

UC Santa Barbara

UC Santa Barbara Electronic Theses and Dissertations

Title

Donor-Acceptor Stenhouse Adducts – Opportunity in Complexity

Permalink

<https://escholarship.org/uc/item/4168v7zx>

Author

Stricker, Friedrich

Publication Date

2022

Peer reviewed|Thesis/dissertation

UNIVERSITY OF CALIFORNIA

Santa Barbara

Donor-Acceptor Stenhouse Adducts – Opportunity in Complexity

A dissertation submitted in partial satisfaction of the
requirements for the degree Doctor of Philosophy
in Chemistry

by

Friedrich Johannes Maximilian Stricker

Committee in charge:

Professor Javier Read de Alaniz, Chair

Professor Christopher M. Bates

Professor Megan T. Valentine

Professor Craig J. Hawker

September 2022

The dissertation of Friedrich Johannes Maximilian Stricker is approved.

Christopher M. Bates

Megan T. Valentine

Craig J. Hawker

Javier G. Read de Alaniz, Committee Chair

July 2022

Donor-Acceptor Stenhouse Adducts – Opportunity in Complexity

Copyright © 2014

by

Friedrich Johannes Maximilian Stricker

To my mother – who would've guessed?

Acknowledgements

I still don't quite understand how I ended up writing this thesis after trying to quit multiple times. How you, Javier, have managed to not only convince me to finish but also managed to convince me that a postdoctoral research position is the right idea will be forever a mystery to me. So, I think I need to thank you first and foremost in these acknowledgements. I also want to thank you for allowing me the freedom to pursue the scientific questions how and when I wanted even though I really should have started writing just about everything earlier. I want to thank Chris Bates, Craig Hawker and Megan Valentine for agreeing to be on my committee.

I also want to thank everyone who taught me along the way without whom none of my projects would have been possible. There is too many to count so this is not in any particular order. Starting with Jimmy Hemmer, who introduced me to DASA and photoswitches. Neil Dolinski, who taught me basically everything I needed to study DASA properties as well as for always having a good suggestion. David Sanchez and Umberto Raucci from whom I learned most my limited knowledge about theory and who opened another viewpoint on DASA. Michele Clerc who figured everything out alongside me on our first project and who always forced me to take that extra step. Miranda Sroda, who's enthusiasm for anything and everything to this day is unparalleled. Michael Lerch who has always taken the time to answer any questions I had and who has taught me a tremendous amount about academia. Julie Peterson who was always there to talk DASA which is honestly how most of this thesis came about in the first place. Jamie Shaum for introducing me to the outdoors and proving that

canned sardines in the wilderness are NOT a thing. Sophia Bailey for being the most annoying little sister a grad student can hope for. Kyle Clark for not being stressed like ever. Manuel Zayas for forgiving me my attempt to drown him in the ocean (learnt an important lesson about cultural differences that day). Jeffrey Self for teaching me about material properties. Guillen Campos for learning liquid crystals with me. Lindsay Robinson for reminding me about what is important in grad school. Serena Seshadri for reminding me about what is important in life. To my undergrads Aurora, Rowina and Jose who reminded me that science can be fascinating and for cleaning all my NMR tubes (Seriously thank you for that last one). To all the other people I overlapped with during my time in the Read de Alaniz, Hawker and Bates groups – there is too many to count!

The biggest thanks however is reserved to my family who have never questioned my decision but asked the right questions at times. Thank you, dad, for all the support on the way and providing the safety net which allowed me to do all this without having to worry (too much at least). Also thank you for not complaining (too much) about me being away for what feels like forever now. And finally, Kate Culhane. Thank you for being there for me during the last few years and putting up with my constant complaining and ranting. I don't think I could've done it without you.

Friedrich Johannes Maximilian Stricker

July 2022

Summary of Skills: Researcher in organic and materials chemistry. Leading and supervising of research projects in organic and materials chemistry in Germany and the USA. Supervising and training of undergraduate and graduate student researchers. Teaching of lectures and lab courses in German and English. Effectively conveying technical and non-technical information to scientific or general audiences. Organising and coordinating events with up to 100 participants. Co-authoring a book chapter and twelve scientific articles in high-impact journals.

Languages: German (mother tongue), English (fluent), French (fluent)

Software and Programming Languages: Microsoft Office Suite, MestReNova, ChemDraw, Igor64, LaTeX, Mathematica (Wolfram), Python for data processing and visualisation

Education

PhD program: Chemistry, Department of Chemistry and Biochemistry, University of California, Santa Barbara, USA, since Aug 2018, current GPA 4.0 (out of 4.0), projected graduation April 2022

Master program: Biomedical Chemistry, Johannes Gutenberg-Universität Mainz, Germany, Apr 2016–Mar 2018, final grade 1.1 (scale of 1.0–4.0 with 1.0 as the top grade)

Bachelor program: Biomedical Chemistry, Johannes Gutenberg-Universität Mainz, Germany, Apr 2013–Mar 2016, final grade 2.2 (scale of 1.0–4.0 with 1.0 as the top grade)

Research Experience

Graduate Research Assistant Sep 2018–present

Department of Chemistry and Biochemistry, UCSB, group of Prof. Read de Alaniz, PhD research on Donor-acceptor Stenhouse adducts (DASA) for photomechanical work

- Led the research group's participation in the Multi University Research Initiative (MURI) on photomechanical work since 2019
- Supervised three undergrad student researcher and trained two graduate student researchers
- Responsible for maintaining, operating and training users for a home-built photo NMR and pump-probe UV-Vis spectroscopy setup and their supporting software
- Co-authored eight scientific publications, with another two journal articles and a book chapter being submitted

Graduate Research Assistant Sep 2017–Mar 2018

Institute for Organic Chemistry, Johannes Gutenberg-Universität, group of Prof. Besenius

- Master thesis on the synthesis of redox active flavin-peptide conjugates, grade 1.0
- Responsible for an independent research project resulting in a first-author publication

Graduate Research Intern Oct 2016–Mar 2017

Department of Chemistry and Biochemistry, UCSB, group of Prof. Read de Alaniz

- Research on water-soluble photochromic molecules on an interdisciplinary project
- Co-authored one publication

Undergraduate Research Assistant May 2015–Aug 2015

Institute for Organic Chemistry, Johannes Gutenberg-Universität, group of Prof. Besenius

- Bachelor thesis on surface-initiated supramolecular polymerisations, grade 1.0
- Co-authored one publication.

Work Experience

Teaching Assistant

University of California, Santa Barbara, Department of Chemistry and Biochemistry, 20 hrs/week, Jan–Jun 2020

- Led organic chemistry lab sections with 20 students, being responsible for both laboratory lectures and quizzes
- Transitioned into a virtual lab at the start of the COVID-19 pandemic, preparing the laboratory videos for the entire organic lab series in a team of four

Johannes Gutenberg-Universität Mainz, Institute for Organic Chemistry, 4 hrs/week, Apr 2016–Apr 2018

- Held a seminar accompanying the lecture of Organic Chemistry 1 for 20 to 30 students, preparing weekly practice problems to discuss, preparing the final exam

- Was selected based on high academic achievements in organic chemistry

Scientific Assistant

Johannes Gutenberg-Universität Mainz, Institute for Chemistry, 12 hrs/week, Jul–Nov 2017

- Organised an inaugural study-abroad information and alumni event by coordinating with the university's department of chemistry, alumni board, and international exchange office
- Set up a databank of former students and their study-abroad destinations and their respective hosts

Scholarships & Awards

- Academic Senate Doctoral Student Travel Award, Dec 2021 & Jun 2022
- Chair Fellowship, for excellence in research and graduate studies, Summer 2021
- Organic Platform Talk Award, UC Chemical Symposium, Mar 2021
- ERP-Fellowship of the German Academic Scholarship Foundation, for postgraduate studies at US elite universities, 2018–2019
- Phi Lambda Upsilon Society Award (National Honorary Chemical Society), for academic excellence, 2019
- Robert H. DeWolfe Graduate Teaching Award, 2019
- DowMI/MRL Travel Grant Winter/Spring, Mar 2019
- GSA Travel Grant, Mar 2019
- Foreign Exchange Fellowship German Academic Scholarship Foundation, Oct 2016–Mar 2017
- Travel Fellowship of German Academic Scholarship Foundation, Sep 2015
- German Academic Scholarship Foundation Scholarship, May 2015–Apr 2018

Publications (*authors contributed equally)

1. Stricker, F., et al. Donor-acceptor Stenhouse Adducts. In *Molecular Photoswitches: Synthesis, Properties, and Applications*, Pianowski, P., Wiley-VCH, 2022.
2. Stricker, F., et al., *Nature Chemistry*, *accepted*.
3. Duan, Y., Zhao, H., Xue, G., Sun, F., Stricker, F., et al., *The Journal of Physical Chemistry B*, **2022**, *126*, 3347–3354.
4. Peterson, J., Stricker, F., Read de Alaniz, J., *Chem. Comm.*, **2022**, *58*, 2303–2306.
5. Sroda, M., Lee, J., Kwon, Y., Stricker, F., et al., *ACS Appl. Polym. Mater.*, **2022**, *4*, 141–149.
6. Stricker, F., et al., *Org. Synth.* **2022**, *99*, 79.
7. Seshadri, S., Bailey, S., Zhao, L., Fisher, J., Sroda, M., Chiu, M., Stricker, F., et al., *Langmuir*, **2021**, *37*, 9939–9951.
8. Bailey, S., Stricker, F., et al., *ACS Appl. Mater. Interfaces*, **2021**, *13*, 35422–35430.
9. Stricker, F., et al., *Org. Biomol. Chem.*, **2021**, *19*, 4483–4486.
10. Clerc, M.*, Stricker, F.*, et al. *Angew. Chem. Int. Ed.*, **2021**, *60*, 10219–10227.
11. Sroda, M.*, Stricker, F.*, et al., *Chem. Eur. J.*, **2021**, *27*, 4183–4190.
12. Mostafavi, S., Li, W., Clark, K., Stricker, F., et al. *Macromolecules*, **2019**, *52*, 6311–6317.
13. Hemmer, J., Page, Z., Clark, K., Stricker, F., et al. *J. Am. Chem. Soc.*, **2018**, *140*(33), 10425–10429.
14. Frisch, H.*, Fritz, E.-C.*, Stricker, F., et al. *Angew. Chem. Int. Ed.*, **2016**, *55*, 7242–7246.

Selected Presentations

Oral, Pacificchem 2021, virtual, 16–21 Dec 2021

Oral, MRS Fall Meeting, Boston, 29 Nov–02 Dec 2021

Oral, UC Chemical Symposium, virtual, 25–27 Mar 2021

Oral, MURI on Photomechanical Materials grant review, virtual, 10–21 Mar 2021

Oral, MURI on Photomechanical Materials grant review, Caltech, Pasadena, 19–20 Feb 2020

Poster, ACS Spring National Meeting, Orlando, 31 Mar–8 Apr, 2019

Poster, APME, IUPAC 11th Adv. Polym. via Macromol. Eng., Yokohama, 18–22 Oct, 2015

ABSTRACT

Donor-acceptor Stenhouse adducts – Opportunity in complexity

by

Friedrich Johannes Maximilian Stricker

Our ability to visually perceive our environment is driven by small molecules – retinal – in our eyes. Upon exposure to light retinal undergoes a change in shape which is translated to the very image of this text. Synthetic versions undergoing similar transformations are called photoswitches. These small molecular machines have been used in a range of applications to control by example pharmacological activity, polarity, conductivity and mechanical properties. Over the years several classes of photoswitches have been developed with different photophysical properties. One key design principle which drives photoswitch development is to combine a simple synthetic strategy with visible light response.

In 2014 our group has introduced a novel class of photochromic molecules called donor-acceptor Stenhouse adducts (DASA). DASAs combine a number of promising properties such as a straightforward synthesis, visible light response as well as a large molecular shape and polarity change. From 2014 significant effort has been made to understand their switching mechanism and structure-property relationships. Since then their multi-step mechanism has been identified while their donor and acceptor design space has been explored. However, the design space of DASA is limited by the reactivity of both donor and acceptor groups. Furthermore while the multi-step mechanism is understood little efforts have been made to take advantage of the unique and promising characteristics of multiple steps photoswitches.

To address some of these problems both the synthetic access to DASA photoswitches as well as the understanding on how structural changes relates to energy landscape have to be improved. If these conditions can be met, DASAs multi-step reaction pathway promises unique photoswitching properties and responses. To widen the synthetic access to DASA we showcase a catalytic method to accelerate the DASA forming reaction and widen the design space of DASA through the use of 1,1,1,3,3,3-hexafluoroisopropanol. By using solvatochromatic shift analysis we were able to link the ground state charge separation of the open form of DASA to the kinetics as well as the effect of concentration and environment on DASA switching properties. We were able to understand the effect of polarity on the switching pathway and by targeting key barriers in the switching pathway we demonstrate how the same two stimuli can provide a multitude of outcomes in a complex DASA mixture through pathway selectivity. By intercepting intermediates along the reaction pathway, we introduced DASA as a negative multi-stage photoswitch. The multi-stage character of the mechanism allows for dual-wavelength control of DASA as well as unique switching properties. To employ the desirable photophysical properties of DASA in applications such as photomechanical work a new chemistry has to be developed for main chain incorporation due to DASA susceptibility to nucleophile and radical chemistry. Through Diels–Alder chemistry we demonstrated main chain incorporation of DASA in liquid crystalline networks.

Through this work we hope to open the door to widespread use of DASA by realizing the full potential of DASA multi-step switching mechanism in solution as well as in solid materials.

TABLE OF CONTENTS

<u>1</u>	<u>DONOR-ACCEPTOR STENHOUSE ADDUCTS – A NOVEL CLASS OF PHOTOSWITCHES</u>	<u>1</u>
1.1	PHOTOSWITCHES AND THEIR PARAMETERS	1
1.2	DONOR-ACCEPTOR STENHOUSE ADDUCTS (DASA).	3
1.3	DASA SYNTHESIS.	6
1.4	PHOTOSWITCHING PROPERTIES	12
1.5	CURRENT CHALLENGES FOR DASAs USE IN MATERIALS.	23
1.6	REFERENCES.	25
<u>2</u>	<u>INCREASING THE EFFICIENCY OF DASA SYNTHESIS THROUGH HFIP</u>	<u>32</u>
2.1	DASA SYNTHESIS THROUGH CATALYSIS.	32
2.2	HFIP AS PROMOTER IN DASA SYNTHESIS.	38
2.3	HFIP AS MODULATOR OF THERMODYNAMIC EQUILIBRIUM AND PHOTOSWITCHING.	42
2.4	NOVEL DASA DERIVATIVES.	45
2.5	ABSORPTION PROPERTIES OF NOVEL DASAs.	46
2.6	PHOTOSWITCHING OF NOVEL DASAs.	49
2.7	FLUORESCENCE OF DASA-9.	51
2.8	POLYMER CONJUGATION.	52
2.9	CONCLUSION.	53
2.10	ADDITIONAL INFORMATION	55
2.11	REFERENCES.	173
<u>3</u>	<u>DASA GROUND STATE CHARGE SEPARATION</u>	<u>182</u>

3.1	DASAs SYNTHETIC EVOLUTION AND GROUND STATE CHEMISTRY	182
3.2	SOLID-STATE ANALYSIS OF THE IONIC CHARACTER OF DASAs	186
3.3	SOLUTION-STATE ANALYSIS OF THE IONIC CHARACTER OF DASAs	188
3.4	COMPUTATIONAL CALCULATIONS ON GROUND STATE CHARGE SEPARATION	192
3.5	INFLUENCE OF IONIC CHARACTER OF DASA ON PHOTOSWITCHING.....	195
3.6	INFLUENCE OF IONIC CHARACTER MIMICS OBSERVED CONCENTRATION EFFECTS.....	196
3.7	CONCLUSION.....	197
3.8	ADDITIONAL INFORMATION	199
3.9	REFERENCES.....	296
4	<u>CONTROLLING DASA PATHWAY SELECTION THROUGH ENVIRONMENT</u>	<u>301</u>
4.1	MULTI-STAGE MECHANISM AS AN INTERNAL ORTHOGONAL STIMULI	301
4.2	UNDERSTANDING DASA ENVIRONMENTAL DEPENDENCE	303
4.3	CONCLUSION.....	312
4.4	ADDITIONAL INFORMATION	314
4.5	REFERENCES.....	441
5	<u>DASA AS A MULTI-STAGE PHOTOSWITCH</u>	<u>446</u>
5.1	MULTI-STAGE PHOTOSWITCHING	446
5.2	DESIGN OF STRUCTURE–PROPERTY RELATIONSHIP STUDIES TOWARDS A MULTISTAGE PHOTOSWITCH.	450
5.3	MULTI-STAGE PHOTOSWITCHING THROUGH A STABLE B/B' POPULATION.	457
5.4	CONCLUSION.....	460
5.5	ADDITIONAL INFORMATION	461

5.6	REFERENCES.....	552
6	<u>DASA IN LIQUID CRYSTALLINE MATERIALS.....</u>	<u>559</u>
6.1	INTRODUCTION.....	559
6.2	A DIELS–ALDER BASED LIQUID CRYSTALLINE NETWORK.	562
6.3	MATERIAL CHARACTERIZATION.....	566
6.4	CONCLUSION.....	568
6.5	ADDITIONAL INFORMATION	570
6.6	REFERENCES.....	631

LIST OF FIGURES

- Figure 1.1.** Photoswitches and their classification due to recovery type.2
- Figure 1.2.** DASAs, a new platform of visible light organic photoswitches. Reproduced with the permission of Wiley & Sons. (Stricker, F., Seshadri, S. and Read de Alaniz, J. (2022). Donor–Acceptor Stenhouse Adducts. In *Molecular Photoswitches*, Z.L. Pianowski (Ed.). <https://doi.org/10.1002/9783527827626.ch14>)¹ Copyright Wiley & Sons.3
- Figure 1.3.** Schematic representation of Aza-Piancatelli rearrangement, Stenhouse Salt synthesis and DASA synthesis. Reproduced with the permission of Wiley & Sons. (Stricker, F., Seshadri, S. and Read de Alaniz, J. (2022). Donor–Acceptor Stenhouse Adducts. In *Molecular Photoswitches*, Z.L. Pianowski (Ed.). <https://doi.org/10.1002/9783527827626.ch14>)¹ Copyright Wiley & Sons. 4
- Figure 1.4.** Structure and modular synthesis of donor–acceptor Stenhouse adducts. **A:** General structure of DASA photochromes. **B:** Modular synthesis of DASA photochromes and Stenhouse salts. **C:** Synthetic evolution through three generations of DASA photochromes. **D:** Closed form isomers of DASA photochromes.^{6,18,19} Reproduced with the permission of Wiley & Sons. (Stricker, F., Seshadri, S. and Read de Alaniz, J. (2022). Donor–Acceptor Stenhouse Adducts. In *Molecular Photoswitches*, Z.L. Pianowski (Ed.). <https://doi.org/10.1002/9783527827626.ch14>)¹ Copyright Wiley & Sons.7
- Figure 1.5.** Structure of donor–acceptor Stenhouse adducts polymer conjugates. **A:** Examples of backbone functionalization with amines.^{25,27,28} **B:** Examples of backbone functionalization with an Acceptor.²⁹ **C:** Click Chemistry approaches towards

functionalization with DASA photochromes.^{27,30} Reproduced with the permission of Wiley & Sons. (Stricker, F., Seshadri, S. and Read de Alaniz, J. (2022). Donor–Acceptor Stenhouse Adducts. In *Molecular Photoswitches*, Z.L. Pianowski (Ed.). <https://doi.org/10.1002/9783527827626.ch14>)¹ Copyright Wiley & Sons.10

Figure 1.6. Proposed photoswitching mechanism of donor–acceptor Stenhouse adducts.³³

Reproduced with the permission of Wiley & Sons. (Stricker, F., Seshadri, S. and Read de Alaniz, J. (2022). Donor–Acceptor Stenhouse Adducts. In *Molecular Photoswitches*, Z.L. Pianowski (Ed.). <https://doi.org/10.1002/9783527827626.ch14>)¹ Copyright Wiley & Sons.14

Figure 1.7. Effects of donor and acceptor groups on photoswitching properties and open-

closed equilibria in the dark (thermodynamic equilibria). **A:** Photothermal stationary state of DASA photochromes with differing steric demand on the donor side.²² **B:** open-closed equilibria in the dark (thermodynamic equilibria) of DASA photochromes with differing steric demand on the donor side.²² **C:** influence of electronics of both the forward light driven reaction as well as the recovery of the open form of DASA photochromes. Time dependent UV–Vis spectrum measured at 10 μM of DASA in toluene with irradiation with a 617 nm ThorLabs LED. Absorption was measured at the respective λ_{max} of each compound. **D:** Thermodynamic equilibrium of DASA photochromes with differing electronic properties.²⁰ Reproduced with the permission of Wiley & Sons. (Stricker, F., Seshadri, S. and Read de Alaniz, J. (2022). Donor–Acceptor Stenhouse Adducts. In *Molecular Photoswitches*, Z.L. Pianowski (Ed.). <https://doi.org/10.1002/9783527827626.ch14>)¹ Copyright Wiley & Sons.16

Figure 2.1. Donor–acceptor Stenhouse adducts (DASAs). a) General structures for open/colored triene and closed/colorless cyclopentenone isomers. R'/R'': alkyl or aryl; X: O or N; R: electron withdrawing group, 5- or 6 membered ring (a selection of donor and acceptor structures are displayed in Figure 2.2). b) General DASA synthesis in comparison to the closely related transformations aza-Piancatelli rearrangement and Stenhouse reaction. Originally published in *Angew. Chem. Int. Ed.*¹ Reprinted with permission of Wiley & Sons.....34

Figure 2.2. Effect of HFIP on reaction rate and yields in DASA synthesis. a) Reaction scheme of the ring opening of CF₃-pyrazolone derived furan adduct (1) and N-methylaniline. b) Conversion plots from in situ ¹H-NMR experiments of the reaction displayed in a) applying different amounts of HFIP in dichloromethane at 25 °C. The second-order rate constant increases from 3 ± 1 M⁻¹ h⁻¹ (0 vol%) to 11.6 ± 0.2 M⁻¹ h⁻¹ (0.2 vol%, 1 equivalent relative to 1) to 56 ± 5 M⁻¹ h⁻¹ (1 vol%, 5 equivalents relative to 1). c) Comparison on isolated yields and reaction time for the synthesis of a series of DASAs under traditionally used reaction conditions and by application of 20 vol% HFIP in dichloromethane. Yields obtained under uncatalyzed conditions for DASA-3 and DASA-4 were taken from literature.¹⁴ Originally published in *Angew. Chem. Int. Ed.*¹ Reprinted with permission of Wiley & Sons.39

Figure 2.3. DASA solvatochromic shift analysis. a) Solvatochromic shifts using the Dimroth-Reichardt *ETN*⁴¹ solvent polarity scale for first to third generation DASAs and non-hydroxy analogue in solvents of different polarity displaying deviation from non-linearity only for DASAs in HFIP, which indicates the presence of hydrogen bonding interactions with the triene hydroxy group. b) Chemical structures of DASAs in a).

Originally published in *Angew. Chem. Int. Ed.*¹ Reprinted with permission of Wiley & Sons.....43

Figure 2.4. Hydrogen bonding interaction of HFIP and the DASA open form and effect on photoswitching. a) General scheme for proposed hydrogen bonding in DASAs in presence and absence of HFIP. b) Time dependent UV-Vis spectroscopy to observe the photochromic behaviour of DASA-2 (10 μ M) in toluene and toluene/HFIP followed at λ_{max} (625 nm). Originally published in *Angew. Chem. Int. Ed.*¹ Reprinted with permission of Wiley & Sons.....44

Figure 2.5. Novel DASAs bearing weak amine donors that were synthesized using HFIP. a) Different secondary amine donors examined previously and in this report for DASA synthesis ordered according to the pK_a values of their corresponding acid (calculated with SciFinder[®]), which correlate well with the reactivity in the furan ring opening reaction. b) Chemical structures of the novel DASAs from this report and λ_{max} in chloroform. Note: some of the DASAs display split absorption bands (**Figure 2.31–42**). The listed wavelengths correspond to the more red-shifted maximum. CF₃-isoxazolone derived furan adduct.¹⁴ Originally published in *Angew. Chem. Int. Ed.*¹ Reprinted with permission of Wiley & Sons.....45

Figure 2.6. UV-Vis absorption properties of novel DASAs. a) Absorption spectra (chloroform) of novel DASA-1 and DASA-9 in comparison to previously reported DASA derivatives.^{12,13} b) Computational density functional theory modelling of DASA-1 determining HOMO orbital overlap and dihedral angles between donor and acceptor (Φ D \square A) in comparison to the respective second generation DASA¹³ bearing

only one phenyl substituent. Originally published in *Angew. Chem. Int. Ed.*¹ Reprinted with permission of Wiley & Sons.....48

Figure 2.7. Photochromic properties of DASA-12 in comparison to DASA-5. a) Time dependent UV-Vis spectroscopy to observe the photochromism of DASA-5 and DASA-12 in chloroform at 10 μ M (initial absorbance: 0.05 and 0.9) followed at λ_{max} (645 nm and 646 nm). Quantitative conversion of the open form to the closed form under light irradiation with 617 nm for 100 seconds and subsequent thermal recovery in the dark can be observed. b) Comparison of photochromic parameters for DASA-5 and DASA-12 in chloroform.¹³ c) Presumed hydrogen bonding stabilizing the zwitterionic closed form of DASA-12. Originally published in *Angew. Chem. Int. Ed.*¹ Reprinted with permission of Wiley & Sons.....49

Figure 2.8. HFIP-promoted synthesis of DASA-polymer conjugates and properties of resulting polymers. a) *In situ* absorbance monitoring at λ_{max} (open form DASA) of furan ring opening reaction to afford P1 in THF or using HFIP in dichloromethane. b) Absorption spectra (chloroform) and chemical structures of DASA functionalized poly(butyl methacrylate) polymers P1 and P2 (*m*: 4 mol%). Originally published in *Angew. Chem. Int. Ed.*¹ Reprinted with permission of Wiley & Sons.52

Figure 2.9. Similarities between the proposed mechanism of DASA synthesis, aza-Piancatelli rearrangement^{53,54} and Stenhouse reaction.²⁴58

Figure 2.10. UV-Vis kinetic data for the reaction of **1** with *N*-methylaniline as a function of the HFIP concentration in DCM. a) Absorbance change at λ_{max} (375 nm) of **1** as a function of time. b) Absorbance change at 565 nm as a function of time. c) Example of

non-linear fit of absorbance decay at 375 nm. d) Relative reaction rates as a function of the HFIP concentration.	83
Figure 2.11. Absorbance change at λ_{\max} (open form DASA) overtime for the reaction of 1 with a) DEA and b) <i>N</i> -methylaniline in DCM vs. DCM/HFIP 20 vol%.....	84
Figure 2.12. Conversion plots from <i>in situ</i> NMR experiments on the synthesis of DASA- 2 in DCM (k : 3 M ⁻¹ h ⁻¹) and upon addition of small quantities of different additives: <i>i</i> PrOH (2 vol%, k : 9 M ⁻¹ h ⁻¹), Me-ether of HFIP (HFIPMe, 3 vol%, k : 5 M ⁻¹ h ⁻¹), HFIP (0.2 vol%, k : 12 M ⁻¹ h ⁻¹ and 1 vol%, k : 56 M ⁻¹ h ⁻¹). Note: reactions were performed with similar excess of <i>N</i> -methylaniline (1.1–1.2 equivalents), except for the experiment with HFIPMe (1.5 equivalents).	86
Figure 2.13. Kinetic fitting of uncatalyzed reaction of 1 with <i>N</i> -methylaniline in dichloromethane. a) Conversion of each measurement (1) 1.1 eq. (2) 1.2 eq. (3) 1.5 eq. of <i>N</i> -methylaniline. The increase in conversion of (3) in <i>a</i>) is due to the increased excess in <i>N</i> -methylaniline. b) Second-order kinetic fitting for each experiment. Calculated k : (1) 4.2 M ⁻¹ h ⁻¹ ; (2) 1.9 M ⁻¹ h ⁻¹ ; (3) 3.2 M ⁻¹ h ⁻¹ ; 3 ± 1 M ⁻¹ h ⁻¹	88
Figure 2.14. Kinetic fitting of the reaction of 1 with <i>N</i> -methylaniline in presence of 0.2 vol% (or 1 eq. relative to 1) HFIP in dichloromethane. a) Conversion of each measurement (1) 1.3 eq. (2) 1.2 eq. (3) 1.2 eq. of <i>N</i> -methylaniline. b) Second-order kinetic fitting for each experiment. Calculated k : (1) 11.5 M ⁻¹ h ⁻¹ ; (2) 11.8 M ⁻¹ h ⁻¹ ; (3) 11.5 M ⁻¹ h ⁻¹ ; 11.6 ± 0.2 M ⁻¹ h ⁻¹	89
Figure 2.15. Kinetic fitting of the reaction of 1 with <i>N</i> -methylaniline in presence of 1 vol% (or 5 eq. relative to 1) HFIP in dichloromethane. a) Conversion of each measurement (1) 1.4 eq. (2) 1.3 eq. (3) 1.3 eq. of <i>N</i> -methylaniline. b) Second-order kinetic fitting for	

each experiment. Calculated k : (1) $53.5 \text{ M}^{-1} \text{ h}^{-1}$; (2) $51.5 \text{ M}^{-1} \text{ h}^{-1}$; (3) $61.4 \text{ M}^{-1} \text{ h}^{-1}$; $56 \pm 5 \text{ M}^{-1} \text{ h}^{-1}$.	90
Figure 2.16. Kinetic fitting of the reaction of 1 with <i>N</i> -methylaniline in presence of 2 vol% (or 10 eq. relative to 1) <i>i</i> PrOH in dichloromethane. a) Conversion, 1.1 eq. of <i>N</i> -methylaniline. b) Second-order kinetic fitting. Calculated k : $9 \text{ M}^{-1} \text{ h}^{-1}$.	91
Figure 2.17. Kinetic fitting of the reaction of 1 with <i>N</i> -methylaniline in presence of 3 vol% (or 10 eq. relative to 1) HFIPME in dichloromethane. a) Conversion, 1.5 eq. of <i>N</i> -methylaniline. b) Second-order kinetic fitting. Calculated k : $5 \text{ M}^{-1} \text{ h}^{-1}$.	91
Figure 2.18. Normalized UV-Vis spectra of 1 in different solvents.	92
Figure 2.19. UV-Vis spectral changes during titration of 1 in DCM ($2.5 \times 10^{-5} \text{ M}$) with HFIP. The concentration of HFIP is indicated in the legend.	92
Figure 2.20. ^1H NMR (600 MHz, CD_2Cl_2) spectra from kinetic experiments for DASA-2 in dichloromethane at $t=0$ and $t= 2.5 \text{ h}$. No closed form can be observed.	93
Figure 2.21. ^1H NMR (600 MHz, CD_2Cl_2) spectra from kinetic experiments for DASA-2 in dichloromethane at $t=0$ and $t= 2.5 \text{ h}$ with 1 eq. of HFIP regarding 1 . 9% closed form can be observed.	94
Figure 2.22. ^1H NMR (600 MHz, CD_2Cl_2) spectra from kinetic experiments for DASA-2 in dichloromethane at $t=0$ and $t= 2.5 \text{ h}$ with 5 eq. of HFIP regarding 1 . 1% closed form can be observed.	95
Figure 2.23. ^1H NMR (600 MHz, CD_2Cl_2) spectra from kinetic experiments for DASA-2 in dichloromethane at $t=0$ and $t= 2.5 \text{ h}$ with 10 eq. of HFIPMe regarding 1 . No closed form can be observed.	96

Figure 2.24. ^1H NMR (600 MHz, CD_2Cl_2) spectra from kinetic experiments for DASA-2 in dichloromethane at $t=0$ and $t= 2.5$ h with 10 eq. of isopropanol regarding 1 . 45% closed form can be observed.	97
Figure 2.25. ^1H NMR (600 MHz, $\text{ACN-}d_3$) spectra from kinetic experiments for DASA-2 in acetonitrile at $t=0$ and $t= 2.5$ h. 75% closed form can be observed.	98
Figure 2.26. Normalized UV-Vis spectra of DASA-6 and DASA-7 in HFIP.	99
Figure 2.27. Normalized UV-Vis spectra of DASA-4 in a range of solvents.	100
Figure 2.28. Normalized UV-Vis spectra of DASA-5 in a range of solvents.	100
Figure 2.29. Normalized UV-Vis spectra of DASA-2 in DCM/HFIP mixtures and in <i>i</i> PrOH.	101
Figure 2.30. Time dependent UV-Vis spectroscopy to observe the photochromism of DASA-2 in dichloromethane at 10 μM followed at λ_{max} (609 nm). Upon the addition of 0.5 vol% HFIP the photothermalstationary state (PTSS) decreases from 81% to 11% closed isomers.	102
Figure 2.31. Normalized UV-Vis spectra of DASA-1 in toluene. λ_{max} : 590 nm.	102
Figure 2.32. Normalized UV-Vis spectra of DASA-1 in chloroform. λ_{max} : 588 nm.	103
Figure 2.33. Normalized UV-Vis spectra of DASA-2 in toluene. λ_{max} : 625 nm.	103
Figure 2.34. Normalized UV-Vis spectra of DASA-2 in chloroform. λ_{max} : 617 nm.	104
Figure 2.35. Normalized UV-Vis spectra of DASA-8 in toluene. λ_{max} : 598/624 nm.	104
Figure 2.36. Normalized UV-Vis spectra of DASA-8 in chloroform. λ_{max} : 594/621 nm.	105
Figure 2.37. Normalized UV-Vis spectra of DASA-9 in toluene. λ_{max} : 631 nm.	105
Figure 2.38. Normalized UV-Vis spectra of DASA-9 in chloroform. λ_{max} : 625 nm.	106

Figure 2.39. Normalized UV-Vis spectra of DASA-10 in toluene. λ_{max} : 630/662 nm.	106
Figure 2.40. Normalized UV-Vis spectra of DASA-10 in chloroform. λ_{max} : 625/656 nm.	107
Figure 2.41. Normalized UV-Vis spectra of DASA-11 in toluene. λ_{max} : 623 nm....	107
Figure 2.42. Normalized UV-Vis spectra of DASA-11 in chloroform. λ_{max} : 616 nm.	108
Figure 2.43. Normalized UV-Vis spectra of DASA-12 in toluene. λ_{max} : 647 nm....	108
Figure 2.44. Normalized UV-Vis spectra of DASA-12 in chloroform. λ_{max} : 646 nm.	109
Figure 2.45. Normalized UV-Vis spectra of P1 in toluene. λ_{max} : 613 nm.	109
Figure 2.46. Normalized UV-Vis spectra of P1 in chloroform. λ_{max} : 609 nm.	110
Figure 2.47. Normalized UV-Vis spectra of P2 in toluene. λ_{max} : 641 nm.	110
Figure 2.48. Normalized UV-Vis spectra of P2 in chloroform. λ_{max} : 640 nm.	111
Figure 2.49. Geometry optimized structures of the open form of a) DASA-1, b) DASA-8, c) DASA-9, d) DASA-10 and e) DASA-11 calculated with DFT.....	114
Figure 2.50. DFT predicted frontier orbitals of the open form. HOMOs are on the left, LUMOs on the right.....	115
Figure 2.51. irradiance of Thorlabs 530 nm and 617 nm LED used in experiments. Total irradiance for 530 nm: 69.7 mW/cm ² ; 617 nm: 240.2 mW/cm ² . Measured using an Ocean Optics hand-held spectrometer with cosine corrector and radiometric calibration (model USB 2000).....	117
Figure 2.52. Time dependent UV-Vis spectroscopy to observe the photochromism of DASA-1 in toluene at 10 μM (initial absorbance: 0.35) followed at λ_{max} (590 nm). Quantitative conversion of the open form to the closed form under light irradiation with	

617 nm for 100 seconds. No subsequent thermal recovery in the dark can be observed.

..... 120

Figure 2.53. Time dependent UV-Vis spectroscopy to observe the photochromism of
DASA-1 in chloroform at 10 μ M (initial absorbance: 0.41) followed at λ_{max} (588 nm).
Quantitative conversion of the open form to the closed form under light irradiation with
617 nm for 100 seconds and subsequent thermal recovery in the dark can be observed.

..... 120

Figure 2.54. Time dependent UV-Vis spectroscopy to observe the photochromism of
DASA-2 in toluene at 10 μ M (initial absorbance: 0.4) followed at λ_{max} (625 nm).
Quantitative conversion of the open form to the closed form under light irradiation with
617 nm for 100 seconds and subsequent thermal recovery in the dark can be observed.

..... 121

Figure 2.55. Time dependent UV-Vis spectroscopy to observe the photochromism of
DASA-2 in chloroform at 10 μ M (initial absorbance: 1.1) followed at λ_{max} (617 nm).
Quantitative conversion of the open form to the closed form under light irradiation with
617 nm for 100 seconds and subsequent thermal recovery in the dark can be observed.

..... 121

Figure 2.56. Time dependent UV-Vis spectroscopy to observe the photochromism of
DASA-8 in chloroform at 100 μ M (initial absorbance: 0.35) followed at λ_{max} (619 nm).
Conversion of 60% of the open form to the closed form under light irradiation with
617 nm for 100 seconds and subsequent thermal recovery in the dark can be observed.

..... 122

Figure 2.57. Time dependent UV-Vis spectroscopy to observe the photochromism of
DASA-9 in toluene at 10 μ M (initial absorbance: 0.32) followed at λ_{max} (631 nm).
Quantitative conversion of the open form to the closed form under light irradiation with
617 nm for 100 seconds and subsequent thermal recovery in the dark can be observed.
..... 122

Figure 2.58. Time dependent UV-Vis spectroscopy to observe the photochromism of
DASA-9 in chloroform at 10 μ M (initial absorbance: 0.56) followed at λ_{max} (625 nm).
Conversion of 87% the open form to the closed form under light irradiation with
617 nm for 100 seconds and subsequent thermal recovery in the dark can be observed.
..... 123

Figure 2.59. Time dependent UV-Vis spectroscopy to observe the photochromism of
DASA-10 in toluene at 10 μ M (initial absorbance: 0.41) followed at λ_{max} (630 nm).
Quantitative conversion of the open form to the closed form under light irradiation with
617 nm for 100 seconds and minimal subsequent thermal recovery in the dark can be
observed..... 123

Figure 2.60. Time dependent UV-Vis spectroscopy to observe the photochromism of
DASA-10 in chloroform at 10 μ M (initial absorbance: 0.41) followed at λ_{max} (625 nm).
Quantitative conversion of the open form to the closed form under light irradiation with
617 nm for 100 seconds and minimal subsequent thermal recovery in the dark can be
observed..... 124

Figure 2.61. Time dependent UV-Vis spectroscopy to observe the photochromism of
DASA-11 in toluene at 10 μ M (initial absorbance: 0.31) followed at λ_{max} (623 nm).
Quantitative conversion of the open form to the closed form under light irradiation with

617 nm for 100 seconds and subsequent thermal recovery in the dark can be observed.

..... 124

Figure 2.62. Time dependent UV-Vis spectroscopy to observe the photochromism of DASA-11 in chloroform at 10 μ M (initial absorbance: 0.56) followed at λ_{max} (616 nm). Conversion of 18% of the open form to the closed form under light irradiation with 617 nm for 100 seconds and subsequent thermal recovery in the dark can be observed.

..... 125

Figure 2.63. Time dependent UV-Vis spectroscopy to observe the photochromism of DASA-12 in toluene at 10 μ M (initial absorbance: 0.43) followed at λ_{max} (647 nm). Quantitative conversion of the open form to the closed form under light irradiation with 617 nm for 100 seconds and subsequent thermal recovery in the dark can be observed.

..... 125

Figure 2.64. Time dependent UV-Vis spectroscopy to observe the photochromism of DASA-12 in chloroform at 10 μ M (initial absorbance: 0.05) followed at λ_{max} (646 nm). Quantitative conversion of the open form to the closed form under light irradiation with 617 nm for 100 seconds and subsequent thermal recovery in the dark can be observed.

..... 126

Figure 2.65. Time dependent UV-Vis spectroscopy to observe the photochromism of **P1** in toluene at 0.01 mg/mL (initial absorbance: 0.76) followed at λ_{max} (613 nm). Conversion of 40% of the open form to the closed form under light irradiation with 617 nm for 150 seconds and subsequent thermal recovery in the dark can be observed.

..... 126

Figure 2.66. Time dependent UV-Vis spectroscopy to observe the photochromism of **P1** in chloroform at 0.01 mg/mL (initial absorbance: 0.73) followed at λ_{\max} (609 nm).

Conversion of 29% of the open form to the closed form under light irradiation with 617 nm for 150 seconds and subsequent thermal recovery in the dark can be observed.

.....127

Figure 2.67. Time dependent UV-Vis spectroscopy to observe the photochromism of **P2** in toluene at 0.3 mg/mL (initial absorbance: 0.76) followed at λ_{\max} (641 nm). Conversion

of 85% of the open form to the closed form under light irradiation with 617 nm for 150 seconds and subsequent thermal recovery in the dark can be observed.127

Figure 2.68. Time dependent UV-Vis spectroscopy to observe the photochromism of **P2** in chloroform at 0.15 mg/mL (initial absorbance: 0.88) followed at λ_{\max} (640 nm).

Conversion of 72% of the open form to the closed form under light irradiation with 617 nm for 150 seconds and subsequent thermal recovery in the dark can be observed.

.....128

Figure 2.69. Time dependent UV-Vis spectroscopy to observe the photochromism of **DASA-5** and **DASA-12** in chloroform at 10 μM and 100 μM (initial absorbance: 0.9 and 1.0) followed at λ_{\max} (645 nm and 646 nm). Quantitative conversion of the open

form to the closed form under light irradiation with 617 nm for 100 seconds and subsequent thermal recovery in the dark can be observed. The half-life of the closed isomer of **DASA-12** is 1545 s at 100 μM . This difference from the value of 10 μM is due to the concentration dependence of **DASA**.128

Figure 2.70. ^1H NMR (600 MHz, CDCl_3) spectra of the equilibrated **DASA-1**.129

Figure 2.71. ^1H NMR (600 MHz, $\text{Tol}-d_8$) spectra of the equilibrated **DASA-1**.130

Figure 2.72. ^1H NMR (600 MHz, CDCl_3) spectra of the equilibrated DASA-2.	131
Figure 2.73. ^1H NMR (600 MHz, Tol- d_8) spectra of the equilibrated DASA-2.....	131
Figure 2.74. ^1H NMR (600 MHz, CDCl_3) spectra of the equilibrated DASA-8. No equilibration to the open form can be observed, but a zwitterionic closed isomer is formed over time.....	132
Figure 2.75. ^1H NMR (600 MHz, CDCl_3) spectra of the equilibrated DASA-9. No closed form can be observed.....	133
Figure 2.76. ^1H NMR (600 MHz, Tol- d_8) spectra of the equilibrated DASA-9.....	134
Figure 2.77. ^1H NMR (600 MHz, CDCl_3) spectra of the equilibrated DASA-10. No open form can be observed.....	135
Figure 2.78. ^1H NMR (600 MHz, CDCl_3) spectra of the equilibrated DASA-11. ...	136
Figure 2.79. ^1H NMR (600 MHz, Tol- d_8) spectra of the equilibrated DASA-11.....	137
Figure 2.80. ^1H NMR (600 MHz, CDCl_3) spectra of the equilibrated DASA-12. ...	138
Figure 2.81. ^1H NMR (600 MHz, Tol- d_8) spectra of the equilibrated DASA-12.....	139
Figure 2.82. HSQC NMR (600 MHz, 297 K, CDCl_3) spectra of DASA-8.	140
Figure 2.83. HMBC NMR (600 MHz, 297 K, CDCl_3) spectra of DASA-12.....	141
Figure 2.84. HSQC NMR (600 MHz, 297 K, CDCl_3) spectra of DASA-12.....	142
Figure 2.85. Absorption, emission and excitation spectra of DASA-9 (equilibrated solution in toluene) and 2,2'-dinaphthylamine in toluene. a) Absorption spectra showing the absorbance bands characteristic for the naphthyl-units at 325–350 nm (2,2'- dinaphthylamine, 20 μM ; DASA-9, 100 μM , before and after visible light irradiation for ~ 100 s). b) Excitation vs emission spectrum of an equilibrated solution of DASA-9 in toluene (10 μM). c) Normalized excitation and emission spectra: $\lambda_{\text{em}} = 400 \text{ nm} / \lambda_{\text{exc}} =$	

350 nm (2 nm slit widths) and $\lambda_{em} = 670$ nm/ $\lambda_{exc} = 630$ nm (5 nm slit widths). d) Emission spectra of DASA-9 in toluene (10 μ M) for different excitation wavelengths. e) Excitation spectra of DASA-9 in toluene (10 μ M) for different emission wavelengths. f) Emission spectra of 2,2'-dinaphthylamine in toluene (20 μ M) for different excitation wavelengths (1 nm slit widths). 144

Figure 2.86. Changes in emission and excitation spectra of DASA-9 (10 μ M, toluene). a) Emission spectra ($\lambda_{exc} = 350$ nm) before and after visible light irradiation (MINTF4 fiber-coupled LED, Thorlabs, nominal wavelength 554 nm) for ~60 seconds. b) Excitation spectra ($\lambda_{em} = 395$ nm) before and after visible light irradiation. c) Fluorescence intensity monitoring at 400 nm ($\lambda_{exc} = 350$ nm, 2 nm slit widths) and 660 nm ($\lambda_{exc} = 630$ nm, 5 nm slit widths) before and after visible light irradiation (MINTF4 fiber-coupled LED, Thorlabs, nominal wavelength 554 nm for ~60 seconds inside fluorimeter, temperature: 31 °C)..... 146

Figure 2.87. Control experiments for luminescence of DASA-9. a) Fluorescence intensity change at 400 nm ($\lambda_{exc} = 350$) upon constant irradiation at 350 nm (excitation light source of fluorimeter) for solutions of dinaphthylamine (20 μ M in toluene) and DASA-9 (10 μ M in toluene). b) Emission spectra at different excitation wavelengths of dinaphthylamine (0.1 μ M) in a solution of DASA-2 in toluene (20 μ M). Slit widths set to 3 nm. c) Fluorescence intensity monitoring at 400 nm ($\lambda_{exc} = 350$ nm) before and after visible light irradiation (MINTF4 fiber-coupled LED, Thorlabs, nominal wavelength 554 nm for ~60 seconds inside fluorimeter, temperature: 31 °C) of dinaphthylamine in toluene (20 μ M) or in a toluene solution (0.1 μ M) of DASA-2 (20 μ M). 147

Figure 2.88. ^1H NMR (500 MHz, CD_2Cl_2) spectra of DASA-2 upon addition of different additives. The signal of hydroxy proton on the triene is shown.....	148
Figure 2.89. ^1H NMR (500 MHz) spectra of DASA-2 (10 mg /mL) in CD_2Cl_2 and CD_2Cl_2 containing 2 vol% HFIP.	149
Figure 2.90. a) DASA-6. b) IR spectra of DASA-6 in DCM and HFIP showing the spectral changes in carbonyl region.	150
Figure 2.91. ^1H NMR (500 MHz, CDCl_3) spectra of the closed isomer of DASA-1. Some open form can also be observed.....	151
Figure 2.92. ^{13}C NMR (125 MHz, CDCl_3) spectra of the closed isomer of DASA-1.	152
Figure 2.93. ^1H NMR (500 MHz, CDCl_3) spectra of the open isomer of DASA-2. Some closed form can also be observed.	153
Figure 2.94. ^{13}C NMR (125 MHz, CDCl_3) spectra of the open isomer of DASA-2	154
Figure 2.95. ^1H NMR (500 MHz, CDCl_3) spectra of the closed isomer of DASA-8.	155
Figure 2.96. ^1H NMR (125 MHz, CDCl_3) spectra of the closed isomer of DASA-8.	156
Figure 2.97. ^1H NMR (500 MHz, CDCl_3) spectra of the open isomer of DASA-9.	157
Figure 2.98. ^{13}C NMR (125 MHz, CDCl_3) spectra of the open isomer of DASA-9.	158
Figure 2.99. ^1H NMR (600 MHz, CDCl_3) spectra of the closed isomer of DASA-10.	158
Figure 2.100. ^{13}C NMR (125 MHz, CDCl_3) spectra of the open isomer of DASA-10. Limited solubility of the compound.	160
Figure 2.101. ^1H NMR (500 MHz, CDCl_3) spectra of the open isomer of DASA-11. Small amounts of closed isomer are also visible.	161
Figure 2.102. ^{13}C NMR (125 MHz, CDCl_3) spectra of the open isomer of DASA-11.	162

Figure 2.103. ^1H NMR (500 MHz, CDCl_3) spectra of the closed isomer of DASA-12. Small amounts of open form are also visible.....	163
Figure 2.104. ^{13}C NMR (125 MHz, CDCl_3) spectra of the closed isomer of DASA-12.	164
Figure 2.105. ^1H NMR (400 MHz, CDCl_3) spectra of S6	165
Figure 2.106. ^{13}C NMR (100 MHz, CDCl_3) spectra of S6	165
Figure 2.107. ^1H NMR (400 MHz, CDCl_3) spectra of activated ester polymer S8 and amine-modified polymers S9 and S10 (top to bottom).....	166
Figure 2.108. ^1H NMR (400 MHz, CDCl_3) spectra of DASA-polymers P1 (top) and P2 (bottom). In solution the DASAs are in equilibrium between open and closed state resulting in a complex spectrum. ^{17,18} Characteristic peaks are marked by colored dots.	167
Figure 2.109. ^{19}F NMR (376 MHz, CDCl_3) of S8 , S9 and S10 (top to bottom) showing complete disappearance of the fluorine signals after aminolysis of the pentafluorophenyl ester.	168
Figure 2.110. ^{19}F NMR (376 MHz, CDCl_3) spectra of DASA-polymers P1 (top) and P2 (bottom).	169
Figure 2.111. ^{19}F NMR (376 MHz, CDCl_3) spectra of DASA-polymers S8 , S9 and S10	170
Figure 2.112. IR absorbance spectra of polymers S8 (top), S9 (middle) and P1 (bottom).	171
Figure 2.113. IR absorbance spectra of polymers S8 (top), S10 (middle) and P2 (bottom).	172

Figure 3.1. Synthetic efforts have resulted in three generations of DASAs which vary in photoswitching properties including control of thermodynamic equilibrium, solvent compatibility and switching kinetics. The closed form is only depicted with the acceptor group in the enol form, however, as reported in the literature the closed form can reside in either a zwitterionic, enol, or keto form depending on the architecture and conditions.^{2,4,15} Reproduced with the permission of Wiley & Sons. (Sroda, M.*, Stricker, F.*, et al. *Chem. Eur. J.*, **2021**, *27*, 4183–4190.)¹ Copyright Wiley & Sons.
.....184

Figure 3.2. A. Photoswitches that were used for XRD study. B. Bond length alternation (BLA) patterns along the triene of the open form of DASA from XRD single crystals. For BLA calculations only the C–C bonds are taken into account. DASAs with diethylamine and non-methylated indoline donors were used as model compounds due to increased crystallinity compared to their counterparts with dimethylamine and 2-methylindoline donors. Reproduced with the permission of Wiley & Sons. (Sroda, M.*, Stricker, F.*, et al. *Chem. Eur. J.*, **2021**, *27*, 4183–4190.)¹ Copyright Wiley & Sons.
.....187

Figure 3.3. A. DASA derivatives studied with thermodynamic equilibrium, photothermal stationary state, and thermal half-life in chloroform for each DASA. B. UV–Vis traces of **DASA 3-IP** in a range of solvents, which shows a blue-shift with increasing polarity of the solvent. C. Solvatochromic shift analysis for **DASA 1-MM**, **2-MI**, **3-IP** and **4-II-H** in solvents of different polarity using the Dimroth–Reichardt ET solvent polarity scale. D. Solvatochromic trends of **DASA 3-IP** (top), **DASA 2-IM** (middle) and **DASA 1-MM** (bottom) are visible by eye, where **DASA 3-IP** and **DASA 1-MM** are more

sensitive to the environment than **DASA 2-IM**. Reproduced with the permission of Wiley & Sons. (Sroda. M.* , Stricker, F.* , et al. *Chem. Eur. J.*, **2021**, *27*, 4183–4190.)¹ Copyright Wiley & Sons.191

Figure 3.4. Influence of ionic character of DASA derivatives on its switching kinetics using an ion concentration as an external trigger. Photoswitching kinetics measured using time dependent pump probe UV-Vis spectroscopy measured at 10 μM in chloroform at their respective λ_{max} including a control without IL and the addition of 1 mM or 10 mM IL. Irradiation was started at $t = 0.3$ min and ceased at $t = 2.0$ min and the subsequent thermal recovery in the dark was measured. A. Time dependent UV-Vis of **DASA 1-MM** monitored at 540 nm, λ_{max} , irradiated with a 530 nm LED. B. Time dependent UV-Vis of **DASA 2-IM** monitored at 591 nm, λ_{max} , irradiated with a 595 nm LED. C. Time dependent UV-Vis of **DASA 3-IP** monitored at 647 nm, λ_{max} , irradiated with a 617 nm LED. Reproduced with the permission of Wiley & Sons. (Sroda. M.* , Stricker, F.* , et al. *Chem. Eur. J.*, **2021**, *27*, 4183–4190.)¹ Copyright Wiley & Sons.194

Figure 3.5. Influence of increasing concentration of DASA derivatives on their switching kinetics, determined by using time-dependent pump-probe UV/Vis spectroscopy equipped with a flow cell with variable pathlengths. The concentrations measured were from 125 μm to 10 mm and the samples were irradiated with a 617 nm LED. The irradiation started at $t=0.3$ min and ceased at $t=2.0$ min; the subsequent thermal recovery in the dark was measured. A) Time-dependent UV/Vis analysis of **DASA 2-IM** monitored at 591 nm (λ_{max}). B) Time-dependent UV/Vis analysis of **DASA 3-IP** monitored at 647 nm (λ_{max}). Reproduced with the permission of Wiley & Sons.

(Sroda. M.*, Stricker, F.*, et al. *Chem. Eur. J.*, **2021**, 27, 4183–4190.)¹ Copyright
Wiley & Sons.....196

Figure 3.6. irradiance of Thorlabs 530 nm, 595 nm and 617 nm LED used in experiments.

Total irradiance for 530 nm: 69.7 mW/cm²; 595 nm: 168 mW/cm²; 617 nm:
240.2 mW/cm². Measured using an Ocean Optics hand-held spectrometer with cosine
corrector and radiometric calibration (model USB 2000).204

Figure 3.7. All compounds referenced in either the paper or supporting information.206

Figure 3.8. Current proposed productive mechanism for photoswitching by Feringa.²⁸207

Figure 3.9. ¹H NMR (500 MHz, chloroform-*d*) of **DASA 3-IP-H**.209

Figure 3.10. ¹H NMR (600 MHz, chloroform-*d*) of **DASA 4-IP-H**.211

Figure 3.11. A. Photoswitching of 10 μM **DASA 3-IP** in chloroform followed at 650 nm,
 λ_{\max} . B. Linear photodegradation upon irradiation and no recovery of 10 μM of **DASA**
4-II-H in chloroform followed at 640 nm, λ_{\max} . Data taken from ref 5.⁵.....213

Figure 3.12. Determination of thermodynamic equilibrium of **DASA 1-MM**. Initial
absorbance after mixing at λ_{\max} = 541 nm. Initial absorbance 0.74. Absorbance after
recovery 0.69. See **Figure 3.13** for recovery.....214

Figure 3.13. Recovery after irradiation for 1 min with 530 nm LED for determination of
thermodynamic equilibrium followed at 541 nm.215

Figure 3.14. An ORTEP representation of the X-ray crystal structure of **DASA 2-IM-H**. C:
grey; N: blue; O: red; H: omitted. CCDC Deposition number: 2041883.....216

Figure 3.15. An ORTEP representation of the X-ray crystal structure of **DASA 3-IP-H**. C:
grey; N: blue; O: red; F: yellow; H: omitted. CCDC Deposition number: 2039176.
.....216

Figure 3.16. An ORTEP representation of the X-ray crystal structure of DASA 4-II-H . C: grey; N: blue; O: red; H: omitted. CCDC Deposition number: 2039175.....	217
Figure 3.17. An ORTEP representation of the X-ray crystal structure of DASA NH . C: grey; N: blue; O: red; H: omitted. CCDC Deposition number: 2041877.....	217
Figure 3.18. Summary of compounds included in Figure 3.19 in order to compare bond length alterations (BLA) of open form crystals.....	218
Figure 3.19. Comparison of bond lengths along the triene of 17 open form DASA crystals showing a varying degree of charge-separation.	219
Figure 3.20. Solvatochromic shift of DASA 1-MM	222
Figure 3.21. Solvatochromic shift of DASA 2-IM	223
Figure 3.22. Solvatochromic shift of DASA 2-IB	224
Figure 3.23. Solvatochromic shift of DASA 3-IP	225
Figure 3.24. Solvatochromic shift of DASA 4-II-H	226
Figure 3.25. Solvatochromic slopes of DASA 1-MM, 2-IM, 2-IB, 3-IM, and 4-II-H with error.....	227
Figure 3.26. A. Aniline-based donor studied by Beves and coworkers ¹⁷ B. Reported absorption maximum vs the polarity value of the solvents for the studied DASAs all show negative solvatochromic slopes. C. Negative solvatochromic slopes correlated with the reported relative dark equilibrium in chloroform.	228
Figure 3.27. The maximum absorbance of DASA 1-EM, 2-MM, 3-IP, and 4-II-H in polymer blends (PS, PMMA, PAN) correlated with mu polymer polarity with error.	230

Figure 3.28. $^1\text{H-NMR}$ (600 MHz, $\text{DMSO-}d_6$) of DASA 1-MM . Only the zwitterionic closed form can be observed.....	232
Figure 3.29. $^{13}\text{C-NMR}$ (125 MHz, $\text{DMSO-}d_6$) of DASA 1-MM . Limited solubility of the closed isomer results in minimal signal.....	233
Figure 3.30. HSQC-NMR (600 MHz, $\text{DMSO-}d_6$) of DASA 1-MM . Only the zwitterionic closed form can be observed. Only three C-H interactions in the region between 5.5 and 2.5 ppm can be observed.	234
Figure 3.31. HMBC-NMR (600 MHz, $\text{DMSO-}d_6$) of DASA 1-MM . Only the zwitterionic closed form can be observed.....	235
Figure 3.32. $^1\text{H-NMR}$ (600 MHz, chloroform- <i>d</i>) of DASA 2-IM . The different isomers are marked.	237
Figure 3.33. $^1\text{H-NMR}$ (600 MHz, chloroform- <i>d</i>) of DASA 2-IM between 5.5 and 2.5 ppm. The different isomers are marked. For the keto isomer integrating with 0.3 lower case letters were used.	238
Figure 3.34. $^{13}\text{C-NMR}$ (125 MHz, chloroform- <i>d</i>) of DASA 2-IM . Assignment can be found in Figure 3.8.31 and S32 and above.	239
Figure 3.35. HSQC-NMR (600 MHz, chloroform- <i>d</i>) of DASA 2-IM . The different isomers are marked. For the keto isomer integrating with 0.3 lower case letters were used. Importantly all signals are bound to a carbon.....	240
Figure 3.36. HMBC-NMR (600 MHz, chloroform- <i>d</i>) of DASA 2-IM . The different isomers are marked. For the keto isomer integrating with 0.3 lower case letters were used. Importantly all signals are Signal A interacts with both the carbons of C and B.	241

Figure 3.37. $^1\text{H-NMR}$ (600 MHz, $\text{DMSO-}d_6$) of DASA 3-IP . Two zwitterionic closed isomers can be observed.	243
Figure 3.38. $^{13}\text{C-NMR}$ (126 MHz, $\text{DMSO-}d_6$) of DASA 3-IP . Two zwitterionic closed isomers can be observed. Assignment can be found in Figure 3.41 and above.	244
Figure 3.39. HSQC-NMR (600 MHz, $\text{DMSO-}d_6$) of DASA 3-IP . Two zwitterionic closed isomers can be observed. No C-H interaction for the N-H proton at 11.5 ppm (C) can be observed.	245
Figure 3.40. HMBC-NMR (600 MHz, $\text{DMSO-}d_6$) of DASA 3-IP . Two zwitterionic closed isomers can be observed.	246
Figure 3.41. Bond lengths of optimized structures DASA 1-MM , DASA 2-IM , DASA 3-IP , and DASA 4-II in chloroform.	271
Figure 3.42. Bond lengths of the optimized structure of DASA 1-MM in toluene, chloroform, and acetonitrile.	272
Figure 3.43. Bond lengths of the optimized structure of DASA 2-IM in toluene, chloroform, and acetonitrile.	273
Figure 3.44. Bond lengths of the optimized structure of DASA 3-IP in toluene, chloroform, and acetonitrile.	273
Figure 3.45. Bond lengths of the optimized structure of DASA 4-II in toluene, chloroform, and acetonitrile.	274
Figure 3.46. Comparison of solvent polarity vs dipole moment of DASA 1-MM , DASA 2-IM , DASA 3-IP , and DASA 4-II	275
Figure 3.47. Comparison of solvent polarity vs the hydrogen bond length between the $-\text{OH}$ and the carbonyl of the acceptor of DASA 1-MM , DASA 2-IM , DASA 3-IP , and	

DASA 4-II. The hydrogen bond in DASA 3-IP is strengthened in more polar solvents compared to DASA 2-IM	276
Figure 3.48. Comparison of solvent polarity vs HOMO-LUMO energy levels of DASA 1-MM , DASA 2-IM , DASA 3-IP , and DASA 4-II . The HOMO-LUMO gaps of DASA 2-IM and DASA 4-II are relatively unchanged as a function of solvent polarity, while the gap of DASA 1-MM and DASA 3-IP increases with increasing solvent polarity, in agreement with the observed blue shift in Figure 3B.	277
Figure 3.49. Time dependent UV–Vis spectroscopy of 10 μ M DASA 1-MB in chloroform with various additions of IL followed at λ_{max} 565 nm. The samples were irradiated with 530 nm LED for 100 s and left to recover in the dark. These results differ from previous reported results from Beves and co-workers in the forward reaction and PTSS. ⁷ This is due to different light sources being used.	279
Figure 3.50. Time dependent UV–Vis spectroscopy of 10 μ M DASA 2-IB in chloroform with various additions of IL followed at λ_{max} 616 nm. The samples were irradiated with 595 nm LED for 100 s and left to recover in the dark.	280
Figure 3.51. Time dependent UV–Vis spectroscopy of 10 μ M DASA 1-MM with various addition of IL followed at λ_{max} 541 nm including the fit used to determine equilibration rates. For rates see Table 3.15.	281
Figure 3.52. time dependent UV-Vis spectroscopy of 10 μ M DASA 1-MB with various addition of IL followed at λ_{max} 565 nm including the fit used to determine equilibration rates. For rates see Table 3.15.	282

Figure 3.53. time dependent UV-Vis spectroscopy of 10 μ M DASA 2-IM with various addition of IL followed at λ_{\max} 590 nm including the fit used to determine equilibration rates. For rates see Table 3.15	283
Figure 3.54. time dependent UV-Vis spectroscopy of 10 μ M DASA 2-IB with various addition of IL followed at λ_{\max} 616 nm including the fit used to determine equilibration rates. For rates see Table 3.15.	284
Figure 3.55. time dependent UV-Vis spectroscopy of 10 μ M DASA 3-IP with various addition of IL followed at λ_{\max} 650 nm including the fit used to determine equilibration rates. For rates see Table 3.15.	284
Figure 3.56. Time dependent UV-Vis spectroscopy of 10 μ M DASA 1-MM irradiated for 500 s with a 530 nm LED followed at λ_{\max} 541 nm.	285
Figure 3.57. Time dependent UV-Vis spectroscopy of 10 μ M DASA 3-IP irradiated for 100 s with a 617 nm LED followed at λ_{\max} 650 nm. Addition of IL (1 mM: 20 μ L of 100 mM solution of IL ; 10 mM: 200 μ L of 100 mM solution of IL) before recovery leads to increase in recovery rate. The loss in absorbance upon recovery at 10 mM IL is due to the increase in volume of the solution. The calculated rates can be found in Figure 3.58.	285
Figure 3.58. Time dependent UV-Vis spectroscopy of 10 μ M DASA 3-IP irradiated for 100 s with a 617 nm LED followed at λ_{\max} 650 nm. Addition of IL (1 mM: 20 μ L of 100 mM solution of IL ; 10 mM: 200 μ L of 100 mM solution of IL) before recovery leads to increase in recovery rate (full graph in Figure 3.57). The recovery of the 10 mM solution of IL has been adjusted for loss of absorbance due to increased volume. The calculated k_B (min^{-1}) values are: 0 IL : 7.1, 1 mM IL : 12.3, 10 mM IL : 16.4. These	

values are roughly in line with previously calculated values but due to change in volume are not as accurate.....286

Figure 3.59. Time dependent UV–Vis spectroscopy of 2 mL of a 10 μ M **DASA 3-IP**

irradiated for 100 s with a 617 nm LED followed irradiation at λ_{max} 650 nm. Addition of IL leads to stepwise increase in PTSS from 89 % to 79 % (addition of 20 μ L of 100 mM solution of **IL**) to 64 % (addition of further 200 μ L of 100 mM solution of **IL**). The loss in absorbance upon recovery is due to the increase in volume of the solution.287

Figure 3.60. UV–Vis spectrum of 10 μ M **DASA 1-MM** in chloroform with various addition of **IL**.....288

Figure 3.61. UV–Vis spectrum of 10 μ M **DASA 1-MB** in chloroform with various addition of **IL**.....289

Figure 3.62. UV–Vis spectrum of 10 μ M **DASA 2-IM** in chloroform with various addition of **IL**.....290

Figure 3.63. UV–Vis spectrum of 10 μ M **DASA 2-IB** in chloroform with various addition of **IL**.....291

Figure 3.64. UV–Vis spectrum of 10 μ M **DASA 3-IP** in chloroform with various addition of **IL**.....292

Figure 3.65. Time dependent UV–Vis spectroscopy of **DASA 2-IM** at various concentration in chloroform followed at λ_{max} 590 nm including the fit used to determine equilibration rates. For rates see Table 3.21.294

Figure 3.66. Time dependent UV–Vis spectroscopy of DASA 3-IP at various concentration in chloroform followed at λ_{max} 650 nm including the fit used to determine equilibration rates. For rates see Table 3.21.	295
Figure 4.1. a) Schematic representation of the environmental influence on the ground state chemistry of DASA. b) simplified mechanism of DASA showing the important steps for DASA kinetics.	301
Figure 4.2. a) DASA structures of investigated compounds and their respective solvatochromic shift. b) calculated energy landscape for the three compounds with MO6-2X/6-31+G(d,p)/SMD(Chloroform) level of theory. Energy barriers are shown for each step. Bolded barriers are the rate determining steps for the forward and back reaction respectively.	304
Figure 4.3. a) calculated energy landscape with MO6-2X/6-31+G(d,p)/SMD(Chloroform) level of theory of DASA-1 in changing polarity marked by dielectric constant. b) schematic of the kinetic steps of the DASA mechanism showcasing an explanation for the changing transition states due to a change of charge separation of the DASA ground state.	306
Figure 4.4. a) DASA structures of investigated compounds b) time dependent UV–Vis spectroscopy of 10 μM DASA-1 in dichloromethane with acetonitrile and diethylether respectively. Followed at $\lambda_{\text{max}} = 564$ nm. Irradiated with 530 nm LED for 100 seconds. c) time dependent UV–Vis spectroscopy of 10 μM DASA-2 in dichloromethane with acetonitrile and diethylether respectively. Followed at $\lambda_{\text{max}} = 619$ nm. Irradiated with 617 nm LED for 150 seconds. d) time dependent UV–Vis spectroscopy of 10 μM DASA-3 in dichloromethane with acetonitrile and diethylether respectively. Followed	

at $\lambda_{\text{max}} = 646 \text{ nm}$. Irradiated with 617 nm LED for 100 seconds. e) thermodynamic equilibrium between the open and closed form. f) $^1\text{H-NMR}$ in CDCl_3 of 10 mM DASA-1 after 24 h of equilibration with 0 vol% and 10 vol% EtOD. The zwitterionic closed form C''' is observed. g) $^1\text{H-NMR}$ in CDCl_3 of 10 mM DASA-2 after 24 h of equilibration with 0 vol% and 10 vol% EtOD. The neutral closed form C'''' is observed. h) $^1\text{H-NMR}$ in CDCl_3 of 10 mM DASA-2 after 24 h of equilibration with 0 vol% and 10 vol% EtOD. The zwitterionic or enol closed form C''(') is observed. Due to the stereocenter of the 2-methylindoline donor two signals for the closed form are observed.....308

Figure 4.5. a) Structures of DASA-3, DASA-4 and DASA-5. b) UV-Vis spectra of a mixture of DASA-3 (10 μM), DASA-4 (10 μM) and DASA-5 (25 μM) in toluene before irradiation, after irradiation and recovery and after addition of 25 vol% DMSO. Three distinct states are observable with all DASA in the open form initially; DASA-1 and 4 are in the open form after irradiation and recovery with DASA-5 closed; after the addition of 25 vol% DMSO DASA-4 and 5 are in the open form and DASA-1 is closed. Measurements were normalized to highest absorbance. c) schematic of distinct behavior of DASA-1, 4 and 5 in toluene and in toluene with 25 vol% of DMSO. d) time dependent UV-Vis spectroscopy of DASA-1 (10 μM), DASA-4 (10 μM) and DASA-5 (25 μM) in toluene in two environments demonstrating pathway selectivity. Detail on deconstruction of overlapping absorbances can be found in the additional information section 4.4.13.....311

Figure 4.6. irradiance of Thorlabs 530 nm and 617 nm LED used in experiments. Total irradiance for 530 nm: 69.7 mW/cm^2 ; 617 nm: 240.2 mW/cm^2 . Measured using an

Ocean Optics hand-held spectrometer with cosine corrector and radiometric calibration (model USB 2000).....	316
Figure 4.7. calculated energy landscape with M06-2X/6-31+G(d,p)/SMD(chloroform) of DASA-2 in changing polarity marked by dielectric constant.....	322
Figure 4.8. calculated energy landscape with M06-2X/6-31+G(d,p)/SMD(chloroform)of DASA-3 in changing polarity marked by dielectric constant.....	322
Figure 4.9. calculated bond alternation with M06-2X/6-31+G(d,p)/SMD(chloroform) of DASA-1 depending on solvent polarity.	323
Figure 4.10. calculated bond lengths with M06-2X/6-31+G(d,p)/SMD(chloroform)of DASA-1 for A.....	323
Figure 4.11. calculated bond lengths with M06-2X/6-31+G(d,p)/SMD(chloroform)of DASA-1 for TS _{A-B}	324
Figure 4.12. calculated bond lengths with M06-2X/6-31+G(d,p)/SMD(chloroform)of DASA-1 for B.....	324
Figure 4.13. calculated bond lengths with M06-2X/6-31+G(d,p)/SMD(chloroform) level of theory of DASA-1 for TS _{B-B'}	325
Figure 4.14. calculated bond lengths with M06-2X/6-31+G(d,p)/SMD(chloroform) level of theory of DASA-1 for B'.....	325
Figure 4.15. calculated bond lengths with M06-2X/6-31+G(d,p)/SMD(chloroform) level of theory of DASA-1 for TS _{B'-C}	326
Figure 4.16. calculated bond alternation with M06-2X/6-31+G(d,p)/SMD(chloroform) level of theory of DASA-2 depending on solvent polarity.....	326

Figure 4.17. calculated bond lengths with M06-2X/6-31+G(d,p)/SMD(chloroform) level of theory of DASA-2 for A	327
Figure 4.18. calculated bond lengths with M06-2X/6-31+G(d,p)/SMD(chloroform) level of theory of DASA-2 for TS_{A-B}	327
Figure 4.19. calculated bond lengths with M06-2X/6-31+G(d,p)/SMD(chloroform) level of theory of DASA-2 for B	328
Figure 4.20. calculated bond lengths with M06-2X/6-31+G(d,p)/SMD(chloroform) level of theory of DASA-2 for TS_{B-B'}	328
Figure 4.21. calculated bond lengths with M06-2X/6-31+G(d,p)/SMD(chloroform) level of theory of DASA-2 for B'	329
Figure 4.22. calculated bond lengths with M06-2X/6-31+G(d,p)/SMD(chloroform) level of theory of DASA-2 for TS_{B'-C}	329
Figure 4.23. calculated bond alternation with M06-2X/6-31+G(d,p)/SMD(chloroform) level of theory of DASA-3 depending on solvent polarity.....	330
Figure 4.24. calculated bond lengths with M06-2X/6-31+G(d,p)/SMD(chloroform) level of theory of DASA-3 for A	330
Figure 4.25. calculated bond lengths with M06-2X/6-31+G(d,p)/SMD(chloroform) level of theory of DASA-3 for TS_{A-B}	331
Figure 4.26. calculated bond lengths with M06-2X/6-31+G(d,p)/SMD(chloroform) level of theory of DASA-3 for B	331
Figure 4.27. calculated bond lengths with M06-2X/6-31+G(d,p)/SMD(chloroform) level of theory of DASA-3 for TS_{B-B'}	332

Figure 4.28. calculated bond lengths with M06-2X/6-31+G(d,p)/SMD(chloroform) level of theory of DASA-3 for B'	332
Figure 4.29. calculated bond lengths with M06-2X/6-31+G(d,p)/SMD(chloroform) level of theory of DASA-3 for TS_{B'}-c	333
Figure 4.30. time dependent UV–Vis spectroscopy of 10 μ M DASA-3 in toluene with 0.0 vol%, 1.0 vol%, 5.0 vol% and 10.0 vol% dichloromethane followed at λ_{max} at 649 nm. The sample was irradiated with 617 nm LED for 100 seconds and the subsequent recovery in the dark was observed.....	334
Figure 4.31. time dependent UV–Vis spectroscopy of 10 μ M DASA-3 in toluene with 0.5 vol%, 1.0 vol% and 2.0 vol% ethanol followed at λ_{max} at 649 nm. The sample was irradiated with 617 nm LED for 100 seconds and the subsequent recovery in the dark was observed.....	334
Figure 4.32. UV–Vis spectroscopy of 10 μ M DASA-3 in toluene with 0.0 vol%, 1.0 vol%, 5.0 vol% and 10.0 vol% of dichloromethane after equilibration overnight relative to no addition.	335
Figure 4.33. UV–Vis spectroscopy of 10 μ M DASA-3 in toluene with 0.0 vol%, 0.5 vol%, 1.0 vol% and 2.0 vol% of diethylether after equilibration overnight relative to no addition.	335
Figure 4.34. $^1\text{H-NMR}$ (600 MHz, CDCl_3) of 10 mM solution of DASA-1 in deuterated chloroform with 0 to 10 vol% of deuterated ethanol after equilibration over 24h. An increase of closed form isomer C''' is observed upon addition of ethanol.....	336
Figure 4.35. $^1\text{H-NMR}$ (600 MHz, CDCl_3) of 10 mM solution of DASA-2 in deuterated chloroform with 0 to 10 vol% of deuterated ethanol after equilibration over 24h. an	

increase of open form isomer **A** is observed upon addition of ethanol. The closed form shows as two separate isomers due to the diastereomer formed upon ring closure due to the stereocenter in the 2-methylindoline moiety.337

Figure 4.36. ¹H-NMR (600 MHz, CDCl₃) of 10 mM solution of **DASA-3** in deuterated chloroform with 0 to 10 vol% of deuterated ethanol after equilibration over 24h. an increase of closed form isomer **C'''** is observed upon addition of ethanol. The closed form shows as two separate isomers due to the diastereomer formed upon ring closure due to the stereocenter in the 2-methylindoline moiety.338

Figure 4.37. normalized emission profiles for the light sources used: 532 nm non-polarized Nd:YAG laser (*P1*); 640 nm diode laser (*P2*); 620 nm LED (*Pr1*); a 660 nm LED with (*Pr2-f*), and without (*Pr2*) a 659 nm high pass filter; 700 nm LED (*Pr3*). 340

Figure 4.38. pump probe spectroscopy of 250 μM **DASA-1** in dichloromethane with 0, 5 and 10 vol% acetonitrile and diethylether irradiated with *P1* for 3 s and followed with *P1* (**A**) and *Pr1* (**B/B'**).341

Figure 4.39. pump probe spectroscopy of 250 μM **DASA-2** in dichloromethane with 0, 5 and 10 vol% acetonitrile and diethylether irradiated with *P1* for 3 s and followed with *P2* (**A**) and *Pr2-f* (**B/B'**).342

Figure 4.40. pump probe spectroscopy of 250 μM **DASA-3** in dichloromethane with 0 and 5 10 vol% acetonitrile and diethylether irradiated with *P2* for 3 s and followed with *P2* (**A**) and *Pr3* (**B/B'**).342

Figure 4.41. time dependent UV–Vis spectroscopy of 10 μM **DASA-3** in chloroform with subsequent additions of 1 vol% ethanol and 1 vol% HFIP followed at λ_{max} at 646 nm.

The sample was irradiated with 617 nm LED for 100 seconds and the subsequent recovery in the dark was observed.....343

Figure 4.42. photographic stills of video 1 of 250 μM **DASA-3** in chloroform with either no addition, 2 vol% ethanol and 2 vol% ethanol and 1 vol% HFIP under irradiation with white light.343

Figure 4.43. time dependent UV–Vis spectroscopy of 10 μM **DASA-3** in toluene with subsequent addition of 25 vol% of DMSO. Absorbance followed at 651 nm before and 641 nm after addition of DMSO due to the shift of the absorption maximum Normalized to initial absorbance and absorbance was adjusted to dilution upon addition of DMSO.344

Figure 4.44. time dependent UV–Vis spectroscopy of 10 μM **DASA-4** in toluene with subsequent addition of 25 vol% of DMSO. Absorbance followed at 552 nm before and 543 nm after addition of DMSO due to the shift of the absorption maximum Normalized to initial absorbance and absorbance was adjusted to dilution upon addition of DMSO.344

Figure 4.45. time dependent UV–Vis spectroscopy of 25 μM **DASA-5** in toluene with subsequent addition of 25 vol% of DMSO. Absorbance followed at 597 nm before and 592 nm after addition of DMSO due to the shift of the absorption maximum. Normalized to initial absorbance and absorbance was adjusted to dilution upon addition of DMSO.345

Figure 4.46. time dependent UV–Vis spectroscopy of 10 μM **DASA-3**, 10 μM **DASA-4** and 25 μM **DASA-5** in toluene with subsequent addition of 25 vol% of DMSO. Normalized to initial absorbance at 552 nm and absorbance was adjusted to dilution upon addition

of DMSO. Followed at each DASA λ_{max} overlapping with absorbances of the other DASAs.....	345
Figure 4.47. time dependent UV–Vis spectroscopy of 10 μM DASA-3 in chloroform with different stabilizers at λ_{max} at 646 nm. The sample was irradiated with 617 nm LED for 100 seconds and the subsequent recovery in the dark was observed.	347
Figure 4.48. Time dependent UV–Vis spectroscopy of 10 μM DASA-1 in dichloromethane irradiated for 100 s with a 530 nm LED followed at λ_{max} 617 nm including the fit used to determine k_B listed in Table 4.1.....	349
Figure 4.49. Time dependent UV–Vis spectroscopy of 10 μM DASA-1 in dichloromethane with 10 vol% acetonitrile irradiated for 100 s with a 530 nm LED followed at λ_{max} 617 nm including the fit used to determine k_B listed in Table 4.1.....	349
Figure 4.50. Time dependent UV–Vis spectroscopy of 10 μM DASA-1 in dichloromethane with 5 vol% acetonitrile irradiated for 150 s with a 617 nm LED followed at λ_{max} 617 nm including the fit used to determine k_B listed in Table 4.1.....	350
Figure 4.51. Time dependent UV–Vis spectroscopy of 10 μM DASA-1 in dichloromethane with 1 vol% acetonitrile irradiated for 150 s with a 617 nm LED followed at λ_{max} 617 nm including the fit used to determine k_B listed in Table 4.1.....	350
Figure 4.52. Time dependent UV–Vis spectroscopy of 10 μM DASA-1 in dichloromethane with 1 vol% acetonitrile irradiated for 150 s with a 617 nm LED followed at λ_{max} 617 nm including the fit used to determine k_B listed in Table 4.1.....	351
Figure 4.53. Time dependent UV–Vis spectroscopy of 10 μM DASA-1 in dichloromethane with 10 vol% diethylether irradiated for 150 s with a 617 nm LED followed at λ_{max} 617 nm including the fit used to determine k_B listed in Table 4.1.....	351

Figure 4.54. Time dependent UV–Vis spectroscopy of 10 μM DASA-1 in dichloromethane with 5 vol% diethylether irradiated for 150 s with a 617 nm LED followed at λ_{max} 617 nm including the fit used to determine k_{B} listed in Table 4.1.....	352
Figure 4.55. Time dependent UV–Vis spectroscopy of 10 μM DASA-1 in dichloromethane with 2 vol% diethylether irradiated for 150 s with a 617 nm LED followed at λ_{max} 617 nm including the fit used to determine k_{B} listed in Table 4.1.....	352
Figure 4.56. Time dependent UV–Vis spectroscopy of 10 μM DASA-1 in dichloromethane with 1 vol% diethylether irradiated for 150 s with a 617 nm LED followed at λ_{max} 617 nm including the fit used to determine k_{B} listed in Table 4.1.....	353
Figure 4.57. Time dependent UV–Vis spectroscopy of 10 μM DASA-2 in dichloromethane with 10 vol% acetonitrile irradiated for 150 s with a 617 nm LED followed at λ_{max} 617 nm including the fit used to determine k_{B} listed in Table 4.2.....	355
Figure 4.58. Time dependent UV–Vis spectroscopy of 10 μM DASA-2 in dichloromethane with 5 vol% acetonitrile irradiated for 150 s with a 617 nm LED followed at λ_{max} 617 nm including the fit used to determine k_{B} listed in Table 4.2.....	355
Figure 4.59. Time dependent UV–Vis spectroscopy of 10 μM DASA-2 in dichloromethane with 2 vol% acetonitrile irradiated for 150 s with a 617 nm LED followed at λ_{max} 617 nm including the fit used to determine k_{B} listed in Table 4.2.....	356
Figure 4.60. Time dependent UV–Vis spectroscopy of 10 μM DASA-2 in dichloromethane with 1 vol% acetonitrile irradiated for 150 s with a 617 nm LED followed at λ_{max} 617 nm including the fit used to determine k_{B} listed in Table 4.2.....	356

Figure 4.61. Time dependent UV–Vis spectroscopy of 10 μM DASA-2 in dichloromethane with 10 vol% diethylether irradiated for 150 s with a 617 nm LED followed at λ_{max} 617 nm including the fit used to determine k_{B} listed in Table 4.2.....	357
Figure 4.62. Time dependent UV–Vis spectroscopy of 10 μM DASA-2 in dichloromethane with 5 vol% diethylether irradiated for 150 s with a 617 nm LED followed at λ_{max} 617 nm including the fit used to determine k_{B} listed in Table 4.2.....	357
Figure 4.63. Time dependent UV–Vis spectroscopy of 10 μM DASA-2 in dichloromethane with 2 vol% diethylether irradiated for 150 s with a 617 nm LED followed at λ_{max} 617 nm including the fit used to determine k_{B} listed in Table 4.2.....	358
Figure 4.64. Time dependent UV–Vis spectroscopy of 10 μM DASA-2 in dichloromethane with 1 vol% diethylether irradiated for 150 s with a 617 nm LED followed at λ_{max} 617 nm including the fit used to determine k_{B} listed in Table 4.2.....	358
Figure 4.65. Time dependent UV–Vis spectroscopy of 10 μM DASA-2 in dichloromethane irradiated for 150 s with a 617 nm LED followed at λ_{max} 617 nm including the fit used to determine k_{B} listed in Table 4.2.....	359
Figure 4.66. Time dependent UV–Vis spectroscopy of 10 μM DASA-3 in dichloromethane irradiated for 100 s with a 617 nm LED followed at λ_{max} 650 nm including the fit used to determine k_{B} listed in Table 4.3.....	361
Figure 4.67. Time dependent UV–Vis spectroscopy of 10 μM DASA-3 in dichloromethane with 10 vol% acetonitrile irradiated for 100 s with a 617 nm LED followed at λ_{max} 650 nm including the fit used to determine k_{B} listed in Table 4.3.....	361

Figure 4.68. Time dependent UV–Vis spectroscopy of 10 μM DASA-3 in dichloromethane with 5 vol% acetonitrile irradiated for 100 s with a 617 nm LED followed at λ_{max} 650 nm including the fit used to determine k_{B} listed in Table 4.3.....	362
Figure 4.69. Time dependent UV–Vis spectroscopy of 10 μM DASA-3 in dichloromethane with 2 vol% acetonitrile irradiated for 100 s with a 617 nm LED followed at λ_{max} 650 nm including the fit used to determine k_{B} listed in Table 4.3.....	362
Figure 4.70. Time dependent UV–Vis spectroscopy of 10 μM DASA-3 in dichloromethane with 1 vol% acetonitrile irradiated for 100 s with a 617 nm LED followed at λ_{max} 650 nm including the fit used to determine k_{B} listed in Table 4.3.....	363
Figure 4.71. Time dependent UV–Vis spectroscopy of 10 μM DASA-3 in dichloromethane with 10 vol% diethylether irradiated for 100 s with a 617 nm LED followed at λ_{max} 650 nm including the fit used to determine k_{B} listed in Table 4.3.....	363
Figure 4.72. Time dependent UV–Vis spectroscopy of 10 μM DASA-3 in dichloromethane with 5 vol% diethylether irradiated for 100 s with a 617 nm LED followed at λ_{max} 650 nm including the fit used to determine k_{B} listed in Table 4.3.....	364
Figure 4.73. Time dependent UV–Vis spectroscopy of 10 μM DASA-3 in dichloromethane with 2 vol% diethylether irradiated for 100 s with a 617 nm LED followed at λ_{max} 650 nm including the fit used to determine k_{B} listed in Table 4.3.....	364
Figure 4.74. Time dependent UV–Vis spectroscopy of 10 μM DASA-3 in dichloromethane with 1 vol% diethylether irradiated for 100 s with a 617 nm LED followed at λ_{max} 650 nm including the fit used to determine k_{B} listed in Table 4.3.....	365

Figure 4.75. Time dependent UV–Vis spectroscopy of 10 μM DASA-3 in toluene irradiated for 100 s with a 617 nm LED followed at λ_{max} 650 nm including the fit used to determine k_{B} listed in Table 4.4.	367
Figure 4.76. Time dependent UV–Vis spectroscopy of 10 μM DASA-3 in toluene irradiated with 1 vol% dichloromethane after irradiation for 100 s with a 617 nm LED followed at λ_{max} 650 nm including the fit used to determine k_{B} listed in Table 4.4.	367
Figure 4.77. Time dependent UV–Vis spectroscopy of 10 μM DASA-3 in toluene with irradiated 5 vol% dichloromethane after irradiation for 100 s with a 617 nm LED followed at λ_{max} 650 nm including the fit used to determine k_{B} listed in Table 4.4.	368
Figure 4.78. Time dependent UV–Vis spectroscopy of 10 μM DASA-3 in toluene irradiated with 10 vol% dichloromethane after irradiation for 100 s with a 617 nm LED followed at λ_{max} 650 nm including the fit used to determine k_{B} listed in Table 4.4.	368
Figure 4.79. Comparison of time dependent UV–Vis spectroscopy of 10 μM DASA-3 in toluene with 1 vol%, 5 vol% and 10 vol% dichloromethane after irradiation for 100 s with a 617 nm LED followed at λ_{max} 650 nm.	369
Figure 4.80. Comparison of time dependent UV–Vis spectroscopy of 10 μM DASA-3 in toluene with 1 vol%, 5 vol% and 10 vol% dichloromethane which was after 25 seconds irradiated for 100 s with a 617 nm LED (red shaded area) followed at λ_{max} 650 nm.	370
Figure 4.81. Time dependent UV–Vis spectroscopy of 10 μM DASA-3 in toluene with 0.5 vol% ethanol after irradiation for 100 s with a 617 nm LED followed at λ_{max} 650 nm including the fit used to determine k_{B} listed in Table 4.4.	371

Figure 4.82. Time dependent UV–Vis spectroscopy of 10 μM DASA-3 in toluene with 1.0 vol% ethanol after irradiation for 100 s with a 617 nm LED followed at λ_{max} 650 nm including the fit used to determine k_{B} listed in Table 4.4.....	371
Figure 4.83. Time dependent UV–Vis spectroscopy of 10 μM DASA-3 in toluene with 2.0 vol% ethanol after irradiation for 100 s with a 617 nm LED followed at λ_{max} 650 nm including the fit used to determine k_{B} listed in Table 4.4.....	372
Figure 4.84. Comparison of time dependent UV–Vis spectroscopy of 10 μM DASA-3 in toluene with 0.5 vol%, 1.0 vol% and 2.0 vol% ethanol after irradiation for 100 s with a 617 nm LED followed at λ_{max} 650 nm.....	372
Figure 4.85. Comparison of time dependent UV–Vis spectroscopy of 10 μM DASA-3 in toluene with 0.5 vol%, 1.0 vol% and 2.0 vol% ethanol which was after 25 seconds irradiated for 100 s with a 617 nm LED followed at λ_{max} 650 nm.	373
Figure 4.86. Time dependent UV–Vis spectroscopy of 10 μM DASA-3 in toluene with 0.5 vol% diethylether after irradiation for 100 s with a 617 nm LED followed at λ_{max} 650 nm including the fit used to determine k_{B} listed in Table 4.4.....	374
Figure 4.87. Time dependent UV–Vis spectroscopy of 10 μM DASA-3 in toluene with 1 vol% diethylether after irradiation for 100 s with a 617 nm LED followed at λ_{max} 650 nm including the fit used to determine k_{B} listed in Table 4.4.....	374
Figure 4.88. Time dependent UV–Vis spectroscopy of 10 μM DASA-3 in toluene with 2.0 vol% diethylether after irradiation for 100 s with a 617 nm LED followed at λ_{max} 650 nm including the fit used to determine k_{B} listed in Table 4.4.....	375

- Figure 4.89.** Comparison of time dependent UV–Vis spectroscopy of 10 μM **DASA-3** in toluene with 0.5 vol%, 1.0 vol% and 2.0 vol% diethylether after irradiation for 100 s with a 617 nm LED followed at λ_{max} 650 nm.....375
- Figure 4.90.** Comparison of time dependent UV–Vis spectroscopy of 10 μM **DASA-3** in toluene with 0.5 vol%, 1.0 vol% and 2.0 vol% diethylether which was after 25 seconds irradiated for 100 s with a 617 nm LED followed at λ_{max} 650 nm.376
- Figure 5.1.** a) Schematic representation of two-stage photoswitches. b) Example of **DASA** as a first single photochrome multi-stage photoswitch. Herein, *stage* corresponds to long-lived stable or meta-stable intermediates along the photoswitching pathway that are independently addressable. Originally published in *Nature Chemistry*.¹ Reprinted with permission from Springer Nature.448
- Figure 5.2.** a) Schematic representation of the full **DASA** photoswitching mechanism, which is comprised of three stages: (Stage I, **violet**) The open-form intermediate A. (Stage II, **blue**) The isomerized B/B' intermediates. (Stage III, colorless) The closed-ring intermediates C. C and C' differ in the planarization of the donor amine. b) normalized experimental UV-Vis spectrum of **DASA 2** showing each stage in Toluene. Stage II is showing a mixture of A ($\lambda_{\text{max}} = 565$ nm) and B/B' ($\lambda_{\text{max}} = 619$ nm) isomers under irradiation with a 530 nm LED. Stage III shows minimal rest absorbance of A. The C-isomers do not absorb in the wavelength range shown. The λ_{max} of the isomers A (565 nm), B (621 nm) and B' (633 nm) are calculated and shifted to experiment by 0.55eV using the COSMO ($\epsilon = 2.38$)- $\omega\text{B97x-D3/def2-TZVP(-f)}$ level of theory and are shown as dashed lines. c) Structural modification of sterically hindered dialkylamine DASAs presented in this paper shown as **DASA 1** (yellow) and **2** (blue), respectively.

DASA 1 and 2 consist of dimethylamine/ *N,N'*-dimethylbarbituric acid and adamantyl/*N,N'*-(*t*-butyl) barbituric acid donor/acceptor pairs, respectively. Originally published in *Nature Chemistry*.¹ Reprinted with permission from Springer Nature.

.....451

Figure 5.3. a) Potential energy surfaces of DASA 1 and 2 for the intermediates up to C' including the relevant changes leading to a stabilization of C computed at the ω B97xD3/def2-TZVP(-f) level of theory in COSMO ($\epsilon = 2.38$). DASA 2 does not access C but directly isomerizes to C' due to the planarization of the nitrogen inside the ring system. The potential energy surface for the full photoswitching mechanism is shown in **Figures 5.11-14**. The C/ C' structures are shown with dihedral angles (ϕ) and C-C bond distances (\AA) for DASA 1 (yellow) and 2 (blue). b) Time-dependent UV-Vis spectroscopy of DASA 1 and 2 at 10 μ M in Toluene. The population of A and B/B' is observed by following their respective λ_{max} during irradiation with a 530 nm LED for 8 minutes and subsequent recovery in the dark. The results show differences under irradiation and in the thermal recovery in the dark for the two DASAs and the increase in the stability of B/B' for DASA 2. Originally published in *Nature Chemistry*.¹ Reprinted with permission from Springer Nature.454

Figure 5.4. a) Schematic representation of A as Stage I, B/B' as Stage II and C' (and subsequent C-isomers) as Stage III. A secondary wavelength can be used intercept the switching mechanism at Stage II as observed in c). b) Absorption profile of DASA 2 under irradiation showing both molecules in Stage I (A) and II (B/B') and the emission profiles of the 530 nm and 660 nm LED used. c) Time-dependent pump-probe UV-Vis spectroscopy at 10 μ M in Toluene of 2 showing both A and the B/B' intermediates.

Transformation of A to C through irradiation with a 530 nm LED (1.2 mW/cm²) can be interrupted by irradiation with a 660 nm LED (128.0 mW/cm²) which promotes conversion of B/B' to A. Originally published in *Nature Chemistry*.¹ Reprinted with permission from Springer Nature.456

Figure 5.5. a) Irradiation of a negative three-stage photoswitch leads to a thin layer of the transient intermediate **B**. b) In a negative three-stage photoswitch perpendicular irradiation can be used to selectively stop the transformation from **A** to **C** through a volume filled with either **A** or **C** as seen in c while in a typical two-stage P-type photoswitch the $h\nu_2$ interacts with **B** and will get absorbed if passing through a volume filled with bleached sample. c) Photographic stills showing how 660 nm (73 mW) light can be used to stop the transformation from **A** to **C** in a secondary glass tube (T2) under constant irradiation with 530 nm (1 mW) through a glass tube (T1) containing already converted DASA 2 in isomer **C**. Originally published in *Nature Chemistry*.¹ Reprinted with permission from Springer Nature.458

Figure 5.6. Irradiance of Thorlabs 530 nm, 595 nm and 617 nm LED used in experiments. Total irradiance for white LED: 105 mW/cm²; 530 nm: 70 mW/cm²; 595 nm: 168 mW/cm²; 660 nm: 128 mW/cm² (unless otherwise specified). Measured using an Ocean Optics hand-held spectrometer with cosine corrector and radiometric calibration (model USB 4000). Values reported in mW are measured capturing the whole light output with a Newport Optical Power/Energy Meter (Model 842-PE) equipped with a 818-UV/DB Low-Power UV Photodetector and a 884-UVR attenuator.464

Figure 5.7. The solvent accessible surface (SAS) for the open form (A) of DASAs **1**, **2**, **S1**, and **S2**. The SAS (grey) is constructed from apparent surface charge (ASC) segments with an effective radius of 1.2 times the radius of each atom. The table shows the number of atoms, total number of cavity segments, surface area of the cavity, and the cavity volume.....476

Figure 5.8. The measured (solid) and computed (dashed) UV-Vis electronic absorption spectra of DASA **1** (yellow) **2** (blue) **S1** (red) and **S2** (green) in toluene. Each normalized computed spectrum consisted of 250 structures sampled to a harmonic Wigner distribution and the lowest five singlet excitations (S_0 - S_n , $n = 1, 2, 3, 4, 5$) were homogeneously broadened using a Gaussian function with a FWHM =0.1eV and shifted to experiment by 0.55eV using the (COSMO ($\epsilon = 2.38$)- ω B97x-D3/def2-TZVP(-f) level of theory. The corresponding spectrum maxima are shown in the inset.478

Figure 5.9. Ground-State Minima Benchmarking. The computed energies of the ground-state minima along the 4π -electrocyclization in DASA **1** relative to the open-form A. Geometries were optimized at the COSMO ($\epsilon=2.38$) ω B97xD3/def2-TZVP(-f) level of theory and single-point energies were computed using the labeled methods. All single point energies were computed using the COSMO solvation model except for CCSD(T). The geometries of each intermediate are shown in the bottom of the plot.....479

Figure 5.10. The Actinic Step for Sterically Hindered DASAs. Critical points along the different Z/E photoisomerization coordinates for the two lowest energy singlet states computed at the SA3-CAS(2,2)-SCF/6-31G** level of theory with reference to the ground-state energy of the S_0 minimum. Structures for each critical point along with the

α (green) and β (red) torsion angles are shown in the bottom. The purple and green markers represent the locations of the substitution pertaining to each DASA derivative.

.....480

Figure 5.11. Computed 1D-potential energy surfaces of key intermediates in Stages I and II along the 4π -electrocyclization reaction coordinate for a) DASA **1** and DASA **S1**. b) DASA **1** and DASA **S2**. c) DASA **2** and DASA **S1**. d) DASA **2** and DASA **S2**. **a/c** and **b/d** highlight the influence of sterics isolated to donor or acceptor substitution, respectively. Energies are relative to the open-form intermediate, **A**. For adamantyl amine derived donors **C** is not accessed through the mechanism and instead **C'** is used as the first closed isomer.....481

Figure 5.12. Influence of steric demand in the acceptor and donor moieties on the potential energy surface for stages I, II, and III, respectively. Unlike **Figure 5.10**, which shows the relative energies of each intermediate to **A**, here we show the relative change in the energy difference upon substitution in the acceptor and donor groups. For example, the TS_{A-B} energy barrier increases by approximately 3.5 – 4.0 kcal/mol when introducing steric demand into the donor group of DASAs **1** and **S2**. In contrast, steric demand introduced into the acceptor group leads to an overall decrease in the TS_{A-B} by approximately 2-2.5 kcal/mol shown in DASAs **S1** and **1**. For adamantyl amine derived donors **C** is not accessed through the mechanism and instead **C'** is used as the first closed isomer due to the pyramidalization of the nitrogen in the ring system. .482

Figure 5.13. Computed 1D-potential energy surfaces of intermediates in Stages II and III after the 4π -electrocyclization reaction coordinate for a) DASA **1** and DASA **S1** b) DASA **1** and DASA **S2** c) DASA and DASA **S1** d) DASA **2** and DASA **S2**. e) DASA **1**

and DASA 2. Energies are relative to the open-form intermediate, A. Note: C is not accessed for adamantyl amine derived donors due to the pyramidalization of the nitrogen. C* is an intermediate corresponding to twisting of the acceptor group which was also computed for previous static potential energy surface calculations.²¹ 483

Figure 5.14. Computed 1D-potential alternative pathways along the energy surfaces of intermediates in Stages II and III after the 4π -electrocyclization reaction coordinate for a) DASA 1 and DASA S1 b) DASA 1 and DASA S2 c) DASA and DASA S1 d) DASA 2 and DASA S2. Energies are relative to the open-form intermediate, A. Note: C is not accessed for adamantyl amine derived donors due to the pyramidalization of the nitrogen.²² The keto forming pathways involve proton transfer between the hydroxy and acceptor groups is shown but are considered minor channels due to their relatively high reaction barrier of ~18-20kcal/mol for all DASA derivatives. See supplemental files for trajectory of both pathways shown.484

Figure 5.15. UV-Vis measurements showing the solvatochromic shift of DASA 1.503

Figure 5.16. UV-Vis measurements showing the solvatochromic shift of DASA S1.504

Figure 5.17. UV-Vis measurements showing the solvatochromic shift of DASA S2.505

Figure 5.18. UV-Vis measurements showing the solvatochromic shift of DASA 2.506

Figure 5.19. Solvatochromic slopes of DASA 1, 2, S1 and S2 with error.507

Figure 5.20. Time dependent UV-Vis spectroscopy of DASA 1 in Toluene followed at λ_{\max} 568 nm in the dark after irradiation including the fit used to determine equilibration rates. For rates see Table 5.6.514

Figure 5.21. Time dependent UV–Vis spectroscopy of DASA S1 in Toluene followed at λ_{max} 575 nm in the dark after irradiation including the fit used to determine equilibration rates. For rates see Table 5.6.	514
Figure 5.22. mole fraction of open form obtained by ^1H NMR spectroscopy of DASA S2 in Tol- d_8 in the dark after irradiation including the fit used to determine equilibration rates. For rates see Table 5.6 and 7.	515
Figure 5.23. Time dependent UV–Vis spectroscopy of DASA 2 in Toluene followed at λ_{max} 565 nm in the dark after irradiation including the fit used to determine equilibration rates. For rates see Table 5.6.	515
Figure 5.24. Arrhenius Plot for DASA S2	517
Figure 5.25. Time-dependent UV-Vis spectroscopy of DASA 1 , 2 , S1 and S2 at 10 μM in Toluene. Irradiation with a 530 nm LED for 8 minutes and subsequent recovery in the dark is observed by following their respective λ_{max} . The results show differences under irradiation and in the thermal recovery in the dark for the four DASAs.	518
Figure 5.26. Time-dependent pump probe UV-Vis spectroscopy at 10 μM in Toluene highlighting (irradiated with a 530 nm LED – 65 mW/cm^2) the B/B' intermediates for S1 and 2 highlighting the long half-life of B/B' in 2 . Inset: difference of the N,N' -(<i>t</i> -buty)lbarbituric acid to N,N' -dimethylbarbituric acid carbon acid on the thermal barrier between B and A from S1 to 2	519
Figure 5.27. Time-dependent pump-probe UV-Vis spectrum at 10 μM in toluene under irradiation with a 530 nm LED (65 mW/cm^2) and followed by the respective λ_{max} and maximum of the B/B' shoulder highlighting the B/B' intermediates for DASAs 1 and S1	520

- Figure 5.28.** Time dependent UV-Vis spectroscopy of 10 μM DASA **S1** and **2** under irradiation with a 530 nm LED for 8 minutes followed at λ_{max} for **A** and at maximum of the shoulder for **B/B'**.521
- Figure 5.29.** Time dependent UV-Vis spectroscopy of 10 μM DASA **1** and **S2** under irradiation with a 530 nm LED for 2 minutes followed at λ_{max} for **A** and at maximum of the shoulder for **B/B'**. This shows a smaller population of **B/B'** for **1** than for **S2** as expected by our theoretical predictions.522
- Figure 5.30.** Time dependent UV-Vis spectroscopy of 10 μM DASA **2** in Toluene under irradiation with a 530 nm LED for 0.5 minutes followed at λ_{max} for **A** and at maximum of the shoulder for **B/B'**. The red trace is then irradiated with 660 nm LED (128 mW/cm^2) showing the recovery of **A** upon irradiation of **B/B'**523
- Figure 5.31.** Time dependent UV-Vis spectroscopy of 10 μM DASA **2** in Toluene under irradiation with different light sources followed at λ_{max} for **A** (565 nm). This shows resistance to switching upon irradiation with a light source red shifted to the λ_{max} . Intensity is calculated for overlap of emission with UV-Vis spectrum of **2** as **A**.524
- Figure 5.32.** Time dependent UV-Vis spectroscopy of 10 μM DASA **2** in Toluene under irradiation with a 530 nm LED (1.2 mW/cm^2) for 0.5 minutes followed at λ_{max} for **A** and at maximum of the shoulder for **B/B'**. The red trace is also irradiated with 660 nm LED (128 mW/cm^2) increasing the PTSS from 93 % closed form under irradiation with 530 nm LED to 56 % closed under irradiation with both light sources.525
- Figure 5.33.** Time-dependent UV-Vis spectroscopy of DASA **1** at 10 μM in Toluene. a) DASA **1** is irradiated with 530 nm light (1.2 mW/cm^2 , dark orange trace) or both 530 nm light (1.2 mW/cm^2) and 660 nm (128.0 mW/cm^2) light (red trace). Even though

Stage II (**B/B'**) is not observable in **DASA 1** irradiation with a secondary wavelength leads to a change in PTSS from 88 to 75 % in Stage III (**C**-isomers) under irradiation by influencing the forward reaction kinetics. b) When irradiation with the 660 nm light is stopped the PTSS moves from 75% to 88 % and upon subsequent restart of 660 nm light irradiation thermal recovery from Stage III to Stage I can be observed. ...526

Figure 5.34. a) Schematic representation of a negative photochromic three-stage photoswitch presented in this work. b) Photographic stills showing **A**, the localization of **B** under irradiation with 530 nm (1 mW) and **C** under extended irradiation. c) Photographic stills showing how 660 nm (30 mW) light can be used to stop the transformation from **A** to **C** under constant irradiation with 530 nm (1 mW) light, locking in a bleaching front. d) Photographic stills showing how 660 nm (73 mW) light can be used to stop the transformation from **A** to **C** in a secondary glass tube (T2) under constant irradiation with 530 nm (1 mW) through a glass tube (T1) containing already converted **DASA 2** in isomer **C**. e) Irradiation of a negative photochromic three-stage photoswitch leads to a thin layer of the transient intermediate **B** as seen in a. f) Irradiation with two wavelengths can be used to stop the transformation from **A** to **C** as shown in c while a typical P-type photoswitch reverses the reaction to **A**. g) In a negative photochromic three-stage photoswitch perpendicular irradiation can be used to selectively stop the transformation from **A** to **C** through a volume filled with either **A** or **C** as shown in d while in a typical two-stage P-type photoswitch the $h\nu_2$ interacts with **B** and will get absorbed if it passes through a volume filled with sample.527

Figure 5.35. Photographic still 125 μ M of **DASA 2** in Toluene in a glass tube. Samples are continuously irradiated with 530 nm (1 mW). Right samples are irradiated with 660 nm

(30 mW) light for 5 minutes in between screenshots). a) picture still at 5 min just before 660 nm LED is turned on for the right sample. b) picture still at 10 min just after 660 nm LED is turned off for the right sample. The left sample is continuously bleached while the photoswitching process in the right sample is interrupted through 660 nm LED.....529

Figure 5.36. Photographic still of 250 μ M of DASA **2** in Toluene in a glass tube. Samples are continuously irradiated with strong white light. 660 nm (73 mW) light is used to protect an area from bleaching. The left picture shows the sample prior to bleaching. The right shows after the sample has bleach and the 660 nm is turned off. The area which was irradiated with 660 nm shows DASA **2** in the open form **A**.529

Figure 5.37. Photographic still of 125 μ M of DASA **2** in Toluene in a glass tube. Samples are irradiated with 530 nm LED (1 mW, a) and after 5 min the light is left: turned off; right: left on and a 660 nm (30 mW, coaxial) is turned on. After additional 5 minutes the 530 LED is turned back on for the sample on the left while in the right samples the 660 nm is turned off. This shows turning off the 530 nm light or irradiating with a 660 nm while irradiating the 530 nm light has similar effects.530

Figure 5.38. Molar absorptivity measurements for DASA **1**, **2**, **S1** and **S2**. Results in Table 5.6.531

Figure 5.39. HMBC NMR (600 MHz, CDCl₃) spectra of DASA **S2**. Only the keto form can be observed.532

Figure 5.40. HMBC NMR (600 MHz, Tol-*d*₈) spectra of DASA **S2**. Only the keto form can be observed.533

Figure 5.41. HSQC NMR (600 MHz, CHCl ₃) spectra of DASA S2. Only the keto form can be observed.	534
Figure 5.42. HSQC NMR (600 MHz, Tol- <i>d</i> ₈) spectra of DASA S2. Only the keto form can be observed.	535
Figure 5.43. ¹ H NMR (600 MHz, CDCl ₃) at room temperature of DASA 1. The open isomer <i>EZZ</i> makes up ~5% of the open isomers.	536
Figure 5.44. ¹ H NMR (600 MHz, CDCl ₃) at room temperature of DASA S1. The open isomer <i>EZZ</i> makes up ~4% of the open isomers.	537
Figure 5.45. ¹ H NMR (600 MHz, CDCl ₃) at room temperature of DASA 2. The open isomer <i>EZZ</i> makes up ~2% of the open isomers.	538
Figure 5.46. ¹ H NMR (500 MHz, CDCl ₃) spectra of Compound S2.	539
Figure 5.47. ¹ H NMR (500 MHz, CDCl ₃) spectra of Compound S3.	540
Figure 5.48. ¹³ C NMR (125 MHz, CDCl ₃) spectra of Compound S3.	541
Figure 5.49. ¹ H NMR (600 MHz, CDCl ₃) spectra of DASA S1.	542
Figure 5.50. ¹³ C NMR (125 MHz, CDCl ₃) spectra of DASA S1.	543
Figure 5.51. ¹ H NMR (500 MHz, CDCl ₃) spectra of DASA S2.	544
Figure 5.52. ¹³ C NMR (150 MHz, CDCl ₃) spectra of DASA S2.	545
Figure 5.53. ¹ H NMR (500 MHz, CDCl ₃) spectra of DASA 2.	546
Figure 5.54. ¹³ C NMR (125 MHz, CDCl ₃) spectra of DASA 2.	547
Figure 5.55. ¹ H NMR (600 MHz, Tol- <i>d</i> ₈) spectra of DASA 1 after 24h equilibration. Solubility is limited in Toluene and the closed form isomer cannot be clearly identified.	548

Figure 5.56. ¹ H NMR (600 MHz, Tol- <i>d</i> ₈) spectra of DASA S1 after 24h equilibration. Only open form can be observed.	549
Figure 5.57. ¹ H NMR (600 MHz, Tol- <i>d</i> ₈) spectra of DASA S2 after 24h equilibration.	550
Figure 5.58. ¹ H NMR (600 MHz, Tol- <i>d</i> ₈) spectra of DASA 2 after 24h equilibration. Only open form can be observed.	551
Figure 6.1. a) LC systems rely on mesogen to amplify external stimuli. Schematic of a photoresponsive LCP system amplifying the isomerization of a photoswitch into macroscopic deformation. b) Schematic representation of the mechanical alignment of Liquid Crystal Networks.....	559
Figure 6.2. a) Previous chemistries used to fabricate mechanically aligned LC systems are based on harsh conditions. b) Schematic representation of new two-step DA-Click chemistry used to form Liquid Crystal Networks.....	561
Figure 6.3. (a) Bifunctional monomers bearing maleimide and cyclopentadiene for step-growth DA polymerization. (b) Schematics of the temperature modulated polymerization (c) Kinetics of the linear polymerization followed by ¹ H NMR. Consumption of maleimide (red), Cyclopentadiene (light blue), deprotection of the endo Furan-maleimide adduct (dark blue) and production of the Cp-mal DAA (gray) plotted as a function of time and temperature. (d) Gel Permeation Chromatography traces for the linear polymer after the first (gray) and second (yellow) polymerization.	562
Figure 6.4. (a) Diels–Alder cyclopentadiene-maleimide Liquid Crystal Network. (b) Polarized Optical Microscopy of the DA Cp-mal LCN at 45° and 0° from the two	

light cross polarizers. (c) 2D-Wide Angle X-ray Diffraction of the DA Cp-mal LCN stretched at 400% its initial length. (d) Differential Scanning Calorimetry of the DA Cp-mal LCN where a glass transition temperature of 63 °C can be observed at a temperature ramp of 10 °C/min (left axis) and change in strain as a function of temperature measured by Dynamic Mechanical Analysis under a tensile constant force of 0.005N on a temperature ramp of 3 °C/minute (right axis). A nematic-to-isotropic temperature can be observed 67 °C.564

Figure 6.5. Images of the DA Cp-mal LCN before (a) and (b) after thermal actuation. A 6 cm, 12 mg film lifting 18.6 g, 1.4 cm when heated above the nematic-to-isotropic temperature.567

Figure 6.6. Images of the DA Cp-mal LCN with a DASA (**19**) and an azobenzene (**22**).568

Figure 6.7 ¹H NMR (500 MHz, CDCl₃) spectra of **a**) linear step-growth polymerization of **8** Meso-mal, **12** CE-Cp and **9** Meso Fu-mal after 30 minutes at room temperature. **b**) **8** Meso-mal. **c**) **12** CE-Cp. **d**) **9** Meso Fu-mal.591

Figure 6.8 Differential Scanning Calorimetry of temperature controlled linear step-growth polymerization of **8** Meso-mal, **12** CE-Cp and **9** Meso Fu-mal. Traces at 24 hrs at room temperature and 72 hrs at 70 °C. Temperature ramp of 10 °C/min from -20 to 140 °C. Second cycle shown.593

Figure 6.9. Dimensions of films 1-3 on the polydomain after being taken out of the molds.597

Figure 6.10. Dimensions of films 1-3 on the polydomain before stretching.597

Figure 6.11. Film 1 (LCN) stretched 400% between two perpendicular light polarizers before the second polymerization a) at 0° and b) at 45°. Birefringence is observed.	
.....	597
Figure 6.12. Film 2 (LCN+19 DASA) stretched 400% between two perpendicular light polarizers before the second polymerization a) at 0° and b) at 45°. Birefringence is observed.	
.....	598
Figure 6.13. Swelling of Films 1-3 in DCM. Gel fraction obtained after 24 hrs in DCM	
.....	598
Figure 6.14. Thermogravimetric Analysis curve for Film 1 (LCN) upon heating from 200 °C to 800 °C at a constant rate of 20 °C/min.	
.....	599
Figure 6.15. Thermogravimetric Analysis curve for Film 2 (LCN+19 DASA) upon heating from 200 °C to 800 °C at a constant rate of 20 °C/min.	
.....	599
Figure 6.16. Thermogravimetric Analysis curve for Film 3 (LCN+22 Azobenzene) upon heating from 200 °C to 800 °C at a constant rate of 20 °C/min	
.....	600
Figure 6.17. Differential Scanning Calorimetry of Film 1 (LCN) from -20 °C to 140 °C at a temperature ramp of 10 °C/min. Third cycle shown. Glass transition temperature and nematic-isotropic temperature can be observed.	
.....	601
Figure 6.18. Differential Scanning Calorimetry of Film 2 (LCN + 19 DASA) from -20 °C to 140 °C at a temperature ramp of 10 °C/min. Third cycle shown. Glass transition temperature can be observed. Nematic-isotropic temperature can be observed only on the first cycle.	
.....	601

Figure 6.19. Differential Scanning Calorimetry of Film 3 (LCN + 22 Azobenzene) from -20 °C to 140 °C at a temperature ramp of 10 °C/min. Third cycle shown. Glass transition temperature and nematic-isotropic temperature can be observed.	602
Figure 6.20. Dynamic Mechanical Analysis of Film 1 (LCN) from -20 to 140 °C at 1 Hz on a temperature ramp of 5 °C / min. The logarithm of the storage modulus, loss modulus and the Tan δ as a function of the temperature.....	603
Figure 6.21. Dynamic Mechanical Analysis of Film 2 (LCN + 19 DASA) from -20 to 140 °C at 1 Hz on a temperature ramp of 5 °C / min. The logarithm of the storage modulus, loss modulus and the Tan δ as a function of the temperature.....	603
Figure 6.22. Dynamic Mechanical Analysis of Film 3 (LCN + 22 Azobenzene) from -20 to 140 °C at 1 Hz on a temperature ramp of 5 °C / min. The logarithm of the storage modulus, loss modulus and the Tan δ as a function of the temperature.	604
Figure 6.23. Polarized Optical Microscopy (POM) images of Film 1 (LCN) after the second polymerization. a) 45° and b) 0°.	605
Figure 6.24. Polarized Optical Microscopy (POM) images of Film 2 (LCN + 19 DASA) after the second polymerization. a) 45° and b) 0°.....	605
Figure 6.25. Polarized Optical Microscopy (POM) images of Film 3 (LCN + 22 Azobenzene) after the second polymerization. a) 45° and b) 0°.....	606
Figure 6.26. 2D Wide Angle X-ray Scattering of the DA Cp-mal LCN. The half-width of the distribution is shown. Order parameter determined to be $S = 0.47$	607
Figure 6.27. Percentage of strain by thermal actuation of a 12 mg DA Cp-mal DAA film, 6 cm in length, in function of the mass lifted.	608

Figure 6.28. Normalized work output (by film mass) by thermal actuation of a 12 mg DA Cp-mal DAA film, 6 cm in length, in function of the mass lifted. Work output calculated as $[\text{mass lifted}] \times [\text{Gravitational constant}] \times [\text{distance of contraction}] / [\text{mass of the film}]$.	609
Figure 6.29. ^1H NMR (500 MHz, CDCl_3) spectra of 3 .	610
Figure 6.30. ^{13}C NMR (125 MHz, CDCl_3) spectra of 3 .	611
Figure 6.31. ^1H NMR (500 MHz, CDCl_3) spectra of 6 .	611
Figure 6.32. ^{13}C NMR (125 MHz, CDCl_3) spectra of 6 .	612
Figure 6.33. ^1H NMR (500 MHz, CDCl_3) spectra of 7 .	612
Figure 6.34. ^{13}C NMR (125 MHz, CDCl_3) spectra of 7 .	613
Figure 6.35. ^1H NMR (500 MHz, CDCl_3) spectra of 8 .	614
Figure 6.36. ^{13}C NMR (125 MHz, CDCl_3) spectra of 8 .	615
Figure 6.37. ^1H NMR (500 MHz, CDCl_3) spectra of 9 .	615
Figure 6.38. ^{13}C NMR (125 MHz, CDCl_3) spectra of 9 .	616
Figure 6.39. ^1H NMR (500 MHz, CDCl_3) spectra of 12 .	617
Figure 6.40. ^{13}C NMR (125 MHz, CDCl_3) spectra of 12 .	618
Figure 6.41. ^1H NMR (500 MHz, CDCl_3) spectra of 13 .	619
Figure 6.42. ^{13}C NMR (125 MHz, CDCl_3) spectra of 13 .	620
Figure 6.43. ^1H NMR (500 MHz, CDCl_3) spectra of 14 .	620
Figure 6.44. ^{13}C NMR (125 MHz, CDCl_3) spectra of 14 .	621
Figure 6.45. ^1H NMR (500 MHz, CDCl_3) spectra of 15 .	622
Figure 6.46. ^{13}C NMR (125 MHz, CDCl_3) spectra of 15 .	623
Figure 6.47. ^1H NMR (500 MHz, CDCl_3) spectra of 18 .	623

Figure 6.48. ^{13}C NMR (125 MHz, CDCl_3) spectra of 18 .	624
Figure 6.49. ^1H NMR (500 MHz, CDCl_3) spectra of 19 .	625
Figure 6.50. ^{13}C NMR (125 MHz, CDCl_3) spectra of 19 .	625
Figure 6.51. ^1H NMR (500 MHz, CDCl_3) spectra of 20 , traces of cis isomer can be observed.	626
Figure 6.52. ^{13}C NMR (125 MHz, CDCl_3) spectra of 20 .	627
Figure 6.53. ^1H NMR (500 MHz, CDCl_3) spectra of 21 .	628
Figure 6.54. ^{13}C NMR (125 MHz, $\text{DMSO}-d_6$) spectra of 21 , cis isomer can be observed.	628
Figure 6.55. ^1H NMR (500 MHz, CDCl_3) spectra of 22 Azobenzene.	629
Figure 6.56. ^{13}C NMR (125 MHz, CDCl_3) spectra of 22 Azobenzene.	630

1 Donor-acceptor Stenhouse adducts – a novel class of photoswitches

This chapter was originally published in *Molecular Photoswitches: Chemistry, Properties, and Applications, Volume 1*. Pianowski, Z., (Ed.) © 2022 Wiley-VCH GmbH

Reproduced with the permission of Wiley & Sons. (Stricker, F., Seshadri, S. and Read de Alaniz, J. (2022). Donor–Acceptor Stenhouse Adducts. In *Molecular Photoswitches*, Z.L. Pianowski (Ed.). <https://doi.org/10.1002/9783527827626.ch14>)¹ Copyright Wiley & Sons.

1.1 Photoswitches and their parameters

1.1.1 Photochromism and Photoswitches

Photochromism – the property to undergo a light-induced reversible change of color based on a chemical reaction – was first reported by Fritzsche in 1867² From this initial discovery, many new classes of photochromic molecules such as photoswitches, that undergo a reversible conversion between their stable and (meta)stable isomers triggered by light, have been discovered. Not surprisingly, each photoswitch has its own advantageous properties and drawbacks which have been significantly optimized in the past 30 years. Wide-ranging applications that leverage photoswitching molecules, such as drug delivery, sensing, photopatterning and actuation, is likewise impressive. It is important to note, however, that the initial discovery of numerous classes of ‘modern’ photochromic molecules actually dates back to the 1800’s and early 1900’s when these molecules were being investigated for their dye properties.

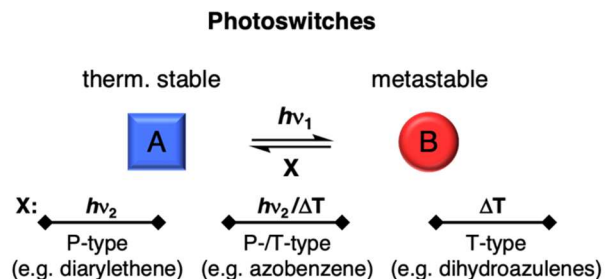


Figure 1.1. Photoswitches and their classification due to recovery type.

1.1.2 T-type and P-type photoswitches

After irradiation of the thermodynamical stable form **A**, a photoswitch undergoes a molecular shape change to a metastable isomer **B**. The recovery to the thermodynamical stable **A** form can either happen spontaneously (driven by heat, T-type photoswitch, e.g., dihydroazulene), by light (P-type, e.g., diarylethene) or by both (P/T-type, e.g., azobenzene). The control over the recovery mechanism, that leads to reversibility, can influence possible applications and is therefore a critical property of all photochromic materials (**Figure 1.1**).³⁻⁵

1.1.3 Negative vs positive photochromism

Another important property inherent to photochromic material is negative and positive photochromism. A positive photochrome has a λ_{\max} of the thermodynamic stable form smaller than the λ_{\max} of the metastable intermediate. A negative photochrome on the other hand has the opposite characteristic. A negative photochrome often promises higher penetration depths due to less overlap of the two isomers upon excitation.³⁻⁵

1.1.4 Photo(thermal)stationary state

A photoswitch under irradiation can reach an equilibrium between the reaction rate from the stable **A** isomer to the metastable isomer **B** and the reverse reaction (**Figure 1.1**). If that reaction equilibrium is driven by light in both directions this is defined as photostationary state (PSS) while if only one direction is driven by light it is called a photothermal stationary state (PTSS).³⁻⁵ In an ideal situation, a photoswitch will have a PSS or PTSS of 100%.

1.2 Donor-acceptor Stenhouse adducts (DASA).

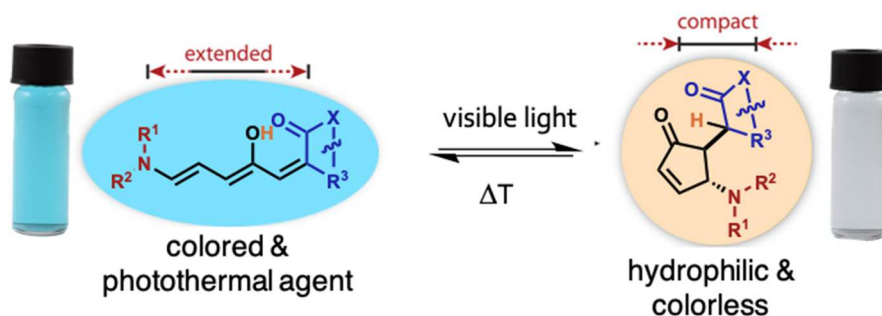
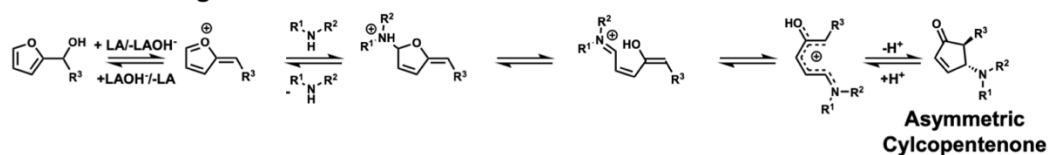


Figure 1.2. DASAs, a new platform of visible light organic photoswitches. Reproduced with the permission of Wiley & Sons. (Stricker, F., Seshadri, S. and Read de Alaniz, J. (2022). Donor–Acceptor Stenhouse Adducts. In *Molecular Photoswitches*, Z.L. Pianowski (Ed.). <https://doi.org/10.1002/9783527827626.ch14>)¹ Copyright Wiley & Sons.

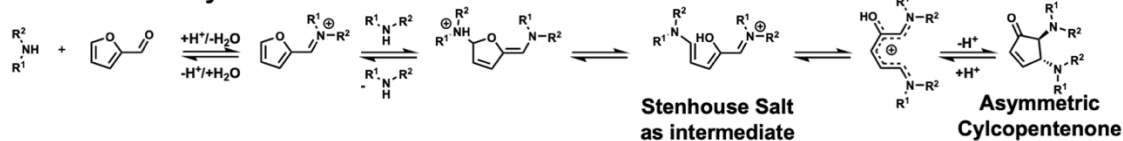
This chapter summarizes an emerging class of negatively photochromic photoswitches discovered in our group in 2014 (**Figure 1.2**)⁶ termed donor–acceptor Stenhouse adducts (DASAs), whose history dates back to a red dye initially reported by J. Stenhouse in 1850 in a lecture at the Royal Society of London.⁷ In this lecture, Stenhouse disclosed that skin, paper,

white velvet, canvas or cotton fabric treated with furfural slowly changes to roseate with the addition of a few drops of aniline. In 1887, Schiff accurately determined the structure of the red dye as a five-carbon cyanine dye with a hydroxyl substituent at the second carbon, commonly referred to as a Stenhouse salt.⁸ Despite these pioneering reports, it would take nearly a century before their photochromic properties were briefly investigated. In 1982, Honda reported the photochromic behavior of more than ten Stenhouse salts.⁹ Although the product of the visible light driven photochromic reaction was not identified, through retrospective mechanistic analysis we now know that the product was a colorless 4,5-diaminocyclopentenone adduct.

Aza-Piancatelli rearrangement



Stenhouse Salt Synthesis



DASA Synthesis

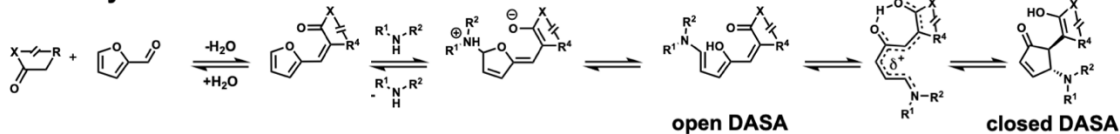


Figure 1.3. Schematic representation of Aza-Piancatelli rearrangement, Stenhouse Salt synthesis and DASA synthesis. Reproduced with the permission of Wiley & Sons. (Stricker, F., Seshadri, S. and Read de Alaniz, J. (2022). Donor–Acceptor Stenhouse Adducts. In *Molecular Photoswitches*, Z.L. Pianowski (Ed.). <https://doi.org/10.1002/9783527827626.ch14>)¹ Copyright Wiley & Sons.

It was the synthesis of 4,5-disubstituted cyclopentenone adducts that led to our serendipitous discovery of DASA based photoswitches. Motivated to replace multistep chemical synthesis of biologically active cyclopentenone scaffolds, we were drawn to the Piancatelli rearrangement.¹⁰ In 1976, Piancatelli and co-workers reported a new method for the synthesis of 4-hydroxycyclopentenone derivatives by an acid-catalyzed rearrangement of furylcarbinols.¹¹ Inspired by this work, in 2010 we developed an efficient aza-Piancatelli rearrangement of furylcarbinols using aniline based nucleophiles (**Figure 1.3**).¹²⁻¹⁵ The overall transformation proceeds through a cascade sequence that terminates with a 4π -electrocyclic ring closure of a pentadienyl cation; a step that is analogous to the ring closing step of DASAs. In an effort to expand the generality of this new methodology to aliphatic amines, we turned our attention to a preliminary study by Safar and coworkers on the rearrangement of activated furans with cyclic secondary aliphatic amines.¹⁶ In contrast to traditional Stenhouse salts that proceeded through imine/iminium activation, this system leveraged the electron-withdrawing nature of Meldrum's acid to facilitate the furan ring opening reaction to generate what we later coined as donor-acceptor Stenhouse adducts (DASAs). Guided by our interest in cascade rearrangements of furfural derived materials, we hypothesized that the photochromic behavior observed by Honda was due to a light driven isomerization of the Stenhouse salt triene which led to the key intermediate for the subsequent 4π electrocyclization and the formation of the closed 4,5-aminocyclopentenone (**Figure 1.3**). With these considerations in mind, we initiated our preliminary studies on the photochromic properties of DASAs and launched a new period in our research group. Herein, we describe the evolution of DASAs, their photophysical properties and highlight a range of applications that have already been demonstrated since their initial report in 2014.

1.3 DASA Synthesis

1.3.1 Molecular Photoswitch

DASA based photochromes all share a general architecture with a triene backbone bearing a hydroxy group in the C2-position, an electron withdrawing carbon acid acceptor and an electron donating secondary amine at the terminal end (**Figure 1.4A**). These structural properties are derived from furfural which serves as the precursor to the triene bridge with the furan oxygen providing the hydroxy group in the final architecture. Using a modular two-step synthesis, furfural is activated with readily available carbon acid acceptor moieties via a Knoevenagel condensation. Subsequently, a secondary amine nucleophile initiates a ring opening reaction of the activated furan core, resulting in the visible light responsive DASA photochrome. This modularity allows straightforward design of DASA photochromes, and has played a major role in the rapid exploration of this new class of photochromic material. The original discovery of DASA photochromes in 2014 was based on dialkylamine donors and acceptors derived from either Meldrum's acid or barbituric acid. This first generation was based on the strongly nucleophilic dialkylamines and relatively weak electron withdrawing acceptor groups, but suffered from a number of drawbacks discussed in Section 1.3.^{6,17}

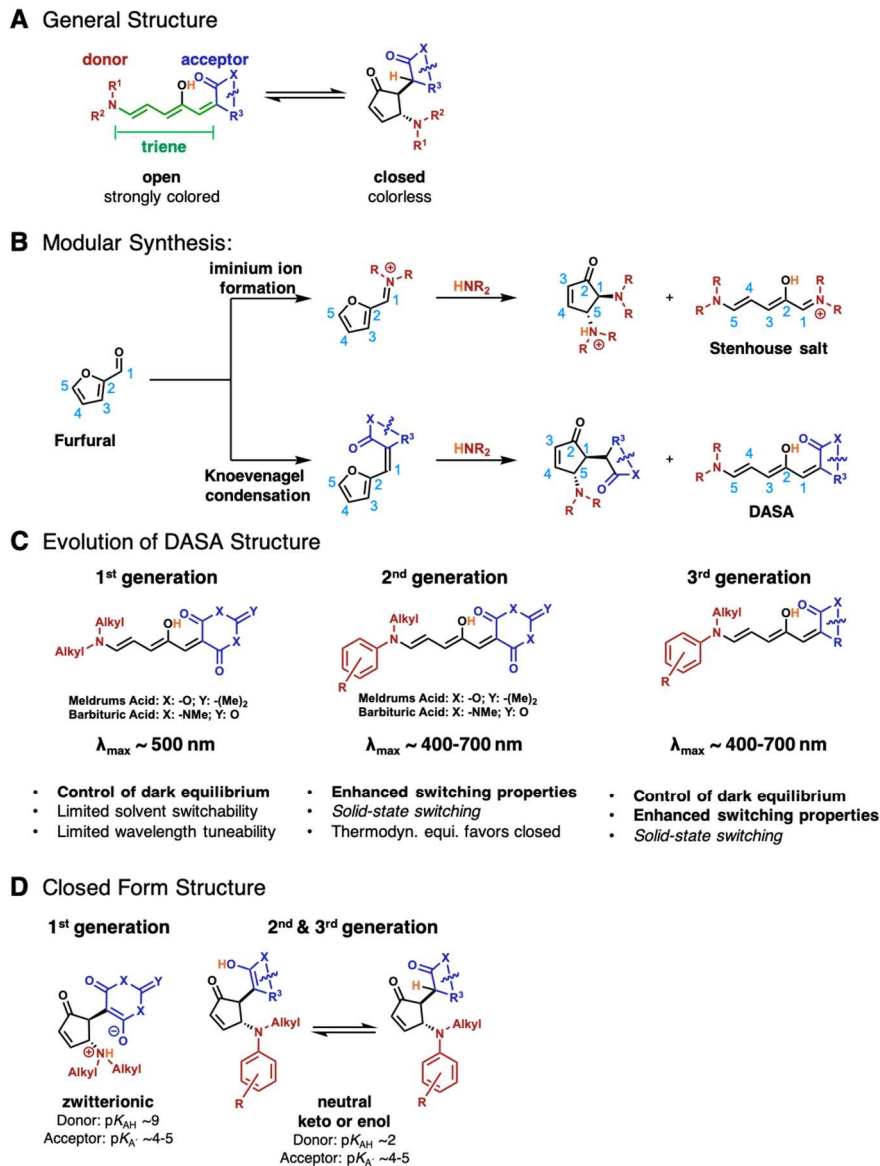


Figure 1.4. Structure and modular synthesis of donor–acceptor Stenhouse adducts. **A:** General structure of DASA photochromes. **B:** Modular synthesis of DASA photochromes and Stenhouse salts. **C:** Synthetic evolution through three generations of DASA photochromes. **D:** Closed form isomers of DASA photochromes.^{6,18,19} Reproduced with the permission of Wiley & Sons. (Stricker, F., Seshadri, S. and Read de Alaniz, J. (2022). Donor–Acceptor Stenhouse Adducts. In Molecular Photoswitches, Z.L. Pianowski (Ed.). <https://doi.org/10.1002/9783527827626.ch14>)¹ Copyright Wiley & Sons.

Due to the strong donating character of the dialkylamines, these compounds show a high bond length alternation (BLA) suggesting a zwitterionic open form, which is supported by theoretical calculations.^{20,21}

In 2016, arylamines (*N*-methylaniline and indoline derivatives) were introduced independently by Read de Alaniz¹⁹ and Beves²⁰ as a second-generation DASA which employed weaker electron donating amines to address a range of shortcomings of the first generation. These derivatives show less BLA suggesting a more hybrid open form triene structure. Although the weakly-donating amines provided improved photoswitching properties, it also introduced several drawbacks, most notably compromised thermodynamic equilibria meaning high amounts of closed form in the dark.¹⁹ As a result, a third generation was developed in 2018 which introduced new classes of more electron-withdrawing acceptor moieties to overcome drawbacks while maintaining the improvements of the second generation.¹⁸ More recently, improved photochromic performance of first generation DASA has been achieved by modifying the steric properties of the donor sidechains using asymmetric alkylamines.²²

When evaluating the effects of the donor and acceptor groups on DASA based photochromes, the closed-form derivative that results from irradiation also play a significant role. DASA has been reported to form a zwitterionic closed form as the kinetic product, in which the acceptor is deprotonated by the amine donor to form an enolate, as well as a thermodynamic ketone form with an enol as the intermediate. More basic donors like alkylamines in the first generation have been reported to exclusively form the zwitterionic

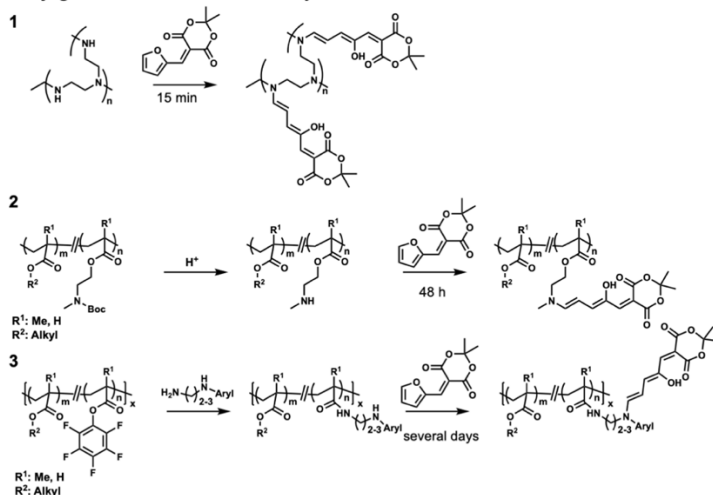
intermediate, while the less basic arylamines in generation 2 and 3 have been reported to form a mixture of the neutral keto and enol acceptors (**Figure 1.4D**) depending on the substitution pattern on the aryl moiety.^{19,20,22,23} The closed form derivatives can also be trapped by the addition of nucleophiles into the Michael acceptor of the cyclopentenone making it possible to drain the equilibrium while also limiting the compatibility with strong nucleophiles.²⁴

1.3.2 Photoswitches in Macromolecules

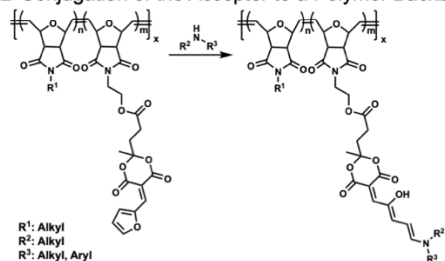
To apply DASA into functional materials, multiple groups have explored ways of conjugating DASA photochromes with polymeric systems.^{17,25–28} However, the presence of radicals or strong nucleophiles in common polymerization methods lead to undesired side reactions with DASA; as a result, only post-polymerization functionalization methods have proven successful to date.

The most common pathway involves the introduction of the donor or acceptor moiety onto a polymer backbone and utilizing the DASA forming reaction as the final functionalization step. Wang and coworkers demonstrated in 2017 the use of a polyethylenimine network to directly form DASA photochromes on a polymeric system.²⁸ (**Figure 1.5A1**) Two research groups have demonstrated two additional ways of including amines as donor groups by utilizing acrylate or methacrylate polymers. Beves and coworkers copolymerized a protected alkylamine acrylate or methacrylate derivative which was unmasked post-polymerization.²⁶ (**Figure 1.5A2**) Read de Alaniz and coworkers employed an activated pentafluorophenolacrylate to functionalize the backbone with a primary amine using either an

A Conjugation of the Donor to a Polymer Backbone



B Conjugation of the Acceptor to a Polymer Backbone



C Functionalization with DASA via Click Chemistry

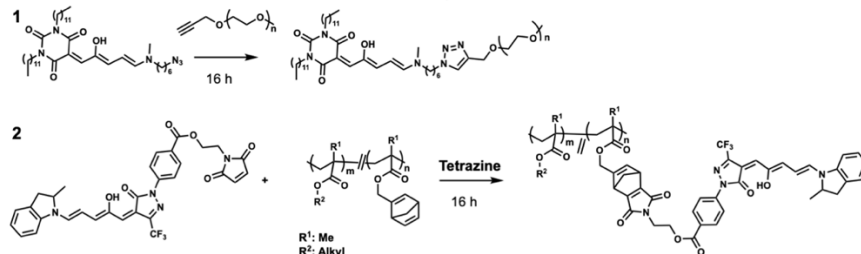


Figure 1.5. Structure of donor–acceptor Stenhouse adducts polymer conjugates. **A:** Examples of backbone functionalization with amines.^{25,27,28} **B:** Examples of backbone functionalization with an Acceptor.²⁹ **C:** Click Chemistry approaches towards functionalization with DASA photochromes.^{27,30} Reproduced with the permission of Wiley & Sons. (Stricker, F., Seshadri, S. and Read de Alaniz, J. (2022). Donor–Acceptor Stenhouse Adducts. In *Molecular Photoswitches*, Z.L. Pianowski (Ed.). <https://doi.org/10.1002/9783527827626.ch14>)¹ Copyright Wiley & Sons.

indoline or *N*-methylaniline pendant group. The subsequent DASA-forming reaction allows for second- and third generation DASA functionalization(**Figure 1.5A3**).²⁵

To introduce an acceptor unit onto a polymer backbone, Read de Alaniz and coworkers developed a synthetic pathway in which a furan adduct acceptor unit is attached to an oxanorbornene derivative and subsequently polymerized through ROMP. The DASA forming reaction was then performed with either dialkyl- or arylamines (**Figure 1.5B**).²⁹

The main challenge with relying on the DASA forming reaction, either from polymer bearing a amine donor or an activated furan, is the slow reaction kinetics when deactivated amines with more desirable photophysical properties are used. One strategy to address this limitation is to rely on “click” chemistry to introduce the DASA photochrome onto the polymer backbone. Here, Read de Alaniz and coworkers demonstrated that a first-generation DASA carrying an azide moiety on the donor alkyl chains could be efficiently conjugated with an alkyne-functionalized polyethyleneglycol in a copper azide click reaction (**Figure 1.5C1**).³⁰ More recently, they developed a metal-free click method to conjugate third-generation DASA using Diels–Alder cycloaddition (**Figure 1.5C2**).²⁷

Additionally, DASA photochromes have been attached to more complicated architectures like nanoparticle (NP) surfaces in several fashions. Schober and coworkers utilized a polyethyleneimine-functionalized surface to directly react a first-generation DASA onto the surface.³¹ In another approach, the synthesis of a catechol functionalized secondary amine was utilized to form a DASA molecule. Upon mixing the catechol-derived DASA with iron(II,III)oxide, NP functionalized particles can be obtained, however reversible

photoswitching was not observed from this system.³² Reliable, general and fast polymer conjugation still remains a challenge in the field due to the slow reaction kinetics of less activated donor amines especially in sterically hindered systems. Novel methods of DASA synthesis reducing necessary reaction time of the DASA formation from days to hours would be highly beneficial towards easily accessible DASA functionalized materials. This is the subject of Chapter 2.

1.4 Photoswitching Properties

1.4.1 Mechanism

The underlying mechanism of DASA photochromes is rather complicated and has been extensively studied by Feringa, Martinez and coworkers.³³⁻³⁸ The currently proposed mechanism consists of an actinic step followed by a series of thermal steps to fully transition from the colored open form to the colorless closed isomer. Through irradiation, the DASA transitions from the original extended open form **A** through an *E/Z*-isomerization around the α -C2 bond next to the hydroxy group to the first isomer **A'** (**Figure 1.6**) This actinic step is a key intermediate since its photostationary state drives the overall forward reaction.³⁶ However, this step can also be driven backwards through irradiation, since **A'** exhibits a red-shifted absorption spectrum.³⁴ The hydrogen bond between the acceptor and the hydroxy group on the triene is responsible for the directionality of the isomerization and is necessary for DASA to form the closed isomer.³⁵ After this actinic step, a thermal bond rotation from **B** to **B'** around the β -bond is proposed to set up the molecule for the subsequent 4π electrocyclization which converts the molecule from the colored isomers to the first closed isomer **C** that is colorless.^{33,36} From **C** the compound can be further stabilized by undergoing

an inversion on the donor nitrogen atom to **C'**, followed by either a bond rotation around the γ -bond to form **C''** or a direct tautomerization to the thermodynamic product **C''''**. Intermediate **C''** either undergoes a proton transfer step towards the kinetic zwitterionic product **C'''**, or can form **C** through tautomerization.³³ Beyond this productive pathway, there are several unproductive pathways which hinder the overall reaction productivity.³³ Most of these seem not to be prominent; however, the stability of the isomer *EZZ* (which can be formed from **A** and **B'**) has been experimentally shown to significantly impact the overall yield of the photoreaction. This is due to the conversion of **B'** into *EZZ* instead of converting into the photoproducts.³³ The mechanism is rather complex with a number of steps making a thorough investigation difficult; however, its complexity also offers opportunity to gain additional control by manipulating the energy landscape of each intermediate.³³ To accomplish this will require a detailed understanding of the factors that influence each intermediate and their corresponding energy barriers. Currently proposed improvements include increasing the stability and lifetime of **B** and **B'**, elimination of *EZZ* formation, optimizing the energy barrier of the key 4π -electrocyclization to improve quantum yield and forward kinetics. For overall equilibrium and recovery rates understanding what governs the stability of the closed isomers **C''**, **C'''** and **C''''** seems to be key.

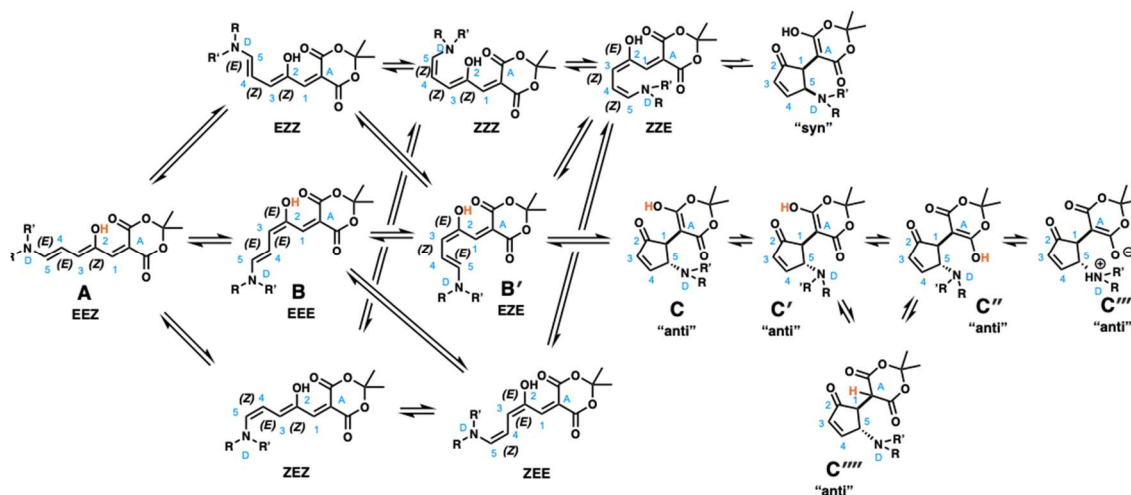


Figure 1.6. Proposed photoswitching mechanism of donor–acceptor Stenhouse adducts.³³

Reproduced with the permission of Wiley & Sons. (Stricker, F., Seshadri, S. and Read de Alaniz, J. (2022). Donor–Acceptor Stenhouse Adducts. In *Molecular Photoswitches*, Z.L. Pianowski (Ed.). <https://doi.org/10.1002/9783527827626.ch14>)¹ Copyright Wiley & Sons.

1.4.2 The Absorption Properties

One of the most promising properties of DASA photochromes is their activation by visible light. The benign properties of long wavelength light make this especially desirable for biomedical and material applications. This low energy activation is due to a strong push-pull system through the triene backbone which results in a π - π^* transition similar to merocyanine dyes. The absorbance profile for the open isomer **A** ranges from a absorption maximum (λ_{max}) around 500 nm for dialkylamines with Meldrum's acid acceptors into the near IR region at 700 nm by extending the conjugation.^{17–19} The closed isomers depend on the carbonyl structure but typically have some absorbance around 250 nm. Extending the conjugation of the open isomers is highly dependent on the planarity of the attached π -system.

An inclusion of an indoline ($\Phi_{D-T} = 0^\circ$) donor increases the absorbance compared to a methylaniline ($\Phi_{D-T} = 39^\circ$) by 30 nm purely due to a lower dihedral angle and better overlap.¹⁹

The λ_{\max} can be further increased using electron donating substituents on the arylamines such as amino or methoxy groups.^{18,19} The introduction of donor groups which possess even larger conjugated systems, such as carbazole or indole, have not succeeded due to their lack of nucleophilicity of the amines in the DASA-forming reaction but this remains a significant goal. Increased conjugation on the acceptor group can also significantly shift the absorption band, as the introduction of an hydroxypyridone derived acceptor increases the λ_{\max} with significant shoulders into 700 nm.¹⁸ Increasing the absorbance even further via the introduction of additional conjugated acceptors is of high interest for DASA photoswitches, in order to expand the absorption further into the IR regions.

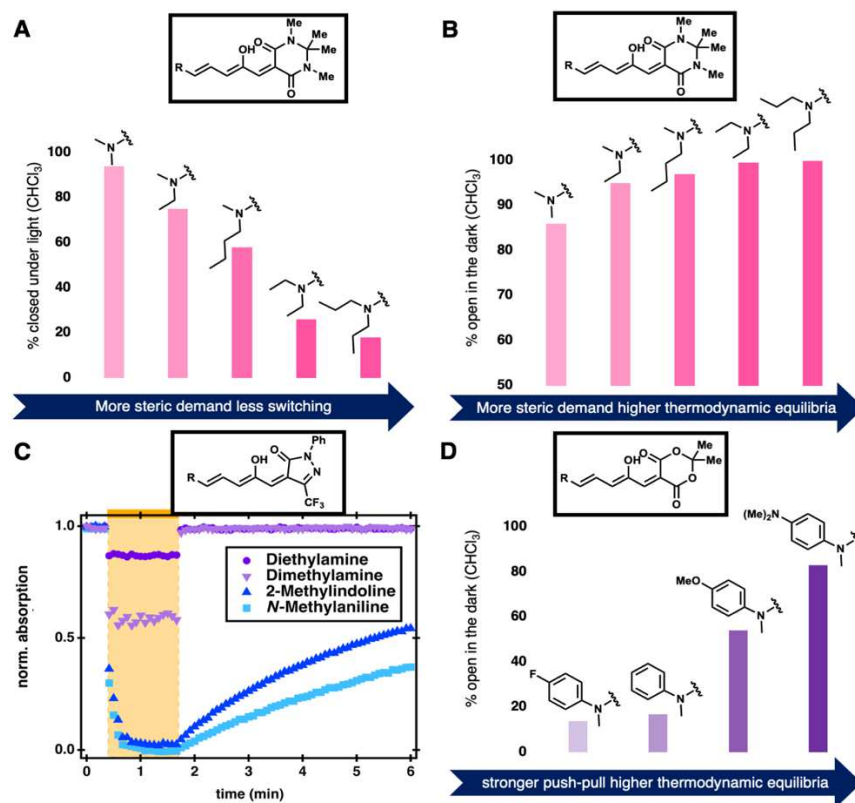


Figure 1.7. Effects of donor and acceptor groups on photoswitching properties and open-closed equilibria in the dark (thermodynamic equilibria). **A:** Photothermal stationary state of DASA photochromes with differing steric demand on the donor side.²² **B:** open-closed equilibria in the dark (thermodynamic equilibria) of DASA photochromes with differing steric demand on the donor side.²² **C:** influence of electronics of both the forward light driven reaction as well as the recovery of the open form of DASA photochromes. Time dependent UV–Vis spectrum measured at 10 μ M of DASA in toluene with irradiation with a 617 nm ThorLabs LED. Absorption was measured at the respective λ_{\max} of each compound. **D:** Thermodynamic equilibrium of DASA photochromes with differing electronic properties.²⁰ Reproduced with the permission of Wiley & Sons. (Stricker, F., Seshadri, S. and Read de Alaniz, J. (2022). Donor–Acceptor Stenhouse Adducts. In *Molecular Photoswitches*, Z.L. Pianowski (Ed.). <https://doi.org/10.1002/9783527827626.ch14>)¹ Copyright Wiley & Sons.

1.4.3 Dark Equilibria

Another important characteristic for T-type photoswitches is thermodynamic equilibrium, which depends on the stability of the open isomer **A** and the closed isomers **C'''** and **C''''**. High thermodynamic equilibrium can be observed with a strongly donating dialkylamine due to the formation of the less stable kinetic product **C'''** as well as a stronger push-pull system stabilizing the open form.⁶ Utilizing a weaker amine, like indoline or an aniline derivative, leads to the formation of a weaker push-pull system and the formation of **C''''**; the resulting thermodynamic equilibria is compromised when weak donor units are used.^{19,20} However, this trend can be reversed by combining a weak donor with a stronger electron-withdrawing carbon acid acceptor.¹⁷ This combination stabilizes the open form and results in high thermodynamic equilibria.^{17-20, 22}

1.4.4 Cyclization Efficiency Under Illumination

In literature, the efficiency of photoswitches is described by the quantum yield of the actinic step. However, quantum yield measurements for DASA photochromes is particularly challenging because that actinic step is coupled with thermal bond rotation and subsequent 4π -electrocyclizations all of which contribute to the overall mechanism. In order to more accurately describe the efficiency of DASA, extended analyses of cyclization efficiencies under illumination have been performed. These consider the thermal steps of both the forward and back reaction while also accounting for the overall stability of the metastable product isomers **C'''** and **C''''**. This efficiency also depends on a number of external effects such as solvent, pH and concentration. Understanding each of these effects is vital for designing a

tailored DASA for specific applications. Here we provide a short summary of each contributing factor.^{17-19, 32-39}

1.4.5 Steric Effects

Another important factor influencing the overall energy landscape and photoswitching efficiency is the steric demand of both the donor and acceptor. Triene substitutions are also important to consider but have not yet been fully explored. The acceptor side has been minimally studied, but similar compounds such as dimethylbarbituric acid acceptors and dioctylbarbituric acid acceptors show very similar behavior.^{17,19} At a minimum, this suggests that steric demand on acceptor that is distal from the triene does not directly interfere with the photoswitching efficiency. On the donor side, Beves and coworkers published an in-depth study on dialkylamine donors with asymmetric substituents.²² It was demonstrated that increasing the size of both sidechains favors the open form and results in faster recovery rates (**Figure 1.7A-B**). Interestingly, increasing the sidechain of one of the substituents has a smaller effect on the photoswitching properties of DASA.^{17,19} This is due to the linear orientation to the open form which allows for the larger substituents to be oriented away from the triene. However, an increase in both sidechains presumably interacts with the closed-form acceptor unit while also destabilizing **B** due to an A^{1,3} strain with the hydrogen on the triene. Both of these effects shift the overall energy landscape to the closed form while also destabilizing the key intermediate **B**, promoting the back reaction to **A** over the forward reaction to **B'**. Taken together these results demonstrate that the photoswitching efficiency can be tuned through both electronic and steric modifications (**Figure 1.7A-B**).^{20,22}

1.4.6 Electronic Effects

The strengths of both donor and acceptor have a direct influence on the actinic step and the amount of DASA which can be cyclized under irradiation. By comparing a diethylamine donor to a *p*-methoxyindoline donor, Feringa and coworkers show that the lifetime of the excited step increased from 2 ps to 24 ps.³⁶ This does not fully explain the different behavior of these two DASA photoswitches which is due to the complicated thermal steps that are involved in the overall mechanism and are also influenced by the push-pull system. Generally, a stronger push-pull system favors the open form in the DASA energy landscape, as seen with strong donors in the first generation and strong acceptors in the third generation. This results in high photothermal equilibria (open form under irradiation) and low closed isomer half lives in the dark (**Figure 1.7C-D**).^{6,17} On the other hand, introducing more electron-poor amines or electron-rich acceptors leads to longer half-life for the closed form and a larger amount of closed form. This pattern is widely observed in the second-generation derivatives.^{19,20} Additionally, the resulting closed-form derivative is different from the strongly donating alkyl amines which are basic enough to easily deprotonate the acceptor proton. This basicity result in the formation of the kinetic zwitterionic product **C'''** while less basic amines like aniline and indoline derivatives mostly form the enol product **C''** and the thermodynamic keto product **C''''** (**Figure 1.5C-D**).¹⁷⁻²⁰

1.4.7 Solvent Effects

One of the biggest developments of DASA over the years is improved solvent compatibility. The first-generation publications only showed formation of the closed isomers in significant amounts in apolar aromatic solvents such as toluene and benzene. However, this limitation was also due to the use of diethylamine and similarly sterically hindered

dialkylamine donors. Beves and coworkers showed in 2018 that using dimethylamine instead enabled reasonable switching in chlorinated solvents like chloroform. Introducing an aryl amine as the donor results in weakening the triene push-pull system and disfavors the open form, allowing for switching at higher concentrations in more polar solvents like ethyl acetate and acetonitrile in addition to apolar and chlorinated solvents.^{17-20, 22} This expansion of compatible solvents is presumably due to a more stable **B** isomer, allowing for a longer lifetime resulting in the reaction to the closed form in weaker push-pull systems. This can also be seen in the subsequent introduction of stronger acceptors increasing the strength of the push-pull system in 2018.¹⁷ These novel acceptors enabled the same solvent compatibility while increasing the thermodynamic equilibrium and while decreasing the closed form half-life. To this date, there has been no DASA reported which is capable of switching reversibly in the presence of protic solvents. Presumably this is due to a lowering in the activation energy of the thermal back reaction from **B** to **A** combined with a spectral overlap of both isomers compromising the photostationary state of the actinic step.³⁷ Additionally, over time the closed isomer is formed even in the dark in these solvents which is assumed to be due to the hydrogen-bonding ability of these solvents stabilizing the closed isomers.⁴¹ Identification of a system that enables reversible switching in protic media such as water will greatly expand the potential of DASA based photochromes and enable their use in biological applications that would benefit from their wavelength tunability.

1.4.8 Concentration Effects

Interestingly, another factor influencing the efficiency of DASA photoswitches is their concentration, as shown by Bardeen and Read de Alaniz in 2019. The thermal back reaction rate was shown to greatly increase at higher concentration with a derivative based on an indoline donor with a pyrazolone acceptor bearing a CF₃ moiety. The quantum yield was also significantly lowered.⁴² This effect is highly interesting and warrants further investigation. However, there is no direct evidence for aggregation explaining these results and potentially long-range coulombic interactions are at play.

1.4.9 Cyclization Under Exclusion of Light

In addition to a light-driven isomerization, a slower purely thermal isomerization from the open form to the closed form (especially in polar, protic solvents) can be observed for DASA. While the actual mechanism is unclear, the DASA photoswitches depend heavily on the relative energy of both the thermodynamic stable isomer **A** and the two metastable isomers **C'''** and **C''''** for cyclization both under light and in the dark. Depending on the structure of the molecule the thermodynamic equilibrium can shift from fully open to fully closed, similar to Stenhouse salt derivatives. This equilibrium can be shifted significantly in favor of the closed form with either solvents or substitutions. Decreasing the overall strength of the push-pull system leads to an increase of the closed isomers.^{17-20,22}

1.4.10 Role of Water and Substituents on Cyclization and Ring-opening

Protic solvents and especially water drive the overall equilibrium towards the closed isomers. Presumably this is due to the stabilization of the isomers through hydrogen bonding, which shifts the overall equilibrium towards the products and water assisted hydrogen transfer

facilitating the 4π electrocyclization. Furthermore, a slow complex formation of the closed form with up to five water molecules is reported to help stabilize the closed form to fully compromise the equilibrium in favor of the closed isomers C''' and C''''.⁴⁰

Interestingly, the effect of the backbone substitution was investigated before DASA compounds were found to have photochromic properties. Safar and coworkers investigated in 2000 the aza- Piantatelli rearrangements of compounds using acyclic secondary amine donors and Meldrum's acid acceptors.¹⁶ In this study, they explored a number of derivatives bearing substitutions (Br, Me, SMe, N₃) at the 3-position of the triene unit. These derivatives resulted directly form the closed adduct with no report of them being in equilibrium with the open form, which is in contrast to unsubstituted triene derivatives. Presumably, the equilibrium shifts to the closed form due to an A^{1,3} strain that arises in the open triene as a result of the sterically demanding substitution (Br, Ph).

1.5 Current Challenges for DASAs use in materials.

Since the first report on the photochromic properties of DASA in 2014⁶ this novel class of molecules has attracted tremendous interest due to its unique combination of desirable photophysical properties. From 2014 to 2020 a number of the initial questions have been answered in an ever increasing synthetic diversity,^{17-19,22} understanding its multi-step mechanism³³⁻³⁶ and postfunctionalization of polymeric materials²¹⁻²⁶ have been solved. However, new challenges have arisen:

1. How do we expand the synthetic scope towards unreactive amines or carbon acids?

To increase the design space of DASA switching parameters sterically hindered and electron poor amines such as *N,N'*-diphenylamine are of interest since they promise high equilibrium while retaining the ability to reversibly in polar solvents. Similarly, the postfunctionalisation of polymeric materials can be slow prohibiting the use of DASA in advanced materials. Catalyzing the DASA forming reaction has the potential of solving many of these issues.

2. Can reversible photoswitching with DASA be achieved in polar protic media?

DASA's photochromic properties are currently limited to aprotic media and the influence of polarity on the switching mechanism is not fully understood. This limits DASA's use in biological media, despite their great promise for biological applications. Understanding how polarity leads to either the formation of the closed adduct or how the photoreaction is inhibited will lead to the development of DASA which can be used successfully in water and biological media.

3. What unique properties does the multi-step mechanism of DASA allow for?

DASA's multi-step switching mechanism is unique in its complexity and promise. However, no use has been made out of the transient intermediates so far. Identifying transient isomers and addressing them independently from the initial and final product has the potential to not only increase the complexity of DASA materials responses but also of photochromic materials in general.

4. How can DASAs be incorporated in the main chain of polymeric systems?

Due to the decomposition of DASA if nucleophiles or radicals are present standard polymerization methods cannot be used to prepare DASA-based materials. This is the main reason DASA-based materials, so far, are limited to post-functionalization methods as described in 1.2.2. For application where main chain incorporation is desirable, such as liquid crystalline elastomeric actuators, a new benign chemistry is needed.

While DASA already has attracted significant attention over the last years, successfully addressing any of these challenges will lead to not only advanced the use of DASA-based light responsive materials but will also further advance the field of photochromic materials.

1.6 References

- (1) Stricker, F., Seshadri, S. and Read de Alaniz, J. (2022). Donor–Acceptor Stenhouse Adducts. In *Molecular Photoswitches*, Z.L. Pianowski (Ed.).
<https://doi.org/10.1002/9783527827626.ch14>
- (2) Fritzsche, M. Note Sur Les Carbures d'hydrogene Solides, Tires Du Goudron de Houille. *C. R. Acad. Sci.* **1867**, *69*, 1035.
- (3) Bouas-Laurent, H. and Dürr, H. Organic photochromism (IUPAC Technical Report). *Pure and Applied Chemistry*, **2001**, *73*, 639–665.
<https://doi.org/10.1351/pac200173040639>.
- (4) Stranius, K., Börjesson, K. Determining the Photoisomerization Quantum Yield of Photoswitchable Molecules in Solution and in the Solid State. *Sci Rep.*, **2017**, *7*, 41145.
<https://doi.org/10.1038/srep41145>.
- (5) Feringa, B. L. & Browne, W. R. (eds) *Molecular Switches* 2nd edn, Vol. 1 (Wiley-VCH Verlag GmbH & Co. KGaA, 2011).
- (6) Helmy, S., Leibfarth, F. A., Oh, S., Poelma, J. E., Hawker, C. J., Read de Alaniz, J. Photoswitching Using Visible Light: A New Class of Organic Photochromic Molecules. *J. Am. Chem. Soc.* **2014**, *136* (23), 8169–8172.
<https://doi.org/10.1021/ja503016b>.
- (7) Stenhouse, J. Ueber Die Oele, Die Bei Der Einwirkung Der Schwefel-. *Justus Liebigs Ann. Chem.* **1850**, *74*, 278–297.
- (8) Schiff, H. Ueber Farbstoff Basen. *Justus Liebigs Ann. Chem.* **1887**, *239*, 349–385.
- (9) Honda, K., Komizu, H., Kawasaki, M. Reverse Photochromism of Stenhouse Salts. *J. Chem. Soc. - Ser. Chem. Commun.* **1982**, *4*, 253–254.

- <https://doi.org/10.1039/C39820000253>.
- (10) Palmer, L. I., Read De Alaniz, J. Lewis Acid Catalyzed Rearrangement of Furylcarbinols: The Aza- and Oxa-Piancatelli Cascade Reaction. *Synlett* **2014**, 25 (1), 8–11. <https://doi.org/10.1055/s-0033-1340157>.
- (11) Piancatelli, G., Scettri, A., Barbadoro, S. A Useful Preparation of 4-Substituted 5-Hydroxy-3-Oxocyclopentene. *Tetrahedron Lett.* **1976**, 13 (1976), 3555–3558.
- (12) Veits, G. K., Wenz, D. R., Read De Alaniz, J. Versatile Method for the Synthesis of 4-Aminocyclopentenones: Dysprosium(III) Triflate Catalyzed Aza-Piancatelli Rearrangement. *Angew. Chemie - Int. Ed.* **2010**, 49 (49), 9484–9487. <https://doi.org/10.1002/anie.201005131>.
- (13) Veits, G. K., Wenz, D. R., Palmer, L. I., St. Amant, A. H., Hein, J. E., Read De Alaniz, J. Cascade Rearrangement of Furylcarbinols with Hydroxylamines: Practical Access to Densely Functionalized Cyclopentane Derivatives. *Org. Biomol. Chem.* **2015**, 13 (31), 8465–8469. <https://doi.org/10.1039/c5ob00944h>.
- (14) Palmer, L. I., Read De Alaniz, J. Direct and Highly Diastereoselective Synthesis of Azaspirocycles by a Dysprosium(III) Triflate Catalyzed Aza-Piancatelli Rearrangement. *Angew. Chemie - Int. Ed.* **2011**, 50 (31), 7167–7170. <https://doi.org/10.1002/anie.201102102>.
- (15) Wenz, D. R., Read de Alaniz, J. Aza-Piancatelli Rearrangement Initiated by Ring Opening of Donor-Acceptor Cyclopropanes. *Org. Lett.* **2013**, 15 (13), 3250–3253. <https://doi.org/10.1021/ol401248p>.
- (16) Šafář, P., Považanec, F., Prónayová, N., Baran, P., Kickelbick, G., Kožíšek, J., Breza, M. Dichotomy in the Ring Opening Reaction of 5-[(2-Furyl)methylidene]-2,2-

- Dimethyl-1,3-Dioxane-4,6-Dione with Cyclic Secondary Amines. *Collect. Czechoslov. Chem. Commun.* **2000**, *65* (12), 1911–1938.
<https://doi.org/10.1135/cccc20001911>.
- (17) Hemmer, J. R., Page, Z. A., Clark, K. D., Stricker, F., Dolinski, N. D., Hawker, C. J., Read de Alaniz, J. Controlling Dark Equilibria and Enhancing Donor-Acceptor Stenhouse Adduct Photoswitching Properties through Carbon Acid Design. *J. Am. Chem. Soc.* **2018**, *140* (33). <https://doi.org/10.1021/jacs.8b06067>.
- (18) Hemmer, J. R., Poelma, S. O., Treat, N., Page, Z. A., Dolinski, N. D., Diaz, Y. J., Tomlinson, W., Clark, K. D., Hooper, J. P., Hawker, C., Read de Alaniz, J. Tunable Visible and Near Infrared Photoswitches. *J. Am. Chem. Soc.* **2016**, *138* (42), 13960–13966. <https://doi.org/10.1021/jacs.6b07434>.
- (19) Helmy, S., Oh, S., Leibfarth, F. A., Hawker, C. J., Read de Alaniz, J. Design and Synthesis of Donor-Acceptor Stenhouse Adducts: A Visible Light Photoswitch Derived from Furfural. *J. Org. Chem.* **2014**, *79* (23), 11316–11329.
<https://doi.org/10.1021/jo502206g>.
- (20) Mallo, N., Brown, P. T., Iranmanesh, H., MacDonald, T. S. C., Teusner, M. J., Harper, J. B., Ball, G. E., Beves, J. E. Photochromic Switching Behaviour of Donor-Acceptor Stenhouse Adducts in Organic Solvents. *Chem. Commun.* **2016**, *52* (93), 13576–13579. <https://doi.org/10.1039/C6CC08079K>.
- (21) Laurent, A. D., Medved, M., Jacquemin, D. Using Time-Dependent Density Functional Theory to Probe the Nature of Donor–Acceptor Stenhouse Adduct Photochromes. *ChemPhysChem* **2016**, *17*, 1846–1851.
<https://doi.org/10.1002/cphc.201600041>.

- (22) Mallo, N., Foley, E. D., Iranmanesh, H., Kennedy, A. D. W., Luis, E. T., Ho, J., Harper, J. B., Beves, J. E. Structure-Function Relationships of Donor-Acceptor Stenhouse Adduct Photochromic Switches. *Chem. Sci.* **2018**, *9* (43), 8242–8252. <https://doi.org/10.1039/c8sc03218a>.
- (23) Mallo, N., Tron, A., Andréasson, J., Harper, J. B., Jacob, L. S. D., McClenaghan, N. D., Jonusauskas, G., Beves, J. E. Hydrogen-Bonding Donor-Acceptor Stenhouse Adducts. *ChemPhotoChem* **2020**, *4* (6), 407–412. <https://doi.org/10.1002/cptc.201900295>.
- (24) Alves, J., Wiedbrauk, S., Gräfe, D., Walden, S. L., Blinco, J. P., Barner-Kowollik, C. It's a Trap: Thiol-Michael Chemistry on a DASA Photoswitch. *Chem. - A Eur. J.* **2020**, *26* (4), 809–813. <https://doi.org/10.1002/chem.201904770>.
- (25) Ulrich, S., Hemmer, J. R., Page, Z. A., Dolinski, N. D., Rifaie-Graham, O., Bruns, N., Hawker, C. J., Boesel, L. F., Read de Alaniz, J. Visible Light-Responsive DASA-Polymer Conjugates. *ACS Macro Lett.* **2017**, *6* (7). <https://doi.org/10.1021/acsmacrolett.7b00350>.
- (26) Yap, J. E., Mallo, N., Thomas, D. S., Beves, J. E., Stenzel, M. H. Comparing Photoswitching of Acrylate or Methacrylate Polymers Conjugated with Donor-Acceptor Stenhouse Adducts. *Polym. Chem.* **2019**, *10* (47), 6515–6522. <https://doi.org/10.1039/c9py01345h>.
- (27) Lee, J., Sroda, M. M., Kwon, Y., El-Arid, S., Seshadri, S., Gockowski, L. F., Hawkes, E. W., Valentine, M. T., Read de Alaniz, J. *ACS Appl. Mater. Interfaces* **2020**, *12*, 54075–54082.
- (28) Zhong, D., Cao, Z., Wu, B., Zhang, Q., Wang, G. Polymer Dots of DASA-

- Functionalized Polyethyleneimine: Synthesis, Visible Light/PH Responsiveness, and Their Applications as Chemosensors. *Sensors Actuators, B Chem.* **2018**, *254*, 385–392. <https://doi.org/10.1016/j.snb.2017.07.107>.
- (29) Chen, Q., Diaz, Y. J., Hawker, M. C., Martinez, M. R., Page, Z. A., Xiao-An Zhang, S., Hawker, C. J., Read de Alaniz, J. Stable Activated Furan and Donor-Acceptor Stenhouse Adduct Polymer Conjugates as Chemical and Thermal Sensors. *Macromolecules* **2019**, *52* (11), 4370–4375. <https://doi.org/10.1021/acs.macromol.9b00533>.
- (30) Poelma, S. O., Oh, S. S., Helmy, S., Knight, A. S., Burnett, G. L., Soh, H. T., Hawker, C. H., Read de Alaniz, J., Controlled Drug Release to Cancer Cells from Modular One-Photon Visible Light-Responsive Micellar System. **2016**, *52* (69), 10525–10528. <https://doi.org/10.1039/c6cc04127b>.
- (31) Singh, S., Mai, P., Borowiec, J., Zhang, Y., Lei, Y., Schober, A. Donor-Acceptor Stenhouse Adduct-Grafted Polycarbonate Surfaces: Selectivity of the Reaction for Secondary Amine on Surface. *R. Soc. Open Sci.* **2018**, *5* (7). <https://doi.org/10.1098/rsos.180207>.
- (32) Ahrens, J., Bian, T., Vexler, T., Klajn, R. Irreversible Bleaching of Donor-Acceptor Stenhouse Adducts on the Surfaces of Magnetite Nanoparticles. *ChemPhotoChem* **2017**, *1* (5), 230–236. <https://doi.org/10.1002/cptc.201700009>.
- (33) Zulfikri, H., Koenis, M. A. J., Lerch, M. M., Di, M., Szyma, W., Filippi, C., Feringa, B. L., Buma, W. J. Taming the Complexity of Donor-Acceptor Stenhouse Adducts: Infrared Motion Pictures of the Complete Switching Pathway. *J. Am. Chem. Soc.* **2019**, *141* (18), 7376–7384. <https://doi.org/10.1021/jacs.9b00341>.

- (34) Lerch, M. M., Wezenberg, S. J., Szymanski, W., Feringa, B. L. Unraveling the Photoswitching Mechanism in Donor-Acceptor Stenhouse Adducts. *J. Am. Chem. Soc.* **2016**, *138* (20), 6344–6347. <https://doi.org/10.1021/jacs.6b01722>.
- (35) Lerch, M. M., Medved, M., Lapini, A., Laurent, A. D., Iagatti, A., Bussotti, L., Szymański, W., Buma, W. J., Foggi, P., Di Donato, M., Feringa, B. L., Tailoring Photoisomerization Pathways in Donor–Acceptor Stenhouse Adducts: The Role of the Hydroxy Group. *J. Phys. Chem. A* **2018**, *122* (4), 955–964. <https://doi.org/10.1021/acs.jpca.7b10255>.
- (36) Di Donato, M., Lerch, M. M., Lapini, A., Laurent, A. D., Iagatti, A., Bussotti, L., Ihrig, S. P., Medved, M., Jacquemin, D., Szymański, W., et al. Shedding Light on the Photoisomerization Pathway of Donor-Acceptor Stenhouse Adducts. *J. Am. Chem. Soc.* **2017**, *139* (44), 15596–15599. <https://doi.org/10.1021/jacs.7b09081>.
- (37) Mallo, N., Foley, E. D., Iranmanesh, H., Kennedy, A. D. W., Luis, E. T., Ho, J., Harper, J. B., Beves, J. E. Structure-Function Relationships of Donor-Acceptor Stenhouse Adduct Photochromic Switches. *Chem. Sci.* **2018**, *9* (43), 8242–8252. <https://doi.org/10.1039/c8sc03218a>.
- (38) Lerch, M. M., Di Donato, M., Laurent, A. D., Medved, M., Iagatti, A., Bussotti, L., Lapini, A., Buma, W. J., Foggi, P., Szymański, W., Feringa, B. L., Solvent Effects on the Actinic Step of Donor–Acceptor Stenhouse Adduct Photoswitching. *Angew. Chemie Int. Ed.* **2018**, *57* (27), 8063–8068. <https://doi.org/10.1002/anie.201803058>.
- (39) Sanchez, D. M., Raucci, U., Martinez, T. J., In Silico Discovery of Multistep Chemistry Initiated by a Conical Intersection: The Challenging Case of Donor–Acceptor Stenhouse Adducts, *J. Am. Chem. Soc.* **2021**, *143*, 20015–20021.

- <https://doi.org/10.1021/jacs.1c06648>.
- (40) Dolinski, N. D., Page, Z. A., Eisenreich, F., Niu, J., Hecht, S., Read de Alaniz, J., Hawker, C. J. A Versatile Approach for In Situ Monitoring of Photoswitches and Photopolymerizations. *ChemPhotoChem* **2017**, *1* (4), 125–131.
<https://doi.org/10.1002/cptc.201600045>.
- (41) Wang, D., Zhao, L., Zhao, H., Wu, J., Wagner, M., Sun, W., Liu, X., Miao, M. sheng, Zheng, Y. Inducing Molecular Isomerization Assisted by Water. *Commun. Chem.* **2019**, *2* (1). <https://doi.org/10.1038/s42004-019-0221-5>.
- (42) Lui, B. F., Tierce, N. T., Tong, F., Sroda, M. M., Lu, H., Read De Alaniz, J., Bardeen, C. J. Unusual Concentration Dependence of the Photoisomerization Reaction in Donor-Acceptor Stenhouse Adducts. *Photochem. Photobiol. Sci.* **2019**, *18* (6), 1587–1595. <https://doi.org/10.1039/c9pp00130a>.

2 Increasing the efficiency of DASA synthesis through HFIP

This chapter was originally published in *Angew. Chem. Int. Ed.* (Stricker, F.*, Clerc, M.*, Ulrich, S., Sroda, M., Bruns, N., Boesel, L. F., Read de Alaniz, J., *Angew. Chem. Int. Ed.*, **2021**, *60*, 10219–10227.)¹ Reprinted with permission of Wiley & Sons.

2.1 DASA synthesis through catalysis

In recent years, photochromic molecules have found increased attention due to their ability to dynamically control physical and chemical properties with high spatial and temporal resolution.^{2,3} Incorporation of these photoresponsive molecules into materials has led to a range of developments from molecular machines to life science applications.^{4–7} Critical to advancing these applications, has been the ability to optimize the photochromic properties, such as absorption profile and quantum yield, through synthetic structural modification. Although clearly beneficial, optimization often also introduces more complicated synthetic strategies with longer synthetic sequences and lower yields. Enabling widespread use of photochromic molecules requires easy accessibility, without compromising their tunability. Therefore, high yielding synthetic approaches using readily available starting materials for both small molecules and macromolecular systems remains an important goal.

Donor–acceptor Stenhouse adducts (DASAs) are a new class of visible light-responsive photoswitches developed in 2014.^{8,9} DASAs exhibit a range of promising properties for photochromic materials such as negative photochromism, visible light activation and modular

synthesis. Their architecture consists of a conjugated triene connecting an amine donor and a carbon acid acceptor, which upon irradiation can undergo a 4π -electrocyclization to a closed cyclopentenone form (**Figure 2.1a**).^{10,11} The “strength” of the electron donating or withdrawing character of the donor and acceptor groups largely governs overall switching properties, with structural modifications enabling these properties to be readily tuned. For example, replacing the dialkylamine donors from first generation derivatives (2014)^{7,8} with arylamines (second generation – 2016)^{12,13} provides access to DASAs with increased solvent compatibility, wavelength tunability and tunable switching kinetics. The introduction of strong carbon acid acceptors (third generation – 2018)¹⁴ retained the advantageous properties of the second generation derivatives while also providing better control over the thermodynamic equilibrium in the dark. In 2018, Beves and co-workers also reported that minor steric modifications to the dialkyl-amine donor (first generation) dramatically improve the photoswitching properties of this class of DASAs.¹⁵

Similar to other classes of photoswitches, however, most of these modifications have come with increased difficulty in synthetic access.

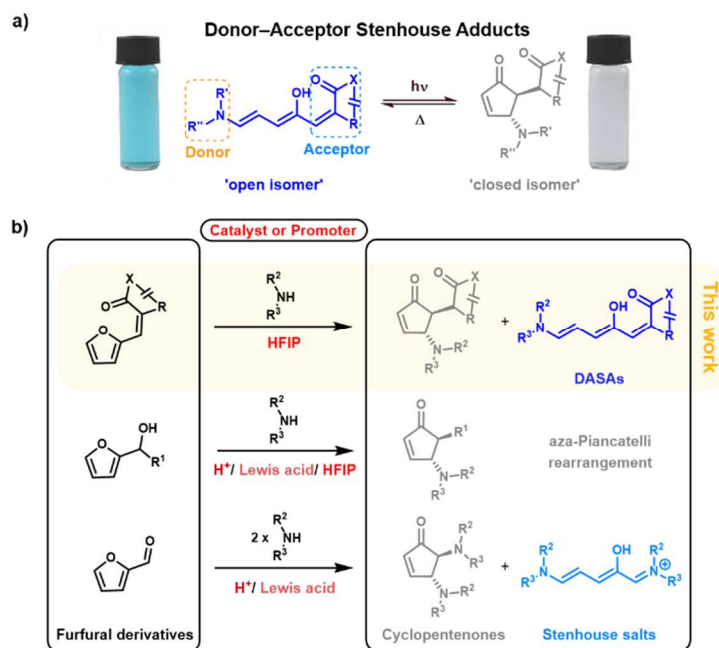


Figure 2.1. Donor–acceptor Stenhouse adducts (DASAs). a) General structures for open/colored triene and closed/colorless cyclopentenone isomers. R¹/R²: alkyl or aryl; X: O or N; R: electron withdrawing group, 5- or 6 membered ring (a selection of donor and acceptor structures are displayed in Figure 2.2). b) General DASA synthesis in comparison to the closely related transformations aza-Piancatelli rearrangement and Stenhouse reaction. Originally published in *Angew. Chem. Int. Ed.*¹ Reprinted with permission of Wiley & Sons.

DASA photochromes are derived from furfural serving as the precursor to the triene bridge with the furan oxygen forming the hydroxy group in the final architecture. Using a straightforward, modular 2-step synthesis, furfural is attached to readily available carbon acid acceptor moieties via a Knoevenagel condensation followed by a ring opening reaction of the furan core by a secondary amine nucleophile resulting in the open form DASA photochrome (**Figure 2.1b**, proposed full mechanism **Figure 2.10.1**). Despite the simplicity of this

approach, some synthetic challenges remain to enable general access to this class of photochromes. Most importantly, the rate of the furan ring opening reaction strongly depends on the nucleophilicity of the amine donor and the electrophilicity of the acceptor group.^{13,14,16,17} By introducing arylamines as donors (second and third generation DASAs) reaction times can increase drastically, from minutes to multiple hours.^{13,14} The slow rate is particularly problematic when performed on polymers due to concentration constraints and additional deceleration caused by steric effects from the polymer backbone. Here, reactions can take up to three weeks to reach full conversion, even with moderately reactive furan adducts derived of Meldrum's acid.^{18,19} Attempts to promote the ring opening reaction by using excess of the amine component leads to partial degradation of the DASA. Presumably, this results from nucleophilic attack on the triene and/or 1,4-addition to the cyclopentenone closed form.^{20,21} Besides long reaction times, purification can also be a major challenge. Purification of DASA photochromes often relies on trituration or precipitation of the more hydrophobic open form, which takes advantage of the solubility differences between the open and closed form of DASAs and corresponding degradation products. Common purification methods such as column chromatography are often low yielding predominantly due to the conversion between open and closed form that occurs during purification. This challenge is highlighted by the low yields (typically <50%)^{12,13} observed for the construction of second generation DASAs. Decreasing the required reaction time, simplifying the purification of DASAs, and expanding the design space to enable the use of unreactive donors or acceptors would therefore further expand the utility of this new class of photochromes.

The intrinsic similarities between the DASA furan ring opening reaction and the Stenhouse reaction²¹ and aza-Piancatelli rearrangement^{23,24} might provide the key to overcome some of the limitations currently associated with DASA synthesis (**Figure 2.1b**). In 2007, Li and Batey rendered the cascade condensation/ring opening/electrocyclization reaction between furfural and two equivalents of an amine practical and synthetically useful using lanthanide(III) catalysts.²⁵ Subsequently, it was demonstrated by Read de Alaniz and co-workers that rare-earth Lewis acids such as dysprosium triflate (Dy(OTf)₃) also serve as excellent catalysts for the rearrangement of furylcarbinols with a range of aniline nucleophiles.²⁴ Since these initial reports, a number of Brønsted and Lewis acid catalysts have been shown to promote the ring opening reaction of furfural or 2-furylcarbinols under mild conditions in the presence of a range nucleophilic amines.²⁴⁻³⁰ A challenge remained to identify conditions applicable to DASA synthesis that can simultaneously increase the rate of the furan ring opening reaction and inhibit the formation of the closed isomer during synthesis for streamlining the purification process and synthetic access. Interestingly, Gandon and co-workers reported several outstanding examples of the aza-Piancatelli rearrangement, for which the Lewis acid catalyzed reaction proceeds in 1,1,1,3,3,3-hexafluoro-2-propanol (HFIP) as a medium at room temperature in under an hour (selected substrates even reacted without additional catalyst when HFIP was used as solvent).²⁷ HFIP has recently gained much attention for efficiently promoting a wide range of Lewis and Brønsted acid-catalyzed organic reactions.^{31,32}

In this Chapter, we report the use of HFIP in DASA synthesis as a mild Lewis/Brønsted acid to promote the ring opening reaction of furan adducts for facile access to a broad range

of DASA photoswitches including a range of novel DASA derivatives bearing deactivated amine donors that were previously unreactive. Furthermore, we show that HFIP shifts the DASA equilibrium to the open form through hydrogen bonding interactions, simplifying work-up and purification procedures and increasing the overall isolated yields. This method is also applied to prepare DASA-polymer conjugates, reducing the required time for functionalization from days to several hours and allowing for the preparation of more structurally diverse DASA materials.

2.2 HFIP as Promoter in DASA Synthesis.

Initial attempts to promote the ring opening reaction commenced with the use of Lewis acid catalysts such as dysprosium triflate ($\text{Dy}(\text{OTf})_3$), a commonly used catalyst in the aza-Piancatelli reaction.^{24,28} Unfortunately, all our attempts to use metal-based Lewis acids in DASA synthesis resulted in degradation of the product or starting materials. Inspired by Gandon and co-workers and their successful application of HFIP in the aza-Pinacatelli rearrangement,^{27,32} we next explored the use of HFIP as mild Lewis/Brønsted acid in DASA synthesis. HFIP has high polarity and ionization potential, moderate acidity ($\text{p}K_{\text{a}} = 9.3$) in combination with low nucleophilicity and a strong hydrogen bond donor ability, possibly providing a way of assisting in electrophilic activation of the furan adduct and stabilizing charged intermediates.^{31,32} Furthermore, due to its low boiling point (bp.: $59\text{ }^\circ\text{C}$)³¹ HFIP can be easily separated from the reaction mixture by evaporation *in vacuo* before purification. Initial experiments were conducted examining the effect of HFIP as a co-solvent with dichloromethane for the reaction of 4,4'-dimethoxydiphenylamine with the furan adduct derived from Meldrum's acid. The former compound is unreactive under standard reported conditions for DASA formation with this acceptor.¹⁴ In contrast, rapid color formation was observed by the naked eye supporting the formation of DASA-1 and the promising activity of HFIP to promote DASA synthesis. $^1\text{H-NMR}$ and UV-Vis kinetic studies were then used to confirm this qualitative evaluation. For this we utilized the third generation CF_3 -pyrazolone derived furan adduct (**1**) and *N*-methylaniline (**Figure 2.2a**) as readily available starting materials providing good signal separation in $^1\text{H-NMR}$. The reaction progress in the synthesis

of DASA-2 was monitored via continuous *in situ* analysis in deuterated dichloromethane in the presence and absence of HFIP. Dichloromethane is a suitable co-solvent for HFIP as it is inert under acidic conditions and does not form hydrogen bond complexes with HFIP. As

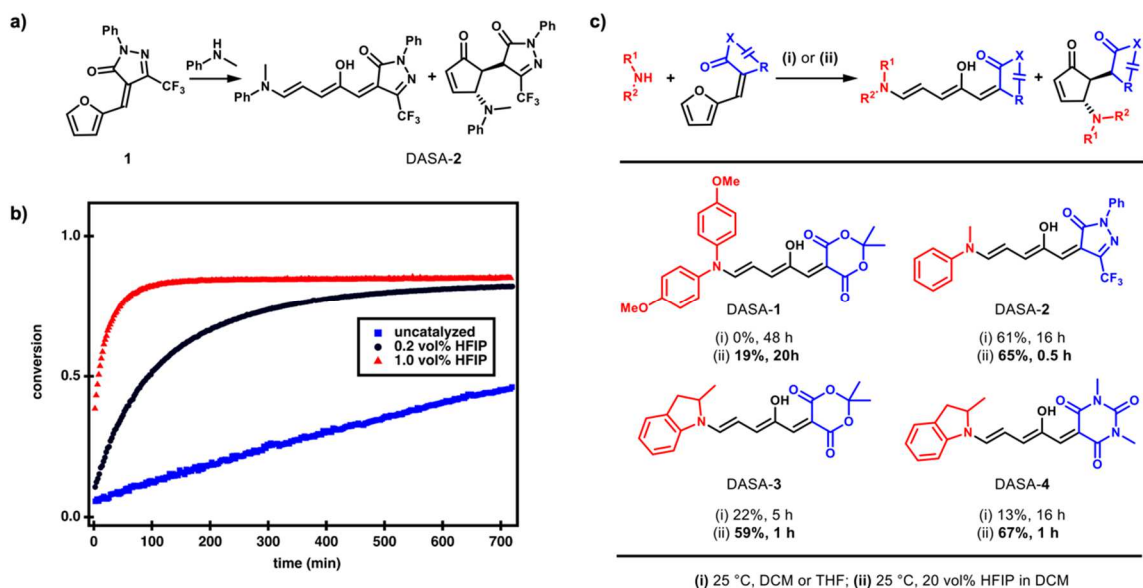


Figure 2.2. Effect of HFIP on reaction rate and yields in DASA synthesis. a) Reaction scheme of the ring opening of CF₃-pyrazolone derived furan adduct (1) and N-methylaniline. b) Conversion plots from *in situ* ¹H-NMR experiments of the reaction displayed in a) applying different amounts of HFIP in dichloromethane at 25 °C. The second-order rate constant increases from $3 \pm 1 \text{ M}^{-1} \text{ h}^{-1}$ (0 vol%) to $11.6 \pm 0.2 \text{ M}^{-1} \text{ h}^{-1}$ (0.2 vol%, 1 equivalent relative to 1) to $56 \pm 5 \text{ M}^{-1} \text{ h}^{-1}$ (1 vol%, 5 equivalents relative to 1). c) Comparison on isolated yields and reaction time for the synthesis of a series of DASAs under traditionally used reaction conditions and by application of 20 vol% HFIP in dichloromethane. Yields obtained under uncatalyzed conditions for DASA-3 and DASA-4 were taken from literature.¹⁴ Originally published in *Angew. Chem. Int. Ed.*¹ Reprinted with permission of Wiley & Sons.

shown in **Figure 2.2b**, a drastic rate increase was observed using only 0.2 and 1 vol % of

HFIP (corresponding to 1 and 5 equivalents relative to **1**) with second-order rate constants (k) increasing from $3 \pm 1 \text{ M}^{-1} \text{ h}^{-1}$ to 11.6 ± 0.2 and $56 \pm 5 \text{ M}^{-1} \text{ h}^{-1}$, respectively (**Table 2.1**). The accelerating effect was strongly enhanced at higher concentrations (**Figure 2.10**) and importantly, no signs for the formation of side products or degradation were detectable by ^1H -NMR spectroscopy even when going up to 20 vol% HFIP while also improving isolated yields (**Figure 2.2c**). Utilizing higher amounts did accelerate the reaction further, however, degradation of the product and starting material could be observed for concentrations $>50 \text{ vol}\%$ (**Figure 2.10**). In this study a maximum of 20 vol% HFIP (1 to 10 equivalents relative to the furan adduct) was therefore utilized for all syntheses. Reactions can be performed open to air. Importantly removing HFIP by evaporation *in vacuo* enables purification by trituration, similar to previously reported procedures.^{8,13}

Encouraged by this initial result, we next explored the generality of this method toward the synthesis of various other first, second and third generation DASAs. Synthesis of first generation based DASAs bearing strongly basic alkyl amines (as compared to anilines used for second and third generation DASAs) were inhibited by the addition of HFIP (**Figure 2.11**). Presumably, this is due to the basicity of the secondary alkyl amines, which are known to form stable hydrogen bond complexes with HFIP leading to an adverse effect on the reaction rate.^{33–35} In contrast, the synthesis of both second and third generation based DASAs greatly benefited from the addition of HFIP (**Figure 2c**). For example, a 5-fold increase in yield was achieved for the synthesis of DASA-4 within a fraction of the usual reaction time, 67% in 1 h vs. 13% in 16 h. This demonstrates that the use of low concentrations of HFIP with a co-solvent improves access to DASA based photoswitches in terms of yield and reaction time, while also expanding the accessible DASA design space.

To better understand the role of HFIP on mediating the ring opening reaction of the furan adduct, we monitored the rate of DASA-2 formation with other polar solvents and alcohols using $^1\text{H-NMR}$ spectroscopy and investigated the electronic ground state properties of the furan adduct via UV-Vis spectroscopy in various solvents. Analogous NMR kinetic experiments were conducted with isopropanol instead of HFIP (**Figures 2.12–17**). As previously observed for polar protic solvents,^{14,17} we found an accelerating effect for isopropanol (k : $9 \text{ M}^{-1} \text{ h}^{-1}$ for 2 vol%), but it was substantially smaller than for its fluorinated analogue (k : $56 \text{ M}^{-1} \text{ h}^{-1}$ for 1 vol%). More interestingly, using the methyl ether of HFIP (HFIPMe) instead of HFIP had only minor effects on the reaction rate (k : $5 \text{ M}^{-1} \text{ h}^{-1}$ for 3 vol%). HFIPMe is comparably polar to HFIP (relative dielectric constant: $\epsilon_{\text{HFIP}} = 17.8^{35}$, $\epsilon_{\text{HFIPMe}} = 15.4^{36}$), exhibits similar hydrogen bond acceptor properties, but lacks the hydrogen bond donor ability suspected to be responsible for the promotion activity seen in many other organic transformations.³⁸ UV-Vis spectroscopy of the CF_3 -pyrazolone derived furan adduct **1** revealed that the spectral properties are largely insensitive to polarity differences in a variety of protic and aprotic solvents but are strongly altered in HFIP (**Figures 2.19–20**). These results suggest that hydrogen bonding of HFIP with the furan adduct plays a role in the observed rate increase, potentially by increasing their electrophilic character. However, the specific mechanism at play here requires further study as it is likely that multiple effects (polarity, hydrogen bond donor ability, possibly acidity) contribute to the observed promotion of the reaction. Moreover, other effects such as off-cycle binding of the amine nucleophile with HFIP (of relevance for strongly basic alkyl amines, **Figure 2.11**) and product inhibition (*vide infra*) further complicate the full mechanistic picture.

2.3 HFIP as Modulator of Thermodynamic Equilibrium and Photoswitching.

We then investigated the impact of HFIP on the thermodynamic equilibrium between the open and closed form DASA. Previous studies showed that protic solvents (e.g. methanol) and polar solvent (e.g. acetonitrile) afford a mixture of open and closed isomers, which renders the purification more difficult and in general results in lower isolated yields (often only the more hydrophobic open form can be isolated in high yield using trituration).^{9,39} ¹H-NMR spectroscopic analysis revealed that in the presence of HFIP minimal formation of closed form was observed despite the polarity and acidity of HFIP (**Figure 2.20–24**). Analogous experiments in polar solvent such as acetonitrile ($\epsilon = 36.6$)⁴⁰ led to mostly the closed form (**Figure 2.25**). These results support that HFIP is unique amongst protic polar solvents for its ability to stabilize the open form of DASA photochromes. To further investigate the effects of solvent on the open form, we analyzed solvatochromic shifts⁴¹ in solvents with varying polarity of first, second and third generation DASAs (DASA-4 to 6) as well as a non-hydroxy DASA analogue (**Figure 2.3** and **Figures 2.26–29**). HFIP showed a clear deviation from the linear trend in solvatochromic shift observed for the other solvents indicating the presence of additional specific interactions in HFIP. Of note, the non-hydroxy DASA analogue (DASA-7) showed a linear trend in its solvatochromic shift with all solvents, including HFIP showing that the hydroxy group is likely responsible for the non-linear behavior of regular DASA compounds. A detailed study on the interpretation of solvatochromic shifts in terms of delocalization of the electronic ground state structure for different DASA generations was recently published by Read de Alaniz and co-workers.⁴² To also evaluate the effects of HFIP on the switching properties, DASA-2 was placed in a solution of dichloromethane with 0.5 vol% of HFIP and irradiated with 530 nm light (**Figure 2.30**). In the presence of HFIP

DASA-2 undergoes an only 11% decrease in absorption upon irradiation, followed by rapid recovery to the open form in the dark. On the other hand, in pure dichloromethane a substantially increased photothermal stationary state (PTSS, equilibrium between the light driven forward reaction and the purely thermal back reaction)⁴³ (81% closed isomers) and a noticeably slower recovery rate were observed. These results highlight that the thermodynamic equilibrium and PTSS clearly shift to the open form in the presence of HFIP, even at low concentrations. We propose that a hydrogen bond donor interaction between the hydroxyl group on the triene backbone and HFIP must be critical for stabilizing the open form and controlling the thermodynamic equilibrium and PTSS. A possible hydrogen bond donor interaction is shown in **Figure 2.4a**.⁴⁴

Building on this hypothesis, we speculated that a modulation of the intramolecular hydrogen bond strength in the open form could also be exploited to systematically shape the

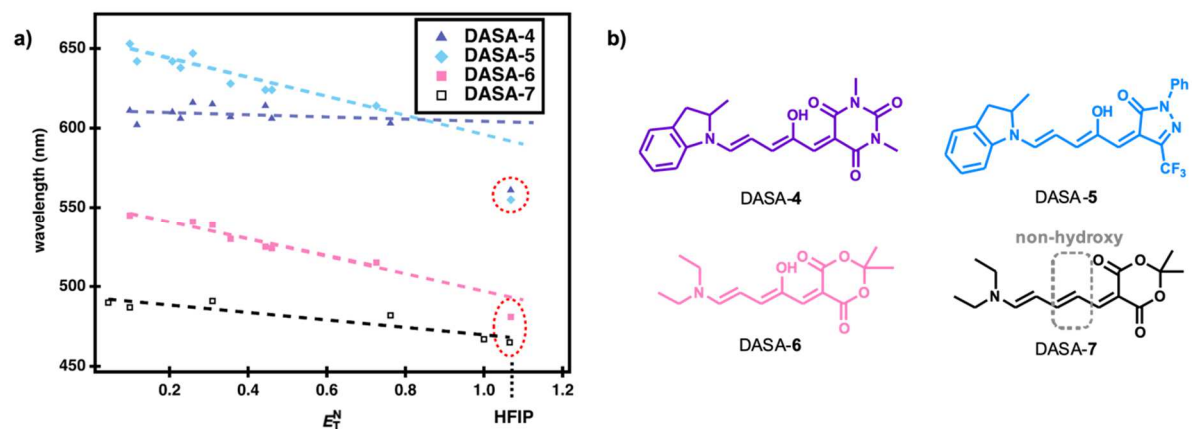


Figure 2.3. DASA solvatochromic shift analysis. a) Solvatochromic shifts using the Dimroth-Reichardt E_T^N solvent polarity scale for first to third generation DASAs and non-hydroxy analogue in solvents of different polarity displaying deviation from non-linearity only for DASAs in HFIP, which indicates the presence of hydrogen bonding interactions with the triene hydroxy group. b) Chemical structures of DASAs in a). Originally published in *Angew. Chem. Int. Ed.*¹ Reprinted with permission of Wiley & Sons.

overall switching kinetics of DASA compounds.^{44,45} To test this idea, we explored the role of HFIP in toluene, in which excellent PTSS performance (>95% closed isomers at PTTS for most DASA derivatives) and slower thermal recovery than in chlorinated solvents is observed. As highlighted in **Figure 2.4b**, the closed form half-life of DASA-2 is reduced from 94 s to 2.5 s upon the addition of only 0.1-0.5 vol% of HFIP reaching a lower value than the substantially more electron rich corresponding 2-methylindoline derivative (DASA-5, 40 s in toluene).¹³ This demonstrates a facile pathway to externally modulate DASA switching kinetics through addition of a simple hydrogen bond donor opening the door to systems relying on finely controlled switching kinetics.

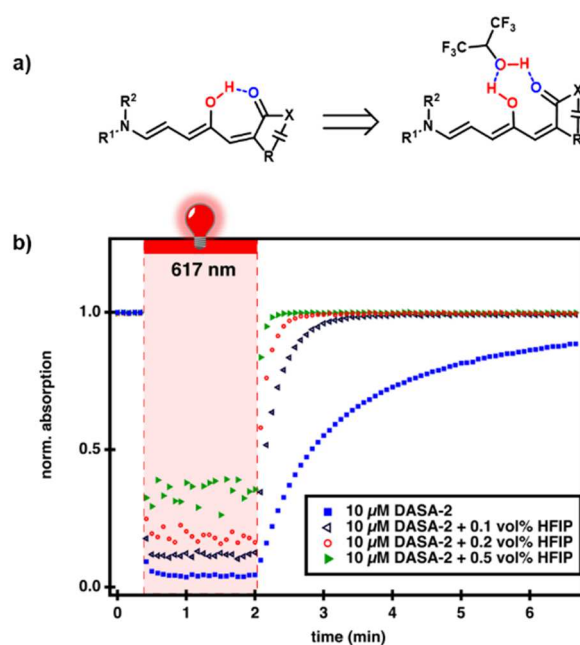


Figure 2.4. Hydrogen bonding interaction of HFIP and the DASA open form and effect on photoswitching. a) General scheme for proposed hydrogen bonding in DASAs in presence and absence of HFIP. b) Time dependent UV-Vis spectroscopy to observe the photochromic behaviour of DASA-2 (10 μM) in toluene and toluene/HFIP followed at λ_{max} (625 nm). Originally published in *Angew. Chem. Int. Ed.*¹ Reprinted with permission of Wiley & Sons.

2.4 Novel DASA Derivatives.

To further illustrate the advantage of this new methodology, we sought to expand the scope of DASAs by including highly unreactive amine donors to prepare previously unattainable DASA derivatives (**Figure 2.5a**). Previously reported DASAs were limited to considerably nucleophilic amine donors with pK_a values of their conjugated acid above ~ 4.8 . One exception being 4,4'-dimethoxydiphenylamine (pK_a conjugated acid of ~ 2.2) that only reacted with a highly electron poor and unusually reactive a number of DASAs bearing extremely non-basic amine donor moieties whose conjugate acids have pK_a values approaching ~ 0.5 (**Figure 2.5a**). Driven by the increased light penetration depth and

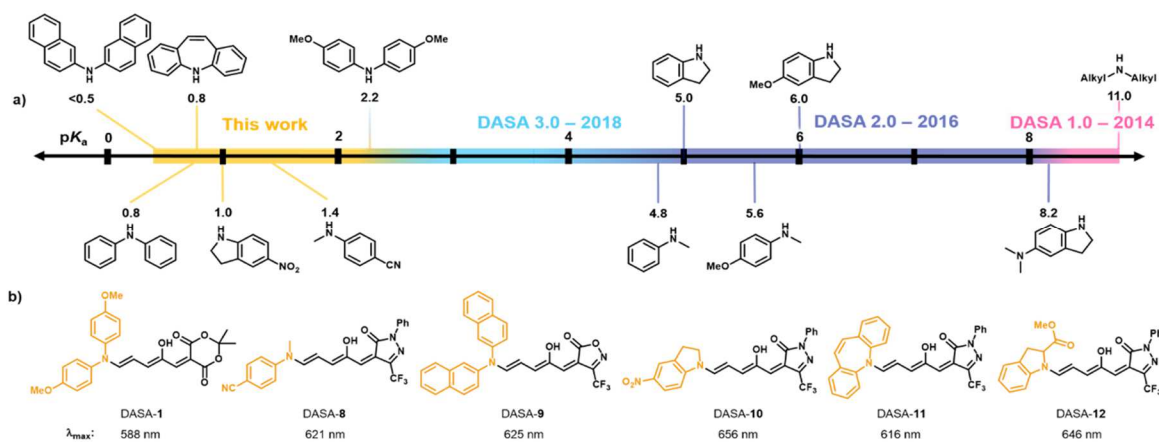


Figure 2.5. Novel DASAs bearing weak amine donors that were synthesized using HFIP.

a) Different secondary amine donors examined previously and in this report for DASA synthesis ordered according to the pK_a values of their corresponding acid (calculated with SciFinder[®]), which correlate well with the reactivity in the furan ring opening reaction. b) Chemical structures of the novel DASAs from this report and λ_{max} in chloroform. Note: some of the DASAs display split absorption bands (**Figure 2.31–42**). The listed wavelengths correspond to the more red-shifted maximum. CF_3 -isoxazolone derived furan adduct.¹⁴ Originally published in *Angew. Chem. Int. Ed.*¹ Reprinted with permission of Wiley & Sons.

biological compatibility of near-IR light, we initially focused on arylamine derivatives with the potential ability to red-shift the λ_{max} through hyperconjugation. Using 20 vol% HFIP in dichloromethane provided access to a range of new DASA derivatives bearing aniline derivatives with highly deactivating groups for the first time, sterically hindered aromatic amines and new acyclic and cyclic aromatic amines (**Figure 2.5b**). To compare the properties of the DASAs synthesized from these new donors, the CF₃-pyrazolone derived furan adducts (**1**) was primarily used as the acceptor compound. For the weakest donor, 2,2'-dinaphthylamine, a more reactive CF₃-isoxazolone derived acceptor (**S4**) was used to yield DASA-9. These furan adducts were synthesized by Knoevenagel condensation of the respective carbon acids with furfural in a first step according to previously reported procedures.^{8,13} The furan ring opening reactions of the furan adducts in 20 vol% HFIP can be conducted at ambient conditions, open to air and after completion, evaporation of the solvents *in vacuo* enables isolation of the desired compounds as solids that can be filtered and purified via trituration with diethyl ether. For example, **1** reacted in 16 h with iminostilbene to afford DASA-11, which was isolated in good yield (65%) after trituration with diethylether. Full characterization data of all compounds can be found in the Supporting Information.

2.5 Absorption Properties of Novel DASAs.

With access to a range of new DASA scaffolds, we explored their absorption profiles through UV-Vis spectroscopy (**Figure 2.6a** and **Figures 2.31-42**). In general, these DASA derivatives have similar properties with the previously reported second and third generation DASAs despite no structural differences.^{8,13,14} For example, two 4-methoxyphenyl substituents in DASA-1 resulted in the same maximum absorption wavelength of ~590 nm in

chloroform as in the respective unsubstituted indoline derivative that formally provides only one phenyl ring (DASA-3).^{13,14} Presumably, this is due to the substantial out-of-plane twist of both aryl substituents on the acyclic amine donors and therefore reduced HOMO overlap/conjugation. This phenomenon was extensively investigated before to explain the bathochromic shift of ~30 nm observed for cyclic indoline relative to the corresponding *N*-methylaniline derivatives.¹³ In analogy to the previous study,¹³ density functional theory (DFT) calculations at B3LYP-GD3BJ/6-31G(d) level of theory were used for geometry optimizations of the open form DASAs in order to compare dihedral angles between the acceptor and donor groups in this new series (**Figure 2.6b**, **Table 2.2**, **Figures 2.49–50**). In agreement with literature,¹³ for the acyclic amine donors a dihedral angle of $\Phi_{D \square A} \approx 40^\circ$ between the acceptor-triene system and the donor aryl group on the opposite side of the hydroxy group was found, whereas the indoline-derivative (DASA-5) is completely planar. The second aryl group in DASA-1 and DASA-9 was predicted to be even more twisted ($\Phi_{D \square A} \approx 60^\circ$) and therefore is expected to contribute even less to homoconjugation and bathochromic absorption shift (**Figure 2.6b**). The iminostilbene moiety in DASA-11 adopts a boat-like conformation similar to experimental solid-state structures⁴⁶ of iminostilbene derivatives causing both phenyl rings to be substantially out-of-plane ($\Phi_{D-A} \approx 60^\circ$), which explains the hypsochromic shift observed relative to the corresponding *N*-methylaniline derivative (DASA-2). A 11 nm red-shift can be achieved with commercially available and stable *p*-nitroindoline in DASA-10 ($\lambda_{\max} = 656$ nm, **Figure 2.39–40**) relative to the respective 2-methylindoline derivative (DASA-5).¹⁴ Since the planarity of the aryl groups of the donors are critical for increasing conjugation and extending the absorption maximum wavelength we attempted to utilize other cyclic amines, including acridone and carbazole derivatives.

However, it was found that these amines, whose conjugated acids have pK_a values <0 , are either unreactive under the optimized reaction conditions or result in unstable adducts that prevented product characterization.

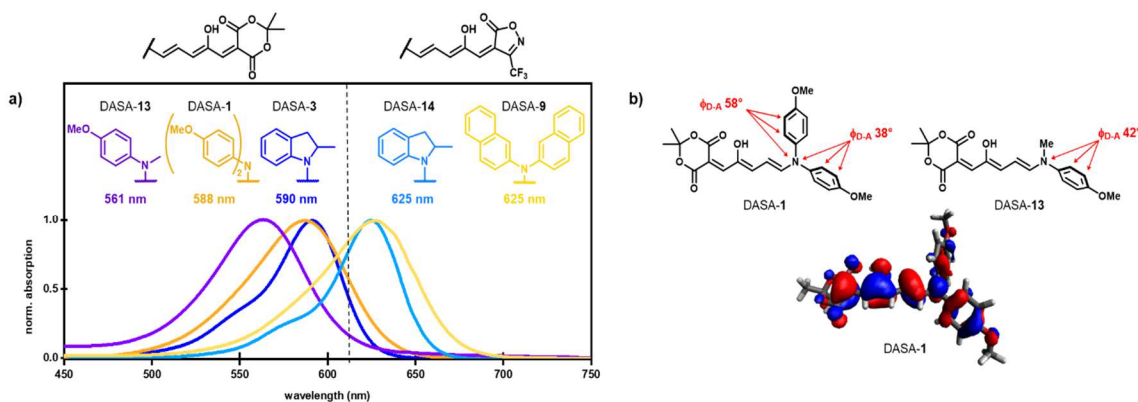


Figure 2.6. UV-Vis absorption properties of novel DASAs. a) Absorption spectra (chloroform) of novel DASA-1 and DASA-9 in comparison to previously reported DASA derivatives.^{12,13} b) Computational density functional theory modelling of DASA-1 determining HOMO orbital overlap and dihedral angles between donor and acceptor (Φ_{D-A}) in comparison to the respective second generation DASA¹³ bearing only one phenyl substituent. Originally published in *Angew. Chem. Int. Ed.*¹ Reprinted with permission of

2.6 Photoswitching of Novel DASAs.

Expanding the scope towards more electron deficient amines allowed us to compare the effect of these weakly donating groups on the photoswitching behavior to the arylamines introduced previously.^{13,14} For this, time dependent UV-Vis spectroscopy for the overall switching kinetics and ¹H-NMR spectroscopy for dark state analysis were utilized (Figures 2.49–54, 2.69–80).

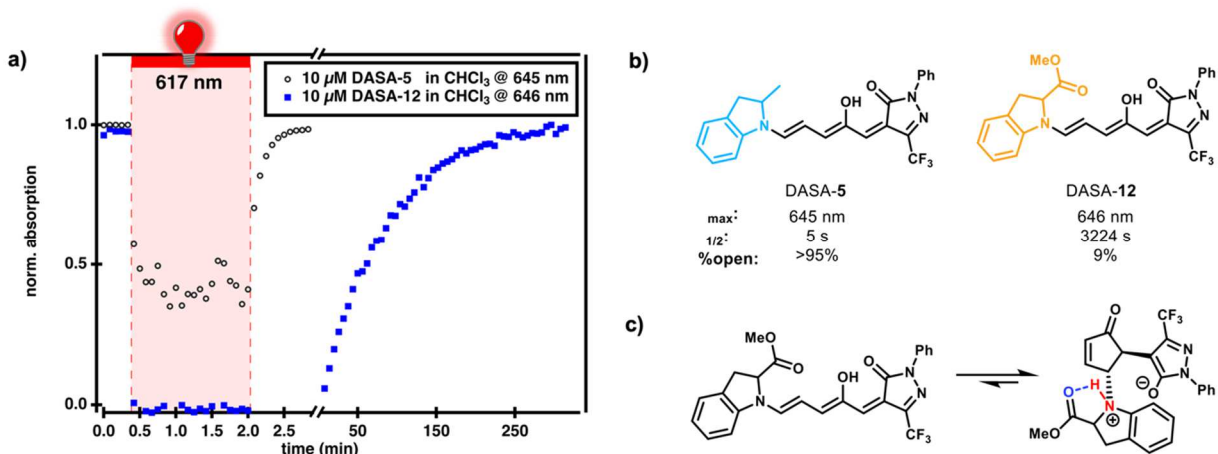


Figure 2.7. Photochromic properties of DASA-12 in comparison to DASA-5. a) Time dependent UV-Vis spectroscopy to observe the photochromism of DASA-5 and DASA-12 in chloroform at 10 μM (initial absorbance: 0.05 and 0.9) followed at λ_{\max} (645 nm and 646 nm). Quantitative conversion of the open form to the closed form under light irradiation with 617 nm for 100 seconds and subsequent thermal recovery in the dark can be observed. b) Comparison of photochromic parameters for DASA-5 and DASA-12 in chloroform.¹³ c) Presumed hydrogen bonding stabilizing the zwitterionic closed form of DASA-12. Originally published in *Angew. Chem. Int. Ed.*¹ Reprinted with permission of Wiley & Sons.

Detailed results are tabulated in the Chapter 2.10 (**Table 2.3**). Similarly to the introduction of arylamines instead of alkylamines for barbituric acid and Meldrum's acid acceptors reported in 2016,¹³ the use of even more electron deficient amines for pyrazolone and isoxazolone derivatives increased the half-life of their closed form while maintaining the red shifted λ_{max} wavelength these acceptor groups enable (e.g., **DASA-5**: 5 s, **DASA-2**: 13 s, **DASA-11**: 202 s). Another similarity is the shift of the thermodynamic equilibrium towards the closed isomer for more weakly donating amines as evidently observed for **DASA-8** and **DASA-10** (both <5% open at equilibrium in chloroform), which is in accordance with previous studies.¹¹ This electronic effect on the equilibrium position can be compensated by introducing sterically hindered groups as shown in 2018,¹⁵ which is in line with what we observed when utilizing amines with bulky secondary phenyl moieties in **DASA-1**, **DASA-9** and **DASA-11** (32%, >95% and 89% open at equilibrium in chloroform). This allows for the formation of DASAs with high amount of open form in the dark while exhibiting long lived closed form isomers after photoswitching, which could previously not be decoupled.¹²⁻¹⁴ One interesting exception to this trend is **DASA-12**, which includes a sterically bulky methylester in the 2-position of an indoline donor. Against expectation, the thermodynamic equilibrium is massively shifted towards the closed form when compared to the previously published 2-methylindoline derivative (**DASA-5**) while the half-life of the closed form after irradiation is immensely increased (>3000 s vs. 5 s, **Figures 2.7a-b**). As a result of the increased stability of the closed form of **DASA-12**, it could be shown by 2D-NMR spectroscopy (**Figures 2.81-82**) to be zwitterionic in chloroform. This is the first report on the nature of the closed form of a DASA with a third generation acceptor and aryl donor

demonstrating a clear difference to the second generation Meldrum's and barbituric acid derivatives residing mostly in the keto isomer closed form.^{12,13,45}

2.7 Fluorescence of DASA-9.

Beyond controlling the half-life, novel properties can be introduced by utilization of functional amines. Subjection of fluorescent 2,2'-dinaphthylamine with furan adduct **S4** in the presence of HFIP 20 vol% in dichloromethane afforded DASA-9. Interestingly, it was found that DASA-9 shows fluorescence emission with a maximum at ~400 nm upon excitation into the absorption bands that are characteristic for the naphthyl groups (300-350 nm, **Figures 2.82–85**). The shape and position of the fluorescence emission band did not change, and the intensity of the emission was found to change only slightly, when the DASA is converted to the closed form (**Figure 2.85**). This is in agreement with DFT calculations that predicted a limited electronic coupling between the naphthyl groups and the acceptor-triene system in the open form (**Table 2.2**). However, we cannot completely exclude that trace amounts of highly fluorescent, free 2,2'-dinaphthylamine is present, which could complicate the fluorescence measurements. DASAs in general are weakly fluorescent when excited at their maximum absorbance wavelength (π - π^* transition of open form) so that prior examples of strongly fluorescent DASAs have been limited to systems that are based on the attachment of separate fluorophores.^{47–50} Introducing easily accessible fluorescent donors could thus enable further development of multifunctional materials and easily identifiable DASA functionalized materials.

2.8 Polymer Conjugation.

The utility of HFIP to promote the formation of DASAs was also explored beyond small molecules by investigating its applicability to the synthesis of DASA-polymer conjugates. Previous synthesis of DASA-polymer conjugates relied on first installing secondary amine precursors onto the polymer and then a subsequent reaction with an excess of furan adduct.^{18,19,51,52} While this approach provided access to DASA-polymer conjugates, it suffered from slow reaction and favoured the use of electron rich amine donors. As such, we were pleased to discover that HFIP improved access to DASA-polymer conjugates reducing the reaction time from days to hours (**Figure 2.8a**). For example, treatment of a

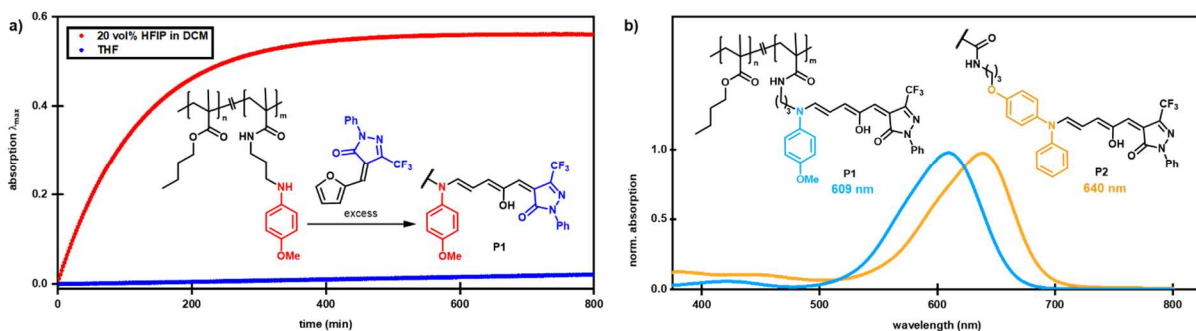


Figure 2.8. HFIP-promoted synthesis of DASA-polymer conjugates and properties of resulting polymers. a) *In situ* absorbance monitoring at λ_{max} (open form DASA) of furan ring opening reaction to afford P1 in THF or using HFIP in dichloromethane. b) Absorption spectra (chloroform) and chemical structures of DASA functionalized poly(butyl methacrylate) polymers P1 and P2 (*m*: 4 mol%). Originally published in *Angew. Chem. Int. Ed.*¹ Reprinted with permission of Wiley & Sons.

N-methoxymethylaniline functionalized simple model poly(butyl methacrylate) with an excess of the CF₃-pyrazolone derived furan adduct in 20 vol% HFIP in dichloromethane for 5 h yielded the novel DASA polymer (**P1**). To further demonstrate the power and generality

of this HFIP-accelerated postfunctionalization approach, we sought to broaden the process to diphenylamine as weak amine donor, which is largely unreactive under previously reported reaction conditions. The polymer bearing diphenylamines was synthesized using aminolysis of activated ester groups.¹⁸ Treatment of this material with an excess of CF₃-pyrazolone furan adduct in 20 vol% HFIP in dichloromethane overnight and subsequent purification by size exclusion chromatography gave DASA-polymer conjugate **P2** (characterization data for the polymers can be found in the Supporting Information). Analysis by UV-Vis spectroscopy confirmed the formation of the novel DASA adduct (**Figure 2.8b**). The DASA-polymer conjugates can be converted to the closed form upon irradiation (PTSS of 40% closed form for **P1** and 85% for **P2** in toluene) and fully recover their initial absorbance in the dark (**Figures 2.65–68**). These examples highlight that the new reaction conditions improve reaction rates and provide access to new DASA-based functional materials with greater tunability of absorption wavelength and photoswitching response.

2.9 Conclusion

In conclusion, we have developed a practical solution for accelerating the furan ring opening reaction in the DASA synthesis by using HFIP. Importantly, the new methodology can be performed at ambient temperature and HFIP can be readily removed from the reaction mixture by simple evaporation. We demonstrate that the addition of HFIP greatly shortens the reaction time and improves isolated yields of novel as well as previously reported adducts, including DASA-polymer conjugates. Furthermore, the method offers access to a broader scope of DASA photoswitches by enabling the use of electron deficient aromatic amines and new furan adducts. The introduction of sterically hindered, electron poor donors allow for the design of DASA derivatives with long closed form half-lives after photoswitching, while

maintaining high amounts of open isomer in the dark. Moreover, the use of HFIP allows more facile and faster access to DASA-polymer conjugates lowering the barrier of entry into the growing field of functional DASA materials. HFIP as external modulator of DASA photoswitching kinetics will further enable the design of systems with tailored response for selected applications.

2.10 Additional Information

2.10.1 General Experimental Procedures for Chemicals and Instruments

2.10.1.1 Chemicals

All commercially obtained reagents were bought from Sigma Aldrich, TCI Europe or Fisher Scientific and were used without purification, except furfural, which was distilled prior to usage. Size exclusion beads (Bio-Beads S-X1 Support, 0.6–14 kDa) were obtained from Bio-Rad Laboratories. Anhydrous solvents were either obtained from Sigma Aldrich or from a solvent purification system.

2.10.1.2 Instruments and Methods

Room temperature reactions were carried out between 22–25 °C. Thin layer chromatography (TLC) was performed using Merck TLC plates (silica gel 60 F254 on aluminum) and visualized by UV light (254/ 366 nm) or staining with KMnO₄/NaOH. Silica gel chromatography was performed using silica gel from Sigma Aldrich (technical grade, 60 Å pore size, 40–63 µm particle size). Size exclusion chromatography (SEC) was performed on Bio-Beads S-X1 Support beads using distilled THF as mobile phase. ¹H and ¹³C nuclear magnetic resonance (NMR) spectra were measured at 298 K on a Bruker Avance III 400 (400 MHz) NMR spectrometer, a Varian Unity Inova 500 MHz, or a Varian Unity Inova AS600 600 MHz spectrometer. ¹⁹F NMR spectra were recorded on a Bruker Avance III 400 (400 MHz) NMR spectrometer. Chemical shifts (δ) are reported in ppm and referenced internally from the proteo-solvent resonance. Coupling constants (J) are reported in Hz. Abbreviations for the peak multiplicities are *s* (singlet), *d* (doublet), *dd* (doublet of doublet), *t* (triplet), *q*

(quadruplet) and *m* (multiplet). For diffusion-edited ^1H NMR spectra, 40% gradient strengths were applied to selectively suppress the signals of low molecular weight species. Gas chromatography/electron impact ionization-mass spectrometry (GC/EI-MS) was measured on a Thermo Scientific ISQ GC/MS equipped with an ISQ 7000 and Trace 1300 GC using a Thermo Scientific TG-SQC capillary column (15 m, 0.25 mm I.D., 0.25 μm thickness). Split/splitless injector at 280 $^\circ\text{C}$; flowrate at 1 mL min^{-1} ; gradient set to 20 $^\circ\text{C min}^{-1}$ from 30 $^\circ\text{C}$ to 300 $^\circ\text{C}$, then isothermal for another 4 min. EI set to 70 eV; single stage quadrupole mass analyzer; mass range 35–600 amu at 2 scans min^{-1} in full scan mode. The retention time (R_t) is reported in min, the mass of molecular ions and characteristic fragments with >15 rel.% are reported as m/z (rel.%). High resolution mass spectrometry (HR-MS) was measured on a Waters LCT Premier ESI TOF. Attenuated total reflection Fourier-transform infrared (ATR FT-IR) spectra were recorded on a Varian 640-IR FT-IR spectrometer equipped with an ATR (attenuated total reflection) accessory or a Thermo Nicolet iS10 FTIR Spectrometer with a Smart Diamond ATR; applied as neat samples and absorbance bands reported as $1/\lambda$ in cm^{-1} . Abbreviations for the relative band intensities are *s* (strong), *m* (medium), *w* (weak). Gel permeation chromatography (GPC) was measured on an Agilent 1100 Series high-performance liquid chromatography (HPLC) system on serial coupled PSS SDV 5 m 100 \AA and PSS SDV 5 m 1000 \AA columns maintained at 30 $^\circ\text{C}$ (allows separation from ca. 1–1000 kDa). Signals were recorded on a diode array detector (235 nm/ 360 nm) and a refractive index (RI) detector (at 35 $^\circ\text{C}$). Measurements were performed in THF as an eluent relative to narrow molecular weight PS standards. UV-Vis absorbance spectra were recorded on an Agilent Cary 4000 UV-Visible spectrophotometer or an Agilent 8453 UV-Visible Spectrophotometer G1103A. Details for UV-Vis absorption and photoswitching measurements are presented in

the respective *section 8*. Photoluminescence spectra were measured on a Horiba Scientific Fluoromax-Plus fluorescence spectrometer at room temperature (excitation and emission slit widths were set to 2 nm unless otherwise stated).

2.10.2 Synthesis

2.10.2.1 Proposed Mechanism

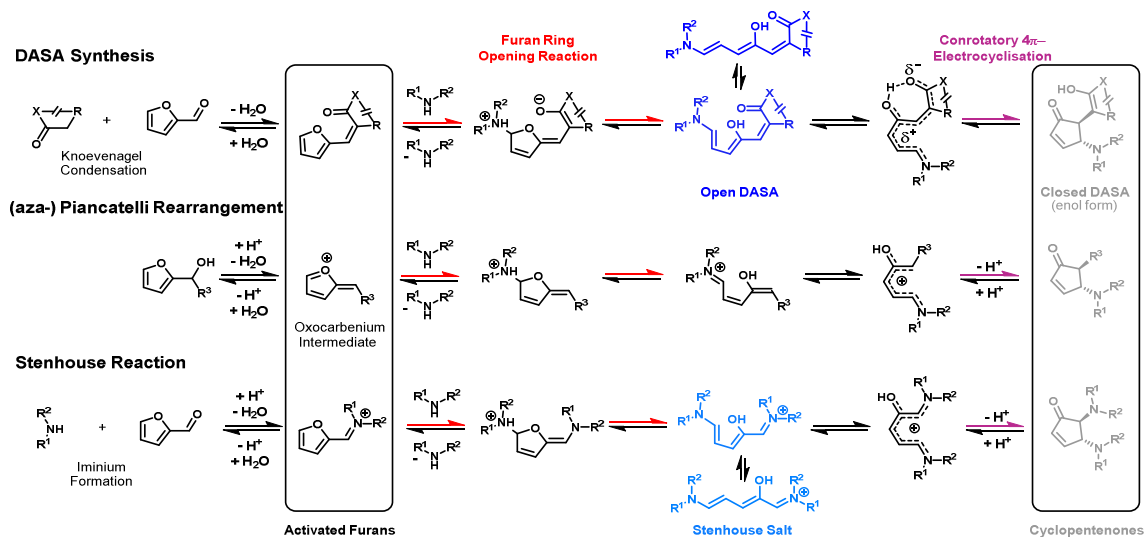
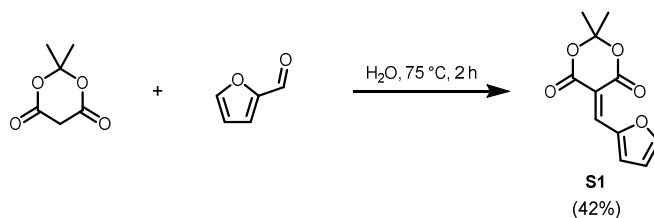


Figure 2.9. Similarities between the proposed mechanism of DASA synthesis, aza-Piancatelli rearrangement^{53,54} and Stenhouse reaction.²⁴

2.10.2.2 Furan Adducts

Compounds **1** and **S1-S4** were prepared similarly to literature procedures and the spectral analysis matched literature data.^{8,14}

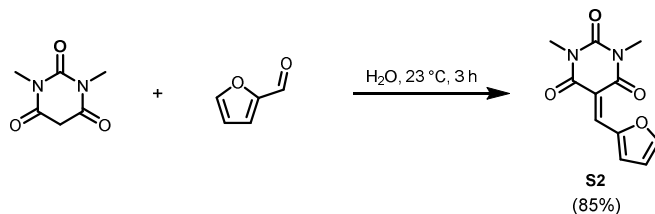
5-(furan-2-ylmethylene)-2,2-dimethyl-1,3-dioxane-4,6-dione (**S1**).



2,2-dimethyl-1,3-dioxane-4,6-dione (11.5 g, 80 mmol, 1.0 eq.) and 2-furaldehyde (7.7 g, 80 mmol, 1.0 eq.) were added to 60 mL H₂O. This suspension was heated to 75 °C and stirred for 2 h when a brown precipitate formed. The mixture was cooled to room temperature

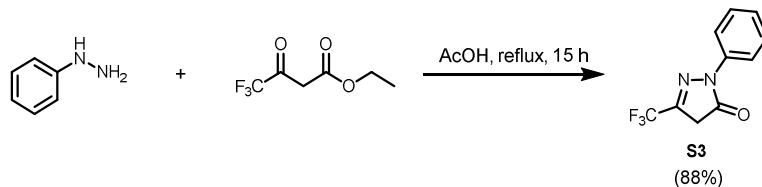
and the precipitate was collected by vacuum filtration and recrystallized from EtOH twice yielding **S1** as a yellow solid (7.5 g, 34 mmol, 42%). ¹H NMR (400 MHz, CDCl₃) δ/ppm: 8.46 (*d*, *J* = 3.9 Hz, 1H, CHCHCHO), 8.35 (*s*, 1H, OCCCH), 7.84 (*d*, *J* = 1.4 Hz, 1H, CHO), 6.75 (*dd*-like *m*, "*J*" = 3.9, 1.0 Hz, 1H, CHCHO), 1.77 (*s*, 6 H, 2 x CH₃); ¹³C NMR (100 MHz, CDCl₃) δ/ppm: 163.4 (C=O), 160.3 (C=O), 150.5 (arom. CH), 150.4 (quart. C), 141.4 (arom. CH), 128.2 (arom. CH), 115.4 (arom. CH), 107.7 (quart. C), 104.6 (quart. C), 27.7 (CH₃); GC/EI-MS (*R*_t = 12.3 min): 222 (100, *M*⁺), 165 (29), 164 (68), 120 (100, [*M*-CO₂-O(CH₃)₂]⁺), 96 (53), 92 (59), 64 (34), 63 (59), 58 (16), 44 (27), 43 (68).

5-(furan-2-ylmethylene)-1,3-dimethylpyrimidine-2,4,6(1H,3H,5H)-trione (S2).



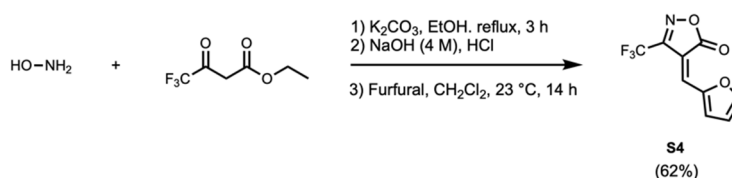
1,3-dimethylpyrimidine-2,4,6(1H,3H,5H)-trione (2.0 g, 13 mmol, 1.0 eq.) and 2-furaldehyde (1.3 g, 14 mmol, 1.1 eq.) were added to 40 mL H₂O and it was stirred for 3 h at room temperature, when reaction control by TLC showed complete consumption of the starting material. A yellow precipitate formed during the course of the reaction, which was collected by vacuum filtration and washed with ice-cooled H₂O (2 x 30 mL). The obtained solid was passed through a silica plug with DCM as the solvent. After removal of the solvent *in vacuo* S2 was obtained as a yellow powder in a yield of 85% (2.6 g, 11 mmol). ¹H NMR (400 MHz, CDCl₃) δ/ppm: 8.63 (*d*, *J* = 3.8 Hz, 1H, CHCHCHO), 8.43 (*s*, 1H, OCCCH), 7.85 (*d*, *J* = 1.4 Hz, 1H, CHO), 6.74 (*ddd*-like *m*, "*J*" = 3.9, 1.6, 0.7 Hz, 1H, CHCHO), 3.41 (*s*, 3 H, CH₃), 3.40 (*s*, 3 H, CH₃); ¹³C NMR (100 MHz, CDCl₃) δ/ppm: 162.6 (C=O), 161.0 (C=O), 151.5 (C=O), 151.3 (quart. C), 150.5 (arom. CH), 141.1 (arom. CH), 128.2 (arom. CH), 115.3 (arom. CH), 111.5 (quart. C), 29.1 (CH₃), 28.4 (CH₃); GC/EI-MS (R_t = 13.9 min): 234 (100, M⁺), 206 (36), 149 (29), 133 (35), 120 (63), 106 (16), 93 (22), 92 (56), 66 (81), 64 (26), 63 (43).

2-phenyl-5-(trifluoromethyl)-2,4-dihydro-3H-pyrazol-3-one (S3).



Phenylhydrazine (2.4 mL, 24 mmol, 1.0 eq.) and ethyl 4,4,4-trifluoroacetoacetate (3.5 mL, 24 mmol, 1.0 eq.) were dissolved in 6 mL AcOH and heated to reflux under N₂ for 15 h while stirring. The reaction mixture was then allowed to cool to room temperature whereupon beige crystals formed. The crystals were filtered off with a Buchner funnel, washed with H₂O (10 mL) and dried in a desiccator overnight (yield 4.8 g, 21 mmol, 88%). NMR characterization is of enol form of product. ¹H NMR (400 MHz, DMSO-*d*₆) δ/ppm: 12.43 (*br s*, 1H, OH), 7.71 (*d-like m*, "J"= 7.6 Hz, 2H, arom. H), 7.51 (*t-like m*, "J"= 7.4 Hz, 2H, arom. H), 7.38 (*tt-like m*, "J"= 7.4, 1.5 Hz, 1H, NCCHCHCH), 5.94 (*s*, 1H, CF₃CCH); ¹³C NMR (100 MHz, DMSO-*d*₆) δ/ppm: 153.7 (COH), 140.4 (*q*, ²J_{CF} = 37 Hz, CCF₃), 137.7 (quart. arom. C), 129.1 (arom. CH), 127.2 (NCCHCHCH), 122.3 (arom. CH), 121.4 (*q*, J_{CF} = 269 Hz, CF₃), 85.6 (*m*, ³J_{CF} = 2 Hz, CHCCF₃); GC/EI-MS (R_t = 11.4 min): 228 (100, M⁺), 105(23), 77(59).

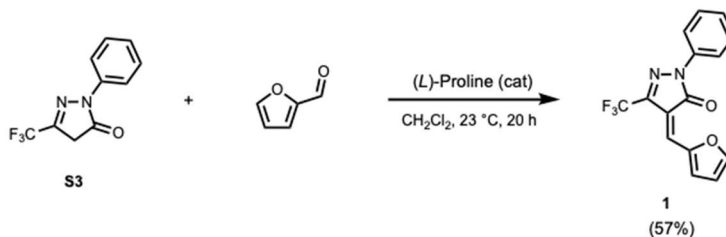
4-(furan-2-ylmethylene)-3-(trifluoromethyl)isoxazol-5(4H)-one (S4).



Hydroxylamine hydrochloride (1.9 g, 27 mmol, 2.3 eq.), 4,4,4-trifluoroacetoacetate (2.4 g, 12 mmol, 1.0 eq.) and K_2CO_3 (3.8 g, 27 mmol, 2.3 eq.) were heated to reflux in EtOH (15 mL) for 3.5 hours while stirring. The reaction mixture was allowed to cool to room temperature, and the solvent was removed under reduced pressure. The yellowish residue was re-dissolved in 10 mL of an aqueous solution of NaOH (4 M) and stirred at 23 °C for 10 min. This solution was then acidified with conc. HCl to a pH value of 2 and extracted with DCM (3 x 50 mL). The organic phase was dried with MgSO_4 , filtered and the solvent was removed *in vacuo* to afford a yellow oil (1.8 g). This oil was re-dissolved in DCM (20 mL), 2-furaldehyde (1.4 g, 15 mmol) was added, and it was stirred at 23 °C for 14 h until the mixture turned brown. H_2O (10 mL) was added and DCM was removed *in vacuo*. The precipitated brown solid was collected by filtration, rinsed with H_2O and dried in a desiccator. Purification was done by passing the product through a silica plug with DCM as an eluent. After removal of the solvent *in vacuo*, the product **S4** was obtained as a yellow solid (1.7 g, 7.4 mmol, 62%). ^1H NMR (400 MHz, CDCl_3) δ /ppm: δ 8.75 (*d*, $J = 3.8$ Hz, 1H, CHCHCHO), 7.94 (*d*, $J = 1.4$ Hz, CHO), 7.72 (*s*, 1H, CF_3CCCH), 6.86 (*ddd*, $J = 3.9, 1.6, 0.7$ Hz, 1H, CHCHO); ^{13}C NMR (100 MHz, CDCl_3) δ /ppm: 167.1 (C=O), 153.9 (*q*, $^2J_{\text{CF}} = 38$ Hz, CCF_3), 152.1 (arom. CH), 150.5 (quart. C), 134.5 (*m*, $^4J_{\text{CF}} = 1$ Hz, CHCCCF_3), 129.7 (arom. CH), 118.8 (*q*, $J_{\text{CF}} = 273$ Hz, CF_3), 116.5 (arom. CH), 106.9 (quart. C); GC/EI-MS ($R_t = 9.8$ min): 231 (87, M^+), 173(100), 162(29), 145(33), 125(28), 106(16), 95(28), 75(19), 63(23).

4-(furan-2-ylmethylene)-2-phenyl-5-(trifluoromethyl)-2,4-dihydro-3H-pyrazol-3-one

(1).

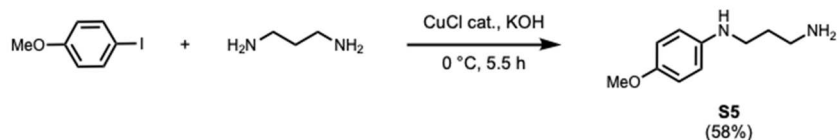


S3 (2.5 g, 11 mmol, 1 eq.) and 2-furaldehyde (1.9 g, 20 mmol, 1.8 eq.) were combined in 30 mL DCM and (*L*)-proline (0.21 g, 1.9 mmol, 0.1 eq.) was added. The mixture was stirred at 23 °C for 20 h and passed through a silica plug with DCM as an eluent. To the orange filtrate was added H₂O (20 mL) and this mixture was subjected to reduced pressure to remove the DCM. The precipitated product was then filtered off and rinsed with water to afford **1** as a dark orange solid (1.9 g, 6.3 mmol, 57%). ¹H NMR (400 MHz, CDCl₃) δ/ppm: 8.92 (*d*, *J* = 3.9 Hz, 1H, *CHCHCHO*), 7.92 (*d*, *J* = 7.9 Hz, 2H, *NCCH*), 7.87 (*d*, *J* = 1.3 Hz, 1H, *CHO*), 7.69 (*s*, 1H, *CF₃CCCH*), 7.46 (*t*, *J* = 8.0 Hz, 2H, *NCCHCH*), 7.29 – 7.26 (*m*, 1H, *NCCHCHCH*), 6.80 (*dd*-like *m*, "*J*" = 3.9, 1.3 Hz, 1H, *CHCHO*); ¹³C NMR (100 MHz, CDCl₃) δ/ppm: 161.5 (C=O), 150.9 (CC=O), 150.8 (*CHO*), 140.0 (*q*, ²*J*_{CF} = 37 Hz, *CCF₃*), 137.8 (*CCHCHCHO*), 131.7 (*m*, ⁴*J*_{CF} = 1 Hz, *CHCCCF₃*), 129.1 (arom. CH), 128.1 (arom. CH), 126.3 (arom. CH), 120.1 (*q*, *J*_{CF} = 272 Hz, *CF₃*), 120.0 (arom. CH), 115.9 (*NCCH*), 115.8 (arom. CH). GC/EI-MS (*R*_t = 14.0 min): 306 (75, *M*⁺), 77(100), 51(21).

2.10.2.3 Amines

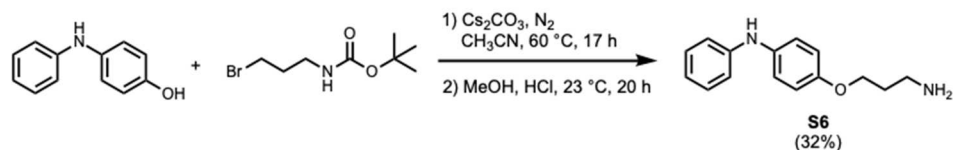
Compound **S5** and **S7** were prepared according to literature procedure and spectral analysis matched literature data.^{55,56}

***N*-(4-Methoxyphenyl)propane-1,3-diamine (S5).**



4-Iodoanisole (3.9 g, 17 mmol, 1.0 eq.), CuCl (freshly recrystallized from MeOH and dry, 0.17 g, 1.7 mmol, 0.1 eq.) and a fine and well dried powder of KOH (1.6 g, 28 mmol, 1.6 eq.) were added to a dry 100 mL round-bottom flask equipped with a stirrer and a septum under N₂. The flask was immersed into an ice-water bath and 1,3-diaminopropane (6.3 mL, 5.6 g, 76 mmol, 4.5 eq.) was added slowly at 0 °C. The reaction mixture turned dark blue overtime. After stirring at 0 °C for 5.5 h, the mixture was exposed to air and 30 mL of H₂O were added. It was extracted with DCM (3 x 150 mL) and the organic phase was dried over MgSO₄, filtered and solvent was removed *in vacuo* to yield the crude product as a brown oil (2.5 g). The product was purified via column chromatography on silica gel (DCM/methanol/ammonia 20:10:1) to afford **S5** as brownish oil (1.8 g, 9.9 mmol, 58%). ¹H NMR (400 MHz, *d*-MeOD) δ/ppm: δ 6.75 (*d-like m*, "J" = 9.1 Hz, 2H, arom. H), 6.65 (*d-like m*, "J" = 8.9 Hz, 2H, arom. H), 3.70 (*s*, 3 H, OCH₃), 3.09 (*t*, J = 7.0 Hz, 2H, CH₂), 2.75 (*t*, J = 7.2 Hz, 2H, CH₂), 1.75 (*q*, J = 7.0 Hz, 2H, CH₂CH₂CH₂); GC/EI-MS (R_t = 12.3 min): 180 (72, M⁺), 148(17), 136(100), 123(30), 108(22).

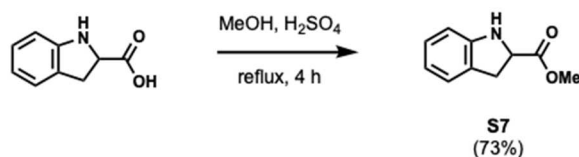
4-(3-Aminopropoxy)-diphenylamine (S6).



3-Bromopropylamine hydrobromide was *N*-*boc* protected as described in literature.⁵⁷ 4-Hydroxydiphenylamine (2.50 g, 13.5 mmol, 1.0 eq.), Cs₂CO₃ (14.6 g, 44.7 mmol, 3.3 eq.) and 3-(*N*-*Boc*)aminopropyl bromide (3.50 g, 14.7 mmol, 1.1 eq.) were added to a two-neck 250 mL round bottom flask equipped with a magnetic stir bar, a septum and a reflux condenser under N₂. CH₃CN (anhydrous, 75 mL) was added and the obtained suspension was heated to 60 °C under N₂ and stirred for 17 h. The mixture was then allowed to cool to room temperature and the solvent was removed *in vacuo*. The residue was taken up in AcOEt (150 mL) and extracted with H₂O (2 x 50 mL) and brine (50 mL). The organic layer was dried over MgSO₄, filtered and the solvent removed *in vacuo* to yield a brown solid, which was re-dissolved in MeOH (15 mL) acidified with conc. HCl (2 mL). This solution was stirred at 23 °C under N₂ for 20 h when reaction control by TLC (AcOEt/heptane 1:2) showed complete deprotection. The solution was then cooled to 0 °C in an ice-water bath and basified with an aqueous solution of NaOH (4 M) to a pH value of 9. H₂O (15 mL) was added and a beige precipitate formed, which was collected by filtration. The product was purified via column chromatography on silica gel (DCM/methanol/ammonia 20:10:1) to afford **S6** as brownish solid (1.05 g, 4.30 mmol, 32%). ¹H NMR (400 MHz, CDCl₃) δ/ppm: 7.21 (*t*-like *m*, "J" = 7.9 Hz, 2H, arom. H), 7.05 (*d*-like *m*, "J" = 8.9 Hz, 2H, arom. H), 6.91 – 6.81 (*m*, 5 H, arom. H), 5.49 (*br s*, 1H, NH), 4.03 (*t*, J = 6.1 Hz, 2H, CH₂), 2.92 (*t*, J = 6.8 Hz, 2H, CH₂), 1.92 (*q*, J =

6.4 Hz, 2H, CH₂CH₂CH₂), 1.31 (*br s*, 2H, NH₂). ¹³C NMR (100 MHz, CDCl₃) δ/ppm: 154.8 (quart. C), 145.3 (quart. C), 135.9 (quart. C), 129.4 (2xCH), 122.3 (2xCH), 119.7 (CH), 115.8 (2xCH), 115.5 (2xCH), 66.4 (CH₂), 39.5 (CH₂), 33.3 (CH₂); IR (ATR, cm⁻¹): 3409*w*, 3369*w*, 3249*w*, 3183*w*, 3098*w*, 3029*w*, 2998*w*, 2931*w*, 2872*w*, 2858*w*, 1596*m*, 1505*s*, 1493*s*, 1471*s*, 1445*m*, 1397*w*, 1321*m*, 1596*m*, 1225*s*, 1174*m*, 1114*m*, 1074*w*, 1025*m*, 993*w*, 941*w*, 877*m*, 818*s*, 792*m*, 741*s*, 693*s*; HR-MS (ESI+) *m/z* 243.1498, calc. 243.1497 for [M + H]⁺; GC/EI-MS (R_t = 15.2 min): 242 (37, M⁺), 186(23), 185(100, [M-C₃H₈N⁺+H]⁺), 184(46).

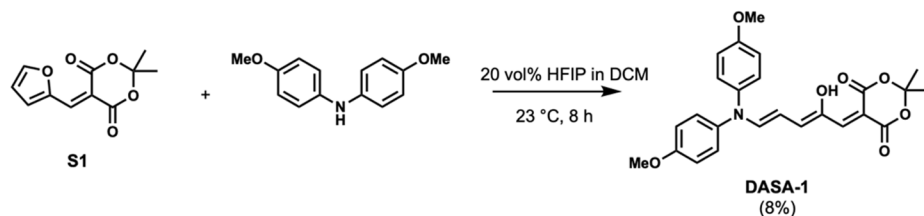
Methyl indoline-2-carboxylate (**S7**).



Indoline-2-carboxylic acid (2 g, 12 mmol, 1 eq.) was dissolved in methanol (25 mL). Concentrated sulfuric acid (5 mL) was added and the solution was heated to reflux for 4 h. After letting the solution cool to room temperature, it was neutralized with sodium bicarbonate and subsequently extracted with AcOEt (2 x 5 mL). After drying with MgSO₄, the solvent was evaporated under reduced pressure which yielded the product **S7** as a colorless oil (1.56 g, 9 mmol, 73%). The spectral analysis matched literature.⁵⁵

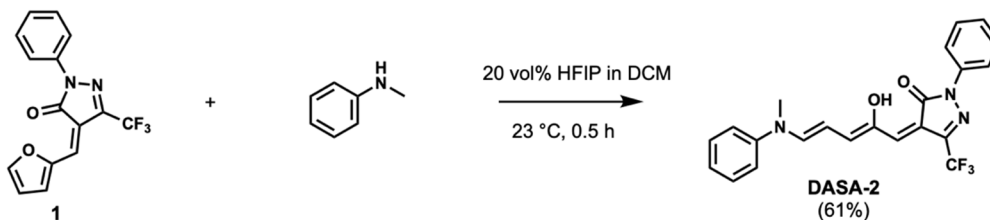
2.10.2.4 DASAs

DASA-1



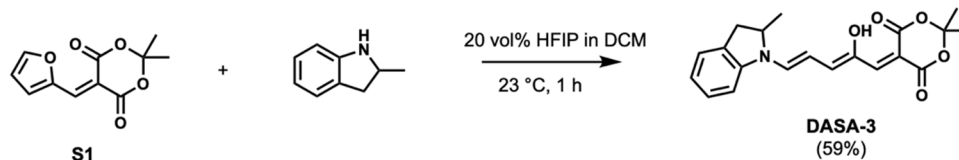
S1 (500 mg, 2.3 mmol, 1.00 eq.) and 4,4'-dimethoxydiphenylamine (500 mg, 2.2 mmol, 0.95 eq.) were dissolved in DCM (0.8 mL). HFIP (0.2 mL) were added and the solution stirred for 8 h. The solvent was removed under reduced pressure and redissolved in 1:1 AcOEt/hexanes (1 mL) and then filtered through a silica plug with first 1:9 AcOEt/hexanes and then 1:1 AcOEt/hexanes as an eluent. The second eluent was collected and the solvent removed under reduced pressure to yield the product as a dark blue solid (80 mg, 0.18 mmol, 8%). ^1H NMR (500 MHz, CDCl_3), closed isomer: δ /ppm: 7.79 (*dd*, $J = 6.0, 1.9$ Hz, 1H), 6.91 – 6.85 (*m*, 4H), 6.85 – 6.79 (*m*, 4H), 6.30 (*dd*, $J = 6.0, 1.9$ Hz, 1H), 5.65 – 5.57 (*m*, 1H), 4.06 – 4.02 (*m*, 1H) 3.77 (*s*, 6H), 3.57 – 3.52 (*m*, 1H), 1.81 (*d*, $J = 8.0$ Hz, 6H); ^{13}C NMR (125 MHz, CDCl_3) δ /ppm: 202.2, 164.8, 164.4, 162.3, 155.7, 144.1, 139.6, 133.8, 123.9, 119.6, 115.3, 114.7, 105.7, 104.0, 62.6, 55.7, 55.6, 55.6, 49.9, 44.1, 28.2, 27.6, 27.6, 27.1, 26.9; HR-MS (ESI+) m/z 474.1522, calc. 474.1525 for $[\text{M} + \text{Na}]^+$; IR (ATR, cm^{-1}): 2923, 1697, 1610, 1592, 1454, 1389, 1376, 1336, 1302, 1243, 1193, 1108, 1020, 926, 908, 826, 767, 728, 714, 680, 623, 601, 545.

DASA-2



1 (100 mg, 0.32 mmol, 1.0 eq.) and *N*-methylaniline (42 mg, 0.40 mmol, 1.2 eq.) were dissolved in DCM (0.8 mL). HFIP (0.2 mL) were added and the solution stirred for 0.5 h. The solvent was removed under reduced pressure and the remaining solid triturated in diethyl ether (1.0 ml). After filtration the product was isolated as a dark blue solid (performed in triplicates: 80/81/87 mg, 0.19/0.19/0.20 mmol, 59/60/64%). ^1H NMR (400 MHz, CDCl_3) δ /ppm: 12.97 (*s*, 1H), 7.93 – 7.88 (*m*, 2H), 7.57 – 7.51 (*m*, 1H), 7.49 – 7.39 (*m*, 5H), 7.31 (*t*, $J = 7.5$ Hz, 1H), 7.25 – 7.18 (*m*, 2H), 6.69 (*d*, $J = 12.1$ Hz, 1H), 6.63 (*s*, 1H), 6.34 (*t*, $J = 12.4$ Hz, 1H), 3.57 (*s*, 3H); ^{13}C NMR (125 MHz, CDCl_3) δ /ppm: 164.3, 163.6, 150.7, 146.9, 138.3, 134.9, 134.4, 130.0, 129.3, 129.0, 128.8, 127.8, 127.0, 125.8, 123.1, 120.5, 119.1, 114.8, 105.9, 68.1, 45.5, 33.1; HR-MS (ESI+) m/z 436.1248, calc. 436.1249 for $[\text{M} + \text{Na}]^+$; IR (ATR, cm^{-1}): 2446, 1604, 1549, 1517, 1497, 1462, 1356, 1309, 1269, 1243, 1228, 1203, 1176, 1159, 1148, 1080, 960, 826, 787, 775, 755, 687.

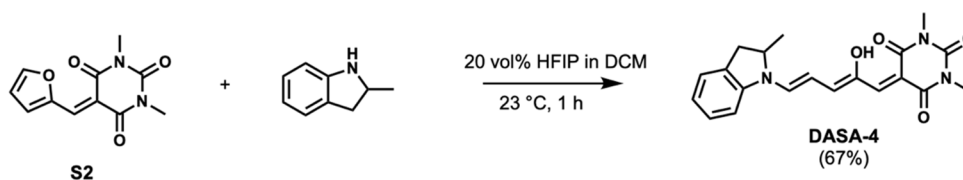
DASA-3



S1 (142 mg, 0.64 mmol, 1.0 eq.) and 2-methylindoline (102 mg, 0.77 mmol, 1.2 eq.) were dissolved in DCM (0.8 mL). HFIP (0.2 mL) were added and the solution stirred for 1 h.

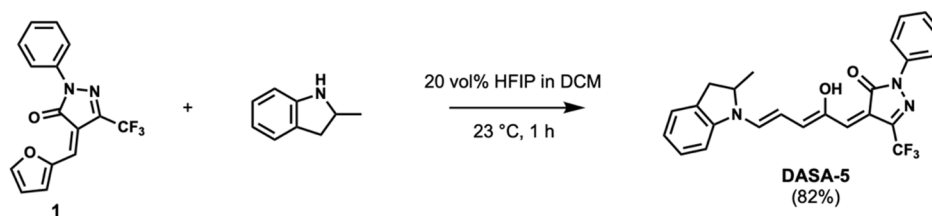
The solvent was removed under reduced pressure and the remaining solid triturated in diethyl ether (1.0 ml). After filtration the product was isolated as a dark blue solid (135 mg, 0.38 mmol, 59%). The spectroscopic data matched literature.¹⁴

DASA-4



S2 (150 mg, 0.64 mmol, 1.0 eq.) and 2-methylindoline (102 mg, 0.77 mmol, 1.2 eq.) were dissolved in DCM (0.8 mL). HFIP (0.2 mL) were added and the solution stirred for 1 h. The solvent was removed under reduced pressure and the remaining solid triturated in diethyl ether (1.0 mL). After filtration the product was isolated as a dark blue solid (158 mg, 0.43 mmol, 67%). The spectroscopic data matched literature.¹⁴

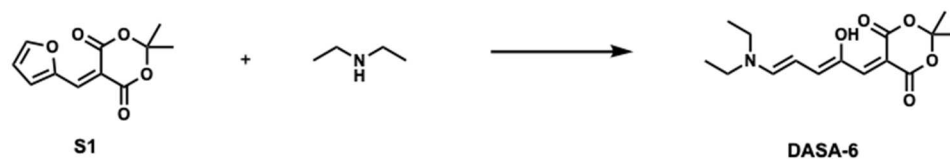
DASA-5



1 (100 mg, 0.32 mmol, 1.0 eq.) and 2-methylindoline (42 mg, 0.32 mmol, 1.0 eq.) were dissolved in DCM (0.8 mL). HFIP (0.2 mL) were added and the solution stirred for 1 h. The solvent was removed under reduced pressure and the remaining solid triturated in diethyl ether

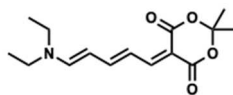
(1.0 mL). After filtration the product was isolated as a dark blue solid (115 mg, 0.26 mmol, 82%). The spectroscopic data matched literature.¹⁴

DASA-6



This compound was prepared analogously to literature procedures. Spectroscopic data matched literature.^{8,9}

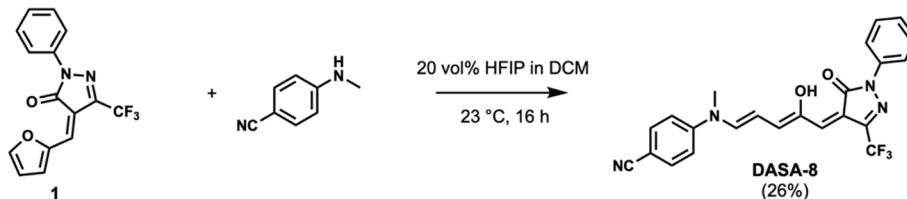
DASA-7



DASA-7

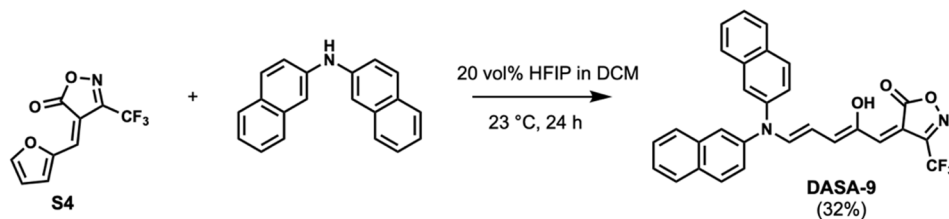
This compound was prepared analogously to literature procedures. Spectroscopic data matched literature.⁴⁴

DASA-8



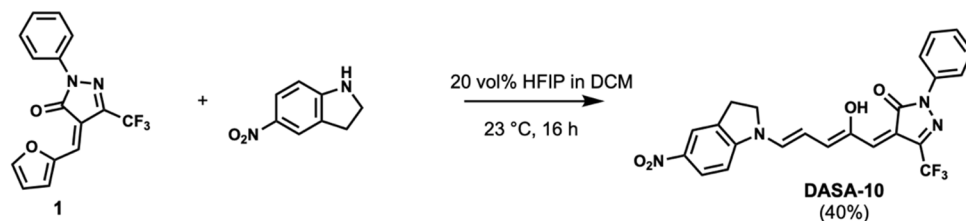
1 (231 mg, 0.75 mmol, 1.0 eq.) and 4-methylaminobenzonitrile (100 mg, 0.75 mmol, 1.0 eq.) were dissolved in DCM (0.8 mL). HFIP (0.2 mL) were added and the solution stirred for 16 h. The solvent was removed under reduced pressure and the remaining solid triturated in diethyl ether (1.0 mL). After filtration the product was isolated as a dark blue solid (84 mg, 0.19 mmol, 26%). ¹H NMR (500 MHz, CDCl₃), closed isomer: δ/ppm: 7.72 – 7.64 (*m*, 1H), 7.60 – 7.52 (*m*, 2H), 7.52 – 7.42 (*m*, 3H), 6.72 – 6.66 (*m*, 2H), 6.58 – 6.49 (*m*, 1H), 5.35 – 5.28 (*m*, 1H), 3.81 – 3.77 (*m*, 1H), 2.91 (*s*, 3H); ¹³C NMR (125 MHz, CDCl₃) δ/ppm: 206.01, 163.2, 152.2, 139.6, 138.8, 137.5, 135.4, 134.0, 129.6, 128.5, 123.5, 123.3, 120.2, 113.1, 100.1, 66.3, 46.7, 32.9; HR-MS (ESI+) *m/z* 461.1194, calc. 461.1201 for [M + Na]⁺; IR (ATR, cm⁻¹): 2223, 1725, 1597, 1518, 1479, 1381, 1347, 1324, 1182, 1141, 1113, 817, 753, 720, 691, 683.

DASA-9



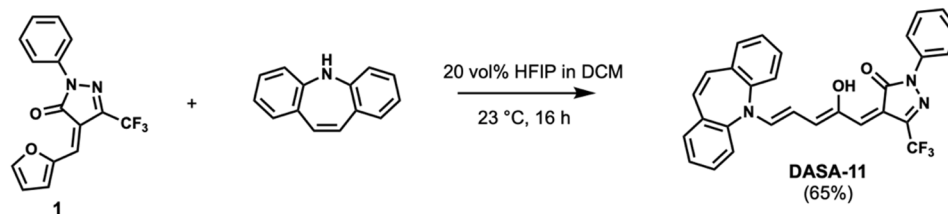
S4 (171 mg, 0.74 mmol, 1.0 eq.) and 2,2'-dinaphthylamine (200 mg, 0.74 mmol, 1.0 eq.) were dissolved in DCM (0.8 mL). HFIP (0.2 mL) were added and the solution stirred for 24 h. The solvent was removed under reduced pressure and the remaining solid triturated in diethyl ether (1.0 mL). After filtration the product was isolated as a dark blue solid (120 mg, 0.24 mmol, 32%). ¹H NMR (500 MHz, CDCl₃) δ/ppm: 11.08 – 11.04 (*m*, 1H), 7.96 – 7.90 (*m*, 2H), 7.86 – 7.80 (*m*, 2H), 7.77 – 7.74 (*m*, 2H), 7.73 – 7.67 (*m*, 2H), 7.67 – 7.56 (*m*, 1H), 7.53 – 7.50 (*m*, 3H), 7.49 – 7.44 (*m*, 1H), 7.38 – 7.32 (*m*, 1H), 7.29 – 7.22 (*m*, 1H), 6.77 (*d*, *J* = 12.6 Hz, 1H), 6.44 (*s*, 1H), 6.30 (*t*, *J* = 12.4 Hz, 1H); ¹³C NMR (125 MHz, CDCl₃) δ/ppm: 175.0, 152.8, 151.7, 150.5, 148.4, 139.2, 134.6, 134.0, 129.3, 128.0, 127.7, 126.6, 126.5, 123.7, 120.3, 116.3, 112.3, 109.5, 96.4; HR-MS (ESI+) *m/z* 523.1233, calc. 523.1240 for [M + Na]⁺; IR (ATR, cm⁻¹): 1660, 1597, 1483, 1457, 1375, 1336, 1291, 1210, 1183, 1133, 982, 942, 769, 739.

DASA-10



1 (100 mg, 0.32 mmol, 1.0 eq.) and 5-nitroindoline (52 mg, 0.75 mmol, 1.0 eq.) were dissolved in DCM (0.8 mL). HFIP (0.2 mL) were added and the solution stirred for 16 h. The solvent was removed under reduced pressure and the remaining solid triturated in diethyl ether (1.0 ml). After filtration the product was isolated as a dark blue solid (60 mg, 0.13 mmol, 40%). ¹H NMR (600 MHz, CDCl₃), closed isomer: δ/ppm: 7.99 – 7.92 (*m*, 2H), 7.75 – 7.70 (*m*, 1H), 7.64 – 7.61 (*m*, 2H), 7.51 – 7.38 (*m*, 3H), 6.59 – 6.55 (*m*, 1H), 6.30 – 6.24 (*m*, 1H), 5.12 – 5.07 (*m*, 1H), 3.98 – 3.95 (*m*, 1H), 3.81 – 3.74 (*m*, 1H), 3.65 – 3.55 (*m*, 1H), 3.18 – 3.11 (*m*, 2H), 2.08 – 1.94 (*m*, 1H); ¹³C NMR (125 MHz, CDCl₃) δ/ppm 162.1, 139.8, 135.6, 129.6, 129.2, 128.7, 126.3, 123.3, 120.9, 105.2, 63.6, 48.9, 44.9, 27.2; HR-MS (ESI+) *m/z* 493.1096, calc. 493.1100 for [M + Na]⁺; IR (ATR, cm⁻¹): 1615, 1599, 1562, 1536, 1493, 1470, 1453, 1364, 1320, 1248, 1214, 1196, 1152, 1107, 978, 944, 914, 899, 878, 781, 755, 742, 709, 685, 660, 582, 559.

DASA-11



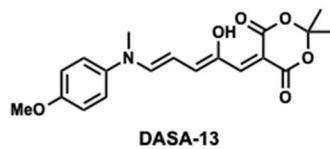
1 (200 mg, 0.65 mmol, 1.2 eq.) and 5H-dibenz[b,f]azepine (101 mg, 0.52 mmol, 1.0 eq.) were dissolved in DCM (0.8 mL). HFIP (0.2 mL) were added and the solution stirred for 16 h. The solvent was removed under reduced pressure and the remaining solid triturated in diethyl ether (1.0 mL). After filtration the product was isolated as a dark blue solid (170 mg, 0.34 mmol, 65%). ^1H NMR (400 MHz, CDCl_3) δ /ppm: 12.81 – 12.77 (*m*, 1H), 7.96 – 7.85 (*m*, 2H), 7.59 – 7.48 (*m*, 3H), 7.50 – 7.34 (*m*, 8H), 7.25 – 7.16 (*m*, 1H), 6.96 – 6.90 (*m*, 2H), 6.63 – 6.55 (*m*, 2H), 6.18 (*t*, $J = 12.5$ Hz, 1H); ^{13}C NMR (125 MHz, CDCl_3) δ /ppm: 164.3, 155.7, 150.6, 146.8, 140.2, 139.9, 138.3, 135.5, 133.3, 132.1, 130.3, 129.7, 129.5, 128.8, 125.8, 123.0, 120.5, 119.9, 119.3, 115.6, 105.1; HR-MS (ESI+) m/z 554.1666, calc. 554.1667 for $[\text{M} + \text{Na} + \text{MeOH}]^+$; IR (ATR, cm^{-1}): 1607, 1554, 1497, 1453, 1430, 1347, 1302, 1202, 1182, 1148, 1108, 1001, 984, 962, 944, 875, 757, 741, 684, 653, 640, 600, 555.

DASA-12



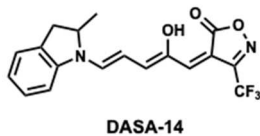
1 (200 mg, 0.65 mmol, 1.1 eq.) and **S7** (104 mg, 0.58 mmol, 1.0 eq.) were dissolved in DCM (0.8 mL). HFIP (0.2 mL) were added and the solution stirred for 16 h. The solvent was removed under reduced pressure and the remaining solid triturated in diethyl ether (1.0 mL). After filtration the product was isolated as a dark blue solid (48 mg, 0.10 mmol, 17%).¹H NMR (500 MHz, CDCl₃) δ/ppm: 7.75 (*d*, *J* = 7.9 Hz, 2H), 7.54 (*d*, *J* = 6.1 Hz, 1H), 7.46 (*t*, *J* = 7.8 Hz, 3H), 7.36 (*q*, *J* = 7.8 Hz, 1H), 7.17 – 7.06 (*m*, 2H), 6.80 (*t*, *J* = 7.4 Hz, 1H), 6.54 (*d*, *J* = 6.1 Hz, 1H), 6.46 (*d*, *J* = 8.0 Hz, 1H), 4.95 – 4.90 (*m*, 1H), 4.37 (*dd*, *J* = 11.5, 5.6 Hz, 1H), 3.89 – 3.81 (*m*, 4H), 3.75 – 3.60 (*m*, 3H), 3.23 (*dd*, *J* = 16.5, 5.6 Hz, 1H); ¹³C NMR (125 MHz, CDCl₃) δ/ppm: 202.4, 158.9, 152.1, 149.7, 137.7, 136.4, 129.0, 128.4, 127.5, 126.5, 124.6, 123.0, 120.3, 109.0, 95.4, 68.0, 60.8, 53.8, 46.5, 34.6; HR-MS (ESI+) *m/z* 506.1297, calc. 506.1304 for [M + Na]⁺; IR (ATR, cm⁻¹): 1739, 1610, 1557, 1489, 1461, 1431 1350, 1315, 1243, 1210, 1162, 1147, 1116, 1042, 984, 961, 945, 869, 835, 788 763, 743, 710, 692, 665, 647.

DASA-13



This compound was prepared analogously to literature procedures. Spectroscopic data matched literature.¹²

DASA-14

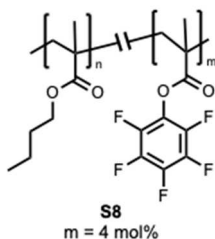


This compound was prepared analogously to literature procedures. Spectroscopic data matched literature.¹³

2.10.2.5 Polymers

Compounds **S8-S10** were prepared similarly to literature procedures.¹⁷

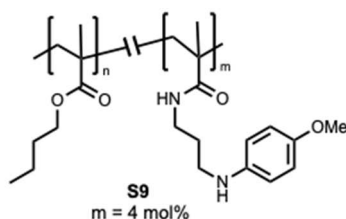
P(BMA-PFPMA) (S8)



The monomers were purified from their polymerization inhibitors by passing them through a basic aluminum oxide plug. Butyl methacrylate (4.95 g, 34.8 mmol, 1.00 eq.), pentafluorophenyl methacrylate (0.370 g, 1.45 mmol, 0.04 eq.) and azobis(isobutyronitrile) (AIBN, recrystallized from MeOH, 70 mg, 0.43 mmol, 0.01 eq.) were dissolved in 10 mL of dry 1,4-dioxane in a round bottom flask equipped with a rubber septum and a magnetic stir bar. The mixture was deoxygenated by bubbling N₂ gas through for 30 minutes. The flask was then immersed into a pre-heated oil bath and the reaction mixture was stirred at 80 °C under nitrogen for 22 h. The solution was allowed to cool to room temperature and diluted with 10 mL of THF. The polymer was precipitated into ice-cold MeOH (175 mL) under rapid stirring, filtered off, washed with MeOH and dried under vacuum to yield **S8** as colorless solid (yield: 4.36 g). ¹H NMR (400 MHz, CDCl₃) δ/ppm: 3.94 (*d*-like *m*, OCH₂), 2.00 – 1.81 (*m*, CH₂), 1.61 (*br s*, CH₂), 1.40 (*d*-like *m*, CH₂), 1.28 – 1.14 (*br*, CH₃), 1.02 (*br s*, CH₃), 0.95 (*br s*, CH₃), 0.87 (*br s*, CH₃); ¹⁹F NMR (377 MHz, CDCl₃) δ/ppm: -149.5 (*s*, 1F), -151.4 (*s*, 1F), - (157.7 – 157.9) (*m*, 1F), -(162.1 – 162.3) (*m*, 2F); IR (ATR, cm⁻¹): 2957*m*, 2932*m*, 2873*w*, 1777*w* (C=O, PFP ester), 1722*s* (C=O, butyl ester), 1519*m* (aryl C-F), 1466*m*, 1450*m*, 1382*w*,

1264m, 1239m, 1171m, 1142s, 1063m, 993m, 964m, 945m, 843w, 748m; GPC: $M_n = 30.3$ kDa, PDI = 2.7.

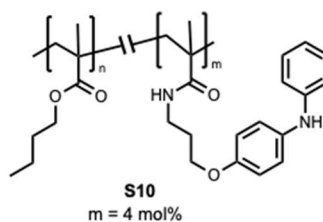
P(BMA-S6MA) (S9)



S8 (1.0 g) was dissolved in 10 mL of anhydrous DMF in a Schlenk tube equipped with rubber septum and magnetic stir bar. **S5** (0.23 g, 1.3 mmol) and TEA (0.20 mL, 0.15 g, 1.5 mmol) were dissolved in 2 mL of anhydrous DMF and added to the polymer solution. The reaction mixture was stirred at 50 °C under nitrogen atmosphere for 5 days until completion. The reaction progress was monitored via IR spectroscopy (disappearance of PFP ester band at 1777 cm^{-1}) of samples precipitated from the reaction mixture by addition to ice-cooled MeOH. After completion of the reaction, the polymer was precipitated into ice-cold methanol/water (5:1, 100 mL) with a few drops of concentrated ammonia and centrifuged. The polymer pellet was dissolved in THF and re-precipitated twice and then dried under vacuum to afford **S9** as white solid (0.98 g). Full conversion of the PFP active ester was confirmed via ^{19}F NMR from the complete disappearance of the fluorine signals. ^1H NMR (400 MHz, CDCl_3) δ /ppm: 6.78 (*d*, $J = 8.3$ Hz, 2 arom. H), 6.63 (*d*, $J = 8.1$ Hz, 2 arom. H), 6.35 – 6.25 (*br*, N-H, amide), 3.94 (*m*, OCH_2), 3.74 (*m*, OCH_3), 3.30 (*br s*, OCNHCH_2), 3.16 (*br s*, CHCNHCH_2), 2.00 – 1.81 (*m*, CH_2), 1.59 (*br s*, CH_2), 1.40 (*d-like m*, CH_2), 1.28 – 1.21 (*br*, CH_3), 1.02 (*br s*, CH_3), 0.94 (*br s*, CH_3), 0.86 (*br s*, CH_3); IR (ATR, cm^{-1}): 3418w, 2956m, 2932m, 2872w, 1721s, 1583w, 1530w, 1465m, 1381w, 1264m, 1239m, 1142s, 1062m, 1019w,

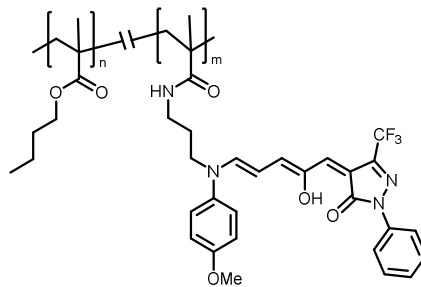
963m, 944m, 844w, 769m, 748m; UV-Vis (DCM) $\lambda_{\text{max}} = 312 \text{ nm}$; GPC: $M_n = 32.0 \text{ kDa}$, PDI = 2.9.

P(BMA-S7MA) (S10)



Same procedure as for **S9** using **S8** (1.0 g) and **S6** (0.26 g, 1.1 mmol). Yield: 0.86 g of an off-white solid. $^1\text{H NMR}$ (400 MHz, CDCl_3) δ/ppm : 7.21 (*t*, $J = 7.5 \text{ Hz}$, 2 arom. H), 7.06 (*d*-like *m*, " J " = 7.1 Hz, 2 arom. H), 6.92 (*d*, $J = 7.7 \text{ Hz}$, 2 arom. H), 6.85–6.81 (*m*, 3 arom. H), 3.93 (*m*, OCH_2 butyl), 3.38 (*br s*, OCNHCH_2), 1.99 – 1.81 (*m*, CH_2), 1.60 (*br s*, CH_2), 1.39 (*d*-like *m*, CH_2), 1.28 – 1.21 (*br*, CH_3), 1.02 (*br s*, CH_3), 0.95 (*br s*, CH_3), 0.87 (*br s*, CH_3); IR (ATR, cm^{-1}): 3420w, 2956m, 2932m, 2872w, 1722s, 1666w, 1600w, 1511w, 1465m, 1385w, 1238m, 1142s, 1062m, 1019m, 996w, 963m, 944m, 843w, 747m, 693w; UV-Vis (DCM) $\lambda_{\text{max}} = 284 \text{ nm}$; GPC: $M_n = 35.5 \text{ kDa}$, PDI = 2.7.

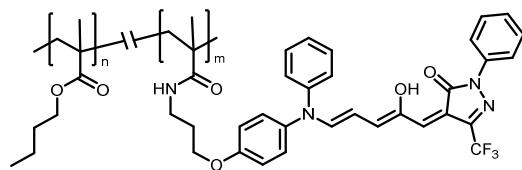
P1



P1
m = 4 mol%

To **S9** (0.25 g) dissolved in DCM (1.5 mL) in a screw cap vial was added **1** (0.30 g, 1 mmol, 0.2 g/mL) and HFIP (0.38 mL). It was stirred at 23 °C in the dark for 5 h. The reaction was monitored via UV-Vis spectroscopy by taking samples and was stopped when the absorbance value of the DASA peak plateaued. Subsequently, the solvent was removed *in vacuo* and the polymer was purified by size exclusion chromatography over Bio-Beads S-X1 Support with distilled THF as the eluent. The excess of **1** could be recovered and reused after separation from the polymer. **P1** was obtained as a deep blue solid (0.25 g). IR (ATR, cm^{-1}): 3420_w, 2956_w, 2932_w, 2872_w, 1721_s, 1600_w, 1558_w, 1471_m, 1455_m, 1379_w, 1239_m, 1145_s, 1114_s, 1062_m, 1020_w, 983_m, 944_m, 878_w, 837_w, 710_w, 785_m, 747_m, 710_m; NMR data in section 11.1.

P2



P2
m = 4 mol%

Same procedure as for **P1** using **S10** (0.20 g) and **1** (0.30 g, 1 mmol, 0.2 g/mL) reacting overnight giving **P2** as a deep blue solid (0.19 g). IR (ATR, cm^{-1}): 3420 w , 2956 w , 2932 w , 2872 w , 1722 s , 1598 w , 1464 m , 1455 m , 1385 w , 1356 w , 1238 m , 1142 s , 1062 m , 1017 w , 945 m , 841 w , 748 m , 692 w ; NMR data in section 11.1.

2.10.3 Kinetics Experiments

2.10.3.1 UV-Vis Spectroscopy

In situ UV-Vis kinetic experiments were performed between 23–25 °C under pseudo-first order conditions using a 100-fold excess of amine reagent. Stock solutions of amine and furan adduct in DCM were freshly prepared and measurements were performed by adding small amounts of stock solutions to the respective DCM/HFIP mixture in a 3 mL quartz cuvette. The absorbance was monitored with an Agilent Cary 4000 UV-Vis spectrophotometer overtime.

2.10.3.2 Rates as Function of HFIP Concentration

Kinetic experiments were done using *N*-methylaniline and **1** for different volumetric ratios of HFIP in DCM (0–90 vol%). Measurements were performed at concentrations of 5×10^{-3} M (amine) and 5×10^{-5} M (furan adduct) at the absorption maximum of **1** (375 nm) and at 565 nm over the time course of 15 to 800 min (**Figure 2.10.2**). Apparent rate constants were obtained by fitting the absorbance changes to one-phase exponential decay functions using Origin 2018 software. R^2 -values reached >0.99 for HFIP concentrations <50 vol%. At concentrations >50 vol% the absorbance changes are not strictly mono-exponential anymore and the rate of DASA formation decreases suggesting the presence of side reactions or degradation of the activated furan. Relative rates ($k_{relative}$) correspond to the apparent rate constants at a given HFIP concentration relative to the apparent rate constant of the reaction in pure DCM (**Figure 2.10.2d**). Note: due to the lower concentrations used in UV-Vis spectroscopic measurements the amount of HFIP relative to **1** was considerably higher than in the NMR kinetic experiments (i.e. 1 vol% HFIP corresponds to a large excess of ~ 1900 equivalents).

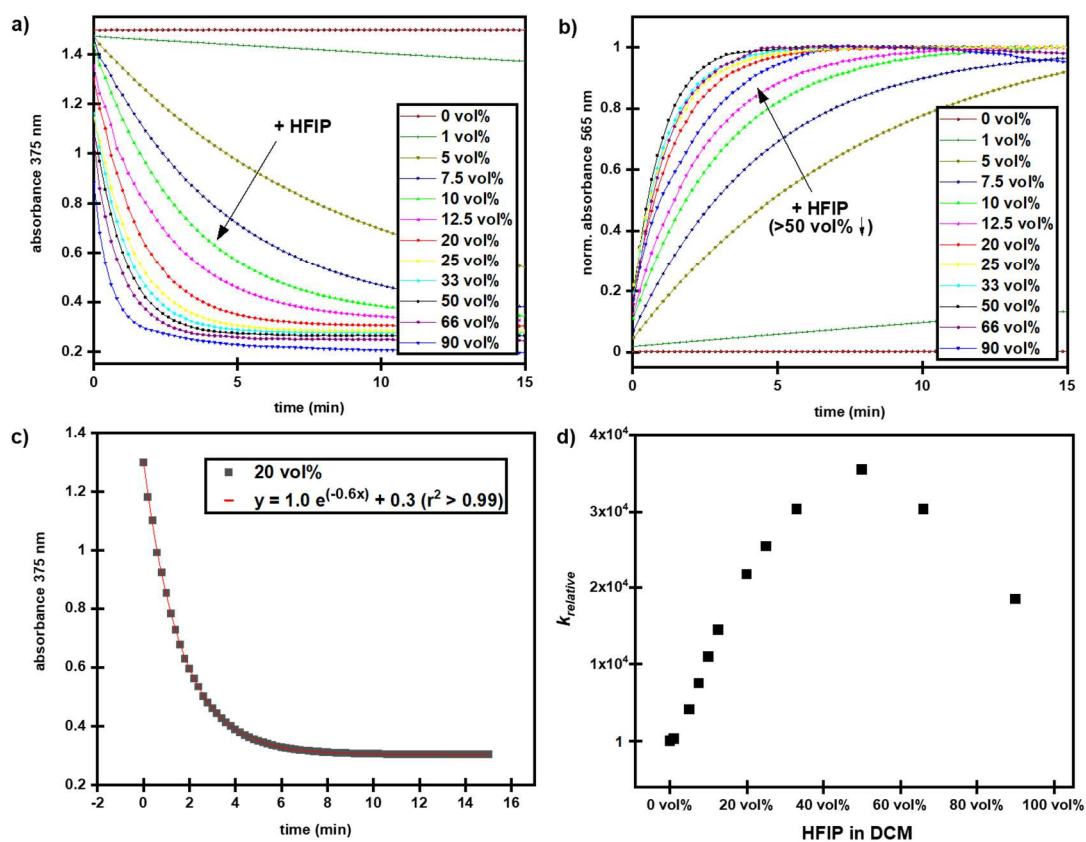


Figure 2.10. UV-Vis kinetic data for the reaction of **1** with *N*-methylaniline as a function of the HFIP concentration in DCM. a) Absorbance change at λ_{max} (375 nm) of **1** as a function of time. b) Absorbance change at 565 nm as a function of time. c) Example of non-linear fit of absorbance decay at 375 nm. d) Relative reaction rates as a function of the HFIP concentration.

Alkyl vs Aryl Amines

The rate of diethylamine (DEA) and *N*-methylaniline in the reaction with **1** was compared in DCM and DCM/HFIP 20 vol%. Measurements were performed at concentrations of 12.5×10^{-4} M (amine) and 12.5×10^{-6} M (furan adduct) at λ_{max} of the formed DASA in the

respective solvent system (with *N*-methylaniline $\lambda_{\max}(\text{DCM}) = 614 \text{ nm}$, $\lambda_{\max}(\text{DCM}/\text{HFIP}) = 566 \text{ nm}$; with DEA $\lambda_{\max}(\text{DCM}) = 580 \text{ nm}$, $\lambda_{\max}(\text{DCM}/\text{HFIP}) = 520 \text{ nm}$).

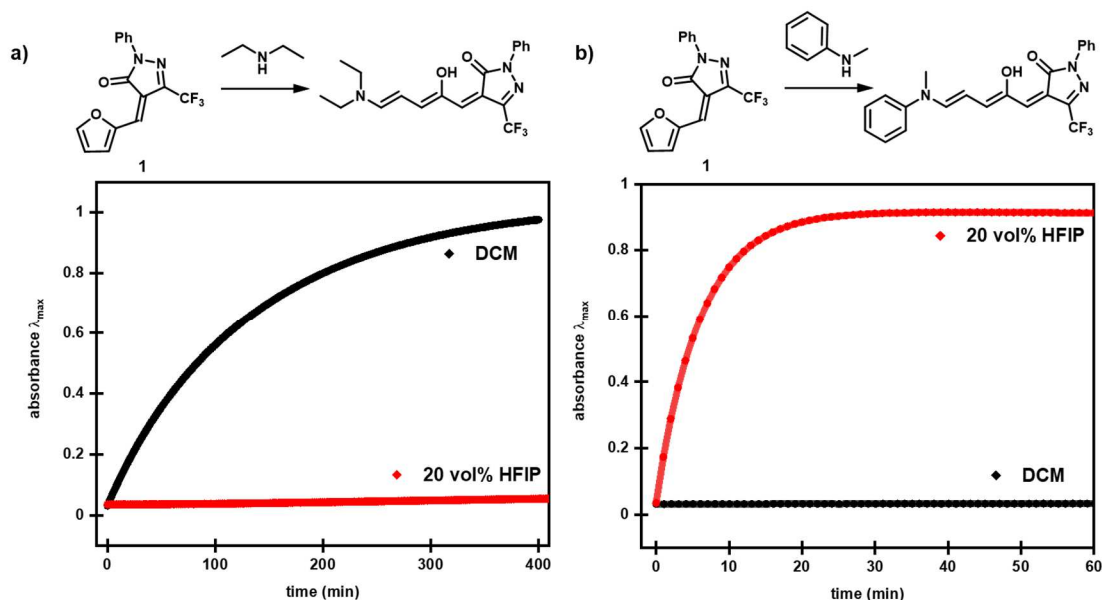


Figure 2.11. Absorbance change at λ_{\max} (open form DASAs) overtime for the reaction of **1** with a) DEA and b) *N*-methylaniline in DCM vs. DCM/HFIP 20 vol%.

Polymers

Experiments were done by preparing stock solutions of the amine modified polymer **S9** (1 mg/mL) and **1** (1.5 mM) in THF and DCM, respectively. Measurements were performed at concentrations of 0.1 mg/mL (polymer) and $1.5 \times 10^{-4} \text{ M}$ (furan adduct) in THF or DCM/HFIP 20 vol% in 3 mL quartz cuvettes and the absorbance at λ_{\max} of the formed DASAs in the respective solvent system for 800 min ($\lambda_{\max}(\text{THF}) = 615 \text{ nm}$, $\lambda_{\max}(\text{DCM}/\text{HFIP}) = 566 \text{ nm}$).

2.10.3.3 NMR Spectroscopy

In situ NMR experiments were performed at a concentration of 25 mM and 298 K. A solution of **1** in CD₂Cl₂ (0.35 mL, 50 mM, 1.0 eq.) and a solution of *N*-methylaniline in CD₂Cl₂ (0.35 mL, targeted at 55 mM, 1.1 eq.) were prepared and to the latter was added deuterated HFIP (0, 1 and 5 eq. relative to **1** or 0, ~0.2 and ~1 vol%). These solutions were combined in a standard 5 mm NMR tube and a series of 300 spectra was acquired on a time course of up to 15 hours on a Varian Unity Inova AS600 600 MHz spectrometer (delay before start of the first scan was 5 min). Conversion plots were calculated from the integrals of the signals of **1** at $\delta = 8.89$ ppm and the signals of the *N*-methyl groups in the open ($\delta = 3.59$ ppm) and closed ($\delta = 2.85$ ppm) DASA respectively as given by:

$$\text{Conversion} = \frac{\mathbf{a}}{\mathbf{a} + \frac{\mathbf{b}}{3} + \frac{\mathbf{c}}{3}}$$

a = integrated signal of **1** (*d*, 1H, OCH, 8.89 ppm)

b = integrated signal *N*-Me group open form (*s*, 3H, CH₃, 3.59 ppm)

c = integrated signal *N*-Me group closed form (*s*, 3H, CH₃, 2.85 ppm)

The measurements were performed in triplicates. The actual amine concentrations (as determined by ¹H-NMR) varied between 1.1–1.5 equivalents relative to **1**. Analogous measurements were performed in acetonitrile-*d*₃ or by exchanging HFIP-*d*₂ with isopropanol or the methyl-ether of HFIP (HFIPME) (**Figure 2.10.4** and **Figures 2.10.8–9**). Similar measurements on the uncatalyzed runs at higher concentration and longer reaction time (50

mM, 15 h) additionally confirmed that similar conversions are reached when the curve plateaus as for the runs with HFIP (80–85%). Also, it was found that higher excess of amine can push the conversion to >95%.

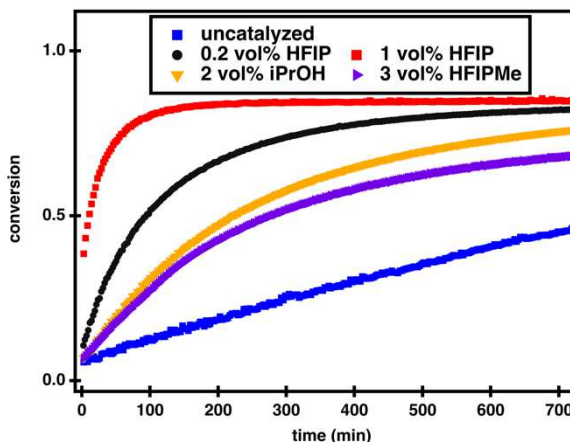


Figure 2.12. Conversion plots from *in situ* NMR experiments on the synthesis of DASA-2 in DCM (k : $3 \text{ M}^{-1} \text{ h}^{-1}$) and upon addition of small quantities of different additives: iPrOH (2 vol%, k : $9 \text{ M}^{-1} \text{ h}^{-1}$), Me-ether of HFIP (HFIPMe, 3 vol%, k : $5 \text{ M}^{-1} \text{ h}^{-1}$), HFIP (0.2 vol%, k : $12 \text{ M}^{-1} \text{ h}^{-1}$ and 1 vol%, k : $56 \text{ M}^{-1} \text{ h}^{-1}$). Note: reactions were performed with similar excess of *N*-methylaniline (1.1–1.2 equivalents), except for the experiment with HFIPMe (1.5 equivalents).

2.10.3.4 Kinetic Fitting

To determine rate constants second-order kinetics was assumed. For this the following differential equation applies:

$$\frac{d[N\text{-methylaniline}]}{dt} = -k[1][N\text{-methylaniline}]$$

The corresponding linearized integrated rate equation is:

$$\ln \frac{[N\text{-methylaniline}]}{[\mathbf{1}]} = k([N\text{-methylaniline}]_0 - [\mathbf{1}]_0)t + \ln \frac{[N\text{-methylaniline}]_0}{[\mathbf{1}]_0}$$

with $[x]$ being the concentration of compound x as a function of time (t) and $[x]_0$ being the initial concentration of compound x . The rate constant k was calculated from the slope of the regression line in the linear regime of a $\ln([N\text{-methylaniline}]/[\mathbf{1}])$ versus time plot (**Figures 2.10.5–9**). The initial ratio of N -methylaniline to $\mathbf{1}$ was calculated through the x-axis intersection.

Table 2.1: Determined rate constants in dichloromethane.

Additive ^[a]	k ($\text{M}^{-1} \text{h}^{-1}$)
-	$3 \pm 1^{[b]}$
0.2 vol% (1 eq.) HFIP	$11.6 \pm 0.2^{[b]}$
1 vol% (5 eq.) HFIP	$56 \pm 5^{[b]}$
2 vol% (10 eq.) iPrOH	9
3 vol% (10 eq.) HFIPMe	5

[a] Equivalentents relative to $\mathbf{1}$. [b] Mean values of three measurements \pm standard deviation.

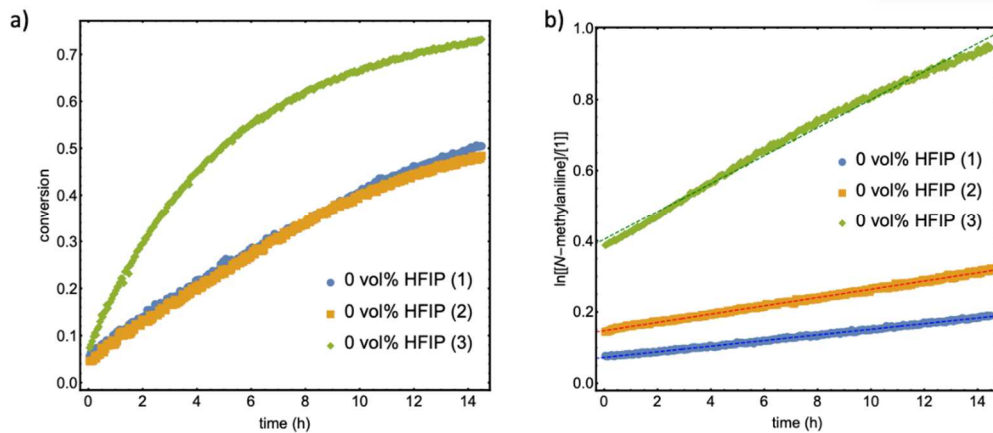


Figure 2.13. Kinetic fitting of uncatalyzed reaction of **1** with *N*-methylaniline in dichloromethane. a) Conversion of each measurement (1) 1.1 eq. (2) 1.2 eq. (3) 1.5 eq. of *N*-methylaniline. The increase in conversion of (3) in a) is due to the increased excess in *N*-methylaniline. b) Second-order kinetic fitting for each experiment. Calculated k : (1) $4.2 \text{ M}^{-1} \text{ h}^{-1}$; (2) $1.9 \text{ M}^{-1} \text{ h}^{-1}$; (3) $3.2 \text{ M}^{-1} \text{ h}^{-1}$; $3 \pm 1 \text{ M}^{-1} \text{ h}^{-1}$.

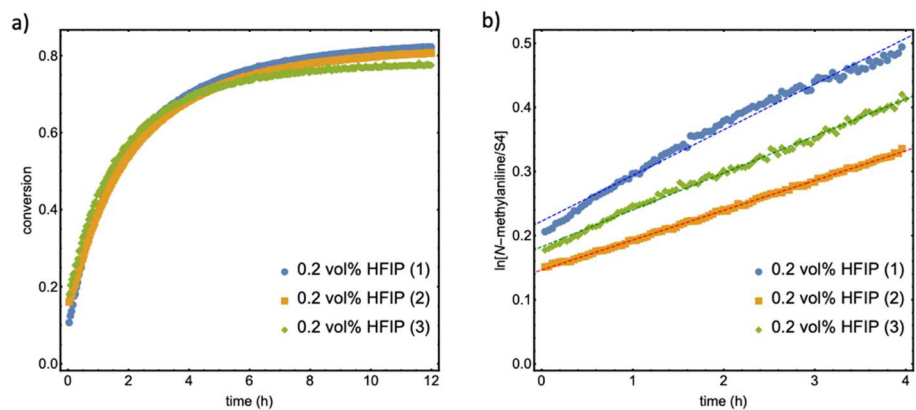


Figure 2.14. Kinetic fitting of the reaction of **1** with *N*-methylaniline in presence of 0.2 vol% (or 1 eq. relative to **1**) HFIP in dichloromethane. a) Conversion of each measurement (1) 1.3 eq. (2) 1.2 eq. (3) 1.2 eq. of *N*-methylaniline. b) Second-order kinetic fitting for each experiment. Calculated k : (1) $11.5 \text{ M}^{-1} \text{ h}^{-1}$; (2) $11.8 \text{ M}^{-1} \text{ h}^{-1}$; (3) $11.5 \text{ M}^{-1} \text{ h}^{-1}$; $11.6 \pm 0.2 \text{ M}^{-1} \text{ h}^{-1}$.

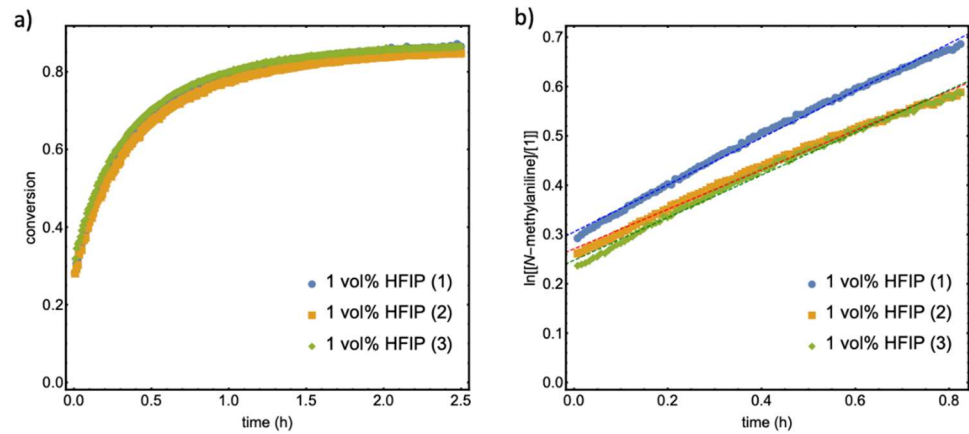


Figure 2.15. Kinetic fitting of the reaction of **1** with *N*-methylaniline in presence of 1 vol% (or 5 eq. relative to **1**) HFIP in dichloromethane. a) Conversion of each measurement (1) 1.4 eq. (2) 1.3 eq. (3) 1.3 eq. of *N*-methylaniline. b) Second-order kinetic fitting for each experiment. Calculated k : (1) $53.5 \text{ M}^{-1} \text{ h}^{-1}$; (2) $51.5 \text{ M}^{-1} \text{ h}^{-1}$; (3) $61.4 \text{ M}^{-1} \text{ h}^{-1}$; $56 \pm 5 \text{ M}^{-1} \text{ h}^{-1}$.

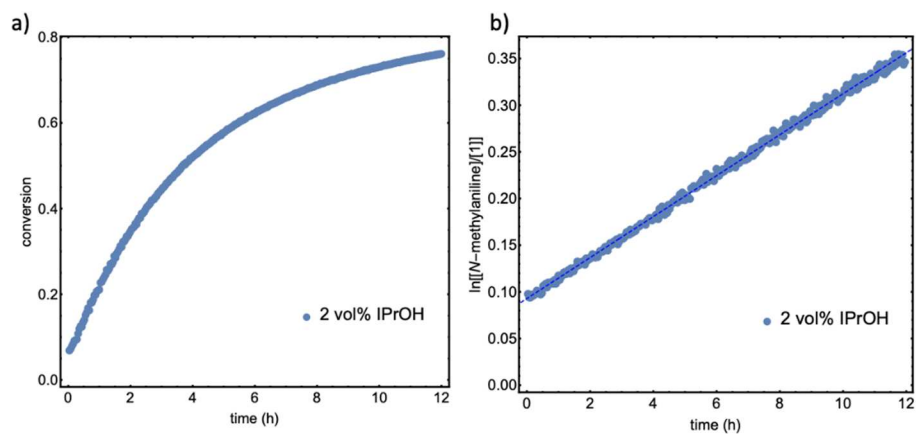


Figure 2.16. Kinetic fitting of the reaction of **1** with *N*-methylaniline in presence of 2 vol% (or 10 eq. relative to **1**) iPrOH in dichloromethane. a) Conversion, 1.1 eq. of *N*-methylaniline. b) Second-order kinetic fitting. Calculated k : $9 \text{ M}^{-1} \text{ h}^{-1}$.

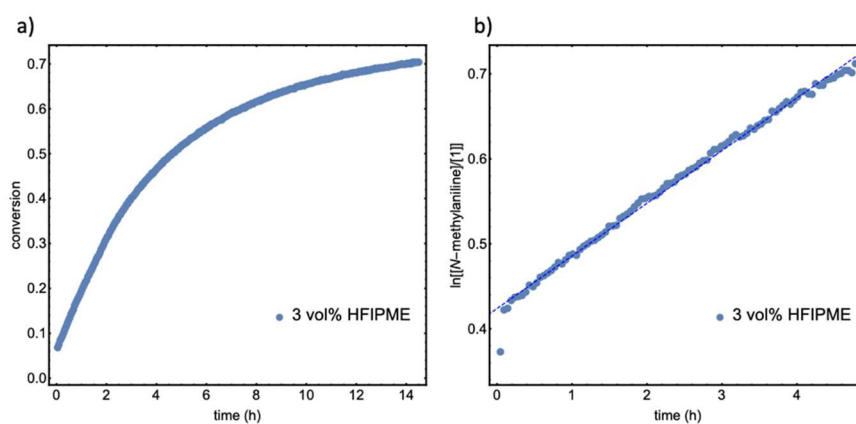


Figure 2.17. Kinetic fitting of the reaction of **1** with *N*-methylaniline in presence of 3 vol% (or 10 eq. relative to **1**) HFIPME in dichloromethane. a) Conversion, 1.5 eq. of *N*-methylaniline. b) Second-order kinetic fitting. Calculated k : $5 \text{ M}^{-1} \text{ h}^{-1}$.

2.10.4 UV-Vis Absorption Spectra of Furan Adducts

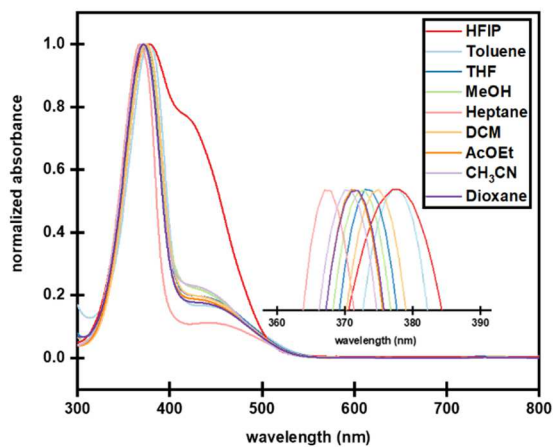


Figure 2.18. Normalized UV-Vis spectra of **1** in different solvents.

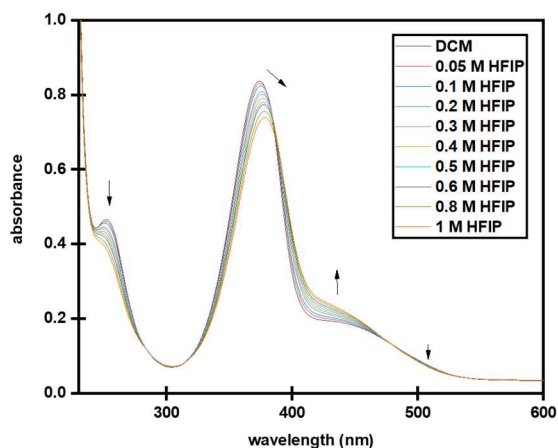


Figure 2.19. UV-Vis spectral changes during titration of **1** in DCM (2.5×10^{-5} M) with HFIP.

The concentration of HFIP is indicated in the legend.

2.10.5 Effects on Thermodynamic Equilibrium

2.10.5.1 NMR Spectroscopy

To analyze closed form formation during synthesis NMR spectra from kinetic experiments in *section 3.2* were compared at 2.5 h for differing conditions ("t= 0 h" refers to the first scan measured 5 min after setting up the reaction (**Figures 2.10.12–17**)).

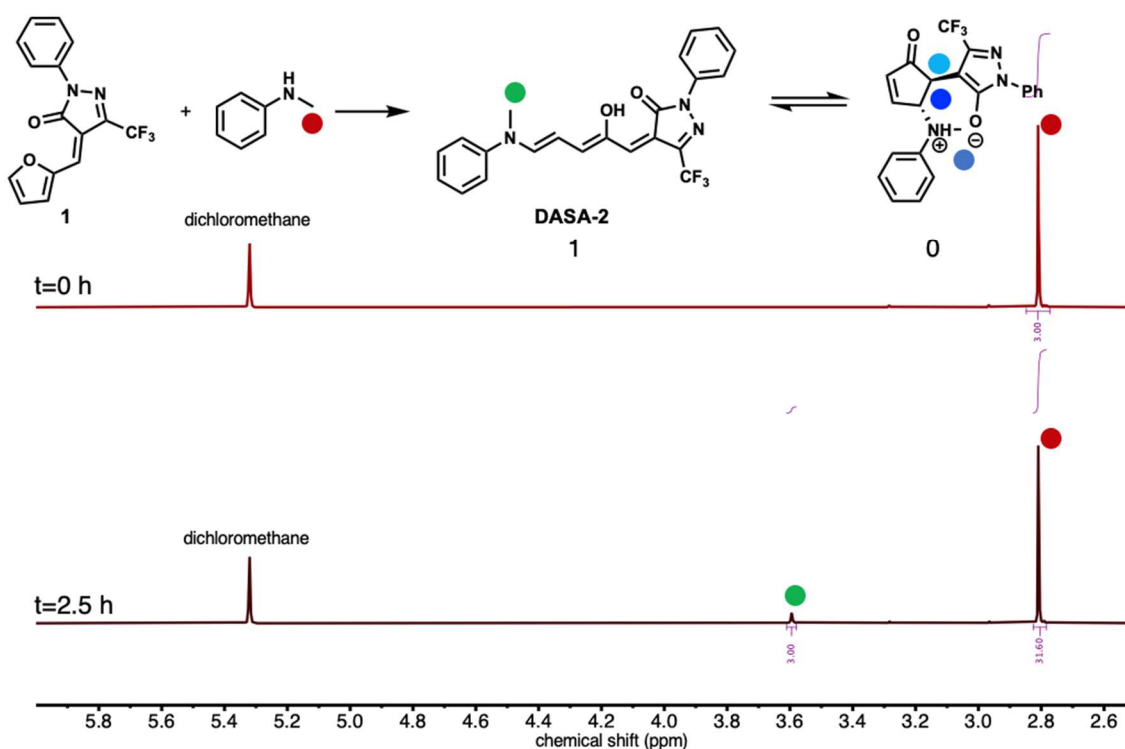


Figure 2.20. ^1H NMR (600 MHz, CD_2Cl_2) spectra from kinetic experiments for DASA-2 in dichloromethane at t=0 and t= 2.5 h. No closed form can be observed.

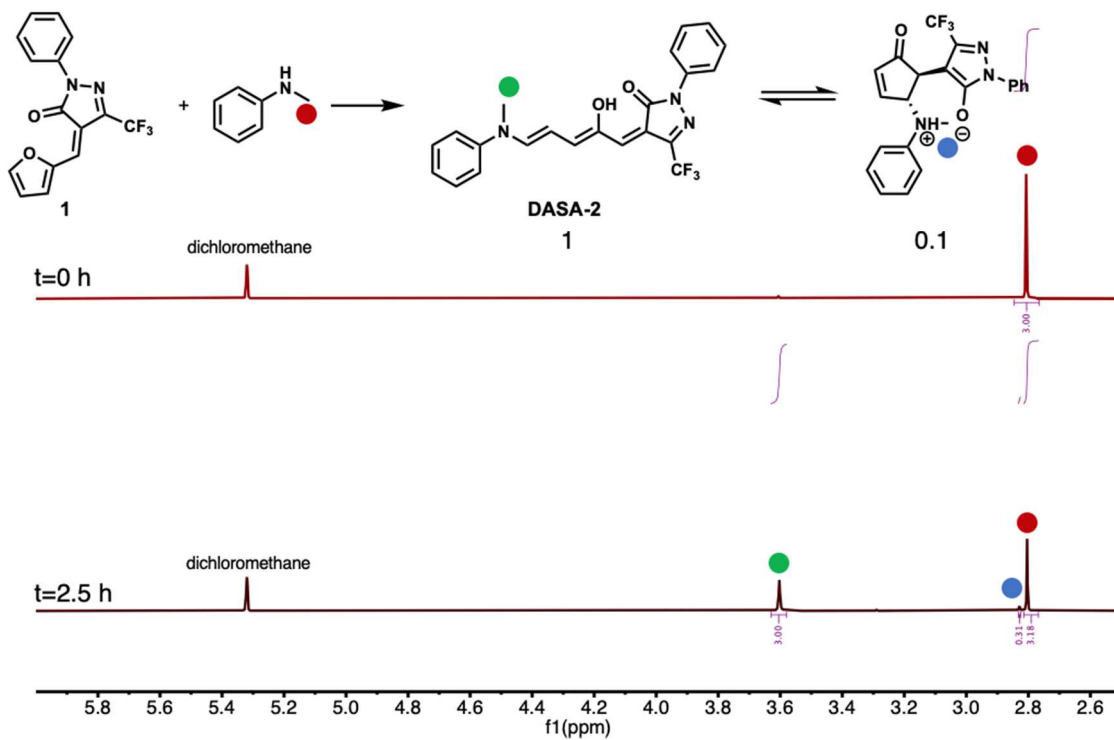


Figure 2.21. ^1H NMR (600 MHz, CD_2Cl_2) spectra from kinetic experiments for DASA-2 in dichloromethane at $t=0$ and $t=2.5$ h with 1 eq. of HFIP regarding **1**. 9% closed form can be observed.

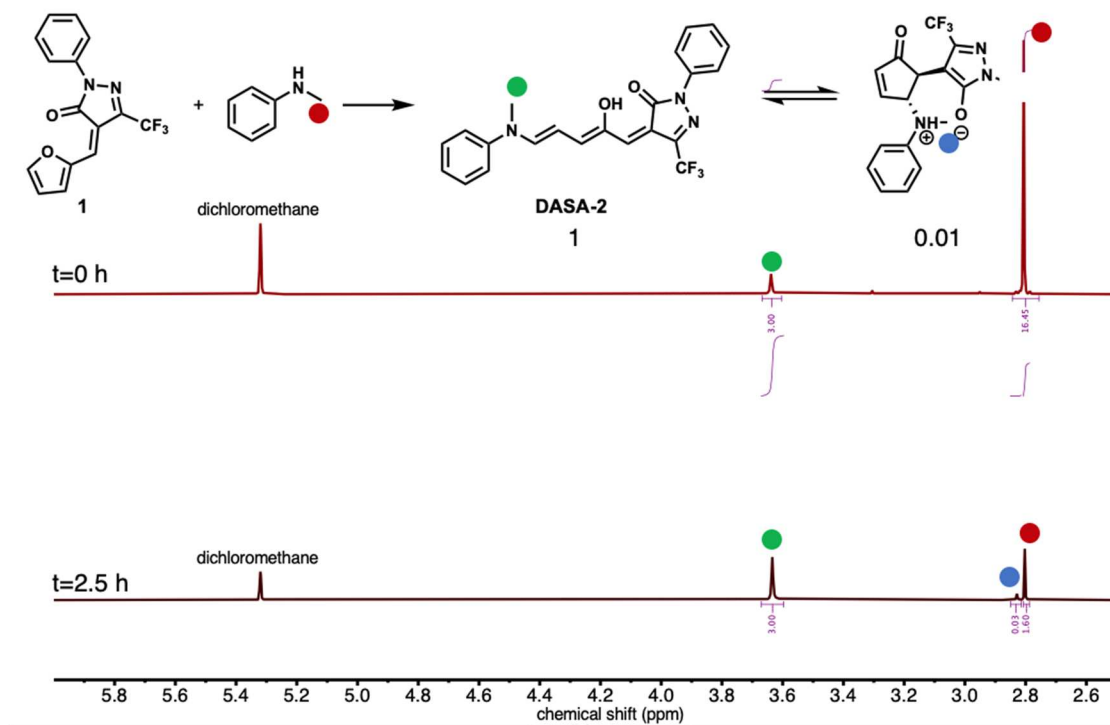


Figure 2.22. ^1H NMR (600 MHz, CD_2Cl_2) spectra from kinetic experiments for DASA-2 in dichloromethane at $t=0$ and $t=2.5$ h with 5 eq. of HFIP regarding **1**. 1% closed form can be observed.

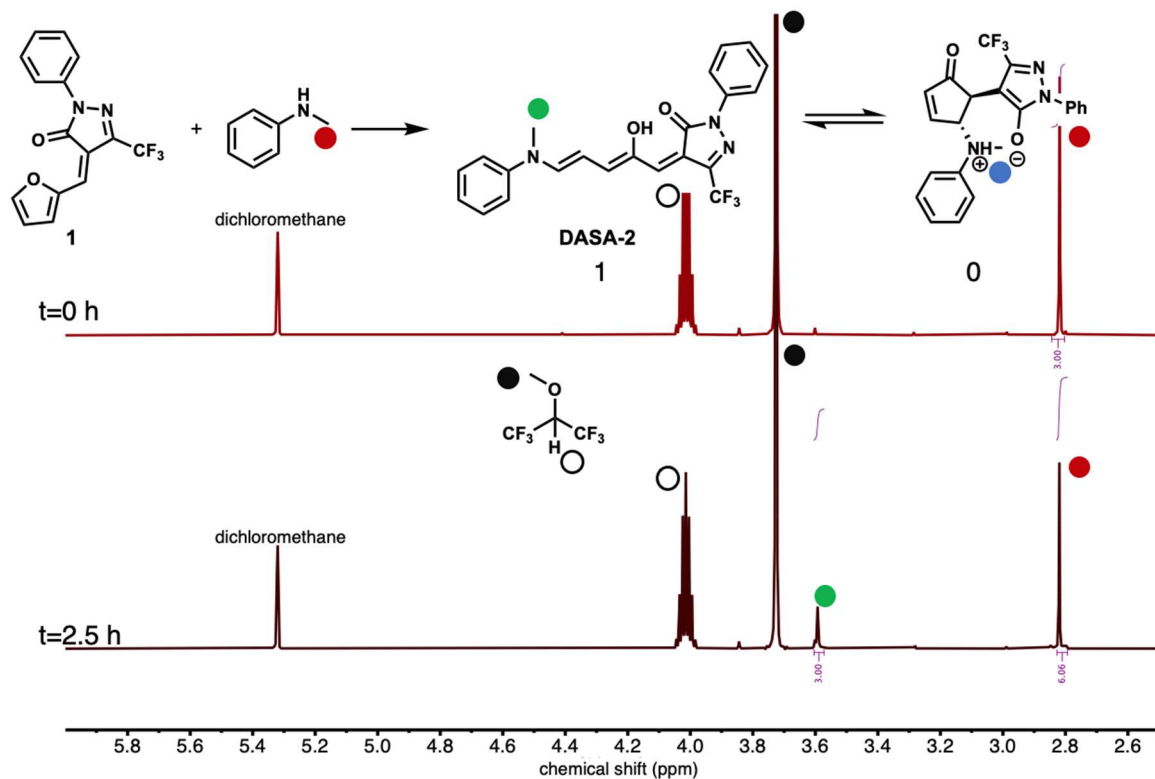


Figure 2.23. ¹H NMR (600 MHz, CD₂Cl₂) spectra from kinetic experiments for DASA-2 in dichloromethane at t=0 and t= 2.5 h with 10 eq. of HFIPMe regarding **1**. No closed form can be observed.

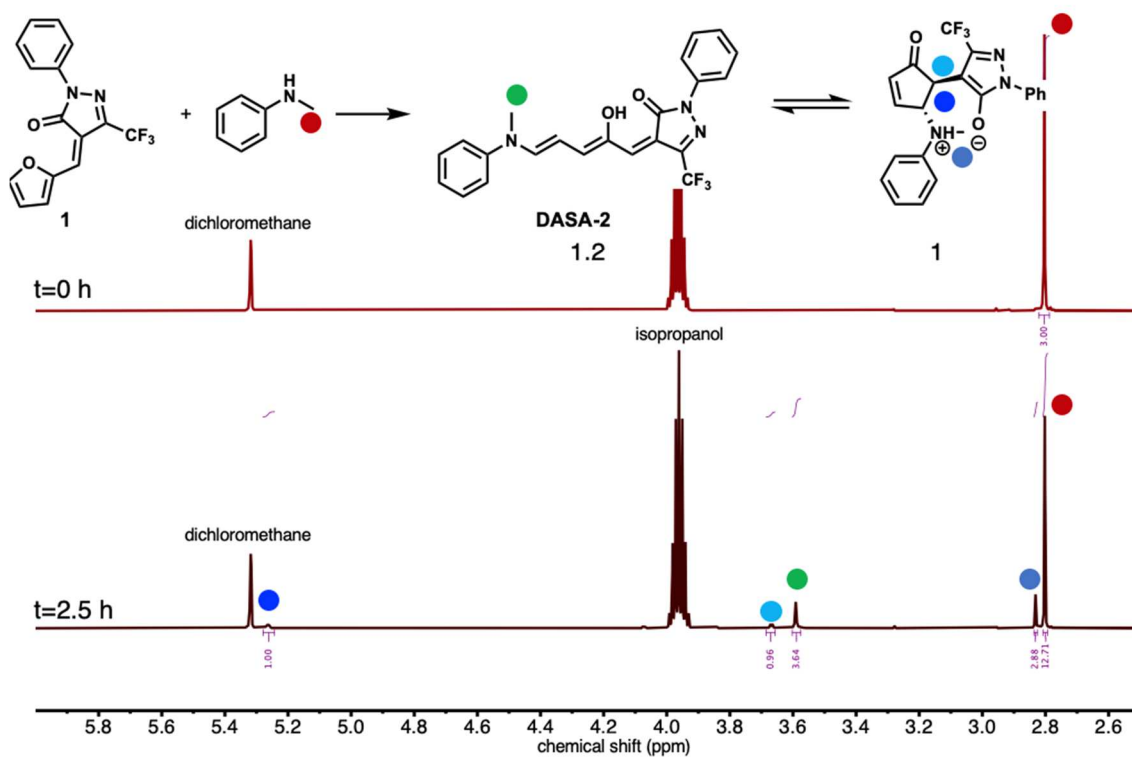


Figure 2.24. ^1H NMR (600 MHz, CD_2Cl_2) spectra from kinetic experiments for DASA-2 in dichloromethane at $t=0$ and $t=2.5$ h with 10 eq. of isopropanol regarding **1**. 45% closed form can be observed.

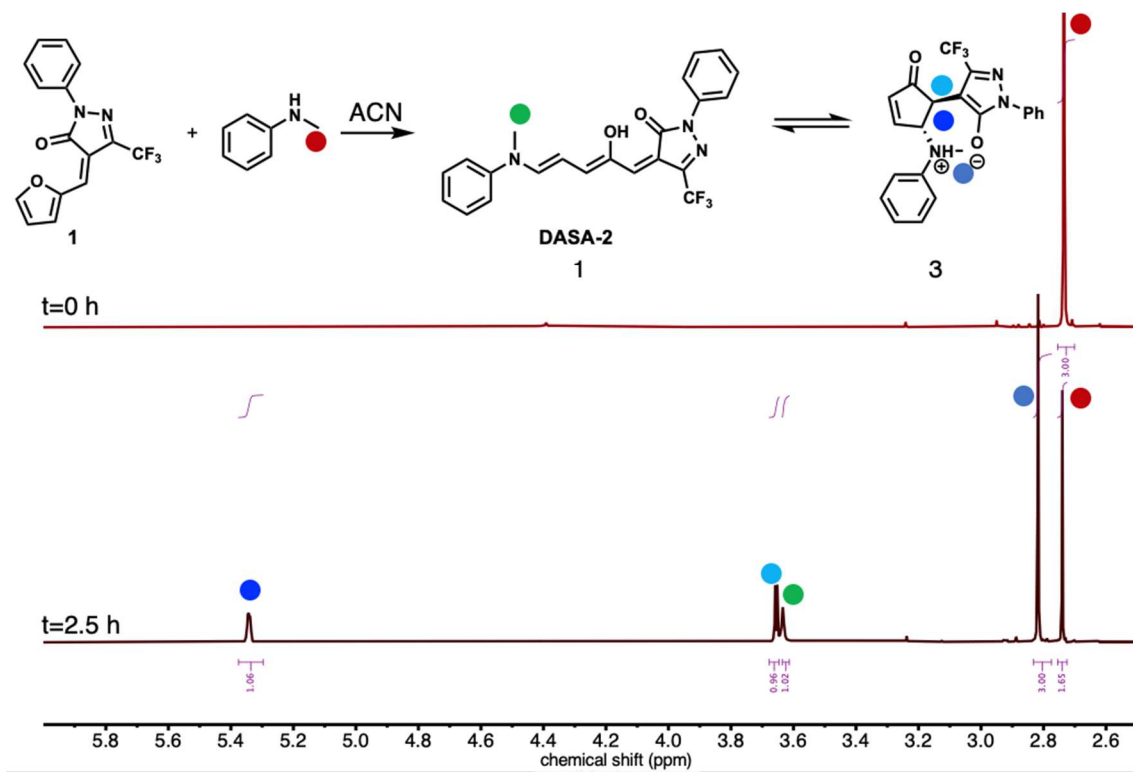


Figure 2.25. ^1H NMR (600 MHz, $\text{ACN-}d_3$) spectra from kinetic experiments for DASA-2 in acetonitrile at $t=0$ and $t=2.5$ h. 75% closed form can be observed.

2.10.5.2 Solvatochromic Shift Analysis

For **Figure 3a** DASA-4, DASA-5, DASA-6 and DASA-7 were measured via UV-Vis spectroscopy at a concentration of 10 μM in the following solvents: toluene (E_{T}^{N} : 0.099), diethyl ether (E_{T}^{N} : 0.117), tetrahydrofuran (E_{T}^{N} : 0.207), ethyl acetate (E_{T}^{N} : 0.228), chloroform (E_{T}^{N} : 0.259), dichloromethane (E_{T}^{N} : 0.309), acetone (E_{T}^{N} : 0.355), dimethyl sulfoxide (E_{T}^{N} : 0.444), acetonitrile (E_{T}^{N} : 0.46), methanol (E_{T}^{N} : 0.726), HFIP (E_{T}^{N} : 1.068).⁴¹ Data for DASA-5, DASA-6 and DASA-7 was partially taken from literature.^{14,39,44}

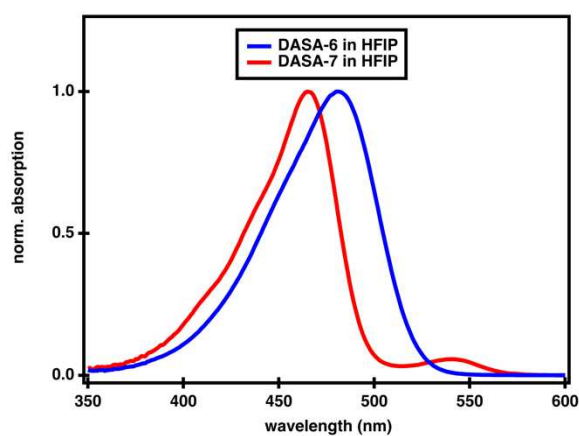


Figure 2.26. Normalized UV-Vis spectra of DASA-6 and DASA-7 in HFIP.

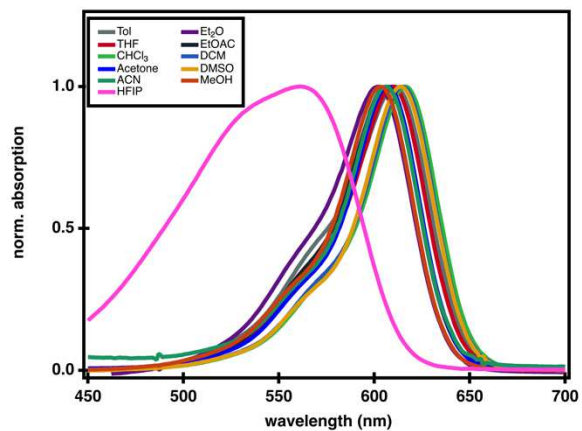


Figure 2.27. Normalized UV-Vis spectra of DASA-4 in a range of solvents.

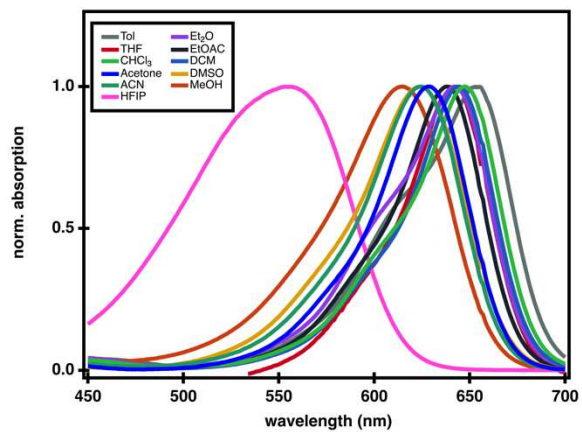


Figure 2.28. Normalized UV-Vis spectra of DASA-5 in a range of solvents.

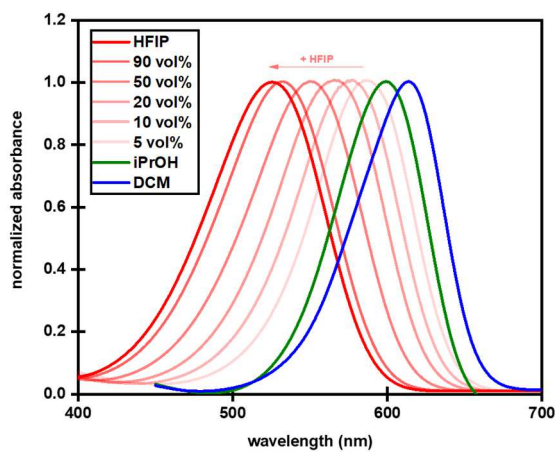


Figure 2.29. Normalized UV-Vis spectra of DASA-2 in DCM/HFIP mixtures and in *iPrOH*.

2.10.5.3 Effect of HFIP on PTSS

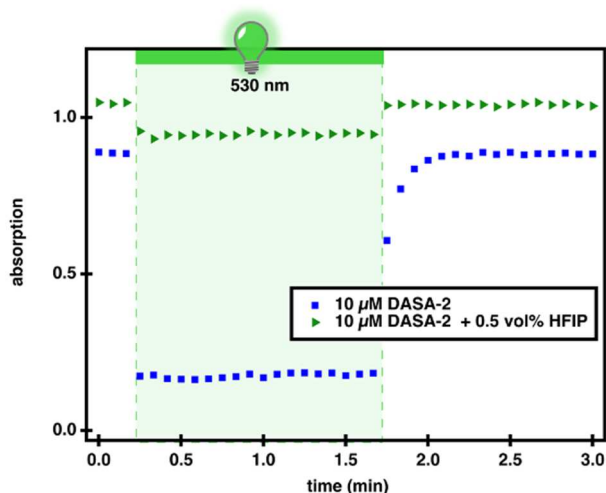


Figure 2.30. Time dependent UV-Vis spectroscopy to observe the photochromism of DASA-2 in dichloromethane at 10 μM followed at λ_{max} (609 nm). Upon the addition of 0.5 vol% HFIP the photothermalstationary state (PTSS) decreases from 81% to 11% closed isomers.

2.10.6 UV-Vis Absorption Spectra

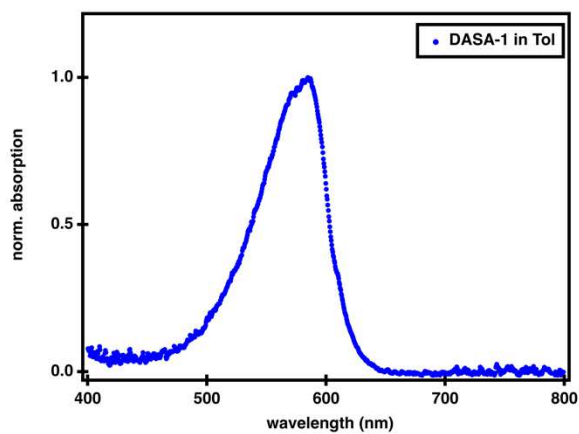


Figure 2.31. Normalized UV-Vis spectra of DASA-1 in toluene. λ_{max} : 590 nm.

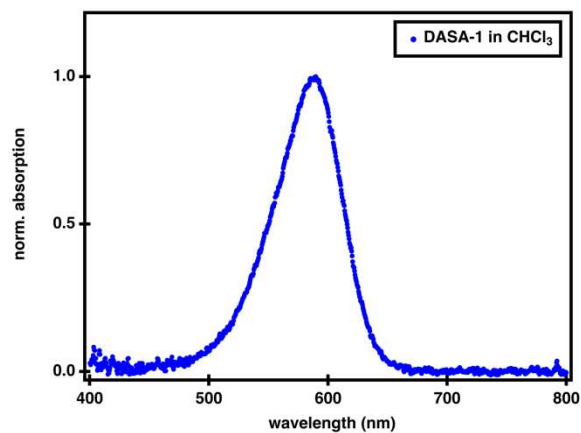


Figure 2.32. Normalized UV-Vis spectra of DASA-1 in chloroform. λ_{max} : 588 nm.

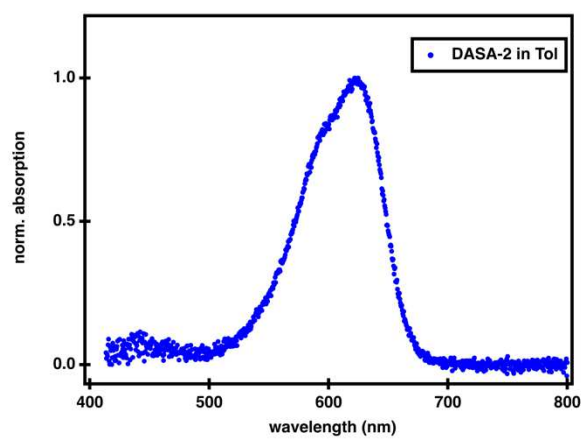


Figure 2.33. Normalized UV-Vis spectra of DASA-2 in toluene. λ_{max} : 625 nm.

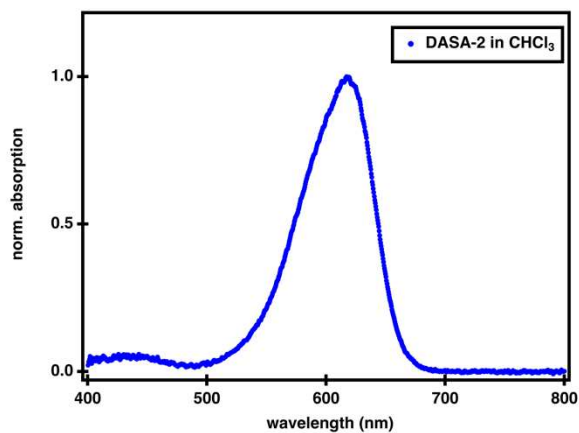


Figure 2.34. Normalized UV-Vis spectra of DASA-2 in chloroform. λ_{max} : 617 nm.

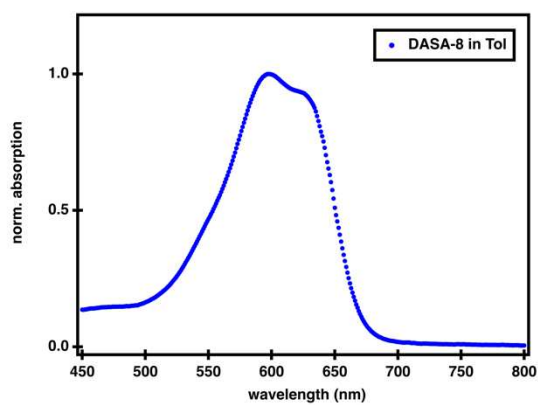


Figure 2.35. Normalized UV-Vis spectra of DASA-8 in toluene. λ_{max} : 598/624 nm.

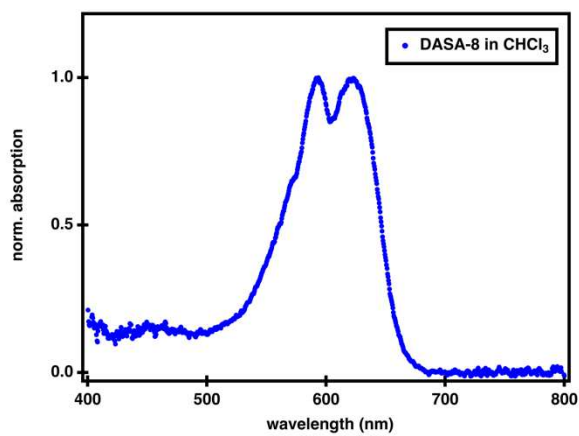


Figure 2.36. Normalized UV-Vis spectra of DASA-8 in chloroform. λ_{max} : 594/621 nm.

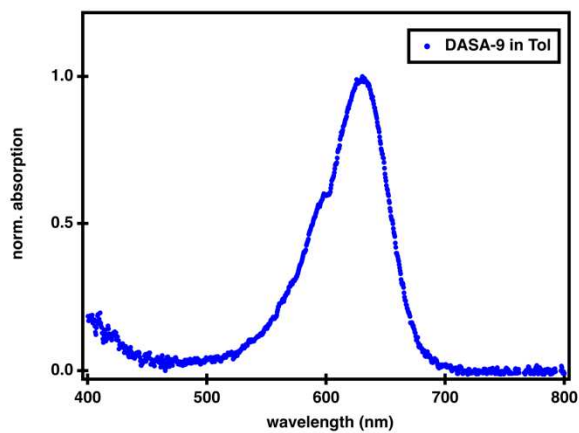


Figure 2.37. Normalized UV-Vis spectra of DASA-9 in toluene. λ_{max} : 631 nm.

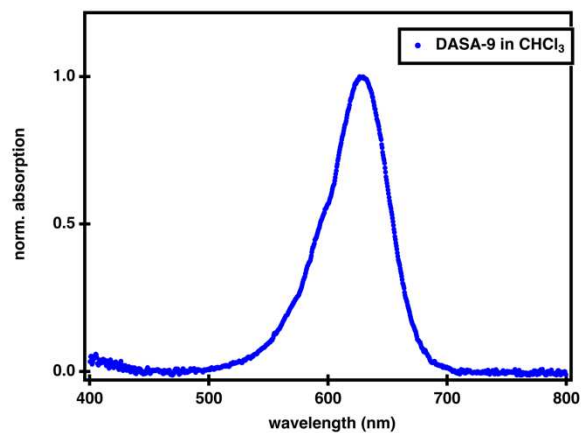


Figure 2.38. Normalized UV-Vis spectra of DASA-9 in chloroform. λ_{max} : 625 nm.

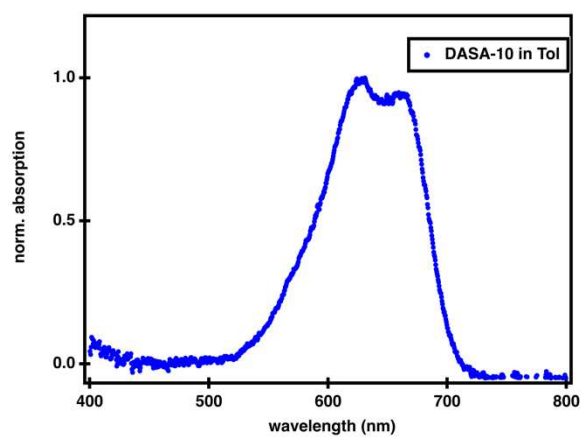


Figure 2.39. Normalized UV-Vis spectra of DASA-10 in toluene. λ_{max} : 630/662 nm.

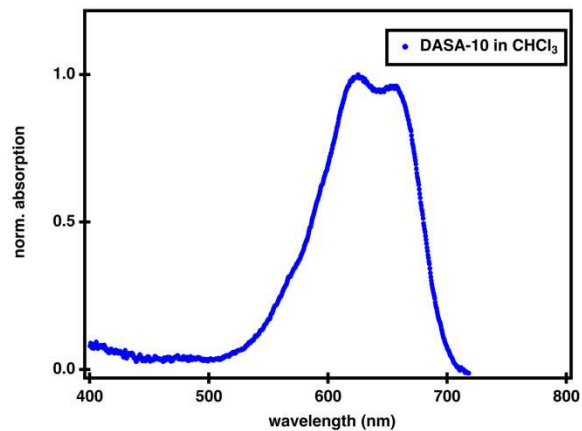


Figure 2.40. Normalized UV-Vis spectra of DASA-10 in chloroform. λ_{max} : 625/656 nm.

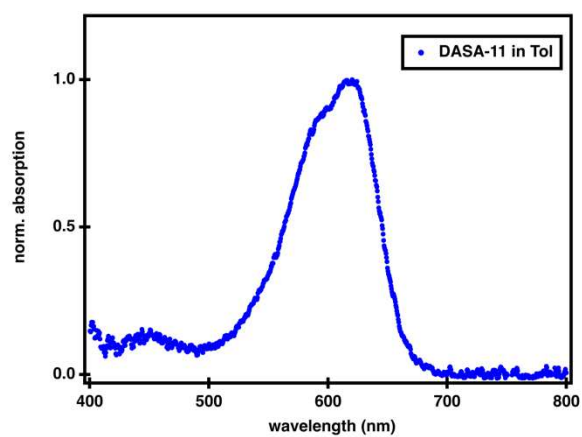


Figure 2.41. Normalized UV-Vis spectra of DASA-11 in toluene. λ_{max} : 623 nm.

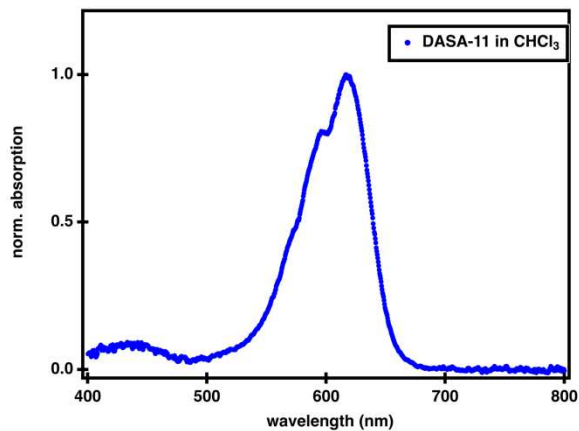


Figure 2.42. Normalized UV-Vis spectra of DASA-11 in chloroform. λ_{max} : 616 nm.

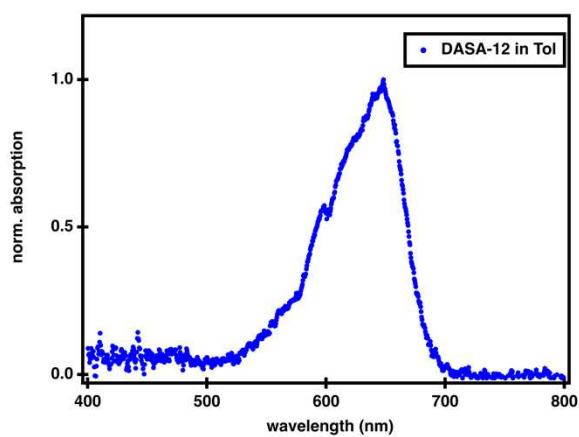


Figure 2.43. Normalized UV-Vis spectra of DASA-12 in toluene. λ_{max} : 647 nm.

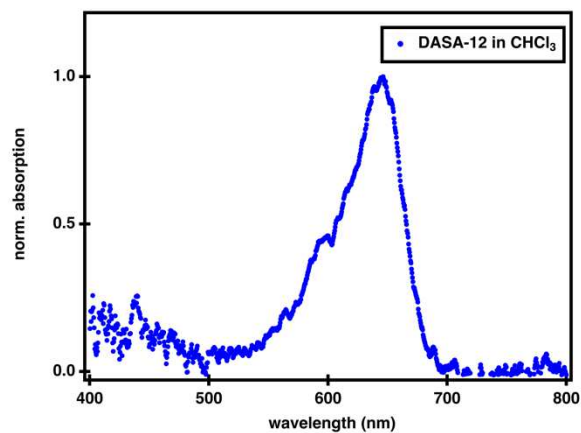


Figure 2.44. Normalized UV-Vis spectra of DASA-12 in chloroform. λ_{max} : 646 nm.

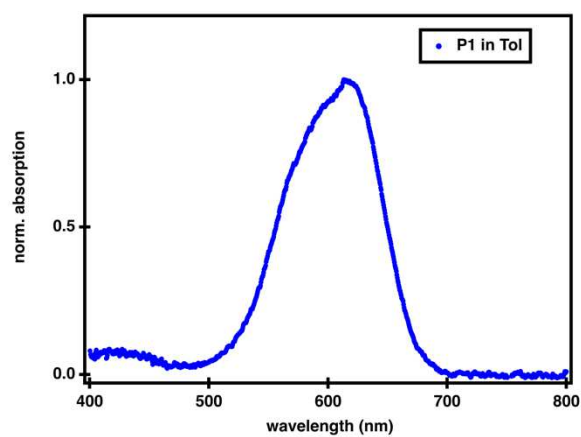


Figure 2.45. Normalized UV-Vis spectra of P1 in toluene. λ_{max} : 613 nm.

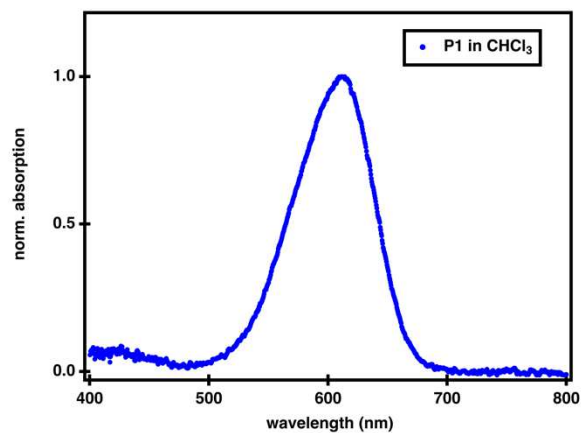


Figure 2.46. Normalized UV-Vis spectra of **P1** in chloroform. λ_{max} : 609 nm.

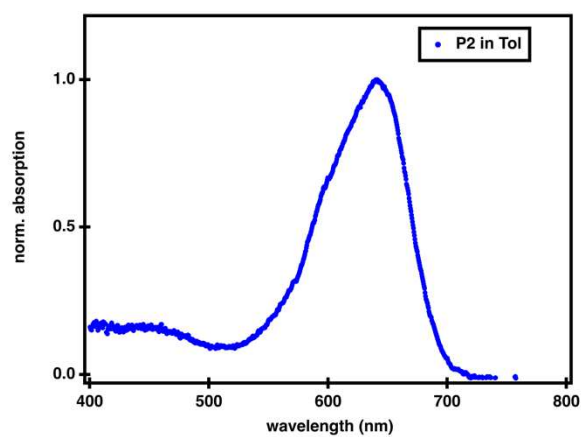


Figure 2.47. Normalized UV-Vis spectra of **P2** in toluene. λ_{max} : 641 nm.

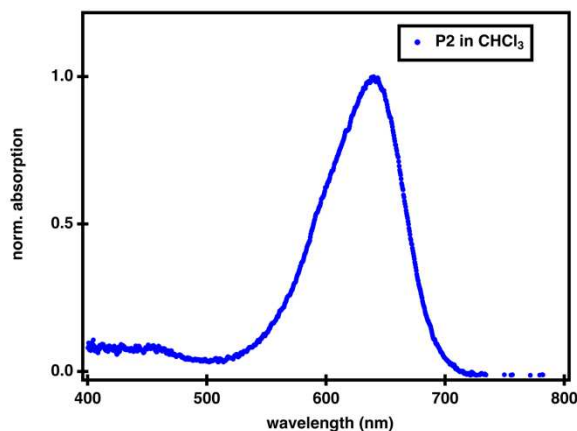


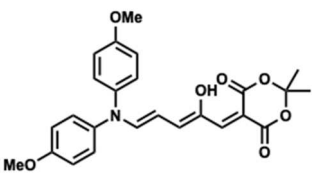
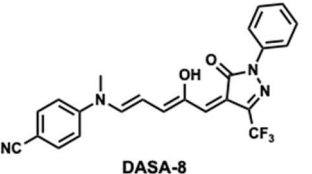
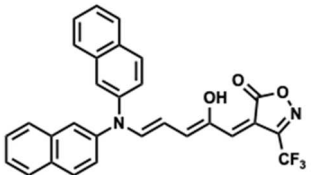
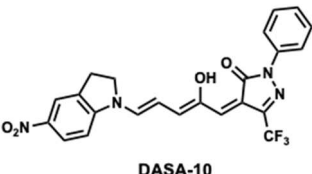
Figure 2.48. Normalized UV-Vis spectra of **P2** in chloroform. λ_{max} : 640 nm.

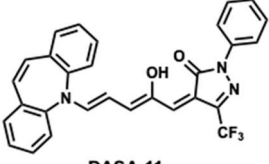
2.10.7 DFT Calculations

Density functional theory (DFT) calculations at B3LYP-GD3BJ/6-31G(d) level of theory were used for geometry optimizations of the open form DASAs to determine the dihedral angle between the acceptor and donor groups, as described before for second generation DASAs.¹³ Calculations at B3LYP-GD3BJ/6-311++(d,p) level of theory were performed to predict the character of the frontier orbitals and the optical excitation energy. The calculations were performed with the Gaussian 16 Rev.A.03 software and solvent effects were considered using a conductor-like polarizable continuum model (CPCM, toluene). The calculated HOMO-LUMO gaps correlate well with the relative ordering of the experimentally observed absorption peaks, however, the absolute energies are systematically over-predicted by 0.4 eV (~ 100 nm blue-shifted λ_{max} relative to experimentally determined value in toluene), which is in accordance with previous findings for second generation DASAs.¹³ The calculated HOMO-LUMO gaps listed in **Table 2.2** were adjusted by this amount. Time-dependent DFT methods and other functionals were also tested but the predictions of the ordering of the HOMO-LUMO gaps in the series were less consistent with experimental results. Dihedral angles ($\Phi_{\text{D}\square\text{A}}$) between acceptor and donor groups were determined from the optimized

geometries and frontier orbitals graphically represented by using the Avogadro software (Figure 2.49–50).

Table 2.2. DFT predicted λ_{\max} of the open form DASA compared to their actual λ_{\max} in nm and dihedral angles between donor and acceptor groups.

DASA	Observed λ_{\max} (nm) ^[a]	Calc. λ_{\max} (nm) ^[b]	Deviation from exp. λ_{\max} (nm)	Dihedral angles Φ_{D-A} [c]	
				R on OH side	R opposite OH side
 <p>DASA-1</p>	590	599	+9	57.6°	37.6°
 <p>DASA-8</p>	598/624 ^[c]	622	-2	-	35.4°
 <p>DASA-9</p>	631	633	+2	55.9°	37.5°
 <p>DASA-10</p>	630/662 ^[c]	664	+2	0.1°	0°

 <p style="text-align: center;">DASA-11</p>	623	611	-12	61.8°	59.3°
---	-----	-----	-----	-------	-------

[a] Measured in toluene at concentrations of approx. 10–20 μM . [b] The energy values were systematically over predicted by 0.4 eV and all the listed values are corrected by this value. [c] Splitted absorbance maxima were observed.

See *section 6* for UV-Vis spectra.

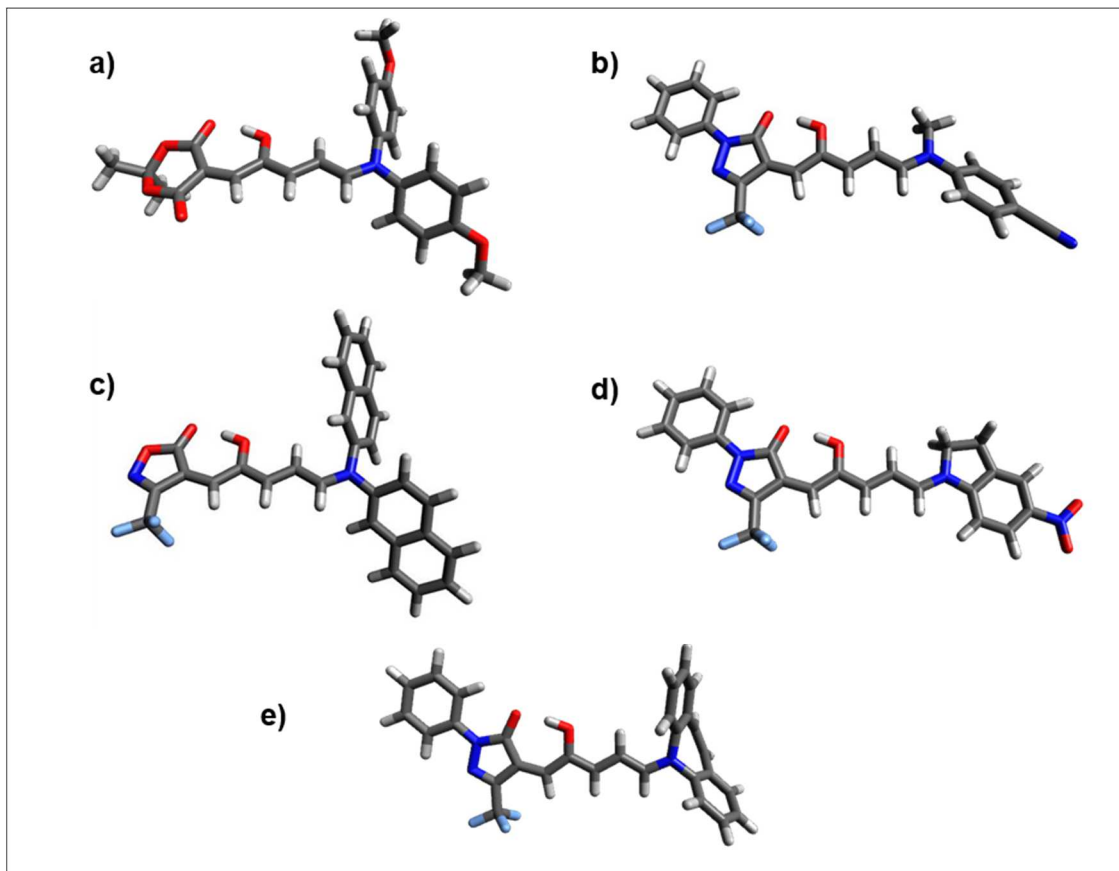


Figure 2.49. Geometry optimized structures of the open form of a) DASA-1, b) DASA-8, c) DASA-9, d) DASA-10 and e) DASA-11 calculated with DFT.

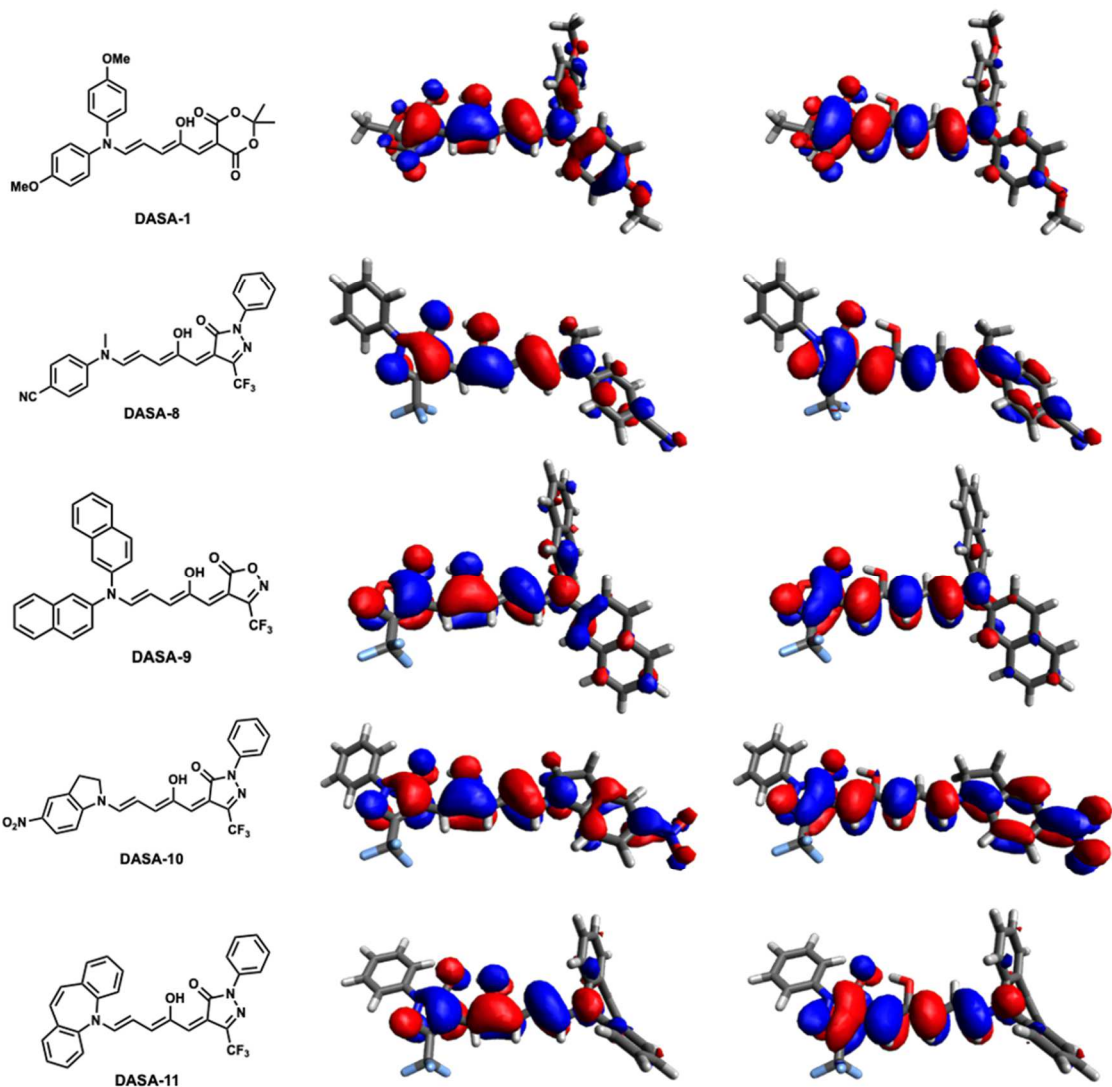


Figure 2.50. DFT predicted frontier orbitals of the open form. HOMOs are on the left, LUMOs on the right.

2.10.8 Photoswitching Experiments

The photoinduced optical absorption kinetics were measured on a pump-probe setup. The pump beam was generated by a light emitting diode (LED) source (Thorlabs) coupled into a multimode optical fiber terminated with an output collimator. The LED intensity was controlled through a digital-to-analog converter (National Instruments USB-6009) using

LabVIEW. The probe beam was produced by High Power MINI Deuterium Tungsten Halogen Source w/shutter 200–2000 nm (Ocean Optics DH-MINI) coupled into a multimode fiber with an output collimator for the light delivery. The probe light was modulated by a shutter (Uniblitz CS25) which could be controlled manually or through a digital output port (National Instruments USB-6009) using LabVIEW. Pump and probe beams were overlapped using steering and focusing optics at a 90° angle inside a sample holder, which allowed for a 10x10 mm rectangular spectrophotometer cells that was connected to a circulating bath for temperature control. Additionally, the solutions were stirred during the measurements by a miniature stirring plate inserted into the sample holder (Starna Cells SCS 1.11). The sample holder was placed into a metal enclosure to prevent exposure to ambient light. Both pump and probe beams were nearly collimated inside the cell with a diameter of about 2 mm. The pump beam was blocked after passing through the sample and the probe beam was directed by a system of lenses into the detector (Ocean Optics Flame-S1-XR spectrometer), which acquired spectra of the probe light. The detector was connected to a PC via USB port. The experiment was controlled by a National Instrument LabVIEW program which collected the probe light spectra, determined sample optical absorption spectra, controlled pump and probe light sources, and stored the data on the computer S3 hard drive according to the experimental protocol. Experiments were performed in at 10 μ M concentration unless otherwise stated. Samples were left to equilibrate overnight prior to measurements unless otherwise stated.

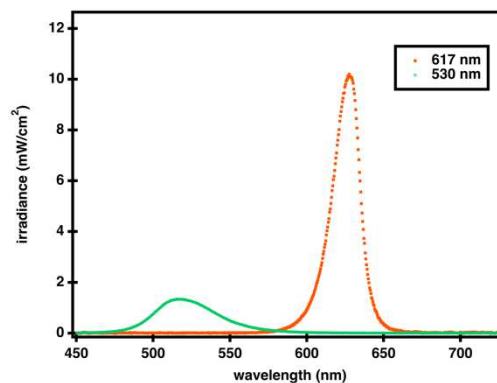
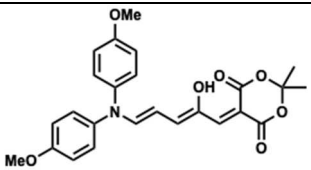
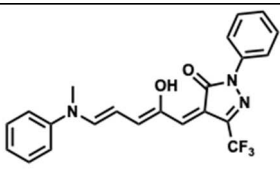
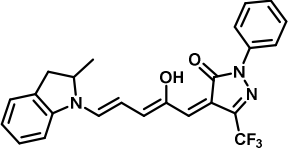
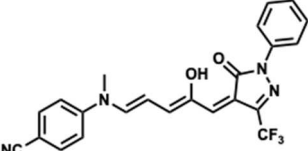
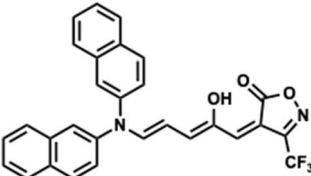
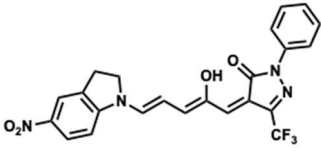
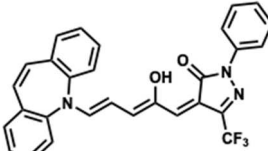
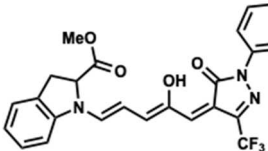


Figure 2.51. irradiance of Thorlabs 530 nm and 617 nm LED used in experiments. Total irradiance for 530 nm: 69.7 mW/cm²; 617 nm: 240.2 mW/cm². Measured using an Ocean Optics hand-held spectrometer with cosine corrector and radiometric calibration (model USB 2000).

2.10.8.1 Overview Switching Parameters

Table 2.3. Photoswitching properties for novel DASAs of this report.

DASA	Solvent	λ_{\max} (nm)	therm. equi.	therm. rec.	$t_{1/2}$ (s ⁻¹)	PTSS
 DASA-1	Toluene	590	19%	-	-	100%
	Chloroform	588	32%	100%	3558	100%
 DASA-2	Toluene	625	84%	100%	94	100%
	Chloroform	617	87%	100%	13	93%
	Chloroform	645 ^[a]	>95% ^[a]	100% ^[a]	5 ^[a]	94% ^[a]

 <p>DASA-5</p>	Toluene	655 ^[a]	100% ^[a]	88% ^[a]	40 ^[a]	100% ^[a]]
 <p>DASA-8</p>	Toluene	598/ 624 ^[b]	insoluble	-	-	-
	Chloroform	594/ 621 ^[b]	<5%	100%	973	n.d. ^[c]
 <p>DASA-9</p>	Toluene	631	83%	100%	868	100%
	Chloroform	625	>95%	100%	67	88%
 <p>DASA-10</p>	Toluene	630/ 662 ^[b]	insoluble	n.d. ^[d]	- ^[d]	100%
	Chloroform	625/ 656 ^[b]	<5% ^[e]	-	-	100%
 <p>DASA-11</p>	Toluene	623	76%	100%	1594	100%
	Chloroform	616	89%	100%	202	15%
 <p>DASA-12</p>	Toluene	647	29%	n.d. ^[d]	17498	100%
	Chloroform	646	9%	100%	3234 ^[g]	100%

P1	Toluene	613	n.d. ^[f]	100%	23	40%
	Chloroform	609	n.d. ^[f]	100%	9	29%
P2	Toluene	641	n.d. ^[f]	100%	53	85%
	Chloroform	640	n.d. ^[f]	100%	24	73%

All compounds were also tested in acetonitrile, but did not show any absorbance after equilibration at 10 μM . [a] Data taken from Hemmer et al.¹⁴ [b] Two absorbance maxima were observed. See *section 6* for complete UV-Vis. [c] Conversion was not completed after 100 s of irradiation [d] Recovery was not completed after 22 h. [e] Limited solubility. [f] Equilibrium DASA signals not clearly observable by NMR spectroscopy for DASA polymers. [g] 1545 s at 100 μM .

2.10.8.2 Time Dependent UV-Vis Absorption Spectra

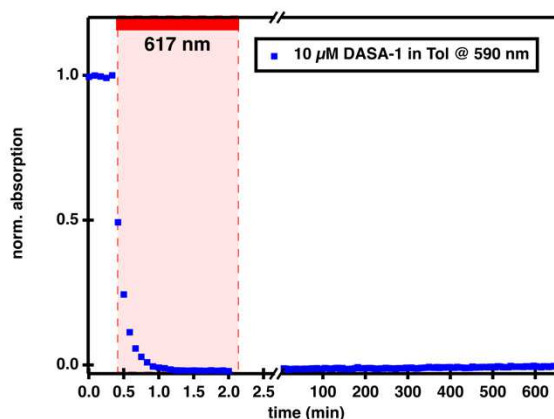


Figure 2.52. Time dependent UV-Vis spectroscopy to observe the photochromism of DASA-**1** in toluene at 10 μM (initial absorbance: 0.35) followed at λ_{max} (590 nm). Quantitative conversion of the open form to the closed form under light irradiation with 617 nm for 100 seconds. No subsequent thermal recovery in the dark can be observed.

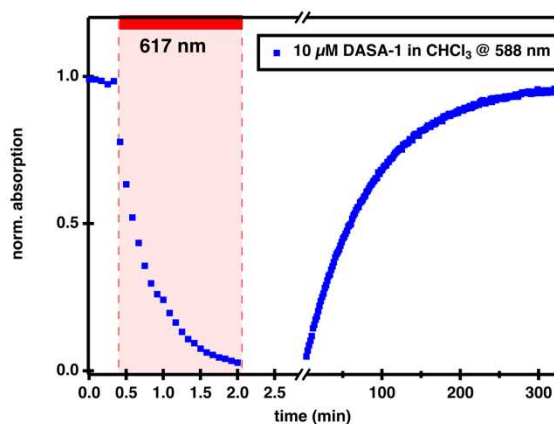


Figure 2.53. Time dependent UV-Vis spectroscopy to observe the photochromism of DASA-**1** in chloroform at 10 μM (initial absorbance: 0.41) followed at λ_{max} (588 nm). Quantitative conversion of the open form to the closed form under light irradiation with 617 nm for 100 seconds and subsequent thermal recovery in the dark can be observed.

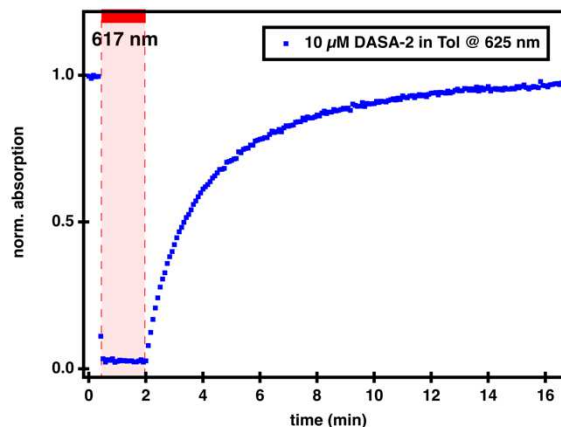


Figure 2.54. Time dependent UV-Vis spectroscopy to observe the photochromism of DASA-2 in toluene at 10 μM (initial absorbance: 0.4) followed at λ_{max} (625 nm). Quantitative conversion of the open form to the closed form under light irradiation with 617 nm for 100 seconds and subsequent thermal recovery in the dark can be observed.

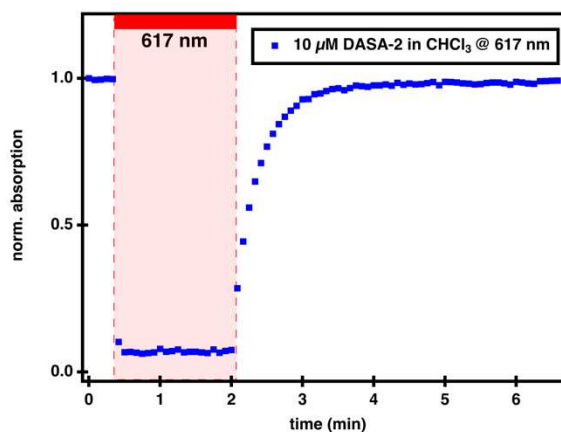


Figure 2.55. Time dependent UV-Vis spectroscopy to observe the photochromism of DASA-2 in chloroform at 10 μM (initial absorbance: 1.1) followed at λ_{max} (617 nm). Quantitative conversion of the open form to the closed form under light irradiation with 617 nm for 100 seconds and subsequent thermal recovery in the dark can be observed.

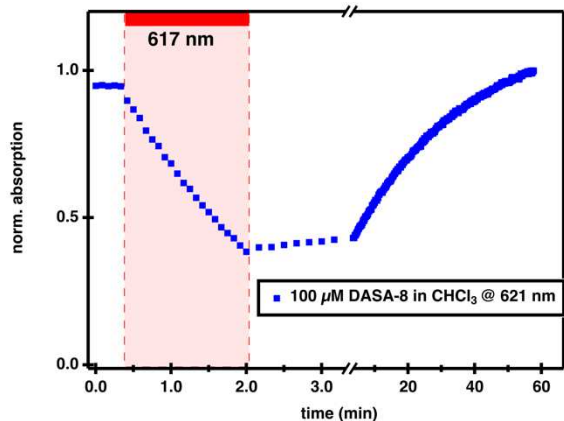


Figure 2.56. Time dependent UV-Vis spectroscopy to observe the photochromism of DASA-**8** in chloroform at 100 μM (initial absorbance: 0.35) followed at λ_{max} (619 nm). Conversion of 60% of the open form to the closed form under light irradiation with 617 nm for 100 seconds and subsequent thermal recovery in the dark can be observed.

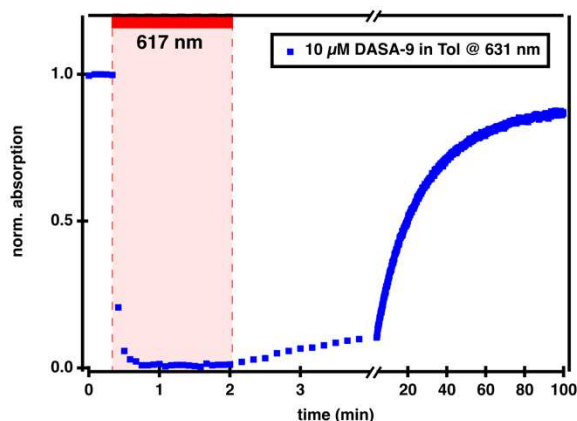


Figure 2.57. Time dependent UV-Vis spectroscopy to observe the photochromism of DASA-**9** in toluene at 10 μM (initial absorbance: 0.32) followed at λ_{max} (631 nm). Quantitative conversion of the open form to the closed form under light irradiation with 617 nm for 100 seconds and subsequent thermal recovery in the dark can be observed.

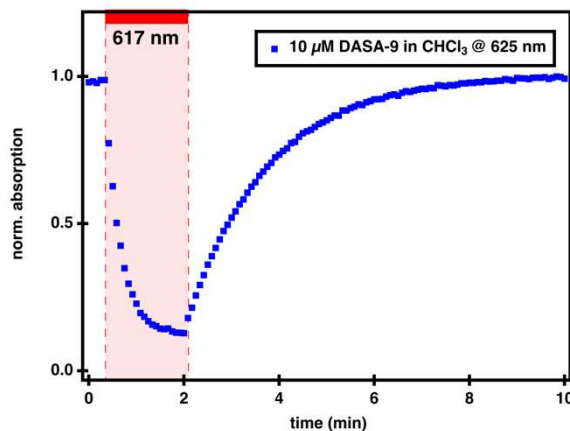


Figure 2.58. Time dependent UV-Vis spectroscopy to observe the photochromism of DASA-**9** in chloroform at 10 μM (initial absorbance: 0.56) followed at λ_{max} (625 nm). Conversion of 87% the open form to the closed form under light irradiation with 617 nm for 100 seconds and subsequent thermal recovery in the dark can be observed.

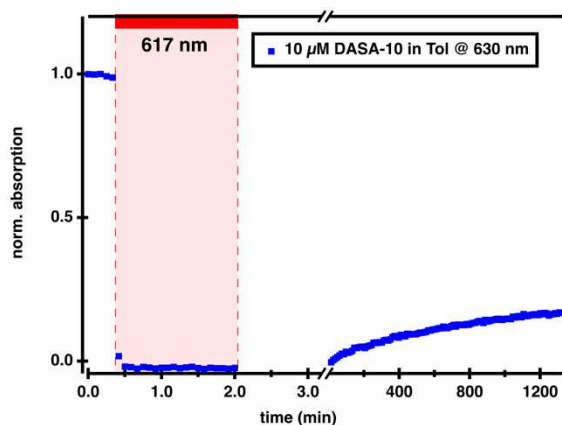


Figure 2.59. Time dependent UV-Vis spectroscopy to observe the photochromism of DASA-**10** in toluene at 10 μM (initial absorbance: 0.41) followed at λ_{max} (630 nm). Quantitative conversion of the open form to the closed form under light irradiation with 617 nm for 100 seconds and minimal subsequent thermal recovery in the dark can be observed.

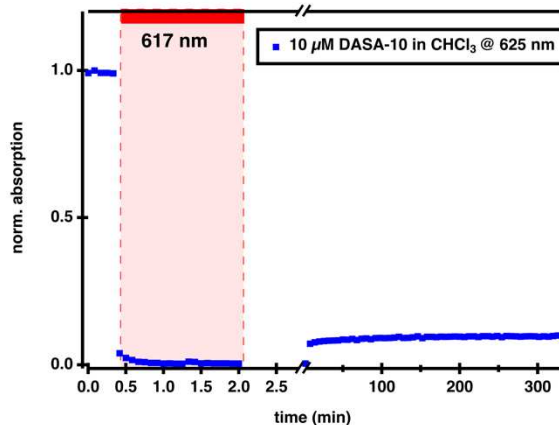


Figure 2.60. Time dependent UV-Vis spectroscopy to observe the photochromism of DASA-**10** in chloroform at 10 μM (initial absorbance: 0.41) followed at λ_{max} (625 nm). Quantitative conversion of the open form to the closed form under light irradiation with 617 nm for 100 seconds and minimal subsequent thermal recovery in the dark can be observed.

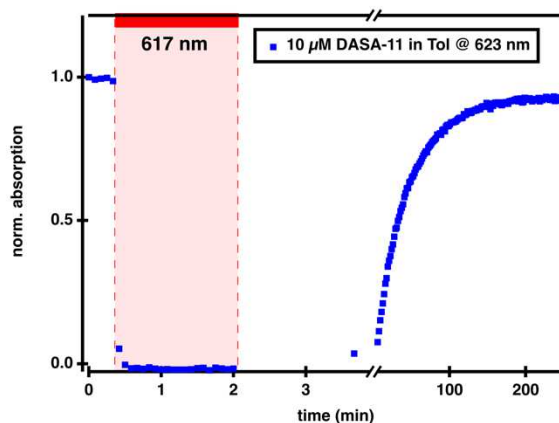


Figure 2.61. Time dependent UV-Vis spectroscopy to observe the photochromism of DASA-**11** in toluene at 10 μM (initial absorbance: 0.31) followed at λ_{max} (623 nm). Quantitative conversion of the open form to the closed form under light irradiation with 617 nm for 100 seconds and subsequent thermal recovery in the dark can be observed.

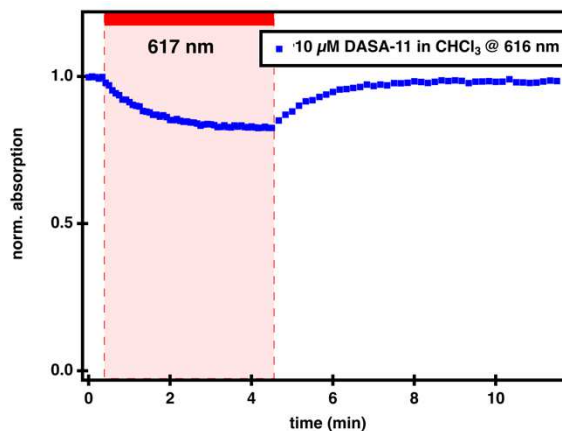


Figure 2.62. Time dependent UV-Vis spectroscopy to observe the photochromism of DASA-**11** in chloroform at 10 μM (initial absorbance: 0.56) followed at λ_{max} (616 nm). Conversion of 18% of the open form to the closed form under light irradiation with 617 nm for 100 seconds and subsequent thermal recovery in the dark can be observed.

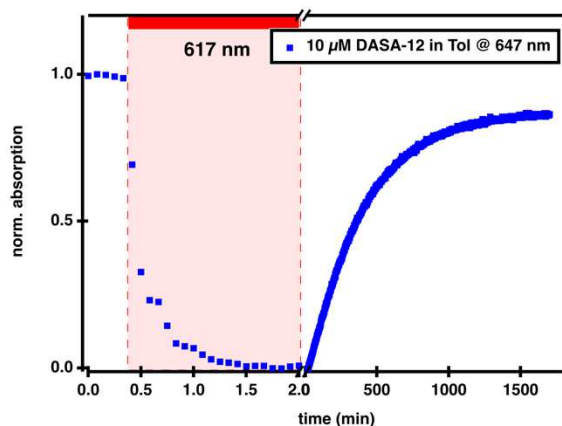


Figure 2.63. Time dependent UV-Vis spectroscopy to observe the photochromism of DASA-**12** in toluene at 10 μM (initial absorbance: 0.43) followed at λ_{max} (647 nm). Quantitative conversion of the open form to the closed form under light irradiation with 617 nm for 100 seconds and subsequent thermal recovery in the dark can be observed.

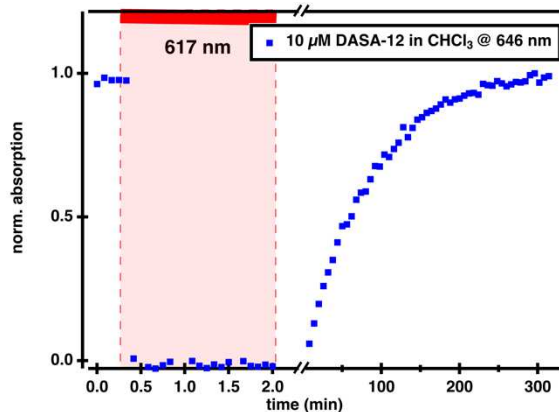


Figure 2.64. Time dependent UV-Vis spectroscopy to observe the photochromism of DASA-12 in chloroform at 10 μM (initial absorbance: 0.05) followed at λ_{max} (646 nm). Quantitative conversion of the open form to the closed form under light irradiation with 617 nm for 100 seconds and subsequent thermal recovery in the dark can be observed.

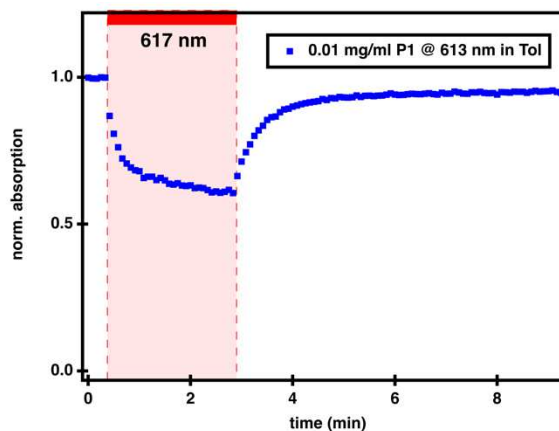


Figure 2.65. Time dependent UV-Vis spectroscopy to observe the photochromism of **P1** in toluene at 0.01 mg/mL (initial absorbance: 0.76) followed at λ_{max} (613 nm). Conversion of 40% of the open form to the closed form under light irradiation with 617 nm for 150 seconds and subsequent thermal recovery in the dark can be observed.

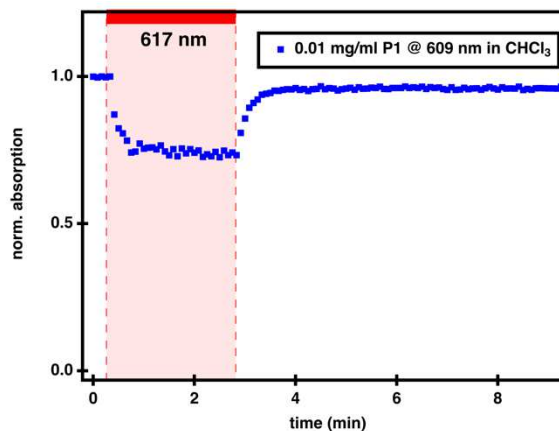


Figure 2.66. Time dependent UV-Vis spectroscopy to observe the photochromism of **P1** in chloroform at 0.01 mg/mL (initial absorbance: 0.73) followed at λ_{max} (609 nm). Conversion of 29% of the open form to the closed form under light irradiation with 617 nm for 150 seconds and subsequent thermal recovery in the dark can be observed.

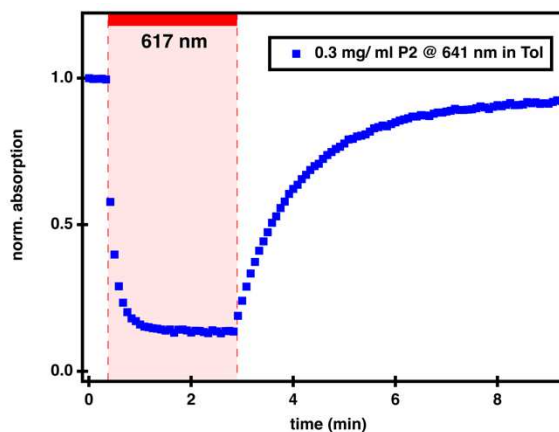


Figure 2.67. Time dependent UV-Vis spectroscopy to observe the photochromism of **P2** in toluene at 0.3 mg/mL (initial absorbance: 0.76) followed at λ_{max} (641 nm). Conversion of 85% of the open form to the closed form under light irradiation with 617 nm for 150 seconds and subsequent thermal recovery in the dark can be observed.

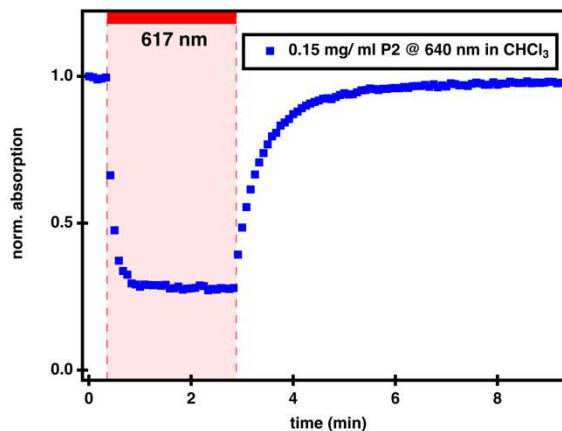


Figure 2.68. Time dependent UV-Vis spectroscopy to observe the photochromism of **P2** in chloroform at 0.15 mg/mL (initial absorbance: 0.88) followed at λ_{max} (640 nm). Conversion of 72% of the open form to the closed form under light irradiation with 617 nm for 150 seconds and subsequent thermal recovery in the dark can be observed.

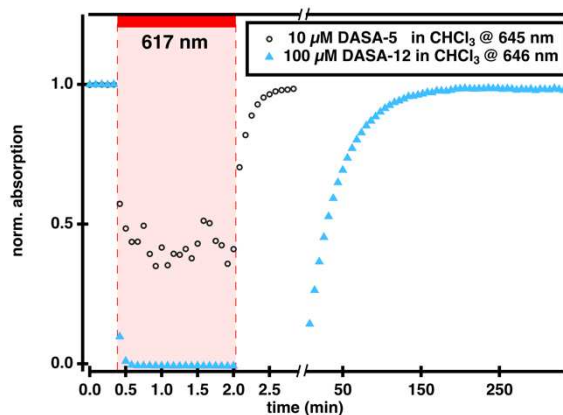


Figure 2.69. Time dependent UV-Vis spectroscopy to observe the photochromism of DASA-5 and DASA-12 in chloroform at 10 μM and 100 μM (initial absorbance: 0.9 and 1.0) followed at λ_{max} (645 nm and 646 nm). Quantitative conversion of the open form to the closed form under light irradiation with 617 nm for 100 seconds and subsequent thermal recovery in the dark can be observed. The half-life of the closed isomer of DASA-12 is 1545 s at 100 μM . This difference from the value of 10 μM is due to the concentration dependence of DASA.

2.10.8.3 Thermodynamic Equilibrium NMR Spectroscopy

Samples were stored in the dark at room temperature overnight. Closed and open isomer were identified by ^1H NMR spectroscopy (Figures 2.10.62–73).

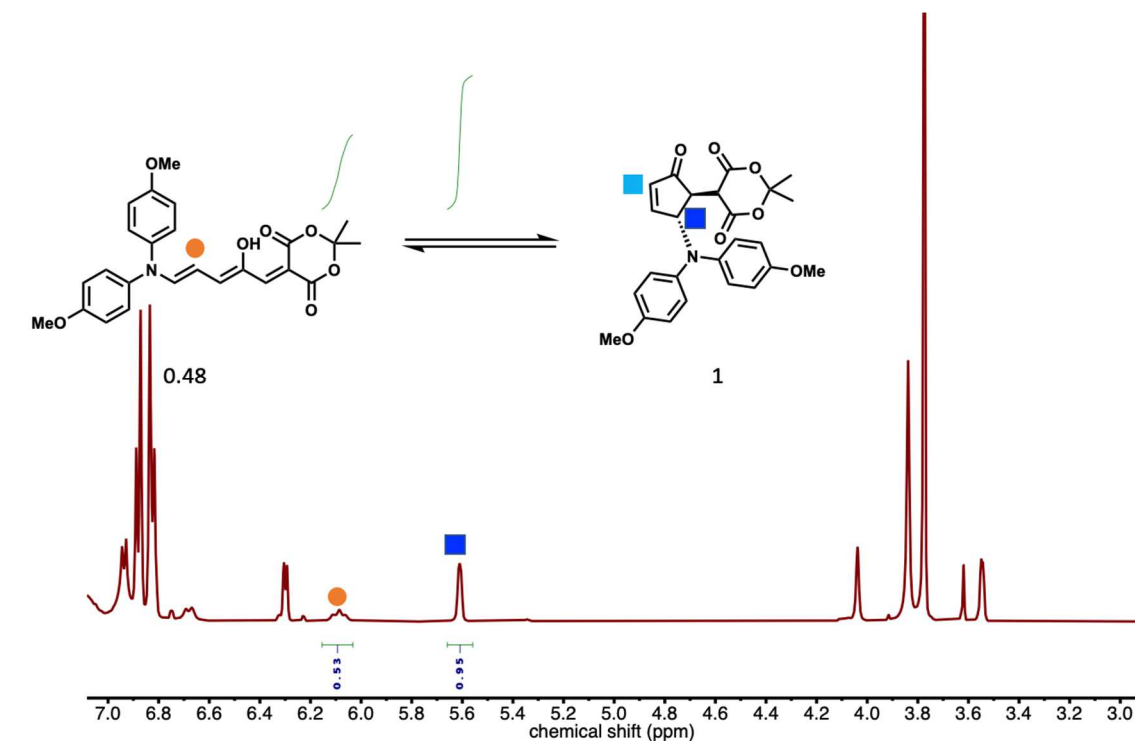


Figure 2.70. ^1H NMR (600 MHz, CDCl_3) spectra of the equilibrated DASA-1.

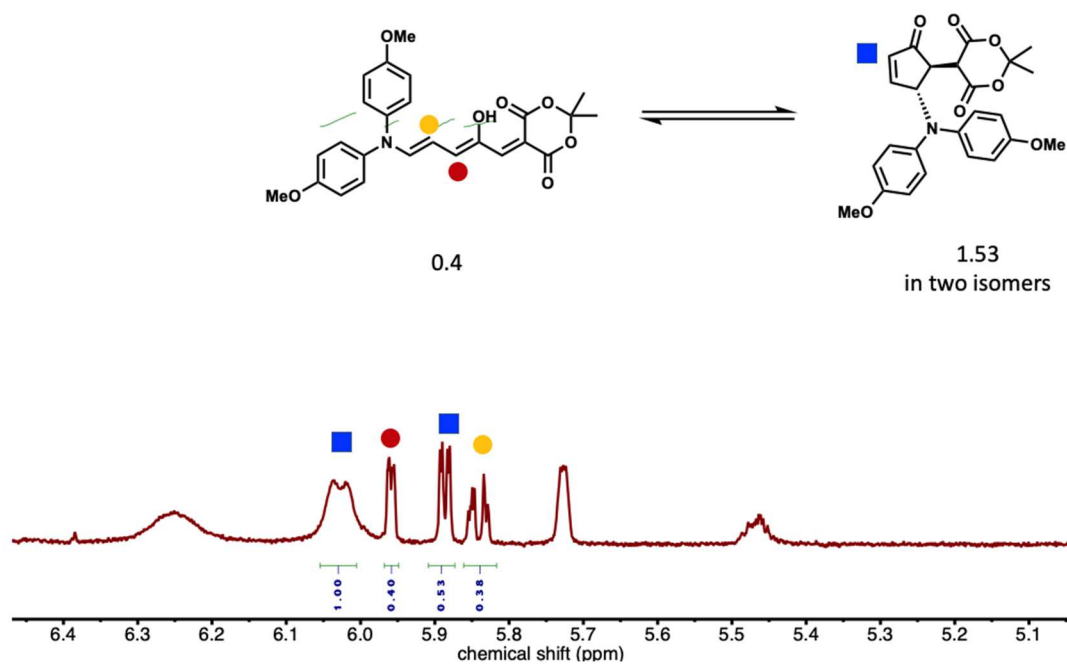


Figure 2.71. ¹H NMR (600 MHz, Tol-*d*₈) spectra of the equilibrated DASA-1.

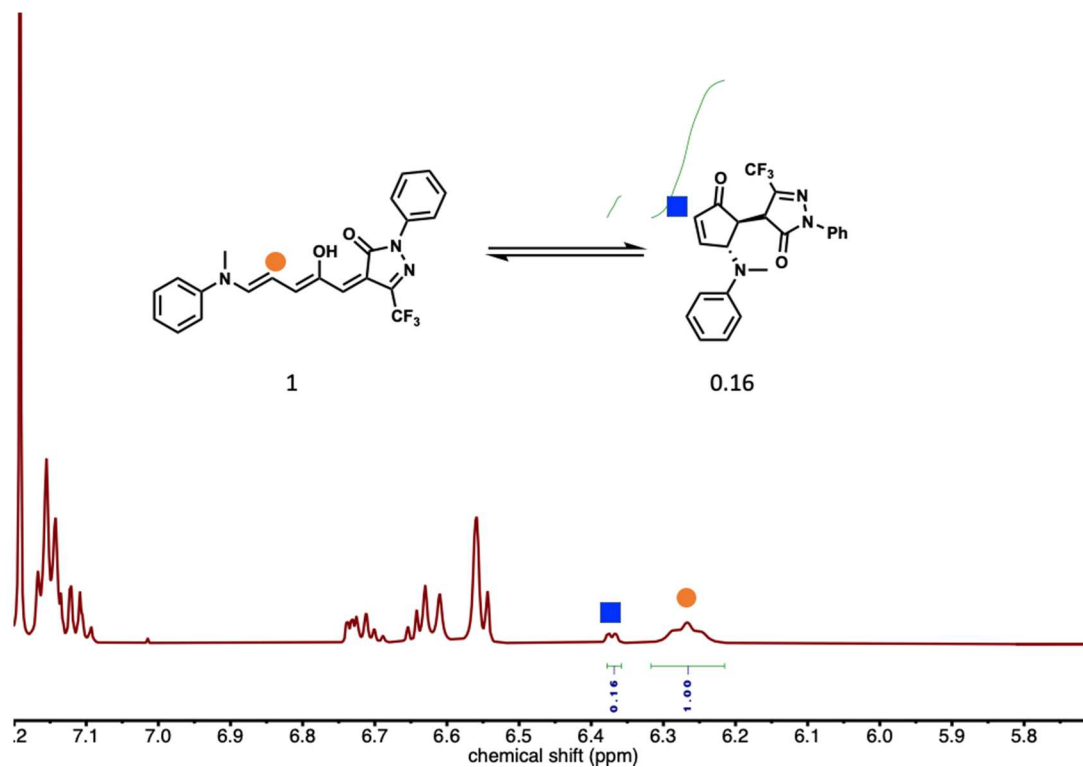


Figure 2.72. ^1H NMR (600 MHz, CDCl_3) spectra of the equilibrated DASA-2.

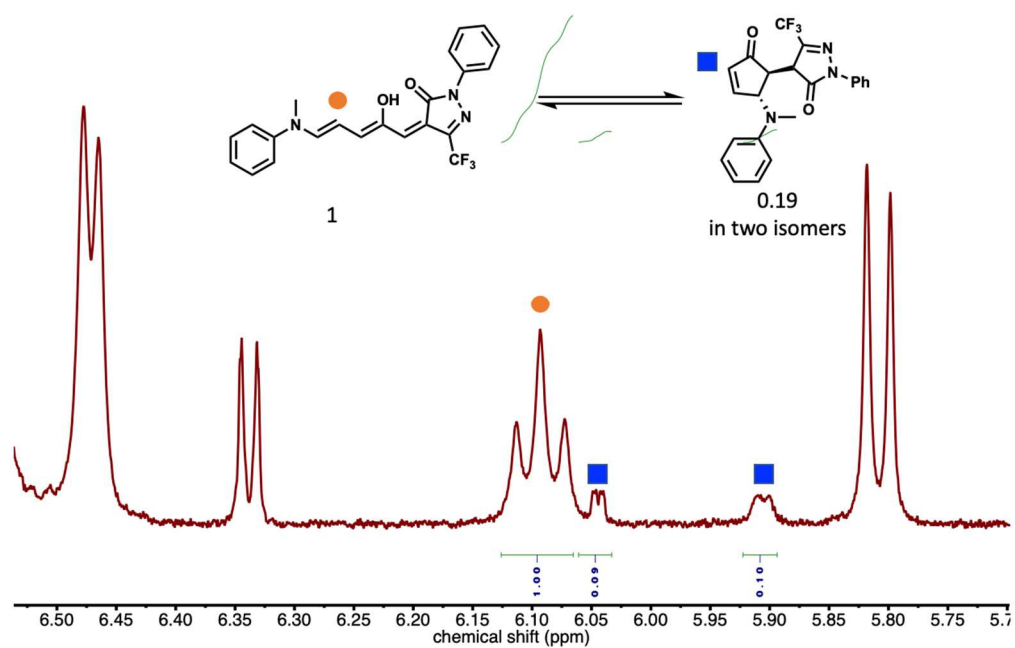


Figure 2.73. ^1H NMR (600 MHz, $\text{Tol-}d_8$) spectra of the equilibrated DASA-2.

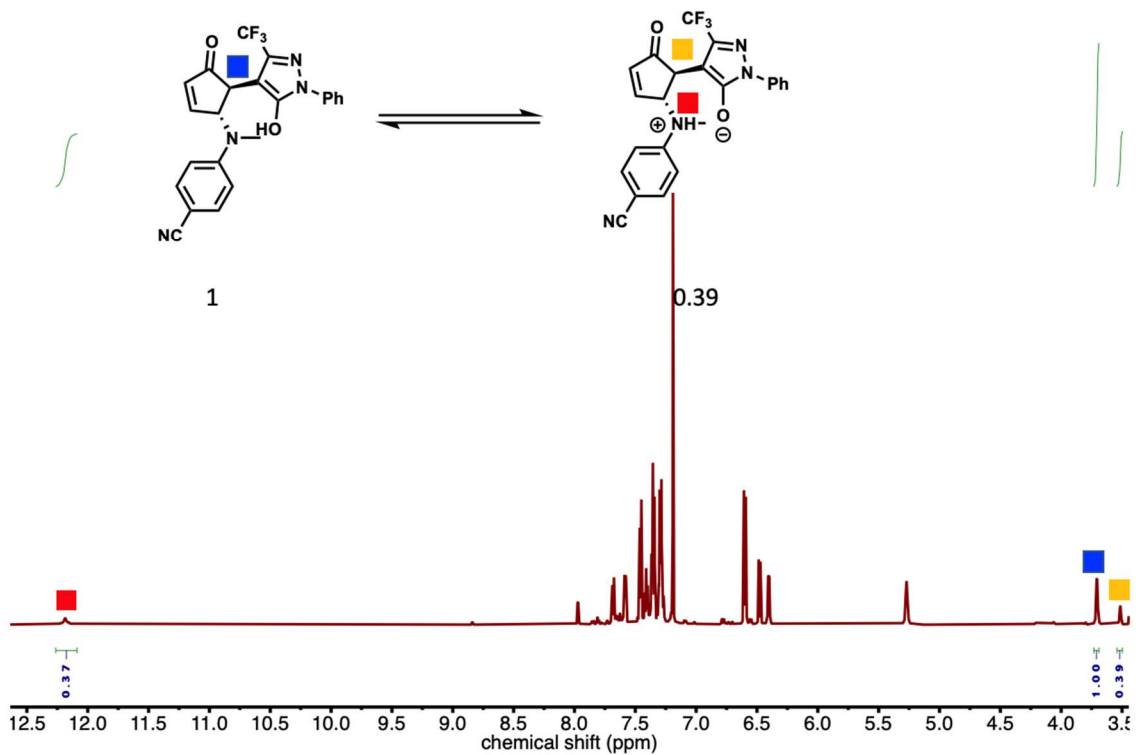


Figure 2.74. ^1H NMR (600 MHz, CDCl_3) spectra of the equilibrated DASA-8. No equilibration to the open form can be observed, but a zwitterionic closed isomer is formed over time.

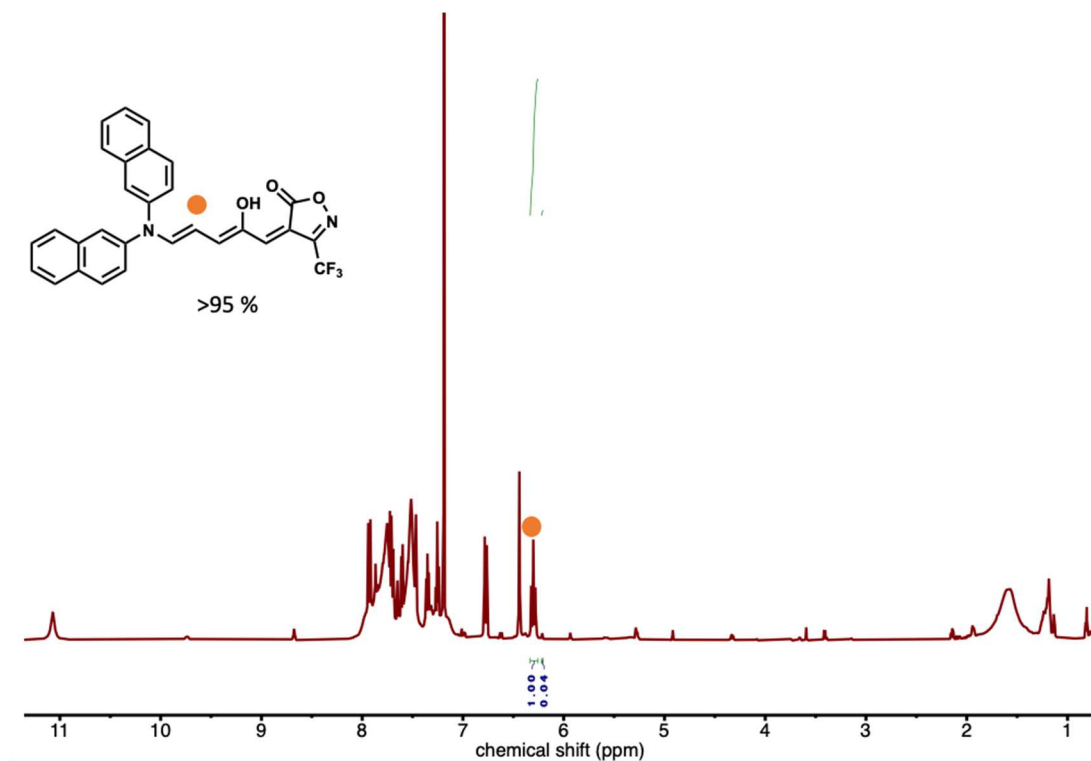


Figure 2.75. ¹H NMR (600 MHz, CDCl₃) spectra of the equilibrated DASA-9. No closed form can be observed.

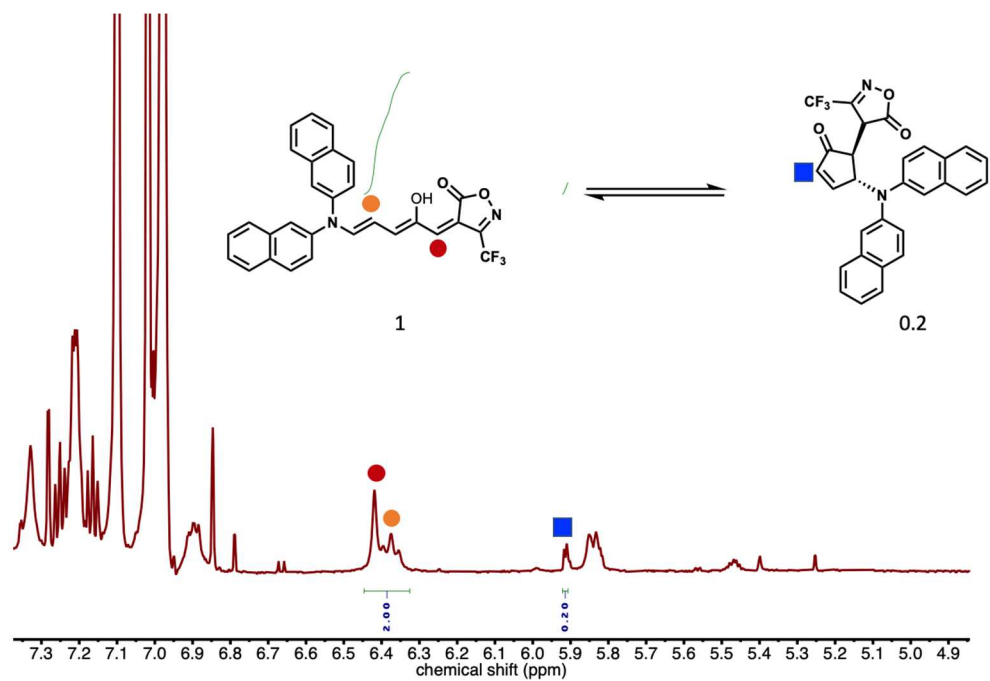


Figure 2.76. ^1H NMR (600 MHz, $\text{Tol-}d_3$) spectra of the equilibrated DASA-9.

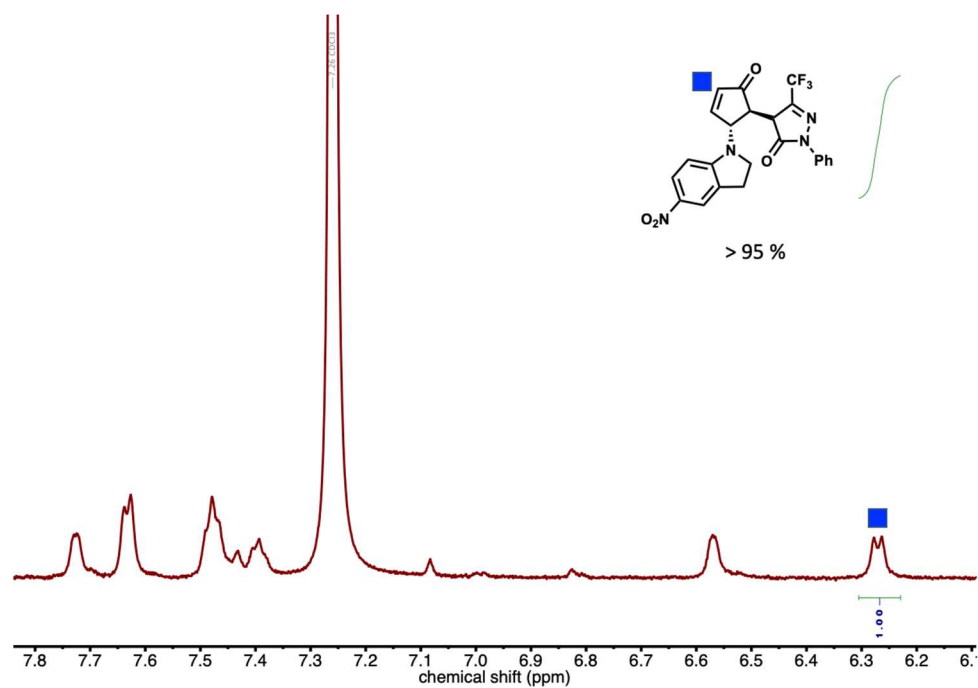


Figure 2.77. ^1H NMR (600 MHz, CDCl_3) spectra of the equilibrated DASA-10. No open form can be observed.

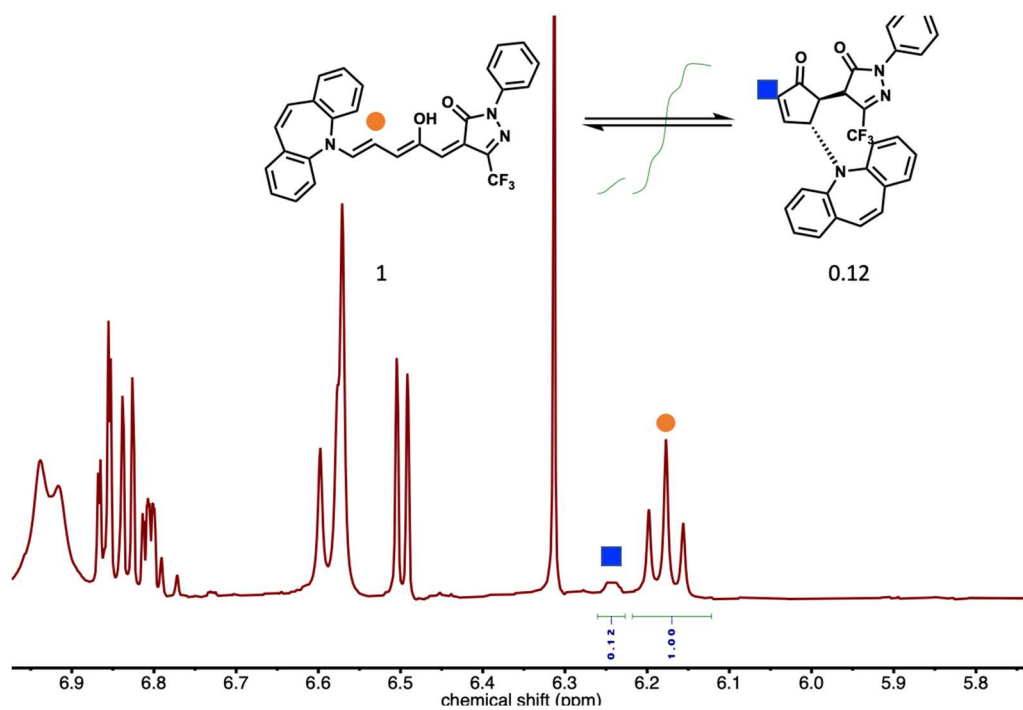


Figure 2.78. ^1H NMR (600 MHz, CDCl_3) spectra of the equilibrated DASA-11.

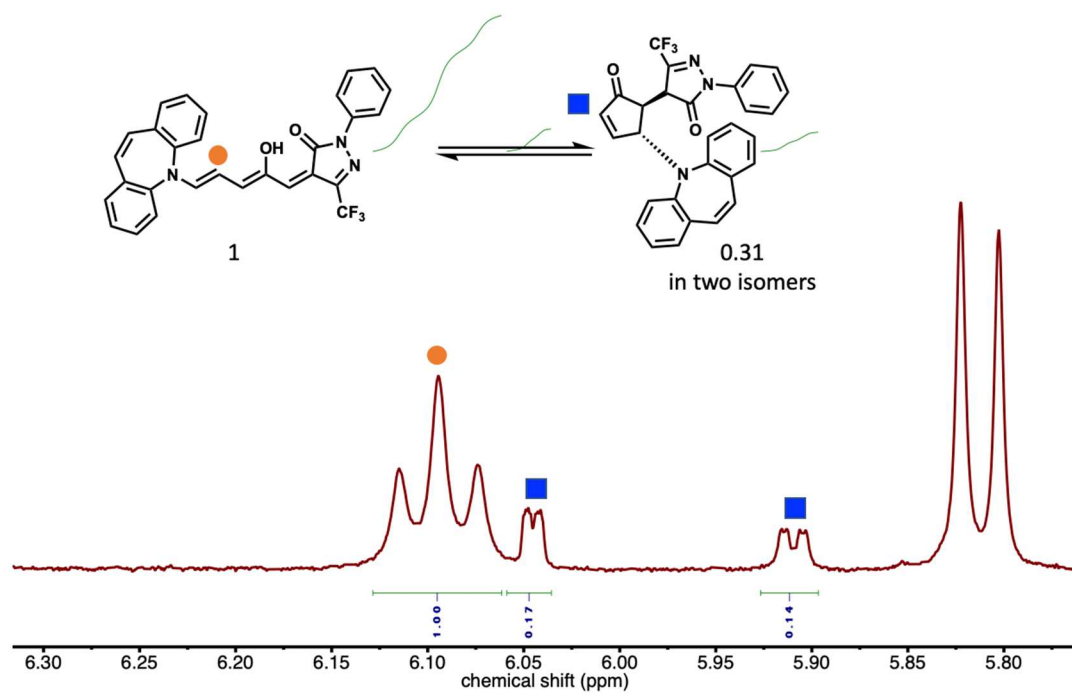


Figure 2.79. ^1H NMR (600 MHz, $\text{Tol-}d_8$) spectra of the equilibrated DASA-11.

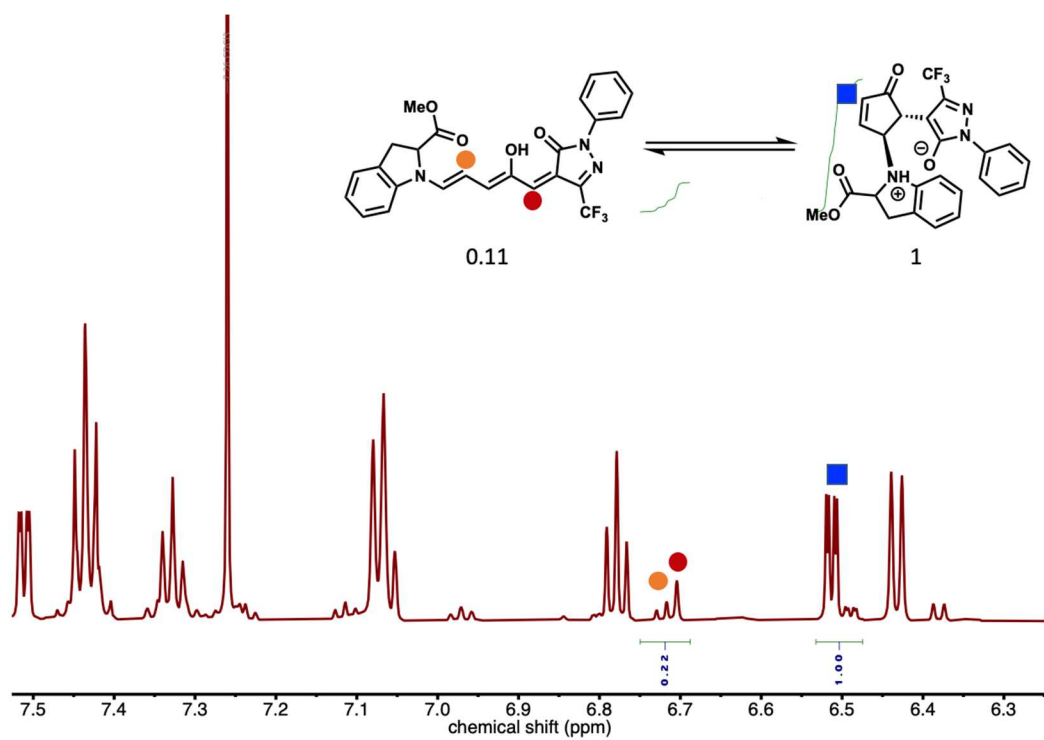


Figure 2.80. ^1H NMR (600 MHz, CDCl_3) spectra of the equilibrated DASA-12.

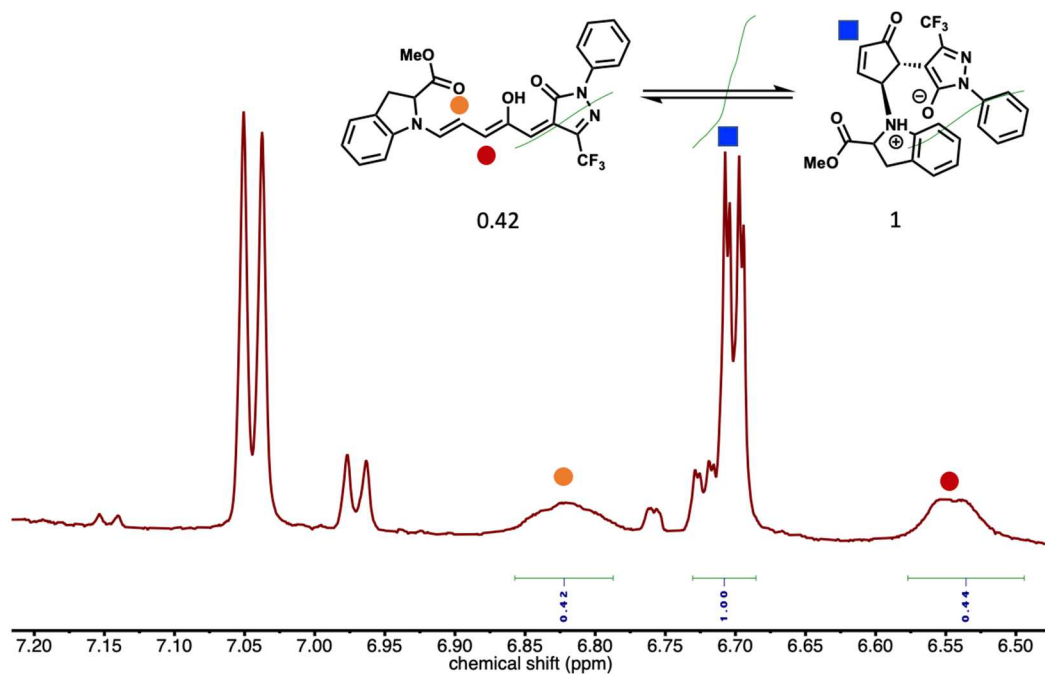


Figure 2.81. ¹H NMR (600 MHz, Tol-*d*₈) spectra of the equilibrated DASA-12.

2.10.8.4 2D-NMR Spectroscopy

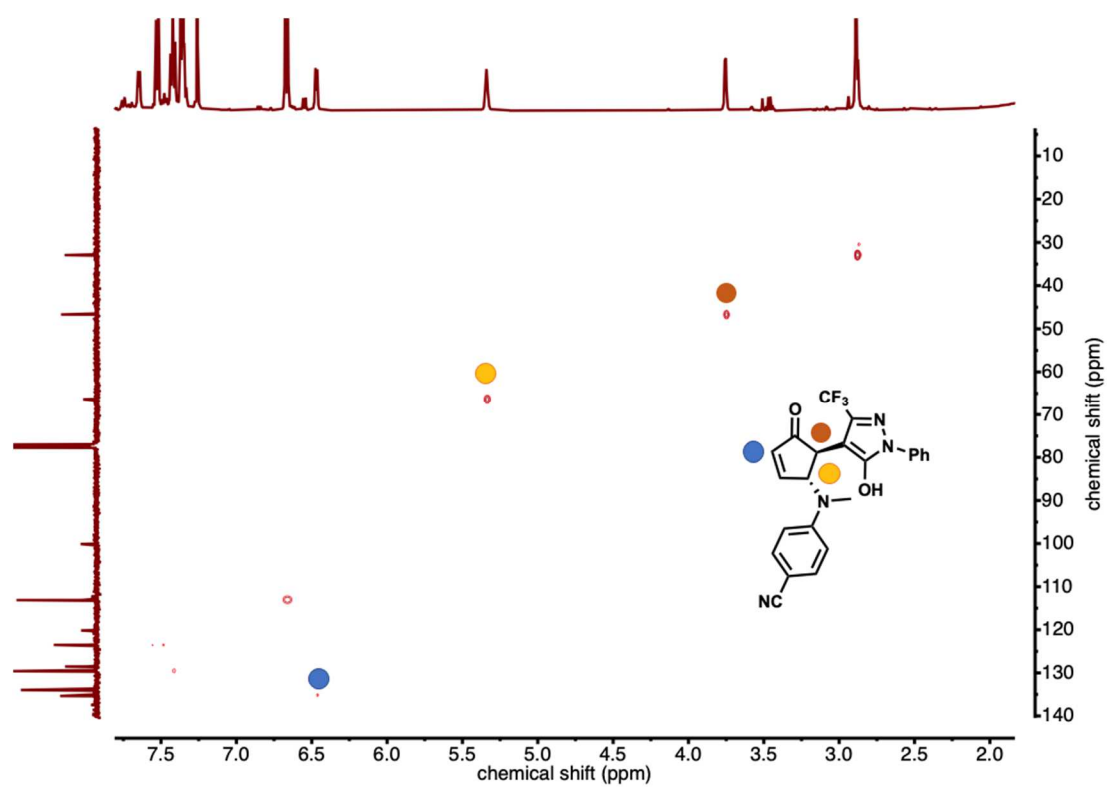


Figure 2.82. HSQC NMR (600 MHz, 297 K, CDCl_3) spectra of DASA-8.

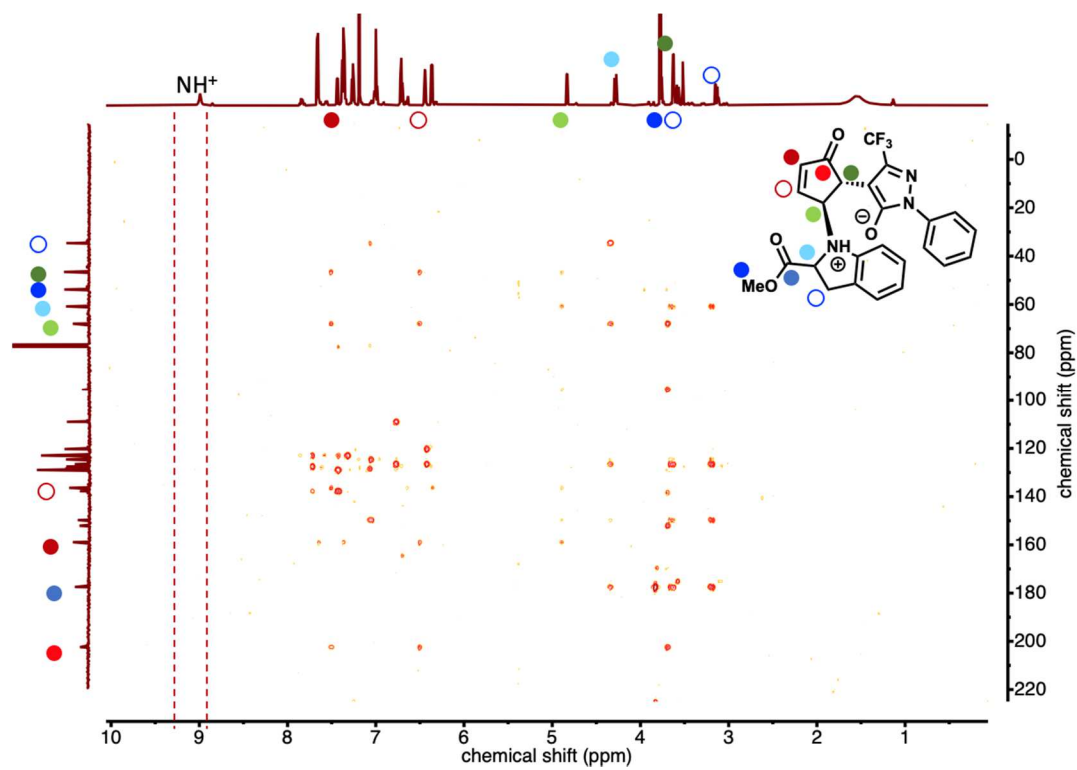


Figure 2.83. HMBC NMR (600 MHz, 297 K, CDCl_3) spectra of DASA-12.

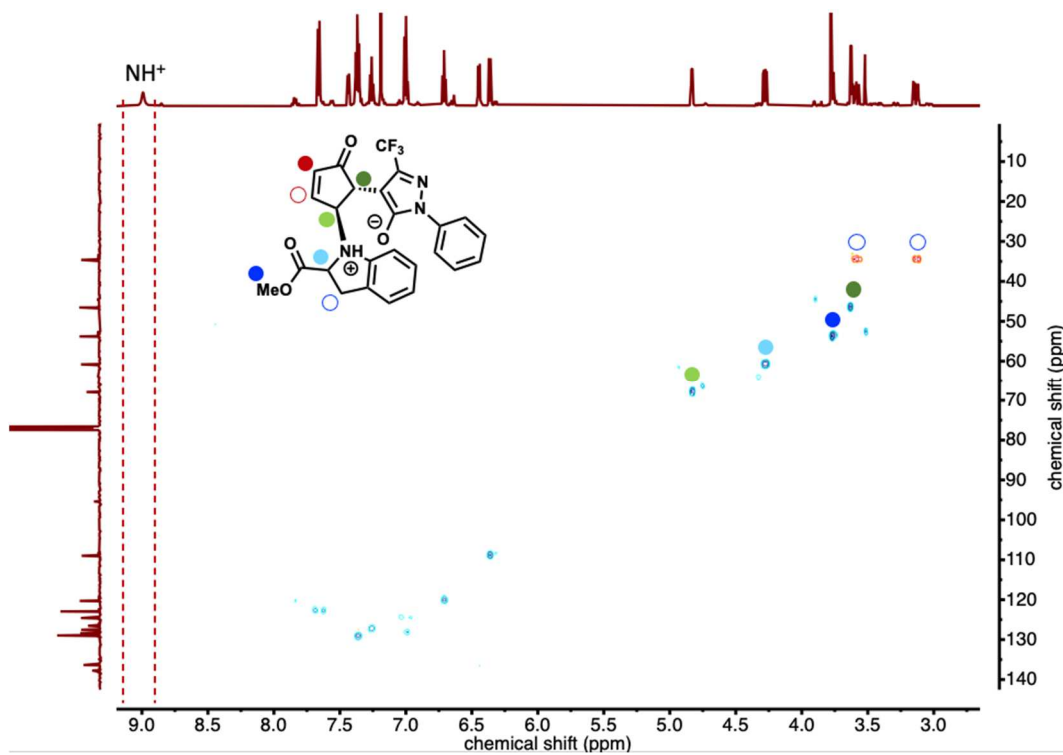


Figure 2.84. HSQC NMR (600 MHz, 297 K, CDCl_3) spectra of DASA-12.

2.10.9 Fluorescence

For **DASA-9** in toluene (in contrast to the parent 2,2'-dinaphthylamine) we found a dependence of the emission spectrum on the excitation wavelength (**Figure 2.85**). This suggests the existence of multiple electronic transitions being involved, which can be explained by the existence of different fluorescent species in the ground state (i.e. open/closed form **DASA** and/or conformers thereof and/or minor amounts of residual free amine and/or conformers thereof). In general, the emission spectra of **DASA-9** are slightly red-shifted when compared to the parent dinaphthylamine in toluene (λ_{max} of 396 nm vs. 388 nm). For dinaphthylamine in toluene we did not observe any visible-light dependence on the fluorescent properties, while for **DASA-9** we observed an increase in intensity, but no change in band shape or position, when repeatedly irradiated with a MINTF4 fiber-coupled LED (Thorlabs, nominal wavelength 554 nm) for ~60 seconds (10 μM in toluene, **Figure 2.86**). Control measurements of dinaphthylamine (0.1 μM) in a toluene solution of **DASA-2** (20 μM), however, did show some degree of excitation wavelength dependent emission spectra and trials with visible light irradiation were inconclusive (**Figure 2.86**). We can therefore not exclude that trace amounts of free dinaphthylamine are causing or interfering with the measured fluorescence response. We additionally found that a toluene solution of **DASA-9** when constantly irradiated with 350 nm light shows irreversible increase in fluorescence emission after some time suggesting possible photodegradation (no such changes were found for dinaphthylamine in toluene in the investigated time window, **Figure 2.87**). As described elsewhere,⁴⁷ open form **DASAs** exhibit weak fluorescence emission when excited at their maximum absorption wavelength ($\pi\text{-}\pi^*$ transition). We also observed fluorescence in **DASA-9** upon excitation at 630 nm but similarly weak in intensity as observed previously for other **DASA** derivatives employing simpler amine donors. The intensity of this fluorescence band

decreases upon converting the DASA to the closed form isomer and increases again upon thermal recovery in the dark (**Figure 2.85**).

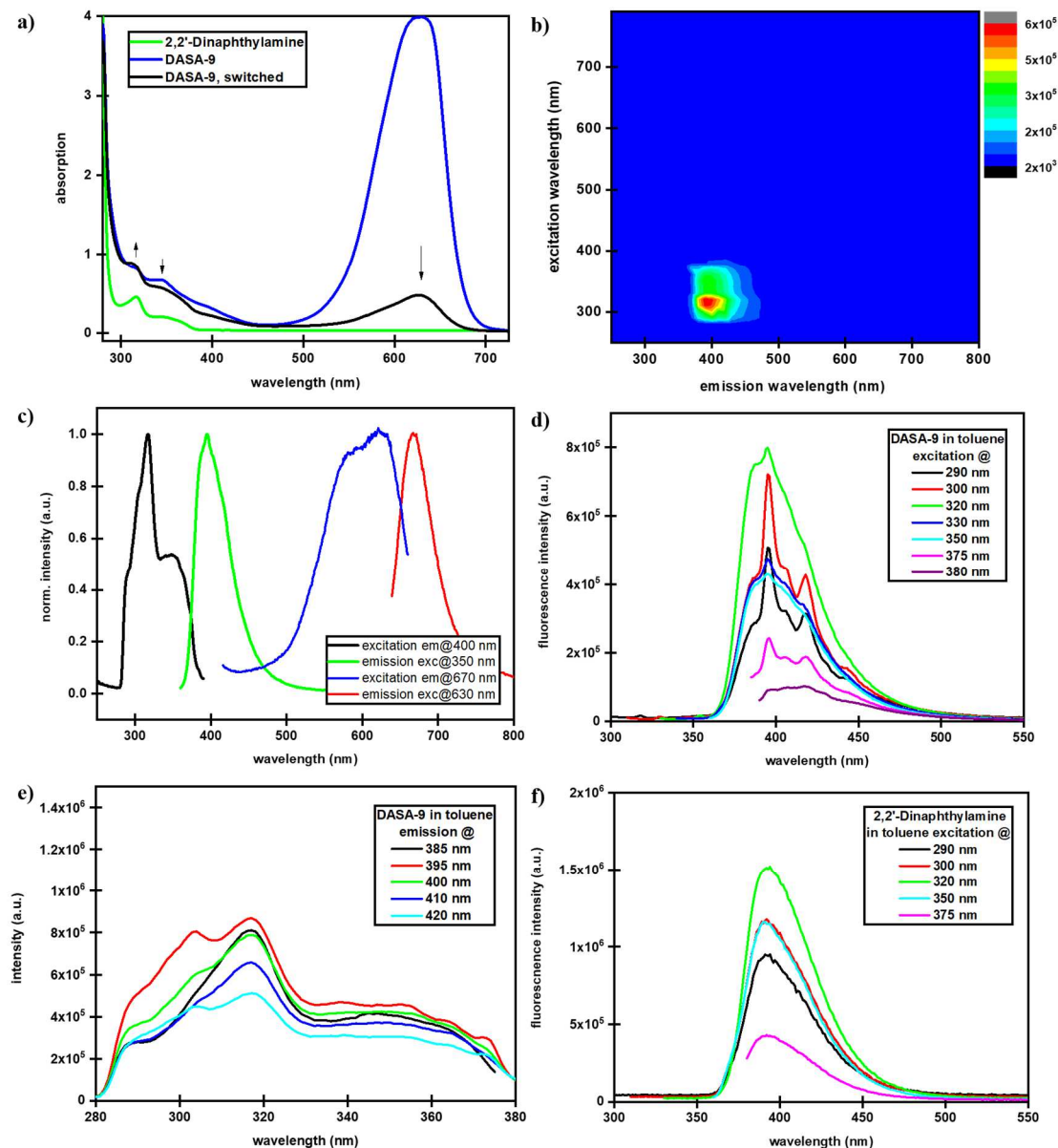


Figure 2.85. Absorption, emission and excitation spectra of DASA-9 (equilibrated solution in toluene) and 2,2'-dinaphthylamine in toluene. a) Absorption spectra showing the absorbance bands characteristic for the naphthyl-units at 325–350 nm (2,2'-dinaphthylamine, 20 μ M; DASA-9, 100 μ M, before and after visible light irradiation for \sim 100 s). b) Excitation

vs emission spectrum of an equilibrated solution of DASA-9 in toluene (10 μM). c) Normalized excitation and emission spectra: $\lambda_{\text{em}} = 400 \text{ nm}$ / $\lambda_{\text{exc}} = 350 \text{ nm}$ (2 nm slit widths) and $\lambda_{\text{em}} = 670 \text{ nm}$ / $\lambda_{\text{exc}} = 630 \text{ nm}$ (5 nm slit widths). d) Emission spectra of DASA-9 in toluene (10 μM) for different excitation wavelengths. e) Excitation spectra of DASA-9 in toluene (10 μM) for different emission wavelengths. f) Emission spectra of 2,2'-dinaphthylamine in toluene (20 μM) for different excitation wavelengths (1 nm slit widths).

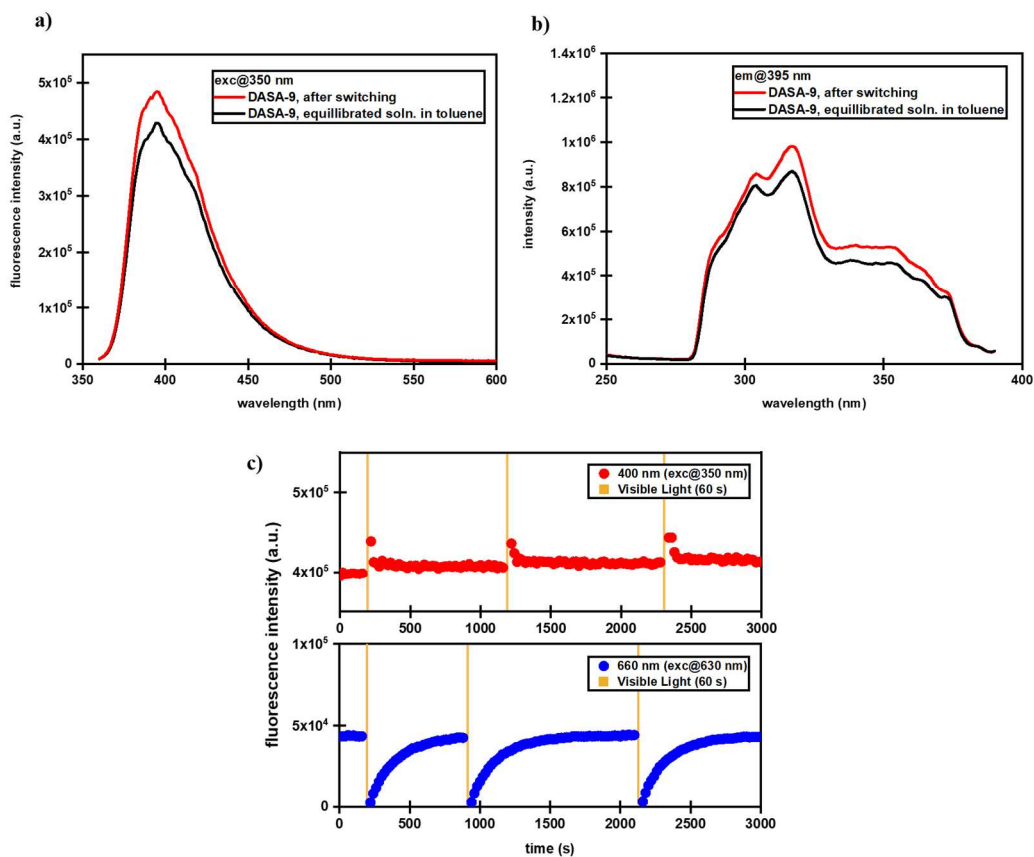


Figure 2.86. Changes in emission and excitation spectra of DASA-9 (10 μ M, toluene). a) Emission spectra ($\lambda_{\text{exc}} = 350$ nm) before and after visible light irradiation (MINTF4 fiber-coupled LED, Thorlabs, nominal wavelength 554 nm) for ~ 60 seconds. b) Excitation spectra ($\lambda_{\text{em}} = 395$ nm) before and after visible light irradiation. c) Fluorescence intensity monitoring at 400 nm ($\lambda_{\text{exc}} = 350$ nm, 2 nm slit widths) and 660 nm ($\lambda_{\text{exc}} = 630$ nm, 5 nm slit widths) before and after visible light irradiation (MINTF4 fiber-coupled LED, Thorlabs, nominal wavelength 554 nm for ~ 60 seconds inside fluorimeter, temperature: 31 $^{\circ}$ C).

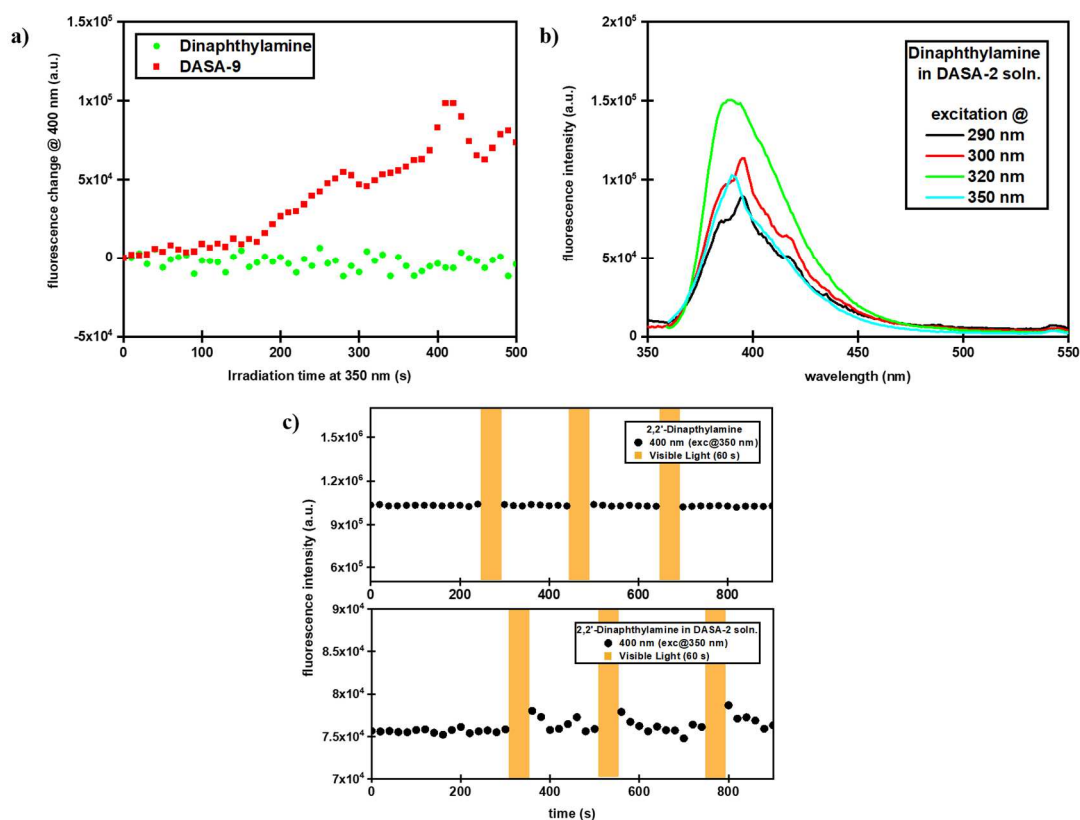


Figure 2.87. Control experiments for luminescence of DASA-9. a) Fluorescence intensity change at 400 nm ($\lambda_{\text{exc}} = 350$) upon constant irradiation at 350 nm (excitation light source of fluorimeter) for solutions of dinaphthylamine (20 μM in toluene) and DASA-9 (10 μM in toluene). b) Emission spectra at different excitation wavelengths of dinaphthylamine (0.1 μM) in a solution of DASA-2 in toluene (20 μM). Slit widths set to 3 nm. c) Fluorescence intensity monitoring at 400 nm ($\lambda_{\text{exc}} = 350$) before and after visible light irradiation (MINTF4 fiber-coupled LED, Thorlabs, nominal wavelength 554 nm for ~ 60 seconds inside fluorimeter, temperature: 31 $^{\circ}\text{C}$) of dinaphthylamine in toluene (20 μM) or in a toluene solution (0.1 μM) of DASA-2 (20 μM).

2.10.10 Probing the H-bonding in the Presence of HFIP

As confirmed in previous studies by other groups,⁴⁴ the hydroxy protons in DASAs are easily exchangeable and their ¹H-NMR signals are completely absent when the spectra are measured in, e.g., deuterated alcohols. We also observed the disappearance of these signals when measuring ¹H-NMR spectra of DASAs in solutions containing larger amounts of HFIP (deuterated and non-deuterated). In the following **Figure 2.88**, the changes of the hydroxy proton ¹H-NMR signal under different conditions are displayed. Here, it is visible that HFIP leads to a disappearance of the hydroxy proton signal, whereas additives such as HFIPMe at similar concentrations have none (or less, only slight broadening is observed) of an effect.

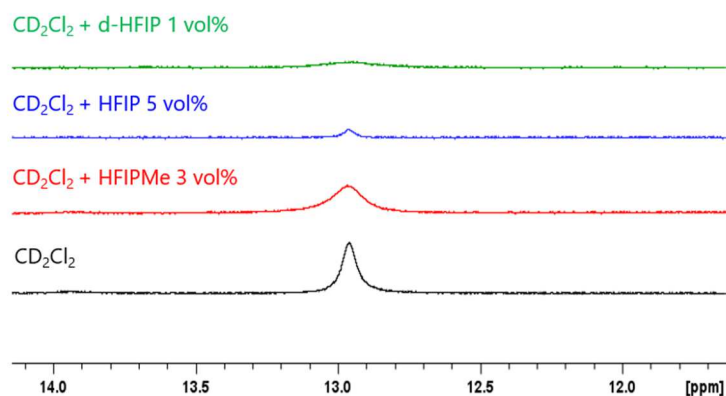


Figure 2.88. ¹H NMR (500 MHz, CD₂Cl₂) spectra of DASA-2 upon addition of different additives. The signal of hydroxy proton on the triene is shown.

As also shown in **Figure 2.89**, the presence of HFIP, however, seems to not effect a change of the chemical shift of the OH-signal. On the other hand, the chemical shifts of the polyene and aromatic protons do change, which we believe can also be a result of simple

solvent effects and not necessarily specific interactions (it is also established that different solvents favor different resonance structures of the DASA open form).

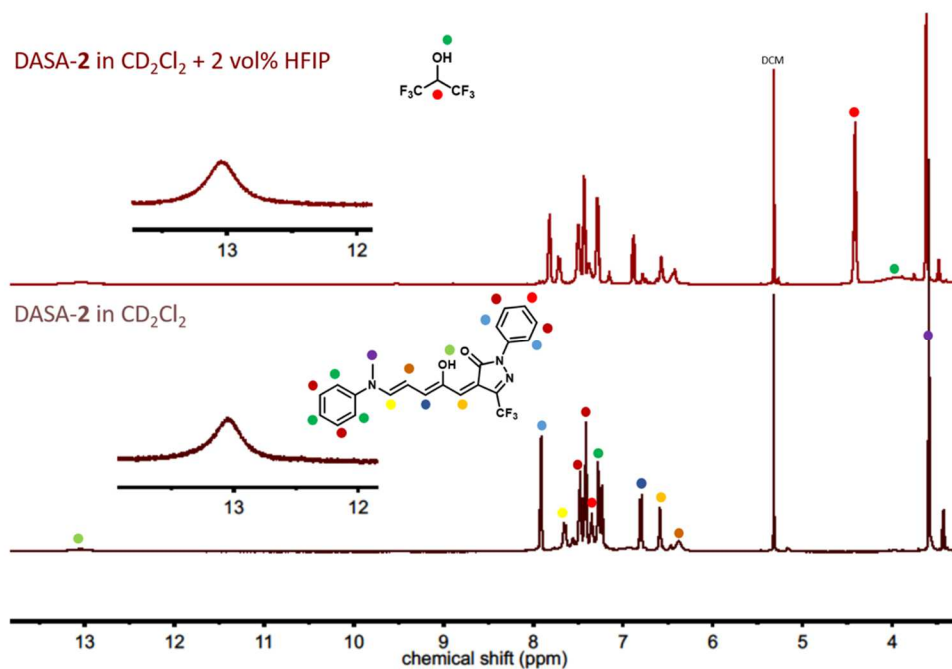


Figure 2.89. ^1H NMR (500 MHz) spectra of DASA-2 (10 mg/mL) in CD_2Cl_2 and CD_2Cl_2 containing 2 vol% HFIP.

To further probe the potential of H-bonding, IR spectroscopic measurements in DCM vs. HFIP on a Meldrum's acid based DASA (DASA-6) were conducted. As indicated in **Figure 2.90** below, the observation of two bands for the carbonyl stretching modes in the Meldrum's acid moiety can be found for measurements in DCM or in the solid state ($\sim 1615\text{ cm}^{-1}$: H-bonded ring carbonyl stretch, $\sim 1700\text{ cm}^{-1}$ second non H-bonded carbonyl, in agreement with previous assignments from literature).⁴⁴ On the other hand, measurements in HFIP did not show a pronounced band at 1700 cm^{-1} for a non H-bonded carbonyl and the band previously observed at $\sim 1615\text{ cm}^{-1}$ red-shifts pointing towards a large change in the strength

of the H-bond. Although further studies are required, this does provide additional supporting evidence for the proposed modulation of the H-bonding.

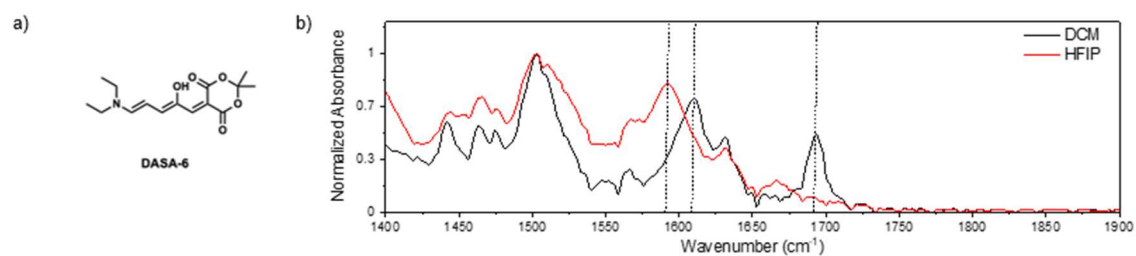


Figure 2.90. a) DASA-6. b) IR spectra of DASA-6 in DCM and HFIP showing the spectral changes in carbonyl region.

2.10.11 Spectra

2.10.11.1 NMR Spectra

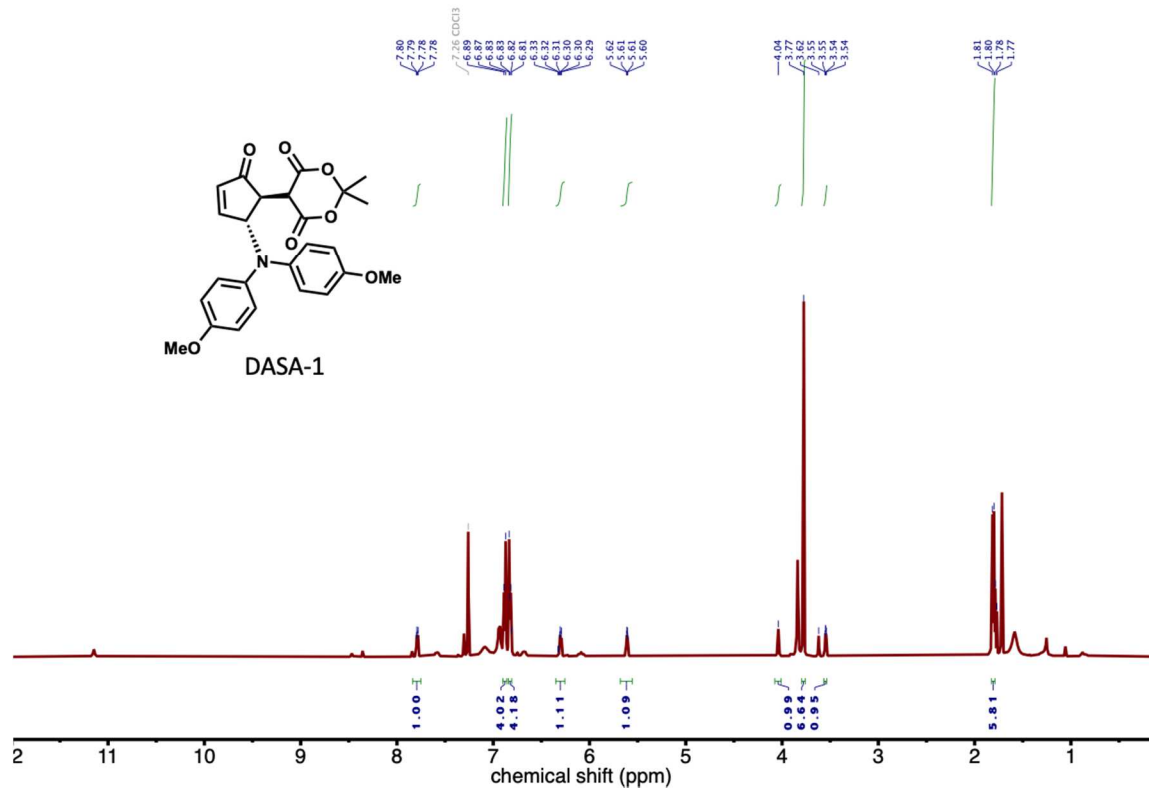


Figure 2.91. ^1H NMR (500 MHz, CDCl_3) spectra of the closed isomer of DASA-1. Some open form can also be observed.

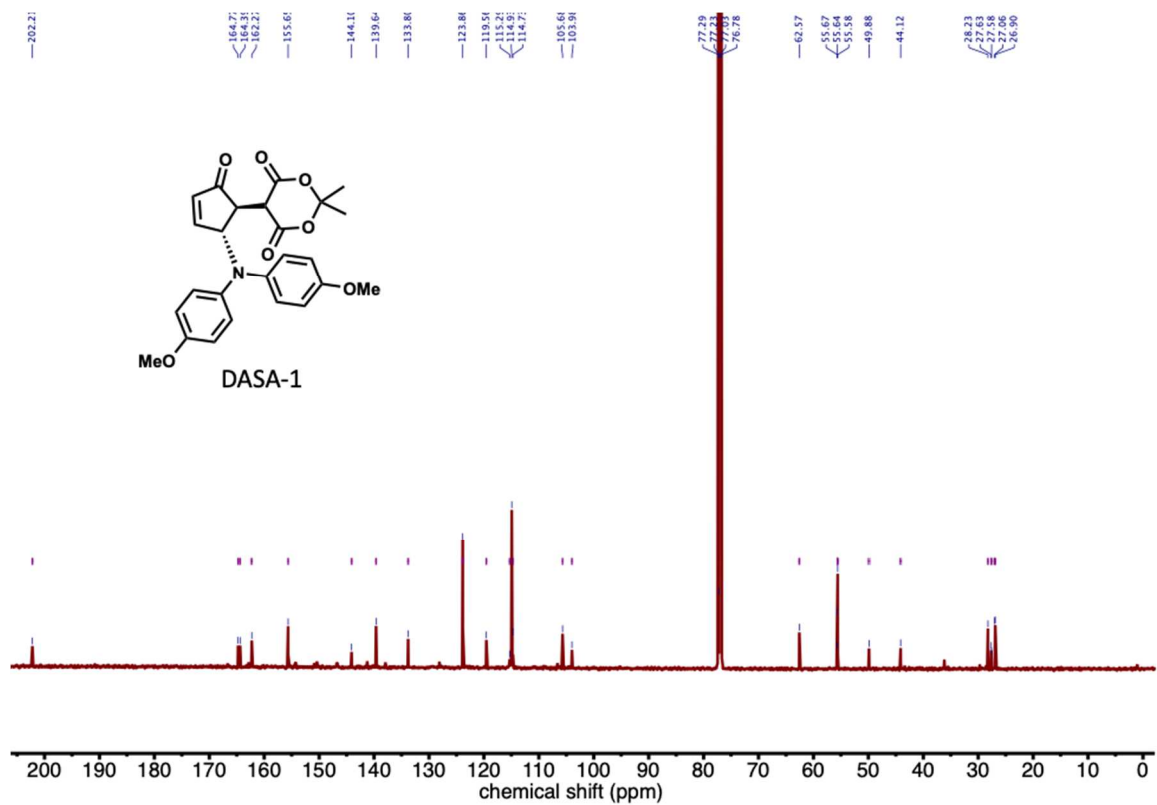


Figure 2.92. ¹³C NMR (125 MHz, CDCl₃) spectra of the closed isomer of DASA-1.

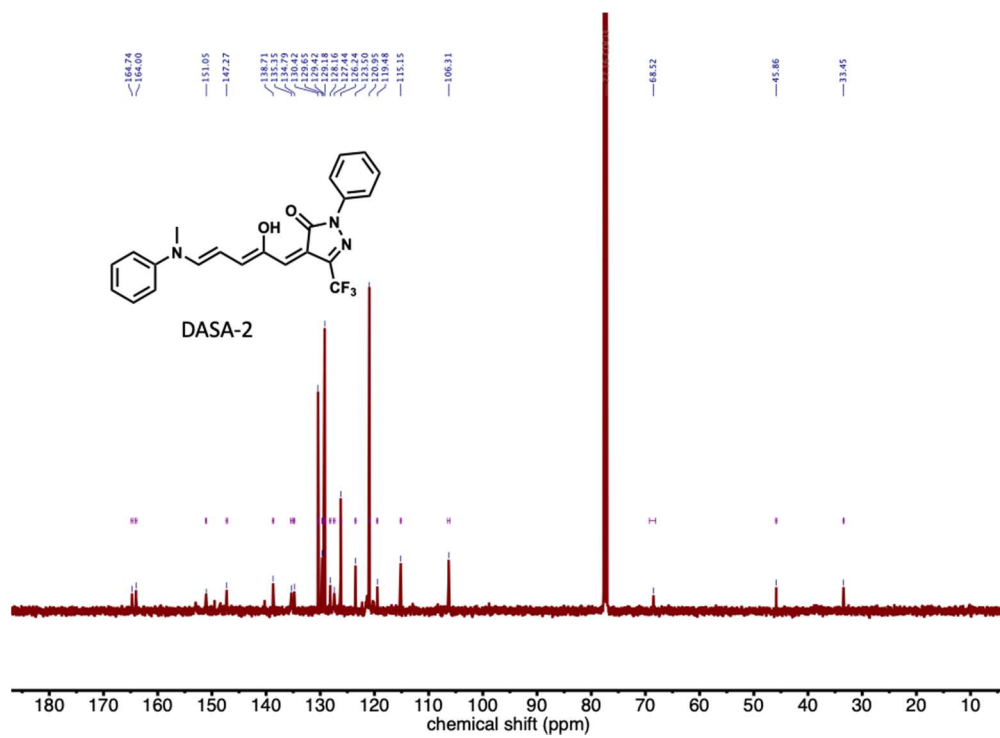


Figure 2.94. ¹³CNMR (125 MHz, CDCl₃) spectra of the open isomer of DASA-2

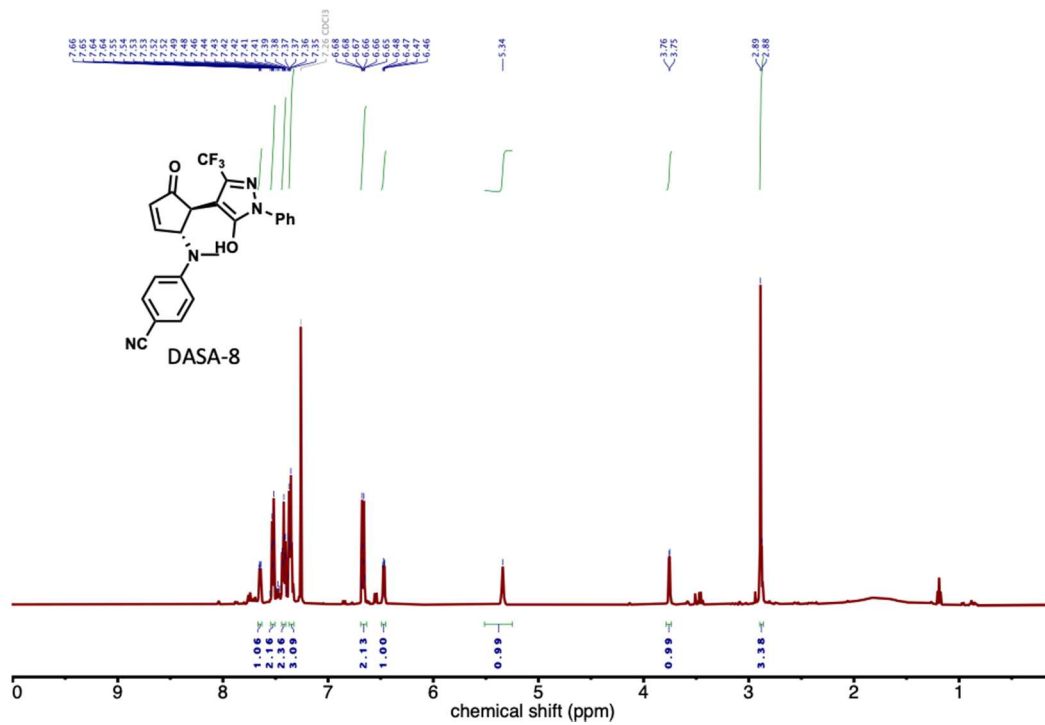


Figure 2.95. ¹H NMR (500 MHz, CDCl₃) spectra of the closed isomer of DASA-8.

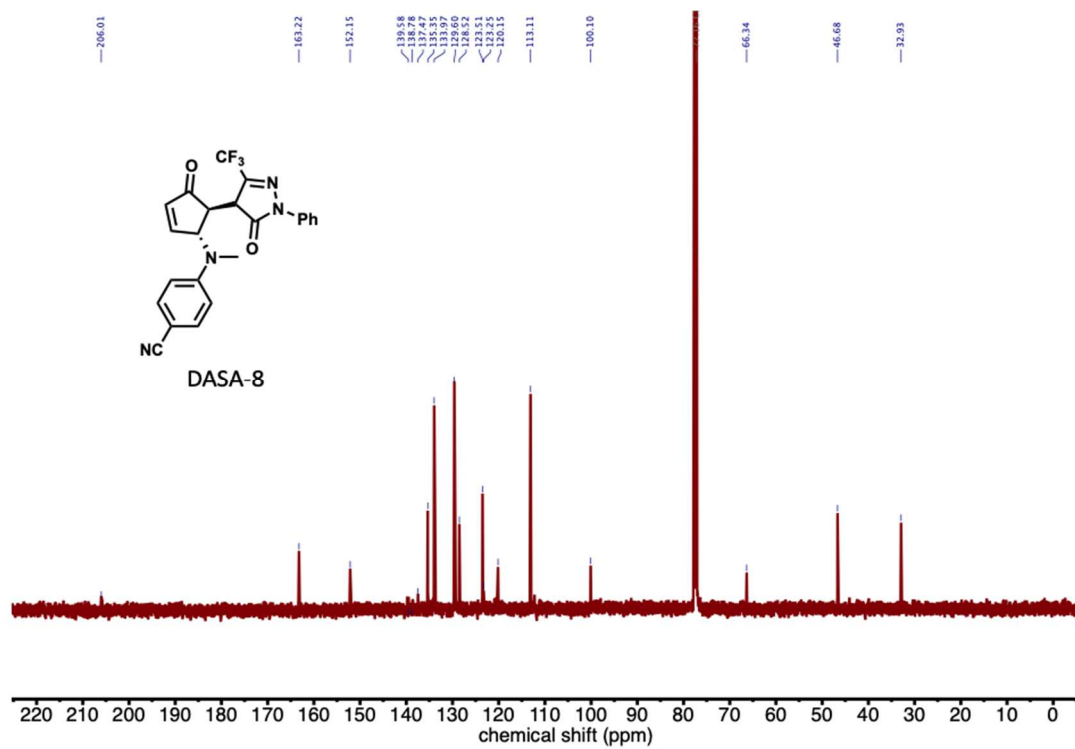


Figure 2.96. ^1H NMR (125 MHz, CDCl_3) spectra of the closed isomer of DASA-8.

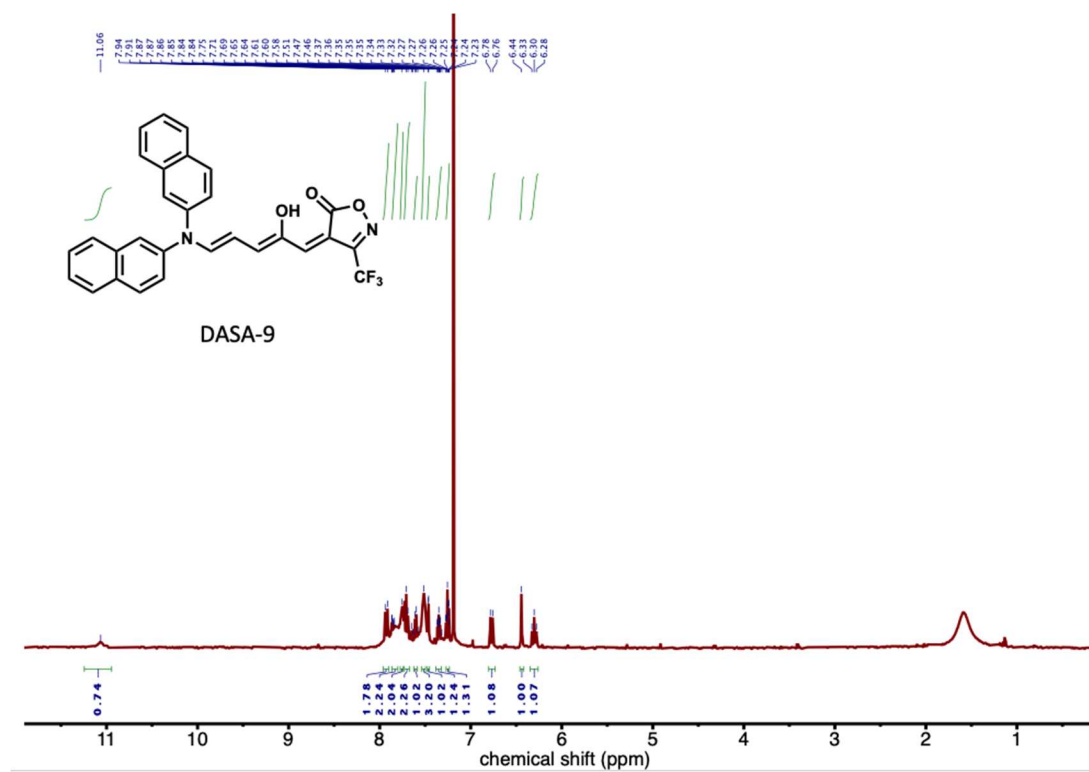


Figure 2.97. ^1H NMR (500 MHz, CDCl_3) spectra of the open isomer of DASA-9.

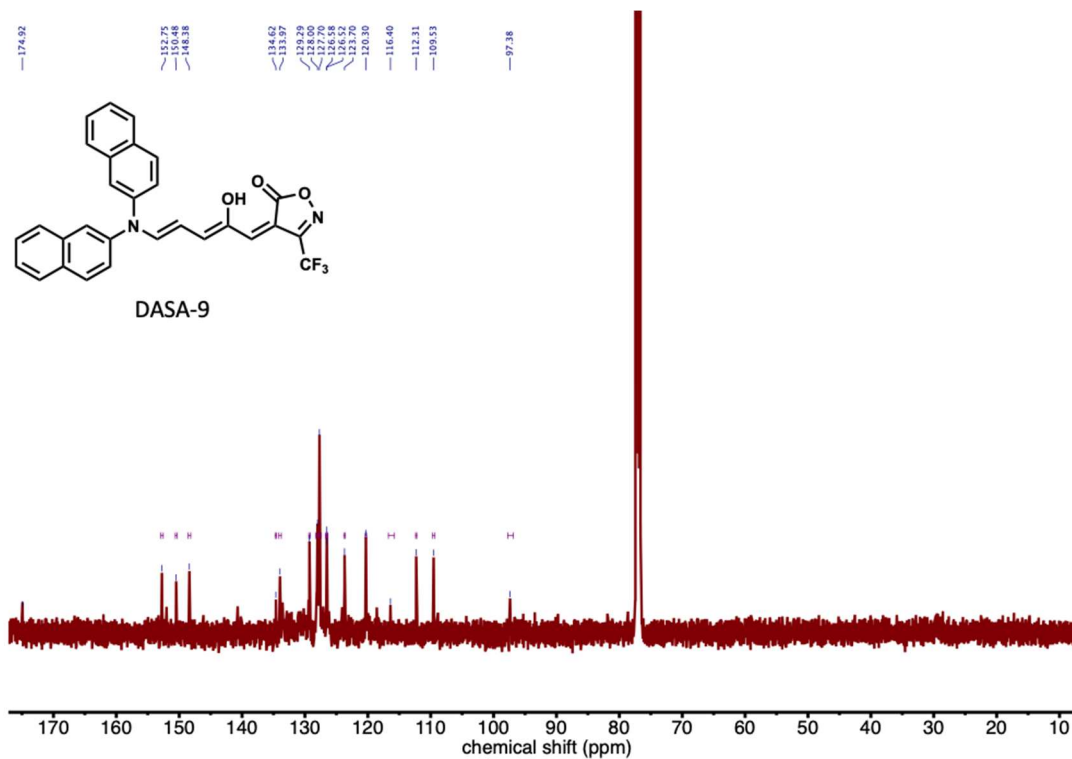


Figure 2.98. ¹³C NMR (125 MHz, CDCl₃) spectra of the open isomer of DASA-9.

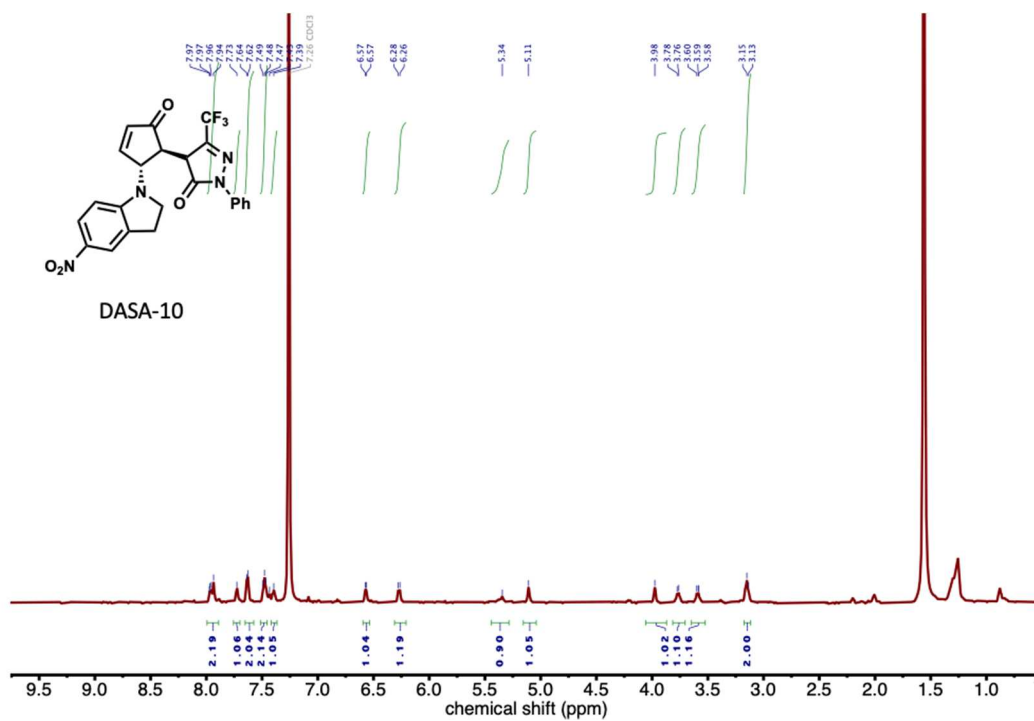


Figure 2.99. ¹H NMR (600 MHz, CDCl₃) spectra of the closed isomer of DASA-10.

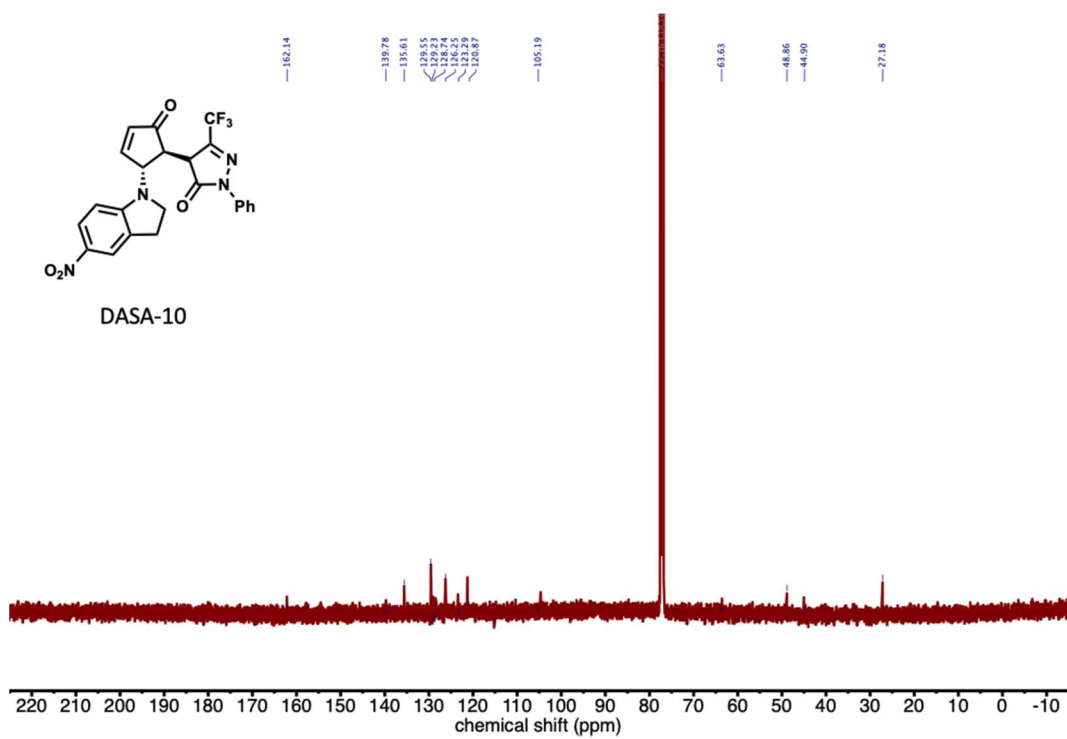


Figure 2.100. ¹³C NMR (125 MHz, CDCl₃) spectra of the open isomer of DASA-10.

Limited solubility of the compound.

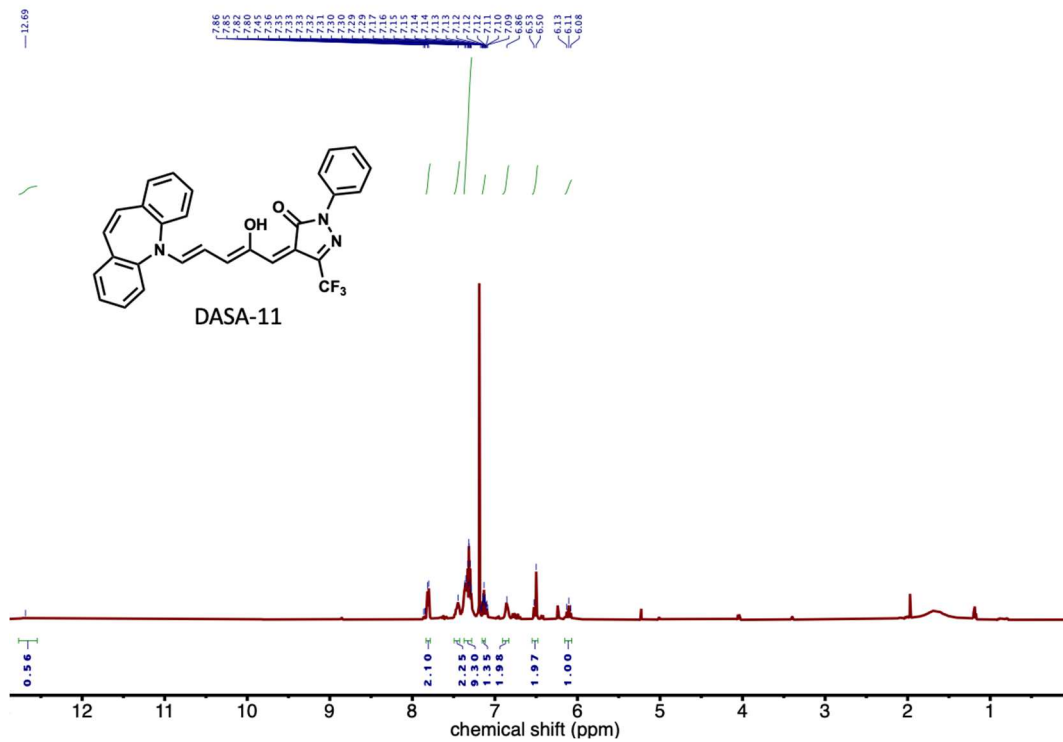


Figure 2.101. ^1H NMR (500 MHz, CDCl_3) spectra of the open isomer of DASA-11. Small amounts of closed isomer are also visible.

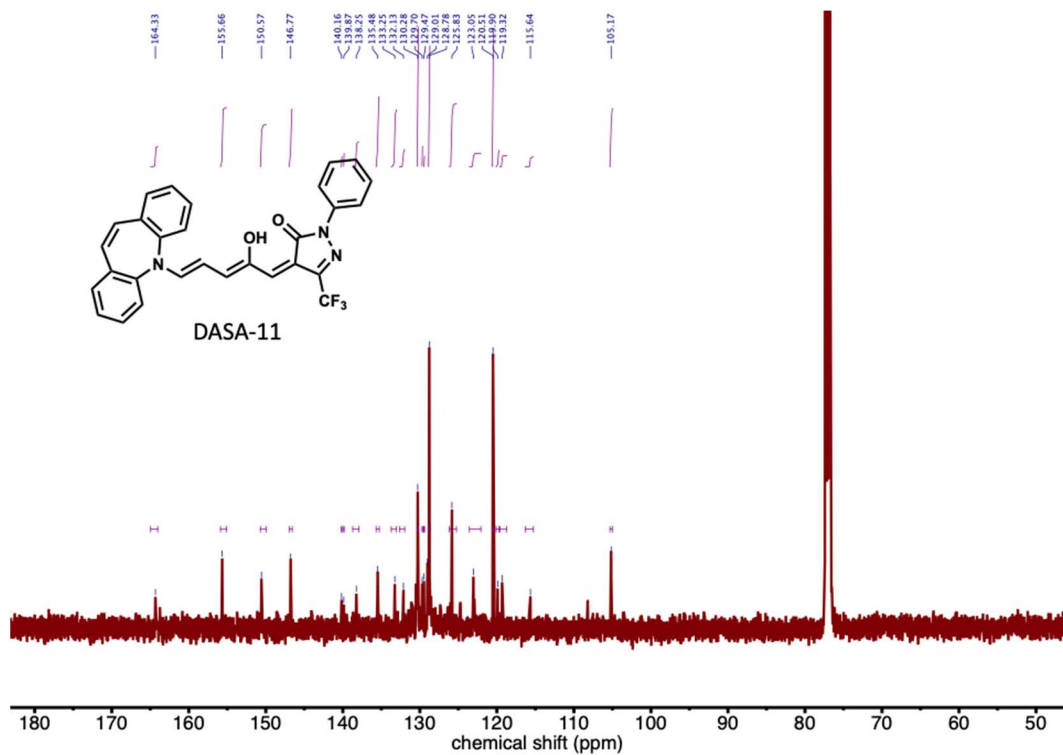


Figure 2.102. ¹³C NMR (125 MHz, CDCl₃) spectra of the open isomer of DASA-11.

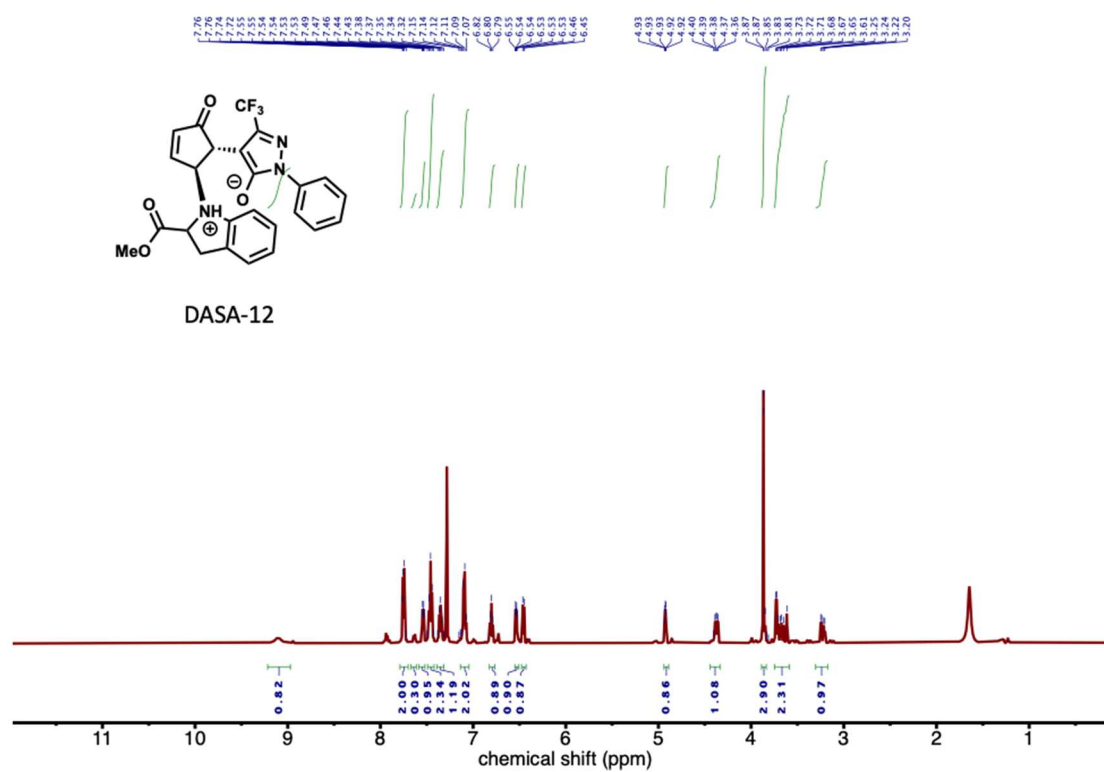


Figure 2.103. ^1H NMR (500 MHz, CDCl_3) spectra of the closed isomer of DASA-12. Small amounts of open form are also visible.

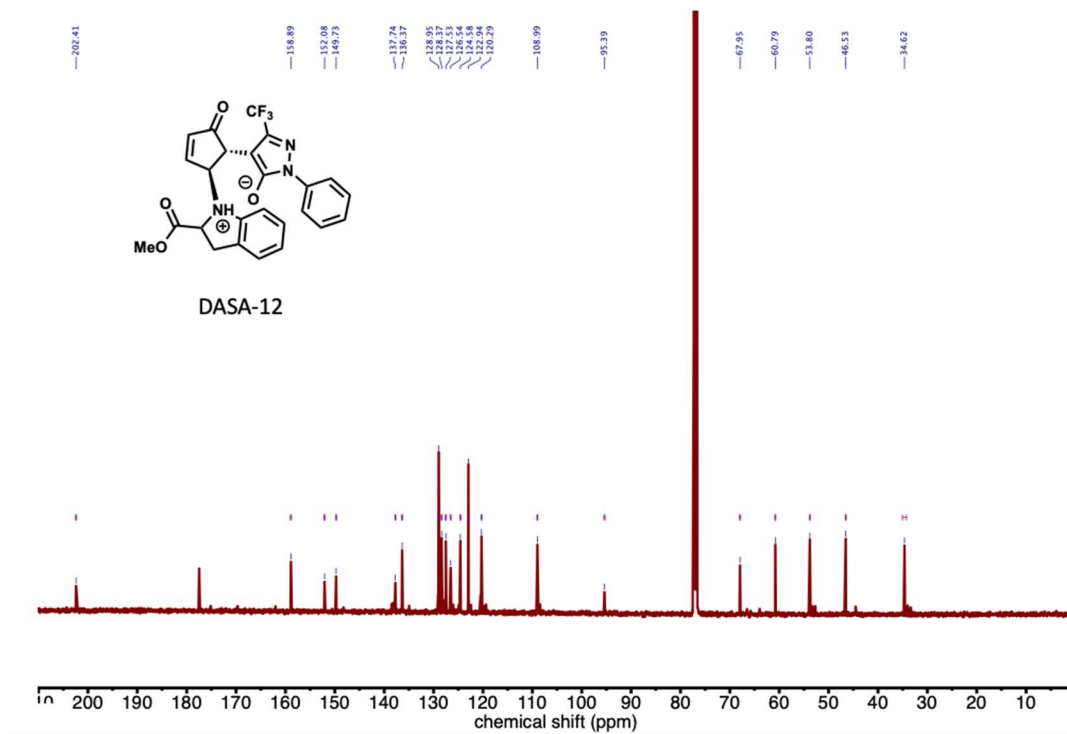


Figure 2.104. ^{13}C NMR (125 MHz, CDCl_3) spectra of the closed isomer of DASA-12.

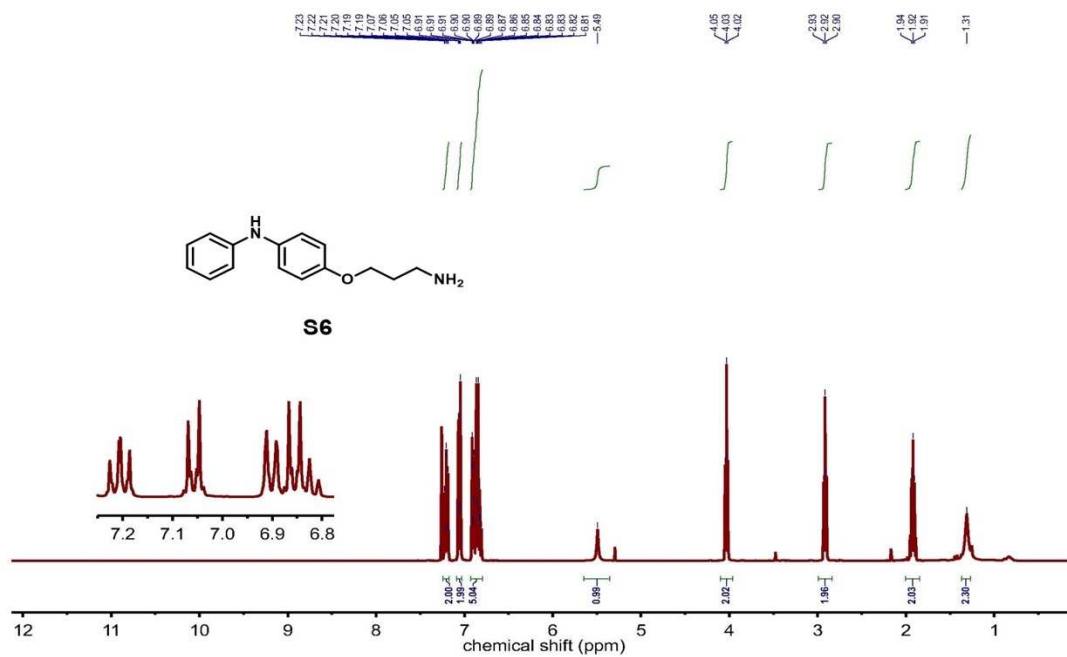


Figure 2.105. ^1H NMR (400 MHz, CDCl_3) spectra of S6.

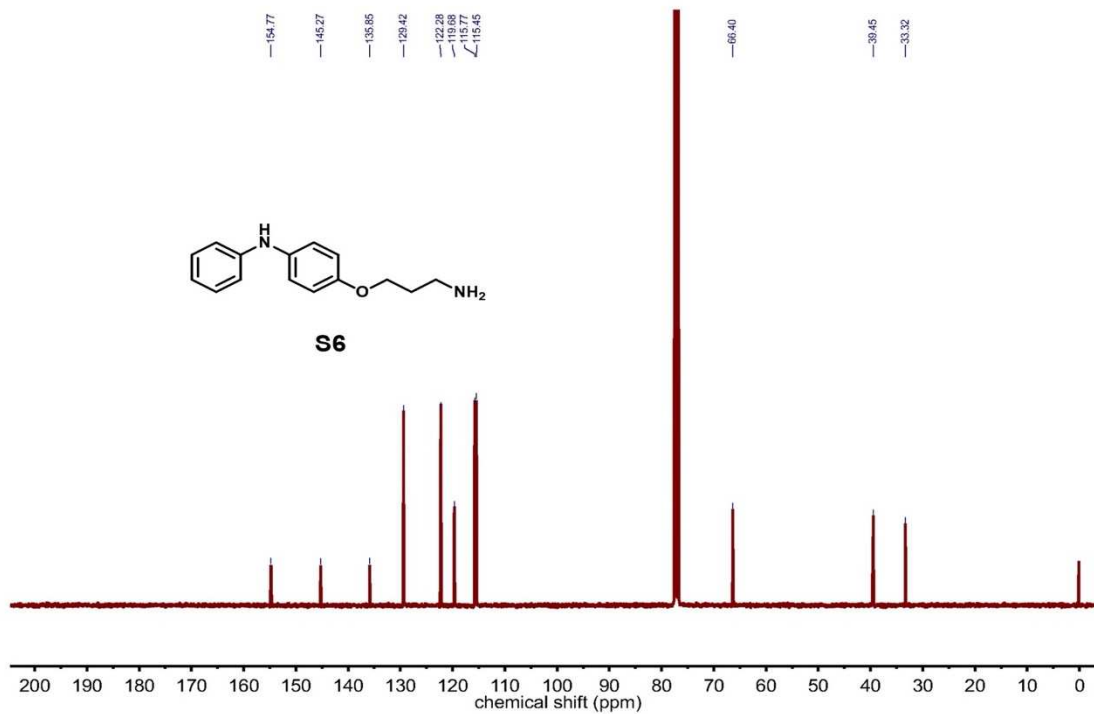


Figure 2.106. ^{13}C NMR (100 MHz, CDCl_3) spectra of S6.

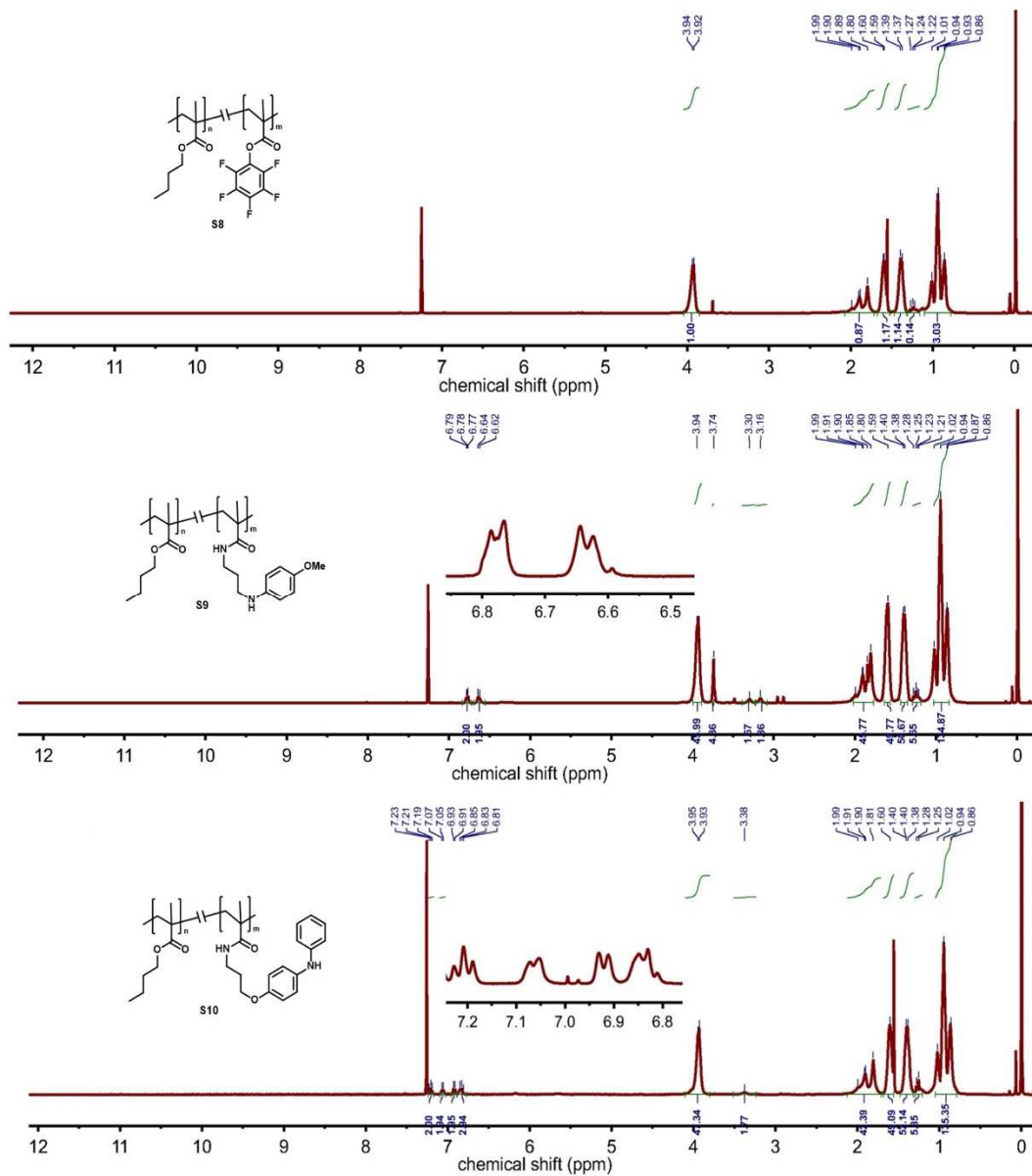


Figure 2.107. ^1H NMR (400 MHz, CDCl_3) spectra of activated ester polymer **S8** and amine-modified polymers **S9** and **S10** (top to bottom).

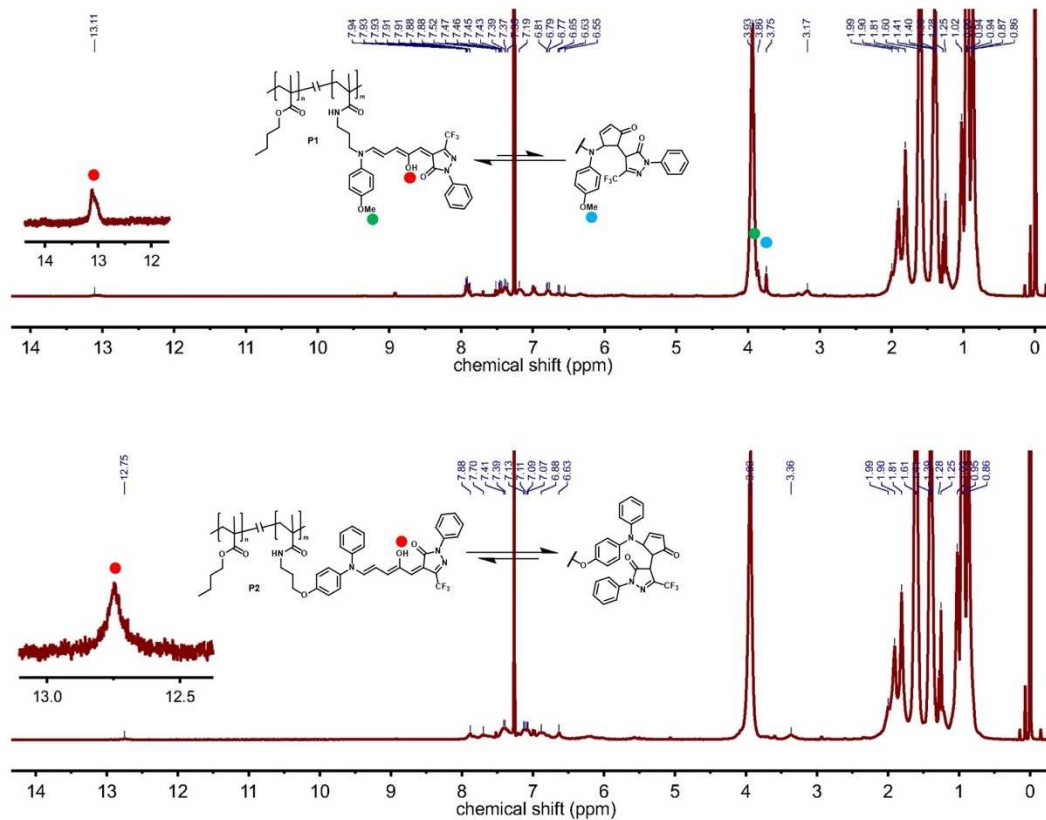


Figure 2.108. ¹H NMR (400 MHz, CDCl₃) spectra of DASA-polymers **P1** (top) and **P2** (bottom). In solution the DASAs are in equilibrium between open and closed state resulting in a complex spectrum.^{17,18} Characteristic peaks are marked by colored dots.

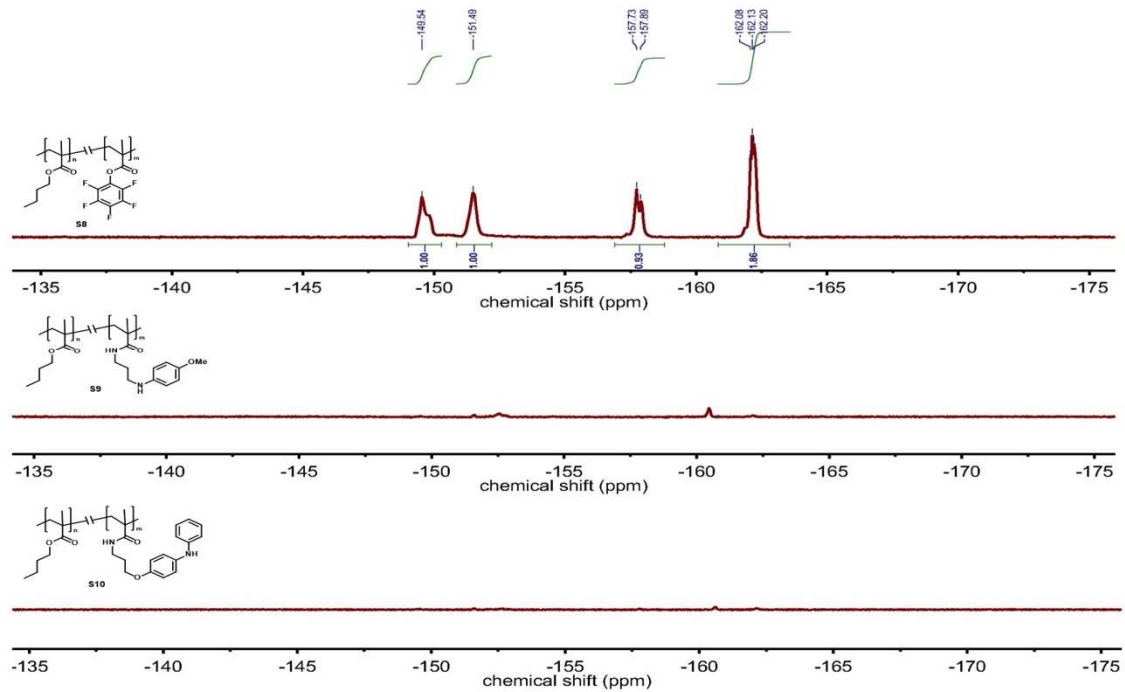


Figure 2.109. ^{19}F NMR (376 MHz, CDCl_3) of **S8**, **S9** and **S10** (top to bottom) showing complete disappearance of the fluorine signals after aminolysis of the pentafluorophenyl ester.

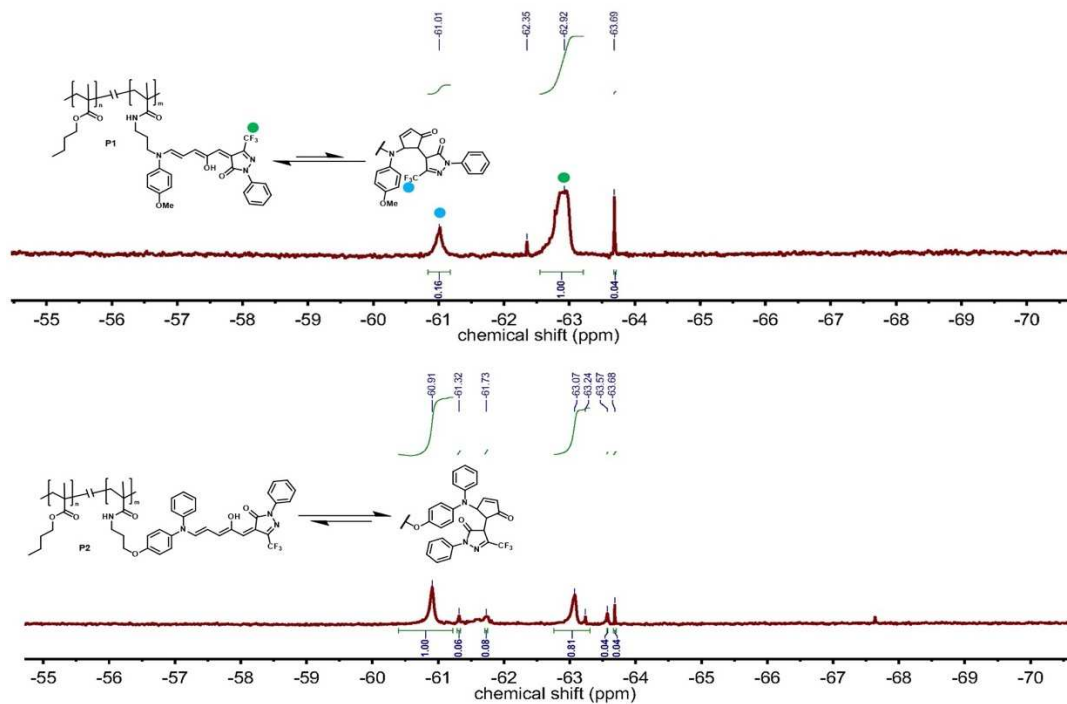


Figure 2.110. ^{19}F NMR (376 MHz, CDCl_3) spectra of DASA-polymers **P1** (top) and **P2** (bottom).

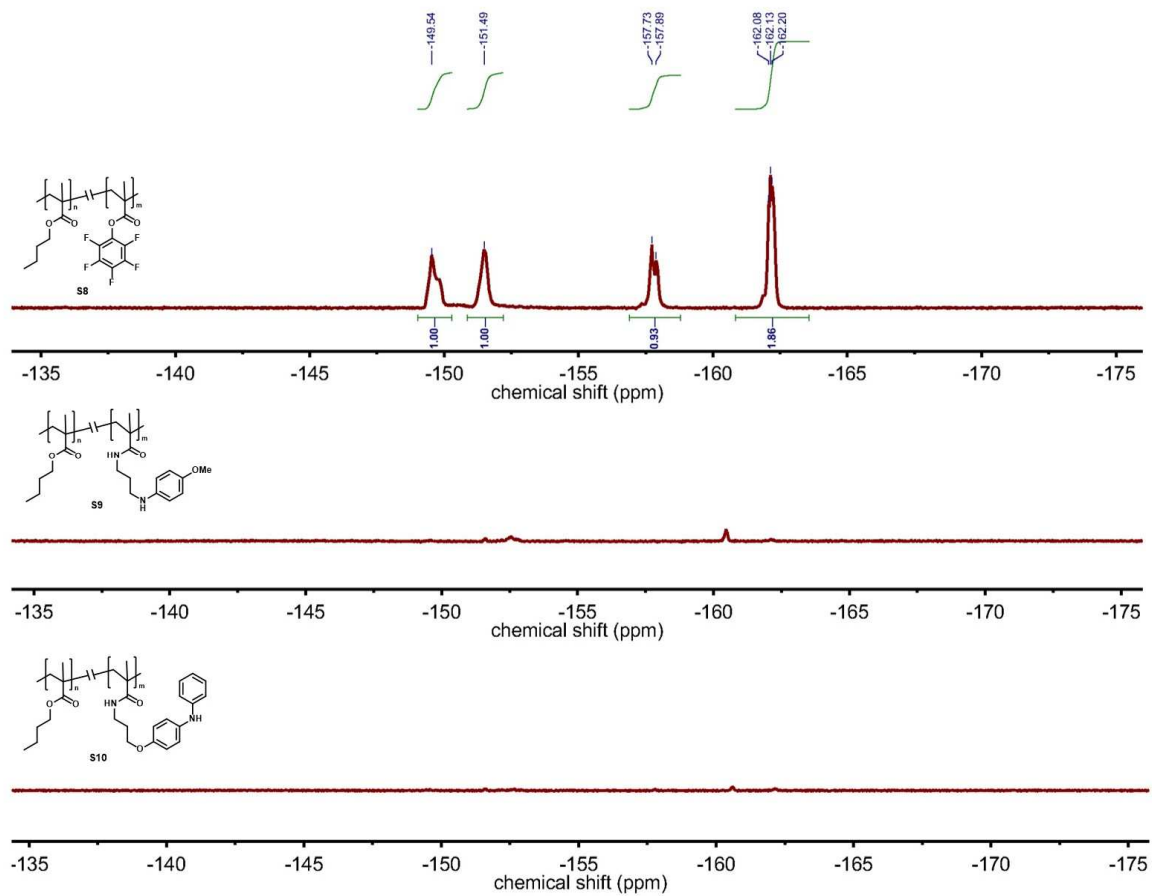


Figure 2.111. ^{19}F NMR (376 MHz, CDCl_3) spectra of DASA-polymers **S8**, **S9** and **S10**.

2.10.11.2 IR Spectra

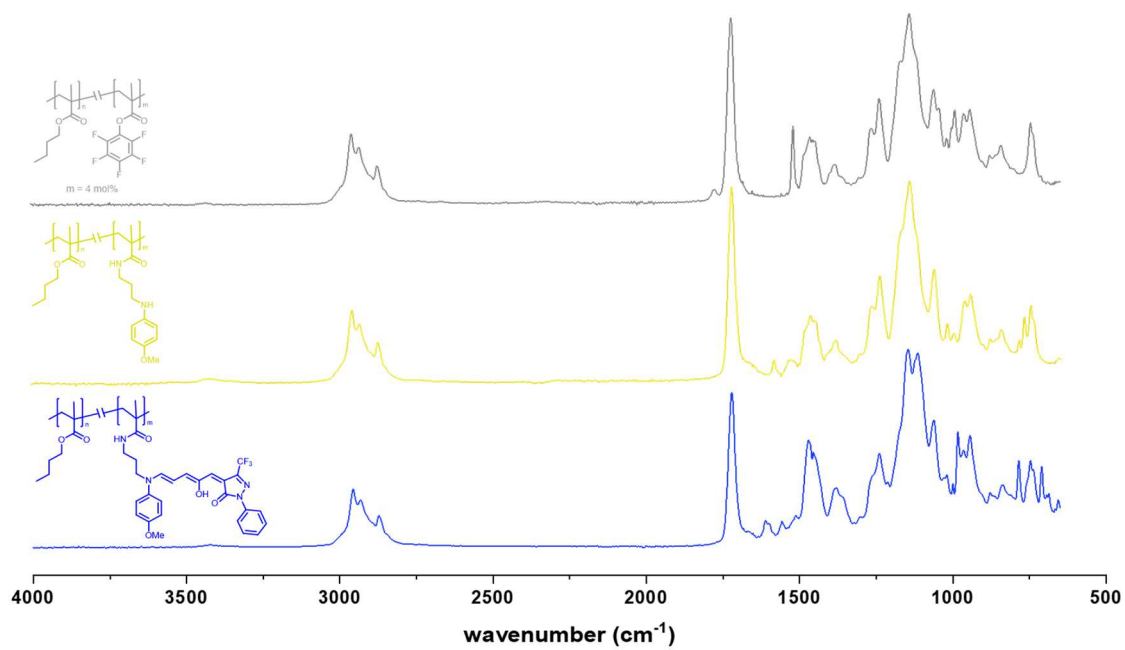


Figure 2.112. IR absorbance spectra of polymers **S8** (top), **S9** (middle) and **P1** (bottom).

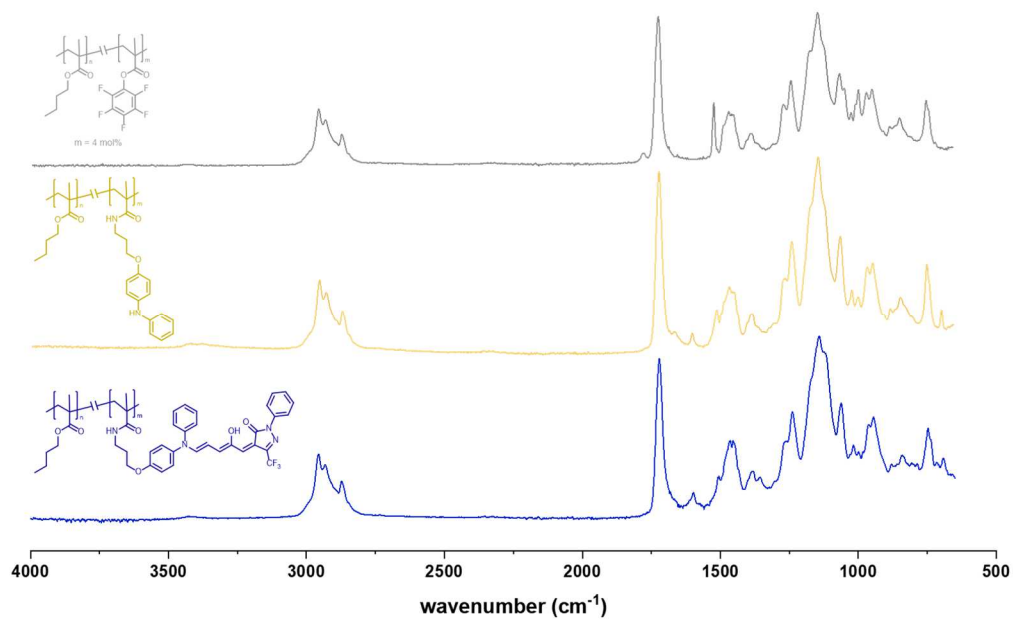


Figure 2.113. IR absorbance spectra of polymers **S8** (top), **S10** (middle) and **P2** (bottom).

2.11 References

- (1) Clerc, M.* , Stricker, F.* , Ulrich, S., Sroda, M., Bruns, N., Boesel, L. F., Read de Alaniz, J., *Angew. Chem. Int. Ed.*, **2021**, *60*, 10219–10227.
<https://doi.org/10.1002/anie.202100115>
- (2) Feringa, B. L., Browne, W. R. *Molecular Switches*, Feringa, B. L., Browne, W. R., Eds., Wiley-VCH Verlag GmbH & Co. KGaA: Weinheim, Germany, 2011, Vol. 1.
<https://doi.org/10.1002/9783527634408>.
- (3) Bouas-Laurent, H., Dürr, H. Organic Photochromism. *Pure Appl. Chem.* **2001**, *73* (4), 639–665. <https://doi.org/10.1351/pac200173040639>.
- (4) Goulet-Hanssens, A., Eisenreich, F., Hecht, S. Enlightening Materials with Photoswitches. *Adv. Mater.* **2020**, *32*, 1905966.
<https://doi.org/10.1002/adma.201905966>.
- (5) Pianowski, Z. L. Recent Implementations of Molecular Photoswitches into Smart Materials and Biological Systems. *Chem. - A Eur. J.* **2019**, *25* (20), 5128–5144.
<https://doi.org/10.1002/chem.201805814>.
- (6) Nie, H., Self, J. L., Kuenstler, A. S., Hayward, R. C., Read de Alaniz, J. Multiaddressable Photochromic Architectures: From Molecules to Materials. *Adv. Opt. Mater.* **2019**, *7*, 1900224. <https://doi.org/10.1002/adom.201900224>.
- (7) Wang, L., Li, Q. Photochromism into Nanosystems: Towards Lighting up the Future Nanoworld. *Chemical Society Reviews*. Royal Society of Chemistry February 2018, pp 1044–1097. <https://doi.org/10.1039/c7cs00630f>.
- (8) Helmy, S., Oh, S., Leibfarth, F. A., Hawker, C. J., Read De Alaniz, J. Design and

- Synthesis of Donor-Acceptor Stenhouse Adducts: A Visible Light Photoswitch Derived from Furfural. *J. Org. Chem.* **2014**, *79* (23), 11316–11329.
<https://doi.org/10.1021/jo502206g>.
- (9) Helmy, S., Leibfarth, F. A., Oh, S., Poelma, J. E., Hawker, C. J., Read de Alaniz, J. Photoswitching Using Visible Light: A New Class of Organic Photochromic Molecules. *J. Am. Chem. Soc.* **2014**, *136* (23), 8169–8172.
<https://doi.org/10.1021/ja503016b>.
- (10) Lerch, M. M., Wezenberg, S. J., Szymanski, W., Feringa, B. L. Unraveling the Photoswitching Mechanism in Donor-Acceptor Stenhouse Adducts. *J. Am. Chem. Soc.* **2016**, *138* (20). <https://doi.org/10.1021/jacs.6b01722>.
- (11) Zulfikri, H., Koenis, M. A. J., Lerch, M. M., Di Donato, M., Szymański, W., Filippi, C., Feringa, B. L., Buma, W. J., Taming the Complexity of Donor–Acceptor Stenhouse Adducts: Infrared Motion Pictures of the Complete Switching Pathway. *J. Am. Chem. Soc.* **2019**, *141* (18), 7376–7384. <https://doi.org/10.1021/jacs.9b00341>.
- (12) Mallo, N., Brown, P. T., Iranmanesh, H., MacDonald, T. S. C., Teusner, M. J., Harper, J. B., Ball, G. E., Beves, J. E. Photochromic Switching Behaviour of Donor-Acceptor Stenhouse Adducts in Organic Solvents. *Chem. Commun.* **2016**, *52* (93), 13576–13579. <https://doi.org/10.1039/C6CC08079K>.
- (13) Hemmer, J. R., Poelma, S. O., Treat, N., Page, Z. A., Dolinski, N. D., Diaz, Y. J., Tomlinson, W., Clark, K. D., Hooper, J. P., Hawker, C., Read de Alaniz, J., Tunable Visible and Near Infrared Photoswitches. *J. Am. Chem. Soc.* **2016**, *138* (42), 13960–13966. <https://doi.org/10.1021/jacs.6b07434>.
- (14) Hemmer, J. R., Page, Z. A., Clark, K. D., Stricker, F., Dolinski, N. D., Hawker, C. J.,

- Read de Alaniz, J. Controlling Dark Equilibria and Enhancing Donor-Acceptor Stenhouse Adduct Photoswitching Properties through Carbon Acid Design. *J. Am. Chem. Soc.* **2018**, *140* (33), 10425–10429. <https://doi.org/10.1021/jacs.8b06067>.
- (15) Mallo, N., Foley, E. D., Iranmanesh, H., Kennedy, A. D. W., Luis, E. T., Ho, J., Harper, J. B., Beves, J. E. Structure-Function Relationships of Donor-Acceptor Stenhouse Adduct Photochromic Switches. *Chem. Sci.* **2018**, *9* (43), 8242–8252. <https://doi.org/10.1039/c8sc03218a>.
- (16) Diaz, Y. J., Page, Z. A., Knight, A. S., Treat, N. J., Hemmer, J. R., Hawker, C. J., Read de Alaniz, J. A Versatile and Highly Selective Colorimetric Sensor for the Detection of Amines. *Chem. - A Eur. J.* **2017**, *23* (15), 3562–3566. <https://doi.org/10.1002/chem.201700368>.
- (17) Lerch, M. M., Szymański, W., Feringa, B. L. The (Photo)Chemistry of Stenhouse Photoswitches: Guiding Principles and System Design. *Chem. Soc. Rev.* **2018**, *47* (6), 1910–1937. <https://doi.org/10.1039/c7cs00772h>.
- (18) Ulrich, S., Hemmer, J. R., Page, Z. A., Dolinski, N. D., Rifaie-Graham, O., Bruns, N., Hawker, C. J., Boesel, L. F., Read de Alaniz, J. Visible Light-Responsive DASA-Polymer Conjugates. *ACS Macro Lett.* **2017**, *6* (7). <https://doi.org/10.1021/acsmacrolett.7b00350>.
- (19) Rifaie-Graham, O., Ulrich, S., Galensowske, N. F. B., Balog, S., Chami, M., Rentsch, D., Hemmer, J. R., Read de Alaniz, J., Boesel, L. F., Bruns, N. Wavelength-Selective Light-Responsive DASA-Functionalized Polymersome Nanoreactors. *J. Am. Chem. Soc.* **2018**, *140* (25), 8027–8036. <https://doi.org/10.1021/jacs.8b04511>.
- (20) Alves, J., Wiedbrauk, S., Gräfe, D., Walden, S. L., Blinco, J. P., Barner-Kowollik, C.

- It's a Trap: Thiol-Michael Chemistry on a DASA Photoswitch. *Chem. - A Eur. J.* **2020**, *26* (4), 809–813. <https://doi.org/10.1002/chem.201904770>.
- (21) Cai, Y. De, Chen, T. Y., Chen, X. Q., Bao, X. Multiresponsive Donor-Acceptor Stenhouse Adduct: Opportunities Arise from a Diamine Donor. *Org. Lett.* **2019**, *21* (18), 7445–7449. <https://doi.org/10.1021/acs.orglett.9b02753>.
- (22) Stenhouse, J. Ueber Die Oele, Die Bei Der Einwirkung Der Schwefelsäure Auf Verschiedene Vegetabilien Entstehen. *Justus Liebigs Ann. Chem* **1850**, *74*, 278–297.
- (23) G. Piancatelli, Scettri, A., Barbadoro, S. A Useful Perparation of 4-Substituted 5-Hydroxy-3-Oxocyclopentene. *Tetrahedron Lett.* **1976**, *13* (December 1966), 3555–3558.
- (24) Veits, G. K., Wenz, D. R., Read De Alaniz, J. Versatile Method for the Synthesis of 4-Aminocyclopentenones: Dysprosium(III) Triflate Catalyzed Aza-Piancatelli Rearrangement. *Angew. Chemie - Int. Ed.* **2010**, *49* (49), 9484–9487. <https://doi.org/10.1002/anie.201005131>.
- (25) Li, S. W., Batey, R. A. Mild Lanthanide(III) Catalyzed Formation of 4,5-Diaminocyclopent-2-Enones from 2-Furaldehyde and Secondary Amines: A Domino Condensation/Ring-Opening/ Electrocyclization Process. *Chem. Commun.* **2007**, *8* (36), 3759–3761. <https://doi.org/10.1039/b709337n>.
- (26) Wenz, D. R., Read de Alaniz, J. R. Aza-Piancatelli Rearrangement Initiated by Ring Opening of Donor-Acceptor Cyclopropanes. *Org. Lett.* **2013**, *15* (13), 3250–3253. <https://doi.org/10.1021/ol401248p>.
- (27) Lebœuf, D., Marin, L., Michelet, B., Perez-Luna, A., Guillot, R., Schulz, E., Gandon, V. Harnessing the Lewis Acidity of HFIP through Its Cooperation with a Calcium(II)

- Salt: Application to the Aza-Piancatelli Reaction. *Chem. - A Eur. J.* **2016**, *22* (45), 16165–16171. <https://doi.org/10.1002/chem.201603592>.
- (28) Hiscox, A., Ribeiro, K., Batey, R. A. Lanthanide(III)-Catalyzed Synthesis of Trans-Diaminocyclopentenones from Substituted Furfurals and Secondary Amines via a Domino Ring-Opening/4 π -Electrocyclization Pathway. *Org. Lett.* **2018**, *20* (21), 6668–6672. <https://doi.org/10.1021/acs.orglett.8b02711>.
- (29) Nunes, J. P. M., Afonso, C. A. M., Caddick, S. Synthesis of 2,4-Bifunctionalised Cyclopentenones from 2-Furaldehyde. *RSC Adv.* **2013**, *3* (35), 14975–14978. <https://doi.org/10.1039/c3ra42663g>.
- (30) Gomes, R. F. A., Coelho, J. A. S., Afonso, C. A. M. Synthesis and Applications of Stenhouse Salts and Derivatives. *Chem. - A Eur. J.* **2018**, *24* (37), 9170–9186. <https://doi.org/10.1002/chem.201705851>.
- (31) Colomer, I., Chamberlain, A. E. R., Haughey, M. B., Donohoe, T. J. Hexafluoroisopropanol as a Highly Versatile Solvent. *Nat. Rev. Chem.* **2017**, *1* (11), 0088. <https://doi.org/10.1038/s41570-017-0088>.
- (32) Pozhydaiev, V., Power, M., Gandon, V., Moran, J., Leboeuf, D. Exploiting Hexafluoroisopropanol (HFIP) in Lewis and Brønsted Acid-Catalyzed Reactions. *Chem. Commun.* **2020**, *56*, 11548–11564. <https://doi.org/10.1039/D0CC05194B>.
- (33) Maiti, N. C., Zhu, Y., Carmichael, I., Serianni, A. S., Anderson, V. E. 1JCH Correlates with Alcohol Hydrogen Bond Strength. *J. Org. Chem.* **2006**, *71* (7), 2878–2880. <https://doi.org/10.1021/jo052389k>.
- (34) Berrien, J. F., Ourevitch, M., Morgant, G., Ghermani, N. E., Crousse, B., Bonnet-Delpon, D. A Crystalline H-Bond Cluster of Hexafluoroisopropanol (HFIP) and

- Piperidine: Structure Determination by X Ray Diffraction. *J. Fluor. Chem.* **2007**, *128* (7), 839–843.
- (35) Vuluga, D., Legros, J., Crousse, B., Slawin, A. M. Z., Laurence, C., Nicolet, P., Bonnet-Delpon, D. Influence of the Structure of Polyfluorinated Alcohols on Brønsted Acidity/Hydrogen-Bond Donor Ability and Consequences on the Promoter Effect. *J. Org. Chem.* **2011**, *76* (4), 1126–1133. <https://doi.org/10.1021/jo1023816>.
- (36) Hong, D. P., Hoshino, M., Kuboi, R., Goto, Y. Clustering of Fluorine-Substituted Alcohols as a Factor Responsible for Their Marked Effects on Proteins and Peptides. *J. Am. Chem. Soc.* **1999**, *121* (37), 8427–8433. <https://doi.org/10.1021/ja990833t>.
- (37) Nakazawa, N., Kawamura, M., Sekiya, A., Ootake, K., Tamai, R., Kurokawa, Y., Murata, J. Liquid Dielectric Constants of Fluorinated Ethers, Fluorinated Ketone and Fluorinated Alcohol. *Trans. Japan Soc. Refrig. Air Cond. Eng.* **2001**, *18* (3), 263–271.
- (38) Berkessel, A., Adrio, J. A., Hüttenhain, D., Neudörfl, J. M. Unveiling the “Booster Effect” of Fluorinated Alcohol Solvents: Aggregation-Induced Conformational Changes and Cooperatively Enhanced H-Bonding. *J. Am. Chem. Soc.* **2006**, *128* (26), 8421–8426. <https://doi.org/10.1021/ja0545463>.
- (39) Lerch, M. M., Di Donato, M., Laurent, A. D., Medved', M., Iagatti, A., Bussotti, L., Lapini, A., Buma, W. J., Foggi, P., Szymański, W., Feringa, B. L., Solvent Effects on the Actinic Step of Donor–Acceptor Stenhouse Adduct Photoswitching. *Angew. Chemie Int. Ed.* **2018**, *57* (27), 8063–8068. <https://doi.org/10.1002/anie.201803058>.
- (40) Gagliardi, L. G., Castells, C. B., Ràfols, C., Rosés, M., Bosch, E. Static Dielectric Constants of Acetonitrile/Water Mixtures at Different Temperatures and Debye-Hückel A and A0B Parameters for Activity Coefficients. *J. Chem. Eng. Data* **2007**,

- 52 (3), 1103–1107. <https://doi.org/10.1021/je700055p>.
- (41) Reichardt, C. Solvatochromic Dyes as Solvent Polarity Indicators. *Chem. Rev.* **1994**, *94* (8), 2319–2358. <https://doi.org/10.1021/cr00032a005>.
- (42) Sroda, M. M., Stricker, F., Peterson, J. A., Bernal, A., Read de Alaniz, J. Donor-Acceptor Stenhouse Adducts: Exploring the Effects of Ionic Character. *Chem. - A Eur. J.* **2020**, <https://doi.org/10.1002/chem.202005110>.
- (43) Stranius, K., Börjesson, K. Determining the Photoisomerization Quantum Yield of Photoswitchable Molecules in Solution and in the Solid State. *Sci. Rep.* **2017**, *7* (January), 41145. <https://doi.org/10.1038/srep41145>.
- (44) Lerch, M. M., Medved, M., Lapini, A., Laurent, A. D., Iagatti, A., Bussotti, L., Szymański, W., Buma, W. J., Foggi, P., Di Donato, M., Feringa, B. L., Tailoring Photoisomerization Pathways in Donor–Acceptor Stenhouse Adducts: The Role of the Hydroxy Group. *J. Phys. Chem. A* **2018**, *122* (4), 955–964. <https://doi.org/10.1021/acs.jpca.7b10255>.
- (45) Mallo, N., Tron, A., Andréasson, J., Harper, J. B., Jacob, L. S. D., McClenaghan, N. D., Jonusauskas, G., Beves, J. E. Hydrogen Bonding Donor–Acceptor Stenhouse Adducts. *ChemPhotoChem* **2020**, *4*, 407–412. <https://doi.org/10.1002/cptc.201900295>.
- (46) Shankar, M. K., Manjunath, B. C., Vinay Kumar, K. S., Pampa, K. J., Sadashiva, M. P., Lokanath, N. K. Crystal Structure, Spectral Studies, and Hirshfeld Surfaces Analysis of 5-Methyl-5 H -Dibenzo[b , f]Azepine and 5-(4-Methylbenzyl)-5 H -Dibenzo[b , f]Azepine. *J. Crystallogr.* **2014**, *2014*, 862067. <https://doi.org/10.1155/2014/862067>.

- (47) Payne, L., Josephson, J. D., Murphy, R. S., Wagner, B. D. Photophysical Properties of Donor-Acceptor Stenhouse Adducts and Their Inclusion Complexes with Cyclodextrins and Cucurbit[7]Uril. *Molecules* **2020**, *25* (21).
<https://doi.org/10.3390/molecules25214928>.
- (48) Yang, S., Liu, J., Cao, Z., Li, M., Luo, Q., Qu, D. Fluorescent Photochromic Donor-Acceptor Stenhouse Adduct Controlled by Visible Light. *Dye. Pigment.* **2018**, *148*, 341–347. <https://doi.org/10.1016/j.dyepig.2017.09.040>.
- (49) Wu, B., Xue, T., Wang, W., Li, S., Shen, J., He, Y. Visible Light Triggered Aggregation-Induced Emission Switching with a Donor-Acceptor Stenhouse Adduct. *J. Mater. Chem. C* **2018**, *6* (31), 8538–8545. <https://doi.org/10.1039/c8tc02621a>.
- (50) Yan, Q., Li, C., Wang, S., Lin, Z., Yan, Q., Cao, D. Visible Light Responsive Donor-Acceptor Stenhouse Adducts with Indoline-Tri/Tetra-Phenylethylene Chromophore: Synthesis, Aggregation-Induced Emission, Photochromism and Solvent Dependence Effect. *Dye. Pigment.* **2020**, *178* (February), 108352.
<https://doi.org/10.1016/j.dyepig.2020.108352>.
- (51) Yap, J. E., Mallo, N., Thomas, D. S., Beves, J. E., Stenzel, M. H. Comparing Photoswitching of Acrylate or Methacrylate Polymers Conjugated with Donor-Acceptor Stenhouse Adducts. *Polym. Chem.* **2019**, *10* (47), 6515–6522.
<https://doi.org/10.1039/c9py01345h>.
- (52) Sinawang, G., Wu, B., Wang, J., Li, S., He, Y. Polystyrene Based Visible Light Responsive Polymer with Donor–Acceptor Stenhouse Adduct Pendants. *Macromol. Chem. Phys.* **2016**, *217* (21), 2409–2414. <https://doi.org/10.1002/macp.201600351>.
- (53) Yu, D., Thai, V. T., Palmer, L. I., Veits, G. K., Cook, J. E., Read de Alaniz, J., Hein,

- J. E. Importance of Off-Cycle Species in the Acid-Catalyzed Aza-Piancatelli Rearrangement. *J. Org. Chem.* **2013**, *78* (24), 12784–12789.
<https://doi.org/10.1021/jo402155b>.
- (54) Gomes, R. F. A., Coelho, J. A. S., Afonso, C. A. M. Synthesis and Applications of Stenhouse Salts and Derivatives. *Chem. - A Eur. J.* **2018**, *24* (37), 9170–9186.
<https://doi.org/10.1002/chem.201705851>.
- (55) Yin, H., Jin, M., Chen, W., Chen, C., Zheng, L., Wei, P., Han, S. Solvent-Free Copper-Catalyzed N-Arylation of Amino Alcohols and Diamines with Aryl Halides. *Tetrahedron Lett.* **2012**, *53* (10), 1265–1270.
<https://doi.org/10.1016/j.tetlet.2011.12.130>.
- (56) Lee, S., Yi, K. Y., Kim, S. K., Suh, J., Kim, N. J., Yoo, S. E., Lee, B. H., Seo, H. W., Kim, S. O., Lim, H. Cardioslective Anti-Ischemic ATP-Sensitive Potassium Channel (KATP) Openers: Benzopyranyl Indoline and Indole Analogues. *Eur. J. Med. Chem.* **2003**, *38* (5), 459–471. [https://doi.org/10.1016/S0223-5234\(03\)00063-1](https://doi.org/10.1016/S0223-5234(03)00063-1).
- (57) Mastitski, A., Kisseljova, K., Järv, J. Fmoc-Aza-Arg(Boc)₂ Prekursori Süntees Hüdrasiini Alküülimise Teel. *Proc. Est. Acad. Sci.* **2014**, *63* (4), 438–443.
<https://doi.org/10.3176/proc.2014.4.09>.

3 DASA ground state charge separation

This chapter was originally published in *Chem. European Journal*.

Reproduced with the permission of Wiley & Sons. (Sroda, M.*, Stricker, F.*, Peterson, J. A., Bernal, A., Read de Alaniz, J., *Chem. Eur. J.*, **2021**, 27, 4183–4190.)¹ Copyright Wiley & Sons.

3.1 DASAs synthetic evolution and ground state chemistry

Donor–acceptor Stenhouse adducts (DASAs) are a particularly interesting new class of photoswitches due to their negative photochromism, visible light activation, polarity and molecular volume change.^{2–5} Upon irradiation DASAs are converted from a highly light-absorbing colored form to a colorless and transparent form with overall switching kinetics highly dependent on the DASA architecture and surrounding environment. Because the closed form of DASA are not light responsive and the recovery to the open form is thermally driven, the obtained steady state upon irradiation is better described as a photothermalstationary (PTSS) state rather than as a photostationary state.⁶ Since their discovery in 2014, these molecules have been exploited in a number of applications including targeted drug release,^{3,7,8} orthogonal photoswitching,⁹ chemical and thermal sensing,^{10–13} and most recently fluid velocity control and photothermal actuation.¹⁴ Synthetic efforts have resulted in three generations of DASAs which vary in photoswitching properties such as thermodynamic equilibrium between the open and closed form in the absence of light irradiation, wavelength tuneability (500–700 nm), switching rates, and solvent dependence.^{2–5} The first generation, published in 2014, consisted of strongly electron donating dialkylamine donors and Meldrum’s or Barbituric acid acceptors (**Figure 3.1**).^{2,3} These derivatives show excellent equilibrium control and fatigue resistance, but are limited in wavelength tuneability and solvent compatibility – defined herein as the ability to switch reversibly upon irradiation in a range of solvents. In 2016 the second generation of

DASAs was introduced by employing weakly donating cyclic and acyclic aryl amines (**Figure 3.1**).^{4,15} These show improved wavelength tuneability (500–700 nm), and enhanced switching properties including low PTSS, higher solvent compatibility and solid-state switching, but show compromised thermodynamic equilibrium in the dark (~50–7% open form in the absence of light) and extended half-lives of the closed form. The third generation in 2018 introduces strongly electron withdrawing carbon acids (**Figure 3.1**). These derivatives have enhanced switching properties such as increased solvent compatibility and tunable half-lives of the closed form, while maintaining high equilibrium control.⁵ The synthetic effort has been tightly coupled with extensive mechanistic studies by Feringa, Beves, Martinez, Marazzi and others.^{15–21} Here it has been demonstrated that the actinic *Z-E* isomerization step is independent of solvent and concentration and occurs on a fs-ns timescale.^{18,22} This is followed by a C₃-C₄ bond rotation and thermal 4 π -electrocyclization leading to the ring-closed cyclopentenone with a *trans* relationship between the C₁ and C₅ groups, that occurs on a ns-ms timescale (**Figure 3.8**). In contrast to the actinic step, the thermal part of the mechanism is highly solvent and concentration dependent.^{18,22} Further use of DASA in more widespread applications has been hampered by limited understanding of solvent compatibility and most importantly concentration dependence. The concentration dependence first reported by Bardeen and our group in 2019 shows decreasing half-lives of the closed isomers at increased concentration while also lowering overall quantum yields.²² This severely hinders applications requiring high concentration of DASA molecules. To further enable the use of DASA photoswitches it is critical that we understand and overcome the factors governing DASAs solvent compatibility and concentration dependency.

Herein we investigate medium effects on the charge-separation of DASAs through a series of XRD analysis, solution-state studies and time dependent pump probe UV-Vis spectroscopy. This work builds on three important independent preliminary studies by Beves,^{15,21} Jacquemin²³ and Feringa²⁴ that show the zwitterionic character of the open form of DASAs.

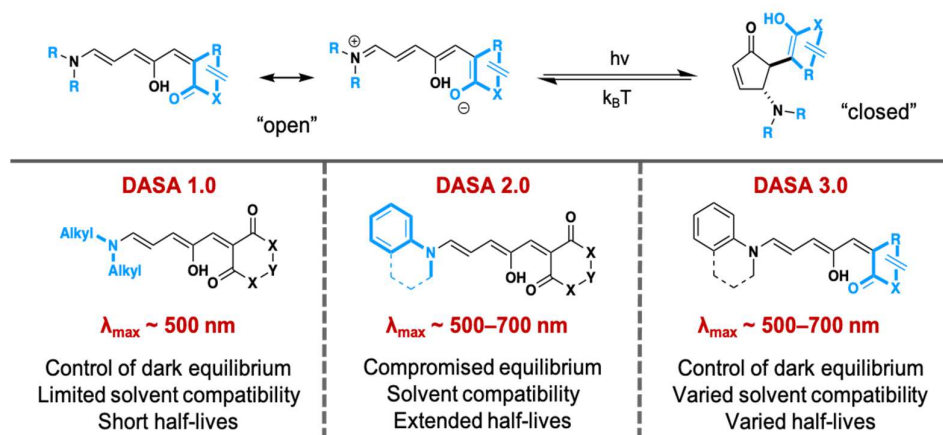


Figure 3.1. Synthetic efforts have resulted in three generations of DASAs which vary in photoswitching properties including control of thermodynamic equilibrium, solvent compatibility and switching kinetics. The closed form is only depicted with the acceptor group in the enol form, however, as reported in the literature the closed form can reside in either a zwitterionic, enol, or keto form depending on the architecture and conditions.^{2,4,15} Reproduced with the permission of Wiley & Sons. (Sroda, M.*, Stricker, F.*, et al. *Chem. Eur. J.*, **2021**, 27, 4183–4190.)¹ Copyright Wiley & Sons.

Using XRD data, Beves and co-workers have reported open linear zwitterionic forms for first and second generation DASAs, concluding the polyene system in second generation DASAs are significantly delocalized.^{15,21} In a separate theoretical investigation, Jacquemin reported that the Mulliken charge for first generation DASAs in both the open and closed form have a significantly negative charge (-0.54 e and -0.56 e, respectively), suggesting both have a zwitterionic nature.²³ Furthermore, they calculated the open and closed DASA isomers which have similar and large ground-state dipole moments that exceed 15D. Feringa used

solvatochromic analysis to investigate the role of the hydroxyl group on the photoisomerization pathway.²⁴ In addition, Wagner recently reported the effect of this zwitterionic character on DASA fluorescence emission and its effects on first generation DASA in protic solvents.²⁵ Despite these initial reports, no effort has been made to understand the implications of the ionic character of the open form of DASA on solvent compatibility and concentration effects. By using solvatochromic shift analyses, XRD and charged ionic liquids as a dopant, we demonstrate how the ionic character of DASA influences their solvent compatibility and concentration effects.

For this study, we selected DASA derivatives which range in photoswitching properties including thermodynamic equilibrium between the open and closed form in the absence of light irradiation, solvent compatibility, photothermal stationary state, and half-life (**Figure 3.3A**, properties summarized in **Table 3.2**). As a first generation DASA we choose **DASA 1-MM** consisting of a dimethylamine donor and a Meldrum's acid derived acceptor. This derivative has high thermodynamic equilibrium control in chloroform with 94% in the open form in the dark (for experimental detail see the supporting information in section 6). This compound also exhibits a short half-life in chloroform (172 s) leading to a PTSS of 76%. For a second generation derivative we choose **DASA 2-IM** bearing an indoline-based donor with a Meldrum's acid acceptor. Compared to **DASA 1-MM**, it suffers from a compromised thermodynamic equilibrium with only 50% residing in the open form in the dark and an extended half-life of the closed form of 3,240 s in chloroform. However it also shows reversible switching in more polar solvents such as acetonitrile.⁵ To represent a third generation DASA derivative we selected **DASA 3-IP** bearing an indoline-based donor and CF₃ pyrazalone-based acceptor. This derivative has excellent thermodynamic equilibrium control with >95% in the open form in the dark and a short-lived closed form with a half-life of 5 s in chloroform. In contrast to **DASA 2-IM** and many second generation DASAs, this compound does not exhibit switching in acetonitrile.⁵ The first and third generation derivatives show very similar behavior

with high thermodynamic equilibria and short half-lives while being limited to apolar solvents like chloroform. To round out this study, DASA derivative **DASA 4-II** was chosen, which shows linear photodegradation upon irradiation and no recovery (**Figure 3.11** compares **DASA 3-IP** and **DASA 4-II-H** photoswitching).⁵

3.2 Solid-state analysis of the ionic character of DASAs

X-ray structural analysis of the open form provides valuable insight into the ground state ionic character in the solid state.^{4,21} Bond length alternation (BLA) patterns were used to analyze the ionic character, where a negative BLA value indicates zwitterionic character.^{15,21} To compare the crystal structures of DASA derivatives we grew single crystals of **DASA 2-IM-H**, **3-IP-H**, and **4-II-H** and used previously reported XRD data.^{2,15,21} Single crystals of **DASA 2-IM-H**, **3-IP-H**, and **4-II-H** were obtained using layer diffusion and slow evaporation crystallization techniques detailed in the supporting information section 4. Previously reported **DASA 1-EM**² was utilized due to increased crystallinity provided by the diethylamine donor in contrast to **DASA 1-MM**. In addition, DASA derivatives bearing non-methylated indoline donors (**DASA 2-IM-H** and **DASA 3-IP-H** indicated by “-H” in the label), were used as model compounds for **DASA 2-IM** and **DASA 3-IP**, respectively. As expected, for **DASA 1-EM**, bearing a strongly donating alkyl donor, the bond length alternation ($BLA_{\text{DASA 1-EM}} = -0.056 \text{ \AA}$) show a more zwitterionic form compared to the weakly donating indoline-based donors for **DASA 2-IM-H** and **DASA 3-IP-H** which have similar, hybrid-zwitterionic ground states ($BLA_{\text{DASA 2-IM}} = -0.013 \text{ \AA}$ and $BLA_{\text{DASA 3-IP}} = -0.018 \text{ \AA}$).

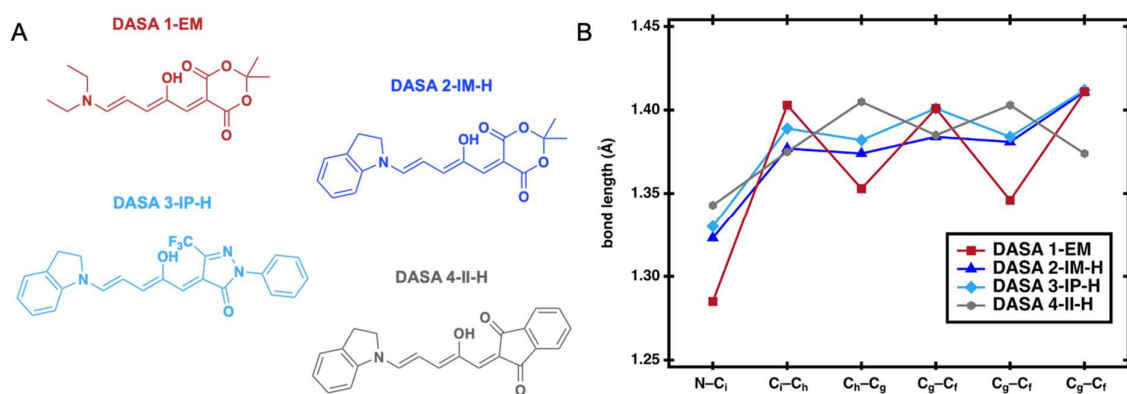


Figure 3.2. A. Photoswitches that were used for XRD study. B. Bond length alternation (BLA) patterns along the triene of the open form of DASA from XRD single crystals. For BLA calculations only the C–C bonds are taken into account. DASAs with diethylamine and non-methylated indoline donors were used as model compounds due to increased crystallinity compared to their counterparts with dimethylamine and 2-methylindoline donors. Reproduced with the permission of Wiley & Sons. (Sroda, M.*, Stricker, F.*, et al. *Chem. Eur. J.*, **2021**, 27, 4183–4190.)¹ Copyright Wiley & Sons.

In this Chapter, we define hybrid as having a more delocalized conjugated triene system. Interestingly, **DASA 4-II-H**, with irreversible photoswitching, reveals opposite alternating bond slopes ($BLA_{\text{DASA 4-II-H}} = 0.026 \text{ \AA}$) and resides in a more neutral ground state, as shown in **Figure 3.2B**. This is in agreement with previous XRD reported results that nonphotochromic spirooxazines predominantly reside in a neutral “quinoidal” structure.²⁶ To further extend this study, we compared the BLA of thirteen previously published open form crystals,^{2,15,21} in addition to the three crystals grown in this study, shown in **Figure 3.19** and **Table 3.3**. In most cases, the XRD data supports that photoswitching DASA molecules evaluated using this approach have some zwitterionic character in the solid state as exemplified by negative bond length alternation values ranging from -0.013 to -0.056 \AA (**Table 3.3**). Inversely, **DASA 4-II-H**, has the most positive BLA of 0.026 \AA and shows linear photodegradation and

irreversible switching. These results suggest that a charge-separated, hybrid/zwitterionic ground state is an important design principal for photoswitchable DASAs. Of note, the BLA from the crystal structures revealed similar results for both the second and third generation derivatives (-0.013 Å and -0.018 Å) which is not consistent with the vastly different photoswitching behavior in solution between the two generations. This is not surprising since XRD relies on single crystalline environment while DASA's photoswitching properties have been shown to be highly dependent on environmental factors like solvent and concentration.

3.3 Solution-state analysis of the ionic character of DASAs

To gain insight into the charge-separation of DASAs in solution, we analyzed solvatochromic shifts of DASA derivatives. For this we utilized the Dimroth–Reichardt E_T solvent polarity scale to explore the dipolar nature of DASA.²⁶ The Dimroth–Reichardt E_T^N solvent polarity scale takes into account solvation effects arising from both nonspecific (e.g., dipole-dipole, induced dipole-induced dipole) and specific (e.g., hydrogen bonding) interactions, where the slope can provide insight into the difference in dipolar character between the ground state and the excited state. A negative solvatochromic slope (blue-shifts in more polar solvents), suggests a stabilization of the zwitterionic ground state with increasing solvent polarity. Inversely, a positive solvatochromic slope suggest a more dipolar excited state which is stabilized with increasing solvent polarity. The scale is based on the electronic transitions of a polarity probe dye in a range of solvents which is normalized to nonpolar tetramethylsilane (TMS) ($E_T^N = 0$) and polar water ($E_T^N = 1.0$). The features of the absorption bands were correlated with the Dimroth-Reichardt E_T^N solvent polarity scale of ten solvents (**Table 3.4**).²⁷ Photoswitches studied and their corresponding photoswitching properties (thermodynamic equilibrium, PTSS, and thermal half-life) in chloroform are shown in **Figure 3.3A**. **Figure 3.3B** shows the blue-shift of the absorption band of **DASA 3-IP** with increasing solvent polarity.

Figure 3.3C shows absorption maximum vs the polarity value of the solvents of the four DASA derivatives. **DASA 1-MM**, **DASA 2-IM**, and **DASA 3-IP** all show negative solvatochromic shifts (blue-shifts in more polar solvents), suggesting a stabilization of the zwitterionic ground state with increasing solvent polarity (with a slope ranging from -7 to -60 nm shown in **Table 3.1** and **Figure 3.25**). Interestingly, **DASA 4-II-H** shows a positive solvatochromic shift with a slope of 14 nm (red-shift in more polar solvents), suggesting a more dipolar excited state which is stabilized with increasing solvent polarity. In agreement with the XRD results, this suggests that the dipolar nature of reversible and non-reversible DASAs are different.

To gain a better understanding of the varying contribution of the zwitterionic resonance form we compared the negative slopes of the reversible switching DASAs. The slopes of **DASA 1-MM** and **DASA 3-IP** are comparable with slopes at -46 and -60 nm. This is in contrast to the XRD data where **DASA 3-IP** seems to have less zwitterionic character than **DASA 1-MM**. **DASA 2-IM**, however, has a significantly lower negative shift, with a slope of -7 nm supporting a hybrid character shown by XRD. The more pronounced negative solvatochromism of **DASA 1-MM** and **DASA 3-IP** suggests that these derivatives have more zwitterionic character than **DASA 2-IM**. These results correlate with the respective electronic character of the donor and acceptor. **DASA 1-MM** has a strongly donating alkylamine donor and a weakly withdrawing Meldrum's acid-based acceptor while **DASA 3-IP** consists of a weaker arylamine donor and a strongly electron withdrawing CF₃-Pyrazolone-based acceptor. **DASA 2-IM** consists of both a weak donor and acceptor, resulting in overall weaker charge separation or hybrid structure. The highly charge-separated DASAs (**DASA 1-MM** and **DASA 3-IP**) show similar behavior in switching properties including a high percent of open form in the dark (94 and >95% in chloroform), fast thermal reversion ($t_{1/2} = 173$ s and 5 s), and limited solvent capability. In contrast, **DASA 2-IM** is less sensitive to the environment and experimentally switches in a wider range of solvents but has a compromised equilibrium. Beves reported absorption profiles for a series of second generation DASAs bearing aniline-based donors in

various solvents. In agreement with our observed trend, these solvatochromic slopes can be correlated with the relative dark equilibrium (**Figure 3.26**).¹⁵ The solvatochromic shifts reveal the dipolar nature of DASA and provides a simple experimental method to help understand switching properties of different DASA derivatives while also providing a more accurate representation of the push-pull system compared to XRD. Feringa²⁸ and Marazzi²⁰ have both independently shown in theoretical studies that the increasing zwitterionic resonance contribution lowers the energy barrier of the thermal reversion between A and B (**Figure 3.8**) which is consistent with our results. This inhibits switching in more polar solvents, as thermal reversion outcompetes electrocyclization. To extend this study to polymers, we analyzed absorbance shifts within polymer blends which have been shown to facilitate photoswitching.^{13,29-31} The same trend in negative slopes were observed in the polymer blends supporting that DASA photoswitching molecules also have a high degree of charge-separation in the ground state in solid macromolecular environments (**Figure 3.27**).

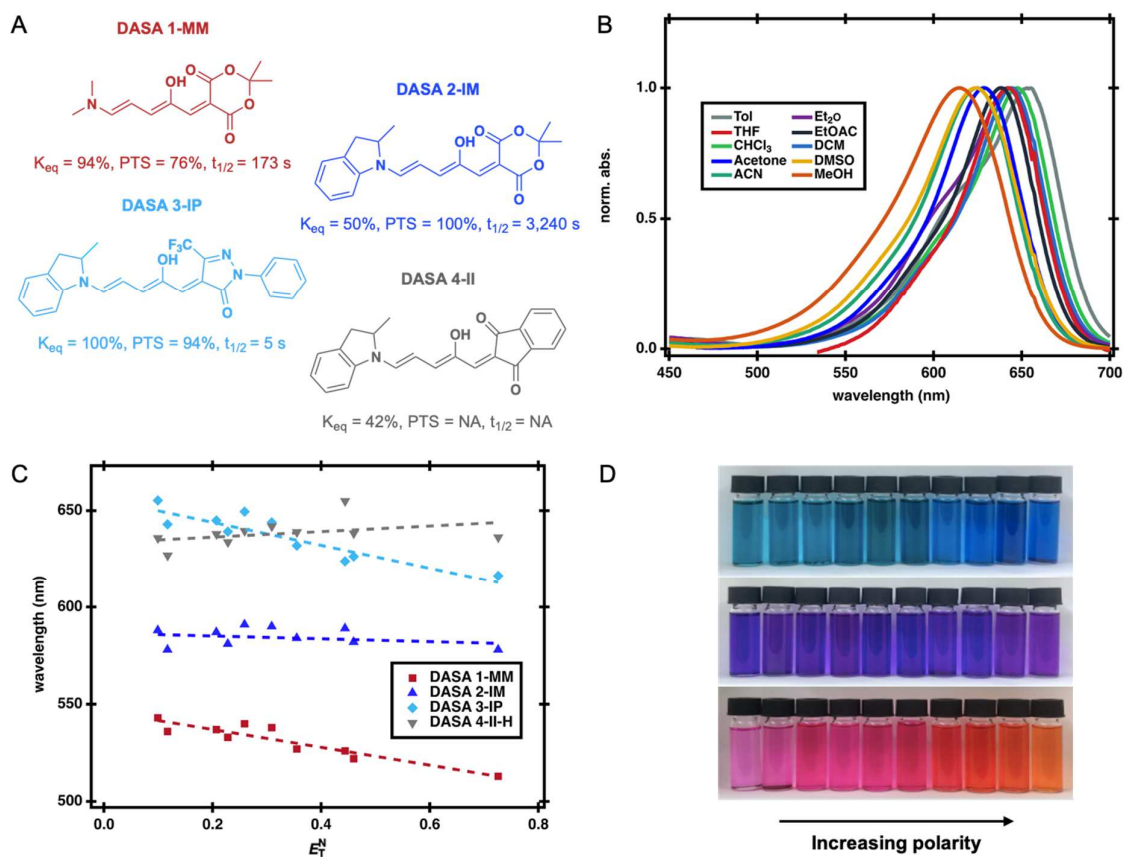


Figure 3.3. A. DASA derivatives studied with thermodynamic equilibrium, photothermal stationary state, and thermal half-life in chloroform for each DASA. B. UV–Vis traces of **DASA 3-IP** in a range of solvents, which shows a blue-shift with increasing polarity of the solvent. C. Solvatochromic shift analysis for **DASA 1-MM**, **2-MI**, **3-IP** and **4-II-H** in solvents of different polarity using the Dimroth–Reichardt ET solvent polarity scale. D. Solvatochromic trends of **DASA 3-IP** (top), **DASA 2-IM** (middle) and **DASA 1-MM** (bottom) are visible by eye, where **DASA 3-IP** and **DASA 1-MM** are more sensitive to the environment than **DASA 2-IM**. Reproduced with the permission of Wiley & Sons. (Sroda. M.*, Stricker, F.*, et al. *Chem. Eur. J.*, **2021**, 27, 4183–4190.)¹ Copyright Wiley & Sons.

With a better understanding of the contribution of the zwitterionic resonance open form, we were also interested in evaluating the ionic character of the closed form (supporting

information section 13). Previous reports have shown the closed form of first generation DASAs with alkyl donors to be zwitterionic while second generation have been shown to form neutral (keto or enol) closed form isomers via 2D-NMR analysis.^{15,21} There have been no reports on closed form isomers for third generation derivatives. In accordance with literature reports, 2D-NMR analysis shows a zwitterionic closed form for **DASA 1-MM** (**Figure 3.30–31**) and a neutral (keto) closed form for **DASA 2-IM** (**Figure 3.35–36**). Interestingly, despite the weakly donating indoline-based donor, 2D-NMR analysis reveals a zwitterionic closed form for **DASA 3-IP** similar to first generation DASAs (**Figure 3.39–40**).

Table 3.1. Experimental data compared to computational calculations.

DASA	Slope ^[a]	BLA ^[b]	Dipole ^[c]	BLA ^[c]
DASA 3-IP	-60	-0.018	17.4	-0.010
DASA 1-MM	-46	-0.056	14.7	-0.007
DASA 2-IM	-7	-0.013	12.0	0.010
DASA 4-II	14	0.026	9.0	0.023

[a] Solvatochromic slopes (nm) extracted by a linear trend from Figure 3B. [b] Bond length alternation (Å) values are extracted from XRD data of the model compounds **DASA 1-EM**, **DASA 2-IM-H**, **DASA 3-IP-H** and **DASA 4-II-H** shown in Figure 2. [c] Dipole (D) and BLA (Å) calculated using M06-2X/6-31+G(d,p) in chloroform using the SMD solvent model.

3.4 Computational calculations on ground state charge separation

Our results from the solvatochromic analysis are supported by theoretical calculations using M06-2X/6-31+G(d,p) in toluene, chloroform, and acetonitrile with the SMD solvent model using Gaussian16 software.^{32–35} The calculated dipole moments and BLAs in chloroform were compared with the experimental results summarized in **Table 3.1** and supporting information section 14. Importantly, the calculations trend with the solvatochromic slopes (extracted from **Figure 3.3B** from linear trends). Where **DASA 1-MM** and **DASA 3-IP** have the highest calculated dipole and most negative BLA values, in agreement with the more

negative solvatochromic slopes. Consistent with experimental results, **DASA 4-II** has the smallest dipole and the most positive BLA. Interestingly, the solvent polarity vs the HOMO-LUMO energy levels show the HOMO-LUMO gap in **DASA 2-IM** is relatively unchanged as a function of solvent, while the gap of **DASA 3-IP** increases with increasing solvent polarity in agreement with the blue-shift observed in the solvatochromic study (**Figure 3.47**). The calculations also revealed the change in the hydrogen bond length between the –OH and the carbonyl of the acceptor as a function of solvent (**Figure 3.48**). The hydrogen bond in **DASA 3-IP** is strengthened in more polar solvents compared to **DASA 2-IM**. It is possible this hydrogen bond plays a key role in stabilizing the open form in the absence of light, resulting in equilibrium control.

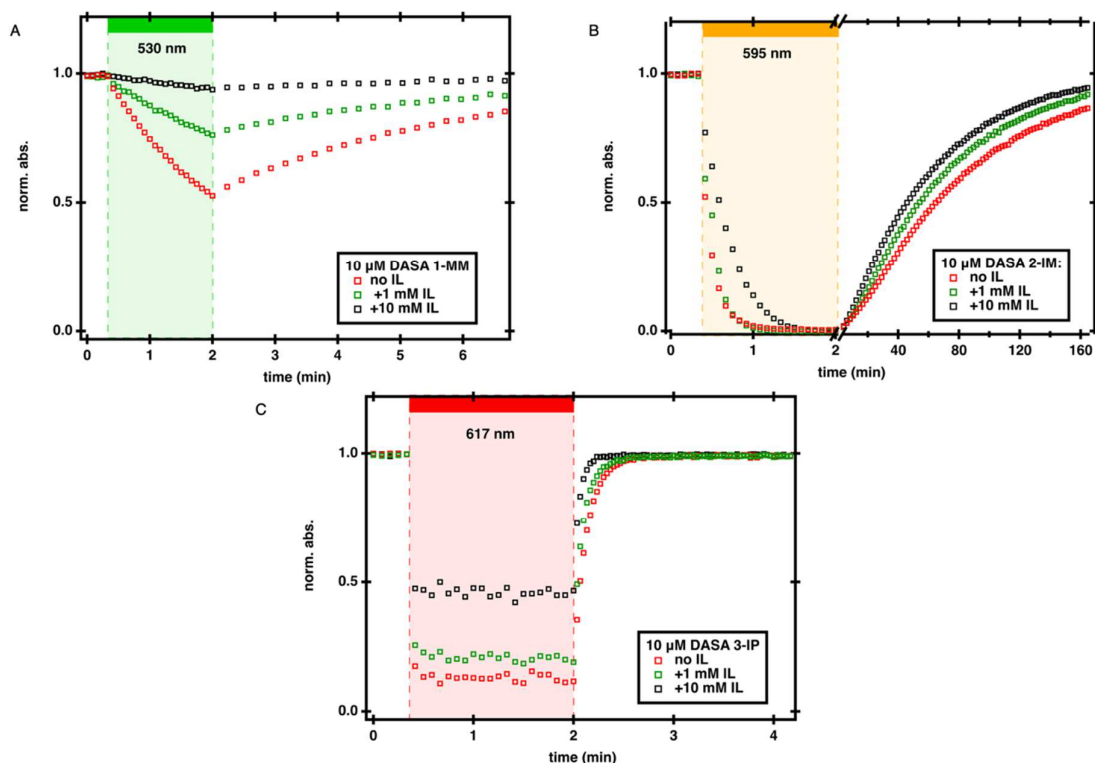


Figure 3.4. Influence of ionic character of DASA derivatives on its switching kinetics using an ion concentration as an external trigger. Photoswitching kinetics measured using time dependent pump probe UV-Vis spectroscopy measured at 10 μM in chloroform at their respective λ_{max} including a control without IL and the addition of 1 mM or 10 mM IL. Irradiation was started at $t = 0.3$ min and ceased at $t = 2.0$ min and the subsequent thermal recovery in the dark was measured. A. Time dependent UV-Vis of **DASA 1-MM** monitored at 540 nm, λ_{max} , irradiated with a 530 nm LED. B. Time dependent UV-Vis of **DASA 2-IM** monitored at 591 nm, λ_{max} , irradiated with a 595 nm LED. C. Time dependent UV-Vis of **DASA 3-IP** monitored at 647 nm, λ_{max} , irradiated with a 617 nm LED. Reproduced with the permission of Wiley & Sons. (Sroda, M.*, Stricker, F.*, et al. *Chem. Eur. J.*, **2021**, *27*, 4183–4190.)¹ Copyright Wiley & Sons.

3.5 Influence of ionic character of DASA on photoswitching

To study the importance of the ionic character of DASA derivatives on their switching kinetics, we next sought to demonstrate the ability to tune switching kinetics by using ion concentration as an external trigger. For this, we utilized 1-butyl-3-methylimidazolium hexafluorophosphate (**IL** for ionic liquid, structure in **Figure 3.7**) as an ion pair soluble in organic solvents. We added 1 mM and 10 mM **IL** to each derivative and monitored the rate of the forward photoswitching and thermal back reaction (k_B) using time dependent pump probe UV-Vis spectroscopy. For experimental detail see the supporting information in section 15. For **DASA 1-MM** upon addition of **IL** we see a significant decrease in the forward reaction rate under light irradiation with 10 mM **IL** almost completely inhibiting photoswitching (**Figure 3.4A**). Due to low solubility of the closed form at higher concentration we were unable to obtain a thermodynamic equilibrium and therefore switching kinetics. For **DASA 2-IM**, bearing the most neutral open and closed form, a slight decrease in the forward reaction kinetics is observed with only a small effect on the recovery to the open form (k_B increases from 0.006 to 0.008 min⁻¹ upon the addition of 10 mM of **IL**; rate increase of 1.4-fold) (**Figure 3.4B**). Although less dramatic than **DASA 1-MM**, the addition of **IL** to a solution of **DASA 3-IP** also resulted in a change in PTSS from 89% to 55% under light irradiation. After irradiation of **DASA 3-IP** is stopped we can observe a 2.3-fold increase in the recovery rate from 7.9 min⁻¹ to 17.8 min⁻¹ upon the addition of 10 mM of **IL**. Taken together, these results highlight that the change in PTSS results out of a combination of a decrease in forward reaction rate and an increased recovery (**Figure 3.4C**).

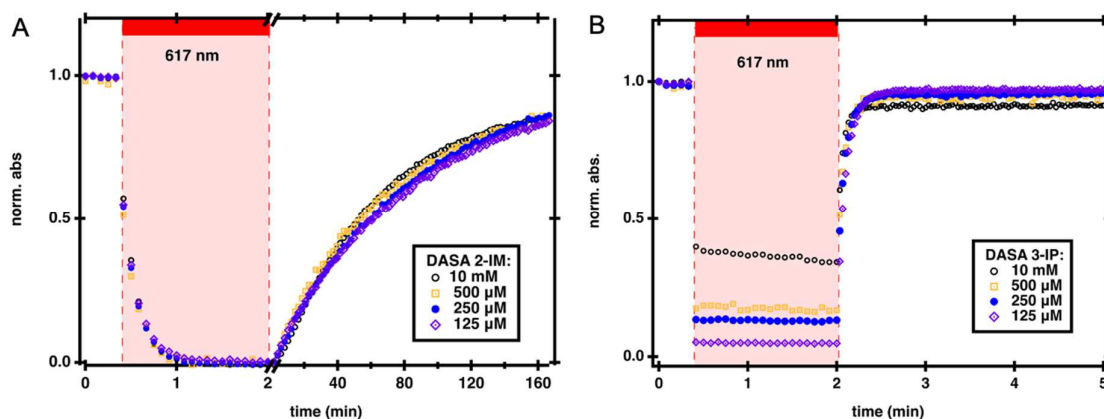


Figure 3.5. Influence of increasing concentration of DASA derivatives on their switching kinetics, determined by using time-dependent pump-probe UV/Vis spectroscopy equipped with a flow cell with variable pathlengths. The concentrations measured were from 125 μM to 10 mM and the samples were irradiated with a 617 nm LED. The irradiation started at $t=0.3$ min and ceased at $t=2.0$ min; the subsequent thermal recovery in the dark was measured. A) Time-dependent UV/Vis analysis of DASA 2-IM monitored at 591 nm (λ_{max}). B) Time-dependent UV/Vis analysis of **DASA 3-IP** monitored at 647 nm (λ_{max}). Reproduced with the permission of Wiley & Sons. (Sroda, M.*, Stricker, F.*, et al. *Chem. Eur. J.*, **2021**, 27, 4183–4190.)¹ Copyright Wiley & Sons.

3.6 Influence of ionic character mimics observed concentration effects

The switching properties of DASA derivatives with highly charge-separated open and closed forms, such as **DASA 1-MM** and **DASA 3-IP**, can be tuned by modifying the ionic character of the solution. In contrast **IL** addition to DASA derivatives with hybrid open and neutral closed forms, such as **DASA 2-IM**, has only a small effect on switching kinetics. These results mirror the previously reported concentration dependence of **DASA 3-IP** suggesting that the higher contribution of the zwitterionic resonance form of **DASA 3-IP** might be responsible for reduced photoswitching observed at high concentrations. To test this hypothesis, we compared the effect of concentration on the less charge-separated **DASA 2-IM** and the more charge-separated **DASA 3-IP** using time dependent pump probe UV-Vis spectroscopy

equipped with a liquid cell with variable pathlengths. For experimental detail see the supporting information in section 1.2.7. The hybrid **DASA 2-IM** shows a negligible change in PTSS at concentrations from 125 μM to 10 mM (**Figure 3.5A**), with a recovery rate increasing from 0.0058 min^{-1} at 125 μM to 0.0067 min^{-1} at 10 mM. In contrast, the concentration effect on **DASA 3-IP** is more dramatic. Here, we see a change in PTSS from 91% to 64% and a 1.6-fold increase in recovery (10 min^{-1} at 125 μM to 16 min^{-1} at 10 mM) as the concentration increases (**Figure 3.5B**), which is consistent with previously reported results.²² Similar experiments with **DASA 1-MM** were unsuccessful due to limited solubility of the closed isomer at concentration above 100 μM . These results reveal that the previously reported concentration dependence is not universal to all DASA derivatives, such as **DASA 2-IM** which has a PTSS of 100% at 10 mM. Importantly, these results provide a path towards designing DASA derivatives able to operate at high concentrations by lowering the ground-state charge-separation in the open form and enabling the formation of a neutral closed isomer.

3.7 Conclusion

The effects of solution-state dielectric and intermolecular interactions on the degree of charge separation provides a route to understand the switching properties and concentration dependence of donor–acceptor Stenhouse adducts (DASAs) in solution. Using easy to perform solvatochromic analysis, the absorption can be used to correlate switching behavior and charge-separation in conjunction with X-ray diffraction (XRD), computational theory, and time dependent pump probe UV–Vis spectroscopy. We show that DASAs bearing the first and third generation architectures have higher contributions of the zwitterionic resonance form and zwitterionic closed forms in solution while the second generation exhibits a hybrid open form and neutral closed isomer. Furthermore, the **DASA 4-II-H** exhibits a different dipolar nature and could be a potential reason for its irreversible switching behavior. Importantly, we highlight the influence of ionic character of DASAs on their photoswitching properties through the

addition of ionic liquids. The more hybrid **DASA 2-IM** shows only limited change in switching behavior upon addition of the ionic liquid, whereas **DASA 1-MM** and **DASA 3-IP** bearing a more zwitterionic open and closed form show a more dramatic effect. Additionally, we show that the previously reported concentration dependence of **DASA 3-IP** relies on the ionic character of the respective open and closed form with more hybrid **DASA 2-IM** being less affected. These results highlight the importance of the charge-separation of DASA on their switching kinetics and the ability to influence certain DASA derivatives through external stimuli. To achieve photoswitching of DASAs at high concentration a more hybrid DASA architecture should be used. Furthermore, these results enable the design of less concentration dependent DASA overcoming a major challenge for applications needing high concentrations of DASA photoswitches as organic photomechanical materials.

3.8 Additional Information

3.8.1 Experimental details

3.8.1.1 Materials

All commercially obtained reagents were bought from Sigma Aldrich, TCI Europe or Fisher Scientific and were used without purification, unless noted. Furfural was distilled before use and stored at -18 °C. Analytical thin-layer chromatography (TLC) was carried out with Merck silica gel 60 F254 glass plates and visualized using combination of UV and potassium permanganate staining or *p*-anisaldehyde. Flash column chromatography was performed with Merck silica gel 60 (70-230 mesh). All chromatographic solvents were of ACS grade and used without further purification.

3.8.2 Characterization methods

3.8.2.1 ¹H NMR

¹H NMR spectra were recorded on Varian spectrometers (400, 500, or 600 MHz) and are reported relative to the residual proteo-signal in deuterated solvents. Data for ¹H NMR spectra are reported as follows: chemical shift (δ ppm), multiplicity, coupling constant (Hz) and integration. ¹³C NMR spectra were recorded on Varian Spectrometers (100, 125, or 150 MHz). Data for ¹³C NMR spectra are reported in terms of chemical shift (δ ppm).

3.8.2.2 Single crystal X-ray diffraction

The crystal was mounted on a glass fiber and transferred to a Bruker Kappa APEX II diffractometer with Mo K-alpha Radiation. The APEX2¹ program was used to determine the unit cell parameters and data collection (10 sec/frame, 0.5 deg./frame Omega scan). The data was collected at room temperature. The raw frame data was processed using SAINT² program. The absorption correction was applied using program SADABS³. Subsequent calculations were carried out using SHELXTL⁴ program. The structure was solved by direct methods and refined on F² by full-matrix least-squares techniques.

1. APEX2 V2014.11-0 Software Users Guide, Bruker Analytical X-ray Systems, Inc.; Madison, WI 2014
2. SAINT Software Users Guide, Version 5.1, Bruker Analytical X-ray Systems, Inc.; Madison, WI 1999
3. Sheldrick, G. M. SADABS, Version 2.05, Bruker Analytical X-ray Systems, Inc.; Madison, WI 2001.
4. Sheldrick, G. M. SHELXTL, Version 6.12, Bruker Analytical X-ray Systems, Inc.; Madison, WI 2001.

3.8.2.3 UV–Vis spectroscopy

UV–Vis absorption spectra were recorded on Agilent 8453 UV–Vis spectrometer from 200 to 1200 nm wavelengths.

3.8.2.4 UV–Vis kinetic measurements

The photoinduced optical absorption kinetics were measured on a pump-probe setup. The pump beam was generated by a light emitting diode (LED) source (Thorlabs) coupled into a multimode optical fiber terminated with an output collimator. The LED intensity was controlled through a digital-to-analog converter (National Instruments USB-6009) using LabVIEW. The probe beam was produced by High Power MINI Deuterium Tungsten Halogen Source w/shutter 200-2000 nm (Ocean Optics DH-MINI) coupled into a multimode fiber with an output collimator for the light delivery. The probe light was modulated by a shutter (Uniblitz CS25) which could be controlled manually or through a digital output port (National Instruments USB-6009) using LabVIEW. Pump and probe beams were overlapped using steering and focusing optics at a 90° angle inside a sample holder, which allowed for a 10 x10 mm rectangular spectrophotometer cells that was connected to a circulating bath for temperature control. Additionally, the solutions were stirred during the measurements by a miniature stirring plate inserted into the sample holder (Starna Cells SCS 1.11). The sample holder was placed into a metal enclosure to prevent exposure to ambient light. Both pump and probe beams were nearly collimated inside the cell with a diameter of about 2 mm. The pump beam was blocked after passing through the sample and the probe beam was directed by a system of lenses into the detector (Ocean Optics Flame-S1-XR spectrometer), which acquired spectra of the probe light. The detector was connected to a PC via USB port. The experiment was controlled by a National Instrument LabVIEW program which collected the probe light spectra, determined sample

optical absorption spectra, controlled pump and probe light sources, and stored the data on the computer S3 hard drive according to the experimental protocol. Experiments were performed in at 10 μM concentration unless otherwise stated. Samples were left to equilibrate overnight prior to measurements unless otherwise stated. Any additives were added prior to equilibration unless otherwise stated.

3.8.2.5 Kinetic modelling

The recovery data obtained from time-dependent UV-Vis spectroscopy was fit to an isomer equilibrium model assuming first order rates of opening and closing. The model used was of the form:

$$\frac{d[\text{Open}]}{dt} = -k_F[\text{Open}]_t + k_B([\text{Open}]_0 - [\text{Open}]_t)$$

For recovery:

$$[\text{Open}]_t = 1 - \frac{k_F + k_B e^{-(k_B+k_F)t}}{k_B + k_F} [\text{Open}]_0$$

where k_F , k_B , and $[\text{Open}]_0$ represent the rate of closing in the dark, the rate of opening in the dark, and the initial concentration. Samples were left to equilibrate overnight, and thermodynamic equilibrium was taken into account for initial concentration. Samples were irradiated for 100 s before recovery. During the recovery 100 measurements were taken at varying time intervals (14 s for **DASA 1-MM**, 5 s for **DASA 1-MB**, 125 s for **DASA 2-IM**, 15 s for **DASA 2-IB**^[a], 2 s for **DASA 3-IP**). ^[a] 450 measurements were taken instead of 100.

3.8.2.6 Light Sources

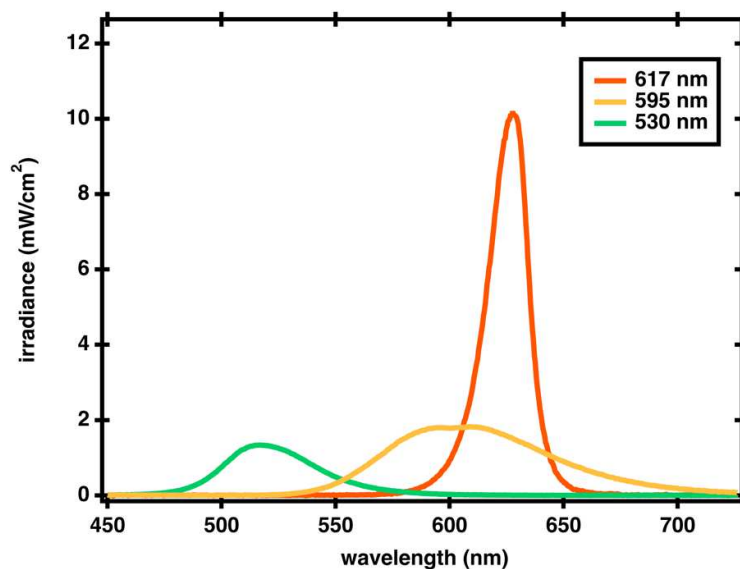


Figure 3.6. irradiance of Thorlabs 530 nm, 595 nm and 617 nm LED used in experiments.

Total irradiance for 530 nm: 69.7 mW/cm²; 595 nm: 168 mW/cm²; 617 nm: 240.2 mW/cm².

Measured using an Ocean Optics hand-held spectrometer with cosine corrector and radiometric calibration (model USB 2000).

3.8.2.7 Demountable liquid cell

A demountable liquid cell (DLC-M13) with variable pathlengths, UV-grade fused silica windows (WAD-U22) and an optical Table 3.8. ample slide holder (HSS-OTE) were purchased from Harrick Scientific Products Inc. The pathlength through the DLC can be varied from 6 μm to 1 mm by selecting the appropriate PTFE spacers.

3.8.2.8 Mass spectrometry

A Waters GCT Premier high-resolution Time-of-flight mass spectrometer is used. The instrument is equipped with electron ionization (EI), chemical ionization (CI), and field ionization/field desorption (FI/FD) ion sources. This instrument has a mass range up to m/z 800 in EI, CI, and FI modes and up to m/z 4000 in FD mode. Accurate mass measurement (<3 mDa) for elemental composition confirmation is available in EI, CI, and FI modes.

3.8.2.9 Ozone cleaning

The hydroxy grown on glass substrates used for spin-coating/drop casting was grown by PSDP-UVT Pro Novascan Ozone Cleaner. The specimens were placed on a mounting stage with the exposed surface requiring cleaning facing upward. The stage height was adjusted to be as close as possible (< 10 mm) to the UV lamps. Each sample was cleaned for 10 min.

3.8.3 All compounds referenced

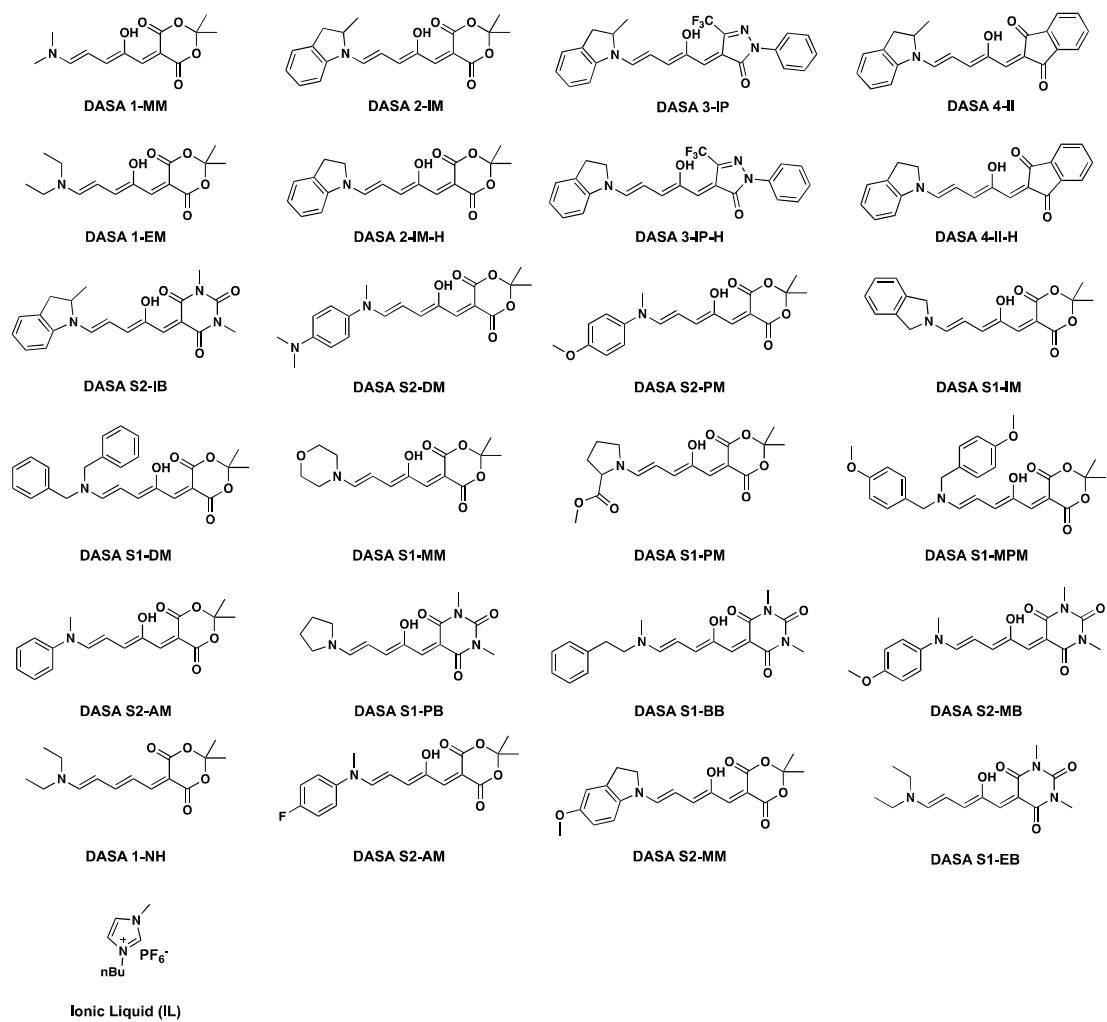


Figure 3.7. All compounds referenced in either the paper or supporting information.

3.8.4 Proposed mechanism

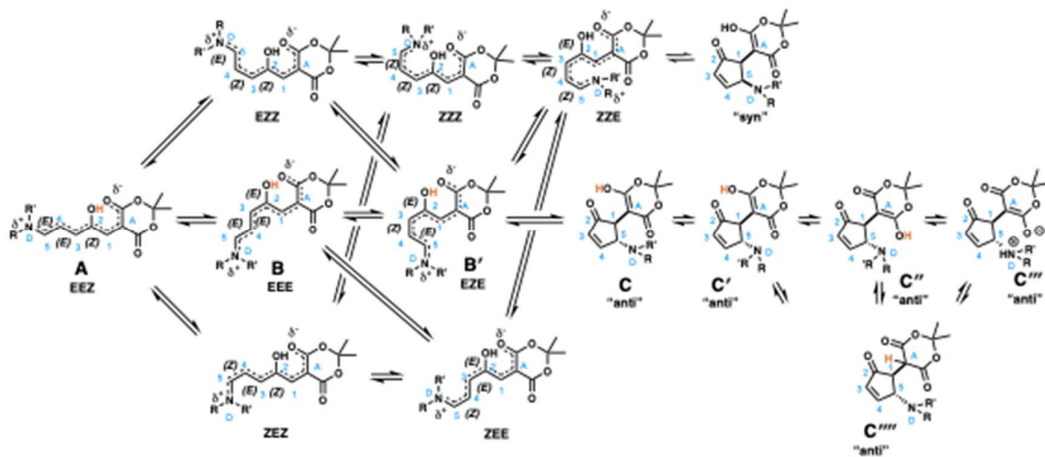
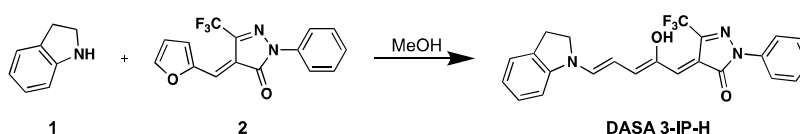


Figure 3.8. Current proposed productive mechanism for photoswitching by Feringa.²⁸

3.8.5 Synthesis of DASAs

Compound **DASA 1-MM**,¹⁷ **DASA 1-DM**,² **DASA-2-IM**,⁵ **DASA 2-IM-H**,⁴ **DASA 2-IB**,⁵ **DASA NH**²⁴ and **DASA 3-IP**⁵ were prepared according to the literature and matched published spectral analysis.



(Z)-4-((2Z,4E)-2-hydroxy-5-(indolin-1-yl)penta-2,4-dien-1-ylidene)-2-phenyl-5-(trifluoromethyl)-2,4-dihydro-3H-pyrazol-3-one (DASA 3-IP-H):

The furan adduct **2**⁵ (500 mg, 1.63 mmol, 1.0 equiv) was stirred in minimal methanol (approximately 5 mL) then indoline **1** (0.28 mL, 292 mg, 2.45 mmol, 1.5 equiv) was added. The reaction was stirred for 4 h and monitored by TLC for consumption of **2**. The reaction mixture was then filtered to yield the product as a green powder and washed with ether to afford the product **DASA 3-IP-H** (458 mg, 1.08 mmol, 66%). Crystals of (**DASA 3-IP-H**) were grown by dissolving 10 mg in 1.5 mL of THF. The solution was stirred, sonicated and filtered. 2.5 mL of ether was layered on top as an anti-solvent. The vial was then capped and allowed to sit in the dark for three days for the crystals to grow. CCDC Deposition number: 2039176.

DASA 3-IP-H: ¹H NMR (500 MHz, chloroform-*d*) δ /ppm: 7.95 (d, $J = 8.1$ Hz, 2H), 7.77 (d, $J = 11.0$ Hz, 1H), 7.52 – 7.36 (m, 2H), 7.17 (t, $J = 7.5$ Hz, 1H), 7.11 (d, $J = 8.2$ Hz, 1H), 6.75 (d, $J = 12.1$ Hz, 1H), 6.66 (s, 1H), 6.34 (t, $J = 12.3$ Hz, 1H), 4.20 (t, $J = 8.0$ Hz, 2H), 3.37 (t, $J = 8.0$ Hz, 2H). IR (thin film) 2920, 2112, 1604, 1556, 1487, 1474, 1354, 1304, 1275, 1253,

1236, 1222, 1205, 1166, 1148, 1094, 1000, 980, 944, 905, 878, 831, 785, 755, 710, 686, 618, 558 cm^{-1} . HRMS (ESI), calculated for $\text{C}_{23}\text{H}_{18}\text{F}_3\text{N}_3\text{NaO}_2^+$ ($\text{M}+\text{Na}^+$): 448.1249, observed 448.1257.

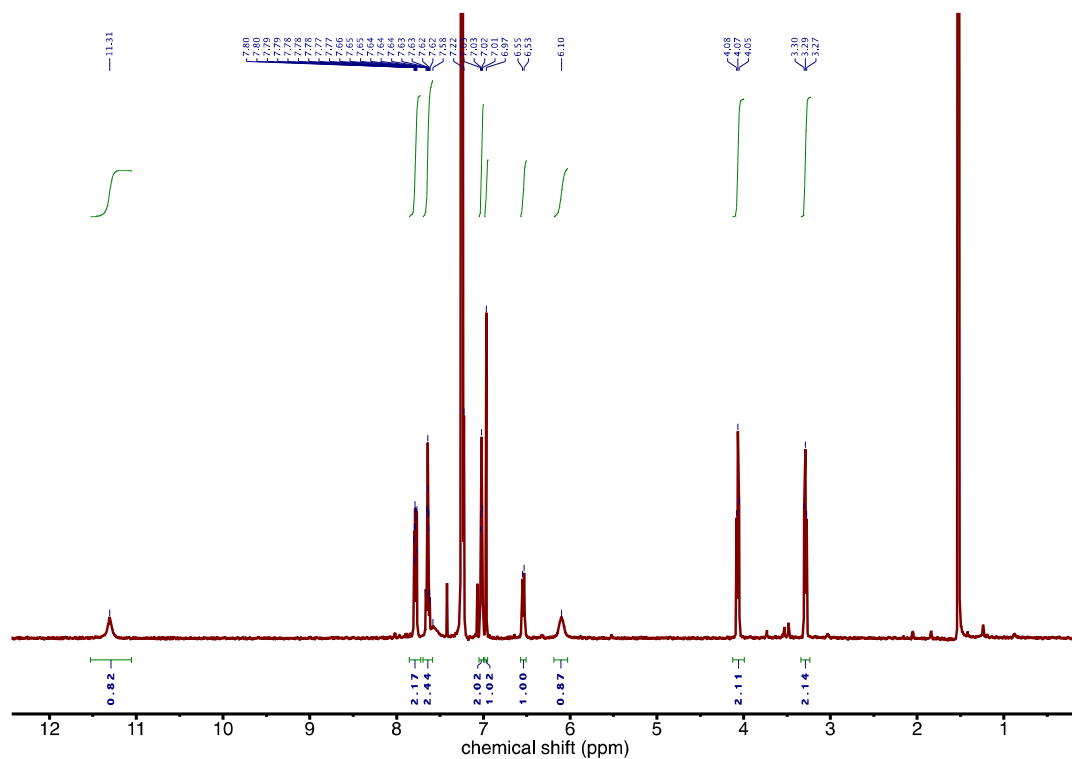
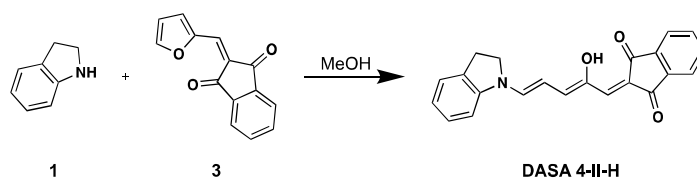


Figure 3.9. ^1H NMR (500 MHz, chloroform-*d*) of **DASA 3-IP-H**.



2-((2Z,4E)-2-hydroxy-5-(indolin-1-yl)penta-2,4-dien-1-ylidene)-1H-indene-1,3(2H)-dione (DASA 4-II-H):

The furan adduct **3**⁴ (200 mg, 0.89 mmol, 1.0 equiv) was stirred in minimal methanol (approximately 4 mL) then indoline **1** (0.12 mL, 127 mg, 1.07 mmol, 1.2 equiv) was added. The reaction was stirred overnight and monitored by TLC for consumption of **3**. The reaction mixture was then filtered to yield the product as a blue powder and washed with ether to afford the product **DASA 4-II-H** (188 mg, 0.55 mmol, 62%). Crystals of (**DASA 4-II-H**) were grown by dissolving 10 mg in 1 mL of THF. The solution was stirred, sonicated, and filtered. A mL of ether was added on top as the anti-solvent. The vial was then capped and allowed to sit in the dark for three days. CCDC Deposition number: 2039175.

DASA 4-II-H: ¹H NMR (600 MHz, chloroform-*d*) δ/ppm: 11.31 (s, 1H), 7.78 (ddd, *J* = 10.7, 6.2, 2.1 Hz, 2H), 7.64 (tt, *J* = 7.3, 5.9 Hz, 2H), 7.58 (s, 1H), 7.23 (d, *J* = 7.2 Hz, 1H), 7.02 (dd, *J* = 8.6, 5.6 Hz, 2H), 6.97 (s, 1H), 6.54 (d, *J* = 11.9 Hz, 1H), 6.10 (s, 1H), 4.07 (t, *J* = 8.2 Hz, 2H), 3.29 (t, *J* = 8.2 Hz, 2H). IR (thin film) 2324, 2062, 1982, 1687, 1615, 1585, 1528, 1487, 1451, 1434, 1328, 1291, 1229, 1202, 1181, 1137, 1112, 932, 875, 846, 812, 798, 750, 728 cm⁻¹. HRMS (ESI), calculated for C₂₂H₁₇NNaO₃⁺ (M+Na⁺): 366.1106, observed 366.1106.

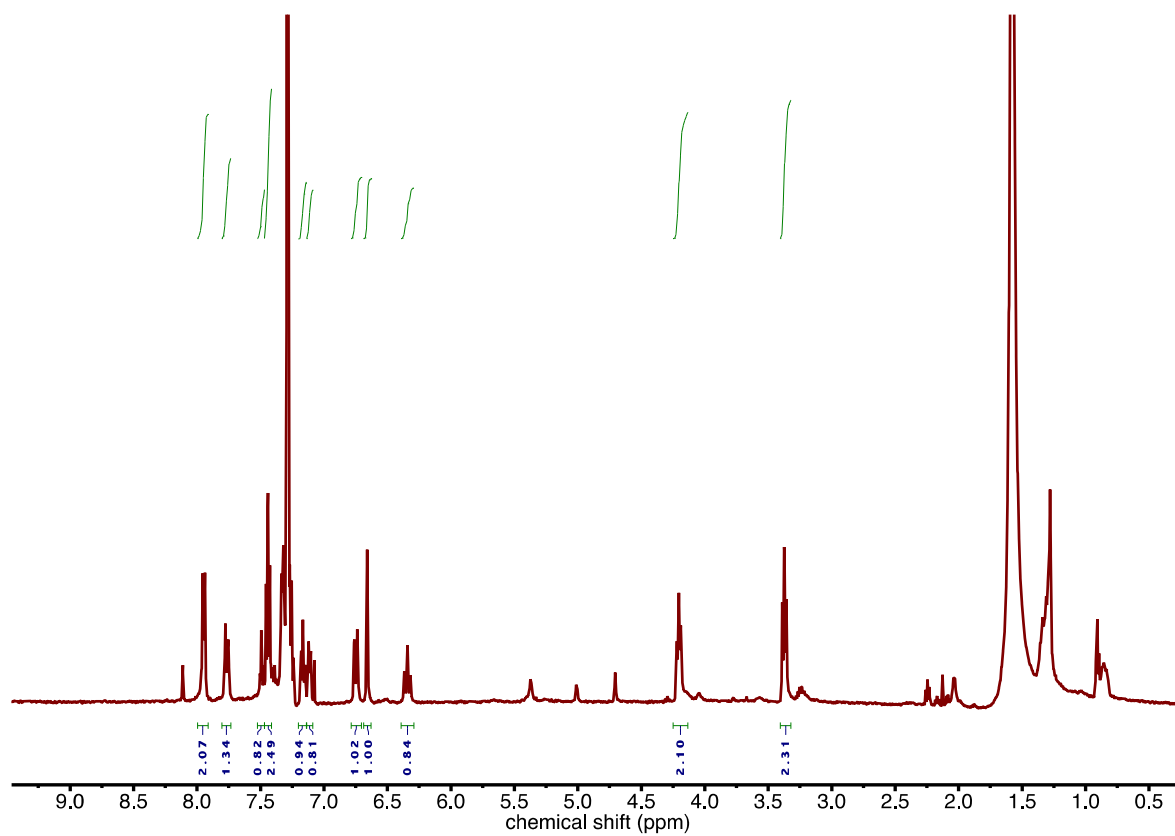


Figure 3.10. ^1H NMR (600 MHz, chloroform-*d*) of DASA 4-IP-H.

3.8.6 Table of photoswitching properties

Table 3.2: Photoswitching properties

DASA Compound	Solvent	λ_{\max} (nm)	therm. equi. (% open form in the dark)	PTSS (% closed under irradi.)	Half-life, $t_{1/2}$ (s)
DASA 1-EM^{1,4}	Chloroform	540	100%	12%	11 s
	Toluene	545	100%	94%	100 s
DASA 1-MM	Chloroform	541	94% ^[a]	76%	172 s
DASA 2-IM⁴	Chloroform	590	50%	100%	3,240 s
DASA 2-IB⁴	Chloroform	616	42%	100%	1,080 s
DASA 3-IP⁴	Chloroform	650	99%	94%	5 s
	Toluene	655	100%	100%	40 s
DASA S4-II⁴	Chloroform	640	42%	-	-
	Toluene	636	N/A	-	-

^[a]determined through UV-Vis. See Figure 3.13–14.

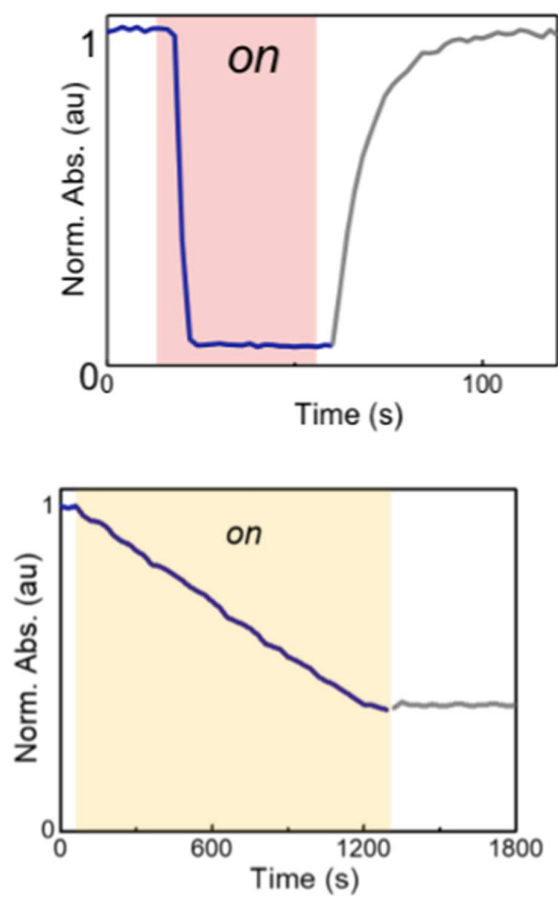


Figure 3.11. A. Photoswitching of 10 μM **DASA 3-IP** in chloroform followed at 650 nm, λ_{max} .
 B. Linear photodegradation upon irradiation and no recovery of 10 μM of **DASA 4-II-H** in chloroform followed at 640 nm, λ_{max} . Data taken from ref 5.⁵

3.8.7 Thermodynamic equilibrium and switching of DASA 1-MM

The thermodynamic equilibrium of **DASA 1-MM** could not be determined by ^1H NMR due to lacking solubility of the closed form at concentrations over $250\ \mu\text{M}$. To obtain a thermodynamic equilibrium a $10\ \mu\text{M}$ solution was made dissolving the open and measuring an initial UV-Vis as fast as possible. The solution then was irradiated for 1 min with a 530 nm LED. Subsequently the absorbance was left in the dark to recover with timepoints being taken every 14 s till recovery was complete. The authors want to point out that the probe light of the UV-Vis will interfere with the equilibrium which is why ^1H -NMR is preferable if possible.

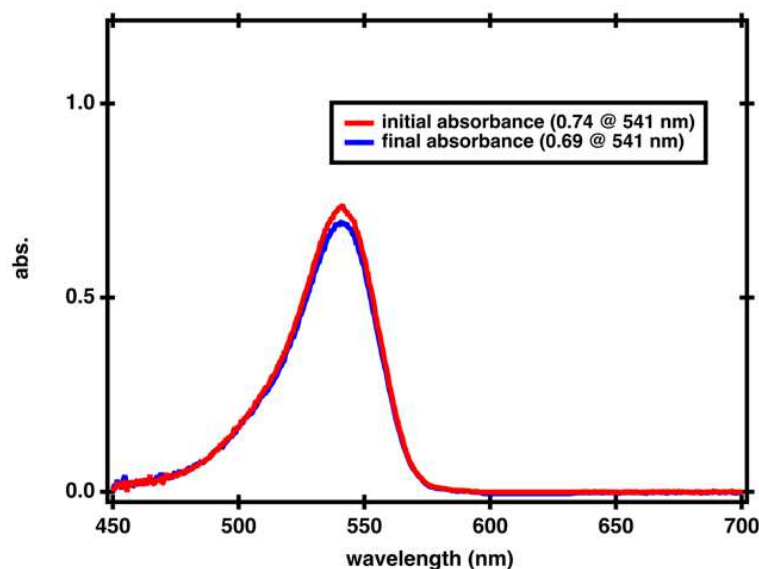


Figure 3.12. Determination of thermodynamic equilibrium of **DASA 1-MM**. Initial absorbance after mixing at $\lambda_{\text{max}} = 541\ \text{nm}$. Initial absorbance 0.74. Absorbance after recovery 0.69. See **Figure 3.13** for recovery.

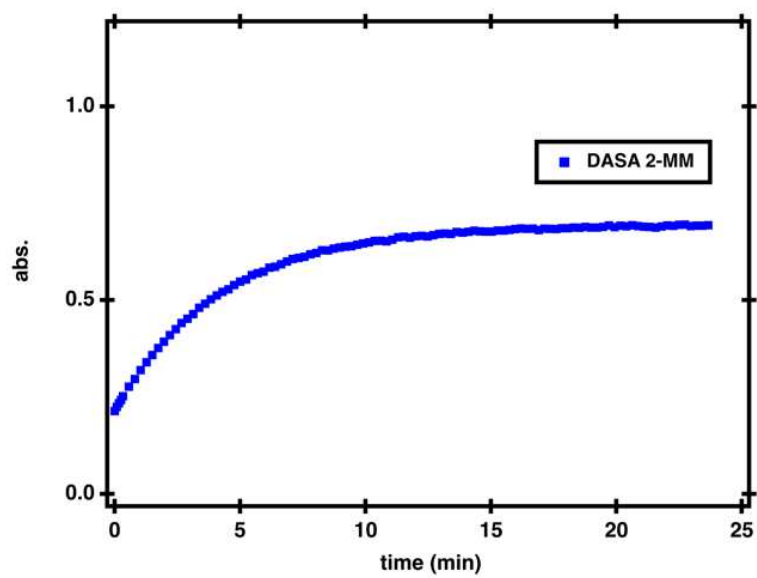


Figure 3.13. Recovery after irradiation for 1 min with 530 nm LED for determination of thermodynamic equilibrium followed at 541 nm.

3.8.8 X-ray crystal structures

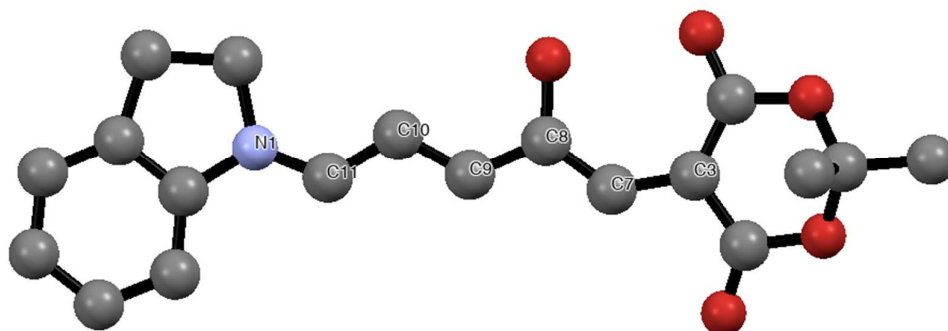


Figure 3.14. An ORTEP representation of the X-ray crystal structure of **DASA 2-IM-H**.

C: grey; N: blue; O: red; H: omitted. CCDC Deposition number: 2041883.

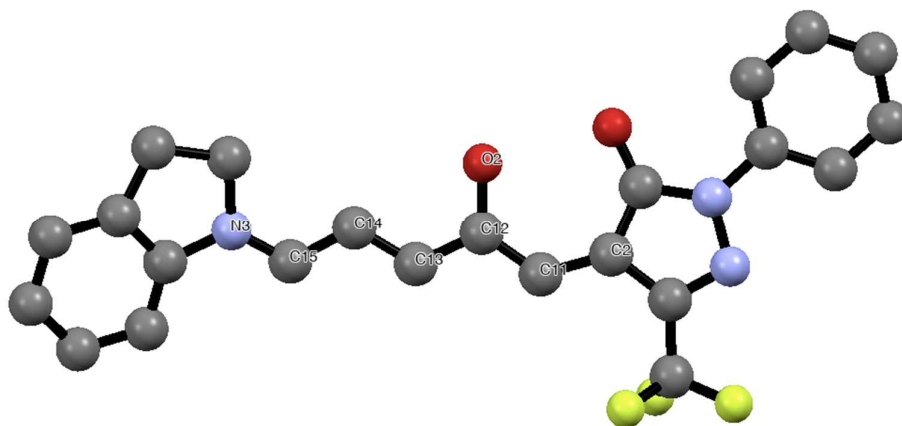


Figure 3.15. An ORTEP representation of the X-ray crystal structure of **DASA 3-IP-H**.

C: grey; N: blue; O: red; F: yellow; H: omitted. CCDC Deposition number: 2039176.

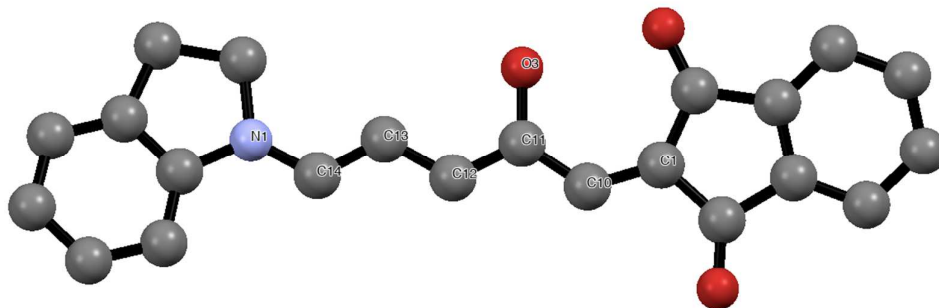


Figure 3.16. An ORTEP representation of the X-ray crystal structure of **DASA 4-II-H**. C: grey; N: blue; O: red; H: omitted. CCDC Deposition number: 2039175.

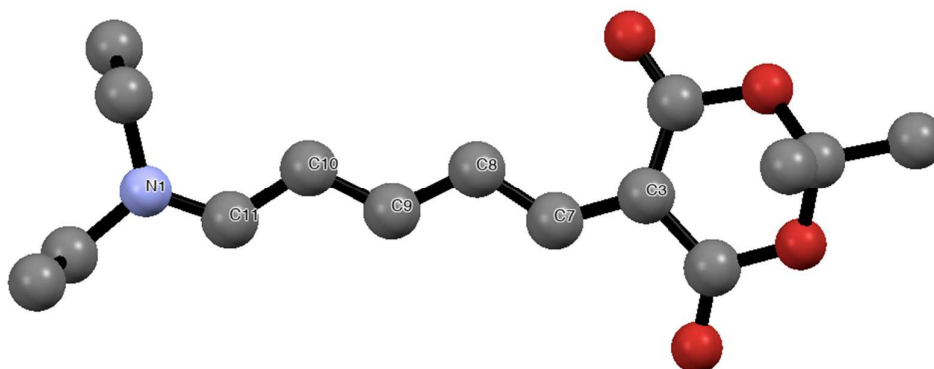


Figure 3.17. An ORTEP representation of the X-ray crystal structure of **DASA NH**. C: grey; N: blue; O: red; H: omitted. CCDC Deposition number: 2041877.

3.8.9 Comparison of bond lengths within the conjugated polyene system of all published linear isomers

Beves, et al. reported bond lengths within the conjugated triene system of **DASA S2-DM**, **S2-PM**, **S1-EB**, **S2-AM**, **S1-PB**, **S1-BB**, and **S2-MB**. This analysis showed the bond lengths within the conjugated triene system suggest that the charge-separated zwitterion is a better representation of the solid-state structure.^{17,21}

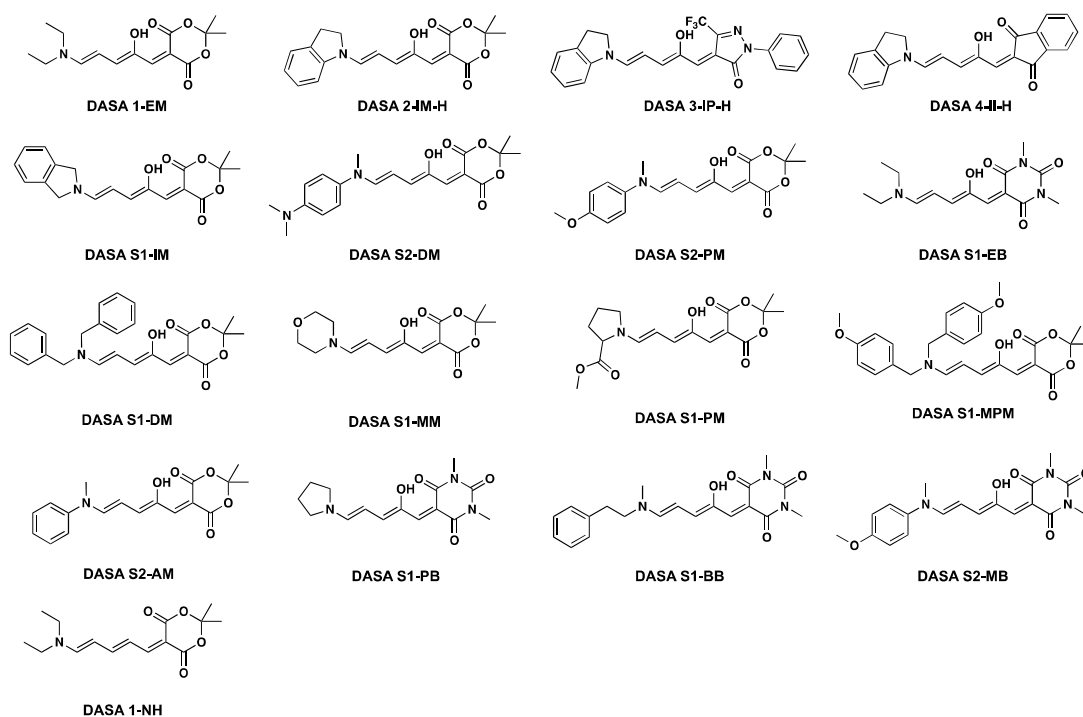


Figure 3.18. Summary of compounds included in Figure 3.19 in order to compare bond length alterations (BLA) of open form crystals.

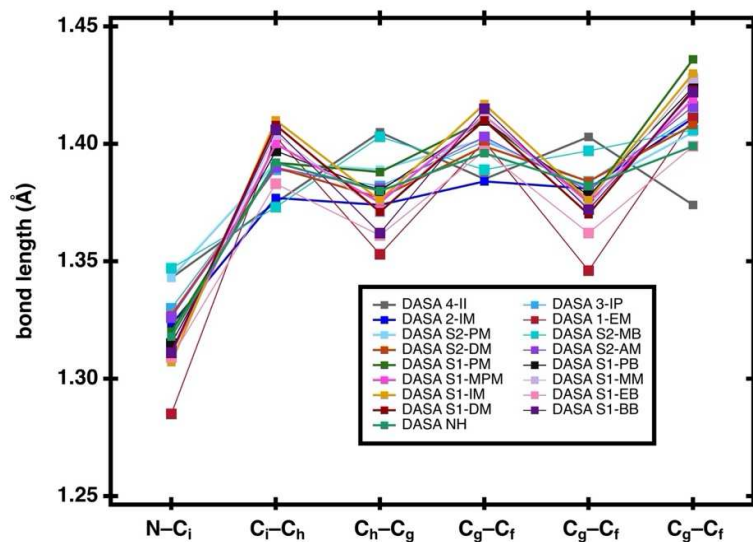


Figure 3.19. Comparison of bond lengths along the triene of 17 open form DASA crystals showing a varying degree of charge-separation.

Table 3.3: Bond lengths along the conjugated triene of seventeen linear DASA compounds as determined by single crystal X-ray structures. Bond length alterations (BLA) defined as the difference between the average bond length of the C-C single bonds and the average bond length of the C-C double bonds.

	N-Ci	Ci-Ch	Ch-Cg	Cg-Cf	Cf-Ce	Ce-Cd	BLA
DASA 1-EM³	1.285	1.403	1.353	1.401	1.346	1.411	-0.056
DASA 2-IM-H	1.323	1.377	1.374	1.384	1.381	1.411	-0.013
DASA 3-IP-H	1.330	1.389	1.382	1.401	1.384	1.412	-0.018
DASA 4-II-H	1.343	1.375	1.405	1.385	1.403	1.374	0.026
DASA S1-IM³	1.307	1.410	1.376	1.417	1.376	1.430	-0.043
DASA S2-DM²	1.327	1.390	1.377	1.399	1.384	1.408	-0.018
DASA S2-PM²	1.343	1.392	1.389	1.402	1.381	1.405	-0.015
DASA S1-EB³	1.309	1.383	1.361	1.397	1.362	1.399	-0.032
DASA S1-DM³	1.311	1.408	1.371	1.410	1.370	1.423	-0.043
DASA S1-MM³	1.311	1.404	1.371	1.412	1.373	1.428	-0.043
DASA S1-PM³	1.320	1.392	1.388	1.410	1.376	1.436	-0.031
DASA S1-MPM²	1.311	1.400	1.375	1.412	1.375	1.419	-0.035
DASA S2-AM²	1.326	1.390	1.381	1.403	1.380	1.416	-0.022
DASA S1-PB⁷	1.315	1.397	1.380	1.410	1.378	1.424	-0.031
DASA S1-BB⁷	1.311	1.406	1.362	1.415	1.372	1.422	-0.047
DASA S2-MB⁷	1.347	1.373	1.403	1.389	1.397	1.406	0.011
DASA NH	1.318	1.392	1.38	1.396	1.382	1.399	-0.015

3.8.10 E_T^N values

Table 3.4: The ten solvents and corresponding E_T^N solvent polarity value using the Dimroth—Reichardt E_T solvent polarity scale. The E_T^N scale is based on the electronic transitions of a polarity probe dye in a range of solvents which is normalized to nonpolar tetramethylsilane (TMS) ($E_T^N = 0$) and polar water ($E_T^N = 1.0$).²⁷

Solvent	Tol	Et ₂ O	THF	EtOAc	CHCl ₃
E_T^N	0.099	0.117	0.207	0.228	0.259
Solvent	CH ₂ Cl ₂	Acetone	DMSO	ACN	MeOH
E_T^N	0.309	0.355	0.444	0.460	0.762

3.8.11 Absorption properties of the linear compounds measured by UV–Vis

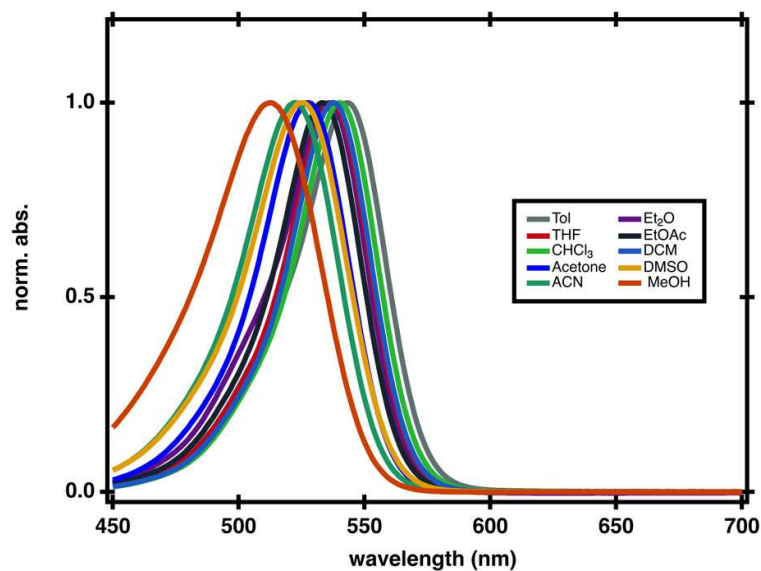


Figure 3.20. Solvatochromic shift of **DASA 1-MM**.

Table 3.5: λ_{max} (nm) values of **DASA 1-MM** in a range of solvents.

Solvent	Tol	Et ₂ O	THF	EtOAc	CHCl ₃
λ_{max} (nm)	543	536	537	533	541
Solvent	CH ₂ Cl ₂	Acetone	DMSO	ACN	MeOH
λ_{max} (nm)	538	527	526	522	513

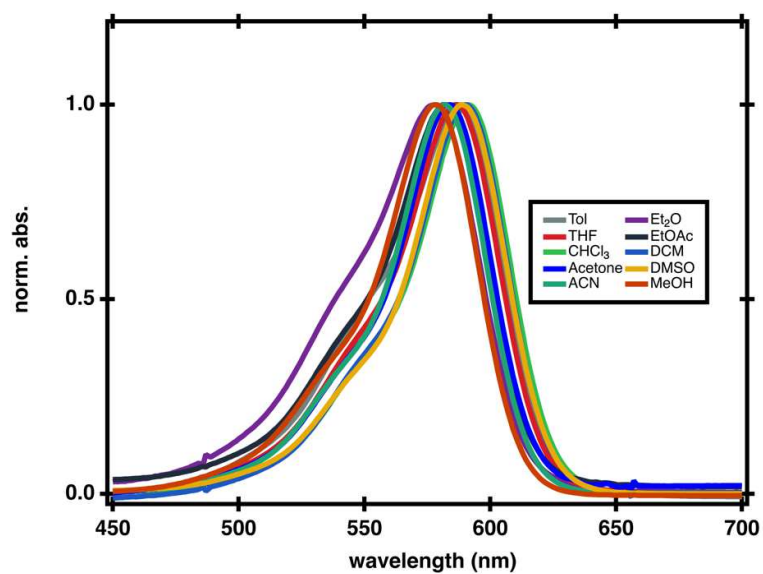


Figure 3.21. Solvatochromic shift of **DASA 2-IM**.

Table 3.6: λ_{\max} (nm) values of **DASA 2-IM** in a range of solvents.

Solvent	Tol	Et ₂ O	THF	EtOAc	CHCl ₃
λ_{\max} (nm)	588	578	587	581	590
Solvent	CH ₂ Cl ₂	Acetone	DMSO	ACN	MeOH
λ_{\max} (nm)	590	584	589	582	578

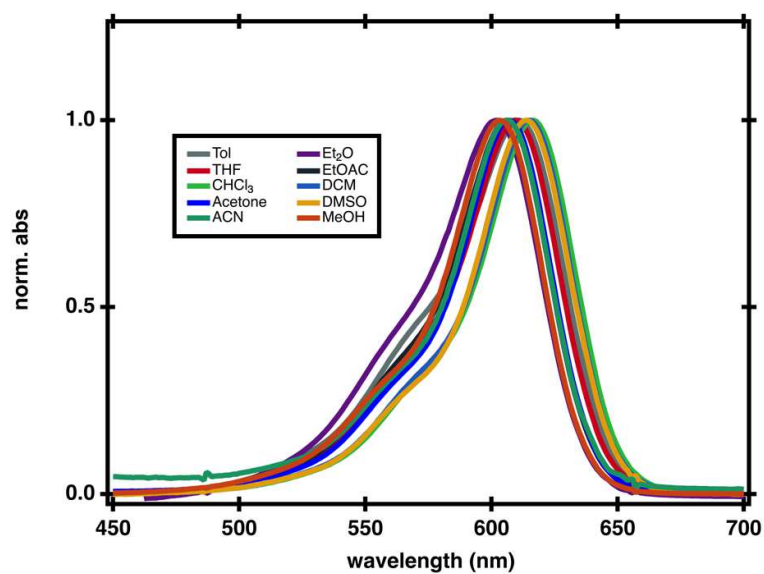


Figure 3.22. Solvatochromic shift of **DASA 2-IB**.

Table 3.7: λ_{\max} (nm) values of **DASA 2-IB** in a range of solvents.

Solvent	Tol	Et ₂ O	THF	EtOAc	CHCl ₃
λ_{\max} (nm)	611	602	610	606	616
Solvent	CH ₂ Cl ₂	Acetone	DMSO	ACN	MeOH
λ_{\max} (nm)	615	607	614	606	603

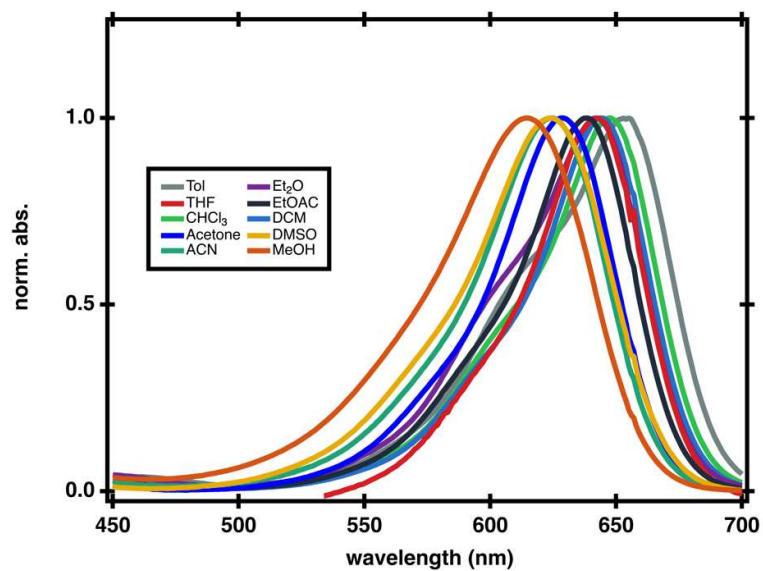


Figure 3.23. Solvatochromic shift of **DASA 3-IP**.

Table 3.8: λ_{\max} (nm) values of **DASA 3-IP** in a range of solvents.

Solvent	Tol	Et ₂ O	THF	EtOAc	CHCl ₃
λ_{\max} (nm)	655	643	645	639	650
Solvent	CH ₂ Cl ₂	Acetone	DMSO	ACN	MeOH
λ_{\max} (nm)	644	632	624	626	616

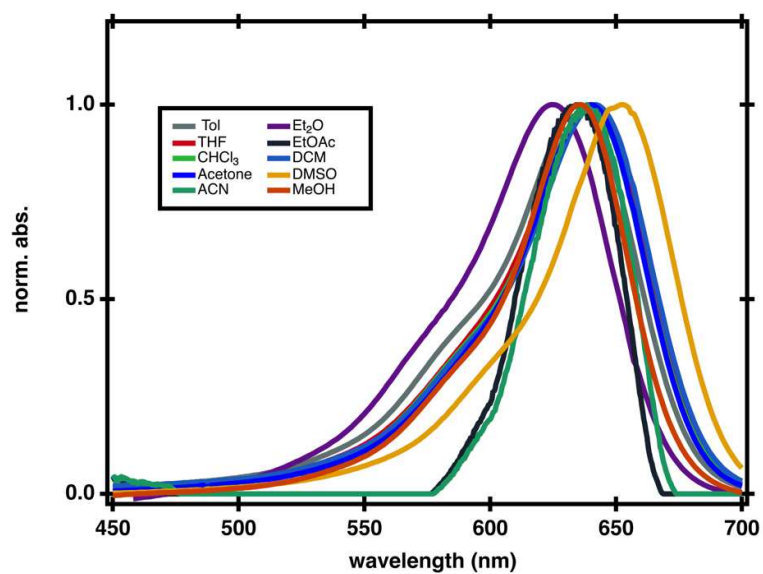


Figure 3.24. Solvatochromic shift of **DASA 4-II-H**.

Table 3.9: λ_{\max} (nm) values of **DASA 4-II-H** in a range of solvents.

Solvent	Tol	Et ₂ O	THF	EtOAc	CHCl ₃
λ_{\max} (nm)	636	627	638	634	640
Solvent	CH ₂ Cl ₂	Acetone	DMSO	ACN	MeOH
λ_{\max} (nm)	642	639	655	638	636

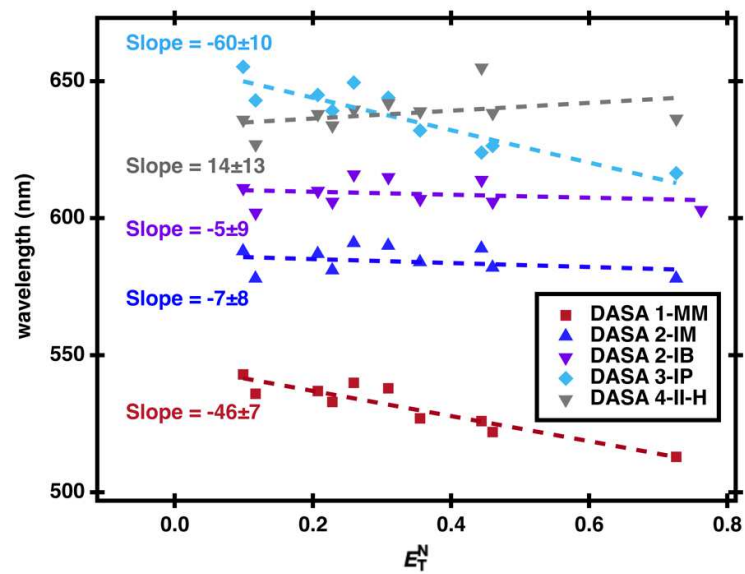


Figure 3.25. Solvatochromic slopes of **DASA 1-MM, 2-IM, 2-IB, 3-IM, and 4-II-H** with error.

3.8.12 Solvatochromic shifts correlated with equilibrium studies

Beves, et al. reported absorption profiles for a series of second generation DASAs bearing aniline-based donors and in agreement with our observed trend, the negative solvatochromic slopes can be correlated with the relative dark equilibrium.¹⁷

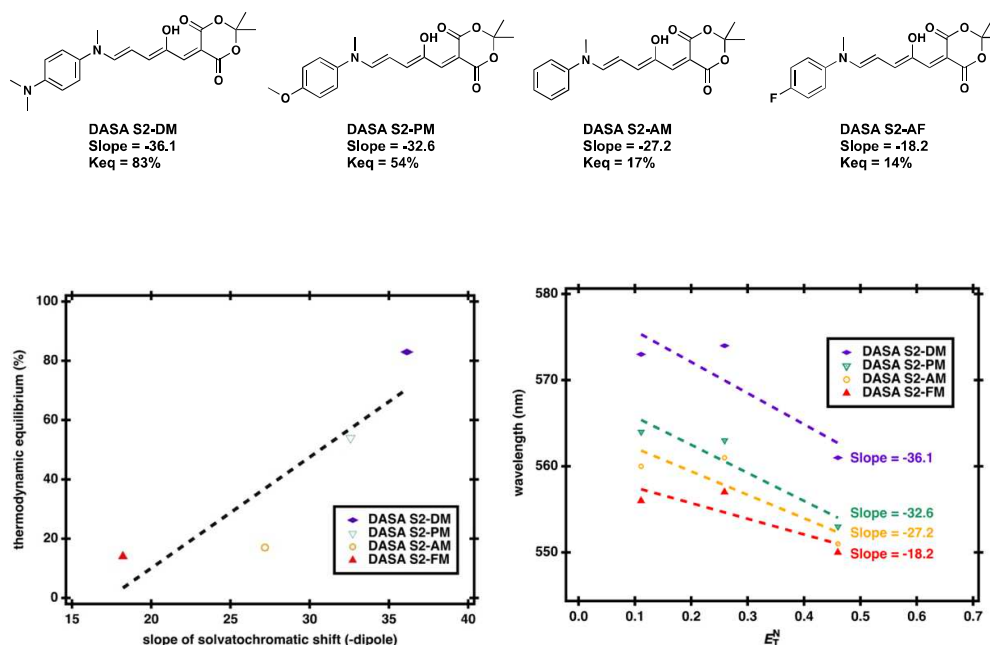


Figure 3.26. A. Aniline-based donor studied by Beves and coworkers¹⁷ B. Reported absorption maximum vs the polarity value of the solvents for the studied DASAs all show negative solvatochromic slopes. C. Negative solvatochromic slopes correlated with the reported relative dark equilibrium in chloroform.

3.8.12.1 Shifting absorbance in polymer matrix blends

To emphasize the role of the environment we extended this analysis to the solid-state. We blended the DASAs into polymer matrices varying in polarity. For the polarity values of the polymer study, we extracted and predicted polarity value based on the well-defined value of the solvent small molecules. For example, $E_T^N \sim \mu$ of polyacrylonitrile was estimated to have similar polarity as acetonitrile, polystyrene to toluene and poly (methyl methacrylate) to ethyl acetate. Although this assumption does not take into account factors such as intermolecular interactions specific to the polymer blends. We observed the same trends for the polymer blends as we did for the solution solvatochromatic study (Figure 3). Taken together, these results show that DASA photoswitching molecules have a high degree of charge-separation in the ground state in both solution and solid-state media.

Thin film DASA blends were prepared by spin coating on an ozone treated microscope glass slide. First, an 89 mg/mL polymer solution in DCM or DMF was prepared in a vial and sonicated at room temperature for 1 hr. Separately the corresponding DASA solution (an approximately 7 mg/mL was prepared in DCM or DMF and 0.15 mL was added to the polymer solution resulting in a 90 mg/mL solution.) After spin-coating, the slides were put in a vacuum oven at 60 °C for 2 hours and the maximum absorbance was measured using UV-Vis spectroscopy.

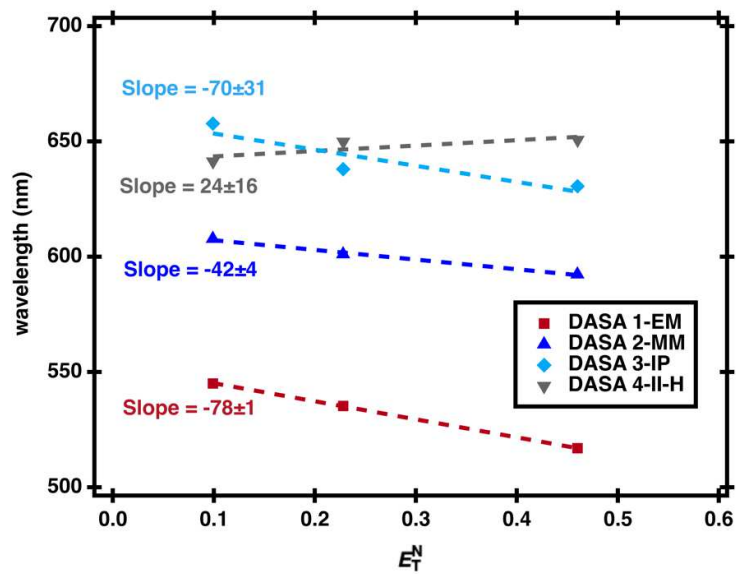
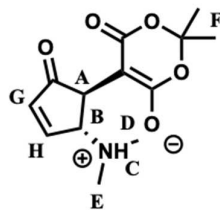


Figure 3.27. The maximum absorbance of DASA 1-EM, 2-MM, 3-IP, and 4-II-H in polymer blends (PS, PMMA, PAN) correlated with mu polymer polarity with error.

3.8.13 Closed form analysis by 2D-NMR



DASA 1-MM: ^1H NMR (600 MHz, $\text{DMSO-}d_6$) δ /ppm: 10.01 – 9.40 (m, 1H, NH_C), 7.81 – 7.65 (m, 1H, H_H), 6.47 – 6.44 (m, 1H, H_G), 4.33 – 4.30 (m, 1H, H_A), 3.29 – 3.27 (m, 1H, H_B), 2.81 (s, 6H, H_E), 1.50 – 1.47 (m, 6H, H_F). ^{13}C NMR^[a] (125 MHz, $\text{DMSO-}d_6$) δ /ppm: 190.1 (CO-C_A), 164.5(C_H), 138.1(C_G), 99.9(C-C_F), 71.6 (C_B), 45.4 (C_A), 26.0 (C_F).

^[a]Limited solubility of the closed isomer limited signal.

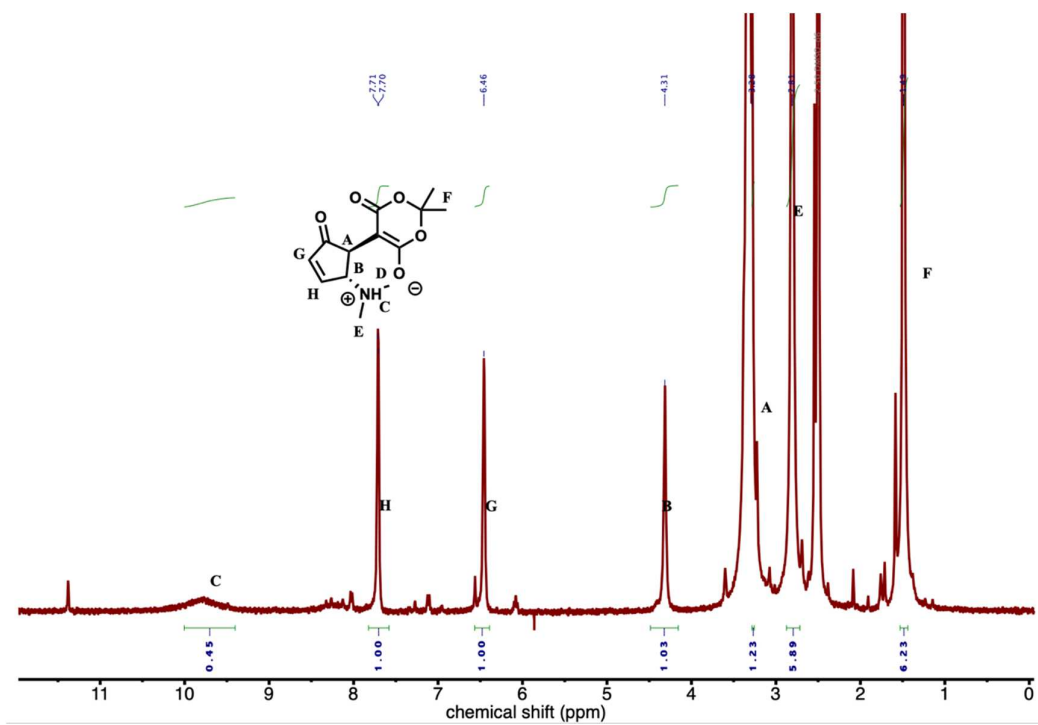


Figure 3.28. ¹H-NMR (600 MHz, DMSO-*d*₆) of DASA 1-MM. Only the zwitterionic closed form can be observed.

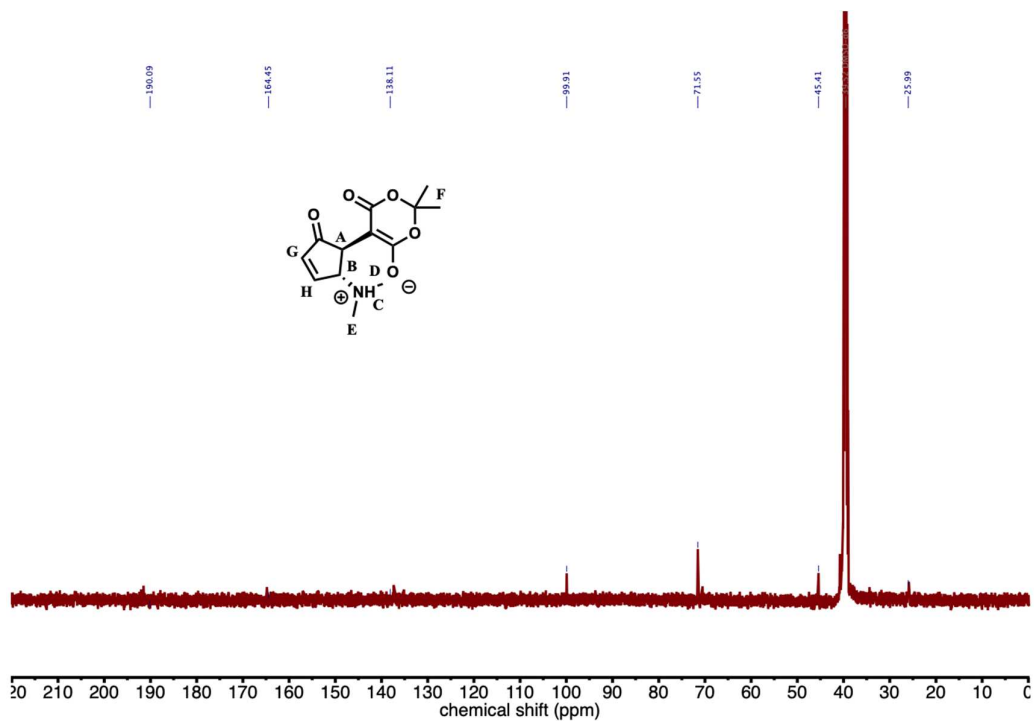


Figure 3.29. ^{13}C -NMR (125 MHz, $\text{DMSO-}d_6$) of **DASA 1-MM**. Limited solubility of the closed isomer results in minimal signal.

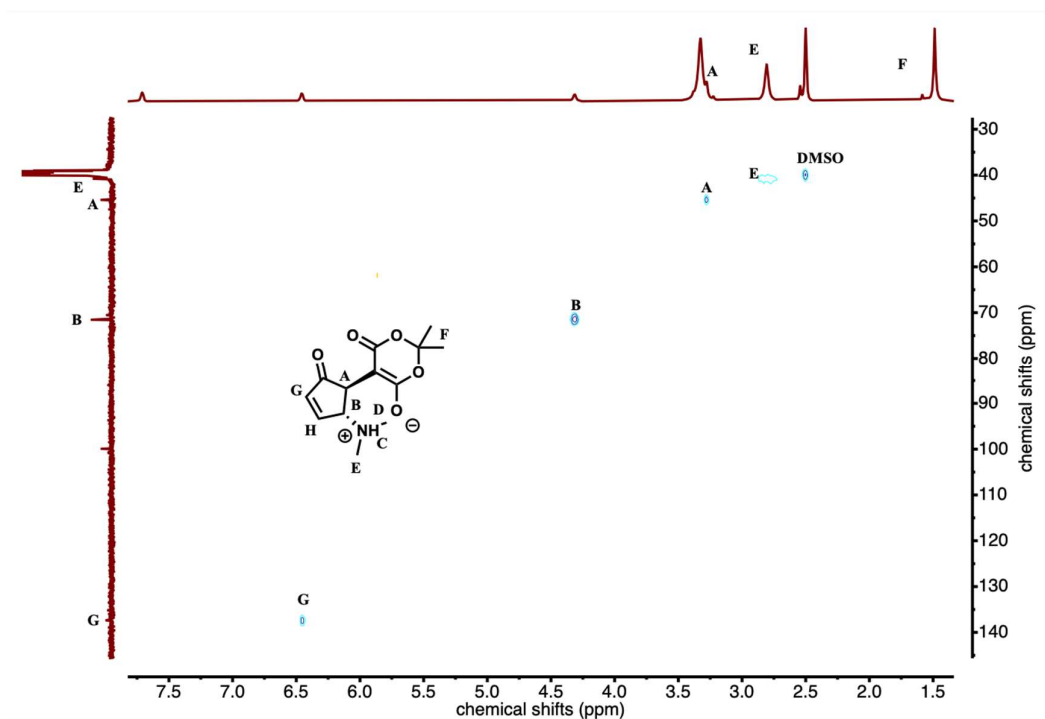


Figure 3.30. HSQC-NMR (600 MHz, DMSO-*d*₆) of **DASA 1-MM**. Only the zwitterionic closed form can be observed. Only three C-H interactions in the region between 5.5 and 2.5 ppm can be observed.

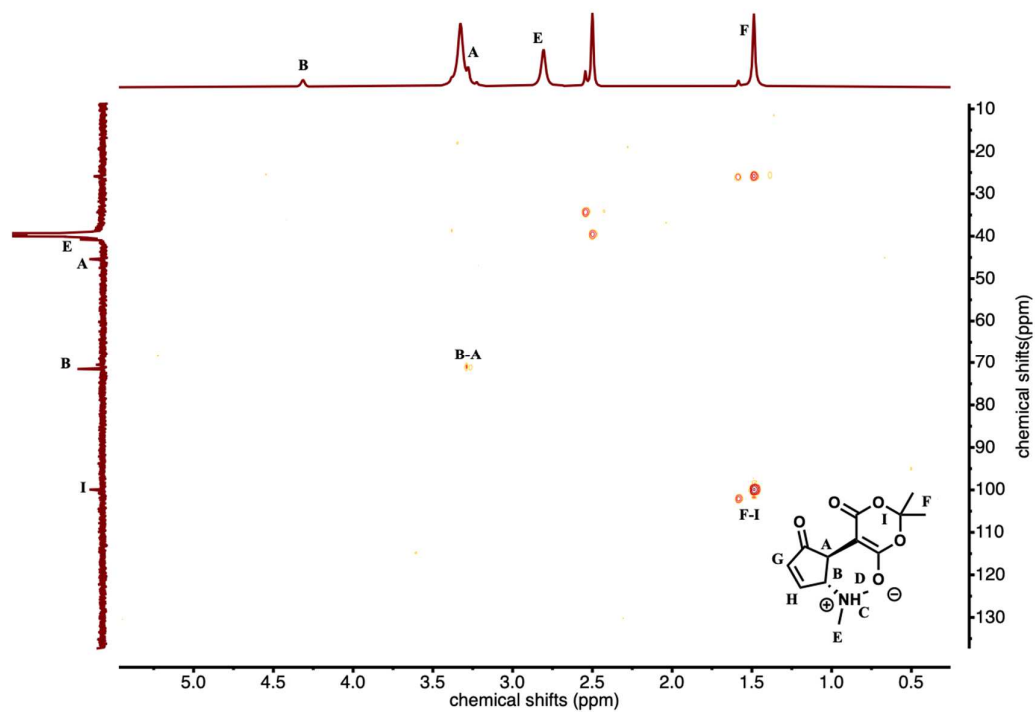
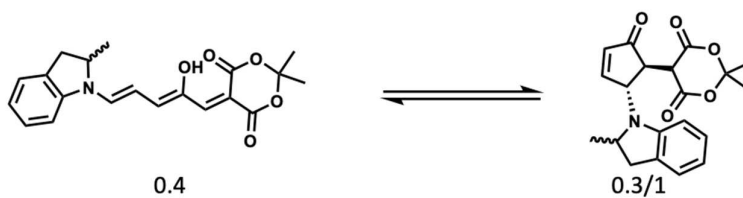


Figure 3.31. HMBC-NMR (600 MHz, DMSO- d_6) of **DASA 1-MM**. Only the zwitterionic closed form can be observed.

DASA 2-IM:



Mixture of open (0.4) and two keto closed forms (0.3/1 labeled closed 1/2 subsequently). presumably diastereomers at the C2 of the indoline.

DASA 2-IM: ^1H NMR (600 MHz, chloroform-*d*) δ /ppm: 11.34 (s, 0.4H, open), 7.78 – 7.72 (m, 1.3H, closed 1/2), 7.62 – 7.54 (m, 0.4H, open), 7.37 – 7.28 (m, 1H, 2x open), 7.16 – 7.10 (m, 1H, open/closed 1), 7.08 – 7.02 (m, 1H, closed 2), 7.02 – 6.92 (m, 1H, closed 2), 6.72 – 6.63 (m, 2H, open/closed 1/2), 6.53 – 6.46 (m, 0.3H, closed 1), 6.45 – 6.37 (m, 2H, 2x closed 2), 6.33 – 6.24 (m, 0.4H, open), 5.27 – 5.24 (m, 1H, closed 2), 5.00 – 4.89 (m, 0.3H, closed 1), 4.68 – 4.61 (m, 0.4H, open), 4.10 – 4.06 (m, 0.3H, closed 1), 4.02 (s, 1H, closed 2), 3.98 – 3.93 (m, 1H, closed 2), 3.88 – 3.83 (m, 0.3H, closed 1), 3.81 – 3.77 (m, 0.3H, closed 1), 3.76 – 3.75 (m, 1H, closed 2), 3.55 – 3.45 (m, 0.4H, open), 3.27 – 3.20 (m, 1.3H, closed 1/2), 2.85 – 2.79 (m, 0.4H, open), 2.68 – 2.55 (m, 1.3H, closed 1/2), 1.42 (d, $J = 6.5$ Hz, 1.5H, open), 1.35 (d, $J = 6.2$ Hz, 1H, closed 1), 1.26 (d, $J = 6.2$ Hz, 3H, closed 2). ^{13}C NMR (125 MHz, chloroform-*d*) δ /ppm: 204.3, 164.8, 164.6, 164.4, 163.8, 150.6, 147.0, 146.6, 143.7, 142.6, 141.5, 134.3, 133.0, 131.4, 129.1, 128.6, 127.6, 127.5, 126.6, 125.6, 125.2, 125.1, 119.0, 110.2, 107.6, 106.7, 105.8, 104.6, 103.9, 61.1, 60.1, 59.5, 57.6, 57.1, 48.4, 46.7, 44.9, 44.4, 37.7, 37.5, 36.4, 28.2, 27.2, 27.1, 27.0, 22.3, 21.6, 19.7.

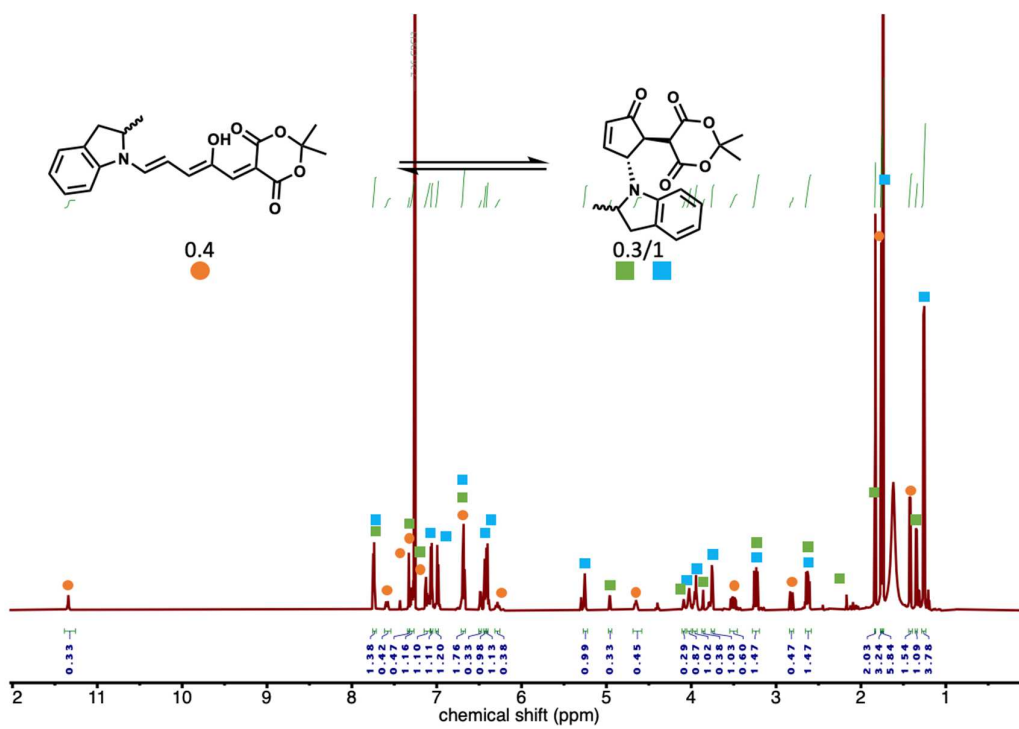


Figure 3.32. $^1\text{H-NMR}$ (600 MHz, chloroform- d) of DASA 2-IM. The different isomers are marked.

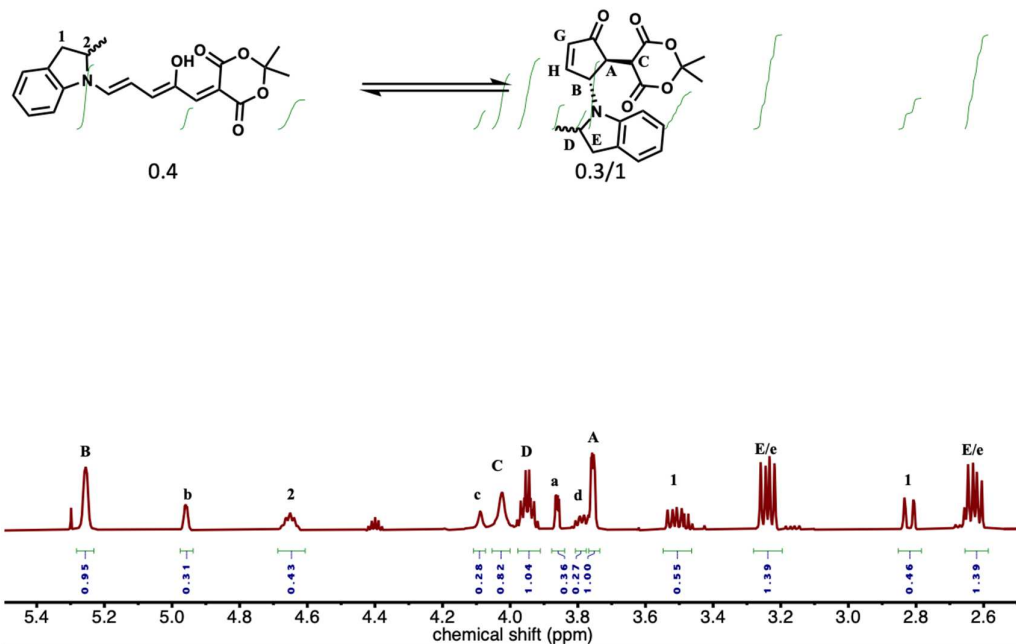


Figure 3.33. $^1\text{H-NMR}$ (600 MHz, chloroform-*d*) of **DASA 2-IM** between 5.5 and 2.5 ppm.

The different isomers are marked. For the keto isomer integrating with 0.3 lower case letters were used.

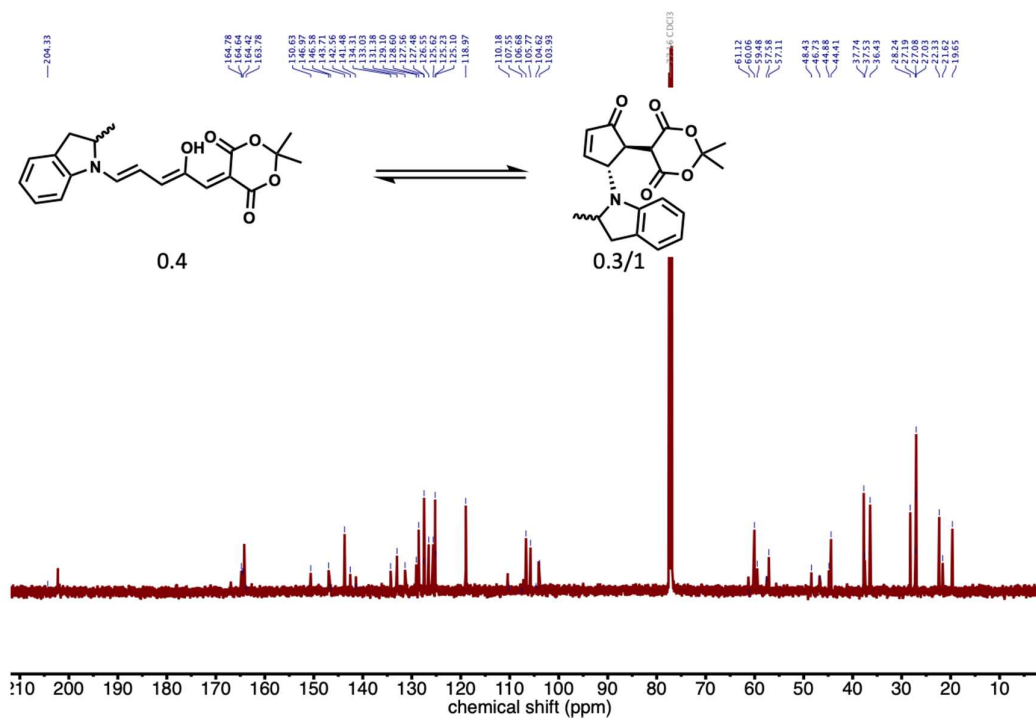


Figure 3.34. ¹³C-NMR (125 MHz, chloroform-*d*) of DASA 2-IM. Assignment can be found in Figure 3.8.31 and S32 and above.

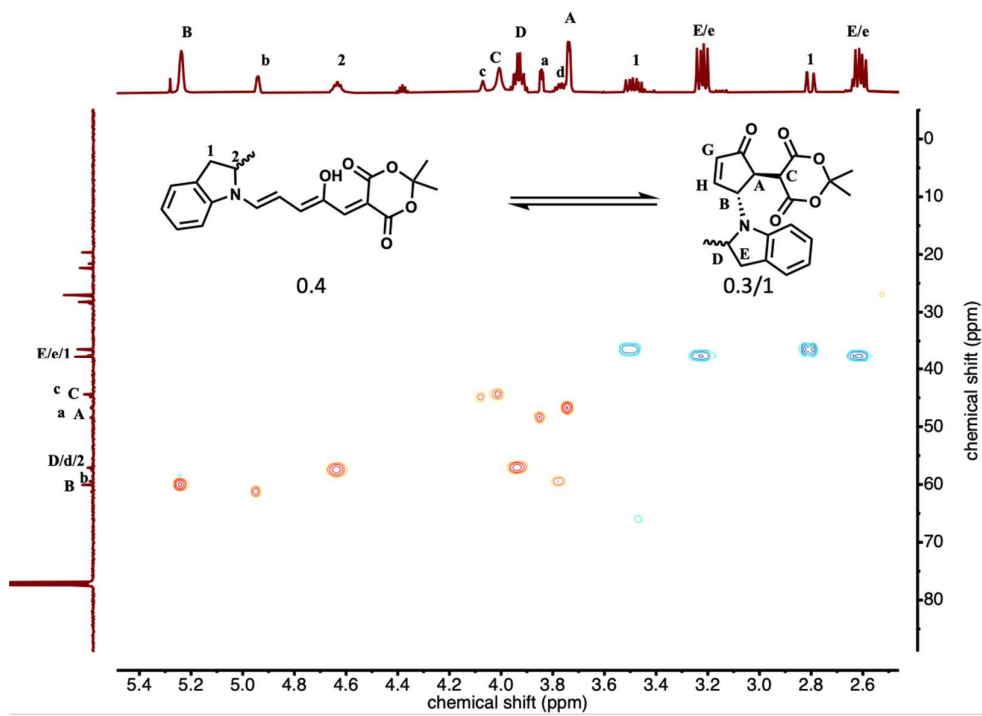


Figure 3.35. HSQC-NMR (600 MHz, chloroform-*d*) of **DASA 2-IM**. The different isomers are marked. For the keto isomer integrating with 0.3 lower case letters were used. Importantly all signals are bound to a carbon.

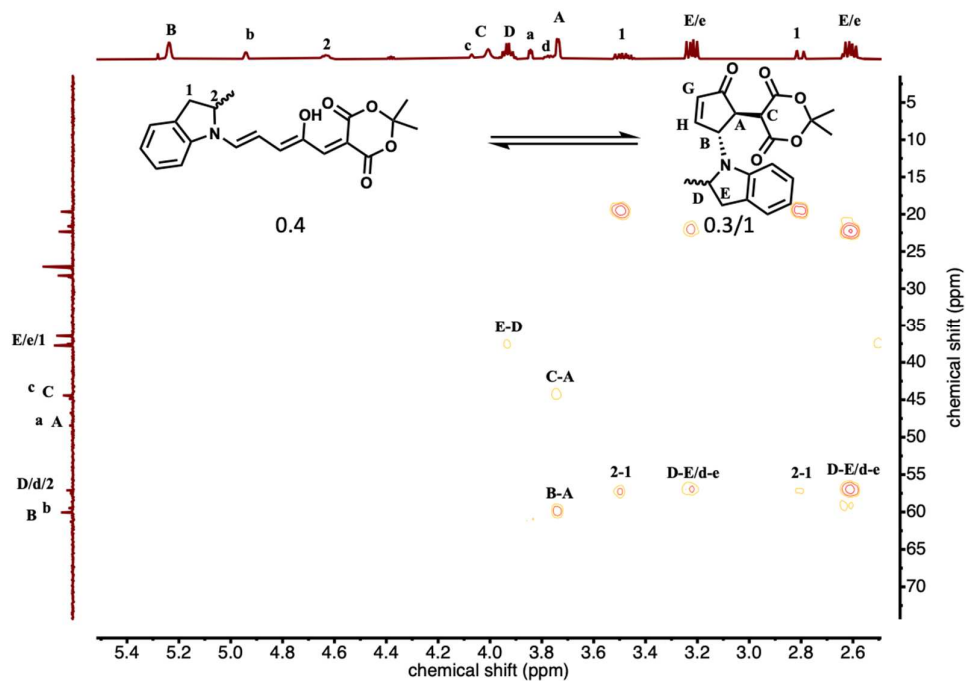
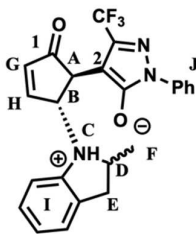


Figure 3.36. HMBC-NMR (600 MHz, chloroform-*d*) of **DASA 2-IM**. The different isomers are marked. For the keto isomer integrating with 0.3 lower case letters were used. Importantly all signals are Signal A interacts with both the carbons of C and B.

DASA 3-IP:



A mixture of two closed isomers observable in a 1:1 ratio. presumably diastereomers at the C2 of the indoline.

DASA 3-IP: ^1H NMR (600 MHz, DMSO- d_6) δ /ppm: 11.55 (s, 2H, NH), 8.08 (dd, $J_{\text{H-G}} = 5.9, 2.2$ Hz, 1H, H_H), 7.94 (dd, $J = 6.0, 2.1$ Hz, 1H, H_H), 7.71 – 7.66 (m, 2H, H_{J,ortho}), 7.62 – 7.59 (m, 2H, H_{J,ortho}), 7.55 – 7.48 (m, 4H, H_{J,meta}), 7.45 – 7.35 (m, 2H, H_{I,meta}), 7.04 (d, $J_{\text{I,meta-para}} = 7.3$, 1H, H_{I,meta}), 6.99 (d, $J_{\text{I,meta-para}} = 7.3$, 1H, H_{I,meta}), 6.91 (t, $J_{\text{I,para-meta}} = 7.7$ Hz, 1H, H_{I,para}), 6.84 (t, $J_{\text{I, para-meta}} = 7.7$ Hz, 1H, H_{I,para}), 6.61 (t, $J_{\text{I,para-meta}} = 7.4$, 1H, H_{I,para}), 6.58 – 6.48 (m, 3H, 2H_G, H_{I,para}), 6.38 (d, $J_{\text{J,ortho-meta}} = 7.9$ Hz, 1H, H_{J,para}), 6.24 (d, $J_{\text{J,ortho-meta}} = 7.9$ Hz, 1H, H_{J,para}), 4.84 (d, $J = 17.6$ Hz, 2H, H_B), 4.08 – 4.03 (m, 1H, H_A), 3.97 – 3.89 (m, 2H, H_A, H_D), 3.74 – 3.66 (m, 1H, H_D), 3.19 (dd, $J_{\text{E-E,E-D}} = 15.8, 9.1$ Hz, 1H, H_E), 3.07 (dd, $J_{\text{E-E,E-D}} = 15.7, 8.6$ Hz, 1H, H_E), 2.53 (d, $J_{\text{E-D}} = 8.2$ Hz, 1H, H_E)^[a], 2.47 (d, $J_{\text{E-D}} = 9.7$ Hz, 1H, H_E)^[a], 1.23 (d, $J = 6.1$ Hz, 3H, H_F), 1.08 (d, $J = 6.1$ Hz, 3H, H_F). ^{13}C NMR (125 MHz, DMSO- d_6) δ /ppm: 203.5 (C_I), 203.33(C_I), 164.6 (C_H), 164.0 (C_H), 149.7 (C_{I,quart.}), 149.6 (C_{I,quart.}), 137.5 (C_{J,quart.}), 133.5 (C_G), 133.3 (C_G), 129.2 (C_{J,meta.}), 129.2 (C_{J,meta.}), 128.5 (C_{I,quart.}), 127.6 (C_{I,quart.}), 127.6 (C_{I, quart.}), 127.1 (C_{I, para.}), 126.8 (C_{I,para.}), 124.5 (C_{I,meta.}), 124.4 (C_{I,meta.}), 122.7 (C_{J,ortho.}), 122.6 (C_{J,ortho.}), 118.1 (C_{I,meta.}), 117.4 (C_{I,meta.}), 107.0 (C_{J,para.}), 99.2 (C₂), 98.5 (C₂), 63.9 (C_B), 63.3 (C_B), 59.3 (C_D), 57.2 (C_D), 43.9 (C_A), 43.7 (C_A), 36.8 (C_E), 36.7 (C_E), 21.6 (C_f), 19.7 (C_f).

^[a] $J_{\text{E-E}}$ is covered by DMSO- d_6

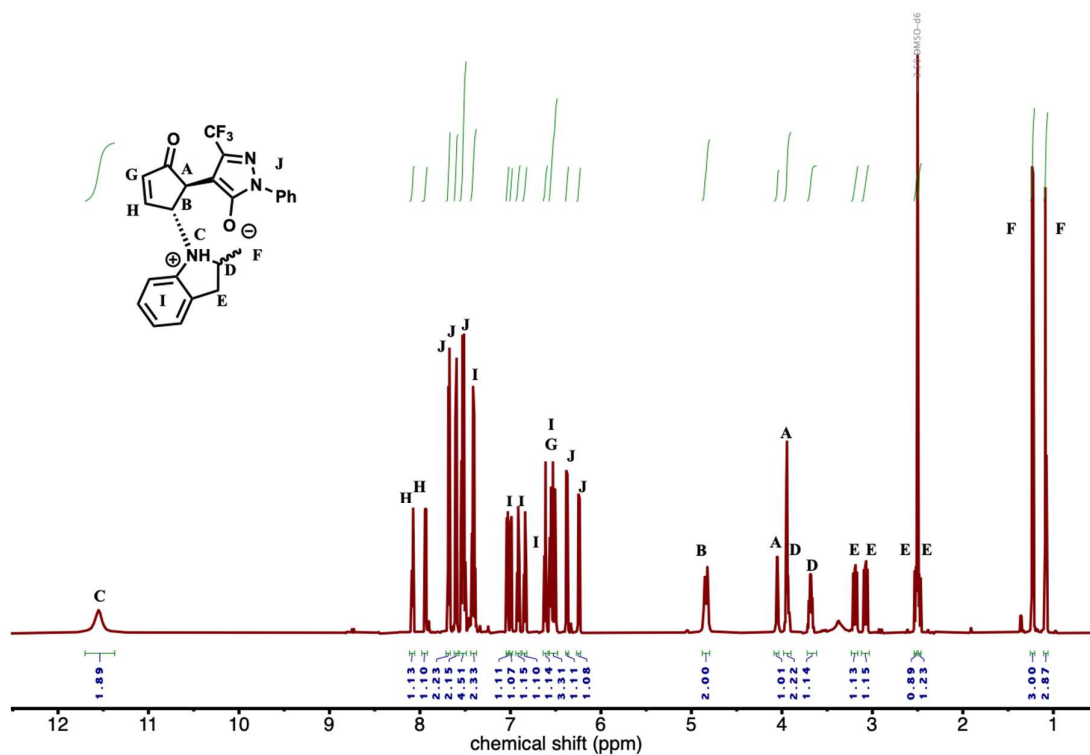


Figure 3.37. ¹H-NMR (600 MHz, DMSO-*d*₆) of **DASA 3-IP**. Two zwitterionic closed isomers can be observed.

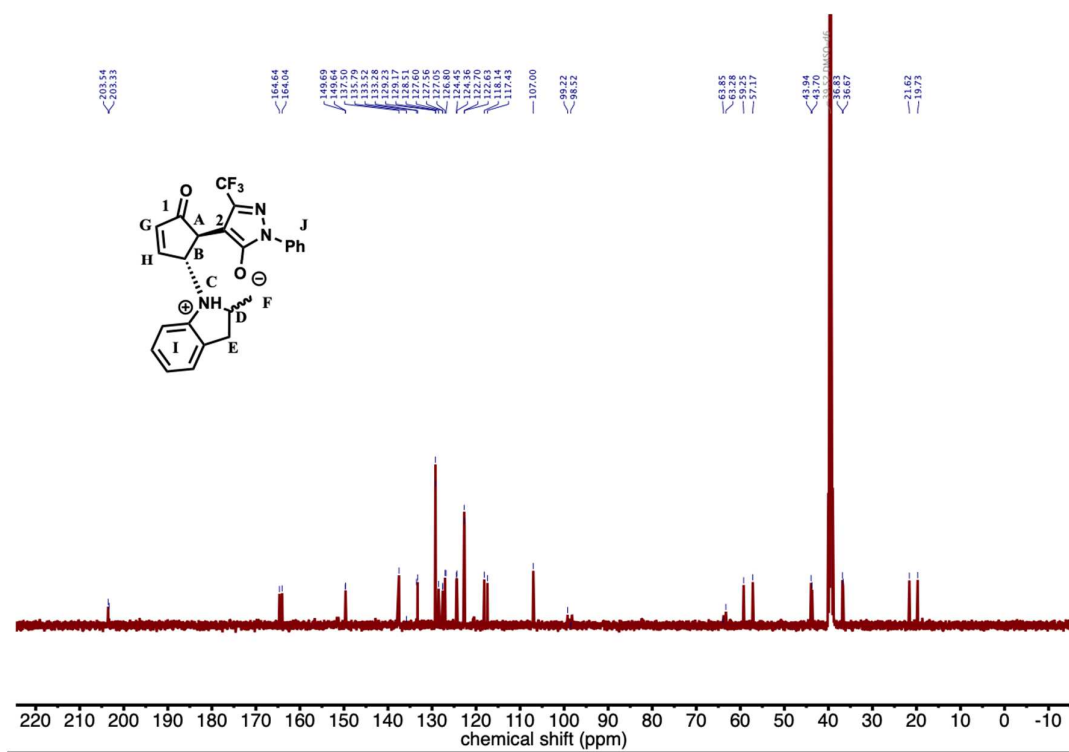


Figure 3.38. ^{13}C -NMR (126 MHz, $\text{DMSO-}d_6$) of **DASA 3-IP**. Two zwitterionic closed isomers can be observed. Assignment can be found in Figure 3.41 and above.

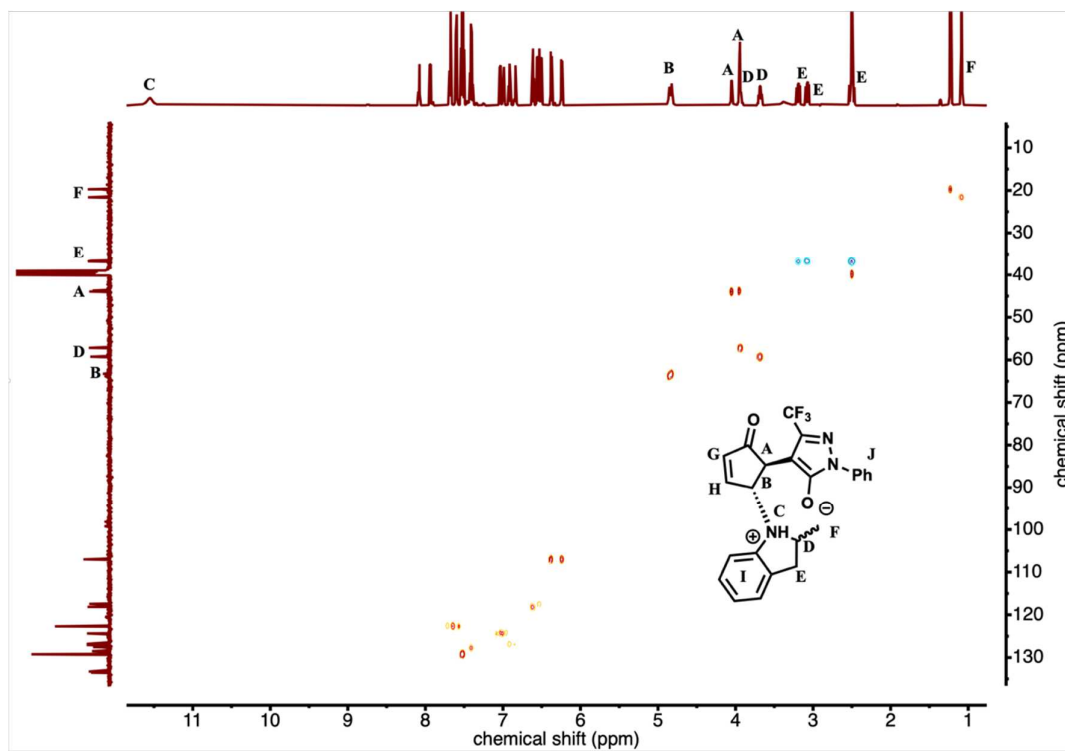


Figure 3.39. HSQC-NMR (600 MHz, DMSO-*d*₆) of **DASA 3-IP**. Two zwitterionic closed isomers can be observed. No C-H interaction for the N-H proton at 11.5 ppm (C) can be observed

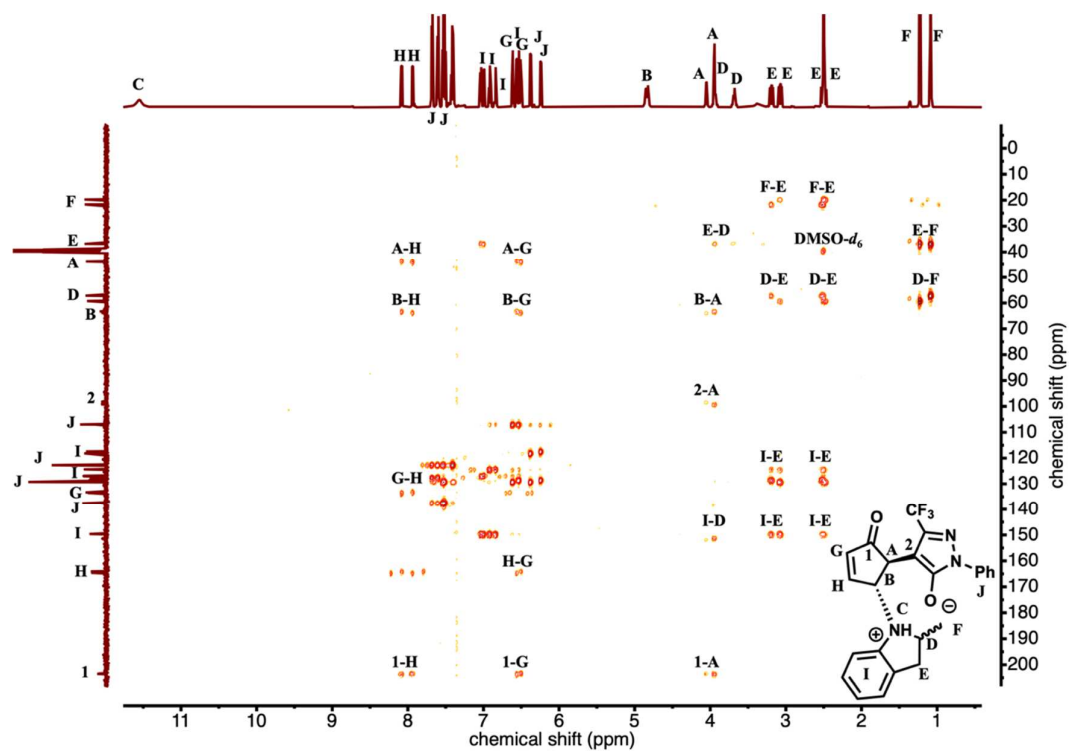


Figure 3.40. HMBC-NMR (600 MHz, DMSO- d_6) of **DASA 3-IP**. Two zwitterionic closed isomers can be observed.

3.8.14 Computational calculations of dipole

Computational detail:

Optimizations and frequencies of **DASA 1-MM**, **DASA 2-IM**, **DASA 3-IP**, and **DASA 4-II** were conducted with Gaussian16 software using the M06-2X/6-31+G(d,p) level of theory in toluene, chloroform, and acetonitrile using the SMD solvent model to calculate bond lengths and dipole moments for each compound.³³⁻³⁵ Cartesian coordinates of the optimized geometries are listed below.

DASA 1-MM (Toluene)

C	-2.14685400	-1.03692700	-0.36219000
O	-3.49030100	-1.15924800	-0.33236800
C	-4.26352500	-0.10557600	0.24962800
O	-3.85060100	1.15044300	-0.27258500
C	-2.52021400	1.44221800	-0.28009100
C	-1.60021700	0.29933300	-0.22493100
C	-0.24260800	0.61566000	-0.15948100
O	-1.50690100	-2.06484000	-0.56408600
C	-5.68496000	-0.32041300	-0.21514300
O	-2.18983500	2.60434000	-0.37837000
C	0.92472800	-0.16077900	-0.08306200
C	-4.12165200	-0.12892600	1.76419200
C	2.14160700	0.51300500	-0.03265600
C	3.38758500	-0.12981200	0.02513300
C	4.55099800	0.61955000	0.06494800

N	5.79037400	0.13510500	0.10592700
O	0.96535100	-1.51266800	-0.03069500
H	4.48091300	1.70620700	0.06226500
C	6.01739800	-1.30150200	0.11474700
C	6.95633800	1.00257700	0.14140500
H	5.54852900	-1.75876800	0.99252500
H	7.09027500	-1.48995200	0.14690300
H	5.60165700	-1.76090500	-0.78828500
H	6.63932900	2.04582800	0.12137000
H	7.59629800	0.80945700	-0.72540800
H	7.53293800	0.82354900	1.05459500
H	-3.08284200	0.02120900	2.07067800
H	-4.46523800	-1.09256600	2.14745900
H	-4.73240300	0.66751800	2.19545900
H	-5.72095200	-0.29602400	-1.30630400
H	-6.32427900	0.46954800	0.18470700
H	-6.04501500	-1.28949300	0.13707400
H	3.41249500	-1.21352600	0.02661400
H	2.10939200	1.59990300	-0.03612700
H	0.06900600	-1.86907200	-0.25527000
H	-0.05617900	1.68668500	-0.15990700

Electronic Energy: -936.168290 Hartree

DASA 2-IM (Toluene)

C	-4.18129400	-0.97614400	-0.30160900
---	-------------	-------------	-------------

C	-4.43578500	1.52446500	-0.30228300
C	-3.56758500	0.33925600	-0.21265000
C	-2.20167400	0.59285800	-0.16497000
O	-3.59160000	-2.03719200	-0.47479800
C	-1.06503100	-0.23709700	-0.07376900
C	0.17651500	0.38151000	-0.05751800
C	1.39628700	-0.32098100	0.00822200
C	2.59080000	0.36327800	0.01568300
O	-1.09165600	-1.58544900	0.02223500
H	2.58013400	1.45040300	-0.02880700
H	1.36559000	-1.40448600	0.04158100
H	0.19658600	1.46773100	-0.09690200
H	-2.00524200	-1.90628600	-0.18426900
H	-1.96514800	1.65348300	-0.19814400
C	5.03170600	0.51761900	0.06554200
C	4.06993200	-1.64044300	0.19776700
C	6.07586700	-0.34520500	0.41169900
C	5.25528400	1.85201300	-0.25937700
C	5.51486600	-1.70718400	0.74125900
H	3.35041500	-2.06336900	0.90399600
C	7.37898800	0.12714900	0.44335300
C	6.57225200	2.31532300	-0.21731100
H	4.44848100	2.51630300	-0.55077200
H	5.52370500	-1.87025800	1.82438100
C	7.62555700	1.46769100	0.12729700
H	8.19697100	-0.53522600	0.71217000

H	6.77549800	3.35147500	-0.46874900
H	8.64111700	1.84932000	0.14527200
N	3.81155100	-0.18420300	0.09292200
C	3.93404800	-2.29885600	-1.17212500
H	2.94281000	-2.13356900	-1.60174900
H	4.68305000	-1.89175400	-1.85972600
H	4.09543400	-3.37689300	-1.08217000
H	6.07431900	-2.52162600	0.27307800
O	-4.04995600	2.66345500	-0.44446600
O	-5.77635000	1.29498400	-0.27485900
O	-5.52653200	-1.03057200	-0.25599300
C	-6.24457500	0.07905500	0.29448300
C	-7.67812300	-0.08329400	-0.15314200
H	-8.08110400	-1.02129300	0.23470200
H	-8.27529800	0.74971300	0.22376100
H	-7.72215300	-0.09415000	-1.24420100
C	-6.08895000	0.10059100	1.80725200
H	-5.04117400	0.21152200	2.09998000
H	-6.65714400	0.93910400	2.21615700
H	-6.47347800	-0.83215700	2.22618300

Electronic Energy: -1205.254317 Hartree

DASA 3-IP (Toluene)

C	3.05002700	-0.60612400	-0.01108300
C	3.40237400	1.62540100	0.02724800

C	2.34364700	0.66152300	0.00315200
C	0.97058600	0.91046500	-0.00480100
O	2.60795800	-1.77182800	-0.04654700
C	-0.08734900	-0.00689000	-0.03150300
C	-1.38982700	0.49352900	-0.02698600
C	-2.52631800	-0.32539600	-0.04908300
C	-3.78904700	0.23698400	-0.03566700
O	0.06151000	-1.34621500	-0.05901100
H	-3.88721900	1.32027000	0.00282300
H	-2.38639600	-1.40047200	-0.07313300
H	-1.51358300	1.57339300	-0.00183700
H	1.02882200	-1.60833900	-0.06100400
H	0.66699500	1.95450100	0.01315500
C	3.25550500	3.11331600	0.05025900
N	4.58766900	1.09394800	0.03226900
N	4.39257500	-0.26236300	0.01641800
C	5.52501000	-1.11651100	-0.01653800
C	5.40668800	-2.47809400	0.27999900
C	6.77120000	-0.56881000	-0.33924600
C	6.54422300	-3.28243600	0.24305700
H	4.44196900	-2.89772800	0.52933600
C	7.89486200	-1.38834300	-0.36605700
H	6.84954400	0.48829200	-0.56176900
C	7.78992100	-2.74866000	-0.07793600
H	6.44725500	-4.33890000	0.47381900
H	8.85846100	-0.95592100	-0.61743600

H	8.66953700	-3.38398400	-0.10228000
F	4.42932000	3.74539800	0.07155100
F	2.57441900	3.55580800	-1.02781800
F	2.55327800	3.52131200	1.12813800
C	-6.23047400	0.13970000	-0.04294900
C	-5.05136100	-1.91103300	-0.16924900
C	-7.18292700	-0.83014400	-0.36483400
C	-6.58280500	1.44815400	0.27131500
C	-6.49136200	-2.13290700	-0.68310500
H	-4.30562900	-2.26374900	-0.88621900
C	-8.52805200	-0.49277800	-0.38497400
C	-7.93985300	1.77490100	0.24182900
H	-5.84251600	2.19154300	0.54710900
H	-6.50319100	-2.31694500	-1.76268200
C	-8.90479900	0.81950200	-0.08103300
H	-9.27772800	-1.23768900	-0.63578400
H	-8.24495900	2.78753900	0.48553200
H	-9.95401100	1.09581500	-0.09058700
N	-4.94222600	-0.43283200	-0.08172100
C	-4.81998500	-2.53314800	1.20437300
H	-3.84296500	-2.25882200	1.61015700
H	-5.59379400	-2.19803700	1.90313600
H	-4.86837400	-3.62300700	1.12914400
H	-6.95655400	-2.99054300	-0.18973600

Electronic Energy: -1540.309952 Hartree

DASA 4-II (Toluene)

C	4.03700500	-0.83393900	-0.04241000
C	4.38216500	1.51639200	0.00235400
C	3.35352300	0.45643900	-0.02170000
C	2.01026000	0.76523900	-0.01967700
O	3.54771700	-1.96570500	-0.06561500
C	0.87894900	-0.08215500	-0.03842400
C	-0.37663300	0.49529200	-0.02770800
C	-1.58209400	-0.24287000	-0.04096100
C	-2.79316400	0.40530800	-0.02907200
O	0.95496200	-1.43320800	-0.06560900
H	-2.81305600	1.49275600	0.00033200
H	-1.52181600	-1.32580200	-0.05860100
H	-0.42536200	1.58106700	-0.00657500
H	1.89524600	-1.73956700	-0.06837600
H	1.78918000	1.83182200	0.00039100
C	-5.23890800	0.49078500	-0.02918100
C	-4.22190600	-1.64065200	-0.15146000
C	-6.26807100	-0.40439800	-0.33887300
C	-5.49188400	1.82473600	0.27681300
C	-5.67727000	-1.75642100	-0.65864600
H	-3.50792000	-2.05317000	-0.86967000
C	-7.58317700	0.03343900	-0.35175500
C	-6.82133100	2.25301300	0.25382100
H	-4.69715200	2.51437100	0.54086000

H	-5.70738500	-1.93872200	-1.73835100
C	-7.85905500	1.37288600	-0.05405700
H	-8.38870800	-0.65450100	-0.59279400
H	-7.04626900	3.28810300	0.49112500
H	-8.88437500	1.72783900	-0.05816800
N	-4.00314400	-0.17782000	-0.07156700
C	-4.03398300	-2.27770300	1.22248200
H	-3.03806800	-2.07732500	1.62569400
H	-4.77788800	-1.88321000	1.92297100
H	-4.16548100	-3.36119900	1.15050500
H	-6.20270600	-2.57755000	-0.16348600
O	4.20386900	2.72203400	0.02399800
C	5.71376700	0.82541500	-0.00353700
C	6.99267300	1.36017100	0.01312800
C	5.50474100	-0.55525200	-0.02982900
C	8.06898000	0.46734100	0.00288200
H	7.14629600	2.43466400	0.03347900
C	6.56654900	-1.44814000	-0.04011800
C	7.85914800	-0.91605700	-0.02327500
H	9.08475700	0.85034000	0.01548800
H	6.39349200	-2.51959800	-0.06040400
H	8.71513000	-1.58376400	-0.03042000

Electronic Energy: -1167.912682 Hartree

DASA 1-MM (Chloroform)

C	-2.14640000	-1.02602700	-0.36899100
O	-3.49071700	-1.15609000	-0.33405900
C	-4.26614800	-0.10748800	0.25560900
O	-3.85051400	1.15090500	-0.26327100
C	-2.51818200	1.43788200	-0.27543700
C	-1.60180500	0.30214000	-0.22769700
C	-0.23262100	0.61812600	-0.17141100
O	-1.50735100	-2.05837100	-0.58036300
C	-5.68738600	-0.31897900	-0.21001200
O	-2.19293000	2.60619000	-0.37236900
C	0.92098200	-0.15966100	-0.09165700
C	-4.12330300	-0.13675000	1.76921500
C	2.15364400	0.50541400	-0.04378100
C	3.38621300	-0.14020100	0.02172200
C	4.55551600	0.61869500	0.06137200
N	5.78567600	0.13722900	0.10962500
O	0.95778500	-1.51553400	-0.02894600
H	4.47979000	1.70499500	0.05181100
C	6.02181300	-1.30154400	0.12907400
C	6.95413300	1.00688500	0.14422500
H	5.55321400	-1.75180300	1.00957700
H	7.09573200	-1.48029300	0.16487500
H	5.61052000	-1.76606500	-0.77235400
H	6.63771500	2.04979100	0.11678500
H	7.59344900	0.80080200	-0.71913800
H	7.52360800	0.82549000	1.06052800

H	-3.08522500	0.01637700	2.07629300
H	-4.46448400	-1.10362300	2.14657700
H	-4.73908100	0.65464800	2.20287100
H	-5.72422100	-0.29225900	-1.30140600
H	-6.32476000	0.47086900	0.19347800
H	-6.04881900	-1.28783200	0.14173400
H	3.41795800	-1.22379700	0.03061300
H	2.12839800	1.59272200	-0.05446100
H	0.05806100	-1.86630900	-0.25634500
H	-0.04050400	1.68792100	-0.18014400

Electronic Energy: -936.173724 Hartree

DASA 2-IM (Chloroform)

C	-4.18309500	-0.97236900	-0.29125900
C	-4.43047500	1.51579200	-0.32006200
C	-3.56732300	0.33616700	-0.22216400
C	-2.19189400	0.58636600	-0.19062800
O	-3.59859900	-2.04170500	-0.45954700
C	-1.06767600	-0.24472500	-0.08989300
C	0.18667100	0.36358600	-0.08496700
C	1.39526300	-0.34163300	-0.00575700
C	2.59330900	0.35084900	-0.00117400
O	-1.09992600	-1.59532400	0.03062000
H	2.57595100	1.43732000	-0.05798400
H	1.36997100	-1.42477600	0.04305500

H	0.21426900	1.44906400	-0.14337600
H	-2.01738700	-1.91194600	-0.17016000
H	-1.94878000	1.64449200	-0.24427700
C	5.02803100	0.52008200	0.06857700
C	4.07730900	-1.64799700	0.18709600
C	6.07280400	-0.33957200	0.41673000
C	5.24222700	1.85858600	-0.24524500
C	5.52005400	-1.70677100	0.73512200
H	3.35814100	-2.07680500	0.88928300
C	7.37374200	0.14104300	0.45909800
C	6.55592700	2.32981200	-0.19310900
H	4.43046600	2.51954700	-0.53109400
H	5.52580000	-1.87632500	1.81711600
C	7.61264500	1.48493100	0.15211100
H	8.19424000	-0.51773100	0.72918400
H	6.75440900	3.36914600	-0.43542300
H	8.62584600	1.87294600	0.17847100
N	3.80856700	-0.19021100	0.08425000
C	3.94996900	-2.30024300	-1.18596100
H	2.95639800	-2.14524900	-1.61435200
H	4.69552500	-1.88225500	-1.87084400
H	4.12430400	-3.37625500	-1.09749100
H	6.08749800	-2.51343100	0.26342700
O	-4.04673400	2.65672700	-0.48517300
O	-5.77228500	1.29554100	-0.27495600
O	-5.52894600	-1.02822900	-0.23453000

C	-6.24364700	0.08665400	0.31135900
C	-7.67917700	-0.07583900	-0.12814900
H	-8.08183600	-1.00866000	0.27252800
H	-8.27184100	0.76193600	0.24559900
H	-7.72927400	-0.09728000	-1.21908300
C	-6.07962100	0.12400200	1.82197100
H	-5.02986600	0.23149800	2.10853900
H	-6.64291300	0.96989700	2.22264900
H	-6.46923600	-0.80206300	2.25099300

Electronic Energy: -1205.2590098 Hartree

DASA 3-IP (Chloroform)

C	3.04894100	-0.58835700	-0.00366400
C	3.40474000	1.63427400	0.03848400
C	2.34867500	0.67383100	0.01259500
C	0.96449000	0.92217000	0.00390400
O	2.60923200	-1.76159100	-0.04649300
C	-0.07867600	0.00325800	-0.03113000
C	-1.39590600	0.49140100	-0.02407700
C	-2.51661800	-0.33273100	-0.05437900
C	-3.78737600	0.23364300	-0.03529400
O	0.07543900	-1.33875800	-0.06986700
H	-3.88236800	1.31696400	0.01416000
H	-2.37833800	-1.40775500	-0.08755700
H	-1.52963800	1.57020700	0.01051600

H	1.04890600	-1.59419400	-0.06848500
H	0.65571500	1.96438300	0.02838900
C	3.25964300	3.12134200	0.06537000
N	4.59525700	1.10349900	0.04299600
N	4.39191400	-0.25002200	0.02747900
C	5.51337500	-1.11702400	-0.01536100
C	5.40892700	-2.43861600	0.42855900
C	6.73105000	-0.62373100	-0.49401800
C	6.53194700	-3.26276600	0.37977100
H	4.46462600	-2.81209400	0.80214100
C	7.84372800	-1.45923000	-0.52778000
H	6.79746500	0.40405100	-0.83128400
C	7.75089200	-2.78228500	-0.09544700
H	6.44780300	-4.28874000	0.72510700
H	8.78699500	-1.07112500	-0.89993300
H	8.62066800	-3.43096800	-0.12696500
F	4.43602900	3.75290900	0.09248600
F	2.58489800	3.57244200	-1.01354000
F	2.55648900	3.53131700	1.14230300
C	-6.22380500	0.13750700	-0.04458700
C	-5.04354100	-1.91604100	-0.18305200
C	-7.17213200	-0.83067400	-0.37869200
C	-6.57394300	1.44325600	0.28237400
C	-6.48125500	-2.13121300	-0.70356100
H	-4.29586600	-2.26450100	-0.89910500
C	-8.51827900	-0.49290000	-0.39955400

C	-7.93072000	1.77024700	0.25243400
H	-5.83227500	2.18216100	0.56676800
H	-6.48868600	-2.30734000	-1.78432700
C	-8.89445400	0.81647800	-0.08363600
H	-9.26728800	-1.23543500	-0.65922600
H	-8.23723700	2.78019300	0.50566500
H	-9.94383000	1.09307900	-0.09346400
N	-4.93138100	-0.43514100	-0.08502400
C	-4.81875000	-2.54317300	1.18870100
H	-3.84002800	-2.27672100	1.59598900
H	-5.59263500	-2.20703600	1.88696400
H	-4.87430500	-3.63197900	1.10561400
H	-6.95004900	-2.99070200	-0.21725400

Electronic Energy: -1540.316502 Hartree

DASA 4-II (Chloroform)

C	4.03493900	-0.82840100	-0.04241900
C	4.37895200	1.51357300	0.00747300
C	3.35383800	0.45746800	-0.01723300
C	2.00326300	0.76490900	-0.01209000
O	3.54446000	-1.96327900	-0.06756500
C	0.88144700	-0.08295200	-0.03214100
C	-0.38394400	0.48639700	-0.01925800
C	-1.57973000	-0.25530300	-0.03547700
C	-2.79457300	0.39860700	-0.02287800

O	0.96045500	-1.43792800	-0.06381800
H	-2.81017000	1.48610600	0.01061500
H	-1.52404800	-1.33850100	-0.05582100
H	-0.43898300	1.57215400	0.00576300
H	1.90443500	-1.73858100	-0.06797600
H	1.77730000	1.83039100	0.01166700
C	-5.23593900	0.49212200	-0.02980600
C	-4.22472400	-1.64588500	-0.14651300
C	-6.26423900	-0.40111500	-0.34430400
C	-5.48344600	1.82710200	0.27558400
C	-5.67767100	-1.75532400	-0.65985600
H	-3.50953100	-2.06197300	-0.86068800
C	-7.57881200	0.04108300	-0.36261900
C	-6.81148900	2.25962000	0.24742000
H	-4.68597600	2.51331300	0.54095900
H	-5.70321800	-1.93827200	-1.73944300
C	-7.85066200	1.38145800	-0.06543200
H	-8.38554200	-0.64432800	-0.60693000
H	-7.03454300	3.29539100	0.48391900
H	-8.87504100	1.73972600	-0.07365700
N	-3.99903100	-0.18121700	-0.06709400
C	-4.04603900	-2.27907000	1.22980800
H	-3.04852600	-2.08757400	1.63372800
H	-4.78865000	-1.87622900	1.92701600
H	-4.18827100	-3.36110400	1.15790300
H	-6.20916200	-2.57303000	-0.16579600

O	4.20154400	2.72271800	0.03242700
C	5.71272600	0.82674900	-0.00398400
C	6.99098800	1.36187800	0.01043100
C	5.50376500	-0.55421700	-0.03310500
C	8.06836700	0.46835400	-0.00504600
H	7.14751200	2.43611800	0.03302200
C	6.56472800	-1.44711200	-0.04842800
C	7.85857600	-0.91451800	-0.03396300
H	9.08405800	0.85179700	0.00569200
H	6.39351600	-2.51910200	-0.07064500
H	8.71444700	-1.58242000	-0.04499900

Electronic Energy: -1167.916810 Hartree

DASA 1-MM (Acetonitrile)

C	-2.14381500	-1.01211200	-0.38158300
O	-3.48980200	-1.15033300	-0.35736700
C	-4.26848800	-0.11349700	0.24918600
O	-3.85380400	1.15249000	-0.25482700
C	-2.51936000	1.43808200	-0.26064500
C	-1.60486000	0.30824900	-0.22368400
C	-0.22285600	0.62576200	-0.17285400
O	-1.50184200	-2.04602900	-0.60420700
C	-5.69043700	-0.32131800	-0.21552000
O	-2.19883900	2.61171200	-0.34591200
C	0.91607200	-0.15423300	-0.08015400

C	-4.12637100	-0.16264100	1.76218400
C	2.16797900	0.50142400	-0.04485700
C	3.38508200	-0.14863500	0.02724600
C	4.56396400	0.61844400	0.05485700
N	5.78304900	0.13593100	0.10307100
O	0.94492600	-1.51038300	0.00932500
H	4.48496500	1.70429400	0.03468400
C	6.02508500	-1.30509400	0.13268900
C	6.95583100	1.00466500	0.12986600
H	5.56791900	-1.74432600	1.02369700
H	7.10002700	-1.47616700	0.15671300
H	5.60301500	-1.77419200	-0.76023300
H	6.64127300	2.04763100	0.10153800
H	7.58667000	0.78581400	-0.73570100
H	7.52458600	0.81508200	1.04409400
H	-3.08953200	-0.01109700	2.07352600
H	-4.46793600	-1.13480200	2.12553800
H	-4.74711300	0.61997200	2.20478900
H	-5.73329900	-0.27903100	-1.30640900
H	-6.32839100	0.45972300	0.20402400
H	-6.04882200	-1.29532500	0.12505400
H	3.42161100	-1.23196300	0.05260300
H	2.15213500	1.58885700	-0.07223800
H	0.04448500	-1.85423100	-0.23291700
H	-0.02500900	1.69400200	-0.19675700

Electronic Energy: -936.181787 Hartree

DASA 2-IM (Acetonitrile)

C	-4.18117000	-0.96323300	-0.30128500
C	-4.43013100	1.51444800	-0.31596500
C	-3.56887200	0.33951100	-0.22607400
C	-2.18293200	0.58939000	-0.20398600
O	-3.59647900	-2.03528700	-0.48107200
C	-1.07113400	-0.24242600	-0.09415000
C	0.19770900	0.35661800	-0.09909400
C	1.39321500	-0.35221700	-0.00998800
C	2.59716900	0.34772400	-0.01316300
O	-1.10947100	-1.59265900	0.04891400
H	2.57413100	1.43337500	-0.08367100
H	1.37198000	-1.43465400	0.05510100
H	0.23416100	1.44117400	-0.17303900
H	-2.02865600	-1.90282600	-0.15984900
H	-1.93477000	1.64536500	-0.27126500
C	5.02678600	0.52093400	0.06545400
C	4.07724500	-1.65117100	0.18662500
C	6.06775800	-0.33809200	0.42321300
C	5.23894300	1.85912300	-0.25118700
C	5.51696500	-1.70526900	0.74011600
H	3.35569600	-2.07838500	0.88617100
C	7.36896500	0.14420000	0.47263000
C	6.55182100	2.33162300	-0.19243800

H	4.42643300	2.51677900	-0.54242700
H	5.51814400	-1.87375300	1.82204400
C	7.60728900	1.48741800	0.16280100
H	8.18811500	-0.51323000	0.74985500
H	6.75115800	3.37044100	-0.43648200
H	8.62004500	1.87676300	0.19460900
N	3.80453100	-0.19138100	0.07646600
C	3.95709100	-2.30281800	-1.18668000
H	2.96216800	-2.15518100	-1.61491300
H	4.70163900	-1.87943300	-1.86940000
H	4.14034500	-3.37685200	-1.09464000
H	6.08870600	-2.50997800	0.27072300
O	-4.05050500	2.65990000	-0.47854400
O	-5.77362400	1.29558600	-0.26954000
O	-5.52832000	-1.02580100	-0.24259100
C	-6.24143300	0.08408900	0.31709700
C	-7.68091200	-0.07720800	-0.10911500
H	-8.07871400	-1.01174700	0.29250100
H	-8.27035500	0.75672700	0.27816500
H	-7.74478500	-0.09291100	-1.19965800
C	-6.06715800	0.11503900	1.82658500
H	-5.01682100	0.22848200	2.10802800
H	-6.63586300	0.95424700	2.23388500
H	-6.45054800	-0.81475000	2.25329700

Electronic Energy: -1205.265092 Hartree

DASA 3-IP (Acetonitrile)

C	3.05328900	-0.57835500	-0.01719400
C	3.40050900	1.63609700	0.05795000
C	2.35303500	0.67493100	0.01619100
C	0.95328400	0.91757000	0.00314300
O	2.62101100	-1.75969200	-0.08579200
C	-0.07026400	-0.00715300	-0.02425000
C	-1.40701600	0.46720900	-0.02558600
C	-2.51035200	-0.36068900	-0.04387200
C	-3.78987900	0.21686700	-0.04128600
O	0.09119800	-1.34969200	-0.04212000
H	-3.87406500	1.30185500	-0.01739900
H	-2.37769900	-1.43694300	-0.05649900
H	-1.55070100	1.54546900	-0.00650400
H	1.06998300	-1.59482600	-0.06499500
H	0.63478800	1.95672000	0.01925500
C	3.25072100	3.12141100	0.10628200
N	4.60041700	1.11258500	0.05797700
N	4.39667300	-0.23864000	0.02218100
C	5.51413400	-1.10860100	-0.03590600
C	5.42724300	-2.40804700	0.47276300
C	6.70932700	-0.64304800	-0.59272800
C	6.54437100	-3.23986600	0.41070700
H	4.49989300	-2.75763600	0.90839300
C	7.81894100	-1.48353000	-0.63713800

H	6.76238200	0.36657800	-0.98439200
C	7.74205200	-2.78540500	-0.14062100
H	6.47483700	-4.24863700	0.80643800
H	8.74534500	-1.11745300	-1.06922200
H	8.60826800	-3.43841000	-0.18115500
F	4.42727100	3.75415900	0.18928300
F	2.62010700	3.59761900	-0.98830200
F	2.51045000	3.51431700	1.16413800
C	-6.21992900	0.13685400	-0.06959900
C	-5.05029500	-1.93255500	-0.11823900
C	-7.16854400	-0.84032600	-0.36967900
C	-6.56053000	1.45913500	0.19570000
C	-6.48674400	-2.15769300	-0.63407400
H	-4.30244000	-2.31260500	-0.81657000
C	-8.51365900	-0.49562200	-0.41507300
C	-7.91470300	1.79220800	0.14156300
H	-5.81418400	2.20550800	0.44640300
H	-6.49101100	-2.37996300	-1.70603500
C	-8.88215100	0.82841700	-0.15894200
H	-9.26511600	-1.24458500	-0.64748100
H	-8.21710100	2.81438800	0.34593900
H	-9.92977300	1.11102900	-0.18869600
N	-4.92644500	-0.44581900	-0.07587500
C	-4.83540200	-2.50124500	1.27952800
H	-3.85130100	-2.23381200	1.67315400
H	-5.60438200	-2.12299300	1.96143700

H	-4.91047400	-3.59112800	1.23943300
H	-6.96450800	-2.99061100	-0.11210900

Electronic Energy: -1540.321469 Hartree

DASA 4-II (Acetonitrile)

C	4.03308000	-0.82352600	-0.04752100
C	4.37361700	1.51123700	0.01965400
C	3.35433700	0.45629800	-0.01016700
C	1.99322000	0.76028600	0.00124700
O	3.54416700	-1.96282800	-0.07971400
C	0.88395300	-0.08924300	-0.02493700
C	-0.39417500	0.47273300	-0.00613000
C	-1.57764400	-0.27176200	-0.02981800
C	-2.79753700	0.39070300	-0.01426200
O	0.96612200	-1.44542200	-0.07022300
H	-2.80610300	1.47803800	0.02739300
H	-1.52722600	-1.35499700	-0.05962500
H	-0.45663000	1.55811200	0.02955500
H	1.91426100	-1.73814300	-0.07693400
H	1.76029200	1.82373600	0.03556800
C	-5.23335400	0.49438600	-0.03367800
C	-4.22867800	-1.65187800	-0.13322000
C	-6.26099900	-0.39916400	-0.34519400
C	-5.47427000	1.83358000	0.25827000

C	-5.68045400	-1.75782600	-0.64743800
H	-3.51395800	-2.07456700	-0.84286500
C	-7.57512500	0.04751000	-0.37139000
C	-6.80071100	2.27012000	0.22294000
H	-4.67279200	2.51870600	0.51447800
H	-5.70487700	-1.94981500	-1.72524000
C	-7.84211900	1.39113000	-0.08548200
H	-8.38312300	-0.63736400	-0.61283100
H	-7.02121900	3.30881800	0.44890500
H	-8.86541000	1.75291400	-0.09972100
N	-3.99509600	-0.18466500	-0.06067800
C	-4.05534200	-2.27280500	1.24871700
H	-3.05472100	-2.08849000	1.64857400
H	-4.79421800	-1.85643400	1.94196000
H	-4.21010700	-3.35331500	1.18325600
H	-6.21698800	-2.56776000	-0.14651200
O	4.19695700	2.72248900	0.05479300
C	5.71179800	0.82906100	-0.00132400
C	6.98887300	1.36556300	0.01313600
C	5.50418800	-0.55218100	-0.04074500
C	8.06910700	0.47322000	-0.01285400
H	7.14735400	2.43953000	0.04368600
C	6.56595800	-1.44306200	-0.06662700
C	7.86093700	-0.90884000	-0.05205600
H	9.08412700	0.85850300	-0.00232700
H	6.39993000	-2.51580200	-0.09702300

H 8.71716100 -1.57616400 -0.07113400

Electronic Energy: -1167.920412 Hartree

Table 3.10: Calculated bond lengths (\AA) of **DASA 1-MM**, **DASA 2-IM**, **DASA 3-IP**, and **DASA 4-II** in chloroform

	N-Ci	Ci-Ch	Ch-Cg	Cg-Cf	Cf-Ce	Ce-Cd	BLA
DASA 1-MM	1.322	1.395	1.393	1.401	1.394	1.406	-0.007
DASA 2-IM	1.333	1.384	1.402	1.394	1.402	1.398	0.009
DASA 3-IP	1.326	1.391	1.391	1.405	1.391	1.406	-0.010
DASA 4-II	1.338	1.380	1.407	1.388	1.406	1.385	0.022

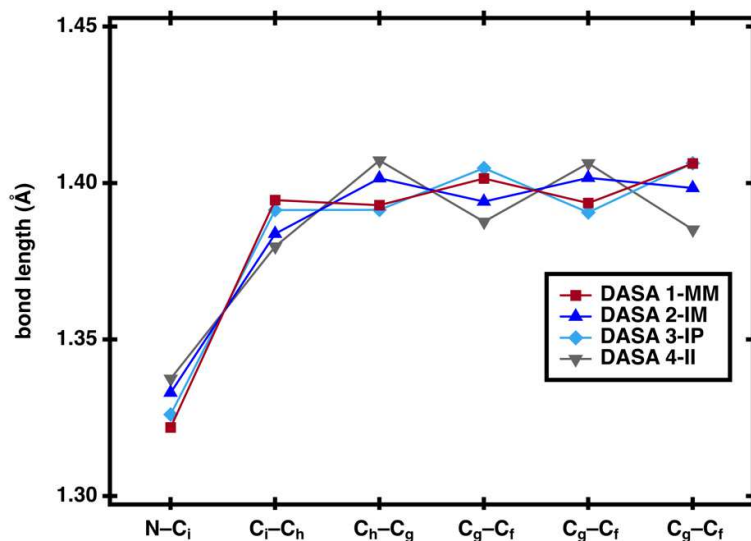


Figure 3.41. Bond lengths of optimized structures **DASA 1-MM**, **DASA 2-IM**, **DASA 3-IP**, and **DASA 4-II** in chloroform

Table 3.11: Calculated bond lengths (Å) for **DASA 1-MM**, **DASA 2-IM**, **DASA 3-IP**, and **DASA 4-II** in toluene, chloroform, and acetonitrile.

		N-C _i	C _i -C _h	C _h -C _g	C _g -C _f	C _f -C _e	C _e -C _d	BLA
DASA 1-MM	Tol	1.331	1.384	1.403	1.392	1.404	1.396	0.013
	CHCl ₃	1.322	1.395	1.393	1.402	1.394	1.406	-0.007
	ACN	1.312	1.407	1.382	1.414	1.384	1.419	-0.030
DASA 2-IM	Tol	1.340	1.377	1.409	1.387	1.410	1.390	0.025
	CHCl ₃	1.333	1.384	1.402	1.394	1.402	1.398	0.010
	ACN	1.325	1.393	1.393	1.403	1.393	1.409	-0.009
DASA 3-IP	Tol	1.334	1.382	1.401	1.395	1.401	1.396	0.010
	CHCl ₃	1.326	1.391	1.391	1.405	1.391	1.406	-0.010
	ACN	1.316	1.404	1.380	1.418	1.380	1.421	-0.035
DASA 4-II	Tol	1.344	1.374	1.414	1.382	1.414	1.378	0.036
	CHCl ₃	1.337	1.380	1.407	1.388	1.406	1.385	0.023
	ACN	1.329	1.388	1.398	1.396	1.398	1.395	0.005

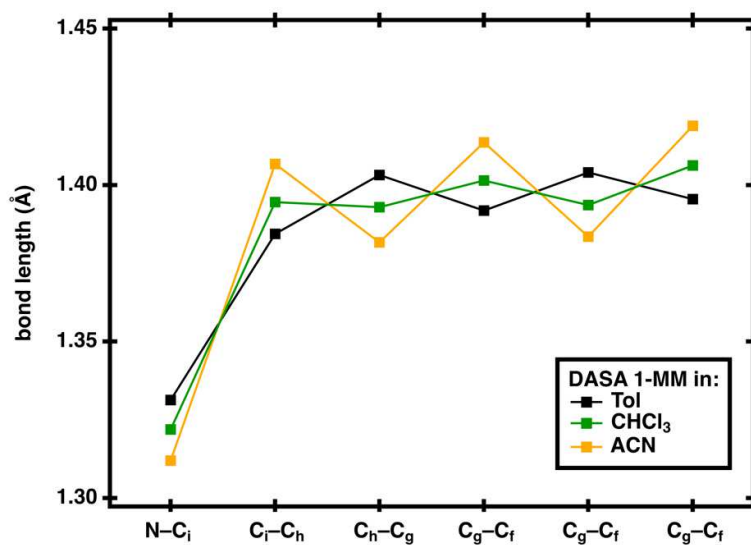


Figure 3.42. Bond lengths of the optimized structure of **DASA 1-MM** in toluene, chloroform, and acetonitrile

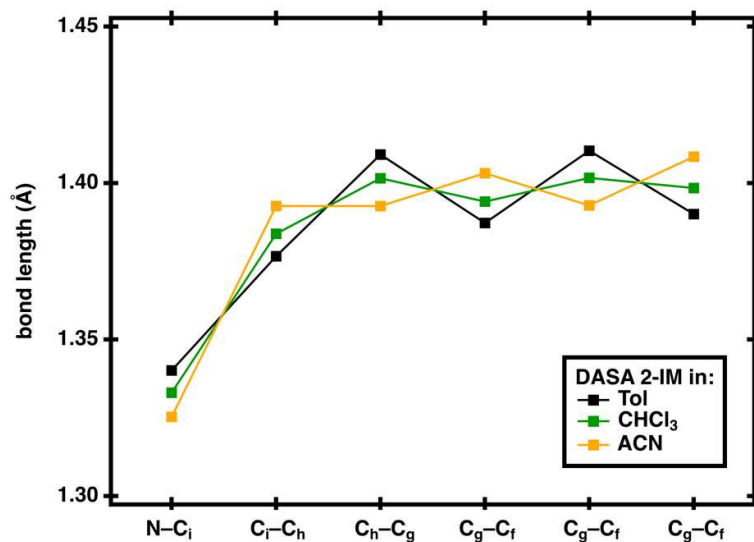


Figure 3.43. Bond lengths of the optimized structure of **DASA 2-IM** in toluene, chloroform, and acetonitrile

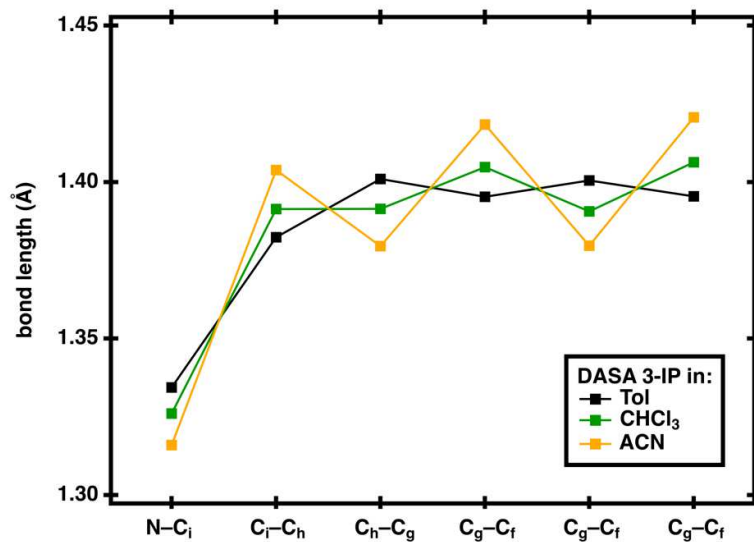


Figure 3.44. Bond lengths of the optimized structure of **DASA 3-IP** in toluene, chloroform, and acetonitrile

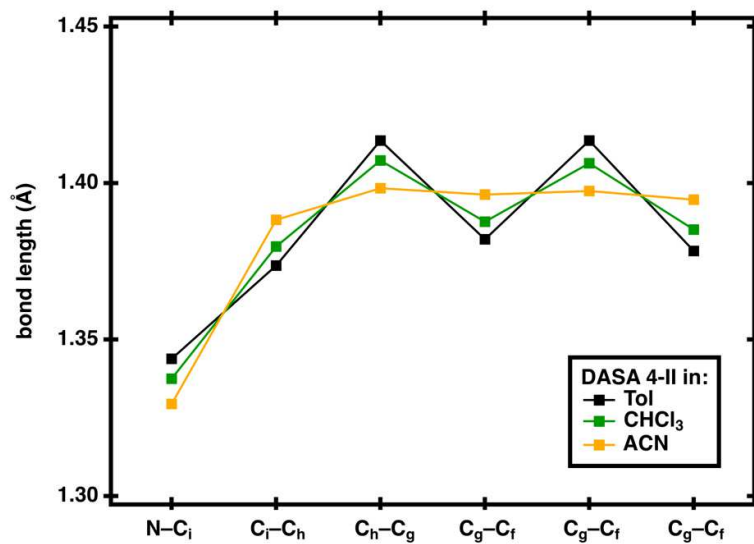


Figure 3.45. Bond lengths of the optimized structure of **DASA 4-II** in toluene, chloroform, and acetonitrile

Table 3.12: Calculated dipole of **DASA 1-MM**, **DASA 2-IM**, **DASA 3-IP**, and **DASA 4-II** in toluene, chloroform and acetonitrile.

Dipole (D)				
Solvent	DASA 1-MM	DASA 2-IM	DASA 3-IP	DASA 4-II
Tol	11.63	9.40	14.01	6.79
CHCl ₃	14.69	12.00	17.40	9.00
ACN	18.12	14.90	21.90	12.08

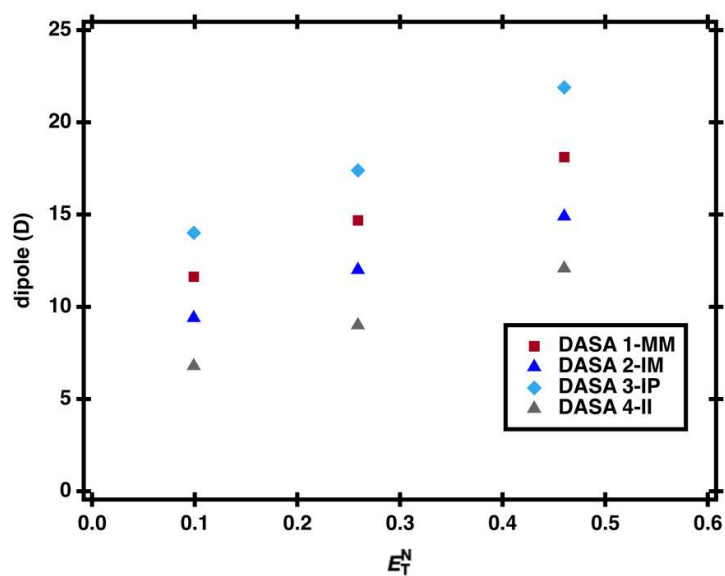


Figure 3.46. Comparison of solvent polarity vs dipole moment of **DASA 1-MM**, **DASA 2-IM**, **DASA 3-IP**, and **DASA 4-II**.

Table 3.13: Calculated hydrogen bond length between the –OH and the carbonyl of the acceptor of **DASA 1-MM**, **DASA 2-IM**, **DASA 3-IP**, and **DASA 4-II** in toluene, chloroform and acetonitrile.

	H-bond length (Å)			
	DASA 1-MM	DASA 2-IM	DASA 3-IP	DASA 4-II
Tol	1.618	1.618	1.588	1.668
CHCl ₃	1.610	1.613	1.569	1.655
ACN	1.602	1.606	1.560	1.645

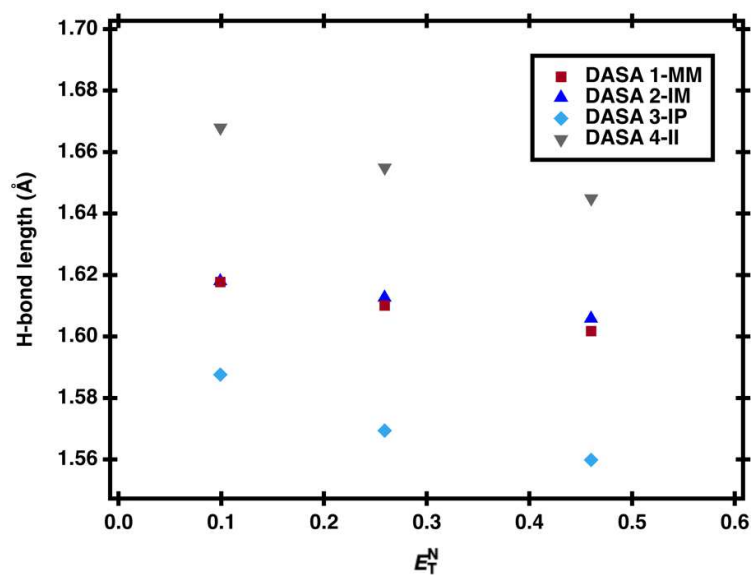


Figure 3.47. Comparison of solvent polarity vs the hydrogen bond length between the –OH and the carbonyl of the acceptor of **DASA 1-MM**, **DASA 2-IM**, **DASA 3-IP**, and **DASA 4-II**. The hydrogen bond in **DASA 3-IP** is strengthened in more polar solvents compared to **DASA 2-IM**.

Table 3.14: HOMO-LUMO energy levels of **DASA 1-MM**, **DASA 2-IM**, **DASA 3-IP**, and **DASA 4-II** in toluene, chloroform and acetonitrile.

	HOMO-LUMO gap (eV)			
	DASA 1-MM	DASA 2-IM	DASA 3-IP	DASA 4-II
Tol	4.450	4.223	3.932	3.998
CHCl ₃	4.477	4.221	3.967	3.984
ACN	4.562	4.247	4.083	3.987

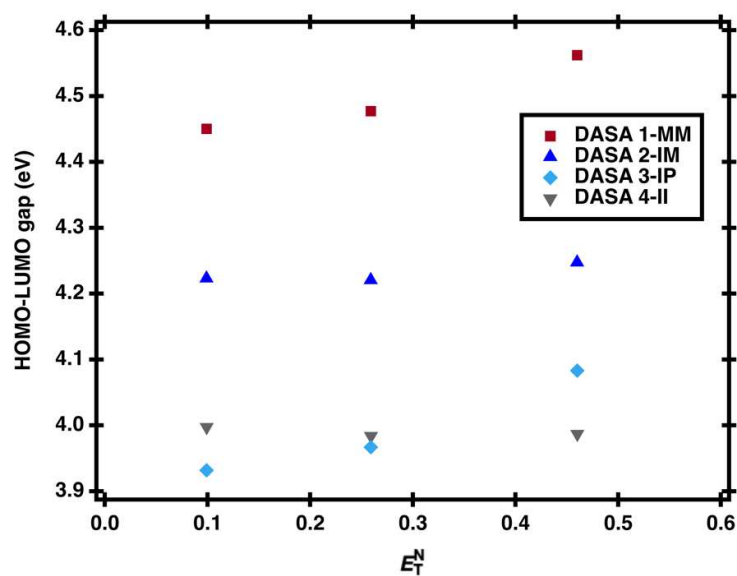


Figure 3.48. Comparison of solvent polarity vs HOMO-LUMO energy levels of **DASA 1-MM**, **DASA 2-IM**, **DASA 3-IP**, and **DASA 4-II**. The HOMO-LUMO gaps of **DASA 2-IM** and **DASA 4-II** are relatively unchanged as a function of solvent polarity, while the gap of **DASA 1-MM** and **DASA 3-IP** increases with increasing solvent polarity, in agreement with the observed blue shift in Figure 3B.

3.8.15 Photoswitching experiments monitored by UV–Vis with ionic liquid

Table 3.8.15: Results of kinetic fit analysis of DASA compounds with addition of ionic liquid.

Cmpds	IL addition (mM)	k_B (min ⁻¹) ¹⁾	k_F (min ⁻¹) ¹⁾	PTSS (% closed u. irradi.)	rate vs 0 mM (k_B/k_F)	light source (nm)
DASA 1-MM	0 mM	0.23	0.02	76 ^[a]	-	530
	1 mM	0.21	0.01	n.d. ^[b]	- ^[c]	
	10 mM	0.21	0.02	n.d. ^[b]	- ^[c]	
DASA 1-MB	0 mM	1.54	0.28	32	-	530
	1 mM	1.55	0.26	23	- ^[c]	
	10 mM	1.44	0.27	7	- ^[c]	
DASA 2-IM	0 mM	0.005 8	0.005 3	100	-	595
	1 mM	0.006 9	0.006 7	100	1.2/1.3	
	10 mM	0.008 0	0.007 8	100	1.4/1.5	
DASA 2-IB	0 mM	0.015	0.020	100	-	595
	1 mM	0.018	0.025	100	1.2/1.3	
	10 mM	0.022	0.031	100	1.5/1.6	
DASA 3-IP	0 mM	7.9	0.09	89	-	617
	1 mM	10.8	0.12	78	1.4/1.3	
	10 mM	17.8	0.13	55	2.3/1.4	

^[a] determined in separate experiment. See Figure 3.56 ^[b] not determined due to slow photoconversion. ^[c] changes are minimal, no rate increase was determined.

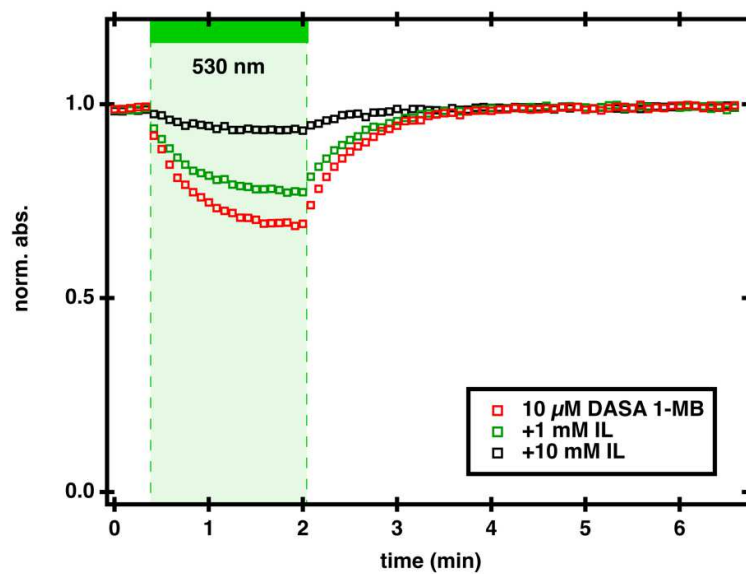


Figure 3.49. Time dependent UV–Vis spectroscopy of 10 μM DASA 1-MB in chloroform with various additions of IL followed at λ_{max} 565 nm. The samples were irradiated with 530 nm LED for 100 s and left to recover in the dark. These results differ from previous reported results from Beves and co-workers in the forward reaction and PTSS.⁷ This is due to different light sources being used.

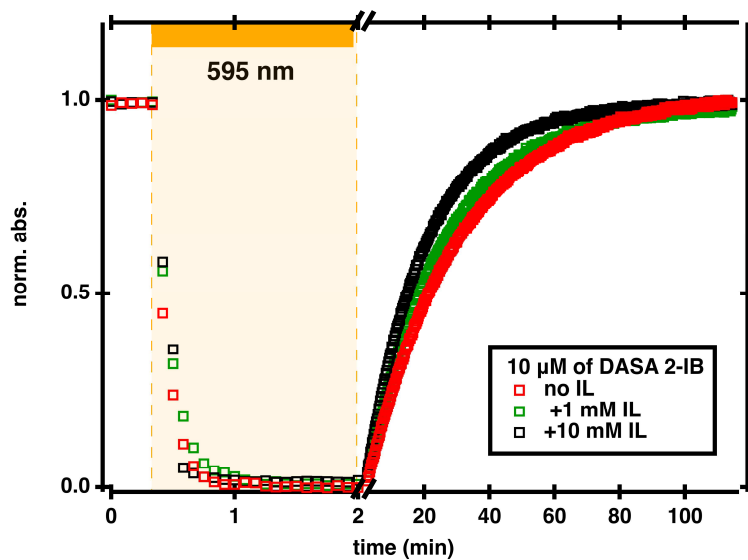


Figure 3.50. Time dependent UV–Vis spectroscopy of 10 μM DASA 2-IB in chloroform with various additions of IL followed at λ_{max} 616 nm. The samples were irradiated with 595 nm LED for 100 s and left to recover in the dark.

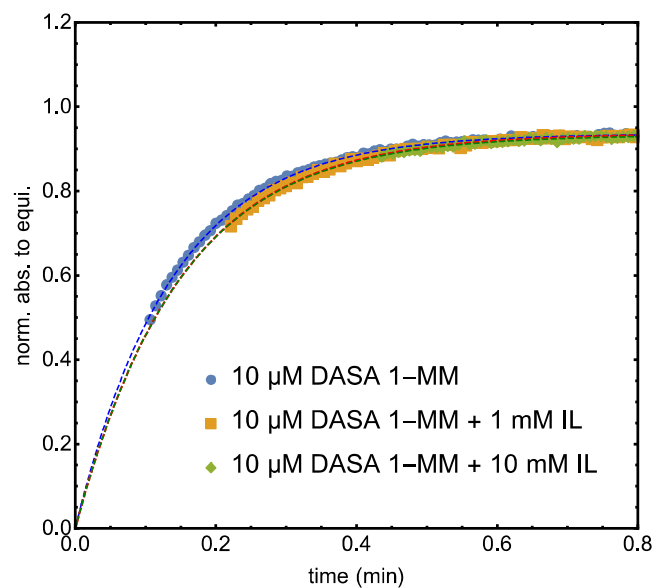


Figure 3.51. Time dependent UV–Vis spectroscopy of 10 μM DASA 1-MM with various addition of IL followed at λ_{max} 541 nm including the fit used to determine equilibration rates. For rates see Table 3.15.

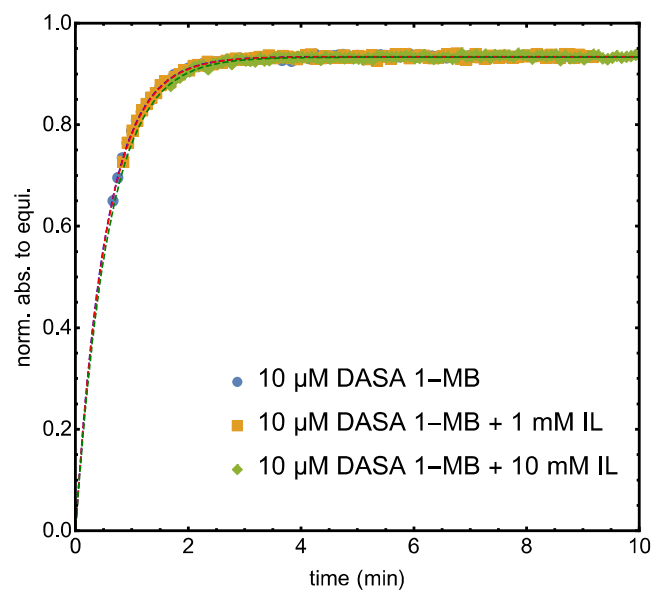


Figure 3.52. time dependent UV-Vis spectroscopy of 10 μM **DASA 1-MB** with various addition of **IL** followed at λ_{max} 565 nm including the fit used to determine equilibration rates. For rates see Table 3.15.

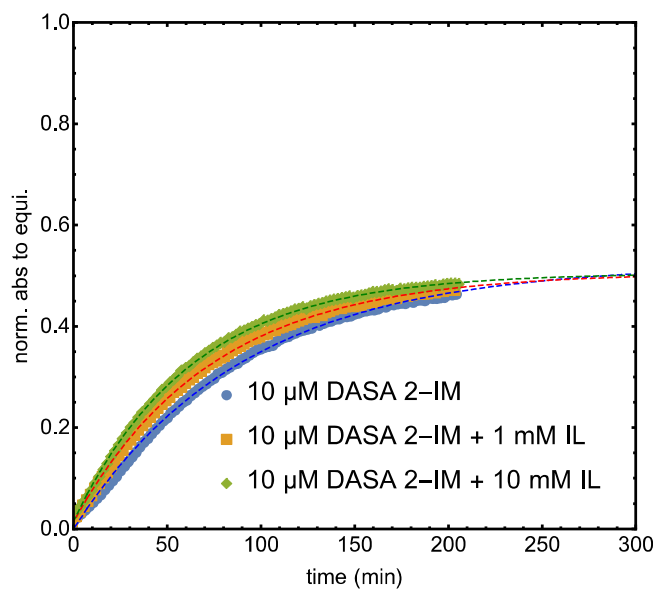


Figure 3.53. time dependent UV-Vis spectroscopy of 10 μM **DASA 2-IM** with various addition of **IL** followed at λ_{\max} 590 nm including the fit used to determine equilibration rates.

For rates see Table 3.15

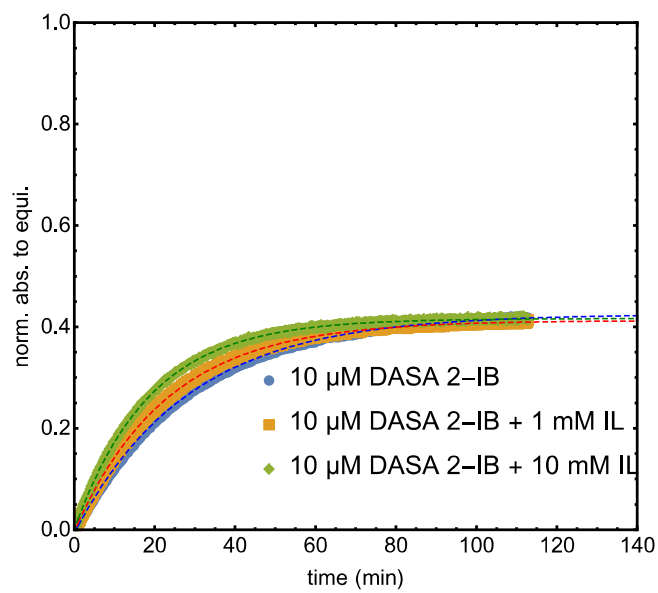


Figure 3.54. time dependent UV-Vis spectroscopy of 10 μM **DASA 2-IB** with various addition of **IL** followed at λ_{max} 616 nm including the fit used to determine equilibration rates.

For rates see Table 3.15.

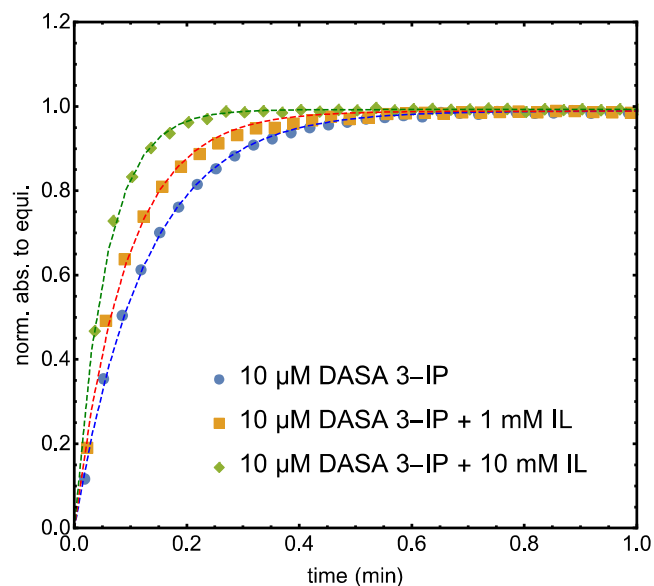


Figure 3.55. time dependent UV-Vis spectroscopy of 10 μM **DASA 3-IP** with various addition of **IL** followed at λ_{max} 650 nm including the fit used to determine equilibration rates.

For rates see Table 3.15.

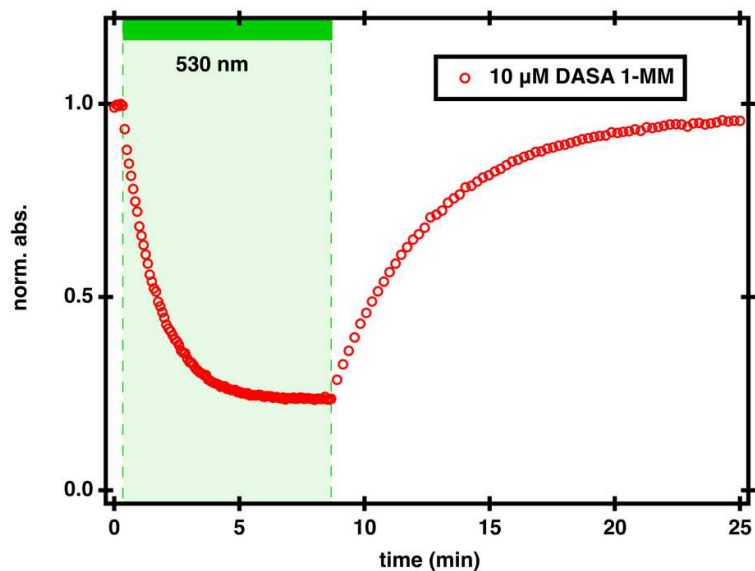


Figure 3.56. Time dependent UV-Vis spectroscopy of 10 μM **DASA 1-MM** irradiated for 500 s with a 530 nm LED followed at λ_{max} 541 nm.

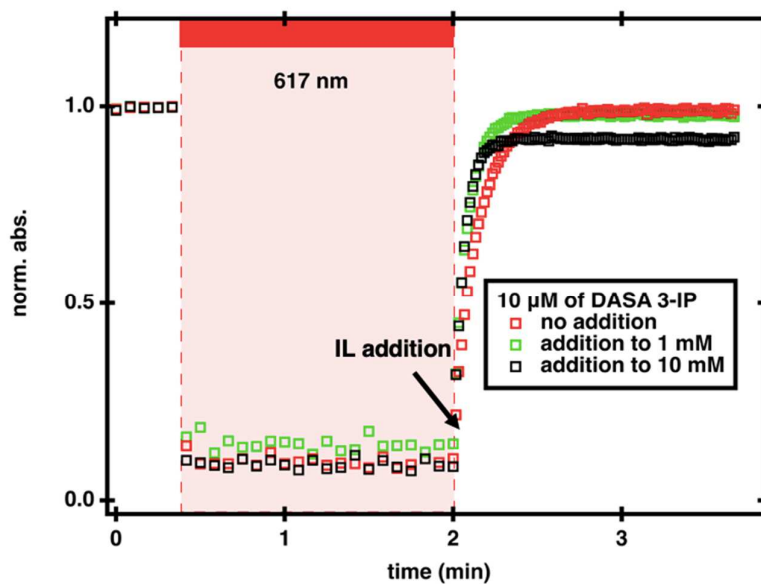


Figure 3.57. Time dependent UV-Vis spectroscopy of 10 μM **DASA 3-IP** irradiated for 100 s with a 617 nm LED followed at λ_{max} 650 nm. Addition of IL (1 mM: 20 μL of 100 mM solution of **IL**; 10 mM: 200 μL of 100 mM solution of **IL**) before recovery leads to increase in recovery rate. The loss in absorbance upon recovery at 10 mM **IL** is due to the increase in volume of the solution. The calculated rates can be found in Figure 3.58.

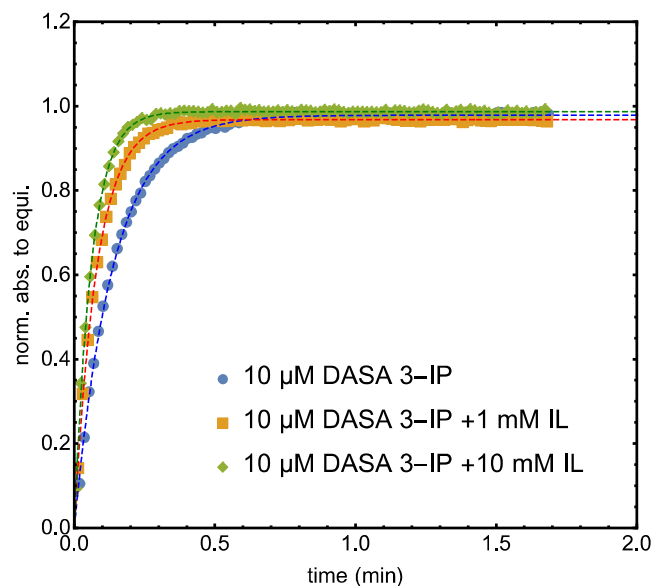


Figure 3.58. Time dependent UV-Vis spectroscopy of 10 μM **DASA 3-IP** irradiated for 100 s with a 617 nm LED followed at λ_{max} 650 nm. Addition of **IL** (1 mM: 20 μL of 100 mM solution of **IL**; 10 mM: 200 μL of 100 mM solution of **IL**) before recovery leads to increase in recovery rate (full graph in Figure 3.57). The recovery of the 10 mM solution of **IL** has been adjusted for loss of absorbance due to increased volume. The calculated k_B (min^{-1}) values are: 0 **IL**: 7.1, 1 mM **IL**: 12.3, 10 mM **IL**: 16.4. These values are roughly in line with previously calculated values but due to change in volume are not as accurate.

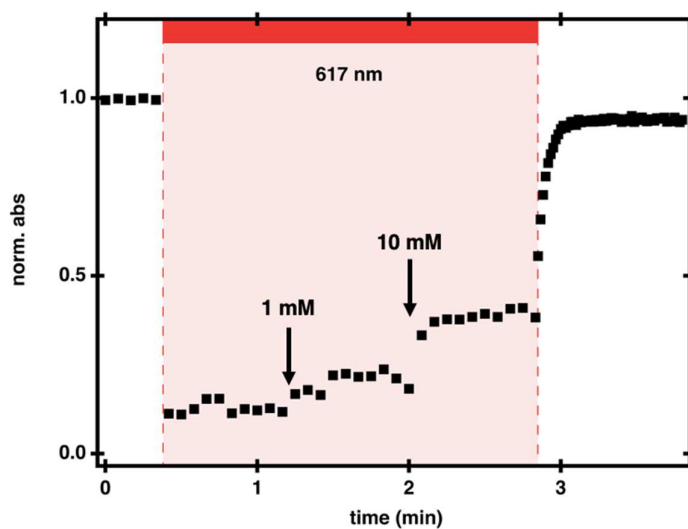


Figure 3.59. Time dependent UV–Vis spectroscopy of 2 mL of a 10 μ M **DASA 3-IP** irradiated for 100 s with a 617 nm LED followed irradiation at λ_{max} 650 nm. Addition of **IL** leads to stepwise increase in PTSS from 89 % to 79 % (addition of 20 μ L of 100 mM solution of **IL**) to 64 % (addition of further 200 μ L of 100 mM solution of **IL**). The loss in absorbance upon recovery is due to the increase in volume of the solution.

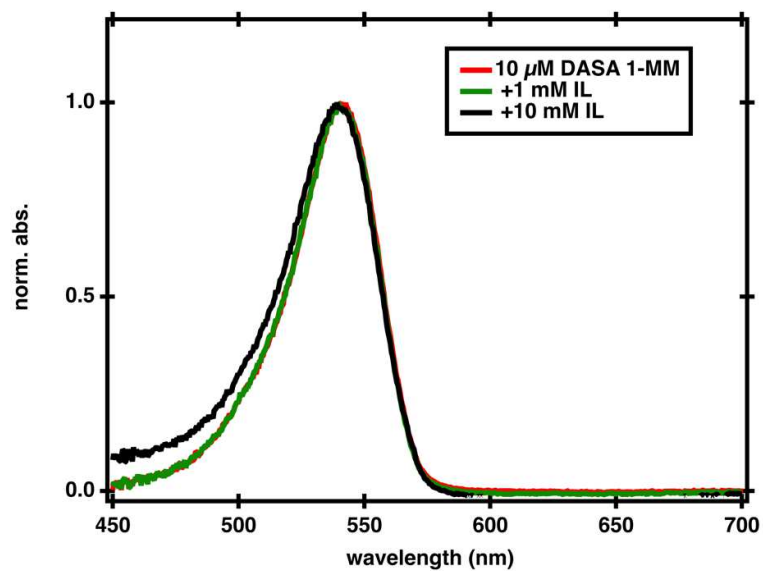


Figure 3.60. UV–Vis spectrum of 10 μM DASA 1-MM in chloroform with various addition of **IL**.

Table 3.16: λ_{max} (nm) values of DASA I-MM in chloroform with a various addition of **IL**.

addition of IL	0 mM	1 mM	10 mM
λ_{max} (nm)	541	540	539

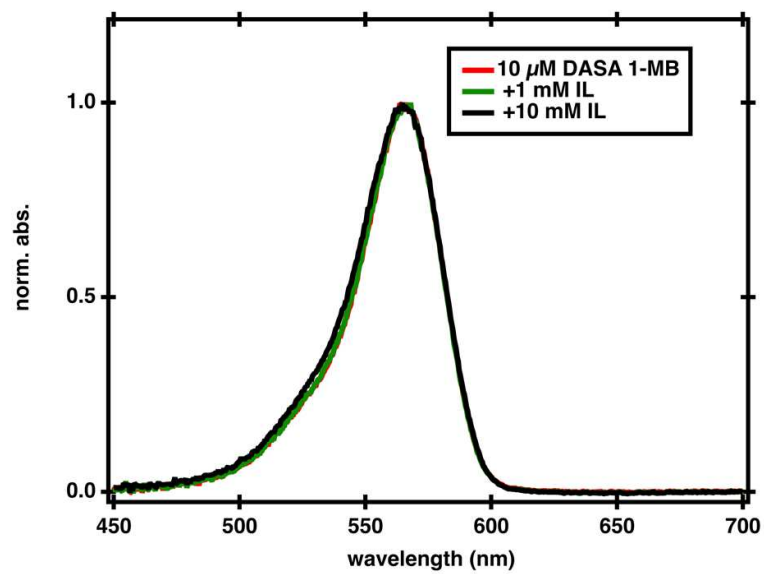


Figure 3.61. UV–Vis spectrum of 10 μM DASA 1-MB in chloroform with various addition of IL.

Table 3.17: λ_{\max} (nm) values of **DASA 1-MB** in chloroform with a various addition of **IL**.

addition of IL	0 mM	1 mM	10 mM
λ_{\max} (nm)	565	565	565

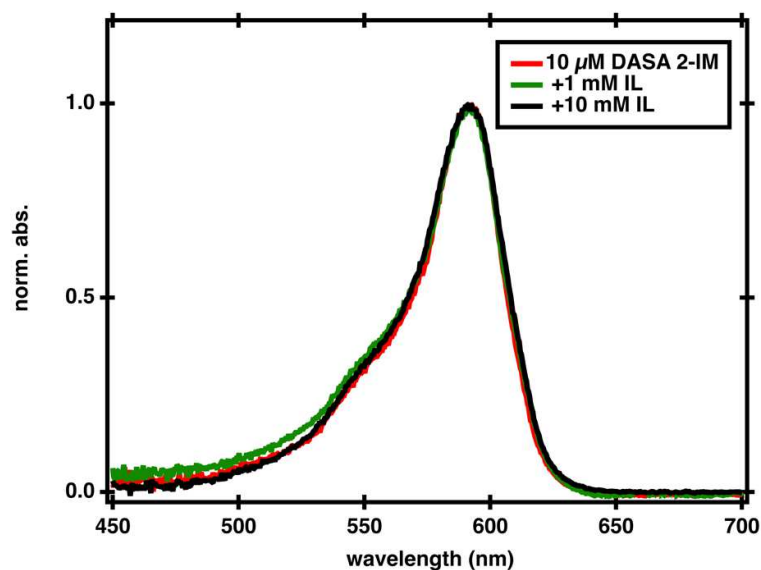


Figure 3.62. UV–Vis spectrum of 10 μ M **DASA 2-IM** in chloroform with various addition of **IL**.

Table 3.18: λ_{\max} (nm) values of **DASA 2-IM** in chloroform with a various addition of **IL**.

addition of IL	0 mM	1 mM	10 mM
λ_{\max} (nm)	590	589	590

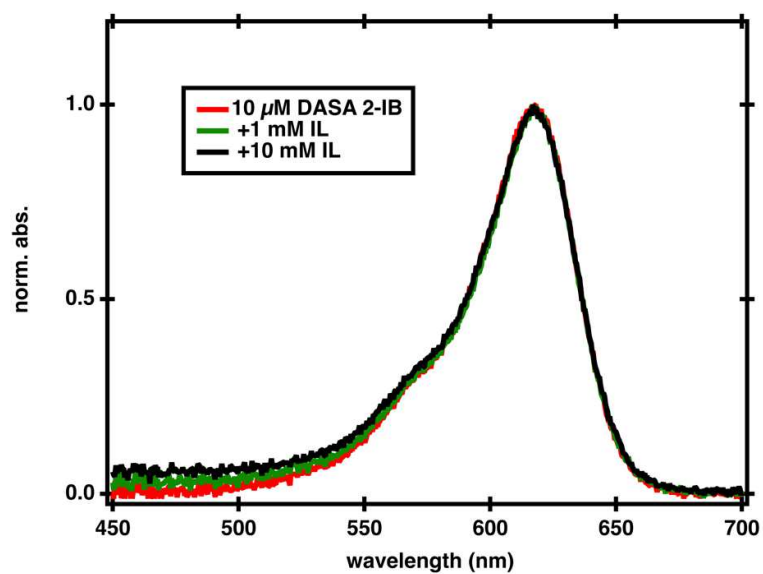


Figure 3.63. UV–Vis spectrum of 10 μM **DASA 2-IB** in chloroform with various addition of **IL**.

Table 3.19: λ_{max} (nm) values of **DASA 2-IB** in chloroform with a various addition of **IL**.

addition	0	1	10
of IL	mM	mM	mM
λ_{max} (nm)	616	616	615

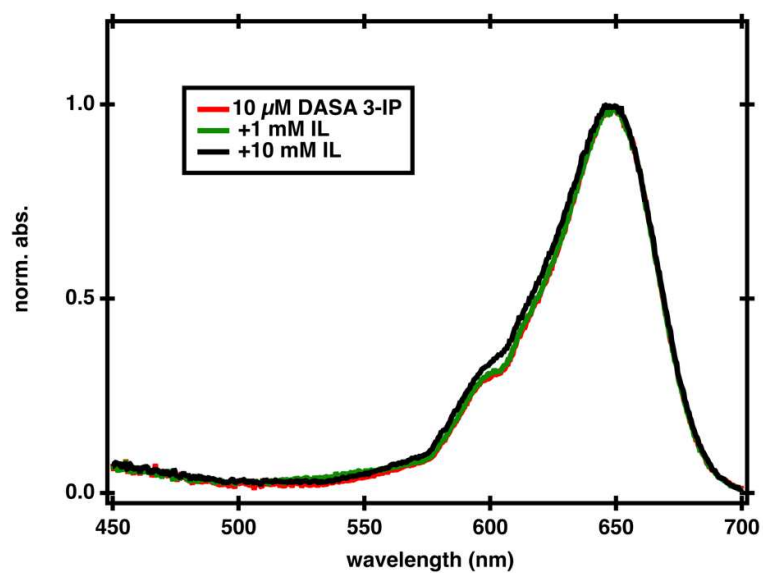


Figure 3.64. UV–Vis spectrum of 10 μM DASA 3-IP in chloroform with various addition of IL.

Table 3.20. λ_{max} (nm) values of DASA 3-IP in chloroform with a various addition of IL.

addition	0	1	10
of IL	mM	mM	mM
λ_{max} (nm)	650	6 49	64 6

3.8.16 Concentration dependency of photoswitching measured by UV–Vis

Table 3.21: Results of kinetic fit analysis of DASA compounds at increasing concentration.

Compounds	[DASA] (mM)	k_B (min ⁻¹)	$k_F^{[a]}$ (min ⁻¹)	PTSS (% closed under irrad.)	rate + vs 125 μ M (k_B/k_F)	light source
DASA 2-IM	0.125	0.0058	0.0061	100	-	617 nm
	0.25	0.0060	0.0060	100	1/1	
	0.5	0.0068	0.0078	100	1.2/1.3 ^[a]	
	10	0.0075	0.0087	100	1.3/1.4 ^[a]	
DASA 3-IP	0.125	10.1	0.33	91	-	617 nm
	0.25	12.1	0.56	87	1.2/1.7 ^[a]	
	0.5	13.5	0.76	83	1.4/2.3 ^[a]	
	10	16.0	1.56	64	1.6/4.8 ^[a]	

^[a] increase in k_F could be due to increase photodegradation at higher concentration decreasing the recovery achieved and artificially increasing the forward reaction rate in the model.

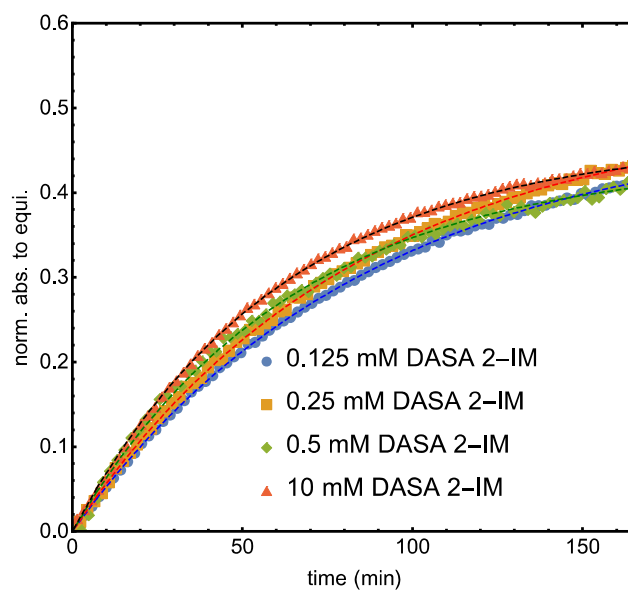


Figure 3.65. Time dependent UV-Vis spectroscopy of **DASA 2-IM** at various concentration in chloroform followed at λ_{max} 590 nm including the fit used to determine equilibration rates. For rates see Table 3.21.

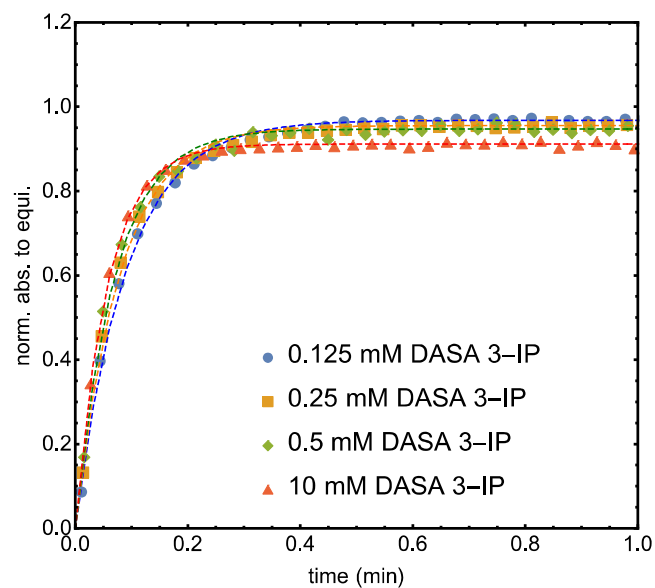


Figure 3.66. Time dependent UV–Vis spectroscopy of **DASA 3-IP** at various concentration in chloroform followed at λ_{max} 650 nm including the fit used to determine equilibration rates. For rates see Table 3.21.

3.9 References

- (1) Sroda*, M. M., Stricker*, F., Peterson, J. A., Bernal, A., Read de Alaniz, J., *Chem. Eur. J.* **2021**, *27*, 4183–4190. <https://doi.org/10.1002/chem.202005110>.
- (2) Helmy, S., Oh, S., Leibfarth, F. A., Hawker, C. J., Read de Alaniz, J. Design and Synthesis of Donor-Acceptor Stenhouse Adducts: A Visible Light Photoswitch Derived from Furfural. *J. Org. Chem.* **2014**, *79* (23), 11316–11329. <https://doi.org/10.1021/jo502206g>.
- (3) Helmy, S., Leibfarth, F. A., Oh, S., Poelma, J. E., Hawker, C. J., Read de Alaniz, J. Photoswitching Using Visible Light: A New Class of Organic Photochromic Molecules. *J. Am. Chem. Soc.* **2014**, *136* (23), 8169–8172. <https://doi.org/10.1021/ja503016b>.
- (4) Hemmer, J. R., Poelma, S. O., Treat, N., Page, Z. A., Dolinski, N. D., Diaz, Y. J., Tomlinson, W., Clark, K. D., Hooper, J. P., Hawker, C., Read de Alaniz, J., Tunable Visible and Near Infrared Photoswitches. *J. Am. Chem. Soc.* **2016**, *138* (42), 13960–13966. <https://doi.org/10.1021/jacs.6b07434>.
- (5) Hemmer, J. R., Page, Z. A., Clark, K. D., Stricker, F., Dolinski, N. D., Hawker, C. J., Read de Alaniz, J. Controlling Dark Equilibria and Enhancing Donor-Acceptor Stenhouse Adduct Photoswitching Properties through Carbon Acid Design. *J. Am. Chem. Soc.* **2018**, *140* (33), 10425–10429. <https://doi.org/10.1021/jacs.8b06067>.
- (6) Stranius, K., Börjesson, K. Determining the Photoisomerization Quantum Yield of Photoswitchable Molecules in Solution and in the Solid State. *Sci. Rep.* **2017**, *7* (January), 41145. <https://doi.org/10.1038/srep41145>.
- (7) Burnett, G. L., Soh, H. T., Hawker, J., Read de Alaniz, J. Controlled Drug Release to Cancer Cells from Modular One-Photon Visible Light-Responsive Micellar System. *ChemComm* **2016**, *52*, 10525–10528. <https://doi.org/10.1039/c6cc04127b>.
- (8) Yap, J. E., Zhang, L., Lovegrove, J. T., Beves, J. E., Stenzel, M. H. Visible Light-

Responsive Drug Delivery Nanoparticle via Donor–Acceptor Stenhouse Adducts (DASA). *Macromol. Rapid Commun.* **2020**, *21*, 2000236.

<https://doi.org/10.1002/marc.202000236>.

- (9) Lerch, M. M., Hansen, M. J., Velema, W. A., Szymanski, W., Feringa, B. L. Orthogonal Photoswitching in Multifunctional Molecular System. *Nat. Commun.* **2016**, *7*, 12054. <https://doi.org/10.1038/ncomms12054>.
- (10) Diaz, Y. J., Page, Z. A., Knight, A. S., Treat, N. J., Hemmer, J. R., Hawker, C. J., Read de Alaniz, J. A Versatile and Highly Selective Colorimetric Sensor for the Detection of Amines. *Chem. - A Eur. J.* **2017**, *23* (15), 3562–3566. <https://doi.org/10.1002/chem.201700368>.
- (11) Balamurugan, A., Lee, H. II. A Visible Light Responsive On-Off Polymeric Photoswitch for the Colorimetric Detection of Nerve Agent Mimics in Solution and in the Vapor Phase. *Macromolecules* **2016**, *49* (7), 2568–2574. <https://doi.org/10.1021/acs.macromol.6b00309>.
- (12) Ulrich, S., Moura, S. O., Diaz, Y., Clerc, M., Géraldine, A., Read de Alaniz, J., Martins, A., Neves, N. M., Rottmar, M., Rossi, R. M., Fortunato, G., Boesel, L. F., Chemical Electrospun Colourimetric Sensors for Detecting Volatile Amines. *Sensors Actuators B. Chem.* **2020**, *322*, 128570. <https://doi.org/10.1016/j.snb.2020.128570>.
- (13) Chen, Q., Diaz, Y. J., Hawker, M. C., Martinez, M. R., Page, Z. A., Xiao-An Zhang, S., Hawker, C. J., Read de Alaniz, J. Stable Activated Furan and Donor-Acceptor Stenhouse Adduct Polymer Conjugates as Chemical and Thermal Sensors. *Macromolecules* **2019**, *52* (11), 4370–4375. <https://doi.org/10.1021/acs.macromol.9b00533>.
- (14) Seshadri, S., Gockowski, L. F., Lee, J., Sroda, M., Helgeson, M. E., Read de Alaniz, J., Valentine, M. T. Self-Regulating Photochemical Rayleigh-Bénard Convection Using a Highly-Absorbing Organic Photoswitch. *Nat. Commun.* **2020**, *11*, 2599.

<https://doi.org/10.1038/s41467-020-16277-7>.

- (15) Mallo, N., Brown, P. T., Iranmanesh, H., MacDonald, T. S. C., Teusner, M. J., Harper, J. B., Ball, G. E., Beves, J. E. Photochromic Switching Behaviour of Donor-Acceptor Stenhouse Adducts in Organic Solvents. *Chem. Commun.* **2016**, 52 (93), 13576–13579. <https://doi.org/10.1039/C6CC08079K>.
- (16) Lerch, M. M., Wezenberg, S. J., Szymanski, W., Feringa, B. L. Unraveling the Photoswitching Mechanism in Donor-Acceptor Stenhouse Adducts. *J. Am. Chem. Soc.* **2016**, 138 (20). <https://doi.org/10.1021/jacs.6b01722>.
- (17) Lerch, M. M., Szymański, W., Feringa, B. L. The (Photo)Chemistry of Stenhouse Photoswitches: Guiding Principles and System Design. *Chem. Soc. Rev.* **2018**, 47 (6), 1910–1937. <https://doi.org/10.1039/c7cs00772h>.
- (18) Lerch, M. M., Di Donato, M., Laurent, A. D., Medved', M., Iagatti, A., Bussotti, L., Lapini, A., Buma, W. J., Foggi, P., Szymański, W., Feringa, B. L., Solvent Effects on the Actinic Step of Donor–Acceptor Stenhouse Adduct Photoswitching. *Angew. Chemie Int. Ed.* **2018**, 57 (27), 8063–8068. <https://doi.org/10.1002/anie.201803058>.
- (19) Sanchez, D. M., Raucci, U., Ferreras, K. N., Martínez, T. J. Putting Photomechanical Switches to Work: An Ab Initio Multiple Spawning Study of Donor-Acceptor Stenhouse Adducts. *J. Phys. Chem. Lett.* **2020**, 11 (18), 7901–7907. <https://doi.org/10.1021/acs.jpcclett.0c02401>.
- (20) García-Iriepa, C., Marazzi, M., Sampedro, D. From Light Absorption to Cyclization: Structure and Solvent Effects in Donor-Acceptor Stenhouse Adducts. *ChemPhotoChem* **2019**, 3 (9), 866–873. <https://doi.org/10.1002/cptc.201900102>.
- (21) Mallo, N., Foley, E. D., Iranmanesh, H., Kennedy, A. D. W., Luis, E. T., Ho, J., Harper, J. B., Beves, J. E. Structure-Function Relationships of Donor-Acceptor Stenhouse Adduct Photochromic Switches. *Chem. Sci.* **2018**, 9 (43), 8242–8252. <https://doi.org/10.1039/c8sc03218a>.

- (22) Lui, B. F., Tierce, N. T., Tong, F., Sroda, M. M., Lu, H., Read de Alaniz, J., Bardeen, C. J. Unusual Concentration Dependence of the Photoisomerization Reaction in Donor-Acceptor Stenhouse Adducts. *Photochem. Photobiol. Sci.* **2019**, *18* (6), 1587–1595. <https://doi.org/10.1039/c9pp00130a>.
- (23) Laurent, A. D., Medved, M., Jacquemin, D. Using Time-Dependent Density Functional Theory to Probe the Nature of Donor–Acceptor Stenhouse Adduct Photochromes. *ChemPhysChem* **2016**, *17*, 1846–1851. <https://doi.org/10.1002/cphc.201600041>.
- (24) Lerch, M. M., Medved, M., Lapini, A., Laurent, A. D., Iagatti, A., Bussotti, L., Szymański, W., Buma, W. J., Foggi, P., Di Donato, M., Feringa, B. L., Tailoring Photoisomerization Pathways in Donor–Acceptor Stenhouse Adducts: The Role of the Hydroxy Group. *J. Phys. Chem. A* **2018**, *122* (4), 955–964. <https://doi.org/10.1021/acs.jpca.7b10255>.
- (25) Payne, L., Josephson, J. D., Murphy, R. S., Wagner, B. D. Photophysical Properties of Donor-Acceptor Stenhouse Adducts and Their Inclusion Complexes with Cyclodextrins and Cucurbit[7]Uril. *Molecules* **2020**, *25* (21). <https://doi.org/10.3390/molecules25214928>.
- (26) Patel, D. G., Paquette, M. M., Kopelman, R. A., Kaminsky, W., Ferguson, M. J., Frank, N. L. A Solution- and Solid-State Investigation of Medium Effects on Charge Separation in Metastable Photomerocyanines. *J. Am. Chem. Soc.* **2010**, *132* (36), 12568–12586. <https://doi.org/10.1021/ja100238h>.
- (27) Reichardt, C. Solvatochromic Dyes as Solvent Polarity Indicators. *Chem. Rev.* **1994**, *94* (8), 2319–2358. <https://doi.org/10.1021/cr00032a005>.
- (28) Zulfikri, H., Koenis, M. A. J., Lerch, M. M., Di, M., Szyma, W., Filippi, C., Feringa, B. L., Buma, W. J. Taming the Complexity of Donor-Acceptor Stenhouse Adducts: Infrared Motion Pictures of the Complete Switching Pathway. *J. Am. Chem. Soc.* **2019**, *141* (18), 7376–7384. <https://doi.org/10.1021/jacs.9b00341>.

- (29) Sinawang, G., Wu, B., Wang, J., Li, S., He, Y. Polystyrene Based Visible Light Responsive Polymer with Donor – Acceptor Stenhouse Adduct Pendants. *Macromol. Chem. Phys.* **2016**, *217*, 2409–2414.
- (30) Ulrich, S., Hemmer, J. R., Page, Z. A., Dolinski, N. D., Rifaie-Graham, O., Bruns, N., Hawker, C. J., Boesel, L. F., Read de Alaniz, J. Visible Light-Responsive DASA-Polymer Conjugates. *ACS Macro Lett.* **2017**, *6* (7).
<https://doi.org/10.1021/acsmacrolett.7b00350>.
- (31) Yap, J. E., Mallo, N., Thomas, D. S., Beves, J. E., Stenzel, M. H. Comparing Photoswitching of Acrylate or Methacrylate Polymers Conjugated with Donor-Acceptor Stenhouse Adducts. *Polym. Chem.* **2019**, *10* (47), 6515–6522.
<https://doi.org/10.1039/c9py01345h>.
- (32) Zhao, Y., Truhlar, D. G. The M06 Suite of Density Functionals for Main Group Thermochemistry, Thermochemical Kinetics, Noncovalent Interactions, Excited States, and Transition Elements: Two New Functionals and Systematic Testing of Four M06-Class Functionals and 12 Other Function. *Theor. Chem. Acc.* **2008**, *120* (1–3), 215–241. <https://doi.org/10.1007/s00214-007-0310-x>.
- (33) Zhao, Y., Truhlar, D. G. Density Functionals with Broad Applicability in Chemistry. *Acc. Chem. Res.* **2008**, *41* (2), 157–167. <https://doi.org/10.1021/ar700111a>.
- (34) Marenich, A. V., Cramer, C. J., Truhlar, D. G. Universal Solvation Model Based on Solute Electron Density and on a Continuum Model of the Solvent Defined by the Bulk Dielectric Constant and Atomic Surface Tensions. *J. Phys. Chem. B* **2009**, *113* (18), 6378–6396. <https://doi.org/10.1021/jp810292n>.
- (35) Frisch, M.J., Trucks, G.W., Schlegel, H.B., Scuseria, G.E., Robb, M.A., Cheeseman, J.R., Scalmani, G., Barone, V., Mennucci, B., Petersson, G.A., Nakatsuji, H., Caricato, M., Li, X., Hratchian, H.P., Izmaylov, A.F., Bloino, J., Zheng, G., Sonnenberg, J.L., Hada, M., Ehara, M., Toyota, K., Fukuda, R., Hasegawa, J., Ishida, M., Nakajima, T.,

Honda, Y., Kitao, O., Nakai, H., Vreven, T., Montgomery Jr., J.A., Peralta, J.E., Oglario, F., Bearpark, M., Heyd, J.J., Brothers, E., Kudin, K.N., Staroverov, V.N., Kobayashi, R., Normand, J., Raghavachari, K., Rendell, A., Burant, J.C., Iyengar, S.S., Tomasi, J., Cossi, M., Rega, N., Millam, J.M., Klene, M., Knox, J.E., Cross, J.B., Bakken, V., Adamo, C., Jaramillo, J., Gomperts, R., Stratmann, R.E., Yazyev, O., Austin, A.J., Cammi, R., Pomelli, C., Ochterski, J.W., Martin, R.L., Morokuma, K., Zakrzewski, V.G., Voth, G.A., Salvador, P., Dannenberg, J.J., Dapprich, S., Daniels, A.D., Farkas, O., Foresman, J.B., Ortiz, J.V., Cioslowski, J. and Fox, D.J. G16_C01. 2016, p Gaussian 16, Revision C.01, Gaussian, Inc., Wallin.

4 Controlling DASA pathway selection through environment

4.1 Multi-stage mechanism as an internal orthogonal stimuli

The design of “smart” stimuli-responsive materials have attracted considerable attention due to their potential ability to mimic nature’s multi-purpose systems.^{1,2} These synthetic

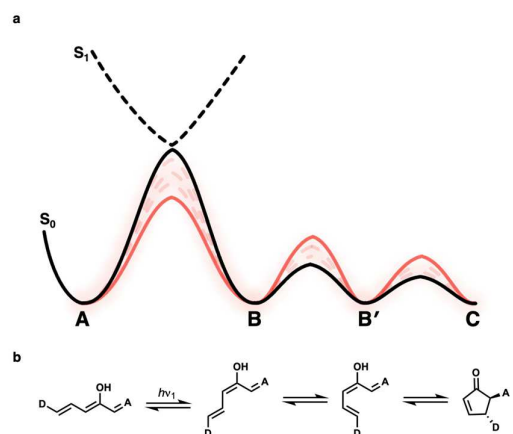


Figure 4.1. a) Schematic representation of the environmental influence on the ground state chemistry of DASA. b) simplified mechanism of DASA showing the important steps for DASA kinetics.

systems have been demonstrated in applications such as soft robotics^{3,4}, sensors⁵, and advanced

actuator systems.^{6,7} To enable greater orthogonality and increased complexity, some of these systems have been designed to respond to both a physical stimulus (e.g., light, electricity, temperature and pressure) and a chemical stimulus (e.g., solvent vapor, chemical analyte, and change in pH).⁸⁻¹⁰ Multiaddressable systems are more capable of sophisticated functions and complex behavior due to the interplay between different stimuli, which are key for a number of applications such as logic systems and life-like materials. Another approach to achieve orthogonality are multi-step processes with small changes in the energy landscape resulting in pathway selectivity. Especially multi-step mechanism can be used towards pathway selectivity due to the multitude of addressable levers.^{8,11} Through this approach, complex mixtures can be independently by separating molecules into different states.

One such multistep system are donor-acceptor Stenhouse adducts (DASAs).¹²⁻¹⁶ DASA are promising novel class of visible light responsive photoswitches.^{13,16} Changing the structure of the donor moiety,^{15,22-24} carbon acid acceptor¹⁴ and modifying the triene backbone²⁵ has been proven to dramatically influence the photochromic properties of DASAs. Beyond DASA architecture, the chemical environment in solution such as concentration,^{26,27} solvent polarity,^{23,28} and hydrogen bonding²⁹ ability also plays a critical role in controlling the potential energy surface (**Figure 4.1**) and therefore the ratio of colored and colorless form, photoswitching kinetics and reversibility. DASAs complex mechanism that combines both light-triggered and thermal isomerization steps allows for unique photoswitching behavior **Figure 4.1** (full mechanism **Scheme 4.1**).¹⁷⁻²⁰ We recently showed a multistage dual-wavelength controlled DASA-based platform by increasing the lifetime of colored intermediates along the reaction pathway (Chapter 3).²¹ We envisioned that the complexity of the DASA mechanism would allow external stimuli to guide pathway selection of DASAs in the mechanisms. In this Chapter, we present a means to tune kinetics and thermodynamics of DASA with different architectures using small amounts of additives. In contrast to prior work where additives were used to influence the properties of photoswitches[ref], this work uses the

additives to control the energy barriers along the photoswitching pathway to enable selectivity. Key to this work is that different classes of DASA react orthogonally to environmental cues. Through this novel approach, we can generate a multi-photochromic system with pathway selectivity by environmental change, opening up new opportunities in controlling material properties.

4.2 Understanding DASA environmental dependence

Due to the multi-step character of DASA's photoswitching mechanism small changes in the initial energy landscape of each DASA-based photoswitch should generate different responses by shuttling the DASA molecules to separate locations along the energy landscape. To test this hypothesis, we selected three commonly used DASAs with different electronic properties. To measure the ground state charge separation of each DASA derivative, we used their solvatochromic shift.²⁷ **DASA-1** consists of a dialkylamine donor with strong electron-donating properties combined with a weakly withdrawing acceptor in *N,N'*-dimethylbarbituric acid resulting in a solvatochromic slope of -43 nm.²¹ **DASA-2** retains the weakly withdrawing acceptor but replaces the donor with a weakly donating 2-methylindoline resulting in a more hybrid ground state, which is supported by the solvatochromic slope of -5 nm. **DASA-3** also retains the weakly donating 2-methylindoline, however, employs a

strongly withdrawing CF_3 -pyrazolone carbon acid as the acceptor. **DASA-3** has the most charge separated ground state with a solvatochromic slope of -60 nm (**Figure 4.2a**).²⁷ Through this change in charge separation, we observe changes in the calculated energy landscape of the kinetically relevant steps of DASA (**Figure 4.2**). The first important change is a difference to the barrier from **B** to **A**; less charge separation, which corresponds to more double bond character, results in a higher barrier. The second key difference is the stability of the first closed isomer **C** in comparison to **A**. Here, we observe **C** form of **DASA-3** to be more stable than the corresponding **C** form of **DASA-2** and **DASA-1**, respectively. Presumably, this is due to

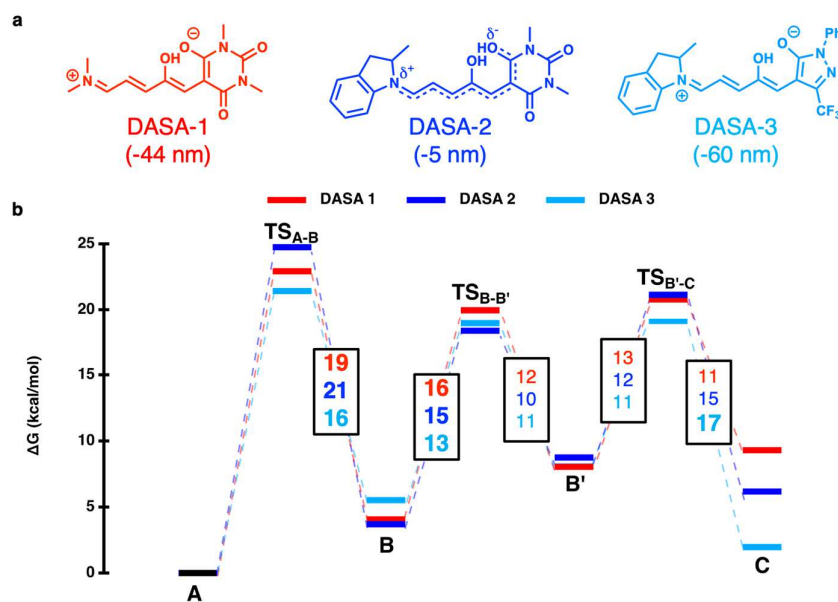


Figure 4.2. a) DASA structures of investigated compounds and their respective solvatochromic shift. b) calculated energy landscape for the three compounds with MO6-2X/6-31+G(d,p)/SMD(Chloroform) level of theory. Energy barriers are shown for each step. Bolded barriers are the rate determining steps for the forward and back reaction respectively.

aromatic character of the pyrazolone in the closed form for **DASA-3**. For **DASA-1** the relative destabilization is most likely due to increased stabilization of the triene form **A** which is broken upon electrocyclization.

In order to design a multi-step system which can use a single stimulus to generate multiple outputs the stimuli must influence the mechanism of the reaction at multiple points. We chose to investigate solvent polarity to target the charge-separation of the ground state of DASA molecules. The double bond character along the triene is directly related to the transition state barriers of each thermal bond rotation both forward (**B-B'-C**) as well as back (**C-B'-B-A**) (**Figure 4.3a**). A key design principle here is that the barrier between **A-B** behaves opposite to the barriers between **B-B'** and **B'-C** upon addition of polarity due to the bond alternation along the triene (**Figure 4.3a, Figure 4.7-29**). As such, upon an increase of polarity the double bond character of the **C4-C5** decreases leading to a decrease in the energy barrier for the corresponding bond rotation (**A to B**) (**Figure 4.3, 4.7-29**). The same effect leads to an increase in the double bond character around the **C3-C4** bond leading to an increase in the energy barrier of the corresponding bond rotation (**B to B'**) (**Figure 4.9-29**). The subsequent 4π -electrocyclization is influenced by the distance between **C5** and **C1** which seems to be governed by the bond angles of the single vs double bonds along the triene (**Figure 4.3 and 4.7-8**). These trends are similar for all DASA investigated here (**DASA-1–DASA-3; Figure 2a, Figure 4.7-8**).

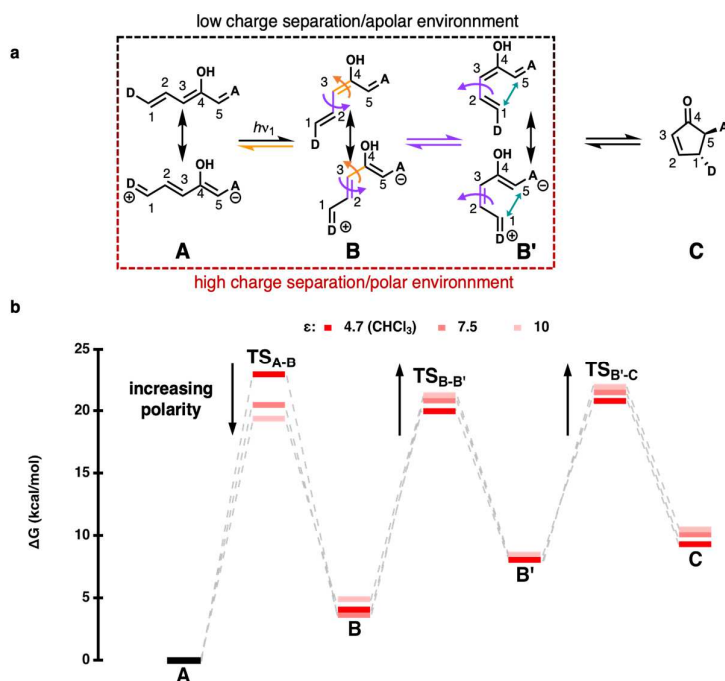


Figure 4.3. a) calculated energy landscape with MO6-2X/6-31+G(d,p)/SMD(Chloroform) level of theory of **DASA-1** in changing polarity marked by dielectric constant. b) schematic of the kinetic steps of the DASA mechanism showcasing an explanation for the changing transition states due to a change of charge separation of the DASA ground state.

To investigate how these trends in the energy landscape translate into changes in both kinetics and thermodynamics we utilized time-dependent UV-Vis spectroscopy and $^1\text{H-NMR}$ (**Figure 4.4**). **DASA-1** can be irradiated with 530 nm light in dichloromethane ($\epsilon=8.9$) resulting in 10 % loss of absorbance in 100 s. If acetonitrile (ACN) is added (more polar solvent than dichloromethane; $\epsilon=37.5$) the amount of DASA which can be turned into the closed form decreases, which can be experimentally observed by monitoring the absorbance change. In the presence of 10 vol% of CAN the absorbance decreases is only 4 %. In contrast, adding 10 vol% diethyl ether (DEE, $\epsilon=4.3$) slightly increases the amount of DASA closing, resulting in a loss of absorbance of 15 %. (**Figure 4.4b**). Importantly, the recovery slows down with the addition of ACN, while DEE does not affect k_{back} (**Table 4.1**). This data is in line with expectation that increasing barrier from **B** to **B'** combined with a decrease in the back reaction barrier from **B** to

A would result in a decreasing rate of closing. This is confirmed by monitoring the formation of **B** form through pump-probe spectroscopy. Using this technique, we monitored the population of **B** upon addition of ACN and observed a decrease in the population of **B**. Consistent with our hypothesis, adding DEE slightly increases the population of **B** under irradiation (**Figure 4.38**). Moreover, we observe a slowdown of the recovery rates upon addition of ACN suggesting that the rate-determining step is not **B** to **A** but rather either **B'** to **B** or a closed isomer.

For **DASA-2** we observe slightly different trends. In contrast to **DASA-1** 150 s of irradiation with a 617 nm LED led to full loss of absorbance. In the dark, we observe recovery to initial absorbance with a k_{back} of 0.031 min^{-1} (**Table 4.2**). Additional ACN does not change the absorbance loss, however, the rate of the recovery increases to 0.036 min^{-1} at 10 vol%. DEE on the other hand leads to a slowing down of the recovery rate to 0.026 min^{-1} . This seems to be reflective of the high barrier from **B** to **A** being solely responsible for the changes in the recovery kinetics. Observing the photoreaction then reflects **DASA-1** with a drop in population of **B** and less **C** population generated over a set irradiation time if ACN is added (**Figure 4.39**). The opposite is observed with DEE reflecting the respective increase in **B** to **A** and decrease in **B** to **B'** barriers (**Figure 4.4c**).

Irradiation of **DASA-3** in dichloromethane results in a photothermalstationary of 67% open form, which corresponds to a 33% loss of absorbance. Interestingly both ACN and DEE lead to a decrease in PTSS to a decrease in absorbance of 56% and 89% at 10 vol% respectively while the recovery rate k_{back} drops from 17.5 min^{-1} to 3.5 and 2.4 min^{-1} (**Table 4.3**). While the **B** population is not detectable through our methods, we do observe the same trend as in **DASA-1** and **DASA-2** regarding the generation of the **C** isomers with additional ACN leading to a decrease in **C** isomers being generated while DEE leads to an increase (**Figure 4.39**). This suggest that **B** for **DASA-3** also favors the back reaction to upon addition of polarity reaction due to the respective barriers from **B** to either **A** or **B'** (**Figure 4.4d**).

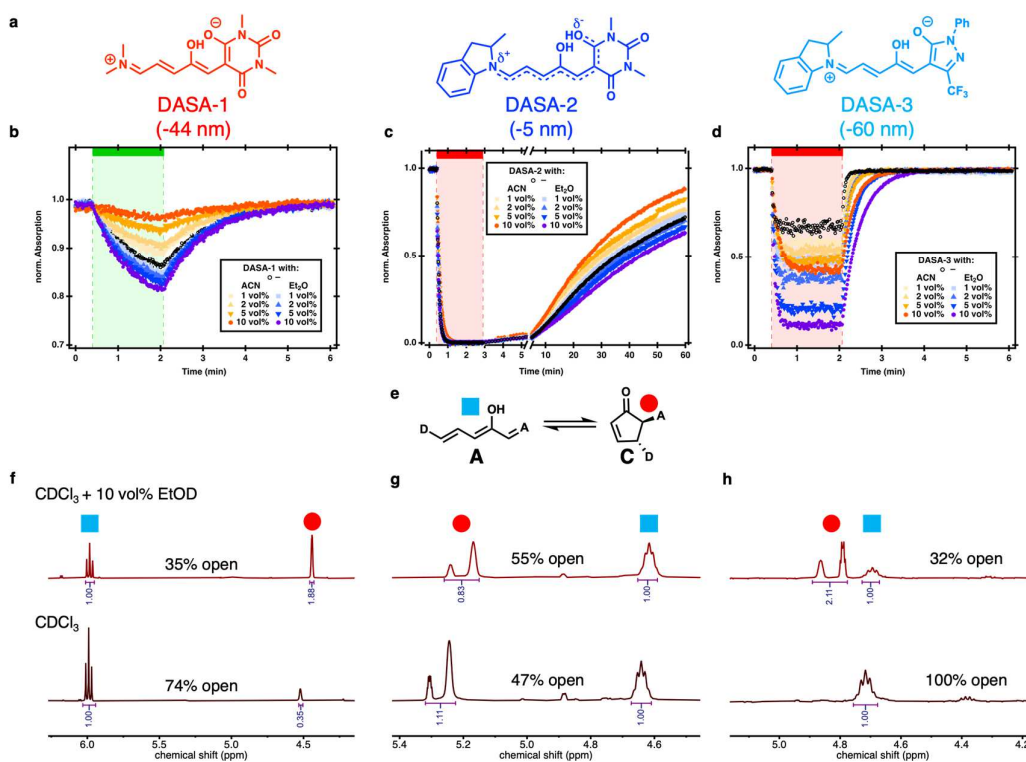


Figure 4.4. a) DASA structures of investigated compounds b) time dependent UV–Vis spectroscopy of 10 μM **DASA-1** in dichloromethane with acetonitrile and diethylether respectively. Followed at $\lambda_{\text{max}} = 564$ nm. Irradiated with 530 nm LED for 100 seconds. c) time dependent UV–Vis spectroscopy of 10 μM **DASA-2** in dichloromethane with acetonitrile and diethylether respectively. Followed at $\lambda_{\text{max}} = 619$ nm. Irradiated with 617 nm LED for 150 seconds. d) time dependent UV–Vis spectroscopy of 10 μM **DASA-3** in dichloromethane with acetonitrile and diethylether respectively. Followed at $\lambda_{\text{max}} = 646$ nm. Irradiated with 617 nm LED for 100 seconds. e) thermodynamic equilibrium between the open and closed form. f) ^1H -NMR in CDCl_3 of 10 mM **DASA-1** after 24 h of equilibration with 0 vol% and 10 vol% EtOD. The zwitterionic closed form **C'''** is observed. g) ^1H -NMR in CDCl_3 of 10 mM **DASA-2** after 24 h of equilibration with 0 vol% and 10 vol% EtOD. The neutral closed form **C''''** is observed. h) ^1H -NMR in CDCl_3 of 10 mM **DASA-2** after 24 h of equilibration with 0 vol% and 10 vol% EtOD. The zwitterionic or enol closed form **C''(')** is observed. Due to the stereocenter of the 2-methylindoline donor two signals for the closed form are observed.

By measuring $^1\text{H-NMR}$ after 24h in the dark we can observe the relative equilibrium between the open and closed form for each DASA. Upon addition of EtOD we observe a shift in the equilibrium for **DASA-1** from 74% open to 35% (**Figure 4.4f, 4.34**). **DASA-2** on the other hand sees a slight increase in the equilibrium from 47% to 55% open (**Figure 4.4g, 4.35**). **DASA-3** on the other hand sees a drop in equilibrium from 100% to 32% upon the addition of 10% EtOD (**Figure 4.4h, 4.36**). This is most likely due to **DASA-1** and **DASA-3** forming a different closed form in C'' (or C''') than **DASA-2** which forms C'''' with the former being stabilized in polar media and the latter being favored in apolar environments.^{13,16,23,30,31}

As highlighted by the data above, each of these DASAs observes the same de facto change in its energy landscape but due to different starting energy landscapes the overall observed output is different. Because the energy landscape is altered for each derivative, small changes in the environment results in pathway selectivity and control of the reaction pathway using a single additive. To showcase the uniqueness of this system, we investigated the ability to independently control three different DASAs (**DASA-3**, **DASA-4**, and **DASA-5**) in toluene (**Figure 4.5a-b**). **DASA-4** and **DASA-5** were chosen as analogues to **DASA-1** and **DASA-2** with improved wavelength separation from **DASA-3**. Upon irradiation in toluene with no additives, **DASA-3** and **DASA-4** close and recover in the dark in minutes (**Figure 4.5b-c, 4.43–45**) while **DASA-5** closes but shows no recovery to the open form over extended periods of time (**Figure 4.5b, c, 4.45**) (i.e., **DASA-5** is kinetically trapped in the closed form). Upon addition of 25 vol% of DMSO to toluene each DASA has a distinctive change in switching properties (**Figure 5.4b-d**). The addition of 25 vol% DMSO causes **DASA-3** to quickly thermally isomerize to the closed form (**Figure 4b-d, 4.43**) being now thermodynamically trapped in the **C**-isomers. **DASA-4** thermally converts, slowly (over hours) to the closed form, and is also unresponsive to irradiation (**Figure 5.4b, 4.44**). This is due to the barrier from **B** to **A** being lower than to **B'** shutting down the “effective” photoinduced pathway to **C**. The addition of DMSO causes **DASA-5** to recover from the kinetically trapped closed form to the

open form and allows for reversible photoswitching (**Figure 4.5b-d, 4.45**). Because each of these DASA react uniquely to the same environmental change, we can use the addition of a single stimuli to change the overall behavior of a complex system without requiring the stimuli to react with the photoswitching molecule.

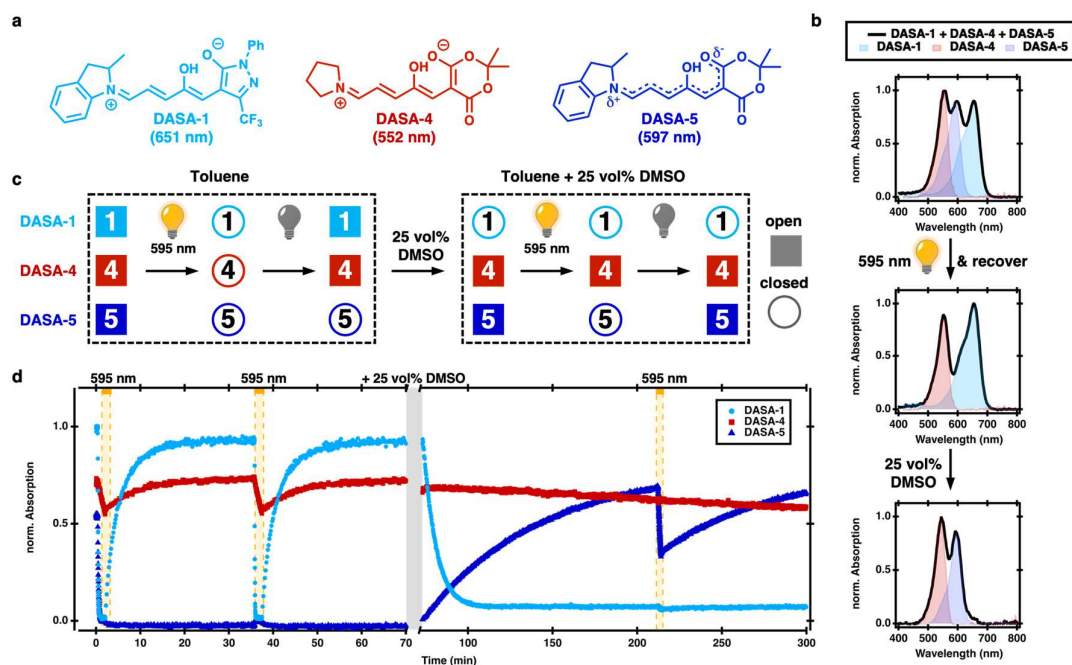


Figure 4.5. a) Structures of **DASA-3**, **DASA-4** and **DASA-5**. b) UV-Vis spectra of a mixture of **DASA-3** (10 μM), **DASA-4** (10 μM) and **DASA-5** (25 μM) in toluene before irradiation, after irradiation and recovery and after addition of 25 vol% DMSO. Three distinct states are observable with all DASA in the open form initially; **DASA-1** and **4** are in the open form after irradiation and recovery with **DASA-5** closed; after the addition of 25 vol% DMSO **DASA-4** and **5** are in the open form and **DASA-1** is closed. Measurements were normalized to highest absorbance. c) schematic of distinct behavior of **DASA-1**, **4** and **5** in toluene and in toluene with 25 vol% of DMSO. d) time dependent UV-Vis spectroscopy of **DASA-1** (10 μM), **DASA-4** (10 μM) and **DASA-5** (25 μM) in toluene in two environments demonstrating pathway selectivity. Detail on deconstruction of overlapping absorbances can be found in the additional information section 4.4.13.

When **DASA-3**, **DASA-4** and **DASA-5** are mixed, we observe three overlapping absorbances with distinctive peaks (**Figure 4.5b,d**). Following each DASA (for details on how

each population is followed see Section 4.6 in the supporting information) we can see a loss of absorbance upon irradiation with 595 nm light, a result of all three DASA derivatives converting to the closed form (**Figure 4.5d**). After irradiation we can observe recovery of **DASA-3** and **DASA-4** while **DASA-5** remains kinetically trapped in the closed form. This change can be observed in **Figure 4.5b** at with only two absorbance peaks being visible after irradiation. In this regime **DASA-3** and **DASA-4** can now be switched repeatedly with 595 nm light while **DASA-5** is kinetically trapped in the closed form. To this solution we add 25 vol% of DMSO (**Figure 4.5d**). Upon addition we observe the absorbance of **DASA-3** decrease in the dark to 4% of the initial absorbance. The absorbance of **DASA-4** is relatively stable after addition, but slowly decreases over time due to a slow thermal conversion to the closed form. Conversely, we observe an increase in the absorbance of **DASA-5**. This now results in a different regime where **DASA-4** and **DASA-5** are in the open form while **DASA-3** is closed as can be observed in **Figure 4.5b**. If this mixture is now irradiated, we observe reversible switching of **DASA-5** upon irradiation while **DASA-4** is kinetically trapped in the open form and **DASA-3** is thermodynamically trapped in the closed form (**Figure 4.5d**). Through the addition of one stimulus each DASA reacts differently to light showcasing the ability to control a complex system through multi-stimuli responsive DASA materials.

4.3 Conclusion

In conclusion we highlight the importance of the environment for DASA photoswitching. Through a combined theoretical and experimental approach, we can explain the effects of DASA on the energy landscape of DASA and the resulting changes in switching properties. Understanding this relationship enables to design set reaction pathways in DASA molecules by changing barriers between isomers. By addressing a complex mixture of DASA molecules with different starting energy landscapes we can orthogonally address the photoswitches through

two stimuli by pathway selectivity. By addressing a complex energy landscape to achieve orthogonality we hope to open the door to more advanced stimuli responsive materials.

4.4 Additional Information

4.4.1 General Experimental

4.4.1.1 Chemicals

All commercially obtained reagents were bought from Sigma Aldrich, TCI Europe or Fisher Scientific and were used without purification, except furfural, which was distilled prior to usage. Size exclusion beads (Bio-Beads S-X1 Support, 0.6–14 kDa) were obtained from Bio-Rad Laboratories. Anhydrous solvents were either obtained from Sigma Aldrich or from a solvent purification system. All additives were stored over sieves (3A, 2-5 mm beads, Alfa Aesar) before use.

4.4.1.2 Instruments and Methods

Room temperature reactions were carried out between 22–25 °C. Thin layer chromatography (TLC) was performed using Merck TLC plates (silica gel 60 F254 on aluminum) and visualized by UV light (254/ 366 nm) or staining with $\text{KMnO}_4/\text{NaOH}$. Silica gel chromatography was performed using silica gel from Sigma Aldrich (technical grade, 60 Å pore size, 40–63 μm particle size). ^1H - and ^{13}C -nuclear magnetic resonance (NMR) spectra were measured at 298 K on a Bruker Avance III 400 (400 MHz) NMR spectrometer, a Varian Unity Inova 500 MHz, or a Varian Unity Inova AS600 600 MHz spectrometer. Chemical shifts (δ) are reported in ppm and referenced internally from the proteo-solvent resonance. Coupling constants (J) are reported in Hz. Abbreviations for the peak multiplicities are *s* (singlet), *d* (doublet), *dd* (doublet of doublet), *t* (triplet), *q* (quadruplet) and *m* (multiplet). For diffusion-edited ^1H NMR spectra, 40% gradient strengths were applied to selectively suppress the signals of low molecular weight species.

4.4.1.3 Time dependent UV-Vis and kinetic rate determination

The photoinduced optical absorption kinetics were measured on a pump-probe setup. The pump beam was generated by a light emitting diode (LED) source (Thorlabs) coupled into a

multimode optical fiber terminated with an output collimator. The LED intensity was controlled through a digital-to-analog converter (National Instruments USB-6009) using LabVIEW. The probe beam was produced by High Power MINI Deuterium Tungsten Halogen Source w/shutter 200–2000 nm (Ocean Optics DH-MINI) coupled into a multimode fiber with an output collimator for the light delivery. The probe light was modulated by a shutter (Uniblitz CS25) which could be controlled manually or through a digital output port (National Instruments USB-6009) using LabVIEW. Pump and probe beams were overlapped using steering and focusing optics at a 90° angle inside a sample holder, which allowed for a 10x10 mm rectangular spectrophotometer cells that was connected to a circulating bath for temperature control. Additionally, the solutions were stirred during the measurements by a miniature stirring plate inserted into the sample holder (Starna Cells SCS 1.11). The sample holder was placed into a metal enclosure to prevent exposure to ambient light. Both pump and probe beams were nearly collimated inside the cell with a diameter of about 2 mm. The pump beam was blocked after passing through the sample and the probe beam was directed by a system of lenses into the detector (Ocean Optics Flame-S1-XR spectrometer), which acquired spectra of the probe light. The detector was connected to a PC via USB port. The experiment was controlled by a National Instrument LabVIEW program which collected the probe light spectra, determined sample optical absorption spectra, controlled pump and probe light sources, and stored the data on the computer S3 hard drive according to the experimental protocol. Experiments were performed in at 10 μ M concentration unless otherwise stated. Samples were left to equilibrate overnight prior to measurements unless otherwise stated.

4.4.1.4 Light Sources

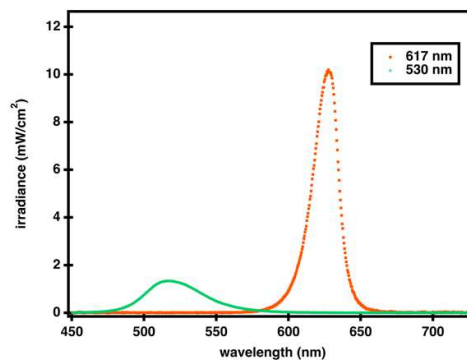


Figure 4.6. irradiance of Thorlabs 530 nm and 617 nm LED used in experiments. Total irradiance for 530 nm: 69.7 mW/cm²; 617 nm: 240.2 mW/cm². Measured using an Ocean Optics hand-held spectrometer with cosine corrector and radiometric calibration (model USB 2000).

4.4.1.5 Kinetic modelling

As second model, we use a first order exponential recovery function³² The model was used in the form:¹

$$Abs_t = Abs_{rec} - (Abs_{rec} - Abs_{PTSS})e^{-k_{back} * t}$$

where $k_{B,1st}$ represents the rate of opening in the dark, Abs_{rec} represents the absorption of open form at full recovery (the absorbance at $t = 15000$ s after full recovery is used), Abs_{PTSS} represents the absorption of open form at the photothermalstationary state (PTSS, the absorbance at $t = 200$ s as the last data point under irradiation was used) and Abs_t represents the absorption of the open form at time t . In this model we plot and fit the measured absorbance without normalization.

The authors want to acknowledge that this model does not take changes of equilibrium into account. However, due to the multi-step nature of DASA switching mechanism the authors

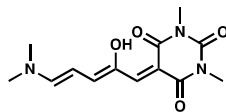
think this model captures the kinetic process better than a dynamic equilibrium model which overestimates the role of equilibrium due to the assumption of two state system.

4.4.1.6 Video Capture

For all videos, neutrally buoyant hollow spherical silica particles ($D_{\text{avg}} = 10 \mu\text{m}$, TSI Inc.) were added to 400 μL of solution in a quartz cuvette (pathlength 2 mm, inner dimensions: $40 \times 12 \times 2 \text{ mm}^3$). Samples were irradiated 2 cm from the bottom at which distance the maximum irradiance was determined to be 214 mW cm^{-2} . All samples were irradiated with a Schott ACE Halogen Light Source with intensities determined using a Field Max II TOP Laser Power Energy Meter. A Canon Rebel SL2 (100 mm f/2.8 Macro USM fixed lens, 1x magnification, 29.97 frames per second) was used to image photoreactions occurring in the UV/Vis quartz cuvette. Experimental Setup was as shown in Seshadri et al.³³

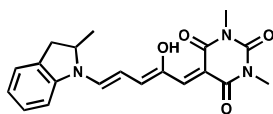
4.4.2 Synthesis

DASA-1



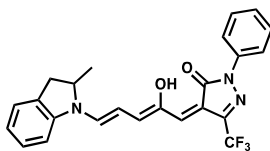
DASA-1 was synthesized as previously reported. The characterization data matched literature.¹⁵

DASA-2



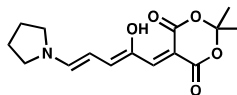
DASA-2 was synthesized as previously reported. The characterization data matched literature.¹⁴

DASA-3



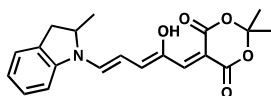
DASA-3 was synthesized as previously reported. The characterization data matched literature.¹⁴

DASA-4



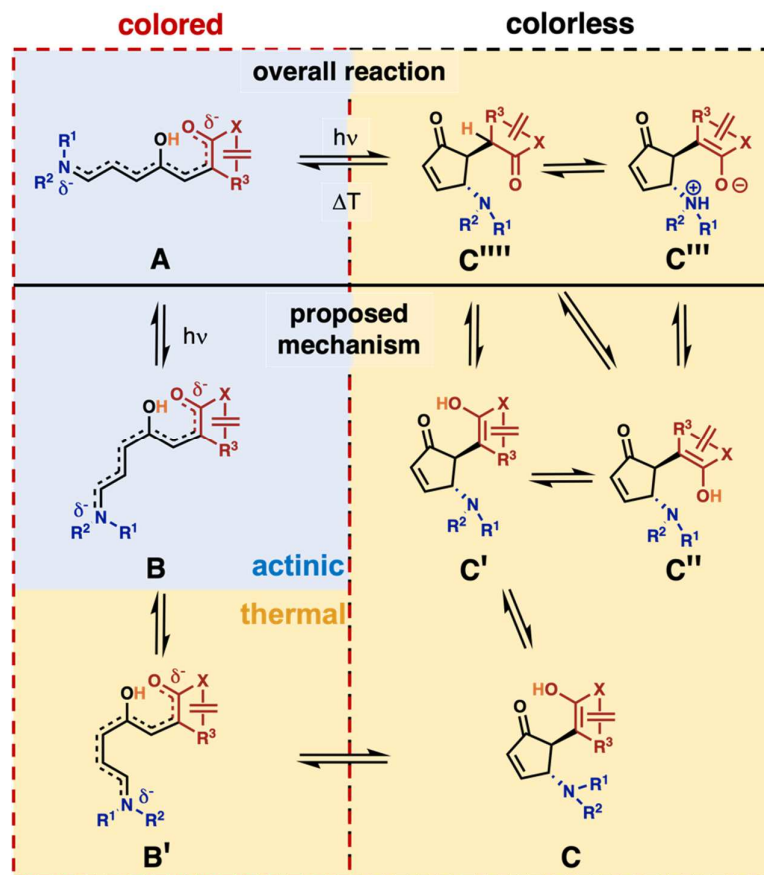
DASA-4 was synthesized as previously reported. The characterization data matched literature.³⁴

DASA-5



DASA-5 was synthesized as previously reported. The characterization data matched literature.¹⁴

4.4.3 DASA Mechanism



Scheme 4.1: Schematic of full DASA mechanism showing all described isomers.^{19,20}

4.4.4 Theoretical calculations

4.4.4.1 General computational details

DFT calculations of the DASA derivatives in various solvents were conducted using M06-2X/6-31+G(d,p) in chloroform using the SMD solvent model. In order to look at the effect of dielectric constant on the energies of the various isomers and transition state, the SMD=(chloroform,read) keyword was used along with Eps=7.5 or 10. Geometries were found starting from the initial isomer A. Transition states were found by doing relaxed scans around the coordinate of interest (XXXX) and the highest energy geometries were used to do transition state searches using keywords opt=(ts,calcfc,noeigentest). In cases where convergence was difficult, opt=(maxstep=1) was included. Bond length alternation were calculated by subtracting the average of the C-C bond lengths from the average of the C-C bond lengths. More positive BLA indicates that the C-C bonds have more single bond character (more zwitterionic resonance form) while more negative BLA indicates that the C-C bonds have more negative bond character (more neutral resonance form). Then relaxed scans were done around the C3-C4. The highest energy geometry was used in a transition state search.

4.4.5 Changes in energy landscape through polarity of solvent

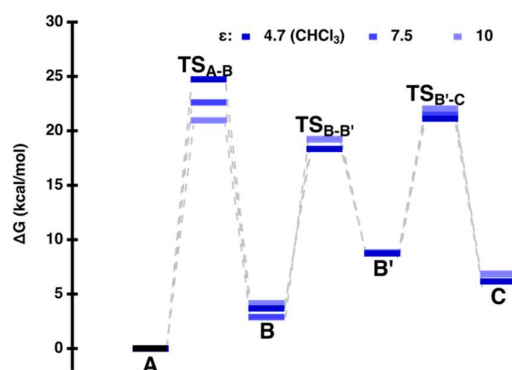


Figure 4.7. calculated energy landscape with M06-2X/6-31+G(d,p)/SMD(chloroform) of DASA-2 in changing polarity marked by dielectric constant.

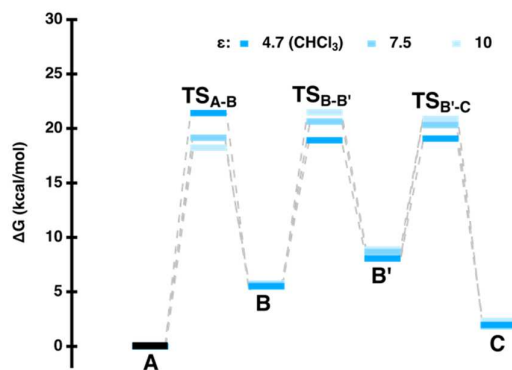


Figure 4.8. calculated energy landscape with M06-2X/6-31+G(d,p)/SMD(chloroform) of DASA-3 in changing polarity marked by dielectric constant.

4.4.6 BLA changes due to environment

DASA-1

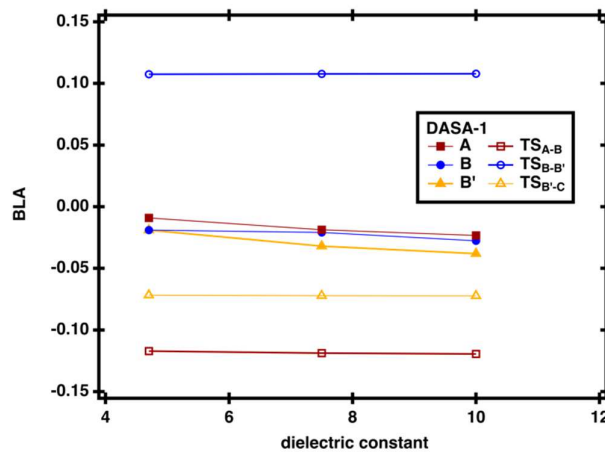


Figure 4.9. calculated bond alternation with M06-2X/6-31+G(d,p)/SMD(chloroform) of **DASA-1** depending on solvent polarity.

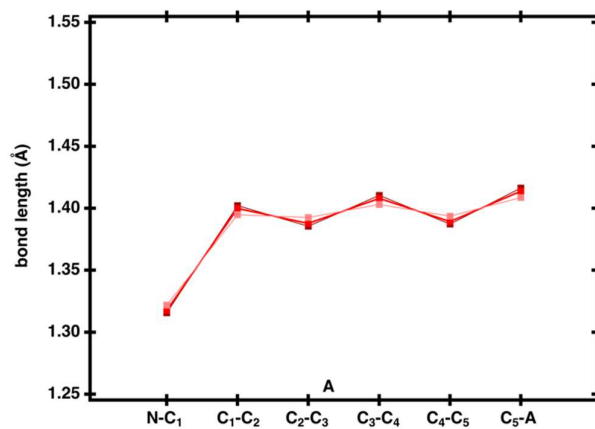


Figure 4.10. calculated bond lengths with M06-2X/6-31+G(d,p)/SMD(chloroform) of **DASA-1** for A.

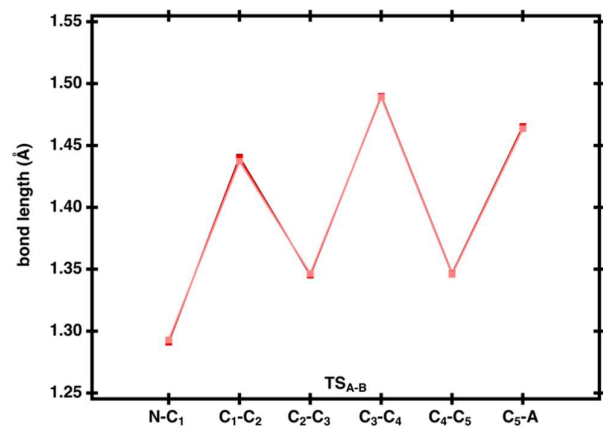


Figure 4.11. calculated bond lengths with M06-2X/6-31+G(d,p)/SMD(chloroform)of **DASA-1** for TS_{A-B}.

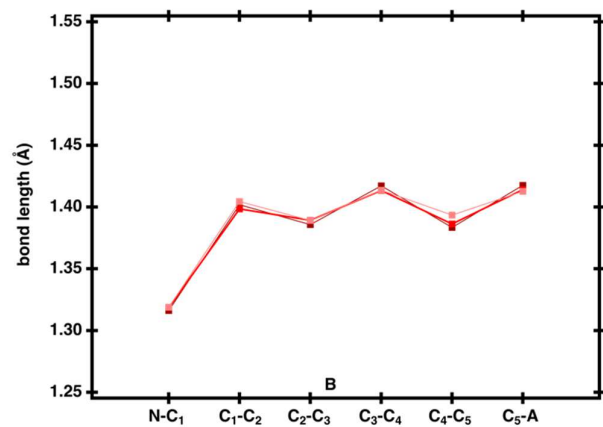


Figure 4.12. calculated bond lengths with M06-2X/6-31+G(d,p)/SMD(chloroform)of **DASA-1** for **B**.

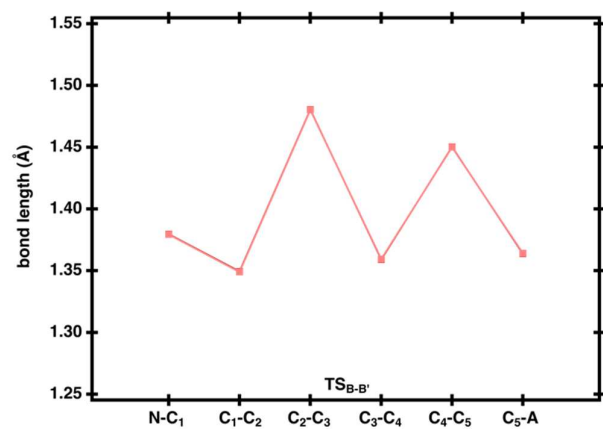


Figure 4.13. calculated bond lengths with M06-2X/6-31+G(d,p)/SMD(chloroform) level of theory of **DASA-1** for **TS_{B-B'}**.

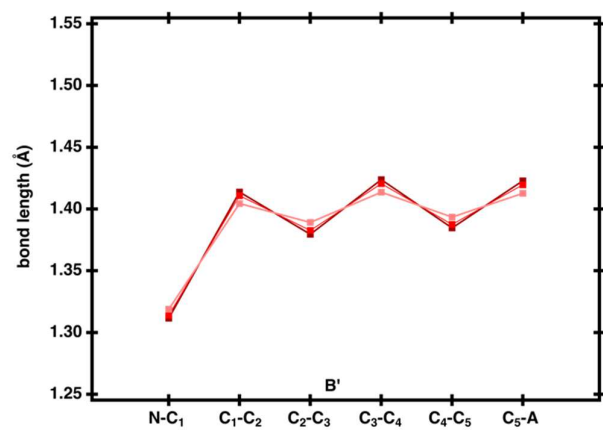


Figure 4.14. calculated bond lengths with M06-2X/6-31+G(d,p)/SMD(chloroform) level of theory of **DASA-1** for **B'**.

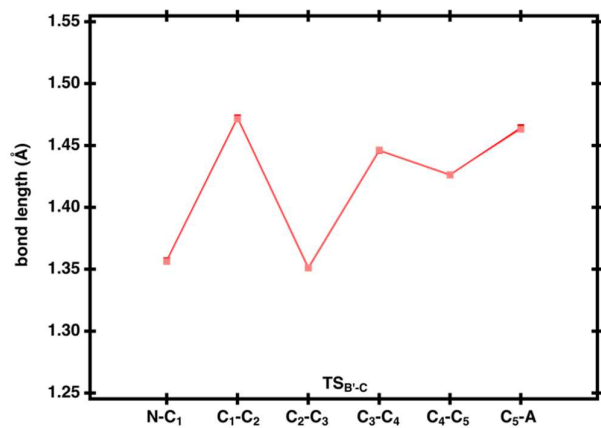


Figure 4.15. calculated bond lengths with M06-2X/6-31+G(d,p)/SMD(chloroform) level of theory of **DASA-1** for $TS_{B'-C}$.

DASA-2

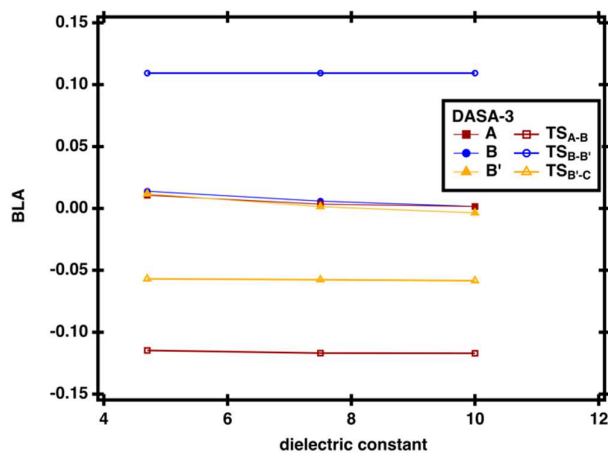


Figure 4.16. calculated bond alternation with M06-2X/6-31+G(d,p)/SMD(chloroform) level of theory of **DASA-2** depending on solvent polarity.

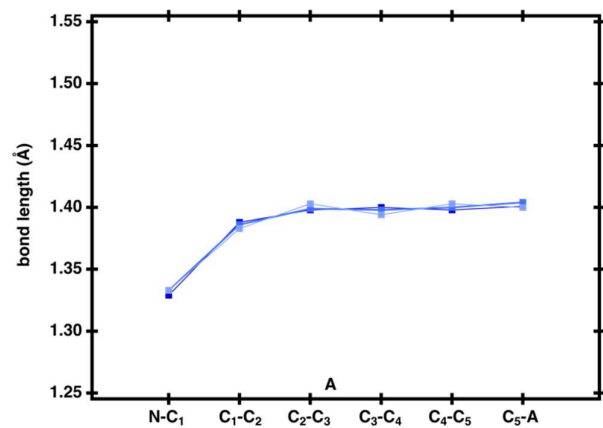


Figure 4.17. calculated bond lengths with M06-2X/6-31+G(d,p)/SMD(chloroform) level of theory of **DASA-2** for **A**.

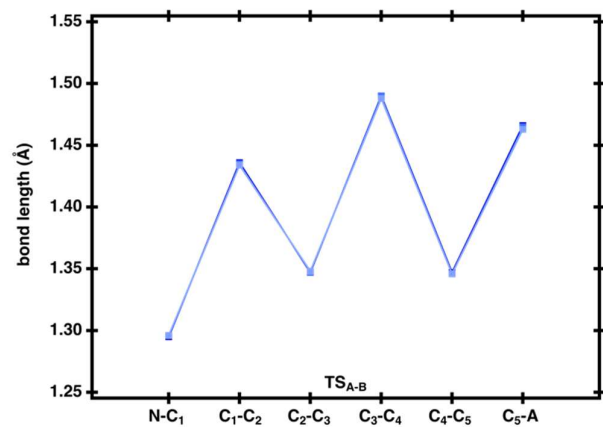


Figure 4.18. calculated bond lengths with M06-2X/6-31+G(d,p)/SMD(chloroform) level of theory of **DASA-2** for **TSA-B**.

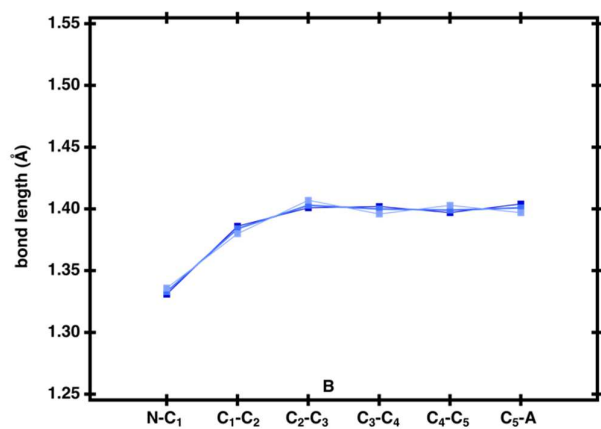


Figure 4.19. calculated bond lengths with M06-2X/6-31+G(d,p)/SMD(chloroform) level of theory of **DASA-2** for **B**.

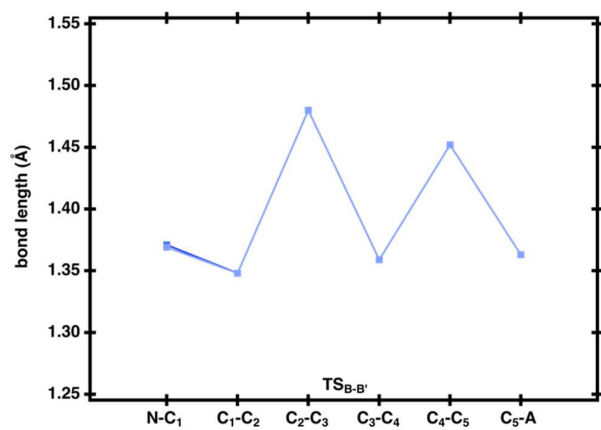


Figure 4.20. calculated bond lengths with M06-2X/6-31+G(d,p)/SMD(chloroform) level of theory of **DASA-2** for **TS_{B-B'}**.

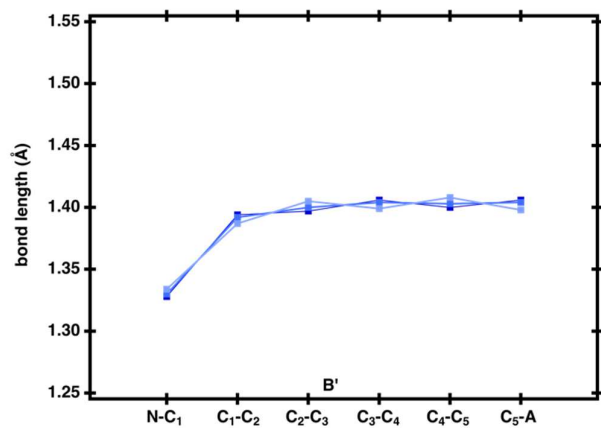


Figure 4.21. calculated bond lengths with M06-2X/6-31+G(d,p)/SMD(chloroform) level of theory of **DASA-2** for **B'**.

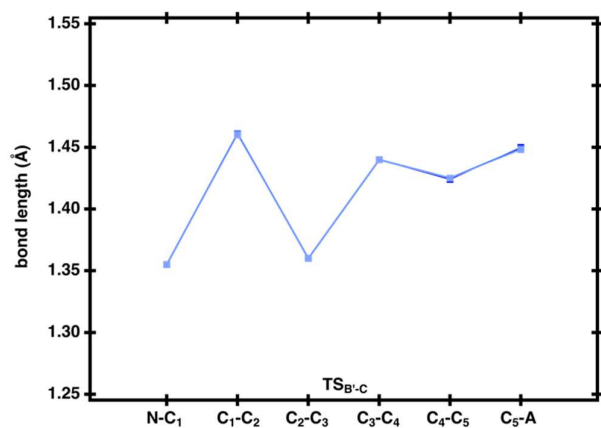


Figure 4.22. calculated bond lengths with M06-2X/6-31+G(d,p)/SMD(chloroform) level of theory of **DASA-2** for **TS_{B'-C}**.

DASA-3

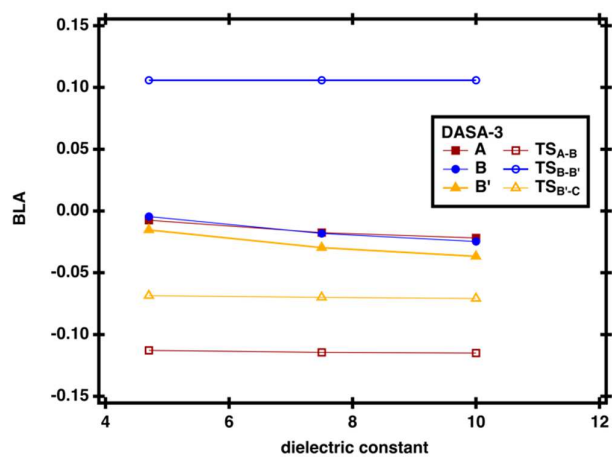


Figure 4.23. calculated bond alternation with M06-2X/6-31+G(d,p)/SMD(chloroform) level of theory of **DASA-3** depending on solvent polarity.

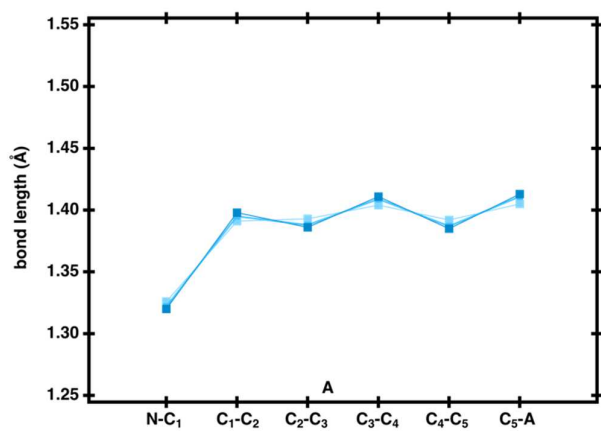


Figure 4.24. calculated bond lengths with M06-2X/6-31+G(d,p)/SMD(chloroform) level of theory of **DASA-3** for **A**.

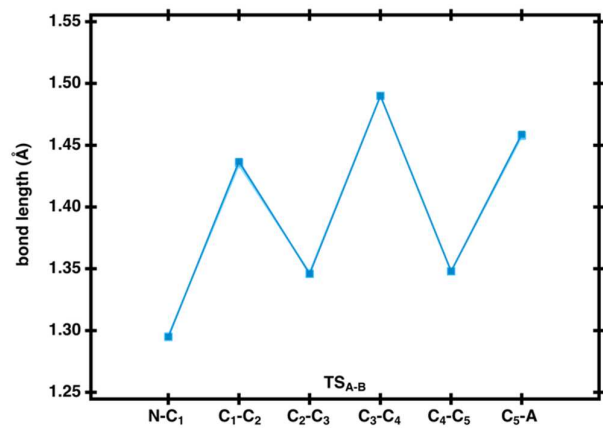


Figure 4.25. calculated bond lengths with M06-2X/6-31+G(d,p)/SMD(chloroform) level of theory of **DASA-3** for TSA-B.

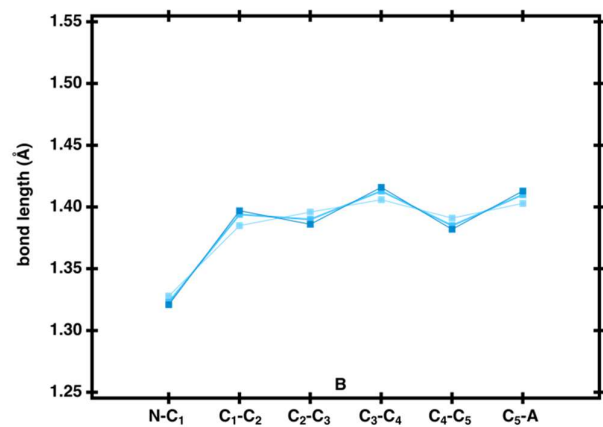


Figure 4.26. calculated bond lengths with M06-2X/6-31+G(d,p)/SMD(chloroform) level of theory of **DASA-3** for **B**.

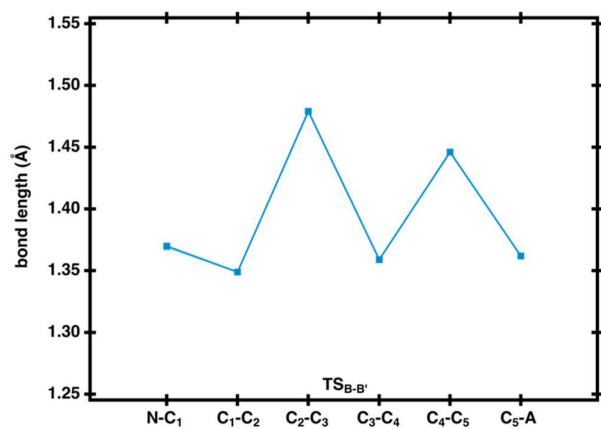


Figure 4.27. calculated bond lengths with M06-2X/6-31+G(d,p)/SMD(chloroform) level of theory of **DASA-3** for **TS_{B-B'}**.

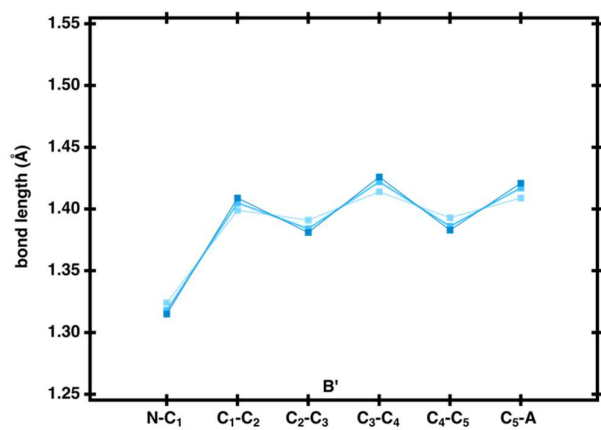


Figure 4.28. calculated bond lengths with M06-2X/6-31+G(d,p)/SMD(chloroform) level of theory of **DASA-3** for **B'**.

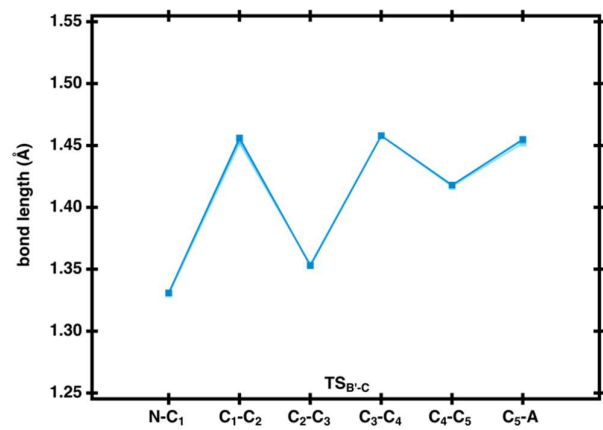


Figure 4.29. calculated bond lengths with M06-2X/6-31+G(d,p)/SMD(chloroform) level of theory of **DASA-3** for TS_{B'-C}.

4.4.7 Photoswitching kinetics upon additives

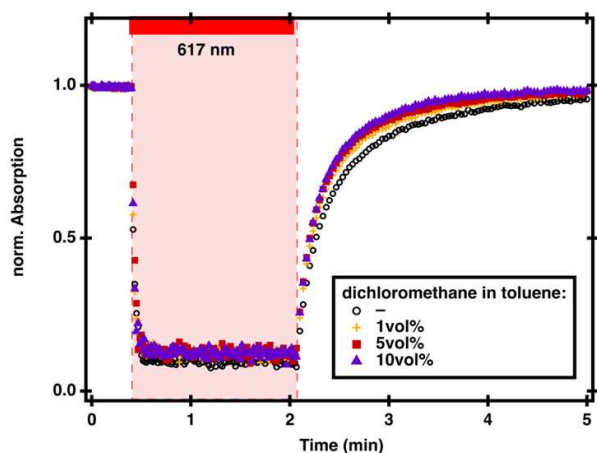


Figure 4.30. time dependent UV-Vis spectroscopy of 10 μM DASA-3 in toluene with 0.0 vol%, 1.0 vol%, 5.0 vol% and 10.0 vol% dichloromethane followed at λ_{\max} at 649 nm. The sample was irradiated with 617 nm LED for 100 seconds and the subsequent recovery in the dark was observed.

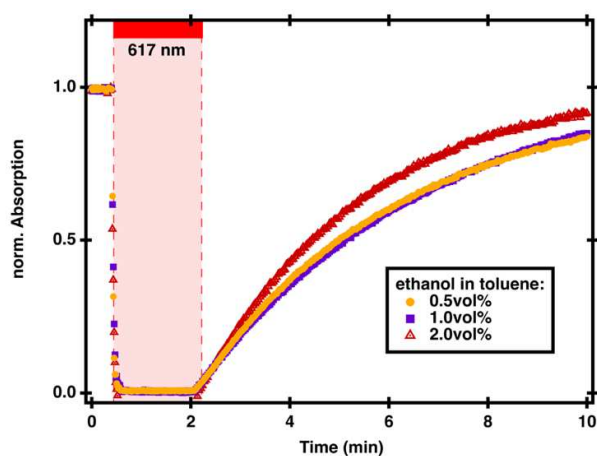


Figure 4.31. time dependent UV-Vis spectroscopy of 10 μM DASA-3 in toluene with 0.5 vol%, 1.0 vol% and 2.0 vol% ethanol followed at λ_{\max} at 649 nm. The sample was irradiated with 617 nm LED for 100 seconds and the subsequent recovery in the dark was observed.

4.4.8 Open and closed form ratios by UV-Vis upon additives

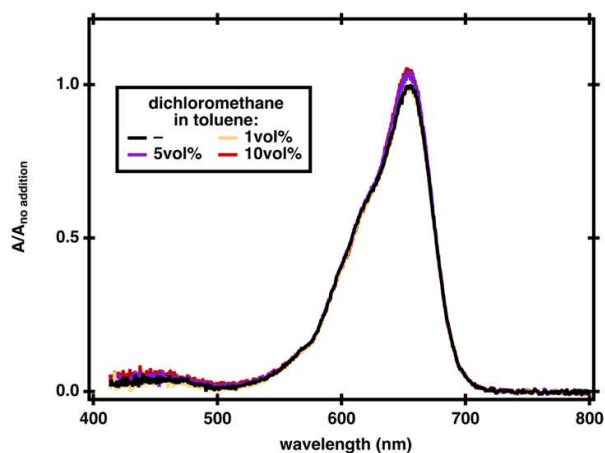


Figure 4.32. UV-Vis spectroscopy of 10 μM DASA-3 in toluene with 0.0 vol%, 1.0 vol%, 5.0 vol% and 10.0 vol% of dichloromethane after equilibration overnight relative to no addition.

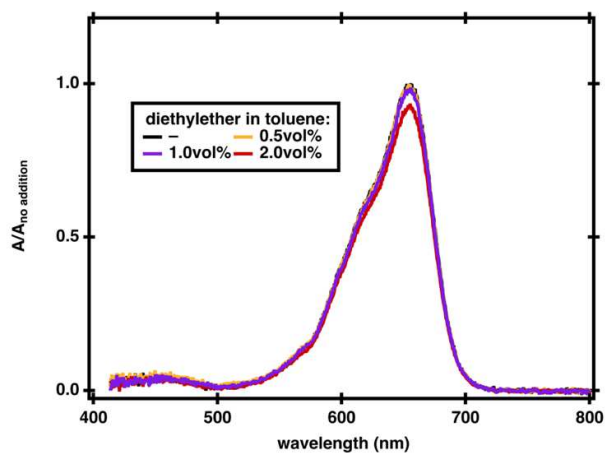


Figure 4.33. UV-Vis spectroscopy of 10 μM DASA-3 in toluene with 0.0 vol%, 0.5 vol%, 1.0 vol% and 2.0 vol% of diethylether after equilibration overnight relative to no addition.

4.4.9 Open and closed form ratios by $^1\text{H-NMR}$ upon additives

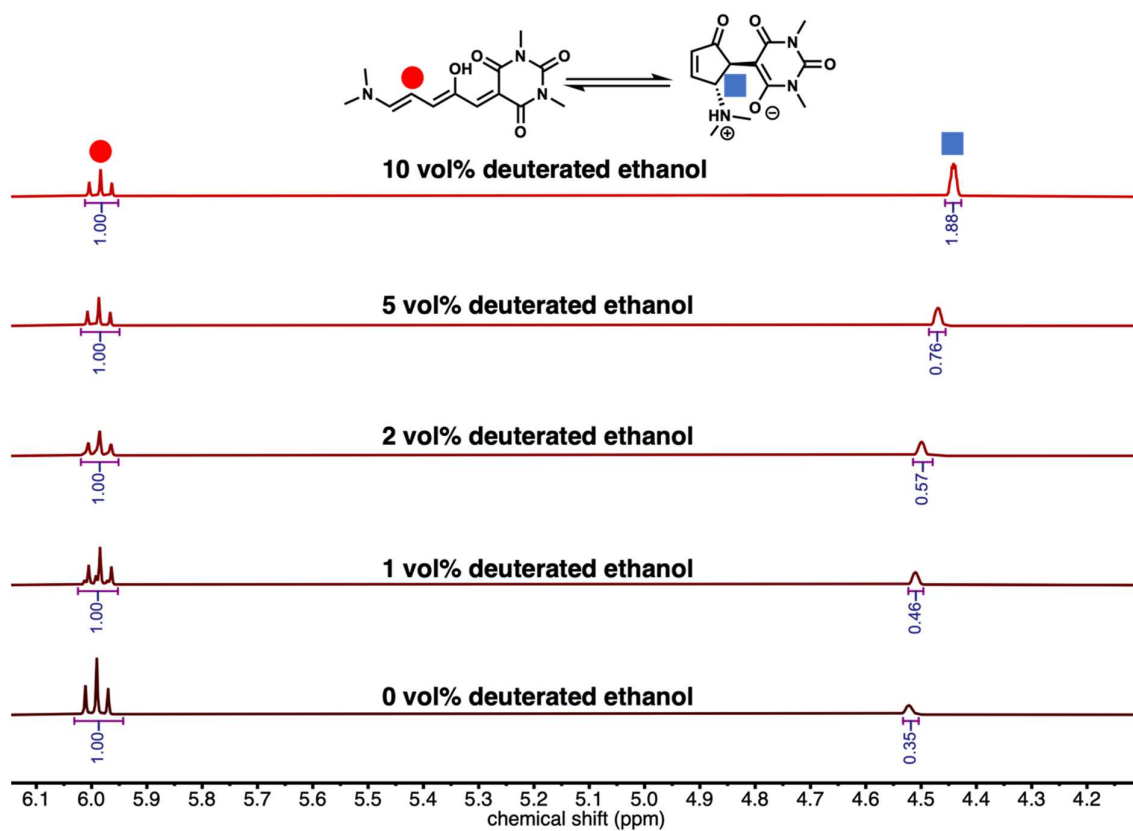


Figure 4.34. $^1\text{H-NMR}$ (600 MHz, CDCl_3) of 10 mM solution of **DASA-1** in deuterated chloroform with 0 to 10 vol% of deuterated ethanol after equilibration over 24h. An increase of closed form isomer **C'''** is observed upon addition of ethanol.

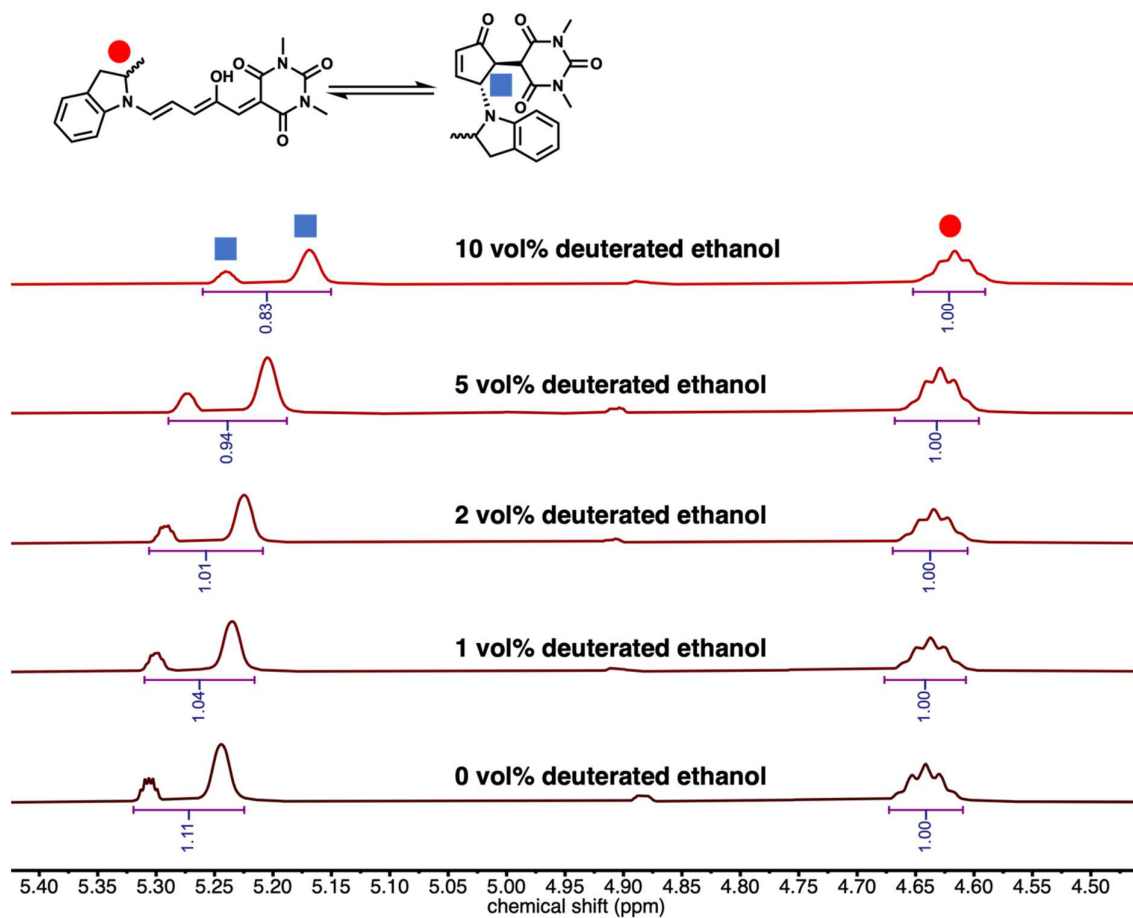


Figure 4.35. ¹H-NMR (600 MHz, CDCl₃) of 10 mM solution of **DASA-2** in deuterated chloroform with 0 to 10 vol% of deuterated ethanol after equilibration over 24h. an increase of open form isomer **A** is observed upon addition of ethanol. The closed form shows as two separate isomers due to the diastereomer formed upon ring closure due the stereocenter in the 2-methylindoline moiety.

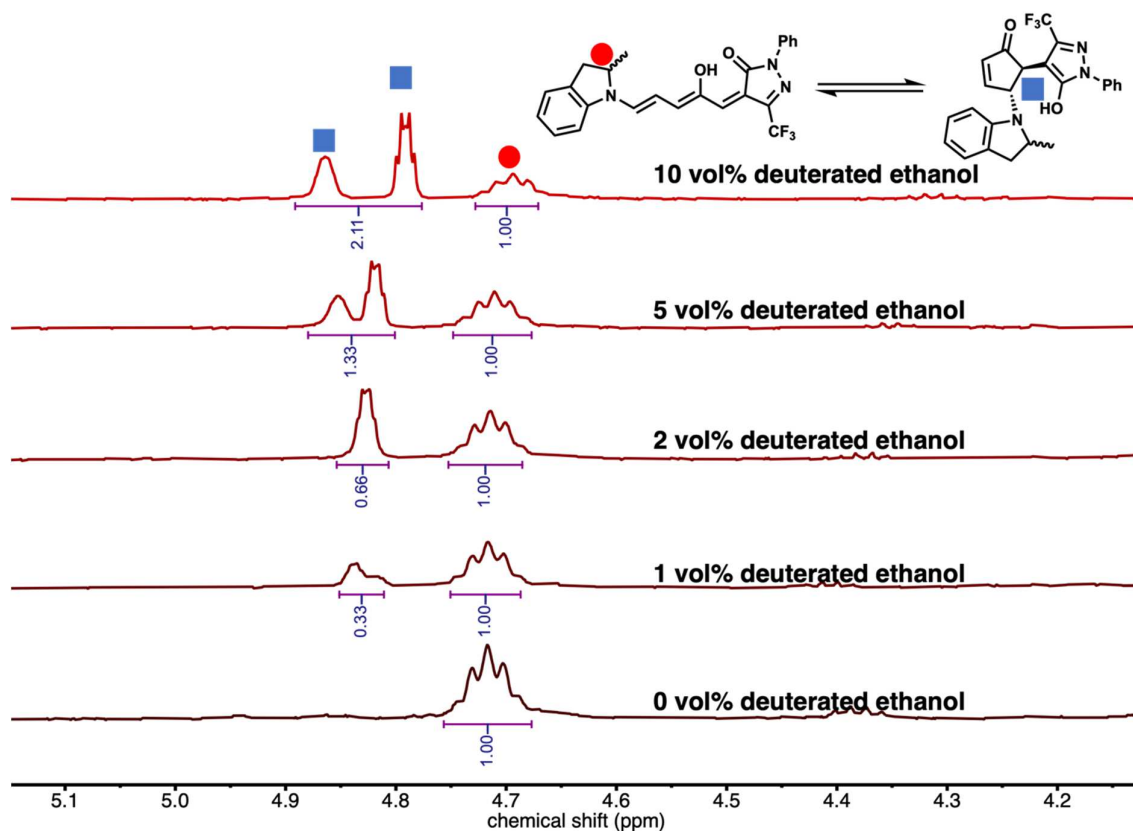


Figure 4.36. $^1\text{H-NMR}$ (600 MHz, CDCl_3) of 10 mM solution of **DASA-3** in deuterated chloroform with 0 to 10 vol% of deuterated ethanol after equilibration over 24h. an increase of closed form isomer C''' is observed upon addition of ethanol. The closed form shows as two separate isomers due to the diastereomer formed upon ring closure due the stereocenter in the 2-methylindoline moiety.

4.4.10 Observing intermediates

Pulse-decay experiments were performed on a custom-built setup consisting of LabVIEW-controlled laser pumping with dual source, rapid, and photochemically “passive” spectroscopic probing. For all measurements, the probe sources were individually modulated at 506 Hz (chopped) and 2.3 kHz (square wave gated), fiber coupled together, and launched normal to a 1 mm thick x 1 cm wide glass cuvette with an active probing area 2 mm in diameter. This frequency modulation step prevented signal contamination with background radiation, including stray pump light, and allowed signals with spectral overlap to be accurately discriminated. The transmitted beam was picked up by a Thorlabs PDA36A Si Switchable Gain Detector and the output signal was passed into a pair of Stanford Research SR830 Lock-In Amplifiers to deconvolve the two probe amplitudes. Lock-In time constants were selected to ensure accurate signal integration over at least 5 periods; 10 ms and 3 ms on the high and low frequency modulated sources, respectively. LabVIEW data acquisition (National Instruments BNC-2110) was used for real-time measurements at 25 Hz of the transmitted probe intensities during photonic excitation and relaxation. The sampling interval was set by slower modulation frequency because its corresponding lock-in time constant was the fastest the system could respond to a discontinuous change in signal amplitude.

Photonic excitation occurred by high intensity laser pumping with an active pump area 1.2 cm in diameter. This area ensured the entire sample volume was subjected to maximally uniform pump intensity and minimized diffusion effects in the observed photoswitching rates. The pump timing was controlled by LabVIEW with a mechanical beam flag, and set to 3 s for all samples in the series. This pump duration ensured the thermal steps governing the overall DASA kinetic process could be followed without fully converting the open form to the metastable closed forms.

The modular nature of this setup allowed the pump and probe sources to be switched out easily to ensure strong overlap with the spectrally shifted absorption profiles of **DASA-1, 2**,

and **3**. This series employed two laser pumping sources: a 532 nm non-polarized Nd:YAG laser (*P1*), and a 640 nm diode laser (*P2*). Two additional probe sources were required: a 620 nm LED (*Pr1*), a 660 nm LED with (*Pr2-f*), and without (*Pr2*) a 659 nm high pass filter and a 700°nm LED (*Pr3*). By splitting the pump laser beam into two lines of high and low intensities, it could simultaneously serve as a pumping and probing source. The pumping wavelength was selected to maximize DASA absorbance, while keeping to wavelengths below the **A** isomer's λ_{\max} to prevent photochemical **B** to **A** isomerization. Additionally, the probe sources were chosen to selectively target the absorption of the **A** and **B/B'** isomers independently. To ensure the absorptions of these species could be separated from one another, a minimum of one probe source was prohibited from overlapping the absorption bands of both **A** and **B/B'**. The pump/probe1/probe2 sources employed for **DASA-1**, **2**, and **3**, respectively, were as follows (asterisk denoting the probe source modulated at 506Hz): *P1/P1*/Pr1*, *P1/P2*/Pr2-f*, and *P2/P2*/Pr2*. The corresponding intensities of these lights were 17.1 mW/2.5 μ W/1.8 μ W, 17.2 mW/13 μ W/21 μ W, and 10.6 mW/14.1 μ W/3.4 μ W.

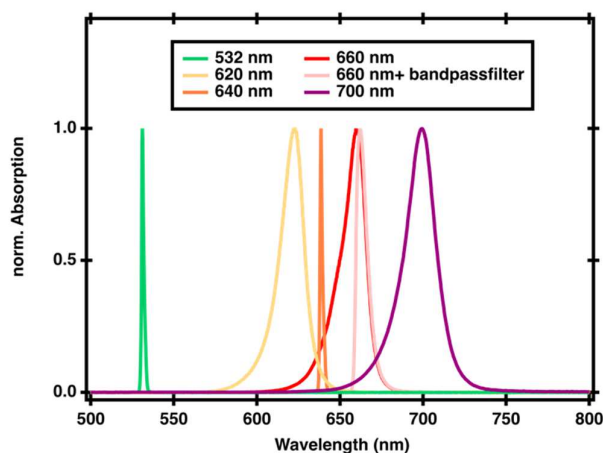


Figure 4.37. normalized emission profiles for the light sources used: 532 nm non-polarized Nd:YAG laser (*P1*); 640 nm diode laser (*P2*); 620 nm LED (*Pr1*); a 660 nm LED with (*Pr2-f*), and without (*Pr2*) a 659 nm high pass filter; 700 nm LED (*Pr3*).

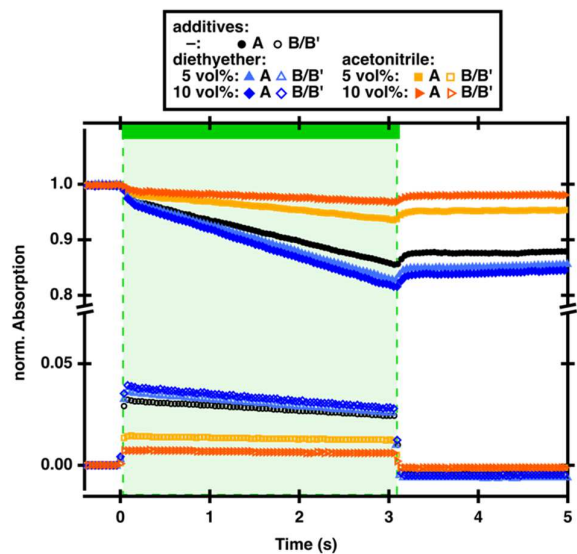


Figure 4.38. pump probe spectroscopy of 250 μM DASA-1 in dichloromethane with 0, 5 and 10 vol% acetonitrile and diethylether irradiated with *PI* for 3 s and followed with *PI* (A) and *PrI* (B/B').

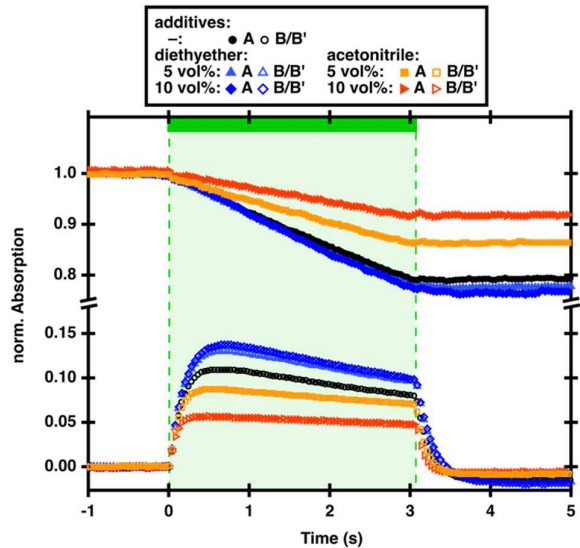


Figure 4.39. pump probe spectroscopy of 250 μM DASA-2 in dichloromethane with 0, 5 and 10 vol% acetonitrile and diethylether irradiated with *P1* for 3 s and followed with *P2* (A) and *Pr2-f* (B/B').

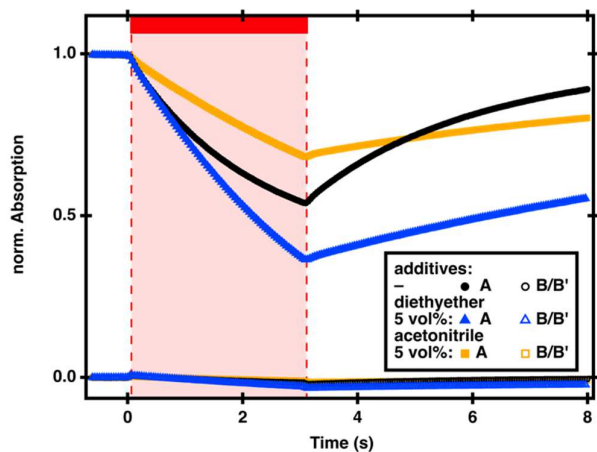


Figure 4.40. pump probe spectroscopy of 250 μM DASA-3 in dichloromethane with 0 and 5 10 vol% acetonitrile and diethylether irradiated with *P2* for 3 s and followed with *P2* (A) and *Pr3* (B/B').

4.4.11 Control of DASA switching

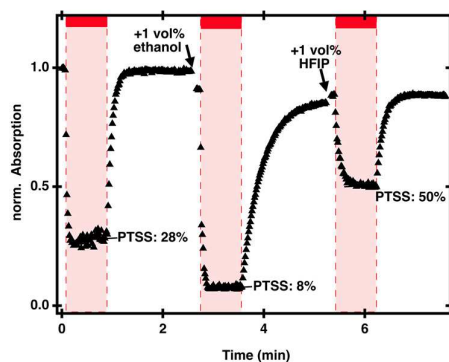


Figure 4.41. time dependent UV–Vis spectroscopy of 10 μM **DASA-3** in chloroform with subsequent additions of 1 vol% ethanol and 1 vol% HFIP followed at λ_{max} at 646 nm. The sample was irradiated with 617 nm LED for 100 seconds and the subsequent recovery in the dark was observed.



Figure 4.42. photographic stills of video 1 of 250 μM **DASA-3** in chloroform with either no addition, 2 vol% ethanol and 2 vol% ethanol and 1 vol% HFIP under irradiation with white light.

4.4.12 Environmental Gating of DASA photoswitching

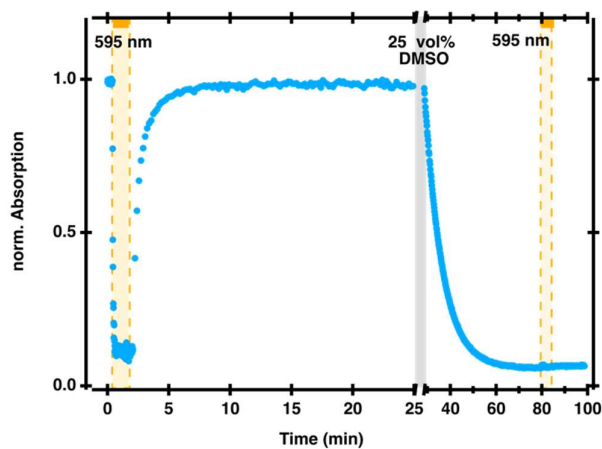


Figure 4.43. time dependent UV–Vis spectroscopy of 10 μM DASA-3 in toluene with subsequent addition of 25 vol% of DMSO. Absorbance followed at 651 nm before and 641 nm after addition of DMSO due to the shift of the absorption maximum Normalized to initial absorbance and absorbance was adjusted to dilution upon addition of DMSO.

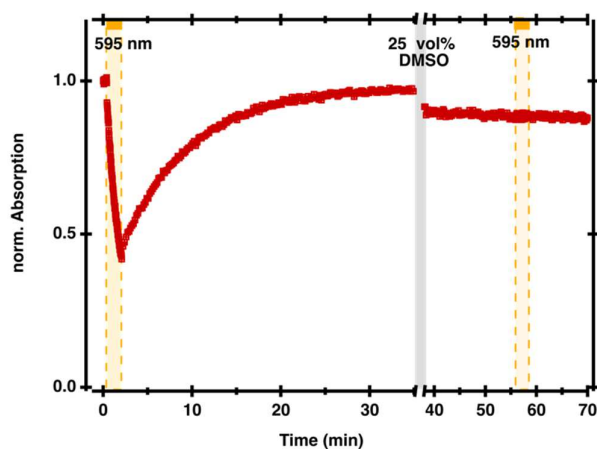


Figure 4.44. time dependent UV–Vis spectroscopy of 10 μM DASA-4 in toluene with subsequent addition of 25 vol% of DMSO. Absorbance followed at 552 nm before and 543 nm after addition of DMSO due to the shift of the absorption maximum Normalized to initial absorbance and absorbance was adjusted to dilution upon addition of DMSO.

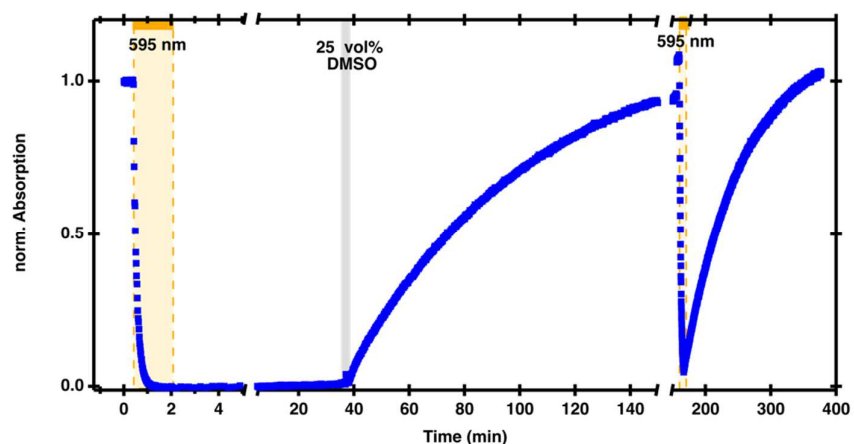


Figure 4.45. time dependent UV–Vis spectroscopy of 25 μM **DASA-5** in toluene with subsequent addition of 25 vol% of DMSO. Absorbance followed at 597 nm before and 592 nm after addition of DMSO due to the shift of the absorption maximum. Normalized to initial absorbance and absorbance was adjusted to dilution upon addition of DMSO.

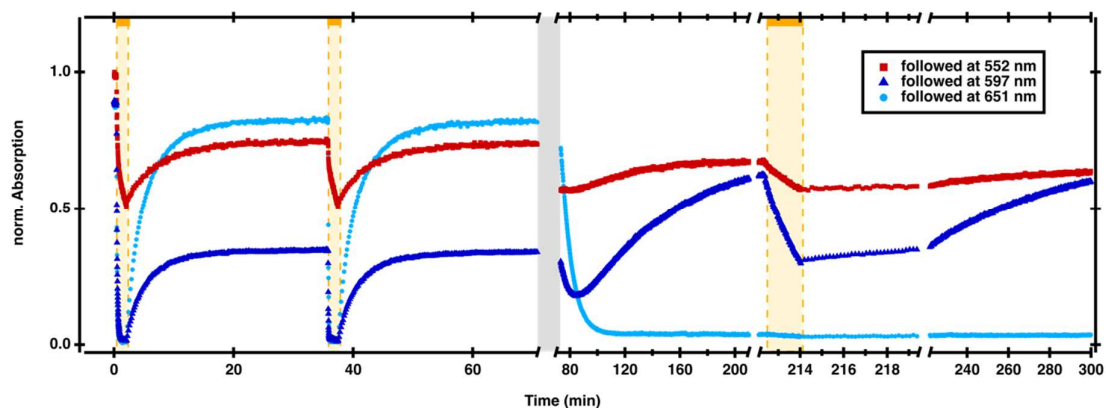


Figure 4.46. time dependent UV–Vis spectroscopy of 10 μM **DASA-3**, 10 μM **DASA-4** and 25 μM **DASA-5** in toluene with subsequent addition of 25 vol% of DMSO. Normalized to initial absorbance at 552 nm and absorbance was adjusted to dilution upon addition of DMSO. Followed at each DASA λ_{max} overlapping with absorbances of the other DASAs.

4.4.13 Deconvolution of Figure 4.5c.

To separate overlapping absorbances the absorbance of the mixture of **DASA-3, 4 and 5**, the normalized absorbance (at 651 nm) of **DASA-3** was subtracted from the absorbance of the mixture normalized at 651 nm (**Figure 4.43**) resulting in the absorbance of the mixture of **DASA 4 and 5** and the normalization was reversed. The absorbance of **DASA-3 (Figure 4.43)** normalized at 552 nm was then subtracted from the absorbance of the mixture of **DASA-4 and 5** leaving the absorbance of **DASA-5**. To obtain the absorbance of **DASA-4** the absorbance of **DASA-5** at 597 nm (**Figure 4.44**) was subtracted from the previously obtained mixture of **DASA-4 and 5** now normalized at 597 nm. To obtain the absorbance of **DASA-3** the absorbances of **DASA-4 and 5** were subtracted in analogous fashion as above. The script to do so was written with Wolfram Language using the Wolfram Mathematica v12 environment. Code available upon request from the authors.

4.4.14 Relevance on stabilizer for DASA switching

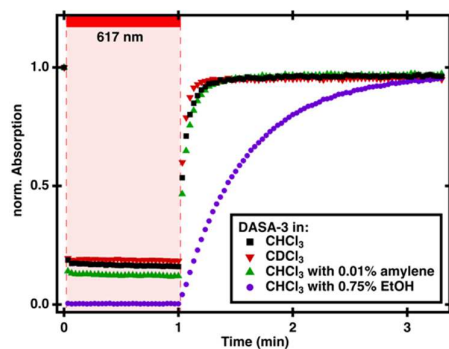


Figure 4.47. time dependent UV–Vis spectroscopy of 10 μM **DASA-3** in chloroform with different stabilizers at λ_{max} at 646 nm. The sample was irradiated with 617 nm LED for 100 seconds and the subsequent recovery in the dark was observed.

4.4.15 DASA photophysical properties upon additives

4.4.15.1 Additives in dichloromethane for DASA-1

Table 4.1: photophysical properties of DASA 1 in toluene with 1 vol% additives.

vol% of additive	A	k_B min^{-1}
	0.77	1.04
acetonitrile		
1	0.69	0.82
2	0.71	0.80
5	0.69	0.75
10	0.66	0.50
diethylether		
1	0.74	0.99
2	0.74	0.98
5	0.68	1.01
10	0.67	0.98

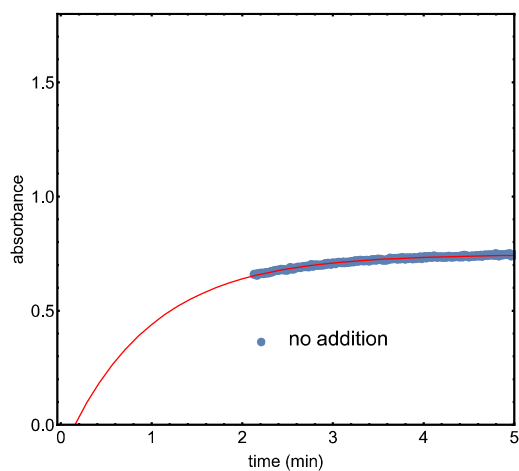


Figure 4.48. Time dependent UV–Vis spectroscopy of 10 μM **DASA-1** in dichloromethane irradiated for 100 s with a 530 nm LED followed at λ_{max} 617 nm including the fit used to determine k_{B} listed in Table 4.1.

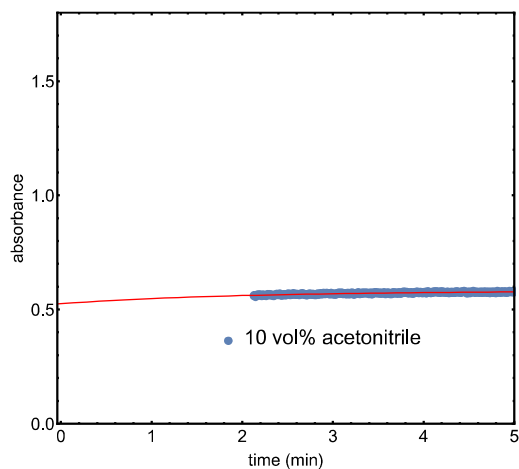


Figure 4.49. Time dependent UV–Vis spectroscopy of 10 μM **DASA-1** in dichloromethane with 10 vol% acetonitrile irradiated for 100 s with a 530 nm LED followed at λ_{max} 617 nm including the fit used to determine k_{B} listed in Table 4.1.

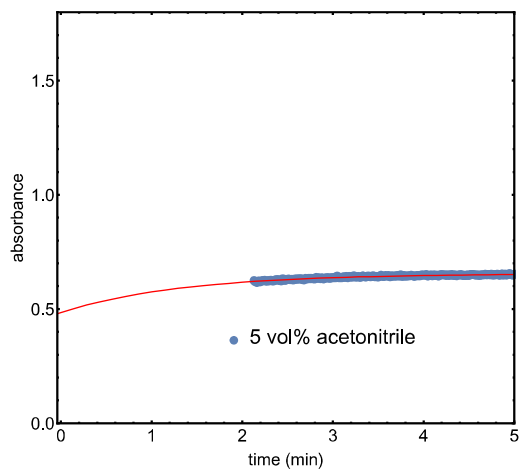


Figure 4.50. Time dependent UV–Vis spectroscopy of 10 μM **DASA-1** in dichloromethane with 5 vol% acetonitrile irradiated for 150 s with a 617 nm LED followed at λ_{max} 617 nm including the fit used to determine k_{B} listed in Table 4.1.

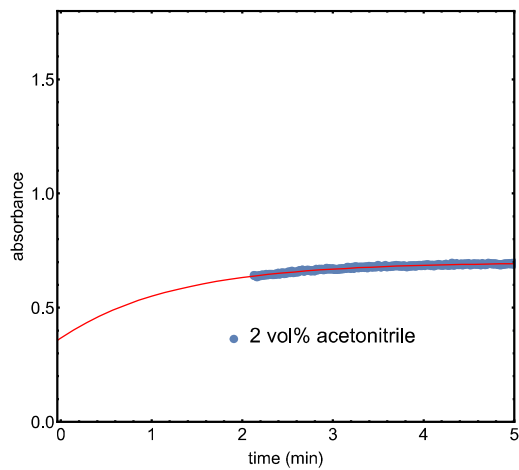


Figure 4.51. Time dependent UV–Vis spectroscopy of 10 μM **DASA-1** in dichloromethane with 1 vol% acetonitrile irradiated for 150 s with a 617 nm LED followed at λ_{max} 617 nm including the fit used to determine k_{B} listed in Table 4.1.

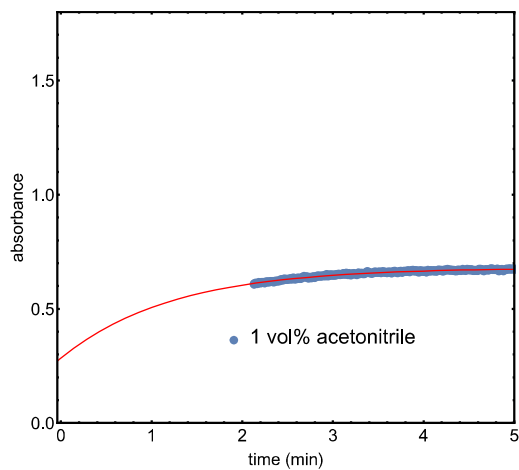


Figure 4.52. Time dependent UV–Vis spectroscopy of 10 μM **DASA-1** in dichloromethane with 1 vol% acetonitrile irradiated for 150 s with a 617 nm LED followed at λ_{max} 617 nm including the fit used to determine k_{B} listed in Table 4.1.

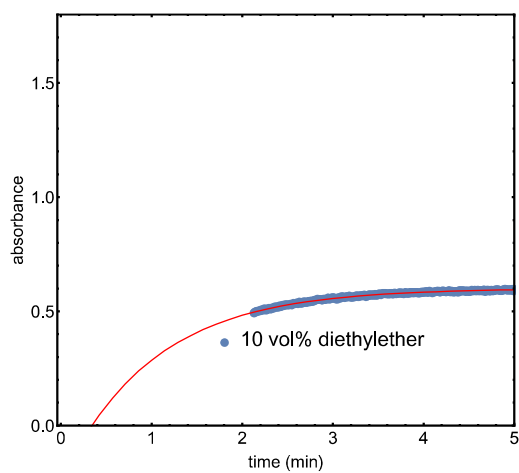


Figure 4.53. Time dependent UV–Vis spectroscopy of 10 μM **DASA-1** in dichloromethane with 10 vol% diethylether irradiated for 150 s with a 617 nm LED followed at λ_{max} 617 nm including the fit used to determine k_{B} listed in Table 4.1.

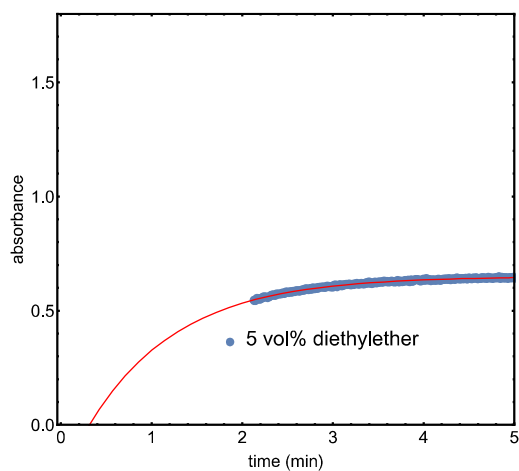


Figure 4.54. Time dependent UV–Vis spectroscopy of 10 μM **DASA-1** in dichloromethane with 5 vol% diethylether irradiated for 150 s with a 617 nm LED followed at λ_{max} 617 nm including the fit used to determine k_{B} listed in Table 4.1.

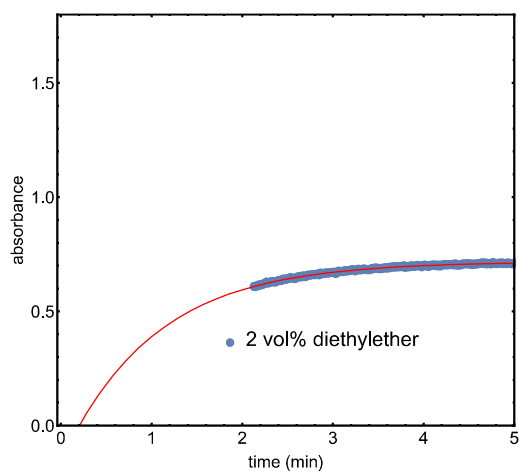


Figure 4.55. Time dependent UV–Vis spectroscopy of 10 μM **DASA-1** in dichloromethane with 2 vol% diethylether irradiated for 150 s with a 617 nm LED followed at λ_{max} 617 nm including the fit used to determine k_{B} listed in Table 4.1.

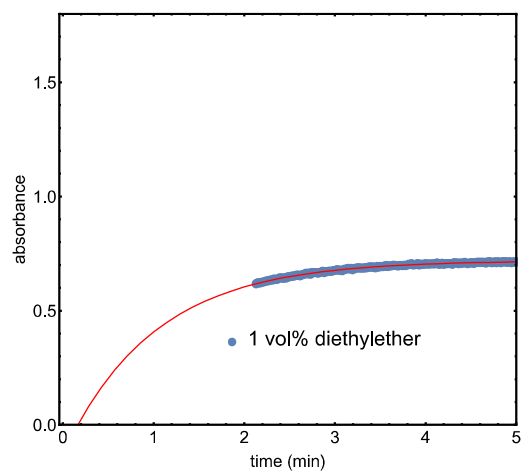


Figure 4.56. Time dependent UV–Vis spectroscopy of 10 μM **DASA-1** in dichloromethane with 1 vol% diethylether irradiated for 150 s with a 617 nm LED followed at λ_{max} 617 nm including the fit used to determine k_B listed in Table 4.1.

4.4.15.2 Additives in dichloromethane for DASA-2

Table 4.2: photophysical properties of DASA 1 in toluene with 1 vol% additives.

vol% of additive	A	k_B min ⁻¹
	0.55	0.022
acetonitrile		
1	0.56	0.024
2	0.59	0.027
5	0.59	0.032
10	0.47	0.029
diethylether		
1	0.74	0.032
2	0.74	0.030
5	0.68	0.029
10	0.67	0.028

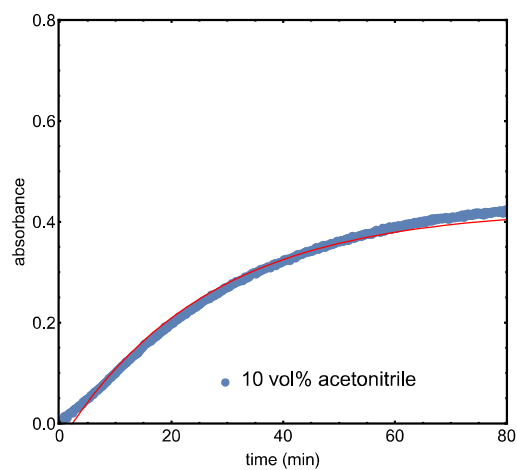


Figure 4.57. Time dependent UV–Vis spectroscopy of 10 μM **DASA-2** in dichloromethane with 10 vol% acetonitrile irradiated for 150 s with a 617 nm LED followed at λ_{max} 617 nm including the fit used to determine k_{B} listed in Table 4.2.

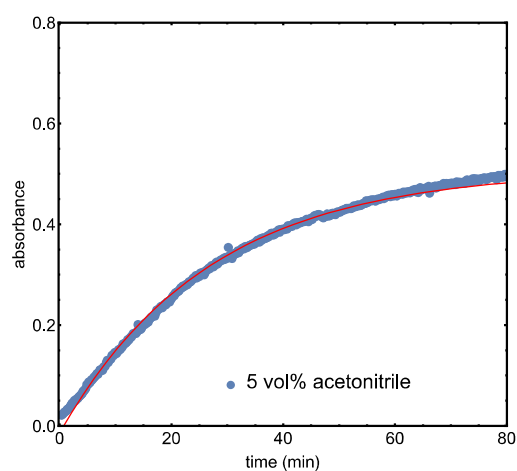


Figure 4.58. Time dependent UV–Vis spectroscopy of 10 μM **DASA-2** in dichloromethane with 5 vol% acetonitrile irradiated for 150 s with a 617 nm LED followed at λ_{max} 617 nm including the fit used to determine k_{B} listed in Table 4.2.

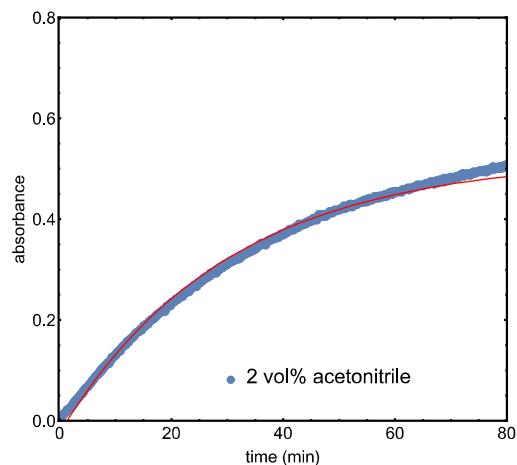


Figure 4.59. Time dependent UV–Vis spectroscopy of 10 μM **DASA-2** in dichloromethane with 2 vol% acetonitrile irradiated for 150 s with a 617 nm LED followed at λ_{max} 617 nm including the fit used to determine k_{B} listed in Table 4.2.

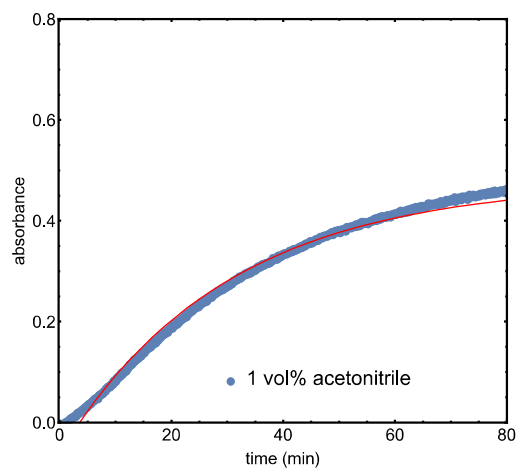


Figure 4.60. Time dependent UV–Vis spectroscopy of 10 μM **DASA-2** in dichloromethane with 1 vol% acetonitrile irradiated for 150 s with a 617 nm LED followed at λ_{max} 617 nm including the fit used to determine k_{B} listed in Table 4.2.

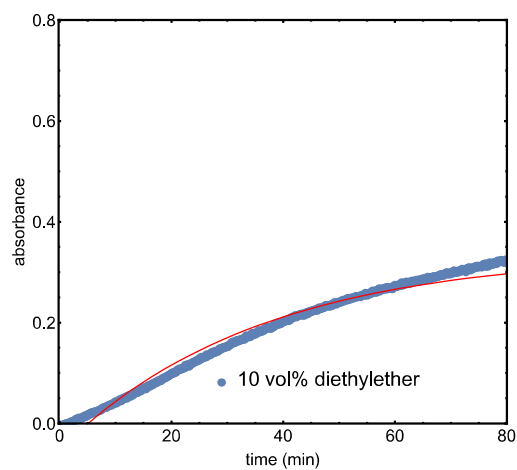


Figure 4.61. Time dependent UV–Vis spectroscopy of 10 μM **DASA-2** in dichloromethane with 10 vol% diethylether irradiated for 150 s with a 617 nm LED followed at λ_{max} 617 nm including the fit used to determine k_{B} listed in Table 4.2.

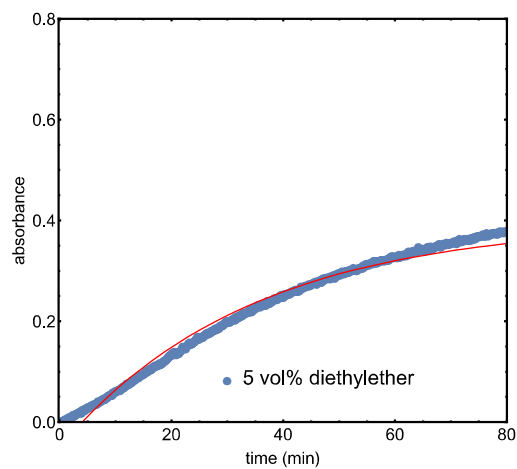


Figure 4.62. Time dependent UV–Vis spectroscopy of 10 μM **DASA-2** in dichloromethane with 5 vol% diethylether irradiated for 150 s with a 617 nm LED followed at λ_{max} 617 nm including the fit used to determine k_{B} listed in Table 4.2.

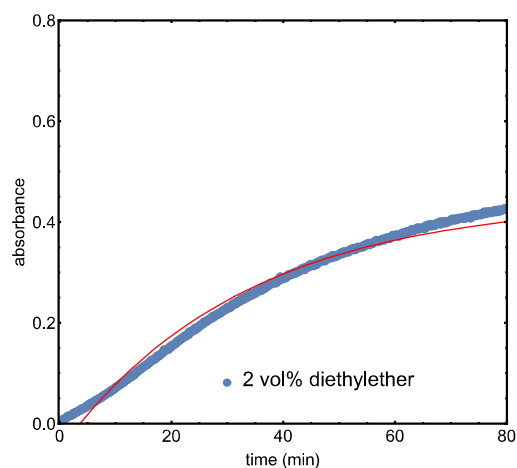


Figure 4.63. Time dependent UV–Vis spectroscopy of 10 μM **DASA-2** in dichloromethane with 2 vol% diethylether irradiated for 150 s with a 617 nm LED followed at λ_{max} 617 nm including the fit used to determine k_{B} listed in Table 4.2.

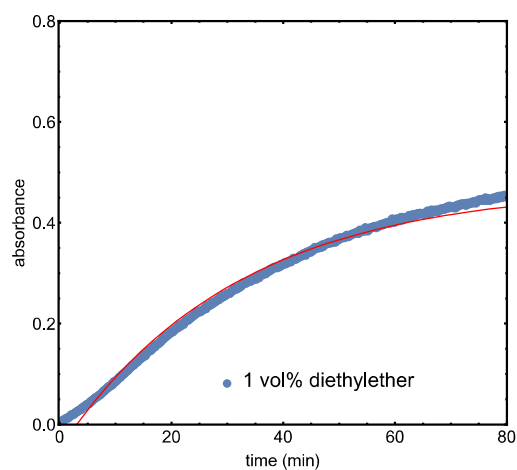


Figure 4.64. Time dependent UV–Vis spectroscopy of 10 μM **DASA-2** in dichloromethane with 1 vol% diethylether irradiated for 150 s with a 617 nm LED followed at λ_{max} 617 nm including the fit used to determine k_{B} listed in Table 4.2.

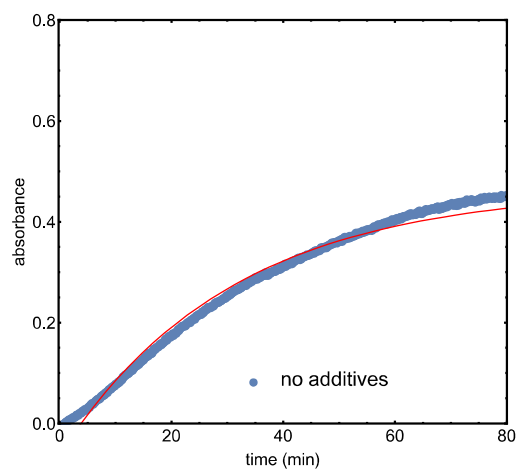


Figure 4.65. Time dependent UV–Vis spectroscopy of 10 μM **DASA-2** in dichloromethane irradiated for 150 s with a 617 nm LED followed at λ_{max} 617 nm including the fit used to determine k_{B} listed in Table 4.2.

4.4.16 Additives in dichloromethane for DASA-3

Table 4.3: photophysical properties of DASA-3 in dichloromethane with 1 vol% additives.

vol% of additive	A	k_B min ⁻¹
	1.26	17.5
acetonitrile		
1	1.26	12.9
2	1.21	9.3
5	1.14	5.9
10	0.9	3.5
diethylether		
1	1.25	10.4
2	1.21	7.4
5	1.14	3.9
10	1.08	2.4

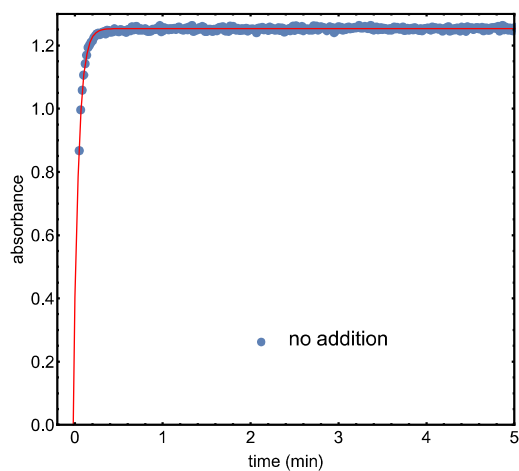


Figure 4.66. Time dependent UV–Vis spectroscopy of 10 μM **DASA-3** in dichloromethane irradiated for 100 s with a 617 nm LED followed at λ_{max} 650 nm including the fit used to determine k_{B} listed in Table 4.3.

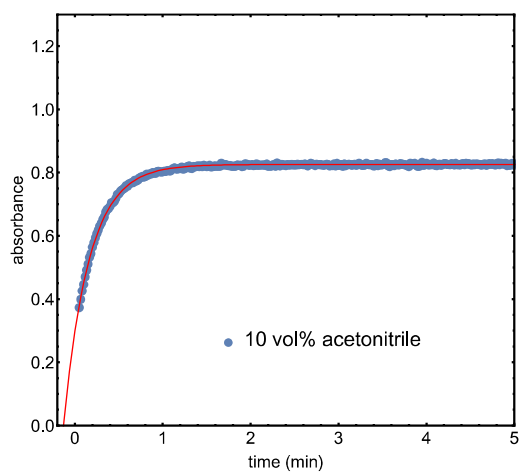


Figure 4.67. Time dependent UV–Vis spectroscopy of 10 μM **DASA-3** in dichloromethane with 10 vol% acetonitrile irradiated for 100 s with a 617 nm LED followed at λ_{max} 650 nm including the fit used to determine k_{B} listed in Table 4.3.

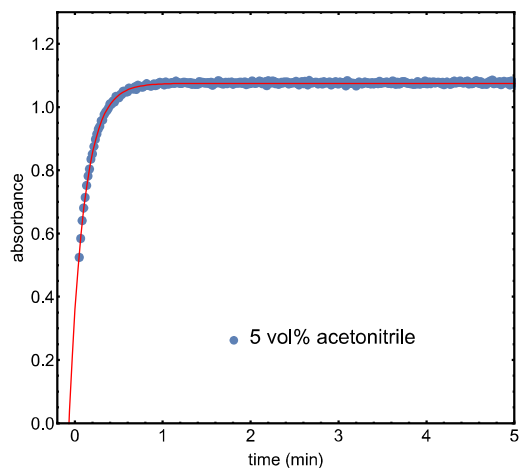


Figure 4.68. Time dependent UV–Vis spectroscopy of 10 μM **DASA-3** in dichloromethane with 5 vol% acetonitrile irradiated for 100 s with a 617 nm LED followed at λ_{max} 650 nm including the fit used to determine k_{B} listed in Table 4.3.

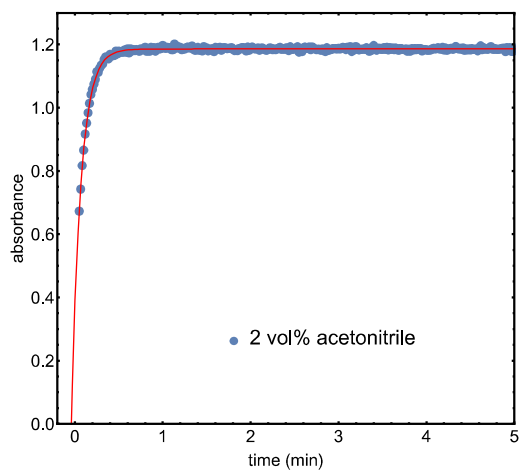


Figure 4.69. Time dependent UV–Vis spectroscopy of 10 μM **DASA-3** in dichloromethane with 2 vol% acetonitrile irradiated for 100 s with a 617 nm LED followed at λ_{max} 650 nm including the fit used to determine k_{B} listed in Table 4.3.

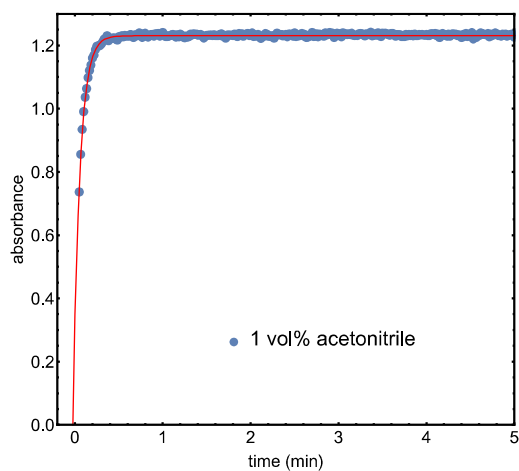


Figure 4.70. Time dependent UV–Vis spectroscopy of 10 μM **DASA-3** in dichloromethane with 1 vol% acetonitrile irradiated for 100 s with a 617 nm LED followed at λ_{max} 650 nm including the fit used to determine k_{B} listed in Table 4.3.

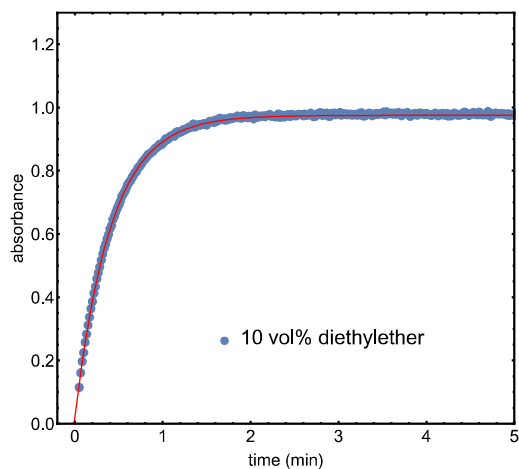


Figure 4.71. Time dependent UV–Vis spectroscopy of 10 μM **DASA-3** in dichloromethane with 10 vol% diethylether irradiated for 100 s with a 617 nm LED followed at λ_{max} 650 nm including the fit used to determine k_{B} listed in Table 4.3.

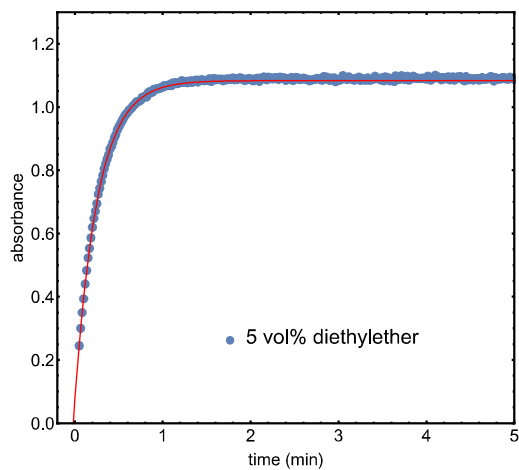


Figure 4.72. Time dependent UV–Vis spectroscopy of 10 μM **DASA-3** in dichloromethane with 5 vol% diethylether irradiated for 100 s with a 617 nm LED followed at λ_{max} 650 nm including the fit used to determine k_{B} listed in Table 4.3.

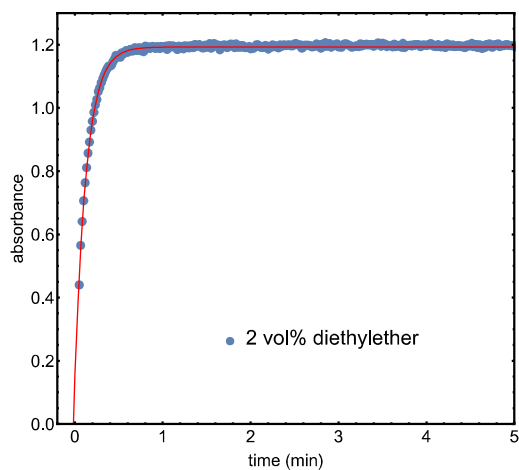


Figure 4.73. Time dependent UV–Vis spectroscopy of 10 μM **DASA-3** in dichloromethane with 2 vol% diethylether irradiated for 100 s with a 617 nm LED followed at λ_{max} 650 nm including the fit used to determine k_{B} listed in Table 4.3.

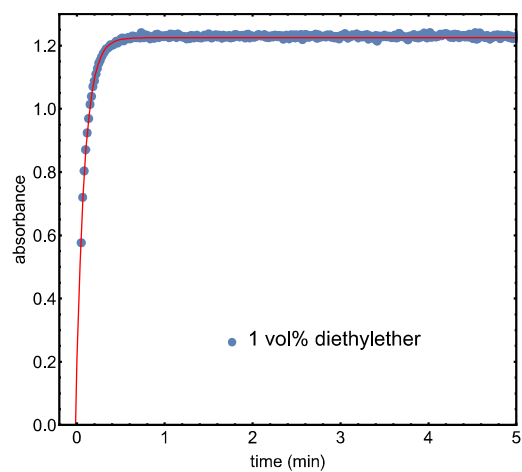


Figure 4.74. Time dependent UV–Vis spectroscopy of 10 μM **DASA-3** in dichloromethane with 1 vol% diethylether irradiated for 100 s with a 617 nm LED followed at λ_{max} 650 nm including the fit used to determine k_B listed in Table 4.3.

4.4.16.1 Additives in toluene for DASA-3

Table 4.4: photophysical properties of DASA-3 in toluene with different vol% of additives.

vol% of additive	A	k_B min ⁻¹
–	1.03	1.39
dichloromethane		
1	1.04	2.18
5	1.07	2.59
10	1.08	2.91
ethanol		
0.5	0.86	0.34
1	0.63	0.32
2	0.39	0.36
diethylether		
0.5	1.03	0.91
1	1.05	0.81
2	0.99	0.52

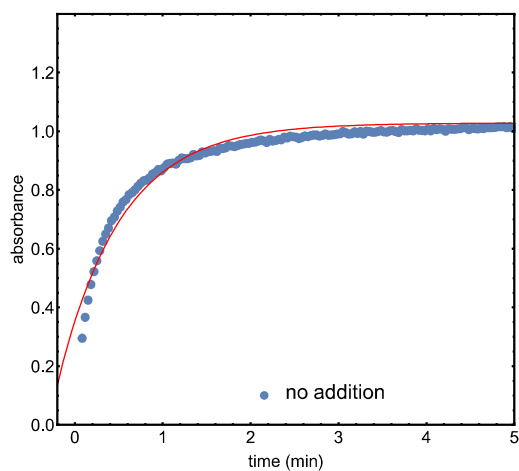


Figure 4.75. Time dependent UV–Vis spectroscopy of 10 μM DASA-3 in toluene irradiated for 100 s with a 617 nm LED followed at λ_{max} 650 nm including the fit used to determine k_B listed in Table 4.4.

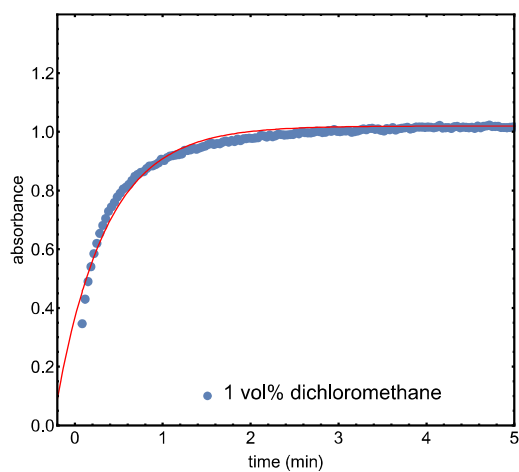


Figure 4.76. Time dependent UV–Vis spectroscopy of 10 μM DASA-3 in toluene irradiated with 1 vol% dichloromethane after irradiation for 100 s with a 617 nm LED followed at λ_{max} 650 nm including the fit used to determine k_B listed in Table 4.4.

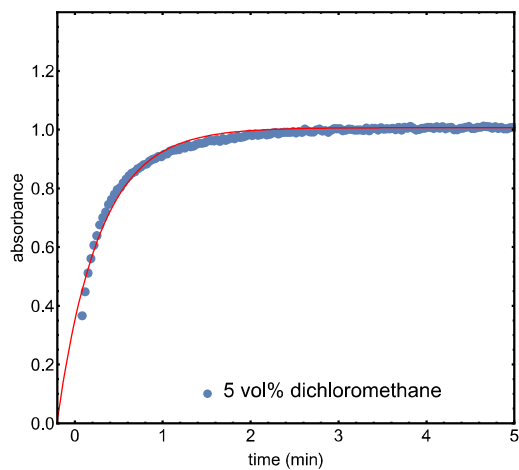


Figure 4.77. Time dependent UV–Vis spectroscopy of 10 μM **DASA-3** in toluene with irradiated 5 vol% dichloromethane after irradiation for 100 s with a 617 nm LED followed at λ_{max} 650 nm including the fit used to determine k_{B} listed in Table 4.4.

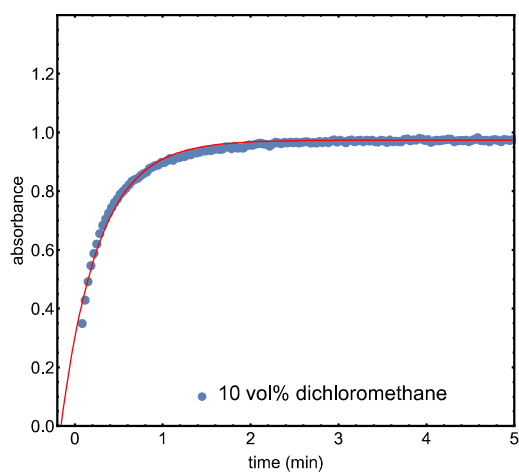


Figure 4.78. Time dependent UV–Vis spectroscopy of 10 μM **DASA-3** in toluene irradiated with 10 vol% dichloromethane after irradiation for 100 s with a 617 nm LED followed at λ_{max} 650 nm including the fit used to determine k_{B} listed in Table 4.4.

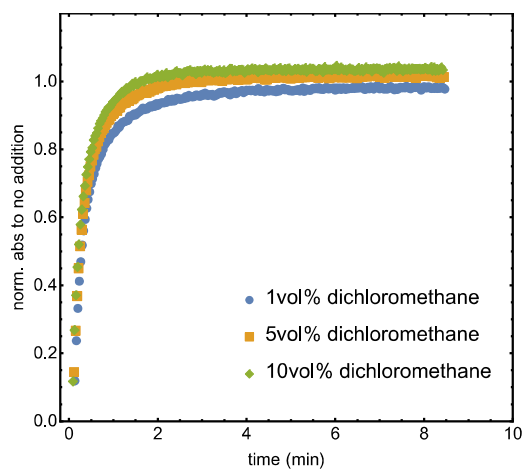


Figure 4.79. Comparison of time dependent UV–Vis spectroscopy of 10 μM **DASA-3** in toluene with 1 vol%, 5 vol% and 10 vol% dichloromethane after irradiation for 100 s with a 617 nm LED followed at λ_{max} 650 nm.

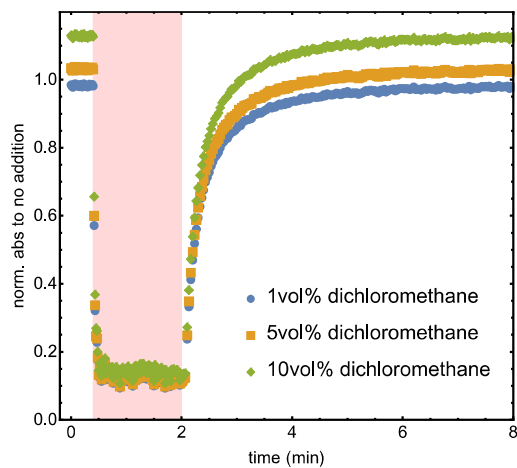


Figure 4.80. Comparison of time dependent UV–Vis spectroscopy of 10 μM **DASA-3** in toluene with 1 vol%, 5 vol% and 10 vol% dichloromethane which was after 25 seconds irradiated for 100 s with a 617 nm LED (red shaded area) followed at λ_{max} 650 nm.

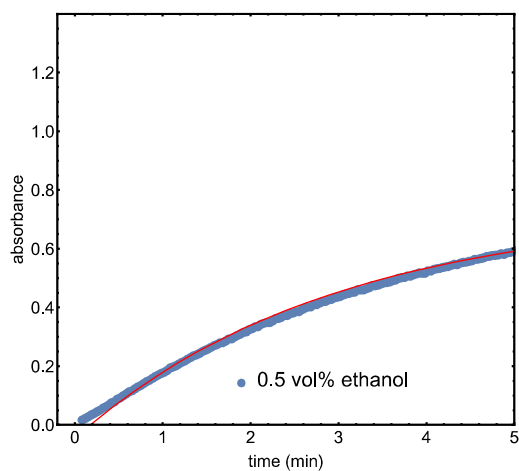


Figure 4.81. Time dependent UV–Vis spectroscopy of 10 μM **DASA-3** in toluene with 0.5 vol% ethanol after irradiation for 100 s with a 617 nm LED followed at λ_{max} 650 nm including the fit used to determine k_{B} listed in Table 4.4.

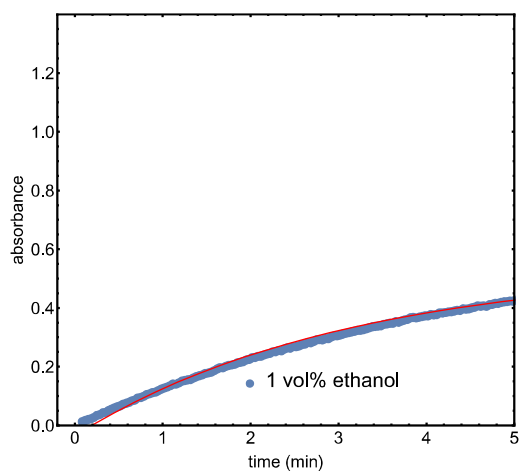


Figure 4.82. Time dependent UV–Vis spectroscopy of 10 μM **DASA-3** in toluene with 1.0 vol% ethanol after irradiation for 100 s with a 617 nm LED followed at λ_{max} 650 nm including the fit used to determine k_{B} listed in Table 4.4.

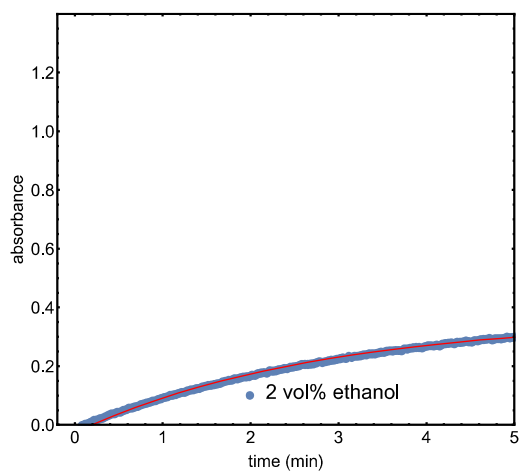


Figure 4.83. Time dependent UV–Vis spectroscopy of 10 μM **DASA-3** in toluene with 2.0 vol% ethanol after irradiation for 100 s with a 617 nm LED followed at λ_{max} 650 nm including the fit used to determine k_{B} listed in Table 4.4.

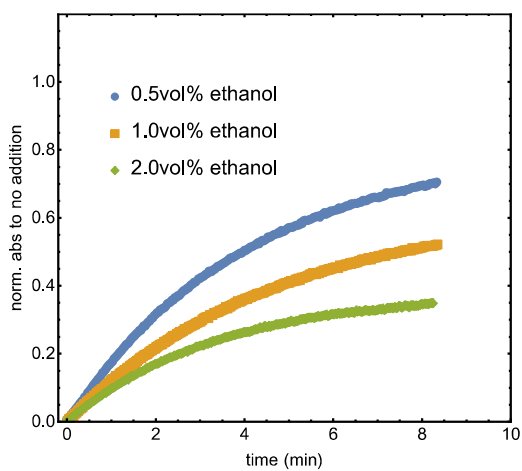


Figure 4.84. Comparison of time dependent UV–Vis spectroscopy of 10 μM **DASA-3** in toluene with 0.5 vol%, 1.0 vol% and 2.0 vol% ethanol after irradiation for 100 s with a 617 nm LED followed at λ_{max} 650 nm.

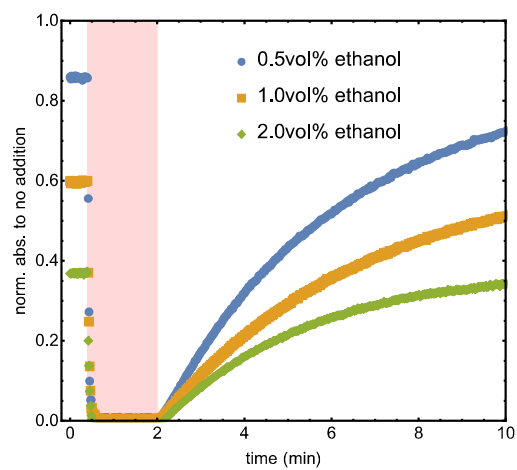


Figure 4.85. Comparison of time dependent UV–Vis spectroscopy of 10 μM DASA-3 in toluene with 0.5 vol%, 1.0 vol% and 2.0 vol% ethanol which was after 25 seconds irradiated for 100 s with a 617 nm LED followed at λ_{max} 650 nm.

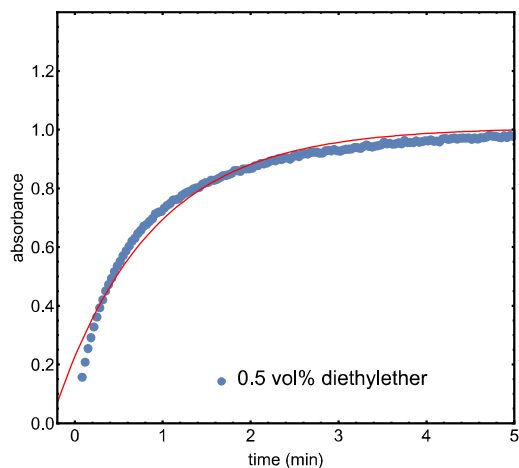


Figure 4.86. Time dependent UV–Vis spectroscopy of 10 μM **DASA-3** in toluene with 0.5 vol% diethylether after irradiation for 100 s with a 617 nm LED followed at λ_{max} 650 nm including the fit used to determine k_{B} listed in Table 4.4.

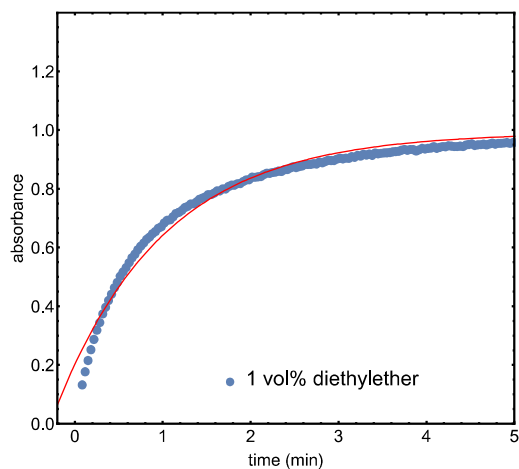


Figure 4.87. Time dependent UV–Vis spectroscopy of 10 μM **DASA-3** in toluene with 1 vol% diethylether after irradiation for 100 s with a 617 nm LED followed at λ_{max} 650 nm including the fit used to determine k_{B} listed in Table 4.4.

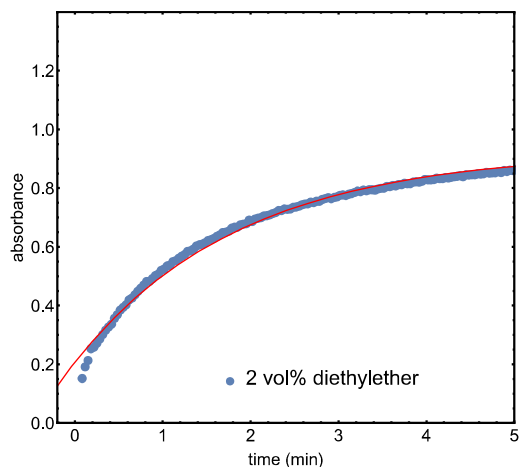


Figure 4.88. Time dependent UV-Vis spectroscopy of 10 μM DASA-3 in toluene with 2.0 vol% diethylether after irradiation for 100 s with a 617 nm LED followed at λ_{max} 650 nm including the fit used to determine k_B listed in Table 4.4.

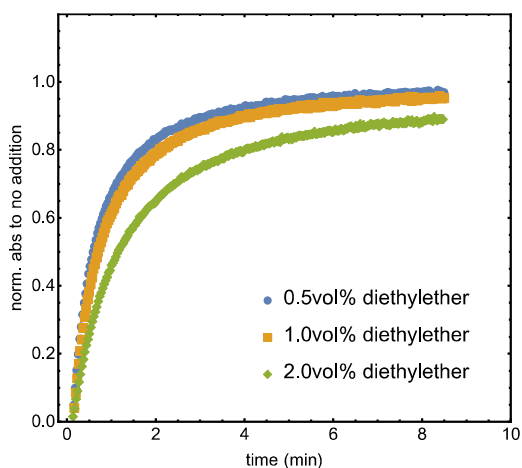


Figure 4.89. Comparison of time dependent UV-Vis spectroscopy of 10 μM DASA-3 in toluene with 0.5 vol%, 1.0 vol% and 2.0 vol% diethylether after irradiation for 100 s with a 617 nm LED followed at λ_{max} 650 nm.

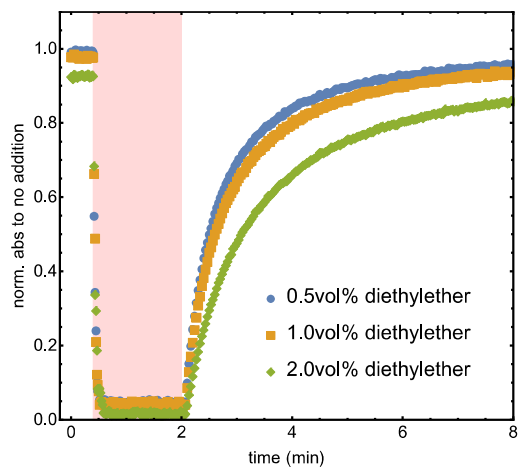


Figure 4.90. Comparison of time dependent UV–Vis spectroscopy of 10 μ M **DASA-3** in toluene with 0.5 vol%, 1.0 vol% and 2.0 vol% diethylether which was after 25 seconds irradiated for 100 s with a 617 nm LED followed at λ_{max} 650 nm.

4.4.17 DFT Calculations

4.4.17.1 General DFT procedure

Initial energy pathway was calculated in SMD chloroform starting from **A**. The bond lengths of Z/E isomerization were scanned from **A-B** etc and transition state search (Berny optimization) was run using the opt=(ts,calcfc,noeigentest,maxstep=1) keywords. The negative frequency of each transition state was visualized using either GaussView or Avogadro to verify that it was along the expected reaction coordinate.

4.4.17.2 DMA MeBarb Geometries

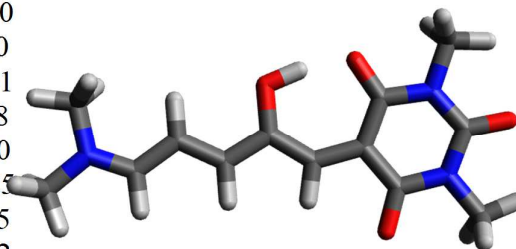
4.4.17.2.1 Chloroform

A

Electronic energy: -970.1522592 Hartree

Free energy: -970.224207 Hartree

C	1.95454	-1.04892	-0.00007
C	4.23325	-0.12133	0.00002
C	2.30982	1.41753	-0.00007
C	1.40648	0.27815	-0.00009
C	0.03367	0.59389	-0.00004
O	1.28857	-2.10377	0.00005
O	1.94775	2.59348	0.00000
C	-1.13087	-0.17170	-0.00010
C	-2.35485	0.51426	0.00000
C	-3.59745	-0.11444	-0.00001
C	-4.75806	0.65916	0.00008
N	-5.99439	0.19131	0.00010
O	-1.19256	-1.52503	-0.00025
H	-4.66934	1.74455	0.00015
C	-6.24577	-1.24489	0.00002
C	-7.15409	1.07314	0.00014
H	-5.81025	-1.70656	-0.89147
H	-7.32201	-1.41280	0.00009
H	-5.81011	-1.70668	0.89138
H	-6.82575	2.11268	0.00024
H	-7.76103	0.88567	0.89074
H	-7.76098	0.88583	-0.89053
H	-3.64374	-1.19767	-0.00009
H	-2.31353	1.60083	0.00009



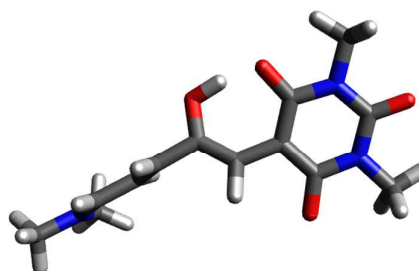
H	-0.25666	-1.87755	-0.00015
H	-0.14849	1.66530	0.00005
O	5.44201	-0.30488	0.00014
N	3.33676	-1.18285	-0.00002
N	3.68212	1.14539	-0.00009
C	4.57909	2.30076	-0.00004
H	5.60304	1.93846	-0.00060
H	4.39296	2.90832	-0.88733
H	4.39375	2.90771	0.88784
C	3.87033	-2.54645	0.00010
H	3.52173	-3.07643	-0.88781
H	4.95456	-2.48580	0.00005
H	3.52181	-3.07627	0.88814

A-B

Electronic energy: -970.1183039 Hartree

Free energy: -970.1876696 Hartree

C	2.03828	-1.08080	-0.10823
C	4.08786	0.22607	0.24688
C	1.96686	1.36959	-0.25917
C	1.30692	0.10149	-0.30633
C	-0.11184	0.11936	-0.66563
O	1.56389	-2.25339	-0.19604
O	1.42211	2.46441	-0.46376
C	-1.05194	-0.81631	-0.43731
C	-2.46387	-0.61030	-0.86284
C	-3.41682	-0.19960	-0.00472
C	-4.76587	-0.06330	-0.48130
N	-5.76303	0.34109	0.23546
O	-0.88859	-2.00499	0.19226
H	-4.98045	-0.31496	-1.51850
C	-5.60784	0.72215	1.64785
C	-7.11656	0.43149	-0.31636
H	-5.33422	-0.15645	2.23601
H	-6.55824	1.11694	2.00091
H	-4.83789	1.48978	1.74004
H	-7.11223	0.09813	-1.35279
H	-7.45371	1.46828	-0.25378
H	-7.77767	-0.20258	0.27845
H	-3.17264	0.02510	1.02880
H	-2.73628	-0.83388	-1.89610
H	0.10660	-2.23322	0.09808
H	-0.44551	1.03083	-1.15479
O	5.29751	0.25483	0.47132
N	3.40461	-0.96990	0.19687
N	3.34348	1.36634	0.03894
C	4.01569	2.66063	0.08751
H	4.04389	3.10977	-0.90851



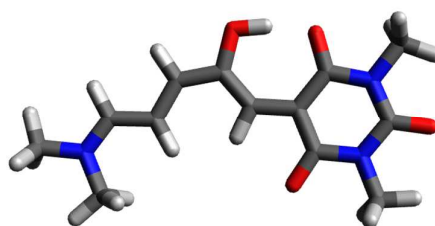
H	3.46798	3.32709	0.75490
H	5.02766	2.50638	0.45270
C	4.20372	-2.17280	0.41758
H	4.90090	-2.32432	-0.41084
H	4.77475	-2.06479	1.34055
H	3.52483	-3.01770	0.48812
B			

Electronic energy: -970.143952 Hartree

Free energy: -970.21775 Hartree

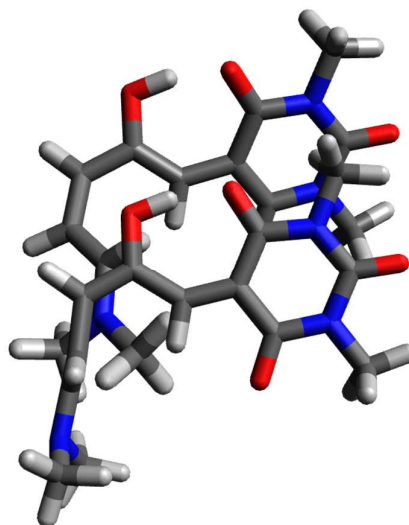
C	-2.18879	-1.12611	0.00051
C	-3.92781	0.61557	-0.00020
C	-1.55820	1.28623	-0.00033
C	-1.16628	-0.11522	-0.00003
C	0.22180	-0.35039	0.00009
O	-1.98561	-2.35526	0.00133
O	-0.76790	2.22983	-0.00043
C	1.01209	-1.49578	-0.00059
C	2.41555	-1.39412	-0.00057
C	3.23384	-0.26422	0.00068
C	4.61487	-0.44705	-0.00041
N	5.52606	0.51271	0.00013
O	0.54106	-2.77400	-0.00196
H	5.01053	-1.46060	-0.00189
C	5.13466	1.91668	0.00234
C	6.95064	0.20964	-0.00070
H	4.54245	2.14873	-0.88843
H	6.03394	2.53170	0.00186
H	4.54483	2.14662	0.89524
H	7.09263	-0.87155	-0.00338
H	7.42187	0.63379	0.89092
H	7.42162	0.63813	-0.89036
H	2.82080	0.73842	0.00228
H	2.92287	-2.36002	-0.00184
H	-0.45467	-2.73976	-0.00073
H	0.78519	0.57739	0.00055
O	-5.11261	0.91664	-0.00033
N	-3.51425	-0.71057	0.00037
N	-2.92755	1.56885	-0.00038
C	-3.30516	2.98198	-0.00080
H	-4.38938	3.04620	-0.00083
H	-2.89792	3.46959	0.88662
H	-2.89791	3.46907	-0.88850
C	-4.53608	-1.75951	0.00094
H	-4.42043	-2.38306	0.88890
H	-5.51135	-1.28200	0.00127
H	-4.42120	-2.38332	-0.88695

B-B'



Electronic energy: -970.1213666 Hartree
Free energy: -970.1923777 Hartree

C	-2.11660	1.09574	0.07691
C	-3.51498	-0.92878	0.04967
C	-1.08156	-1.20629	-0.17170
C	-0.91704	0.26642	-0.08808
C	0.36879	0.71218	-0.18333
O	-2.10364	2.32628	0.16919
O	-0.14718	-1.98023	-0.30314
C	1.00265	2.01592	-0.15161
C	2.35008	2.08416	-0.31893
C	3.26806	0.95169	-0.57542
C	3.97242	0.36401	0.41368
N	4.93523	-0.61458	0.28013
O	0.31874	3.16503	0.04234
H	3.81203	0.68065	1.44384
C	5.10650	-1.20285	-1.03271
C	5.05678	-1.55247	1.38674
H	4.20037	-1.73525	-1.36637
H	5.93777	-1.91025	-1.00046
H	5.34336	-0.42587	-1.76479
H	4.98598	-1.01198	2.33361
H	6.03087	-2.04584	1.34116
H	4.27064	-2.32269	1.36224
H	3.40379	0.64805	-1.61150
H	2.76513	3.09330	-0.29194
H	-0.64900	2.96865	0.11392
H	1.09262	-0.08899	-0.31270
O	-4.62451	-1.42107	0.10701
N	-3.33256	0.45483	0.12689
N	-2.37429	-1.70361	-0.09294
C	-2.52101	-3.15972	-0.17514
H	-3.57568	-3.40306	-0.08789
H	-2.12994	-3.51010	-1.13158
H	-1.95632	-3.62556	0.63370
C	-4.51852	1.30566	0.28064
H	-4.56353	2.01369	-0.54784
H	-5.39689	0.66783	0.28074
H	-4.45063	1.85683	1.21978
B'			



Electronic energy: -970.1397139 Hartree
Free energy: -970.2113926 Hartree

C	1.82440	1.09835	0.25284
C	3.40158	-0.78328	0.13125
C	1.07518	-1.11524	-0.60474
C	0.78935	0.27450	-0.29854

C	-0.55084	0.67881	-0.48855
O	1.67871	2.28349	0.61850
O	0.24154	-1.92157	-1.01981
C	-1.15406	1.93479	-0.50769
C	-2.54414	2.05308	-0.73597
C	-3.52448	1.10111	-0.48618
C	-3.34390	0.06132	0.44060
N	-4.15382	-0.96698	0.60266
O	-0.46911	3.10785	-0.48471
H	-2.50820	0.11141	1.13583
C	-5.27729	-1.20559	-0.29465
C	-4.02054	-1.86816	1.74028
H	-6.12231	-0.55835	-0.03505
H	-5.58509	-2.24722	-0.19823
H	-4.97593	-1.01488	-1.32658
H	-3.16410	-1.56990	2.34486
H	-3.87915	-2.89158	1.38264
H	-4.92709	-1.82526	2.35183
H	-4.50142	1.23277	-0.94118
H	-2.86214	3.00661	-1.15635
H	0.42321	2.92936	-0.07212
H	-1.20415	-0.14314	-0.76541
O	4.51780	-1.23659	0.34280
N	3.08546	0.53751	0.41805
N	2.38984	-1.55379	-0.40900
C	2.68251	-2.94896	-0.73512
H	3.76113	-3.07440	-0.77346
H	2.25936	-3.61328	0.02305
H	2.23612	-3.18468	-1.70046
C	4.12667	1.39389	0.98864
H	3.89044	1.62913	2.02884
H	5.07163	0.86131	0.93335
H	4.17919	2.32179	0.41909

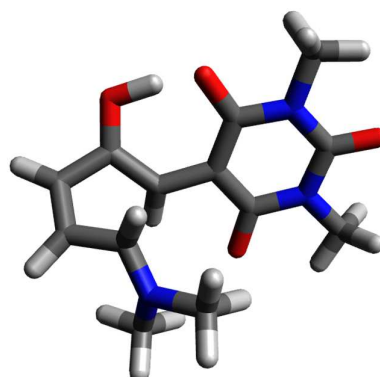
B'-C

Electronic energy: -970.1239689 Hartree

Free energy: -970.1910783 Hartree

C	1.15724	1.29054	0.10721
C	2.95638	-0.35498	0.06660
C	0.70438	-0.97399	-0.71641
C	0.24527	0.34496	-0.38199
C	-1.18223	0.58863	-0.59040
O	0.88087	2.50871	0.37770
O	-0.01776	-1.85636	-1.19569
C	-1.84745	1.84994	-0.61275
C	-3.28699	1.72547	-0.54520
C	-3.64267	0.60390	0.11894
C	-2.51406	-0.10890	0.73796
N	-2.55183	-1.45660	0.88528

O	-1.28274	3.01140	-0.52860
H	-2.04939	0.40511	1.57718
C	-3.06442	-2.29612	-0.18764
C	-1.57383	-2.11584	1.73729
H	-3.60147	-3.14821	0.23894
H	-2.23238	-2.66102	-0.80371
H	-3.75577	-1.73157	-0.81587
H	-1.21889	-1.42272	2.50250
H	-0.72291	-2.47576	1.14452
H	-2.04349	-2.97254	2.23010
H	-4.65933	0.23036	0.21587
H	-3.96116	2.49019	-0.91369
H	-0.24342	2.86210	-0.16329
H	-1.61737	-0.13742	-1.27276
O	4.12168	-0.66791	0.28007
N	2.47390	0.91868	0.32313
N	2.05582	-1.25883	-0.45271
C	2.58480	-2.58965	-0.74589
H	3.39490	-2.51560	-1.47404
H	2.97305	-3.04446	0.16752
H	1.77200	-3.18759	-1.14883
C	3.40037	1.93291	0.82906
H	3.05751	2.29716	1.79875
H	4.37883	1.47129	0.92772
H	3.44694	2.76991	0.13070
C			



Electronic energy: -970.1422979 Hartree
Free energy: -970.2093747 Hartree

C	0.94918	1.20195	0.20867
C	2.94082	-0.16487	0.12477
C	0.80009	-0.98417	-0.78243
C	0.15722	0.23357	-0.33759
C	-1.33163	0.30876	-0.48530
O	0.52256	2.40875	0.59698
O	0.21629	-1.89683	-1.36459
C	-1.94596	1.63095	-0.90767
C	-3.34765	1.63783	-0.46281

C	-3.49976	0.68466	0.46765
C	-2.22654	-0.07708	0.75296
N	-2.47474	-1.46918	1.05355
O	-1.34705	2.56042	-1.43899
H	-1.76290	0.36762	1.64488
C	-2.99093	-2.24594	-0.06658
C	-1.36173	-2.14900	1.70317
H	-3.38937	-3.19245	0.31086
H	-2.21650	-2.47231	-0.81647
H	-3.81031	-1.70722	-0.55345
H	-0.99156	-1.54212	2.53474
H	-0.52804	-2.36533	1.01713
H	-1.71621	-3.10203	2.10837
H	-4.41118	0.46659	1.01805
H	-4.07307	2.37311	-0.78984
H	-0.17060	2.71758	-0.01975
H	-1.60925	-0.39545	-1.28306
O	4.12731	-0.33384	0.36670
N	2.29098	1.02021	0.44468
N	2.16222	-1.12274	-0.49608
C	2.79025	-2.38068	-0.90222
H	3.83011	-2.36039	-0.58904
H	2.26741	-3.21476	-0.43118
H	2.72292	-2.48890	-1.98620
C	3.07451	2.11642	1.02683
H	2.68690	2.36878	2.01470
H	4.10220	1.77482	1.10866
H	3.02005	2.99201	0.37894

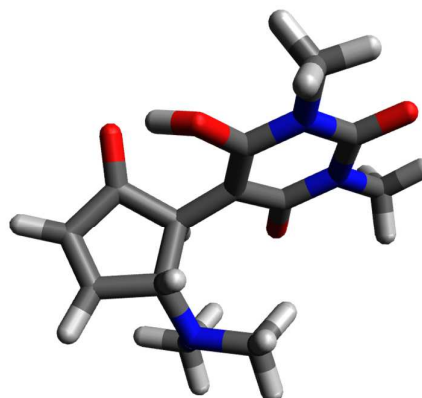
Eps = 7.5

A

Electronic energy: -970.1563494 Hartree

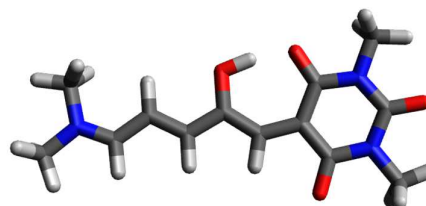
Free energy: -970.2282678 Hartree

C	1.95527	-1.04588	-0.00018
C	4.23379	-0.12110	0.00004
C	2.30963	1.41572	-0.00014
C	1.40809	0.27844	-0.00016
C	0.02992	0.59398	-0.00009



O	1.28898	-2.10287	-0.00009
O	1.94819	2.59352	0.00005
C	-1.12922	-0.17187	-0.00009
C	-2.36048	0.51111	-0.00004
C	-3.59726	-0.11861	0.00000
C	-4.76088	0.65954	0.00005
N	-5.99293	0.19244	0.00011
O	-1.18989	-1.52644	-0.00013
H	-4.66962	1.74472	0.00003
C	-6.24842	-1.24461	0.00014
C	-7.15367	1.07503	0.00011
H	-5.81375	-1.70562	-0.89167
H	-7.32510	-1.40815	0.00023
H	-5.81360	-1.70561	0.89187
H	-6.82535	2.11441	0.00011
H	-7.75882	0.88380	0.89076
H	-7.75883	0.88380	-0.89053
H	-3.64705	-1.20171	0.00000
H	-2.32197	1.59791	-0.00003
H	-0.25151	-1.87555	-0.00000
H	-0.15442	1.66489	-0.00005
O	5.44384	-0.30436	0.00023
N	3.33812	-1.18177	-0.00007
N	3.68282	1.14492	-0.00007
C	4.57925	2.30084	0.00008
H	5.60352	1.93953	-0.00036
H	4.39379	2.90811	-0.88756
H	4.39437	2.90751	0.88826
C	3.87096	-2.54575	0.00004
H	3.52305	-3.07555	-0.88825
H	4.95523	-2.48615	0.00004
H	3.52305	-3.07543	0.88840

A-B

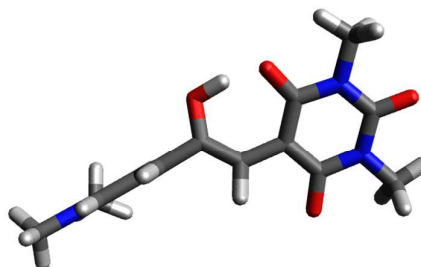


Electronic energy: -970.1258868 Hartree

Free energy: -970.1956473 Hartree

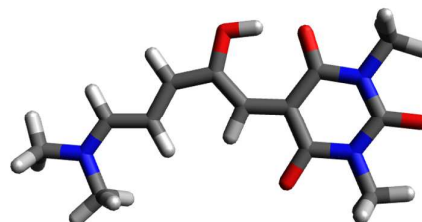
C	2.04128	-1.08033	-0.11063
C	4.09109	0.22477	0.24296
C	1.96992	1.36925	-0.25565
C	1.30872	0.10208	-0.30400
C	-0.11150	0.12018	-0.66229
O	1.56601	-2.25268	-0.20166

O	1.42478	2.46507	-0.45765
C	-1.05341	-0.81222	-0.42573
C	-2.46608	-0.61111	-0.85308
C	-3.42126	-0.19888	0.00040
C	-4.77090	-0.06666	-0.48273
N	-5.76957	0.33855	0.22930
O	-0.88391	-1.99584	0.21306
H	-4.98101	-0.32325	-1.51952
C	-5.62148	0.72539	1.64105
C	-7.12116	0.42597	-0.32817
H	-5.34391	-0.14998	2.23195
H	-6.57588	1.11483	1.98903
H	-4.85660	1.49816	1.73221
H	-7.11178	0.09056	-1.36381
H	-7.45826	1.46284	-0.26738
H	-7.78286	-0.20709	0.26695
H	-3.18330	0.03161	1.03424
H	-2.73511	-0.83909	-1.88605
H	0.10833	-2.22615	0.11154
H	-0.44553	1.02758	-1.15860
O	5.30195	0.25318	0.46382
N	3.40797	-0.97076	0.19292
N	3.34684	1.36567	0.03958
C	4.01994	2.66001	0.08882
H	4.05070	3.10865	-0.90736
H	3.47225	3.32659	0.75598
H	5.03123	2.50599	0.45579
C	4.20722	-2.17487	0.40929
H	4.89929	-2.32762	-0.42317
H	4.78249	-2.06798	1.32967
H	3.52833	-3.01935	0.48385
B			



Electronic energy: -970.1480347 Hartree
 Free energy: -970.2224808 Hartree

C	-2.18605	-1.12305	0.00063
C	-3.93413	0.60785	-0.00008
C	-1.56732	1.28628	0.00029
C	-1.17041	-0.11039	0.00031
C	0.22457	-0.34199	0.00032
O	-1.97833	-2.35390	0.00093
O	-0.78129	2.23556	-0.00016
C	1.01291	-1.48241	-0.00048
C	2.42298	-1.38458	-0.00055
C	3.23847	-0.25987	0.00052
C	4.62431	-0.44766	-0.00041
N	5.53234	0.50857	0.00009
O	0.54514	-2.76308	-0.00174
H	5.01691	-1.46242	-0.00169



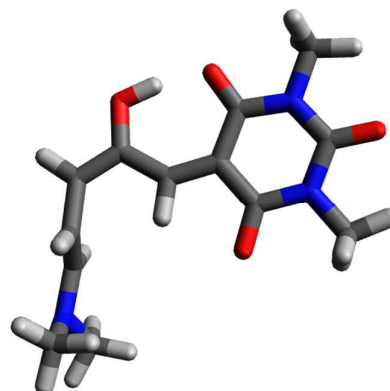
C	5.14537	1.91557	0.00184
C	6.95805	0.20434	-0.00074
H	4.55453	2.14710	-0.88945
H	6.04733	2.52617	0.00138
H	4.55656	2.14545	0.89490
H	7.09929	-0.87670	-0.00243
H	7.42619	0.63191	0.89044
H	7.42567	0.63461	-0.89089
H	2.82879	0.74421	0.00193
H	2.92814	-2.35162	-0.00173
H	-0.45230	-2.72835	-0.00030
H	0.78581	0.58706	0.00086
O	-5.12151	0.90429	-0.00063
N	-3.51497	-0.71524	0.00029
N	-2.93855	1.56469	-0.00006
C	-3.32135	2.97643	-0.00058
H	-4.40575	3.03718	-0.00087
H	-2.91701	3.46578	0.88723
H	-2.91656	3.46527	-0.88848
C	-4.53142	-1.76938	0.00034
H	-4.41400	-2.39216	0.88862
H	-5.50926	-1.29719	0.00032
H	-4.41402	-2.39226	-0.88788

B-B'

Electronic energy: -970.1239785 Hartree

Free energy: -970.1950876 Hartree

C	-2.11715	1.09511	0.07606
C	-3.51465	-0.92819	0.04812
C	-1.08240	-1.20701	-0.16929
C	-0.91726	0.26565	-0.08656
C	0.36849	0.71105	-0.18077
O	-2.10314	2.32625	0.16824
O	-0.14738	-1.98101	-0.30021
C	1.00252	2.01486	-0.14743
C	2.34966	2.08506	-0.31447
C	3.26913	0.95423	-0.57379
C	3.97350	0.36390	0.41408
N	4.93771	-0.61313	0.27717
O	0.31629	3.16310	0.04891
H	3.81225	0.67624	1.44546
C	5.10752	-1.19909	-1.03741
C	5.05847	-1.55520	1.38109
H	4.20113	-1.73178	-1.36989
H	5.93933	-1.90589	-1.00729
H	5.34167	-0.42095	-1.76911
H	4.98778	-1.01793	2.32978
H	6.03175	-2.04980	1.33289
H	4.27138	-2.32429	1.35301

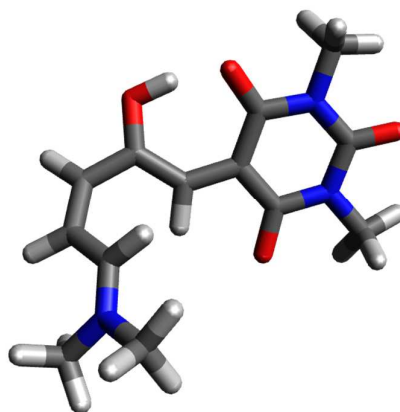


H	3.40583	0.65437	-1.61092
H	2.76392	3.09460	-0.28565
H	-0.65183	2.96329	0.11779
H	1.09261	-0.08968	-0.31030
O	-4.62478	-1.42028	0.10368
N	-3.33292	0.45542	0.12272
N	-2.37436	-1.70407	-0.08951
C	-2.52147	-3.16052	-0.16892
H	-3.57516	-3.40445	-0.07276
H	-2.13892	-3.51213	-1.12843
H	-1.95068	-3.62464	0.63652
C	-4.51932	1.30679	0.27218
H	-4.55847	2.01717	-0.55453
H	-5.39842	0.67013	0.26423
H	-4.45733	1.85373	1.21424
B'			

Electronic energy: -970.1436117

Free energy: -970.2148698 Hartree

C	1.80875	1.09455	0.26006
C	3.41323	-0.76230	0.14198
C	1.09862	-1.11640	-0.61905
C	0.79271	0.26380	-0.30557
C	-0.55810	0.65527	-0.49868
O	1.64386	2.27681	0.63633
O	0.27975	-1.93175	-1.05037
C	-1.16050	1.90475	-0.53345
C	-2.55536	2.02549	-0.77375
C	-3.53794	1.09256	-0.49841
C	-3.35441	0.06051	0.44586
N	-4.16360	-0.96011	0.61923
O	-0.47846	3.08073	-0.51475
H	-2.51980	0.12091	1.14146
C	-5.29097	-1.20992	-0.27313
C	-4.02409	-1.85651	1.76164
H	-6.13658	-0.56664	-0.00782
H	-5.59011	-2.25316	-0.17005
H	-4.99614	-1.01987	-1.30661
H	-3.16878	-1.55078	2.36384
H	-3.87997	-2.87965	1.40515
H	-4.93234	-1.81377	2.36992
H	-4.51993	1.22463	-0.94218
H	-2.86415	2.96446	-1.23222
H	0.40690	2.90626	-0.08045
H	-1.20758	-0.17448	-0.76077
O	4.53411	-1.20365	0.36240
N	3.07779	0.55138	0.43293
N	2.41742	-1.54123	-0.41339
C	2.73043	-2.93024	-0.74684

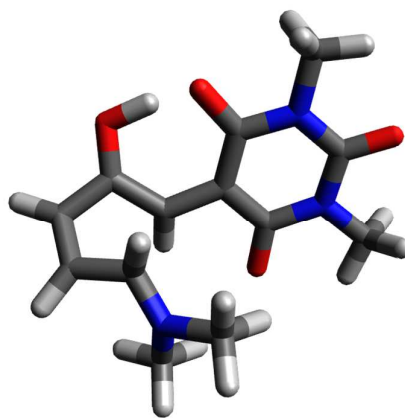


H	3.81077	-3.04244	-0.77634
H	2.30890	-3.60569	0.00245
H	2.29698	-3.16456	-1.71840
C	4.10130	1.41778	1.02005
H	3.85596	1.63688	2.06176
H	5.05544	0.90187	0.96445
H	4.14298	2.35267	0.46122
B'-C			

Electronic energy: -970.1268174 Hartree

Free energy: -970.1940328 Hartree

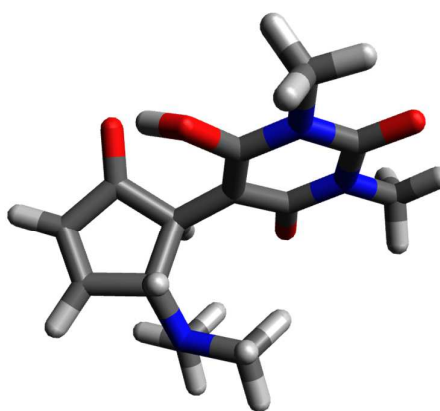
C	1.14939	1.28957	0.11004
C	2.95473	-0.34763	0.06804
C	0.70827	-0.97184	-0.72461
C	0.24236	0.34305	-0.38459
C	-1.18749	0.58134	-0.59068
O	0.86682	2.50636	0.38398
O	-0.00743	-1.85369	-1.21503
C	-1.85387	1.84197	-0.61989
C	-3.29270	1.71658	-0.54595
C	-3.64255	0.59716	0.12487
C	-2.50826	-0.11117	0.74030
N	-2.54423	-1.45890	0.89296
O	-1.28806	3.00438	-0.54543
H	-2.04446	0.40595	1.57829
C	-3.05838	-2.30186	-0.17655
C	-1.55819	-2.11228	1.74056
H	-3.57860	-3.16203	0.25437
H	-2.22893	-2.65519	-0.80319
H	-3.76456	-1.74486	-0.79490
H	-1.20602	-1.41768	2.50570
H	-0.70617	-2.46518	1.14489
H	-2.01979	-2.97358	2.23280
H	-4.65804	0.22271	0.23010
H	-3.97035	2.47799	-0.91501
H	-0.25228	2.85611	-0.16981
H	-1.62059	-0.14622	-1.27290
O	4.12207	-0.65637	0.28145
N	2.46752	0.92292	0.32720
N	2.05892	-1.25412	-0.45365
C	2.59304	-2.58289	-0.74776
H	3.38518	-2.50968	-1.49584
H	3.00503	-3.02543	0.16098
H	1.77699	-3.19200	-1.12658
C	3.38909	1.94009	0.83670
H	3.04285	2.30136	1.80627
H	4.36920	1.48260	0.93751
H	3.43509	2.77777	0.13908
C			



Electronic energy: -970.1449186 Hartree

Free energy: -970.2121902 Hartree

C	-0.94374	-1.19810	0.21357
C	-2.94049	0.15891	0.12609
C	-0.80552	0.98381	-0.78703
C	-0.15666	-0.22893	-0.33872
C	1.33234	-0.30008	-0.48662
O	-0.51223	-2.40064	0.60971
O	-0.22648	1.89729	-1.37395
C	1.94526	-1.61858	-0.92317
C	3.34446	-1.63581	-0.47197
C	3.49768	-0.69033	0.46637
C	2.22658	0.07323	0.75507
N	2.47709	1.46371	1.06490
O	1.34467	-2.53761	-1.47094
H	1.76102	-0.37604	1.64365
C	2.99799	2.24467	-0.05026
C	1.35839	2.14057	1.70859
H	3.39232	3.19109	0.33162
H	2.22671	2.47185	-0.80345
H	3.81999	1.70851	-0.53536
H	0.98446	1.53209	2.53727
H	0.52816	2.35397	1.01724
H	1.70753	3.09485	2.11541
H	4.40908	-0.48085	1.02020
H	4.06891	-2.37052	-0.80275
H	0.18976	-2.70953	0.00479
H	1.60961	0.41083	-1.27839
O	-4.12826	0.32395	0.36840
N	-2.28614	-1.02184	0.44952
N	-2.16750	1.11809	-0.49898
C	-2.80118	2.37258	-0.90747
H	-3.83971	2.35073	-0.59022
H	-2.27960	3.20993	-0.44089
H	-2.73944	2.47667	-1.99222
C	-3.06373	-2.11915	1.03847
H	-2.67629	-2.36126	2.02897
H	-4.09383	-1.78418	1.11626
H	-3.00264	-2.99855	0.39646



Eps = 10

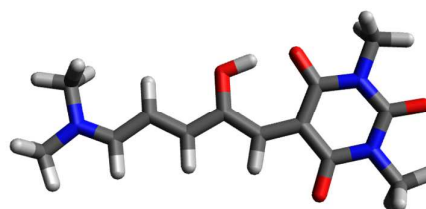
A

Electronic energy: -970.1582549 Hartree

Free energy: -970.2301951 Hartree

C	1.95527	-1.04421	0.00008
C	4.23411	-0.12148	-0.00004
C	2.30989	1.41495	0.00010
C	1.40895	0.27888	0.00007
C	0.02818	0.59472	0.00009
O	1.28859	-2.10207	0.00000
O	1.94902	2.59365	0.00007
C	-1.12842	-0.17131	0.00005
C	-2.36320	0.51043	0.00006
C	-3.59704	-0.12000	0.00003
C	-4.76238	0.65987	0.00002
N	-5.99232	0.19267	-0.00000
O	-1.18866	-1.52624	-0.00002
H	-4.67036	1.74497	0.00004
C	-6.24924	-1.24487	-0.00002
C	-7.15384	1.07523	-0.00003
H	-5.81475	-1.70530	-0.89199
H	-7.32609	-1.40668	-0.00000
H	-5.81471	-1.70533	0.89191
H	-6.82582	2.11462	-0.00000
H	-7.75817	0.88208	0.89059
H	-7.75809	0.88211	-0.89072
H	-3.64803	-1.20308	-0.00001
H	-2.32596	1.59731	0.00009
H	-0.24904	-1.87407	0.00013
H	-0.15689	1.66541	0.00014
O	5.44469	-0.30498	-0.00007
N	3.33847	-1.18146	-0.00003
N	3.68352	1.14436	-0.00006
C	4.57995	2.30027	-0.00012
H	5.60426	1.93916	-0.00074
H	4.39470	2.90749	-0.88786
H	4.39561	2.90694	0.88820
C	3.87049	-2.54574	-0.00008
H	3.52252	-3.07538	-0.88846
H	4.95479	-2.48697	-0.00027
H	3.52283	-3.07534	0.88845

A-B

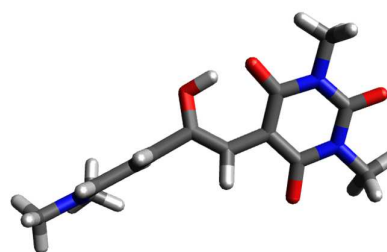


Electronic energy: -970.1292817 Hartree

Free energy: -970.1993221 Hartree

C	2.04261	-1.07999	-0.11168
C	4.09283	0.22393	0.24055
C	1.97154	1.36929	-0.25332
C	1.30958	0.10262	-0.30222
C	-0.11138	0.12100	-0.65972
O	1.56671	-2.25213	-0.20435
O	1.42620	2.46564	-0.45366
C	-1.05400	-0.80993	-0.41914

C	-2.46696	-0.61150	-0.84752
C	-3.42350	-0.19825	0.00337
C	-4.77313	-0.06832	-0.48346
N	-5.77308	0.33702	0.22578
O	-0.88150	-1.99111	0.22400
H	-4.98043	-0.32717	-1.52020
C	-5.62917	0.72613	1.63739
C	-7.12325	0.42366	-0.33539
H	-5.34613	-0.14698	2.22891
H	-6.58671	1.10920	1.98370
H	-4.86950	1.50409	1.72814
H	-7.11064	0.08841	-1.37101
H	-7.46031	1.46053	-0.27467
H	-7.78584	-0.20948	0.25860
H	-3.18875	0.03564	1.03725
H	-2.73426	-0.84220	-1.88025
H	0.10934	-2.22259	0.11854
H	-0.44562	1.02646	-1.15938
O	5.30436	0.25197	0.45906
N	3.40958	-0.97131	0.19056
N	3.34868	1.36529	0.04004
C	4.02248	2.65952	0.08950
H	4.05525	3.10752	-0.90691
H	3.47444	3.32651	0.75589
H	5.03316	2.50551	0.45806
C	4.20886	-2.17613	0.40415
H	4.89815	-2.32924	-0.43054
H	4.78655	-2.07009	1.32308
H	3.52992	-3.02037	0.48064
B			

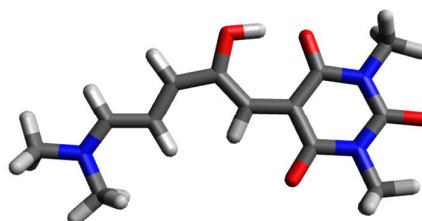


Electronic energy: -970.1498661 Hartree
Free energy: -970.2223971 Hartree

C	2.17174	-1.11857	0.06729
C	3.94187	0.58761	0.02803
C	1.58490	1.29129	-0.07244
C	1.17238	-0.09841	-0.03463
C	-0.22796	-0.31837	-0.04343
O	1.94553	-2.34383	0.16739
O	0.80973	2.24930	-0.12003
C	-1.01247	-1.45482	-0.12659
C	-2.42682	-1.36677	-0.11190
C	-3.24387	-0.25366	0.00493
C	-4.63219	-0.44535	-0.03007
N	-5.54144	0.50186	0.06111
O	-0.53866	-2.72554	-0.27343
H	-5.01932	-1.45641	-0.13973
C	-5.16284	1.90423	0.21110
C	-6.96715	0.19480	0.04040

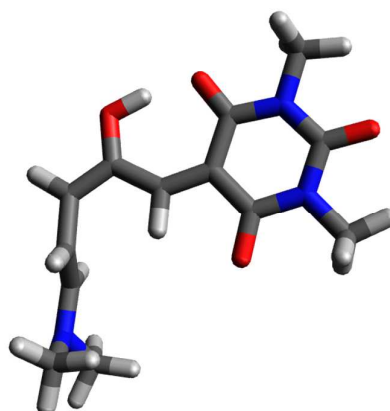
H	-4.64095	2.05557	1.16090
H	-6.06602	2.51256	0.19623
H	-4.51069	2.20843	-0.61209
H	-7.10685	-0.88137	-0.06195
H	-7.43999	0.70804	-0.80129
H	-7.42784	0.53612	0.97165
H	-2.83831	0.74497	0.12441
H	-2.92686	-2.33110	-0.21336
H	0.44762	-2.70492	-0.11504
H	-0.78623	0.61145	0.00462
O	5.13249	0.87201	0.06209
N	3.50670	-0.72851	0.07712
N	2.95984	1.55370	-0.06214
C	3.36308	2.95857	-0.11855
H	4.44357	3.00106	-0.22162
H	2.88255	3.43623	-0.97294
H	3.05473	3.47270	0.79463
C	4.50771	-1.79127	0.18887
H	4.38490	-2.49537	-0.63515
H	5.49243	-1.33534	0.14862
H	4.37863	-2.32330	1.13330

B-B'



Electronic energy: -970.1251708 Hartree
Free energy: -970.1963325 Hartree

C	-2.11747	1.09483	0.07540
C	-3.51441	-0.92801	0.04723
C	-1.08266	-1.20733	-0.16790
C	-0.91733	0.26534	-0.08575
C	0.36834	0.71063	-0.17930
O	-2.10308	2.32627	0.16724
O	-0.14727	-1.98129	-0.29850
C	1.00242	2.01450	-0.14492
C	2.34943	2.08570	-0.31169
C	3.26960	0.95572	-0.57269
C	3.97401	0.36380	0.41436
N	4.93881	-0.61252	0.27547
O	0.31506	3.16223	0.05288
H	3.81245	0.67380	1.44642
C	5.10787	-1.19685	-1.04017
C	5.05904	-1.55709	1.37767
H	4.20136	-1.72954	-1.37231
H	5.93993	-1.90340	-1.01140
H	5.34072	-0.41787	-1.77139
H	4.98847	-1.02181	2.32748
H	6.03187	-2.05239	1.32802
H	4.27140	-2.32552	1.34755
H	3.40663	0.65787	-1.61039
H	2.76331	3.09541	-0.28164

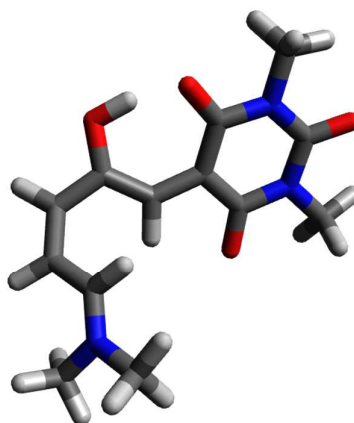


H	-0.65328	2.96083	0.11995
H	1.09265	-0.08987	-0.30883
O	-4.62479	-1.42006	0.10167
N	-3.33310	0.45563	0.12041
N	-2.37421	-1.70434	-0.08748
C	-2.52143	-3.16096	-0.16537
H	-3.57453	-3.40524	-0.06401
H	-2.14374	-3.51320	-1.12662
H	-1.94700	-3.62411	0.63797
C	-4.51979	1.30717	0.26748
H	-4.55617	2.01842	-0.55857
H	-5.39914	0.67096	0.25581
H	-4.46071	1.85237	1.21074
B'			

Electronic energy: -970.1454307 Hartree

Free energy: -970.2166954 Hartree

C	1.80131	1.09320	0.26283
C	3.41747	-0.75245	0.14867
C	1.11056	-1.11578	-0.62927
C	0.79493	0.25952	-0.31092
C	-0.56114	0.64437	-0.50448
O	1.62576	2.27296	0.64679
O	0.29901	-1.93457	-1.07007
C	-1.16345	1.89059	-0.54549
C	-2.56089	2.01288	-0.78938
C	-3.54477	1.08955	-0.50167
C	-3.35939	0.05964	0.44905
N	-4.16822	-0.95753	0.62690
O	-0.48279	3.06804	-0.52873
H	-2.52434	0.12362	1.14379
C	-5.29868	-1.21172	-0.26166
C	-4.02503	-1.85345	1.77011
H	-6.14672	-0.57610	0.01327
H	-5.58842	-2.25782	-0.16172
H	-5.01079	-1.01368	-1.29531
H	-3.17105	-1.54421	2.37216
H	-3.87827	-2.87568	1.41245
H	-4.93452	-1.81310	2.37640
H	-4.52949	1.22349	-0.93872
H	-2.86585	2.94507	-1.26400
H	0.39876	2.89548	-0.08364
H	-1.20874	-0.18910	-0.75930
O	4.53858	-1.18971	0.37975
N	3.07475	0.55925	0.43660
N	2.43082	-1.53446	-0.41742
C	2.75411	-2.92095	-0.75138
H	3.83522	-3.02418	-0.78634
H	2.34242	-3.59998	0.00025



H	2.31836	-3.15905	-1.72087
C	4.09117	1.42765	1.03284
H	3.86512	1.60581	2.08696
H	5.05528	0.93602	0.93981
H	4.09983	2.38071	0.50484

B'-C

Electronic energy: -970.1281166 Hartree
Free energy: -970.1952643 Hartree

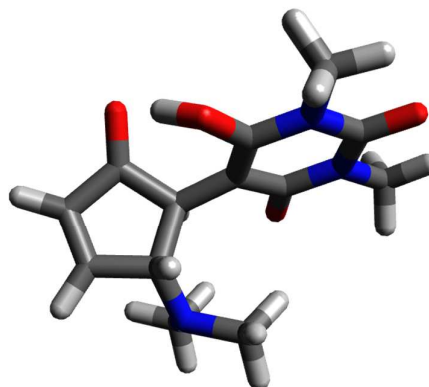
C	1.14583	1.28920	0.11117
C	2.95389	-0.34433	0.06866
C	0.70995	-0.97075	-0.72842
C	0.24102	0.34232	-0.38599
C	-1.18989	0.57815	-0.59093
O	0.86055	2.50539	0.38654
O	-0.00281	-1.85229	-1.22398
C	-1.85683	1.83848	-0.62293
C	-3.29530	1.71262	-0.54588
C	-3.64236	0.59406	0.12781
C	-2.50542	-0.11230	0.74134
N	-2.54050	-1.46006	0.89636
O	-1.29049	3.00128	-0.55280
H	-2.04180	0.40616	1.57868
C	-3.05563	-2.30455	-0.17146
C	-1.55065	-2.11078	1.74170
H	-3.56812	-3.16829	0.26148
H	-2.22762	-2.65265	-0.80310
H	-3.76860	-1.75100	-0.78508
H	-1.19921	-1.41536	2.50643
H	-0.69849	-2.46085	1.14444
H	-2.00859	-2.97389	2.23412
H	-4.65728	0.21915	0.23684
H	-3.97461	2.47260	-0.91489
H	-0.25623	2.85342	-0.17261
H	-1.62213	-0.15000	-1.27315
O	4.12216	-0.65117	0.28197
N	2.46457	0.92483	0.32895
N	2.06014	-1.25200	-0.45401
C	2.59633	-2.58002	-0.74820
H	3.37947	-2.50784	-1.50599
H	3.01983	-3.01627	0.15814
H	1.77871	-3.19444	-1.11477
C	3.38394	1.94327	0.84013
H	3.03578	2.30359	1.80934
H	4.36462	1.48743	0.94256
H	3.43024	2.78101	0.14259

C

Electronic energy: -970.1461261 Hartree

Free energy: -970.2134821 Hartree

C	-0.94112	-1.19622	0.21620
C	-2.94044	0.15596	0.12638
C	-0.80808	0.98358	-0.78914
C	-0.15640	-0.22681	-0.33929
C	1.33271	-0.29590	-0.48732
O	-0.50758	-2.39652	0.61668
O	-0.23127	1.89748	-1.37823
C	1.94511	-1.61246	-0.93108
C	3.34327	-1.63436	-0.47718
C	3.49690	-0.69284	0.46514
C	2.22668	0.07117	0.75594
N	2.47798	1.46078	1.07070
O	1.34384	-2.52642	-1.48653
H	1.76041	-0.38070	1.64282
C	3.00126	2.24425	-0.04166
C	1.35633	2.13585	1.71152
H	3.39334	3.19055	0.34279
H	2.23166	2.47195	-0.79655
H	3.82474	1.70963	-0.52588
H	0.98027	1.52608	2.53827
H	0.52804	2.34823	1.01744
H	1.70276	3.09046	2.11986
H	4.40833	-0.48745	1.02050
H	4.06740	-2.36850	-0.81005
H	0.20086	-2.70479	0.01982
H	1.60966	0.41853	-1.27595
O	-4.12889	0.31897	0.36847
N	-2.28385	-1.02258	0.45188
N	-2.17004	1.11577	-0.50057
C	-2.80632	2.36869	-0.91003
H	-3.84430	2.34599	-0.59114
H	-2.28549	3.20747	-0.44522
H	-2.74690	2.47113	-1.99507
C	-3.05868	-2.12037	1.04399
H	-2.67113	-2.35789	2.03557
H	-4.08983	-1.78839	1.12019
H	-2.99473	-3.00146	0.40462



4.4.17.3 Indoline MeBarb Geometries

4.4.17.3.1 Chloroform

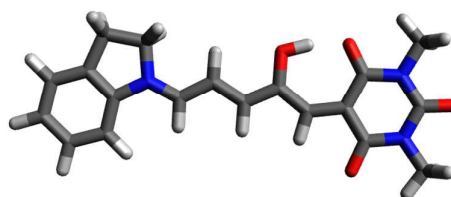
A

Electronic energy: -1199.8736454 Hartree

Free energy: -1199.954509 Hartree

C	-3.81177	-1.02633	-0.02270
C	-3.99663	1.48196	0.03976
C	-3.17773	0.27022	0.02234
C	-1.79525	0.49135	0.04240
O	-3.20047	-2.11002	-0.04340
C	-0.66870	-0.34557	0.04136
C	0.58224	0.27069	0.05225
C	1.79461	-0.43485	0.04269
C	2.99456	0.25263	0.04023
O	-0.69110	-1.69827	0.02866
H	2.98704	1.34021	0.04561
H	1.77020	-1.51911	0.02981
H	0.60501	1.35760	0.06574
H	-1.64510	-1.99153	0.00125
H	-1.54388	1.54825	0.06264
C	5.44137	0.34711	-0.01067
C	4.39349	-1.78221	0.03221
C	6.47893	-0.58746	0.01501
C	5.68327	1.71691	-0.07470
C	5.92119	-1.98762	0.09240
H	3.87474	-2.20789	0.89526
C	7.79701	-0.15539	-0.02106
C	7.01428	2.13698	-0.10911
H	4.87914	2.44459	-0.10109
H	6.21840	-2.47719	1.02398
C	8.06353	1.21616	-0.08307
H	8.61041	-0.87537	-0.00131
H	7.23086	3.19948	-0.15979
H	9.09003	1.56699	-0.11278
N	4.19926	-0.31850	0.03072
H	6.27296	-2.60775	-0.73576
O	-3.53235	2.61816	0.07504
C	-6.00518	0.07166	-0.03033
H	3.95012	-2.19615	-0.87860
C	-5.90468	-2.33924	-0.09213
H	-6.51450	-2.39019	-0.99559
H	-5.16336	-3.13253	-0.09442
H	-6.55319	-2.43113	0.78056
C	-6.26774	2.46618	0.02974
H	-6.88301	2.47550	-0.87173
H	-6.91925	2.42452	0.90436
H	-5.64472	3.35531	0.06777
N	-5.38289	1.30151	0.01458
N	-5.19811	-1.05716	-0.04652
O	-7.22239	-0.02783	-0.05495

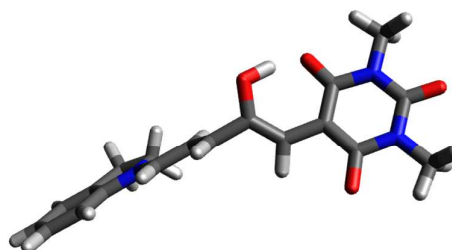
A-B



Electronic energy: -1199.8365872 Hartree

Free energy: -1199.915068 Hartree

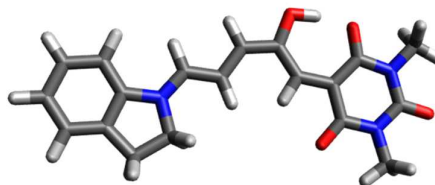
C	3.65409	-0.95853	-0.22342
C	3.79883	1.46711	0.17510
C	3.04902	0.30939	-0.20828
C	1.62349	0.51979	-0.46652
O	3.05462	-2.04800	-0.47199
C	0.75557	-0.25943	-1.13837
C	-0.67328	0.13524	-1.28275
C	-1.63276	-0.28853	-0.43628
C	-2.98866	0.11883	-0.65831
O	1.01589	-1.43070	-1.76708
H	-3.21581	0.74995	-1.51509
H	-1.38304	-0.92036	0.41065
H	-0.94966	0.76642	-2.12982
H	1.86117	-1.80063	-1.31970
H	1.22761	1.45305	-0.07465
C	-5.33734	0.19411	-0.04858
C	-3.84651	-1.06818	1.32502
C	-6.11772	-0.39984	0.93725
C	-5.85486	1.05168	-1.01363
C	-5.28384	-1.27882	1.83102
H	-3.35235	-1.99722	1.03864
C	-7.48344	-0.13858	0.97142
C	-7.22357	1.30366	-0.96712
H	-5.23482	1.51652	-1.77222
H	-5.58510	-2.32563	1.73848
C	-8.03011	0.71531	0.01366
H	-8.11054	-0.59281	1.73248
H	-7.66568	1.96894	-1.70121
H	-9.09396	0.92929	0.02913
N	-3.97847	-0.21085	0.11145
H	-5.37998	-0.99253	2.88067
O	3.33074	2.61100	0.26411
C	5.78971	0.04207	0.43908
H	-3.22194	-0.53252	2.04299
C	5.70508	-2.33279	0.04982
H	6.60145	-2.26067	-0.56799
H	5.99919	-2.62445	1.06146
H	5.01904	-3.06722	-0.36229
C	5.99308	2.39961	0.87040
H	5.37050	3.28980	0.84026
H	6.38304	2.24761	1.87946
H	6.83451	2.50375	0.18223
N	5.16348	1.26561	0.47661
N	5.02299	-1.04161	0.07210
O	6.98121	-0.08180	0.72102
B			



Electronic energy: -1199.8659463 Hartree
Free energy: -1199.9486247 Hartree

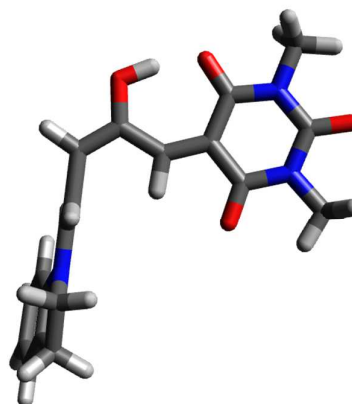
C	3.96259	-1.10037	-0.00005
C	3.15593	1.27803	0.00034
C	2.86707	-0.15715	0.00019
C	1.50951	-0.48691	0.00022
O	3.83943	-2.33705	-0.00021
C	0.78899	-1.69110	0.00014
C	-0.60703	-1.67240	0.00010
C	-1.49339	-0.57993	-0.00014
C	-2.85230	-0.82184	0.00005
O	1.34917	-2.92973	0.00017
H	-3.21228	-1.84779	0.00035
H	-1.13120	0.44248	-0.00051
H	-1.06236	-2.66360	0.00025
H	2.33914	-2.82913	0.00008
H	0.88171	0.39808	0.00036
C	-5.18960	-0.10008	-0.00001
C	-3.50012	1.56626	-0.00048
C	-5.86433	1.12288	-0.00016
C	-5.86670	-1.31678	0.00018
C	-4.87688	2.26456	-0.00028
H	-2.90793	1.80639	0.88745
C	-7.25156	1.14444	-0.00013
C	-7.26253	-1.27958	0.00022
H	-5.34236	-2.26635	0.00030
H	-5.00073	2.89741	0.88235
C	-7.95283	-0.06603	0.00006
H	-7.78506	2.09086	-0.00024
H	-7.81531	-2.21381	0.00036
H	-9.03811	-0.06241	0.00009
N	-3.79901	0.12116	-0.00008
H	-5.00096	2.89749	-0.88280
O	2.28796	2.14649	0.00057
C	5.56239	0.76009	-0.00011
H	-2.90840	1.80598	-0.88883
C	6.34826	-1.56473	-0.00038
H	7.28519	-1.01553	-0.00024
H	6.27922	-2.19482	0.88774
H	6.27926	-2.19435	-0.88884
C	4.86442	3.06574	0.00021
H	5.45449	3.29715	0.88863
H	5.45401	3.29734	-0.88849
H	3.94373	3.64208	0.00052
N	4.50410	1.64723	0.00016
N	5.25110	-0.59447	-0.00013
O	6.71636	1.15836	-0.00030

B-B'



Electronic energy: -1199.8462548 Hartree
Free energy: -1199.9252824 Hartree

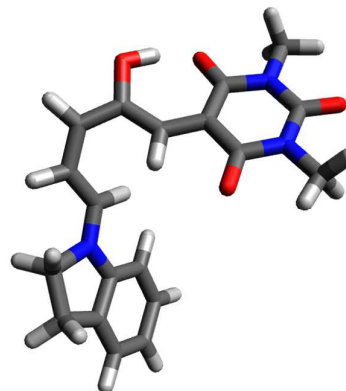
C	-3.73123	0.88603	0.27515
C	-2.42625	-1.21268	-0.33520
C	-2.47560	0.26428	-0.16553
C	-1.30760	0.91423	-0.43566
O	-3.87816	2.09684	0.46356
C	-0.88699	2.30360	-0.43953
C	0.40290	2.58768	-0.75952
C	1.45494	1.61709	-1.13546
C	2.35945	1.17000	-0.24113
O	-1.72074	3.32766	-0.15877
H	2.31371	1.50751	0.79145
H	1.50418	1.29991	-2.17571
H	0.65560	3.64924	-0.75802
H	-2.60626	2.97241	0.10837
H	-0.50073	0.24302	-0.71971
C	4.43869	-0.01448	0.33452
C	3.60695	-0.25192	-1.85292
C	5.32665	-0.88885	-0.30998
C	4.68337	0.44033	1.62905
C	4.77861	-1.24001	-1.67453
H	2.70049	-0.73171	-2.23338
C	6.47265	-1.31923	0.33701
C	5.84416	-0.00549	2.27044
H	4.00707	1.12184	2.13405
H	4.42063	-2.27494	-1.68532
C	6.73548	-0.87228	1.63984
H	7.16089	-1.99720	-0.16124
H	6.05256	0.34049	3.27864
H	7.63242	-1.19929	2.15592
N	3.36427	0.27770	-0.50782
H	5.52175	-1.13572	-2.46835
O	-1.42045	-1.80348	-0.69075
C	-4.78833	-1.32716	0.33876
H	3.86740	0.57575	-2.52740
C	-6.05299	0.69682	0.93680
H	-6.37632	1.41763	0.18454
H	-6.80268	-0.07826	1.06337
H	-5.88115	1.21576	1.88093
C	-3.62482	-3.36570	-0.22014
H	-2.63791	-3.68325	-0.54399
H	-3.87509	-3.82751	0.73595
H	-4.37410	-3.64584	-0.96178
N	-3.60017	-1.90740	-0.07136
N	-4.80666	0.06041	0.49648
O	-5.77374	-2.00582	0.55205
B'			



Electronic energy: -1199.8613716 Hartree
Free energy: -1199.9405668 Hartree

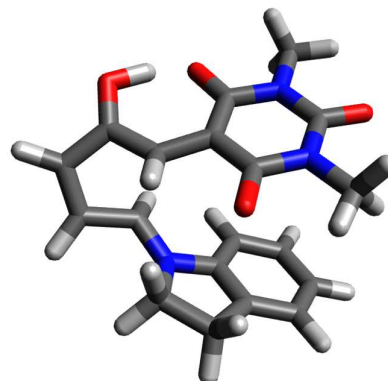
C	-3.21836	0.64626	0.53712
C	-1.90344	-0.81121	-1.02516
C	-2.05460	0.44348	-0.29125
C	-0.98097	1.33318	-0.39717
O	-3.41895	1.64867	1.24705
C	-0.81508	2.67757	-0.01384
C	0.40962	3.32065	-0.22078
C	1.67303	2.73261	-0.39981
C	2.00264	1.47714	0.08994
O	-1.83709	3.46831	0.40242
H	1.32722	0.96766	0.77325
H	2.45178	3.33589	-0.85728
H	0.36051	4.40880	-0.23912
H	-2.55390	2.87812	0.76355
H	-0.15057	0.92763	-0.96793
C	3.60115	-0.33414	0.45968
C	4.15151	1.32201	-1.13775
C	4.77541	-0.77373	-0.15620
C	3.02707	-1.01134	1.53104
C	5.13192	0.14378	-1.30101
H	3.64715	1.59722	-2.06679
C	5.40102	-1.92498	0.29931
C	3.66582	-2.17065	1.97646
H	2.12436	-0.65669	2.01703
H	4.97932	-0.36385	-2.25853
C	4.83956	-2.62550	1.37252
H	6.31348	-2.27774	-0.17312
H	3.24213	-2.71893	2.81202
H	5.32066	-3.52604	1.74048
N	3.14855	0.84486	-0.16618
H	6.17087	0.47758	-1.25951
O	-0.92452	-1.08093	-1.71562
C	-4.07699	-1.55044	-0.13549
H	4.64539	2.20948	-0.72689
C	-5.35340	-0.12847	1.40475
H	-6.02585	-0.97184	1.27771
H	-5.04929	-0.04300	2.44958
H	-5.84493	0.79675	1.10110
C	-2.87258	-3.00353	-1.63405
H	-2.83402	-3.83432	-0.92665
H	-3.75276	-3.11757	-2.26834
H	-1.97086	-2.98662	-2.23961
N	-2.94891	-1.73353	-0.91108
N	-4.17632	-0.35288	0.56298
O	-4.94243	-2.40952	-0.07146

B'-C



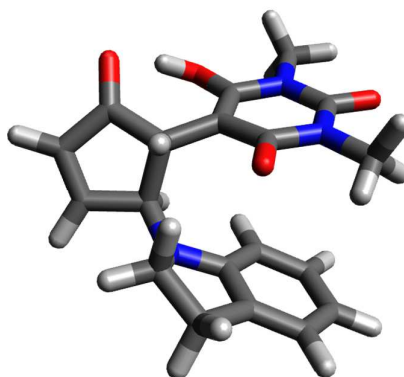
Electronic energy: -1199.8472829 Hartree
Free energy: -1199.9208213 Hartree

C	-2.03038	1.12324	0.11559
C	-0.56159	-0.28523	-1.27925
C	-0.83018	0.95210	-0.59620
C	0.25012	1.91523	-0.61465
O	-2.37286	2.18995	0.71544
C	0.25721	3.27619	-0.19142
C	1.58958	3.80170	-0.03840
C	2.46781	2.81489	0.28440
C	1.80806	1.56038	0.63462
O	-0.79259	3.96141	0.16810
H	1.17325	1.59364	1.51539
H	3.55044	2.91373	0.28428
H	1.82131	4.85774	-0.11904
H	-1.58256	3.26195	0.35937
H	0.96085	1.70882	-1.40932
C	1.82655	-0.85909	0.88554
C	3.24309	0.09851	-0.75581
C	2.29786	-1.93054	0.12450
C	0.92082	-1.03958	1.92731
C	3.23938	-1.43475	-0.94503
H	2.81918	0.61530	-1.62437
C	1.85528	-3.21700	0.39633
C	0.48177	-2.34030	2.18993
H	0.55078	-0.20738	2.51823
H	2.87687	-1.70691	-1.93944
C	0.94051	-3.42160	1.43586
H	2.20754	-4.05456	-0.20009
H	-0.22961	-2.50556	2.99338
H	0.58344	-4.42309	1.65428
N	2.37677	0.35080	0.41320
H	4.24261	-1.85160	-0.81904
O	0.44342	-0.49165	-1.96791
C	-2.67891	-1.17405	-0.39252
H	4.24507	0.48942	-0.56402
C	-4.18441	0.27392	0.89285
H	-4.81984	-0.58856	0.71162
H	-3.99251	0.37601	1.96330
H	-4.66440	1.18246	0.52924
C	-1.26534	-2.62122	-1.70179
H	-0.26118	-2.61469	-2.11806
H	-1.35329	-3.39066	-0.93351
H	-1.99641	-2.81987	-2.48932
N	-1.50769	-1.30821	-1.10752
N	-2.92779	0.06985	0.17133
O	-3.46344	-2.10722	-0.27602
C			



Electronic energy: -1199.8702687 Hartree
Free energy: -1199.9446753 Hartree

C	2.30414	0.22038	-0.18484
C	0.47716	-0.57772	1.17341
C	1.13664	0.50114	0.46516
C	0.39654	1.80429	0.45198
O	3.07413	1.11626	-0.80278
C	1.12883	3.12181	0.32139
C	0.16683	4.11522	-0.18137
C	-0.87449	3.46457	-0.72124
C	-0.72230	1.96470	-0.64049
O	2.32525	3.31068	0.52547
H	-0.30303	1.62285	-1.59573
H	-1.72775	3.92012	-1.21620
H	0.35868	5.18142	-0.18293
H	2.96372	1.99221	-0.36382
H	-0.12644	1.88631	1.41603
C	-2.08739	-0.09224	-0.73961
C	-2.77786	1.55155	0.75333
C	-3.20212	-0.63203	-0.07667
C	-1.29086	-0.88736	-1.56173
C	-3.87331	0.47124	0.70807
H	-2.16904	1.42804	1.65925
C	-3.52929	-1.96760	-0.22836
C	-1.63004	-2.23954	-1.70334
H	-0.41563	-0.48972	-2.06748
H	-4.18808	0.16271	1.70735
C	-2.73256	-2.78300	-1.04774
H	-4.38916	-2.38373	0.29069
H	-1.00939	-2.87394	-2.33033
H	-2.97070	-3.83555	-1.16430
N	-1.96582	1.27184	-0.44452
H	-4.75583	0.83595	0.16810
O	-0.49082	-0.41229	1.91210
C	2.13174	-2.14922	0.25468
H	-3.17648	2.56845	0.71849
C	4.09077	-1.28126	-0.94767
H	4.34190	-2.33144	-0.82875
H	4.00957	-1.03796	-2.00853
H	4.85744	-0.65677	-0.48868
C	0.24468	-3.00175	1.51240
H	0.28944	-3.82832	0.80505
H	0.68623	-3.31387	2.46293
H	-0.78576	-2.69005	1.67023
N	0.97799	-1.86573	0.95440
N	2.80567	-1.05669	-0.27681
O	2.54677	-3.29237	0.12433



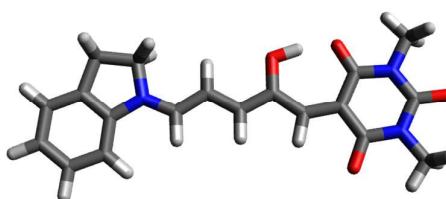
Eps = 7.5

A

Electronic energy: -1199.8777011 Hartree

Free energy: -1199.9589493 Hartree

C	-3.81178	-1.02358	-0.02785
C	-3.99512	1.48021	0.04470
C	-3.17809	0.27019	0.02364
C	-1.79139	0.49023	0.04545
O	-3.20095	-2.10931	-0.05321
C	-0.66977	-0.34711	0.04472
C	0.58679	0.26562	0.05623
C	1.79423	-0.44129	0.04640
C	2.99640	0.24932	0.04289
O	-0.69388	-1.70105	0.03200
H	2.98687	1.33695	0.04733
H	1.77232	-1.52561	0.03302
H	0.61260	1.35259	0.07034
H	-1.64989	-1.99044	-0.00030
H	-1.53784	1.54647	0.06721
C	5.44053	0.34740	-0.01259
C	4.39652	-1.78503	0.03674
C	6.47866	-0.58578	0.01988
C	5.67853	1.71735	-0.08677
C	5.92382	-1.98607	0.10830
H	3.87238	-2.21078	0.89604
C	7.79641	-0.15133	-0.01912
C	7.00872	2.13969	-0.12396
H	4.87217	2.44235	-0.11905
H	6.21630	-2.46404	1.04735
C	8.05972	1.22030	-0.09099
H	8.61115	-0.86962	0.00590
H	7.22357	3.20215	-0.18266
H	9.08564	1.57292	-0.12326
N	4.19809	-0.32050	0.03278
H	6.28201	-2.61420	-0.71088
O	-3.53093	2.61769	0.08622
C	-6.00461	0.07287	-0.03215
H	3.96161	-2.19896	-0.87789
C	-5.90508	-2.33746	-0.10378
H	-6.54919	-2.43582	0.77160
H	-6.51843	-2.38322	-1.00513
H	-5.16399	-3.13082	-0.11430
C	-6.26591	2.46718	0.03442
H	-6.89134	2.47139	-0.85997
H	-6.90669	2.43255	0.91743
H	-5.64242	3.35638	0.05951
N	-5.38201	1.30176	0.01547
N	-5.19871	-1.05539	-0.05330
O	-7.22298	-0.02578	-0.05549

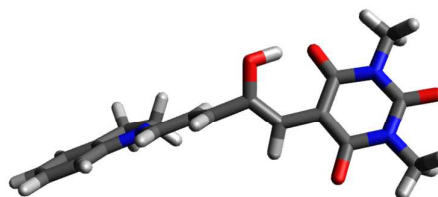


A-B

Electronic energy: -1199.8440386 Hartree

Free energy: -1199.9228984 Hartree

C	3.65667	-0.95744	-0.22376
C	3.80671	1.46522	0.18366
C	3.05237	0.31084	-0.19978
C	1.62405	0.52363	-0.44693
O	3.05386	-2.04499	-0.47379
C	0.75382	-0.24625	-1.12722
C	-0.67563	0.15010	-1.26618
C	-1.63734	-0.29125	-0.43257
C	-2.99279	0.12623	-0.65115
O	1.02021	-1.40789	-1.77245
H	-3.21360	0.77544	-1.49584
H	-1.39456	-0.94267	0.40163
H	-0.94893	0.80109	-2.09876
H	1.86179	-1.78388	-1.32661
H	1.22743	1.44970	-0.03928
C	-5.34223	0.19508	-0.04893
C	-3.85910	-1.09607	1.30713
C	-6.12586	-0.40725	0.92930
C	-5.85551	1.06369	-1.00663
C	-5.29653	-1.29711	1.81604
H	-3.37926	-2.02616	1.00074
C	-7.49113	-0.14240	0.96381
C	-7.22367	1.31905	-0.95985
H	-5.23198	1.53271	-1.75985
H	-5.60663	-2.34091	1.71995
C	-8.03368	0.72296	0.01383
H	-8.12073	-0.60295	1.71906
H	-7.66281	1.99244	-1.68844
H	-9.09709	0.93959	0.02954
N	-3.98473	-0.21557	0.10909
H	-5.38761	-1.01373	2.86696
O	3.34062	2.61020	0.27893
C	5.79574	0.03681	0.43390
H	-3.22396	-0.58161	2.03100
C	5.70696	-2.33634	0.03132
H	6.60705	-2.25918	-0.58020
H	5.99277	-2.64043	1.04173
H	5.02292	-3.06515	-0.39378
C	6.00479	2.39278	0.87427
H	5.38946	3.28732	0.83034
H	6.38029	2.24650	1.88979
H	6.85483	2.48615	0.19552
N	5.17226	1.26138	0.47745
N	5.02719	-1.04361	0.06280
O	6.98802	-0.09021	0.71350
B			

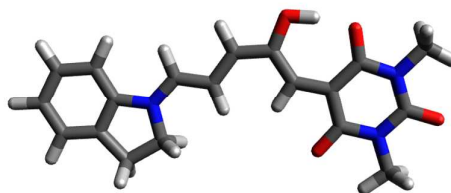


Electronic energy: -1199.8699282 Hartree

Free energy: -1199.9543358 Hartree

C	-3.96081	-1.09942	0.00151
C	-3.16795	1.27879	-0.00229
C	-2.87208	-0.15237	-0.00103
C	-1.50898	-0.47718	-0.00132
O	-3.83191	-2.33734	0.00364
C	-0.78712	-1.67584	-0.00195
C	0.61287	-1.65748	-0.00153
C	1.49653	-0.56793	0.00147
C	2.85796	-0.81514	-0.00042
O	-1.34294	-2.91819	-0.00421
H	3.21373	-1.84257	-0.00358
H	1.13698	0.45543	0.00531
H	1.06834	-2.64870	-0.00384
H	-2.33416	-2.81818	-0.00166
H	-0.88424	0.41004	-0.00160
C	5.19564	-0.10110	0.00022
C	3.51003	1.57133	0.00510
C	5.87229	1.12042	0.00150
C	5.86873	-1.32007	-0.00167
C	4.88859	2.26483	0.00272
H	2.91664	1.81364	-0.88103
C	7.26006	1.13852	0.00092
C	7.26462	-1.28639	-0.00225
H	5.34127	-2.26797	-0.00259
H	5.01338	2.89639	-0.88064
C	7.95779	-0.07392	-0.00094
H	7.79583	2.08365	0.00188
H	7.81523	-2.22193	-0.00368
H	9.04316	-0.07307	-0.00137
N	3.80407	0.12374	0.00120
H	5.01604	2.89751	0.88486
O	-2.30461	2.15365	-0.00384
C	-5.57132	0.75005	0.00028
H	2.92177	1.80975	0.89575
C	-6.34462	-1.57865	0.00452
H	-7.28491	-1.03526	0.00437
H	-6.27348	-2.20926	-0.88306
H	-6.27194	-2.20607	0.89424
C	-4.88546	3.05910	-0.00341
H	-5.47812	3.28651	-0.89116
H	-5.47340	3.28984	0.88665
H	-3.96784	3.64022	-0.00688
N	-4.51834	1.64228	-0.00189
N	-5.25313	-0.60193	0.00181
O	-6.72842	1.14265	0.00088

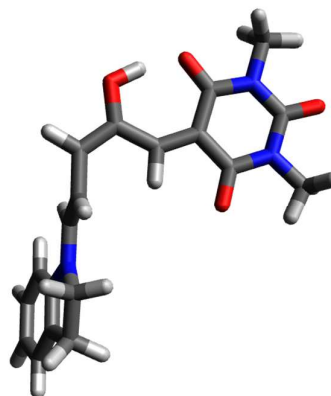
B-B'



Electronic energy: -1199.8494206 Hartree

Free energy: -1199.9282863 Hartree

C	-3.72990	0.88713	0.27677
C	-2.43208	-1.21420	-0.33778
C	-2.47718	0.26286	-0.16873
C	-1.30878	0.91012	-0.44248
O	-3.87259	2.09891	0.46615
C	-0.88579	2.29891	-0.44841
C	0.40450	2.58194	-0.76675
C	1.45683	1.61016	-1.13939
C	2.35918	1.16427	-0.24215
O	-1.72072	3.32398	-0.17102
H	2.31173	1.50308	0.78999
H	1.50739	1.29055	-2.17890
H	0.65844	3.64330	-0.76611
H	-2.60493	2.96690	0.10119
H	-0.50374	0.23774	-0.72864
C	4.43929	-0.01648	0.33678
C	3.61316	-0.25491	-1.85264
C	5.33159	-0.88741	-0.30718
C	4.68104	0.43942	1.63180
C	4.78596	-1.24084	-1.67206
H	2.70929	-0.73518	-2.23824
C	6.47894	-1.31320	0.34088
C	5.84338	-0.00182	2.27425
H	4.00142	1.11808	2.13627
H	4.42955	-2.27635	-1.68187
C	6.73893	-0.86511	1.64428
H	7.17033	-1.98829	-0.15700
H	6.04943	0.34511	3.28269
H	7.63687	-1.18848	2.16110
N	3.36438	0.27099	-0.50648
H	5.52985	-1.13630	-2.46506
O	-1.42717	-1.80765	-0.69320
C	-4.79154	-1.32218	0.34166
H	3.87489	0.57518	-2.52355
C	-6.04875	0.70395	0.94931
H	-6.37603	1.42313	0.19718
H	-6.79906	-0.06940	1.08211
H	-5.87005	1.22366	1.89172
C	-3.63678	-3.36374	-0.22533
H	-4.39606	-3.64078	-0.95775
H	-2.65517	-3.68317	-0.56296
H	-3.87416	-3.82670	0.73358
N	-3.60737	-1.90548	-0.07502
N	-4.80587	0.06478	0.50256
O	-5.77826	-1.99865	0.55804
B'			

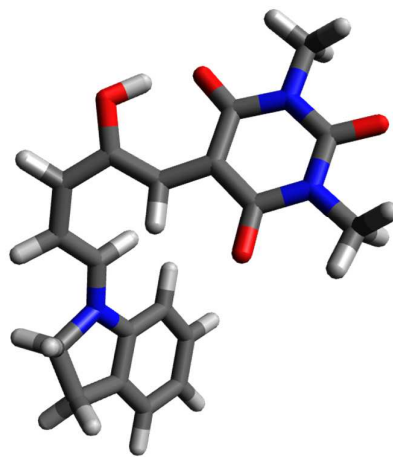


Electronic energy: -1199.8650919 Hartree

Free energy: -1199.9448821 Hartree

C	-3.19852	0.65472	0.55107
C	-1.91271	-0.78755	-1.05003
C	-2.05198	0.45479	-0.29777
C	-0.96759	1.34098	-0.39819
O	-3.36382	1.64674	1.28755
C	-0.79945	2.67944	-0.01409
C	0.42775	3.32780	-0.22468
C	1.68874	2.74353	-0.38885
C	2.00902	1.48028	0.10032
O	-1.81930	3.47251	0.40761
H	1.32875	0.97534	0.78230
H	2.47635	3.34702	-0.83050
H	0.37391	4.41527	-0.26225
H	-2.52627	2.87786	0.78400
H	-0.13816	0.93189	-0.96770
C	3.58918	-0.34474	0.46447
C	4.15857	1.31725	-1.12345
C	4.75873	-0.79117	-0.15445
C	3.00612	-1.02239	1.53082
C	5.12829	0.13131	-1.29053
H	3.65685	1.60038	-2.05118
C	5.37166	-1.95292	0.29328
C	3.63189	-2.19169	1.96820
H	2.10750	-0.66039	2.01904
H	4.97598	-0.36776	-2.25248
C	4.80130	-2.65469	1.36081
H	6.28083	-2.31182	-0.18080
H	3.20220	-2.74131	2.79980
H	5.27239	-3.56310	1.72257
N	3.14886	0.84505	-0.15369
H	6.16996	0.45517	-1.24070
O	-0.94314	-1.05057	-1.75898
C	-4.06497	-1.53305	-0.13311
H	4.65833	2.19806	-0.70666
C	-5.36215	-0.17747	1.39445
H	-6.24008	-0.46836	0.81895
H	-5.28892	-0.81020	2.28250
H	-5.43155	0.86550	1.68969
C	-2.88365	-2.98197	-1.65540
H	-2.78201	-3.81017	-0.95056
H	-3.79401	-3.12081	-2.23974
H	-2.01769	-2.94307	-2.31031
N	-2.95509	-1.71233	-0.93236
N	-4.17019	-0.33565	0.55862
O	-4.92760	-2.39414	-0.03757

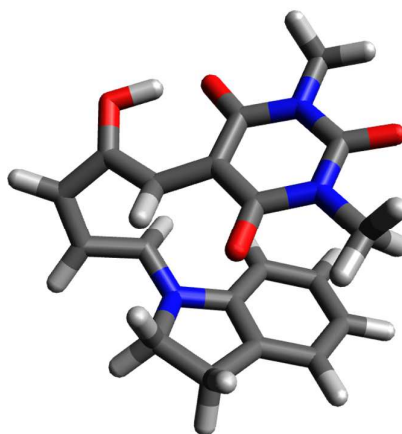
B'-C



Electronic energy: -1199.8505506 Hartree

Free energy: -1199.9246211 Hartree

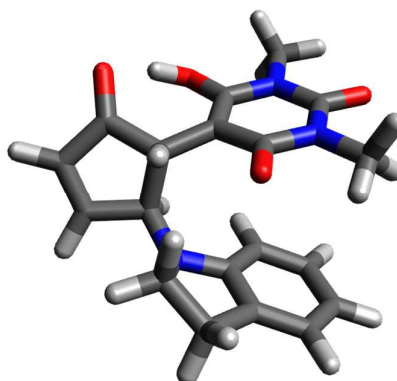
C	-2.11519	0.97515	0.10942
C	-0.54239	-0.32556	-1.27422
C	-0.90354	0.89077	-0.59735
C	0.10717	1.92928	-0.61226
O	-2.53579	2.01515	0.70773
C	0.01335	3.28719	-0.19168
C	1.30281	3.90825	-0.02903
C	2.24752	2.98778	0.29972
C	1.67924	1.68608	0.64078
O	-1.08628	3.89547	0.16053
H	1.04099	1.66633	1.51993
H	3.31997	3.16585	0.31124
H	1.45861	4.97832	-0.10807
H	-1.82271	3.14051	0.35086
H	0.83269	1.77469	-1.40561
C	1.88059	-0.72589	0.87632
C	3.23894	0.34832	-0.74104
C	2.45792	-1.75382	0.12810
C	0.96560	-0.98116	1.89401
C	3.38216	-1.17964	-0.91709
H	2.77507	0.81688	-1.61650
C	2.11913	-3.07310	0.39200
C	0.63129	-2.31460	2.14881
H	0.51067	-0.18121	2.47031
H	3.08161	-1.49133	-1.92059
C	1.19924	-3.35385	1.40955
H	2.55521	-3.87818	-0.19368
H	-0.08428	-2.53897	2.93413
H	0.92272	-4.38195	1.62150
N	2.34107	0.52521	0.41787
H	4.41492	-1.50134	-0.75520
O	0.47590	-0.45932	-1.96186
C	-2.58863	-1.36607	-0.38805
H	4.19673	0.83483	-0.54394
C	-4.20818	-0.02977	0.87561
H	-4.80628	-0.90530	0.63814
H	-4.03540	0.01851	1.95353
H	-4.71939	0.87719	0.55471
C	-1.05812	-2.71486	-1.67202
H	-1.09275	-3.47983	-0.89502
H	-1.76358	-2.97857	-2.46388
H	-0.05335	-2.63629	-2.07944
N	-1.40659	-1.41779	-1.09522
N	-2.93572	-0.14037	0.16123
O	-3.30087	-2.35588	-0.26503
C			



Electronic energy: -1199.8734974 Hartree

Free energy: -1199.9480464 Hartree

C	2.29831	0.25204	-0.19044
C	0.48914	-0.57656	1.17329
C	1.12859	0.51321	0.46439
C	0.36845	1.80508	0.45303
O	3.04984	1.16096	-0.81190
C	1.08356	3.13271	0.32950
C	0.11264	4.11447	-0.17655
C	-0.91901	3.45190	-0.72093
C	-0.74926	1.95408	-0.64163
O	2.27662	3.33573	0.54324
H	-0.32476	1.61816	-1.59659
H	-1.77601	3.89827	-1.21782
H	0.29101	5.18307	-0.17614
H	2.92718	2.03443	-0.37230
H	-0.15759	1.87772	1.41612
C	-2.09030	-0.11860	-0.73849
C	-2.80318	1.51995	0.74896
C	-3.20065	-0.66990	-0.07677
C	-1.28228	-0.90620	-1.55712
C	-3.88692	0.42815	0.70246
H	-2.19419	1.40446	1.65598
C	-3.51168	-2.00986	-0.22567
C	-1.60542	-2.26276	-1.69600
H	-0.41065	-0.49900	-2.06159
H	-4.20357	0.11913	1.70100
C	-2.70305	-2.81793	-1.04124
H	-4.36808	-2.43479	0.29209
H	-0.97605	-2.89138	-2.32026
H	-2.92850	-3.87357	-1.15575
N	-1.98577	1.24716	-0.44711
H	-4.77071	0.78237	0.15756
O	-0.48225	-0.42745	1.91190
C	2.16963	-2.11799	0.25130
H	-3.21200	2.53257	0.71234
C	4.10774	-1.21814	-0.96148
H	4.38063	-2.26249	-0.83966
H	4.01545	-0.98126	-2.02287
H	4.86424	-0.57707	-0.50867
C	0.31096	-3.00837	1.51804
H	0.31318	-3.81414	0.78503
H	0.80466	-3.34981	2.43200
H	-0.70804	-2.70098	1.74203
N	1.01441	-1.85548	0.95613
N	2.82198	-1.01582	-0.28413
O	2.60275	-3.25528	0.12119



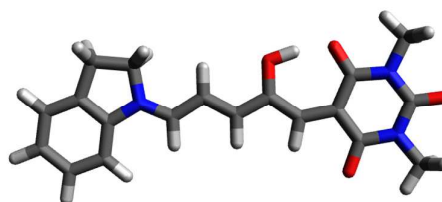
Eps = 10

A

Electronic energy: -1199.8795807 Hartree

Free energy: -1199.9606103 Hartree

C	-3.81146	-1.02209	-0.03183
C	-3.99480	1.47937	0.04777
C	-3.17836	0.27039	0.02502
C	-1.78956	0.49035	0.04676
O	-3.20045	-2.10851	-0.06357
C	-0.67035	-0.34719	0.04985
C	0.58906	0.26389	0.05830
C	1.79396	-0.44381	0.05058
C	2.99731	0.24825	0.04297
O	-0.69530	-1.70168	0.04474
H	2.98682	1.33589	0.04318
H	1.77316	-1.52821	0.04140
H	0.61643	1.35093	0.06829
H	-1.65196	-1.98947	0.00421
H	-1.53519	1.54639	0.06580
C	5.44021	0.34756	-0.01449
C	4.39743	-1.78607	0.04373
C	6.47839	-0.58518	0.02089
C	5.67671	1.71750	-0.09354
C	5.92484	-1.98552	0.11312
H	3.87548	-2.20762	0.90629
C	7.79609	-0.14993	-0.01970
C	7.00659	2.14057	-0.13239
H	4.86950	2.44148	-0.12821
H	6.21933	-2.46150	1.05249
C	8.05822	1.22164	-0.09626
H	8.61127	-0.86763	0.00762
H	7.22086	3.20294	-0.19483
H	9.08394	1.57483	-0.12980
N	4.19746	-0.32112	0.03341
H	6.28215	-2.61454	-0.70575
O	-3.53095	2.61763	0.09050
C	-6.00434	0.07299	-0.03434
H	3.96094	-2.20399	-0.86814
C	-5.90453	-2.33699	-0.11217
H	-6.55934	-2.43219	0.75546
H	-6.50625	-2.38635	-1.02127
H	-5.16364	-3.13059	-0.11082
C	-6.26580	2.46692	0.03994
H	-6.87910	2.48290	-0.86284
H	-6.91810	2.42173	0.91386
H	-5.64269	3.35561	0.08399
N	-5.38202	1.30141	0.01938
N	-5.19866	-1.05484	-0.05653
O	-7.22313	-0.02553	-0.06167

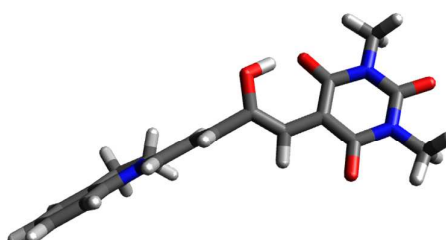


A-B

Electronic energy: -1199.8473509 Hartree

Free energy: -1199.9271863 Hartree

C	3.65668	-0.95626	-0.22582
C	3.81274	1.46376	0.19174
C	3.05446	0.31288	-0.19393
C	1.62487	0.52898	-0.43376
O	3.05063	-2.04139	-0.47911
C	0.75302	-0.23312	-1.12101
C	-0.67658	0.16495	-1.25543
C	-1.63911	-0.28628	-0.42861
C	-2.99428	0.13664	-0.64419
O	1.02183	-1.38729	-1.77917
H	-3.21132	0.80001	-1.47869
H	-1.39950	-0.94912	0.39759
H	-0.94881	0.82703	-2.07943
H	1.86067	-1.76922	-1.33463
H	1.22872	1.45004	-0.01450
C	-5.34493	0.19678	-0.04787
C	-3.86640	-1.11877	1.29025
C	-6.13074	-0.41679	0.92161
C	-5.85569	1.07712	-0.99633
C	-5.30388	-1.31706	1.79991
H	-3.39560	-2.04722	0.96540
C	-7.49597	-0.15119	0.95680
C	-7.22380	1.33294	-0.94905
H	-5.22992	1.55366	-1.74302
H	-5.61876	-2.35871	1.69697
C	-8.03609	0.72591	0.01614
H	-8.12726	-0.62026	1.70540
H	-7.66118	2.01494	-1.67070
H	-9.09943	0.94308	0.03243
N	-3.98801	-0.21682	0.10768
H	-5.39217	-1.04040	2.85289
O	3.34905	2.60949	0.29364
C	5.79906	0.03047	0.43089
H	-3.22473	-0.62238	2.02079
C	5.70449	-2.34092	0.01728
H	6.60713	-2.26134	-0.59003
H	5.98473	-2.65395	1.02655
H	5.02069	-3.06479	-0.41653
C	6.01467	2.38483	0.87867
H	5.40570	3.28311	0.82449
H	6.37943	2.24218	1.89872
H	6.87126	2.46905	0.20721
N	5.17884	1.25646	0.47936
N	5.02794	-1.04646	0.05566
O	6.99145	-0.10045	0.70919

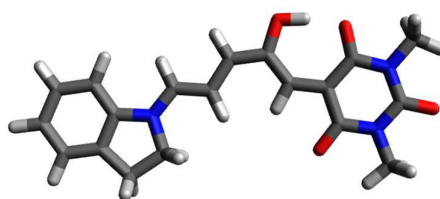


B

Electronic energy: -1199.8717613 Hartree

Free energy: -1199.9536913 Hartree

C	3.95832	-1.09859	-0.03008
C	3.17619	1.27952	0.04130
C	2.87486	-0.14893	0.01887
C	1.50839	-0.46971	0.02711
O	3.82442	-2.33616	-0.07421
C	0.78612	-1.66561	0.04194
C	-0.61604	-1.64839	0.03524
C	-1.49863	-0.56133	0.00257
C	-2.86143	-0.81147	0.01150
O	1.34041	-2.90887	0.07887
H	-3.21491	-1.83928	0.04131
H	-1.14047	0.46196	-0.03198
H	-1.07101	-2.63961	0.05906
H	2.33090	-2.81068	0.02336
H	0.88581	0.41916	0.02877
C	-5.19937	-0.10169	-0.00453
C	-3.51584	1.57325	-0.05008
C	-5.87704	1.11873	-0.03382
C	-5.87039	-1.32141	0.02830
C	-4.89532	2.26406	-0.06701
H	-2.92597	1.83567	0.83252
C	-7.26509	1.13517	-0.02951
C	-7.26628	-1.28941	0.03192
H	-5.34142	-2.26823	0.05032
H	-5.02106	2.92044	0.79786
C	-7.96097	-0.07782	0.00367
H	-7.80199	2.07939	-0.05179
H	-7.81576	-2.22530	0.05732
H	-9.04638	-0.07834	0.00737
N	-3.80728	0.12485	-0.01397
H	-5.02409	2.87069	-0.96710
O	2.31651	2.15831	0.07190
C	5.57701	0.74287	-0.00980
H	-2.92518	1.79205	-0.94389
C	6.34009	-1.58762	-0.08668
H	7.28300	-1.04906	-0.07019
H	6.27174	-2.25393	0.77450
H	6.25947	-2.17722	-1.00143
C	4.90055	3.05373	0.05458
H	5.51518	3.25786	0.93296
H	5.46731	3.30433	-0.84393
H	3.98563	3.63773	0.09416
N	4.52813	1.63854	0.02856
N	5.25332	-0.60703	-0.03538
O	6.73607	1.13119	-0.02113

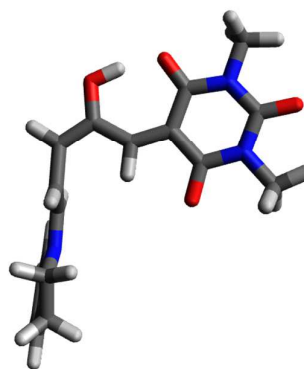


B-B'

Electronic energy: -1199.8508994 Hartree

Free energy: -1199.9299979 Hartree

C	-3.73075	0.88772	0.27469
C	-2.45021	-1.21361	-0.34315
C	-2.48253	0.26204	-0.17987
C	-1.31262	0.90257	-0.46089
O	-3.87163	2.10070	0.45887
C	-0.88703	2.29050	-0.47476
C	0.40398	2.57127	-0.79113
C	1.45719	1.59658	-1.15384
C	2.35677	1.15771	-0.25033
O	-1.72362	3.31747	-0.20723
H	2.30606	1.50398	0.77919
H	1.51079	1.26904	-2.19075
H	0.65873	3.63246	-0.79606
H	-2.60608	2.96176	0.07334
H	-0.51090	0.22586	-0.74674
C	4.43794	-0.01398	0.34206
C	3.61928	-0.26880	-1.84819
C	5.33545	-0.88537	-0.29436
C	4.67513	0.45172	1.63457
C	4.79390	-1.25047	-1.65774
H	2.71848	-0.75313	-2.23565
C	6.48348	-1.30173	0.35881
C	5.83830	0.01992	2.28228
H	3.99152	1.13066	2.13327
H	4.43989	-2.28686	-1.66024
C	6.73899	-0.84366	1.65981
H	7.17882	-1.97704	-0.13328
H	6.04076	0.37463	3.28878
H	7.63741	-1.15950	2.18052
N	3.36342	0.26292	-0.50530
H	5.53925	-1.15026	-2.44989
O	-1.45357	-1.82733	-0.69011
C	-4.80079	-1.32301	0.36216
H	3.88191	0.55892	-2.52167
C	-6.03361	0.71123	0.99395
H	-6.78219	-0.05849	1.15286
H	-5.82968	1.23928	1.92649
H	-6.37817	1.42393	0.24334
C	-3.59078	-3.35662	-0.27425
H	-3.17343	-3.57967	-1.25590
H	-2.96284	-3.80951	0.49595
H	-4.60498	-3.73748	-0.19977
N	-3.62711	-1.90196	-0.09400
N	-4.80271	0.06552	0.52209
O	-5.78907	-1.98559	0.61070

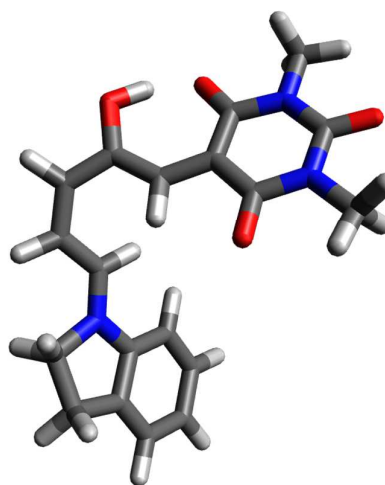


B'

Electronic energy: -1199.8670297 Hartree

Free energy: -1199.9466381 Hartree

C	-3.19356	0.64799	0.54947
C	-1.92715	-0.79761	-1.05031
C	-2.05166	0.44487	-0.30023
C	-0.96232	1.32794	-0.40623
O	-3.36991	1.64349	1.28103
C	-0.79404	2.66484	-0.02555
C	0.43194	3.31782	-0.24453
C	1.69336	2.73845	-0.40249
C	2.01540	1.47567	0.09248
O	-1.81204	3.45743	0.40303
H	1.33533	0.97260	0.77602
H	2.48145	3.34268	-0.84213
H	0.37293	4.40454	-0.29494
H	-2.52022	2.86203	0.77916
H	-0.13405	0.91448	-0.97415
C	3.59702	-0.34512	0.46402
C	4.16817	1.31604	-1.12545
C	4.76928	-0.78943	-0.15092
C	3.01164	-1.02214	1.52958
C	5.14123	0.13231	-1.28654
H	3.66862	1.59572	-2.05523
C	5.38338	-1.94945	0.30048
C	3.63852	-2.18943	1.97056
H	2.11075	-0.66117	2.01443
H	4.99441	-0.36848	-2.24841
C	4.81097	-2.65074	1.36715
H	6.29491	-2.30690	-0.17014
H	3.20759	-2.73881	2.80170
H	5.28285	-3.55767	1.73173
N	3.15581	0.84354	-0.15738
H	6.18183	0.45879	-1.23230
O	-0.96397	-1.06970	-1.76567
C	-4.08830	-1.53027	-0.12857
H	4.66353	2.19882	-0.70809
C	-5.32307	-0.11360	1.44816
H	-6.02127	-0.93250	1.30169
H	-5.00319	-0.07556	2.49132
H	-5.79294	0.83456	1.18448
C	-2.92560	-2.97655	-1.66554
H	-2.86758	-3.81484	-0.96812
H	-3.82318	-3.08221	-2.27645
H	-2.04173	-2.95598	-2.29670
N	-2.97863	-1.71369	-0.92827
N	-4.16547	-0.33929	0.58024
O	-4.95948	-2.38542	-0.05455

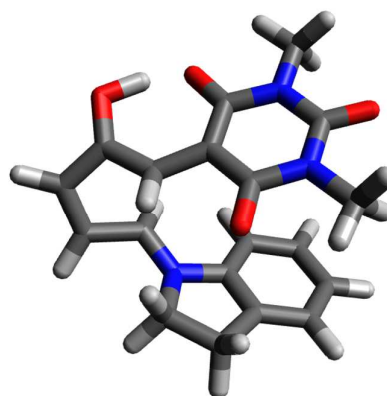


B'-C

Electronic energy: -1199.8521565 Hartree

Free energy: -1199.9254483 Hartree

C	-1.91264	1.31217	0.13148
C	-0.59101	-0.21911	-1.28774
C	-0.74097	1.03190	-0.59313
C	0.43027	1.88701	-0.60884
O	-2.13510	2.40528	0.74117
C	0.56598	3.24360	-0.19545
C	1.94109	3.63845	-0.03266
C	2.71570	2.57141	0.29823
C	1.93360	1.38519	0.63952
O	-0.41705	4.02975	0.15204
H	1.30301	1.47702	1.51937
H	3.80287	2.56429	0.31211
H	2.27600	4.66651	-0.11278
H	-1.26051	3.40563	0.35795
H	1.11654	1.61297	-1.40500
C	1.73325	-1.02811	0.88429
C	3.24647	-0.19828	-0.74094
C	2.10460	-2.13402	0.11591
C	0.82080	-1.13363	1.93122
C	3.08359	-1.71949	-0.95475
H	2.89996	0.37661	-1.60714
C	1.55148	-3.37797	0.38430
C	0.26916	-2.39225	2.18940
H	0.53088	-0.27599	2.53078
H	2.68605	-1.93708	-1.94930
C	0.62618	-3.50625	1.42740
H	1.82657	-4.24065	-0.21702
H	-0.44908	-2.49830	2.99696
H	0.18322	-4.47360	1.64303
N	2.39000	0.12864	0.41735
H	4.03961	-2.23899	-0.84625
O	0.38606	-0.51070	-1.98657
C	-2.76997	-0.91067	-0.39313
H	4.28034	0.07994	-0.52366
C	-4.15101	0.59056	0.90651
H	-4.99483	0.31012	0.27592
H	-4.17842	-0.00229	1.82394
H	-4.19669	1.64840	1.14854
C	-1.51430	-2.47616	-1.72998
H	-1.66544	-3.24379	-0.96959
H	-2.26841	-2.59467	-2.51205
H	-0.51842	-2.56116	-2.15759
N	-1.62445	-1.15344	-1.11807
N	-2.90399	0.34212	0.18197
O	-3.64613	-1.75960	-0.27001

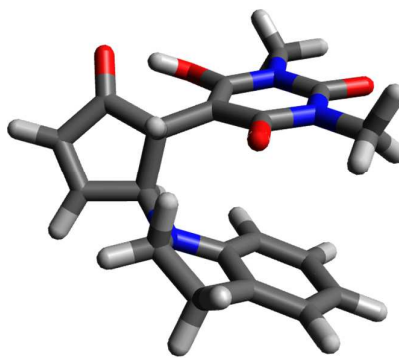


C

Electronic energy: -1199.8750018 Hartree

Free energy: -1199.9496526 Hartree

C	2.29574	0.26445	-0.19340
C	0.49528	-0.57639	1.17382
C	1.12589	0.51783	0.46451
C	0.35743	1.80487	0.45395
O	3.03913	1.17831	-0.81739
C	1.06577	3.13647	0.33405
C	0.09207	4.11347	-0.17493
C	-0.93520	3.44613	-0.72195
C	-0.75879	1.94918	-0.64248
O	2.25715	3.34493	0.55329
H	-0.33159	1.61514	-1.59685
H	-1.79308	3.88883	-1.22061
H	0.26510	5.18298	-0.17392
H	2.91192	2.05093	-0.37821
H	-0.17038	1.87340	1.41634
C	-2.09139	-0.12926	-0.73769
C	-2.81324	1.50869	0.74563
C	-3.20145	-0.68355	-0.07739
C	-1.27859	-0.91542	-1.55323
C	-3.89363	0.41378	0.69777
H	-2.20528	1.39594	1.65378
C	-3.50720	-2.02505	-0.22439
C	-1.59655	-2.27351	-1.69022
H	-0.40731	-0.50589	-2.05642
H	-4.21320	0.10569	1.69567
C	-2.69363	-2.83172	-1.03673
H	-4.36336	-2.45211	0.29207
H	-0.96352	-2.90093	-2.31205
H	-2.91497	-3.88843	-1.14981
N	-1.99280	1.23714	-0.44873
H	-4.77647	0.76461	0.14913
O	-0.47683	-0.43457	1.91344
C	2.18523	-2.10567	0.24924
H	-3.22468	2.52011	0.70757
C	4.11405	-1.19263	-0.96846
H	4.01628	-0.96054	-2.03043
H	4.86577	-0.54309	-0.51987
H	4.39715	-2.23388	-0.84377
C	0.33681	-3.00976	1.52072
H	0.34021	-3.81499	0.78705
H	0.83752	-3.34873	2.43178
H	-0.68303	-2.70970	1.75062
N	1.02954	-1.85157	0.95629
N	2.82838	-0.99956	-0.28790
O	2.62626	-3.24026	0.11910



4.4.17.4 Indoline CF3 Pyrazalone Geometries

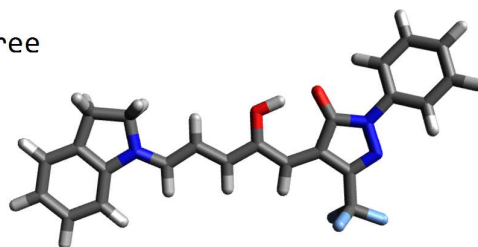
Chloroform

A

Electronic energy: -1500.6157043 Hartree

Free energy: -1500.7019748 Hartree

C	2.88351	-0.62446	0.03680
C	3.20936	1.60419	0.05212
C	2.16569	0.62896	0.05010
C	0.77970	0.85840	0.04975
O	2.45929	-1.80309	0.00976
C	-0.25332	-0.07451	0.04218
C	-1.57431	0.39893	0.03815
C	-2.68813	-0.43764	0.02250
C	-3.96464	0.11325	0.01558
O	-0.08213	-1.41484	0.03754
H	-4.07636	1.19475	0.02782
H	-2.54042	-1.51207	0.01225
H	-1.71970	1.47674	0.04627
H	0.89378	-1.65759	0.02244
H	0.45687	1.89654	0.05492
C	3.04527	3.08965	0.06754
N	4.40624	1.08921	0.04603
N	4.22189	-0.26728	0.04600
C	5.35481	-1.11850	-0.01156
C	5.27595	-2.44042	0.43662
C	6.55767	-0.60942	-0.51075
C	6.40937	-3.24902	0.37107
H	4.34321	-2.82643	0.82611
C	7.68110	-1.42949	-0.56095
H	6.60457	0.41834	-0.85122
C	7.61366	-2.75281	-0.12481
H	6.34488	-4.27535	0.71950
H	8.61263	-1.02902	-0.94919
H	8.49167	-3.38949	-0.16936
F	4.21365	3.73610	0.07157
F	2.34941	3.52149	-1.00576
F	2.35263	3.50053	1.15067
C	-6.40421	-0.06932	-0.02737
C	-5.11687	-2.06768	-0.02772
C	-7.32434	-1.11835	-0.04141
C	-6.80122	1.26507	-0.03741
C	-6.61112	-2.44730	-0.02149
H	-4.59821	-2.41195	-0.92684



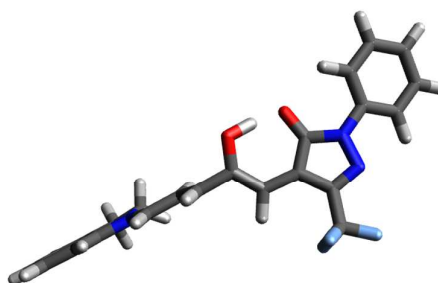
C	-8.68428	-0.84033	-0.06562
C	-8.17120	1.52942	-0.06137
H	-6.08711	2.08168	-0.02792
H	-6.87093	-3.05295	-0.89331
C	-9.10636	0.49198	-0.07557
H	-9.40868	-1.64979	-0.07662
H	-8.50988	2.56051	-0.06998
H	-10.16662	0.72275	-0.09485
N	-5.08987	-0.58871	-0.00575
H	-6.87087	-3.02094	0.87213
H	-4.58155	-2.44151	0.84891

A-B

Electronic energy: -1500.5832707 Hartree

Free energy: -1500.6678346 Hartree

C	2.83295	-0.58653	-0.34948
C	3.01348	1.58805	0.04668
C	2.07213	0.60407	-0.31439
C	0.64079	0.74250	-0.55122
O	2.46599	-1.79129	-0.57934
C	-0.15395	-0.19463	-1.10461
C	-1.61405	0.04296	-1.28040
C	-2.52410	-0.36640	-0.37534
C	-3.91517	-0.13320	-0.63412
O	0.21332	-1.40246	-1.57579
H	-4.19850	0.36673	-1.55828
H	-2.21138	-0.87056	0.53386
H	-1.95009	0.53442	-2.19546
H	1.15718	-1.64741	-1.20203
H	0.16850	1.67491	-0.25299
C	2.74826	3.04225	0.23387
N	4.23889	1.12702	0.21808
N	4.13220	-0.20653	-0.03692
C	5.27195	-1.03065	0.11914
C	5.32789	-2.29979	-0.46797
C	6.35837	-0.55192	0.86090
C	6.46925	-3.08183	-0.29761
H	4.48581	-2.66296	-1.04192
C	7.49224	-1.34400	1.01416
H	6.30481	0.43395	1.30678
C	7.55518	-2.61431	0.44059
H	6.50536	-4.06608	-0.75527
H	8.32972	-0.96349	1.59151
H	8.44021	-3.23022	0.56638
F	3.83782	3.73114	0.59592
F	2.26962	3.62225	-0.89053
F	1.80898	3.26509	1.18407
C	-6.26800	-0.27786	-0.05802
C	-4.66956	-1.16471	1.47727

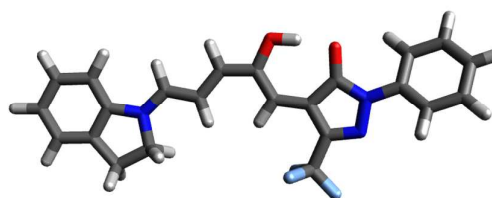


C	-6.98328	-0.69531	1.05905
C	-6.87242	0.24233	-1.19770
C	-6.05844	-1.19460	2.13695
H	-4.28305	-2.16444	1.26715
C	-8.37033	-0.59148	1.05457
C	-8.26129	0.34077	-1.18758
H	-6.30290	0.55558	-2.06621
H	-6.32079	-2.20365	2.46184
C	-9.00290	-0.07134	-0.07446
H	-8.94791	-0.91010	1.91691
H	-8.77146	0.73849	-2.05849
H	-10.08463	0.01373	-0.09272
N	-4.87272	-0.47734	0.16863
H	-6.09313	-0.53869	3.01110
H	-3.93256	-0.60483	2.05341
B			

Electronic energy: -1500.6076115 Hartree

Free energy: -1500.693186 Hartree

C	3.07943	-0.91092	0.03698
C	2.55519	1.28199	0.06747
C	1.94590	-0.01136	0.06830
C	0.57315	-0.29993	0.07687
O	3.12440	-2.15997	-0.00346
C	-0.05714	-1.54029	0.09124
C	-1.45874	-1.64919	0.08251
C	-2.42615	-0.64301	0.06339
C	-3.76698	-1.00284	0.04104
O	0.60319	-2.72640	0.11987
H	-4.03860	-2.05594	0.04000
H	-2.15337	0.40700	0.05531
H	-1.81969	-2.67801	0.09022
H	1.59453	-2.59665	0.06853
H	-0.08922	0.56080	0.07003
C	1.85402	2.60099	0.10768
N	3.85701	1.24690	0.04790
N	4.18898	-0.08106	0.03874
C	5.55530	-0.45260	-0.04281
C	5.98124	-1.69977	0.42298
C	6.47115	0.45468	-0.58356
C	7.33159	-2.03310	0.33313
H	5.26654	-2.39478	0.84411
C	7.81708	0.10789	-0.65713
H	6.12501	1.41897	-0.93731
C	8.25418	-1.13695	-0.20393
H	7.66043	-3.00265	0.69467
H	8.52505	0.81567	-1.07746
H	9.30423	-1.40459	-0.26752
F	2.69966	3.63367	0.07809



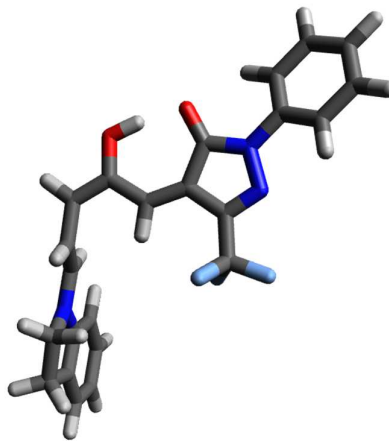
F	1.00612	2.74343	-0.93390
F	1.09992	2.72862	1.22025
C	-6.15100	-0.47553	-0.05576
C	-4.60296	1.32234	0.03032
C	-6.91965	0.68868	-0.01884
C	-6.72270	-1.74020	-0.16000
C	-6.03045	1.90104	0.10803
H	-3.98663	1.59758	0.88962
C	-8.30333	0.60079	-0.08358
C	-8.11508	-1.81336	-0.22267
H	-6.12201	-2.64279	-0.19827
H	-6.19885	2.40992	1.06129
C	-8.90080	-0.65913	-0.18551
H	-8.91171	1.50034	-0.05586
H	-8.58973	-2.78585	-0.30616
H	-9.98157	-0.74161	-0.23845
N	-4.78054	-0.14449	0.01855
H	-6.21194	2.62272	-0.69181
H	-4.08205	1.61841	-0.88536

B-B'

Electronic energy: -1500.5853347 Hartree

Free energy: -1500.6718252 Hartree

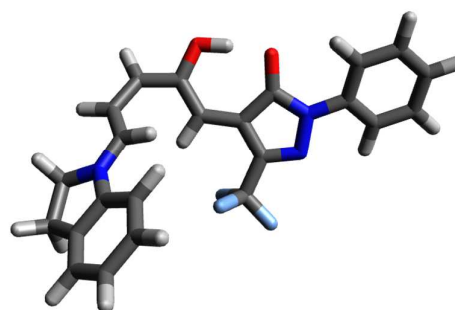
C	-2.89294	0.96020	0.02707
C	-1.79354	-1.00900	-0.34756
C	-1.55350	0.42067	-0.28738
C	-0.36949	1.06045	-0.49573
O	-3.26192	2.12847	0.16738
C	-0.06116	2.47236	-0.45324
C	1.21045	2.87817	-0.70905
C	2.34893	2.00560	-1.07007
C	3.24567	1.58508	-0.15444
O	-0.99358	3.40575	-0.16060
H	3.11877	1.84986	0.89255
H	2.47789	1.75918	-2.12256
H	1.37257	3.95645	-0.66671
H	-1.89161	3.01440	-0.02491
H	0.49371	0.44162	-0.72994
C	-0.78581	-2.08468	-0.62144
N	-3.02192	-1.32301	-0.11627
N	-3.70094	-0.15266	0.12292
C	-5.10444	-0.19699	0.34696
C	-5.72844	0.80519	1.09250
C	-5.83750	-1.26153	-0.18177
C	-7.10548	0.73683	1.29547
H	-5.14982	1.62180	1.50531
C	-7.21036	-1.31826	0.04019
H	-5.33390	-2.03227	-0.75430
C	-7.85037	-0.31961	0.77423



H	-7.59325	1.51550	1.87341
H	-7.78053	-2.14617	-0.36941
H	-8.92189	-0.36613	0.94056
F	-1.34669	-3.29191	-0.68899
F	-0.14660	-1.86122	-1.78531
F	0.15986	-2.12391	0.33453
C	5.15483	0.19146	0.52872
C	4.63137	0.29742	-1.76259
C	6.10731	-0.61528	-0.11057
C	5.09681	0.28079	1.91813
C	5.95927	-0.47241	-1.60814
H	3.80689	-0.36340	-2.06630
C	7.01511	-1.34610	0.63746
C	6.02191	-0.46151	2.66005
H	4.36145	0.89971	2.42154
H	5.93270	-1.43459	-2.12449
C	6.97121	-1.27007	2.03663
H	7.75387	-1.97181	0.14335
H	5.99040	-0.40686	3.74425
H	7.67483	-1.84102	2.63383
N	4.35466	0.82844	-0.42405
H	6.79452	0.10461	-2.01897
H	4.69669	1.11664	-2.48421
B'			

Electronic energy: -1500.6031353 Hartree
Free energy: -1500.6891268 Hartree

C	-2.52933	0.97497	-0.15865
C	-1.43941	-0.67427	0.91590
C	-1.25776	0.65906	0.44303
C	-0.09029	1.44262	0.53062
O	-2.92462	2.02785	-0.71393
C	0.07971	2.77683	0.16939
C	1.33126	3.41177	0.34158
C	2.58327	2.80524	0.35983
C	2.82187	1.55606	-0.22261
O	-0.93098	3.58347	-0.22635
H	2.07123	1.11383	-0.87292
H	3.42351	3.36795	0.75597
H	1.28952	4.49326	0.46405
H	-1.76424	3.05505	-0.42385
H	0.76439	0.97885	1.01292
C	-0.41924	-1.52052	1.60460
N	-2.62304	-1.16230	0.66725
N	-3.29592	-0.16743	0.01097
C	-4.65147	-0.37318	-0.35064
C	-5.23275	0.36397	-1.38659
C	-5.39454	-1.33759	0.33739
C	-6.56625	0.13240	-1.71993

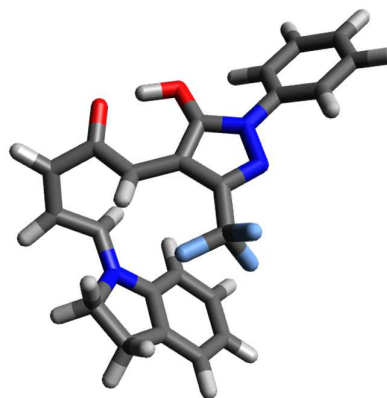


H	-4.65056	1.10612	-1.91687
C	-6.72214	-1.56085	-0.01522
H	-4.92905	-1.90290	1.13629
C	-7.31654	-0.82645	-1.04157
H	-7.01557	0.70700	-2.52421
H	-7.29435	-2.31121	0.52189
H	-8.35370	-1.00110	-1.30995
F	-0.87414	-2.74053	1.89977
F	0.68730	-1.67586	0.84344
F	0.00027	-0.95665	2.75674
C	4.28978	-0.30784	-0.79435
C	5.05768	1.27350	0.79756
C	5.49674	-0.80852	-0.30533
C	3.58196	-0.93142	-1.81736
C	6.00618	0.05965	0.81871
H	5.53928	2.16169	0.37594
C	6.02506	-1.97272	-0.84615
C	4.12342	-2.10287	-2.34841
H	2.64898	-0.53222	-2.20174
H	7.04538	0.36116	0.67139
C	5.33106	-2.61965	-1.87278
H	6.96306	-2.37468	-0.47411
H	3.59638	-2.61319	-3.14815
H	5.73380	-3.52963	-2.30579
N	3.94949	0.87470	-0.09595
H	5.94214	-0.47284	1.77246
H	4.65052	1.52366	1.77934

B'-C

Electronic energy: -1500.590477 Hartree
Free energy: -1500.6715683 Hartree

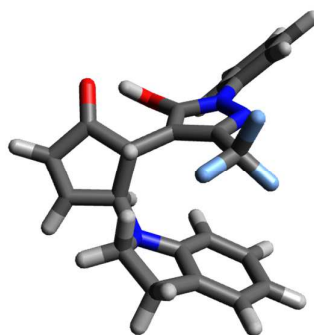
C	-1.90113	1.10932	-0.06768
C	-0.60796	-0.41928	-0.98319
C	-0.59627	0.93725	-0.56438
C	0.48166	1.90918	-0.61175
O	-2.49697	2.16962	0.42000
C	0.36190	3.24887	-0.16470
C	1.64388	3.93669	-0.06984
C	2.68531	3.14317	0.27608
C	2.35708	1.80244	0.72657
O	-0.71942	3.82127	0.22129
H	1.63888	1.68411	1.53031
H	3.72523	3.45984	0.23771
H	1.72036	5.00909	-0.22007
H	-1.77868	2.97199	0.33736
H	1.28511	1.69968	-1.30411
C	0.49022	-1.24140	-1.57906
N	-1.75924	-1.02608	-0.77493
N	-2.55044	-0.08061	-0.21213
C	-3.90519	-0.38677	0.09698
C	-4.54142	0.23047	1.17495
C	-4.57334	-1.32855	-0.68738
C	-5.86698	-0.09567	1.45532
H	-4.00908	0.95235	1.78188
C	-5.89373	-1.65109	-0.38698
H	-4.05667	-1.79714	-1.51744
C	-6.54675	-1.03411	0.68036
H	-6.36476	0.38444	2.29207
H	-6.41421	-2.38361	-0.99609
H	-7.57832	-1.28451	0.90716
F	0.78510	-2.32045	-0.83428
F	0.17404	-1.70167	-2.80472
F	1.63073	-0.53436	-1.71456
C	3.01437	-0.52635	1.05400
C	4.19283	0.76234	-0.55741
C	3.85502	-1.42042	0.39086
C	2.16449	-0.92727	2.07989
C	4.62106	-0.71343	-0.70049
H	3.75329	1.17158	-1.47272
C	3.85955	-2.75915	0.75634
C	2.17687	-2.27773	2.43493
H	1.50606	-0.23177	2.59010
H	4.35282	-1.11199	-1.68304
C	3.01441	-3.18637	1.78515
H	4.50461	-3.46623	0.24234
H	1.52065	-2.62131	3.22828
H	3.00496	-4.23148	2.07737
N	3.16262	0.76778	0.50420
H	5.70091	-0.82651	-0.57756
H	5.02523	1.40215	-0.25318
C			



Electronic energy: -1500.6191188 Hartree

Free energy: -1500.6988444 Hartree

C	1.56760	1.05793	-0.00740
C	0.39688	-0.45791	1.03614
C	0.30053	0.85501	0.51872
C	-0.85927	1.79394	0.46083
O	2.11674	2.12216	-0.61346
C	-0.50946	3.27632	0.52506
C	-1.57113	4.01524	-0.17948
C	-2.27518	3.15183	-0.92423
C	-1.77028	1.73217	-0.81306
O	0.50653	3.74781	1.01525
H	-1.12555	1.54052	-1.68098
H	-3.09659	3.40290	-1.58949
H	-1.67170	5.09324	-0.14014
H	1.85538	2.92191	-0.11928
H	-1.51541	1.62837	1.32440
C	-0.61585	-1.26606	1.78424
N	1.57781	-1.01396	0.82877
N	2.29456	-0.07640	0.18561
C	3.65632	-0.32408	-0.15665
C	4.17837	0.16438	-1.35356
C	4.43715	-1.07704	0.71979
C	5.51142	-0.09639	-1.66440
H	3.55274	0.73235	-2.03237
C	5.76327	-1.34078	0.38853
H	4.00280	-1.44704	1.64211
C	6.30516	-0.84781	-0.79883
H	5.92430	0.28212	-2.59411
H	6.37542	-1.92769	1.06596
H	7.34139	-1.05153	-1.04967
F	-0.83961	-2.46320	1.22629
F	-0.22239	-1.50357	3.05271
F	-1.79920	-0.62979	1.86140
C	-2.58085	-0.58931	-1.10651
C	-3.93003	0.85175	0.13782
C	-3.65425	-1.37720	-0.66051
C	-1.48597	-1.16781	-1.74671
C	-4.69820	-0.47141	-0.04802
H	-3.53842	0.92871	1.16243
C	-3.64686	-2.74717	-0.85641
C	-1.49216	-2.55456	-1.94024
H	-0.63632	-0.57656	-2.07512
H	-5.09945	-0.84962	0.89499
C	-2.55406	-3.34337	-1.50359
H	-4.47756	-3.35526	-0.50698
H	-0.64006	-3.02005	-2.42714
H	-2.53109	-4.41804	-1.65341
N	-2.83113	0.76236	-0.83787



H	-5.53551	-0.33655	-0.74301
H	-4.54720	1.73138	-0.06077

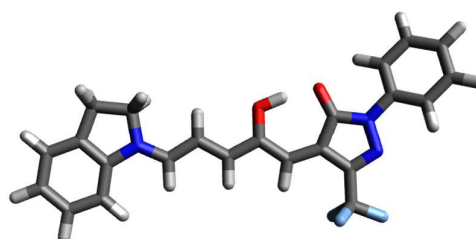
Eps = 7.5

A

Electronic energy: -1500.6202976 Hartree

Free energy: -1500.7069695 Hartree

C	2.88426	-0.61874	0.03506
C	3.20861	1.60618	0.05640
C	2.16767	0.63133	0.05128
C	0.77563	0.85938	0.04998
O	2.46184	-1.80103	0.00186
C	-0.24975	-0.07483	0.04340
C	-1.57835	0.39288	0.03807
C	-2.68504	-0.44498	0.02399
C	-3.96528	0.10949	0.01466
O	-0.07589	-1.41580	0.04206
H	-4.07364	1.19143	0.02383
H	-2.53996	-1.51980	0.01621
H	-1.72793	1.47030	0.04409
H	0.90252	-1.65479	0.02239
H	0.44983	1.89651	0.05384
C	3.04338	3.09112	0.07546
N	4.40878	1.09322	0.05000
N	4.22285	-0.26229	0.04677
C	5.35318	-1.11639	-0.01396
C	5.28075	-2.42623	0.46930
C	6.54621	-0.62318	-0.55110
C	6.41054	-3.23990	0.40077
H	4.35527	-2.79868	0.88885
C	7.66726	-1.44699	-0.60295
H	6.58782	0.39504	-0.92036
C	7.60557	-2.75889	-0.13210
H	6.35156	-4.25699	0.77632
H	8.59158	-1.05919	-1.02025
H	8.48122	-3.39877	-0.17838
F	4.21244	3.73853	0.08650
F	2.35317	3.52776	-0.99960
F	2.34695	3.50038	1.15683
C	-6.40234	-0.06980	-0.03077
C	-5.11703	-2.07156	-0.02219
C	-7.32222	-1.11849	-0.03970
C	-6.79645	1.26537	-0.04844
C	-6.61141	-2.44805	-0.01267
H	-4.60045	-2.41846	-0.92109
C	-8.68240	-0.83902	-0.06602
C	-8.16599	1.53104	-0.07444

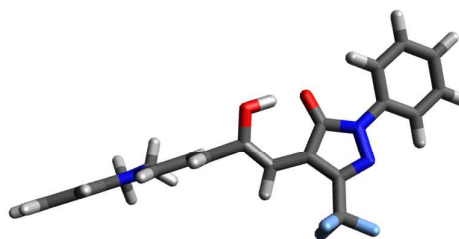


H	-6.08071	2.08064	-0.04333
H	-6.87294	-3.05786	-0.88096
C	-9.10225	0.49374	-0.08332
H	-9.40758	-1.64780	-0.07306
H	-8.50375	2.56238	-0.08902
H	-10.16230	0.72574	-0.10438
N	-5.08669	-0.59081	-0.00593
H	-6.87151	-3.01555	0.88470
H	-4.58144	-2.44146	0.85553

A-B

Electronic energy: -1500.5909926 Hartree
Free energy: -1500.6764479 Hartree

C	2.84133	-0.59030	-0.33253
C	3.01734	1.58729	0.04788
C	2.07598	0.59793	-0.29798
C	0.64182	0.73285	-0.52529
O	2.47801	-1.79852	-0.54994
C	-0.15648	-0.20630	-1.07054
C	-1.61623	0.03280	-1.24957
C	-2.53122	-0.37556	-0.35015
C	-3.92119	-0.13650	-0.61960
O	0.21345	-1.41653	-1.53666
H	-4.19461	0.36672	-1.54491
H	-2.22855	-0.88178	0.56147
H	-1.94673	0.52768	-2.16457
H	1.15639	-1.65677	-1.16771
H	0.17047	1.66660	-0.22990
C	2.75002	3.04216	0.22771
N	4.24675	1.13160	0.21063
N	4.14191	-0.20361	-0.03540
C	5.28501	-1.02492	0.11356
C	5.35388	-2.27739	-0.50672
C	6.36027	-0.55983	0.87954
C	6.49762	-3.05807	-0.34535
H	4.52026	-2.62928	-1.10019
C	7.49770	-1.34928	1.02303
H	6.29649	0.41289	1.35265
C	7.57334	-2.60350	0.41617
H	6.54475	-4.02935	-0.82892
H	8.32713	-0.98007	1.61901
H	8.46074	-3.21753	0.53438
F	3.84380	3.73622	0.56909
F	2.25571	3.61241	-0.89469
F	1.82446	3.27048	1.18906
C	-6.27774	-0.27446	-0.06383
C	-4.69562	-1.17365	1.48225
C	-7.00457	-0.69944	1.04293
C	-6.86961	0.25877	-1.20440

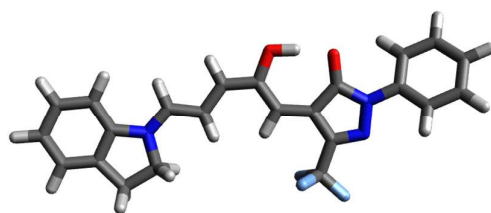


C	-6.09238	-1.21394	2.12412
H	-4.30096	-2.16993	1.27176
C	-8.39130	-0.58983	1.02688
C	-8.25823	0.36281	-1.20575
H	-6.29027	0.57755	-2.06447
H	-6.35851	-2.22800	2.42977
C	-9.01165	-0.05646	-0.10291
H	-8.97770	-0.91435	1.88111
H	-8.75887	0.77113	-2.07738
H	-10.09290	0.03364	-0.12987
N	-4.88516	-0.48065	0.17408
H	-6.13810	-0.57140	3.00753
H	-3.96943	-0.61177	2.06997
B			

Electronic energy: -1500.6123165 Hartree

Free energy: -1500.6979164 Hartree

C	3.07487	-0.90048	0.03189
C	2.56793	1.29128	0.07363
C	1.95148	0.00440	0.06872
C	0.57035	-0.27858	0.07581
O	3.11324	-2.15321	-0.01870
C	-0.05841	-1.51301	0.09452
C	-1.46664	-1.62632	0.08463
C	-2.43053	-0.62562	0.06012
C	-3.77464	-0.99449	0.03841
O	0.59759	-2.70247	0.13154
H	-4.03992	-2.04933	0.04298
H	-2.16265	0.42564	0.04675
H	-1.82532	-2.65588	0.09704
H	1.59109	-2.57443	0.06995
H	-0.08923	0.58425	0.06473
C	1.87642	2.61474	0.12144
N	3.87215	1.24975	0.05363
N	4.19164	-0.08036	0.03803
C	5.55359	-0.46578	-0.04650
C	5.97153	-1.70582	0.44514
C	6.47384	0.41991	-0.61503
C	7.31796	-2.05471	0.35310
H	5.25318	-2.38313	0.88891
C	7.81632	0.05896	-0.69003
H	6.13402	1.37865	-0.98992
C	8.24492	-1.17951	-0.21129
H	7.64078	-3.01855	0.73491
H	8.52790	0.74999	-1.13169
H	9.29198	-1.45850	-0.27617
F	2.73087	3.64199	0.10143
F	1.03286	2.77372	-0.92121
F	1.12108	2.74247	1.23318



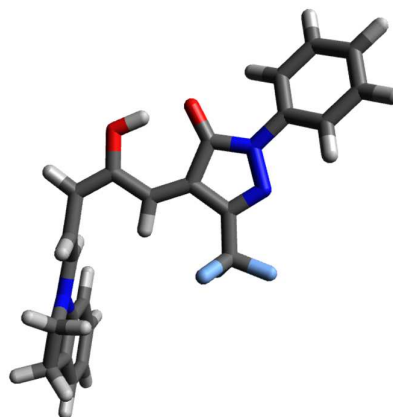
C	-6.15813	-0.48130	-0.05758
C	-4.61829	1.32737	0.01119
C	-6.93107	0.67961	-0.03124
C	-6.72167	-1.75083	-0.14552
C	-6.04893	1.89824	0.07736
H	-4.00848	1.61032	0.87218
C	-8.31513	0.58340	-0.09062
C	-8.11355	-1.83228	-0.20292
H	-6.11497	-2.64980	-0.17463
H	-6.22190	2.42185	1.02164
C	-8.90517	-0.68097	-0.17622
H	-8.92835	1.47984	-0.07101
H	-8.58350	-2.80808	-0.27341
H	-9.98574	-0.77010	-0.22448
N	-4.78707	-0.14263	0.00891
H	-6.23361	2.60470	-0.73520
H	-4.09442	1.61771	-0.90401

B-B'

Electronic energy: -1500.5884542 Hartree

Free energy: -1500.6740814 Hartree

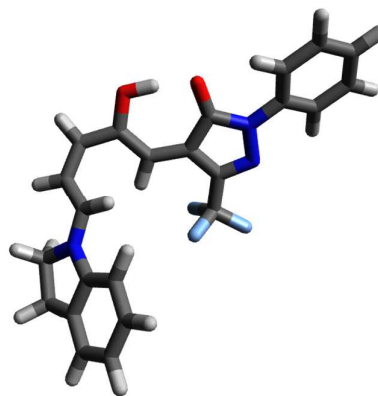
C	-2.88883	0.95487	0.02302
C	-1.79136	-1.01570	-0.34873
C	-1.55059	0.41432	-0.29308
C	-0.36780	1.05500	-0.50711
O	-3.25983	2.12354	0.16025
C	-0.06220	2.46749	-0.47014
C	1.20827	2.87568	-0.72727
C	2.34942	2.00439	-1.08308
C	3.24465	1.58961	-0.16339
O	-0.99777	3.40032	-0.18151
H	3.11558	1.85889	0.88223
H	2.47995	1.75262	-2.13415
H	1.36817	3.95457	-0.68929
H	-1.89411	3.00539	-0.04079
H	0.49577	0.43730	-0.74242
C	-0.78642	-2.09572	-0.61611
N	-3.01993	-1.32831	-0.11444
N	-3.69653	-0.15658	0.12347
C	-5.09979	-0.19449	0.34990
C	-5.70392	0.77245	1.15535
C	-5.85048	-1.21511	-0.23652
C	-7.08110	0.71448	1.36133
H	-5.10902	1.55323	1.61315
C	-7.22333	-1.26432	-0.01035
H	-5.36129	-1.95739	-0.85773
C	-7.84392	-0.29958	0.78378
H	-7.55463	1.46514	1.98631
H	-7.80858	-2.05802	-0.46404



H	-8.91529	-0.33959	0.95309
F	-1.35473	-3.29967	-0.69467
F	-0.13247	-1.87321	-1.77142
F	0.14778	-2.14689	0.35069
C	5.15163	0.19857	0.52917
C	4.63310	0.29348	-1.76382
C	6.10403	-0.61344	-0.10442
C	5.09038	0.29418	1.91836
C	5.95979	-0.47681	-1.60292
H	3.80820	-0.36828	-2.06401
C	7.00854	-1.34295	0.64918
C	6.01239	-0.44691	2.66593
H	4.35514	0.91729	2.41689
H	5.93375	-1.44111	-2.11525
C	6.96158	-1.26048	2.04828
H	7.74702	-1.97253	0.15945
H	5.97844	-0.38712	3.74986
H	7.66269	-1.83028	2.64968
N	4.35543	0.83303	-0.42820
H	6.79654	0.09793	-2.01390
H	4.70018	1.10801	-2.49038
B'			

Electronic energy: -1500.6075899 Hartree
Free energy: -1500.6931798 Hartree

C	-2.52187	0.96466	-0.15174
C	-1.44679	-0.69384	0.91218
C	-1.25762	0.63863	0.44852
C	-0.08172	1.42330	0.54492
O	-2.91448	2.02605	-0.70244
C	0.08553	2.75356	0.19352
C	1.33733	3.40067	0.38355
C	2.58913	2.81041	0.37753
C	2.82893	1.56008	-0.21760
O	-0.91914	3.56188	-0.21574
H	2.07729	1.12244	-0.86985
H	3.43214	3.37628	0.76287
H	1.28355	4.47644	0.54564
H	-1.75547	3.03199	-0.41464
H	0.77137	0.95447	1.02479
C	-0.43507	-1.54962	1.60077
N	-2.63496	-1.17686	0.65947
N	-3.29713	-0.17310	0.00808
C	-4.65383	-0.36135	-0.35729
C	-5.20978	0.35588	-1.42077
C	-5.42385	-1.28720	0.35353
C	-6.54532	0.14402	-1.75952
H	-4.60547	1.06725	-1.96872
C	-6.75313	-1.49308	-0.00485



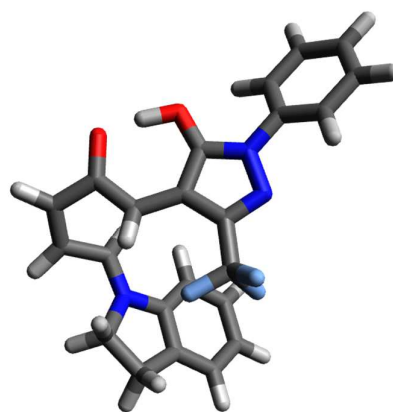
H	-4.97851	-1.83612	1.17530
C	-7.32213	-0.77747	-1.05884
H	-6.97512	0.70268	-2.58546
H	-7.34666	-2.21373	0.54956
H	-8.36051	-0.93791	-1.33155
F	-0.89717	-2.77200	1.88045
F	0.67807	-1.70376	0.84938
F	-0.02376	-1.00099	2.76352
C	4.29556	-0.29849	-0.79667
C	5.06801	1.28602	0.79417
C	5.50708	-0.79300	-0.31438
C	3.58105	-0.92540	-1.81310
C	6.02434	0.07896	0.80225
H	5.53916	2.17986	0.37415
C	6.03546	-1.95703	-0.85719
C	4.12242	-2.09577	-2.34595
H	2.64393	-0.52930	-2.19062
H	7.05902	0.38782	0.63944
C	5.33574	-2.60746	-1.87733
H	6.97757	-2.35499	-0.49142
H	3.59172	-2.60937	-3.14117
H	5.73833	-3.51693	-2.31178
N	3.95566	0.88636	-0.09772
H	5.97763	-0.45356	1.75679
H	4.66306	1.52612	1.77895

B'-C

Electronic energy: -1500.5945421 Hartree

Free energy: -1500.6745719 Hartree

C	1.88591	1.10333	0.06398
C	0.59752	-0.41883	0.99322
C	0.58284	0.93432	0.56517
C	-0.49734	1.90679	0.60737
O	2.48185	2.16034	-0.43411
C	-0.36768	3.25078	0.17456
C	-1.64833	3.93917	0.06143
C	-2.67943	3.14259	-0.30310
C	-2.33593	1.79915	-0.74204
O	0.72051	3.82520	-0.18894
H	-1.62151	1.68290	-1.54991
H	-3.72140	3.45434	-0.28791
H	-1.73042	5.01084	0.21375
H	1.77336	2.96586	-0.33247
H	-1.30223	1.69803	1.29903
C	-0.49613	-1.23816	1.60029
N	1.74987	-1.02653	0.78668
N	2.53733	-0.08387	0.21522
C	3.89190	-0.38636	-0.09863
C	4.50045	0.18735	-1.21577

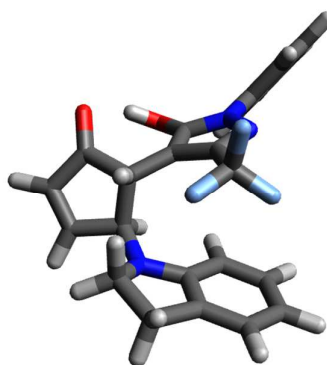


C	4.58663	-1.27776	0.72034
C	5.82675	-0.13109	-1.50196
H	3.94515	0.86892	-1.84882
C	5.90737	-1.59490	0.41404
H	4.09169	-1.71164	1.58224
C	6.53314	-1.02042	-0.69292
H	6.30390	0.31457	-2.36927
H	6.44953	-2.28841	1.04936
H	7.56490	-1.26599	-0.92423
F	-0.78330	-2.33022	0.86980
F	-0.17518	-1.68214	2.83166
F	-1.63987	-0.53823	1.72784
C	-2.99195	-0.53164	-1.06076
C	-4.17284	0.76504	0.54339
C	-3.84222	-1.42058	-0.40227
C	-2.13300	-0.93977	-2.07652
C	-4.62116	-0.70580	0.67473
H	-3.72409	1.15920	1.46119
C	-3.84729	-2.76099	-0.76231
C	-2.14593	-2.29202	-2.42608
H	-1.46817	-0.24769	-2.58327
H	-4.37995	-1.10891	1.66233
C	-2.99281	-3.19559	-1.78077
H	-4.50078	-3.46348	-0.25253
H	-1.48345	-2.64071	-3.21211
H	-2.98433	-4.24194	-2.06891
N	-3.14339	0.76516	-0.51973
H	-5.69933	-0.80581	0.52752
H	-4.99585	1.41992	0.24707
C			

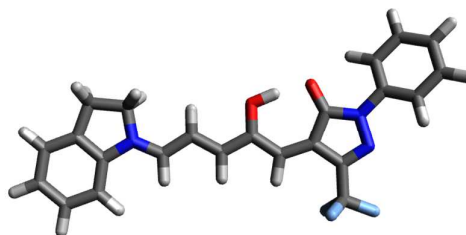
Electronic energy: -1500.6228411 Hartree

Free energy: -1500.7040427 Hartree

C	1.56349	1.05525	-0.01481
C	0.39630	-0.44773	1.05003
C	0.29799	0.85855	0.51794
C	-0.86270	1.79562	0.45388
O	2.11190	2.11075	-0.63569
C	-0.51390	3.27819	0.50859
C	-1.57636	4.01199	-0.19879
C	-2.28078	3.14326	-0.93747
C	-1.77211	1.72559	-0.82024
O	0.50350	3.75175	0.99540
H	-1.12606	1.53323	-1.68689
H	-3.10391	3.38989	-1.60231
H	-1.67886	5.09009	-0.16586
H	1.84542	2.91899	-0.15824
H	-1.51887	1.63542	1.31849
C	-0.61183	-1.24341	1.81647



N	1.57702	-1.00684	0.84577
N	2.29126	-0.07625	0.18952
C	3.65176	-0.32595	-0.15681
C	4.15799	0.12744	-1.37416
C	4.44675	-1.04325	0.73660
C	5.49024	-0.13291	-1.68958
H	3.52052	0.66717	-2.06524
C	5.77194	-1.30773	0.40102
H	4.02547	-1.38456	1.67607
C	6.29816	-0.84963	-0.80743
H	5.89117	0.21802	-2.63524
H	6.39551	-1.86685	1.09148
H	7.33359	-1.05344	-1.06167
F	-0.80184	-2.46821	1.30476
F	-0.23201	-1.42350	3.09928
F	-1.80854	-0.63161	1.85227
C	-2.57604	-0.59853	-1.11116
C	-3.93007	0.84037	0.13323
C	-3.64528	-1.39077	-0.66132
C	-1.48323	-1.17308	-1.75959
C	-4.68943	-0.48966	-0.04211
H	-3.53998	0.93078	1.15701
C	-3.63594	-2.76021	-0.86185
C	-1.48868	-2.55929	-1.95983
H	-0.63742	-0.57845	-2.09195
H	-5.07954	-0.86809	0.90553
C	-2.54667	-3.35226	-1.51977
H	-4.46367	-3.37104	-0.50991
H	-0.63974	-3.02093	-2.45610
H	-2.52366	-4.42616	-1.67551
N	-2.82885	0.75091	-0.84057
H	-5.53420	-0.36368	-0.72957
H	-4.55312	1.71362	-0.07451



Eps = 10

A

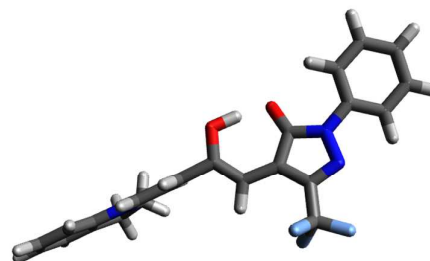
Electronic energy: -1500.6225151 Hartree

Free energy: -1500.7095708 Hartree

C	2.88489	-0.61600	0.03175
C	3.20823	1.60722	0.05886
C	2.16870	0.63242	0.05018
C	0.77371	0.85965	0.04729
O	2.46364	-1.80006	-0.00684
C	-0.24792	-0.07537	0.04126
C	-1.58031	0.38948	0.03486
C	-2.68359	-0.44897	0.02257
C	-3.96569	0.10725	0.01208

O	-0.07256	-1.41656	0.04280
H	-4.07239	1.18941	0.01841
H	-2.53981	-1.52399	0.01701
H	-1.73182	1.46670	0.03905
H	0.90696	-1.65376	0.01940
H	0.44638	1.89625	0.04981
C	3.04225	3.09187	0.08098
N	4.41005	1.09533	0.05314
N	4.22349	-0.25967	0.04665
C	5.35265	-1.11507	-0.01502
C	5.28418	-2.41762	0.48802
C	6.53997	-0.63088	-0.57247
C	6.41213	-3.23387	0.41868
H	4.36298	-2.78222	0.92395
C	7.65989	-1.45652	-0.62443
H	6.57822	0.38170	-0.95768
C	7.60177	-2.76156	-0.13415
H	6.35658	-4.24541	0.80949
H	8.58005	-1.07597	-1.05734
H	8.47626	-3.40304	-0.18075
F	4.21152	3.73978	0.10018
F	2.35834	3.53219	-0.99661
F	2.34033	3.49877	1.15971
C	-6.40152	-0.07018	-0.03269
C	-5.11760	-2.07378	-0.01748
C	-7.32151	-1.11848	-0.03685
C	-6.79385	1.26543	-0.05568
C	-6.61212	-2.44842	-0.00515
H	-4.60243	-2.42364	-0.91587
C	-8.68177	-0.83798	-0.06345
C	-8.16313	1.53205	-0.08189
H	-6.07705	2.07978	-0.05452
H	-6.87509	-3.06121	-0.87087
C	-9.10019	0.49506	-0.08587
H	-9.40756	-1.64623	-0.06678
H	-8.50021	2.56355	-0.10058
H	-10.16010	0.72790	-0.10721
N	-5.08535	-0.59220	-0.00653
H	-6.87203	-3.01185	0.89480
H	-4.58160	-2.44034	0.86121

A-B

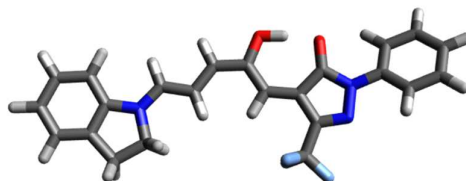


Electronic energy: -1500.5945182 Hartree

Free energy: -1500.6805048 Hartree

C	2.84641	-0.59193	-0.32481
C	3.01924	1.58725	0.04774
C	2.07837	0.59484	-0.29074
C	0.64291	0.72777	-0.51375
O	2.48593	-1.80218	-0.53597

C	-0.15738	-0.21366	-1.05237
C	-1.61681	0.02619	-1.23373
C	-2.53456	-0.37896	-0.33610
C	-3.92377	-0.13779	-0.61199
O	0.21298	-1.42659	-1.51247
H	-4.19200	0.36477	-1.53912
H	-2.23709	-0.88367	0.57816
H	-1.94441	0.52022	-2.15012
H	1.15676	-1.66320	-1.14753
H	0.17229	1.66313	-0.22241
C	2.75015	3.04232	0.22357
N	4.25071	1.13462	0.20664
N	4.14718	-0.20139	-0.03502
C	5.29177	-1.02142	0.11073
C	5.37012	-2.26129	-0.53300
C	6.35764	-0.56766	0.89606
C	6.51451	-3.04192	-0.37573
H	4.54342	-2.60352	-1.14188
C	7.49650	-1.35622	1.03498
H	6.28597	0.39523	1.38812
C	7.58148	-2.59834	0.40470
H	6.56979	-4.00345	-0.87755
H	8.31918	-0.99637	1.64583
H	8.46972	-3.21180	0.51939
F	3.84572	3.73965	0.55355
F	2.24695	3.60690	-0.89765
F	1.83196	3.27328	1.19090
C	-6.28239	-0.27243	-0.06665
C	-4.70799	-1.17309	1.48706
C	-7.01507	-0.70130	1.03477
C	-6.86809	0.26585	-1.20820
C	-6.10928	-1.22195	2.11823
H	-4.30537	-2.16664	1.27928
C	-8.40173	-0.59052	1.01217
C	-8.25666	0.37100	-1.21605
H	-6.28381	0.58774	-2.06379
H	-6.37537	-2.23922	2.41315
C	-9.01602	-0.05206	-0.11858
H	-8.99253	-0.91820	1.86218
H	-8.75256	0.78351	-2.08846
H	-10.09709	0.03920	-0.15050
N	-4.89115	-0.48048	0.17762
H	-6.16307	-0.58700	3.00658
H	-3.99009	-0.60635	2.08028
B			



Electronic energy: -1500.6145794 Hartree
Free energy: -1500.7003681 Hartree

C	3.07288	-0.89523	0.02696
---	---------	----------	---------

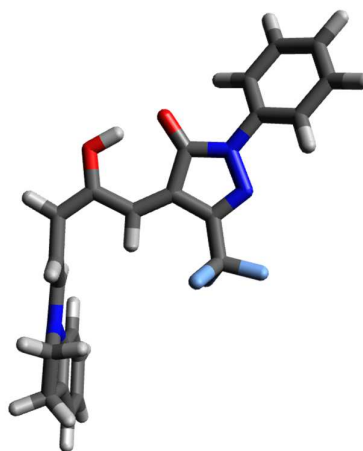
C	2.57437	1.29589	0.07634
C	1.95440	0.01222	0.06674
C	0.56905	-0.26795	0.07200
O	3.10800	-2.14961	-0.03037
C	-0.05901	-1.49949	0.09252
C	-1.47067	-1.61534	0.08203
C	-2.43265	-0.61726	0.05504
C	-3.77857	-0.99028	0.03496
O	0.59484	-2.69051	0.13393
H	-4.04064	-2.04595	0.04278
H	-2.16702	0.43458	0.03879
H	-1.82799	-2.64533	0.09693
H	1.58926	-2.56357	0.06682
H	-0.08903	0.59598	0.05835
C	1.88740	2.62134	0.12877
N	3.87983	1.25118	0.05716
N	4.19317	-0.07990	0.03714
C	5.55300	-0.47217	-0.04741
C	5.96641	-1.70849	0.45730
C	6.47590	0.40262	-0.62843
C	7.31090	-2.06519	0.36569
H	5.24580	-2.37672	0.91139
C	7.81666	0.03456	-0.70265
H	6.13953	1.35845	-1.01398
C	8.24051	-1.20060	-0.21103
H	7.63038	-3.02602	0.75780
H	8.53045	0.71708	-1.15391
H	9.28608	-1.48527	-0.27540
F	2.74605	3.64603	0.11491
F	1.04663	2.78923	-0.91465
F	1.13083	2.74791	1.23978
C	-6.16190	-0.48402	-0.05741
C	-4.62598	1.32995	-0.00078
C	-6.93685	0.67527	-0.03764
C	-6.72148	-1.75604	-0.13364
C	-6.05812	1.89708	0.05829
H	-4.01998	1.61743	0.86121
C	-8.32115	0.57486	-0.09235
C	-8.11316	-1.84165	-0.18648
H	-6.11184	-2.65320	-0.15690
H	-6.23324	2.43075	0.99643
C	-8.90762	-0.69176	-0.16643
H	-8.93677	1.46972	-0.07776
H	-8.58088	-2.81915	-0.24765
H	-9.98813	-0.78420	-0.21072
N	-4.79043	-0.14158	0.00293
H	-6.24444	2.59350	-0.76254
H	-4.09989	1.61661	-0.91555

B-B'

Electronic energy: -1500.5899039 Hartree

Free energy: -1500.6753234 Hartree

C	-2.88728	0.95340	0.02185
C	-1.78962	-1.01677	-0.35031
C	-1.54920	0.41335	-0.29490
C	-0.36685	1.05475	-0.50976
O	-3.25940	2.12210	0.15870
C	-0.06250	2.46743	-0.47293
C	1.20758	2.87714	-0.72931
C	2.34990	2.00704	-1.08433
C	3.24424	1.59264	-0.16362
O	-0.99967	3.39950	-0.18499
H	3.11421	1.86164	0.88198
H	2.48108	1.75486	-2.13524
H	1.36649	3.95621	-0.69120
H	-1.89531	3.00269	-0.04347
H	0.49707	0.43779	-0.74558
C	-0.78530	-2.09761	-0.61699
N	-3.01811	-1.32966	-0.11537
N	-3.69447	-0.15791	0.12297
C	-5.09759	-0.19472	0.35047
C	-5.69628	0.76071	1.17344
C	-5.85307	-1.20207	-0.25236
C	-7.07345	0.70517	1.38059
H	-5.09688	1.53024	1.64455
C	-7.22585	-1.24983	-0.02458
H	-5.36801	-1.93505	-0.88789
C	-7.84114	-0.29605	0.78694
H	-7.54306	1.44673	2.01927
H	-7.81517	-2.03326	-0.49072
H	-8.91242	-0.33470	0.95737
F	-1.35551	-3.30088	-0.69817
F	-0.12845	-1.87534	-1.77045
F	0.14650	-2.15214	0.35197
C	5.14952	0.20013	0.52995
C	4.63336	0.29581	-1.76353
C	6.10142	-0.61333	-0.10299
C	5.08684	0.29523	1.91928
C	5.95914	-0.47564	-1.60156
H	3.80793	-0.36528	-2.06359
C	7.00390	-1.34472	0.65138
C	6.00686	-0.44783	2.66762
H	4.35209	0.91953	2.41709
H	5.93303	-1.43954	-2.11460
C	6.95548	-1.26280	2.05065
H	7.74187	-1.97528	0.16212
H	5.97175	-0.38839	3.75158
H	7.65499	-1.83407	2.65259
N	4.35561	0.83630	-0.42798
H	6.79686	0.09879	-2.01101

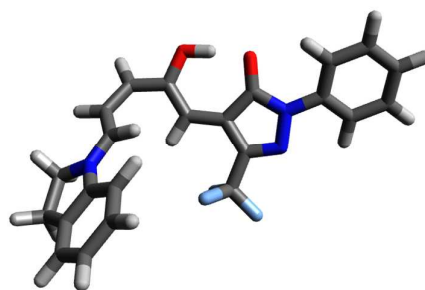


H	4.70153	1.10983	-2.49047
B'			

Electronic energy: -1500.6097405 Hartree

Free energy: -1500.6953916 Hartree

C	-2.51927	0.96157	-0.14664
C	-1.44787	-0.70160	0.90863
C	-1.25715	0.63128	0.45084
C	-0.07777	1.41710	0.55093
O	-2.91240	2.02745	-0.69267
C	0.08839	2.74521	0.20267
C	1.34056	3.39801	0.39930
C	2.59207	2.81524	0.38152
C	2.83164	1.56337	-0.21793
O	-0.91317	3.55402	-0.21413
H	2.07916	1.12736	-0.87031
H	3.43669	3.38272	0.76085
H	1.28144	4.47079	0.57846
H	-1.75171	3.02402	-0.41060
H	0.77475	0.94639	1.02981
C	-0.43855	-1.56147	1.59536
N	-2.63799	-1.18307	0.65488
N	-3.29716	-0.17511	0.00801
C	-4.65432	-0.35696	-0.35830
C	-5.20246	0.35500	-1.42941
C	-5.43290	-1.27080	0.35876
C	-6.53887	0.15053	-1.76954
H	-4.59098	1.05638	-1.98247
C	-6.76297	-1.47008	-0.00108
H	-4.99386	-1.81543	1.18688
C	-7.32414	-0.75914	-1.06255
H	-6.96264	0.70494	-2.60147
H	-7.36330	-2.18134	0.55814
H	-8.36308	-0.91418	-1.33631
F	-0.90117	-2.78703	1.86311
F	0.67882	-1.70965	0.84933
F	-0.03399	-1.02284	2.76527
C	4.29606	-0.29494	-0.79734
C	5.07170	1.29219	0.79113
C	5.50840	-0.78782	-0.31627
C	3.57873	-0.92342	-1.81086
C	6.02913	0.08639	0.79654
H	5.54006	2.18672	0.37008
C	6.03568	-1.95320	-0.85806
C	4.11892	-2.09470	-2.34260
H	2.64084	-0.52763	-2.18680
H	7.06258	0.39624	0.62811
C	5.33353	-2.60536	-1.87524
H	6.97867	-2.35031	-0.49369

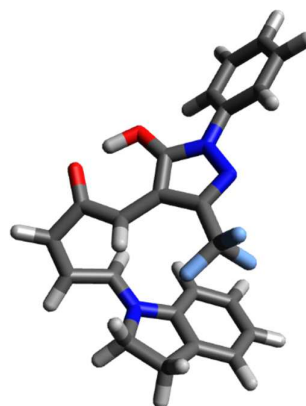


H	3.58676	-2.60989	-3.13584
H	5.73519	-3.51568	-2.30889
N	3.95726	0.89223	-0.09982
H	5.98750	-0.44472	1.75204
H	4.66759	1.53072	1.77643
B'-C			

Electronic energy: -1500.5964676 Hartree

Free energy: -1500.676287 Hartree

C	1.87855	1.10126	0.06137
C	0.59266	-0.41744	0.99809
C	0.57649	0.93386	0.56512
C	-0.50478	1.90646	0.60513
O	2.47405	2.15662	-0.44229
C	-0.37097	3.25223	0.17791
C	-1.65108	3.94038	0.05641
C	-2.67730	3.14156	-0.31522
C	-2.32638	1.79674	-0.74761
O	0.72006	3.82715	-0.17616
H	-1.61368	1.68137	-1.55728
H	-3.72012	3.45080	-0.31064
H	-1.73602	5.01190	0.20819
H	1.77001	2.96339	-0.33235
H	-1.30887	1.69893	1.29835
C	-0.49876	-1.23514	1.61096
N	1.74546	-1.02558	0.79236
N	2.53111	-0.08454	0.21630
C	3.88562	-0.38585	-0.09934
C	4.48287	0.16824	-1.23227
C	4.59112	-1.25529	0.73382
C	5.80941	-0.14746	-1.52068
H	3.91817	0.83199	-1.87614
C	5.91199	-1.57056	0.42539
H	4.10500	-1.67358	1.60850
C	6.52662	-1.01528	-0.69761
H	6.27812	0.28264	-2.40036
H	6.46302	-2.24694	1.07146
H	7.55842	-1.25919	-0.93059
F	-0.78104	-2.33443	0.88851
F	-0.17613	-1.66950	2.84573
F	-1.64457	-0.53926	1.73303
C	-2.98110	-0.53485	-1.06347
C	-4.16698	0.76477	0.53470
C	-3.83505	-1.42236	-0.40738
C	-2.11790	-0.94531	-2.07485
C	-4.61884	-0.70511	0.66447
H	-3.71935	1.15757	1.45370
C	-3.83974	-2.76334	-0.76569
C	-2.13048	-2.29819	-2.42270

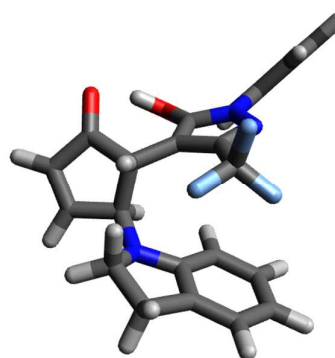


H	-1.45081	-0.25407	-2.57988
H	-4.38461	-1.10791	1.65389
C	-2.98108	-3.20026	-1.77989
H	-4.49657	-3.46437	-0.25812
H	-1.46525	-2.64838	-3.20581
H	-2.97273	-4.24696	-2.06695
N	-3.13477	0.76277	-0.52595
H	-5.69625	-0.80317	0.51057
H	-4.98762	1.42158	0.23647
C			

Electronic energy: -1500.6246052 Hartree

Free energy: -1500.7058315 Hartree

C	1.55885	1.05553	-0.01491
C	0.39490	-0.44362	1.05831
C	0.29423	0.85981	0.52047
C	-0.86809	1.79440	0.45238
O	2.10569	2.10778	-0.64229
C	-0.52113	3.27726	0.50700
C	-1.58177	4.00938	-0.20426
C	-2.28275	3.13921	-0.94472
C	-1.77213	1.72255	-0.82528
O	0.49485	3.75142	0.99680
H	-1.12227	1.53152	-1.68934
H	-3.10414	3.38456	-1.61217
H	-1.68606	5.08737	-0.17261
H	1.83530	2.91961	-0.17321
H	-1.52683	1.63373	1.31496
C	-0.61111	-1.23549	1.83108
N	1.57626	-1.00259	0.85535
N	2.28828	-0.07391	0.19381
C	3.64785	-0.32334	-0.15660
C	4.14338	0.11202	-1.38492
C	4.45224	-1.02136	0.74360
C	5.47476	-0.14719	-1.70517
H	3.49810	0.63672	-2.08051
C	5.77654	-1.28523	0.40342
H	4.03943	-1.34800	1.69210
C	6.29206	-0.84519	-0.81643
H	5.86763	0.18954	-2.65935
H	6.40777	-1.82918	1.09903
H	7.32673	-1.04837	-1.07432
F	-0.77986	-2.47338	1.34195
F	-0.24191	-1.38601	3.12108
F	-1.81569	-0.63965	1.84329
C	-2.56925	-0.60346	-1.11598
C	-3.93273	0.83399	0.11993
C	-3.63776	-1.39826	-0.66809
C	-1.47219	-1.17619	-1.75927



C	-4.68697	-0.49902	-0.05474
H	-3.54687	0.92913	1.14483
C	-3.62288	-2.76829	-0.86454
C	-1.47239	-2.56308	-1.95616
H	-0.62744	-0.57936	-2.09050
H	-5.07929	-0.87649	0.89238
C	-2.52919	-3.35861	-1.51721
H	-4.44985	-3.38094	-0.51387
H	-0.62061	-3.02306	-2.44922
H	-2.50235	-4.43284	-1.67039
N	-2.82682	0.74535	-0.84908
H	-5.52974	-0.37770	-0.74548
H	-4.55767	1.70449	-0.09326

4.5 References

- (1) *Out-of-Equilibrium (Supra)Molecular Systems and Materials*, Giuseppone, N., Walther, A., Eds., Wiley, 2021. <https://doi.org/10.1002/9783527821990>.
- (2) Otto, S. An Approach to the De Novo Synthesis of Life. *Acc. Chem. Res.* **2022**, *55* (2), 145–155. <https://doi.org/10.1021/acs.accounts.1c00534>.
- (3) Pilz da Cunha, M., Debije, M. G., Schenning, A. P. H. J. Bioinspired Light-Driven Soft Robots Based on Liquid Crystal Polymers. *Chem. Soc. Rev.* **2020**, *49* (18), 6568–6578. <https://doi.org/10.1039/D0CS00363H>.
- (4) Li, J., Zhou, X., Liu, Z. Recent Advances in Photoactuators and Their Applications in Intelligent Bionic Movements. *Adv. Opt. Mater.* **2020**, *8*, 2000886. <https://doi.org/10.1002/adom.202000886>.
- (5) Davis, D. A., Hamilton, A., Yang, J., Cremar, L. D., Van Gough, D., Potisek, S. L., Ong, M. T., Braun, P. V., Martínez, T. J., White, S. R., Moore, J. S., Sottos, N. R., Force-Induced Activation of Covalent Bonds in Mechanoresponsive Polymeric Materials. *Nature* **2009**, *459* (7243), 68–72. <https://doi.org/10.1038/nature07970>.
- (6) Lu, X., Zhang, H., Fei, G., Yu, B., Tong, X., Xia, H., Zhao, Y. Liquid-Crystalline Dynamic Networks Doped with Gold Nanorods Showing Enhanced Photocontrol of Actuation. *Adv. Mater.* **2018**, *30* (14), 1706597. <https://doi.org/10.1002/adma.201706597>.
- (7) Iamsaard, S., Abhoff, S. J., Matt, B., Kudernac, T., Cornelissen, J. J. L. M., Fletcher, S. P., Katsonis, N. Conversion of Light into Macroscopic Helical Motion. *Nat. Chem.* **2014**, *6* (3), 229–235. <https://doi.org/10.1038/nchem.1859>.
- (8) Nie, H., Self, J. L., Kuenstler, A. S., Hayward, R. C., Read de Alaniz, J. Multiaddressable Photochromic Architectures: From Molecules to Materials. *Adv. Opt. Mater.* **2019**, *7*, 1900224. <https://doi.org/10.1002/adom.201900224>.
- (9) Andréasson, J., Pischel, U. Light-Stimulated Molecular and Supramolecular Systems

- for Information Processing and Beyond. *Coord. Chem. Rev.* **2021**, *429*, 213695.
<https://doi.org/10.1016/j.ccr.2020.213695>.
- (10) Zarzar, L. D., Aizenberg, J. Stimuli-Responsive Chemomechanical Actuation: A Hybrid Materials Approach. *Acc. Chem. Res.* **2014**, *47* (2), 530–539.
<https://doi.org/10.1021/ar4001923>.
- (11) Fihey, A., Perrier, A., Browne, W. R., Jacquemin, D. Multiphotochromic Molecular Systems. *Chem. Soc. Rev.* **2015**, *44* (11), 3719–3759.
<https://doi.org/10.1039/c5cs00137d>.
- (12) Helmy, S., Leibfarth, F. A., Oh, S., Poelma, J. E., Hawker, C. J., Read de Alaniz, J. Photoswitching Using Visible Light: A New Class of Organic Photochromic Molecules. *J. Am. Chem. Soc.* **2014**, *136* (23), 8169–8172.
<https://doi.org/10.1021/ja503016b>.
- (13) Lerch, M. M., Szymański, W., Feringa, B. L. The (Photo)Chemistry of Stenhouse Photoswitches: Guiding Principles and System Design. *Chem. Soc. Rev.* **2018**, *47* (6), 1910–1937. <https://doi.org/10.1039/c7cs00772h>.
- (14) Hemmer, J. R., Page, Z. A., Clark, K. D., Stricker, F., Dolinski, N. D., Hawker, C. J., Read de Alaniz, J. Controlling Dark Equilibria and Enhancing Donor-Acceptor Stenhouse Adduct Photoswitching Properties through Carbon Acid Design. *J. Am. Chem. Soc.* **2018**, *140* (33), 10425–10429. <https://doi.org/10.1021/jacs.8b06067>.
- (15) Mallo, N., Foley, E. D., Iranmanesh, H., Kennedy, A. D. W., Luis, E. T., Ho, J., Harper, J. B., Beves, J. E. Structure-Function Relationships of Donor-Acceptor Stenhouse Adduct Photochromic Switches. *Chem. Sci.* **2018**, *9* (43), 8242–8252.
<https://doi.org/10.1039/c8sc03218a>.
- (16) Stricker, F., Seshadri, S., Alaniz, J. R. Donor–Acceptor Stenhouse Adducts. In *Molecular Photoswitches*, Wiley, 2022, pp 303–324.
<https://doi.org/10.1002/9783527827626.ch14>.

- (17) Lerch, M. M., Wezenberg, S. J., Szymanski, W., Feringa, B. L. Unraveling the Photoswitching Mechanism in Donor–Acceptor Stenhouse Adducts. *J. Am. Chem. Soc.* **2016**, *138* (20), 6344–6347. <https://doi.org/10.1021/jacs.6b01722>.
- (18) Di Donato, M., Lerch, M. M., Lapini, A., Laurent, A. D., Iagatti, A., Bussotti, L., Ihrig, S. P., Medved, M., Jacquemin, D., Szymański, W., Feringa, B. L., Shedding Light on the Photoisomerization Pathway of Donor-Acceptor Stenhouse Adducts. *J. Am. Chem. Soc.* **2017**, *139* (44), 15596–15599. <https://doi.org/10.1021/jacs.7b09081>.
- (19) Zulfikri, H., Koenis, M. A. J., Lerch, M. M., Di Donato, M., Szymański, W., Filippi, C., Feringa, B. L., Buma, W. J., Taming the Complexity of Donor–Acceptor Stenhouse Adducts: Infrared Motion Pictures of the Complete Switching Pathway. *J. Am. Chem. Soc.* **2019**, *141* (18), 7376–7384. <https://doi.org/10.1021/jacs.9b00341>.
- (20) Sanchez, D. M., Raucci, U., Martínez, T. J. In Silico Discovery of Multistep Chemistry Initiated by a Conical Intersection: The Challenging Case of Donor–Acceptor Stenhouse Adducts. *J. Am. Chem. Soc.* **2021**, *143* (48), 20015–20021. <https://doi.org/10.1021/jacs.1c06648>.
- (21) Stricker, F., Sanchez, D. M., Raucci, U., Dolinski, N. D., Zayas, M. S., Meisner, J., Hawker, C. J., Martínez, T. J., Read de Alaniz, J. A Multi-Stage Single Photochrome System for Controlled Photoswitching Responses. *Nat. Chem.* **2022**. <https://doi.org/10.1038/s41557-022-00947-8>.
- (22) Hemmer, J. R., Poelma, S. O., Treat, N., Page, Z. A., Dolinski, N. D., Diaz, Y. J., Tomlinson, W., Clark, K. D., Hooper, J. P., Hawker, C., Read de Alaniz, J., Tunable Visible and Near Infrared Photoswitches. *J. Am. Chem. Soc.* **2016**, *138* (42), 13960–13966. <https://doi.org/10.1021/jacs.6b07434>.
- (23) Mallo, N., Brown, P. T., Iranmanesh, H., MacDonald, T. S. C., Teusner, M. J., Harper, J. B., Ball, G. E., Beves, J. E. Photochromic Switching Behaviour of Donor-Acceptor Stenhouse Adducts in Organic Solvents. *Chem. Commun.* **2016**, *52* (93), 13576–13579.

<https://doi.org/10.1039/C6CC08079K>.

- (24) Clerc, M., Stricker, F., Ulrich, S., Sroda, M., Bruns, N., Boesel, L. F., Read de Alaniz, J. Promoting the Furan Ring Opening Reaction to Access New Donor–Acceptor Stenhouse Adducts with Hexafluoroisopropanol. *Angew. Chemie Int. Ed.* **2021**, *60* (18), 10219–10227. <https://doi.org/10.1002/anie.202100115>.
- (25) Peterson, J. A., Stricker, F., Read de Alaniz, J. Improving the Kinetics and Dark Equilibrium of Donor–Acceptor Stenhouse Adduct by Triene Backbone Design. *Chem. Commun.* **2022**, *58* (14), 2303–2306. <https://doi.org/10.1039/d1cc06235b>.
- (26) Lui, B. F., Tierce, N. T., Tong, F., Sroda, M. M., Lu, H., Read de Alaniz, J., Bardeen, C. J. Unusual Concentration Dependence of the Photoisomerization Reaction in Donor–Acceptor Stenhouse Adducts. *Photochem. Photobiol. Sci.* **2019**, *18* (6), 1587–1595. <https://doi.org/10.1039/c9pp00130a>.
- (27) Sroda, M. M., Stricker, F., Peterson, J. A., Bernal, A., Read de Alaniz, J. Donor–Acceptor Stenhouse Adducts: Exploring the Effects of Ionic Character. *Chem. – A Eur. J.* **2021**, *27* (12), 4183–4190. <https://doi.org/10.1002/chem.202005110>.
- (28) Lerch, M. M., Di Donato, M., Laurent, A. D., Medved', M., Iagatti, A., Bussotti, L., Lapini, A., Buma, W. J., Foggi, P., Szymański, W., Feringa, B. L., Solvent Effects on the Actinic Step of Donor–Acceptor Stenhouse Adduct Photoswitching. *Angew. Chemie Int. Ed.* **2018**, *57* (27), 8063–8068. <https://doi.org/10.1002/anie.201803058>.
- (29) Mallo, N., Tron, A., Andréasson, J., Harper, J. B., Jacob, L. S. D., McClenaghan, N. D., Jonusauskas, G., Beves, J. E. Hydrogen-Bonding Donor–Acceptor Stenhouse Adducts. *ChemPhotoChem* **2020**, *4* (6), 407–412. <https://doi.org/10.1002/cptc.201900295>.
- (30) Sroda, M. M., Stricker, F., Peterson, J. A., Bernal, A., Read de Alaniz, J. Donor–Acceptor Stenhouse Adducts: Exploring the Effects of Ionic Character. *Chem. – A Eur. J.* **2020**, <https://doi.org/10.1002/chem.202005110>.

- (31) Zulfikri, H., Koenis, M. A. J., Lerch, M. M., Di, M., Szyma, W., Filippi, C., Feringa, B. L., Buma, W. J. Taming the Complexity of Donor-Acceptor Stenhouse Adducts: Infrared Motion Pictures of the Complete Switching Pathway. *J. Am. Chem. Soc.* **2019**, *141* (18), 7376–7384. <https://doi.org/10.1021/jacs.9b00341>.
- (32) Lui, B. F., Tierce, N. T., Tong, F., Sroda, M. M., Lu, H., Read de Alaniz, J., Bardeen, C. J. Unusual Concentration Dependence of the Photoisomerization Reaction in Donor-Acceptor Stenhouse Adducts. *Photochem. Photobiol. Sci.* **2019**, *18* (6), 1587–1595. <https://doi.org/10.1039/c9pp00130a>.
- (33) Seshadri, S., Gockowski, L. F., Lee, J., Sroda, M., Helgeson, M. E., Read de Alaniz, J., Valentine, M. T. Self-Regulating Photochemical Rayleigh-Bénard Convection Using a Highly-Absorbing Organic Photoswitch. *Nat. Commun.* **2020**, *11*, 2599. <https://doi.org/10.1038/s41467-020-16277-7>.
- (34) Helmy, S., Oh, S., Leibfarth, F. A., Hawker, C. J., Read de Alaniz, J. Design and Synthesis of Donor-Acceptor Stenhouse Adducts: A Visible Light Photoswitch Derived from Furfural. *J. Org. Chem.* **2014**, *79* (23), 11316–11329. <https://doi.org/10.1021/jo502206g>.

5 DASA as a multi-stage photoswitch

This chapter was originally published in *Nature Chemistry*. (Stricker, F., Sanchez, D. M., Raucci, U., Dolinski, N. D., Zayas, M. S., Meisner, J., Hawker, C. J., Martinez, T. J., Read de Alaniz, J., *Nature Chemistry*, **2022**, <https://doi.org/10.1038/s41557-022-00947-8>.)¹ Reprinted with permission from Springer Nature.

5.1 Multi-stage photoswitching

The ability to control the properties of a material through the application of external stimuli is of key importance to the ever-growing field of smart materials. Of the stimuli available, light offers numerous attractive features as an external stimulus due to its benign nature, availability, and spatial and temporal control.² To translate the light irradiation into a macroscopic material response, molecular photoswitches that undergo structural changes can be used to enable actuation,^{3,4} control ion conductivity,^{5,6} and enhance energy storage.^{7,8} The advancement of these fields has been tightly coupled with structure-property relationship studies of photoswitches that enable a fundamental understanding of their underlying light-driven mechanisms.⁹

In general, photoswitches are converted from the ground-state isomer to the metastable isomer either through a *Z/E*-isomerization (e.g., azobenzene¹⁰ and hydrazones¹¹) or a pericyclic reaction (e.g., diarylethene,^{12,13} spiropyran,¹⁴ and dihydroazulene¹⁵).¹⁶ The reversion back to the original state can be facilitated by a thermal process (T-type) and/or by irradiation with a secondary wavelength (P-type),¹² whereas select photoswitches such as azobenzene allow for both (P/T-type, **Figure 5.1a**).² These two-stage photoswitch systems have garnered significant attention for their 'on/off' control, as well as their abilities to represent 0/1 binary digits capable of encoding circuit information.

One strategy to move beyond binary systems and to achieve more complex material responses is to synthetically connect individual photoswitches.¹⁷⁻¹⁹ Indeed, this approach enables the design of highly functional materials, allowing for multiaddressable systems, increased information storage and complex logic gates.^{18,20,21} The challenge, however, is ensuring that the photoswitches retain their intrinsic switching properties while maintaining synthetic accessibility.^{18,21} A more common approach to increase complexity uses multi-stimuli concepts combining pH changes or electrochemical regulation with light compromising the spatio- and temporal control of light in the second stimuli.^{18,19,21} The development of a single photoswitch capable of selectively addressing metastable intermediates along a multi-step process provide numerous advantages and opens up complex switching phenomena in a single system (**Figure 5.1b**).

Donor-acceptor Stenhouse adducts (DASAs) are a unique class of state-of-the-art visible-light responsive photoswitches that inherently possess such multi-step pathways.²²⁻²⁴ In addition, DASA building blocks exhibit a range of desirable material properties such as negative photochromism (i.e., photoinduced decolorization and thermal coloration¹⁶), visible light absorption, polarity switching, high fatigue resistance, and a straightforward synthetic route.²⁵⁻³⁰

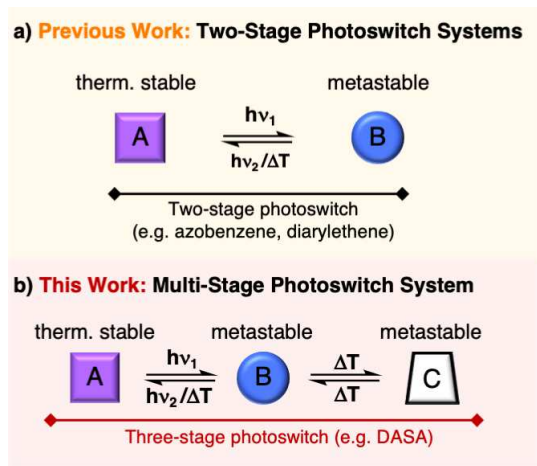


Figure 5.1. a) Schematic representation of two-stage photoswitches. b) Example of DASA as a first single photochromic multi-stage photoswitch. Herein, *stage* corresponds to long-lived stable or meta-stable intermediates along the photoswitching pathway that are independently addressable. Originally published in *Nature Chemistry*.¹ Reprinted with permission from Springer Nature.

Perhaps, however, DASAs' most characteristic property is their multi-step photoswitching mechanism that combines an initial actinic *Z/E*-isomerization with several subsequent thermal steps (**Figure 5.1b, 5.2**).^{22,24,31–35} Understanding DASA's complex photoswitching mechanism has been the topic of a number of experimental^{23,25,26,29,33,36,37} and theoretical studies.^{22,34,35,38–40} The initial actinic *Z/E* isomerization (from **A** to **B** in **Figure 5.2**) is followed by a bond rotation before the rate-determining 4π -electrocyclization.³⁵ The loss of absorbance in the visible region marks the formation of the closed intermediate species **C**, where conjugation along the DASA backbone is lost. Interconversion of this colorless adduct to other tautomeric closed forms (e.g., **C'** to **C''''**) is possible and depends on structure and environment.^{22,26,36,41} As a result of this unique step-wise process, the photoswitching of DASA-based systems is initiated by light with subsequent thermal steps governing their overall switching behavior (property changes).

This multi-step photoswitching mechanism for DASA-based systems (**Figure 5.2a**) has a potential energy surface with several minima and transition states, providing new opportunities to design novel and more complex photomechanical derivatives. Herein, we demonstrate how steric modifications to the DASA moiety can be used to tune this multi-step photoswitching pathway into a system with three independently addressable stages enabling dual-wavelength control for the first time. Herein, 'stage' corresponds to long-lived stable or meta-stable intermediate(s) along the photoswitching pathway that are independently addressable. We show from the computed potential energy surface and measured reaction kinetics how steric modifications to either the donor or acceptor group can be used to stabilize key intermediates (e.g. **B** and **B'**) along the 4π -electrocyclization pathway. An innovative approach where a second wavelength of light is used to gate the conversion between the actinic and the thermal steps is demonstrated, resulting in a novel three-stage, reversible DASA photoswitch. The first stage consists of the isomer **A** which reacts upon irradiation to the colored second stage **B/B'** exhibiting P/T-type behavior. This is followed by the purely thermal 4π -electrocyclization to the third stage which consists of all **C** isomers. Critically, the second stage involving the **B/B'** intermediates can be preferentially addressed via a secondary light stimulus, leading to controlled multistage reactivity. This leads to unique characteristics different from two-stage photoswitches. To our knowledge, the behavior of this negative photochromic three-stage photoswitch cannot be achieved with a traditional two-stage T- or P-type photoswitch. We believe these studies will facilitate the further development of new photoswitches with improved performance and showcases the design principles obtained through combined synthesis/computational studies.

5.2 Design of structure–property relationship studies towards a multistage photoswitch.

It has not gone unnoticed that going beyond photoswitches with “simple” *E/Z* isomerization or electrocyclization pathways can provide new opportunities to design novel photoswitching properties.^{22,36} Inspired by the work of Buma and Feringa²² and guided by computational studies by Martínez and co-workers,^{35,42} we focused on DASA architectures that increase the thermal half-life, stability, and population of **B/B'** to enable a multi-stage photoswitch by introducing a Stage II (**Figure 5.2a**). Both **B** and **B'** can be predicted theoretically and observed experimentally by UV-Vis spectroscopy, although spectroscopically indistinguishable from each other, as a transient ~50 nm red shifted shoulder to the main absorption peak **A** (**Figure 5.2b**).²⁷ Transient absorption experiments below –40 °C demonstrated that irradiation of this shoulder facilitates the reformation of **A**.³² Previously, however, the lifetime of **B** and **B'** was too short-lived to have any practical relevance. To stabilize Stage II (**B/B'**, **Figure 5.2a**), we targeted DASA derivatives that decreased the transition rates from **B** to **A** (Stage II to I) and decreased 4π -electrocyclization rates from **B'** to **C** (Stage II to III, **Figure 5.2a**). The energy barrier controlling the conversion of **B** to **A** (from Stage II to I, **Figure 5.2a**) can be increased by the introduction of a weakly donating arylamine as shown by Buma and coworkers.²²

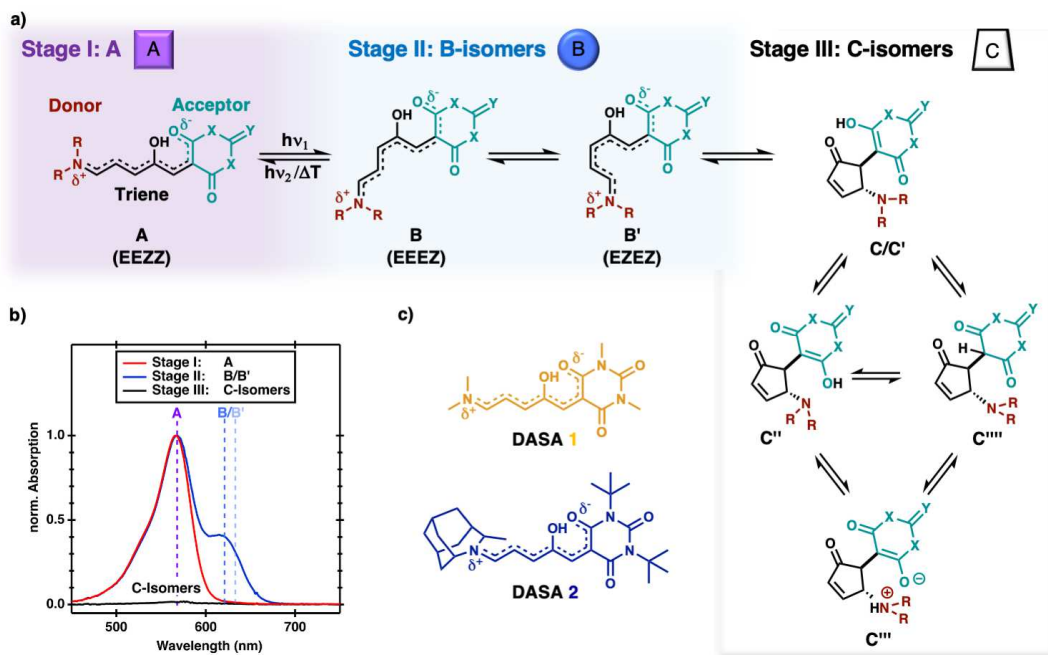


Figure 5.2. a) Schematic representation of the full DASA photoswitching mechanism, which is comprised of three stages: (Stage I, **violet**) The open-form intermediate A. (Stage II, **blue**) The isomerized B/B' intermediates. (Stage III, colorless) The closed-ring intermediates C. C and C' differ in the planarization of the donor amine. b) normalized experimental UV-Vis spectrum of DASA 2 showing each stage in Toluene. Stage II is showing a mixture of A (λ_{\max} = 565 nm) and B/B' (λ_{\max} = 619 nm) isomers under irradiation with a 530 nm LED. Stage III shows minimal rest absorbance of A. The C-isomers do not absorb in the wavelength range shown. The λ_{\max} of the isomers A (565 nm), B (621 nm) and B' (633 nm) are calculated and shifted to experiment by 0.55eV using the COSMO ($\epsilon = 2.38$)- ω B97x-D3/def2-TZVP(-f) level of theory and are shown as dashed lines. c) Structural modification of sterically hindered dialkylamine DASAs presented in this paper shown as DASA 1 (yellow) and 2 (blue), respectively. DASA 1 and 2 consist of dimethylamine/ *N,N'*-dimethylbarbituric acid and adamantyl/*N,N'*-(*t*-butyl) barbituric acid donor/acceptor pairs, respectively. Originally published in *Nature Chemistry*.¹ Reprinted with permission from Springer Nature.

Additionally, a destabilization of C (Stage III, **Figure 5.2a**) can be achieved by increasing steric demand on the donor side, effectively shifting the thermodynamic equilibrium in the dark.^{22,36} Unfortunately, in spite of recent synthetic advances,³⁷ it is still not possible to synthesize DASA derivatives containing a sterically sufficiently demanding arylamine derived donor. We hypothesized, however, that a similar effect on the triene charge separation can be achieved using sterics to destabilize the extended donor-acceptor conjugation of A by restricting the formation of the partial double bond in the acceptor ring system (Scheme 5.1), thereby weakening the extended push-pull donor-acceptor conjugation. Furthermore, increasing the steric demand on the donor group should increase the thermodynamic equilibrium from C to A by destabilizing the C intermediates in Stage III.

Building upon these design principles, we generated a library of sterically-hindered DASA photoswitches based on previously reported first-generation DASA architectures with new acceptor and donor groups (**Figure 5.2c**). DASA **1** has been investigated previously and consists of a dimethyl amine donor and *N,N'*-dimethylbarbituric acid acceptor.³⁶ DASA **2** was constructed by switching the *N,N'*-dimethylbarbituric acid acceptor to the more sterically bulky *N,N'*-(*t*-butyl)barbituric acid. In addition, we introduced steric demand to the donor side by leveraging an adamantyl derived amine (**Figure 5.2c**). To investigate the influence of the sterically bulky acceptor and donor moieties, we also synthesized and characterized DASA derivatives by substituting solely the donor (DASA **S1**) or acceptor groups (DASA **S2**).

To ensure these substitutions did not interfere with the actinic step we computed the critical points along the S_1 adiabatic potential energy surface for DASA **1** and **2** (**Figure 10**). The qualitative features of the potential energy surface for these molecules agree well with our previous Meldrum's acid derived DASA study.³⁵ Furthermore, the quantitative agreement between these critical points suggests that sterics play a small role in the photoisomerization. Sterics is considered to have the greatest influence on the interconversion between ground-state minima along the ring-closing coordinate. Our previous *ab initio* dynamical study of DASA

ground-state chemistry revealed that most of the isomerizing wavepacket population oscillates in Stage II between **B** and **B'** with very little successfully forming Stage III (**C** isomers, **Figure 5.2a**).⁴² This is consistent with the relative energies in **Figure 5.5, 11, 13-14** and previous hypothesis-driven computations that suggest that the ring-closing step from Stage II to III (**B'** to **C/C'**) is the rate-determining step.²⁷ Introducing sterics into the acceptor and/or donor shifts the relative barrier heights separating these intermediates. The most notable difference is observed in **Figure 5.3a** and **Figures 5.5,11-12** where the thermal reverse reaction to reform Stage I (**A**, **Figure 5.2a**) plays a significant role in promoting (DASA **1**) or impeding (DASA **2**) reversion by vibrationally “hot” **B/B'** intermediates in Stage II (**Figure 5.2a**). Furthermore, the relative stability of Stage III (**C** isomers, **Figure 5.2a**), which can shift upwards of 5-6 kcal/mol upon the introduction of more sterically hindered acceptor groups, directly influences both the forward and reverse switching rate. This upwards shift is due to steric interactions between the adamantyl and barbituric acid groups after formation of the 4,5-disubstituted cyclopentenone. This interaction results in the rotation of the donor group for DASAs **S2** and **2** compared to DASA **1** (**Figure 5.3a**).

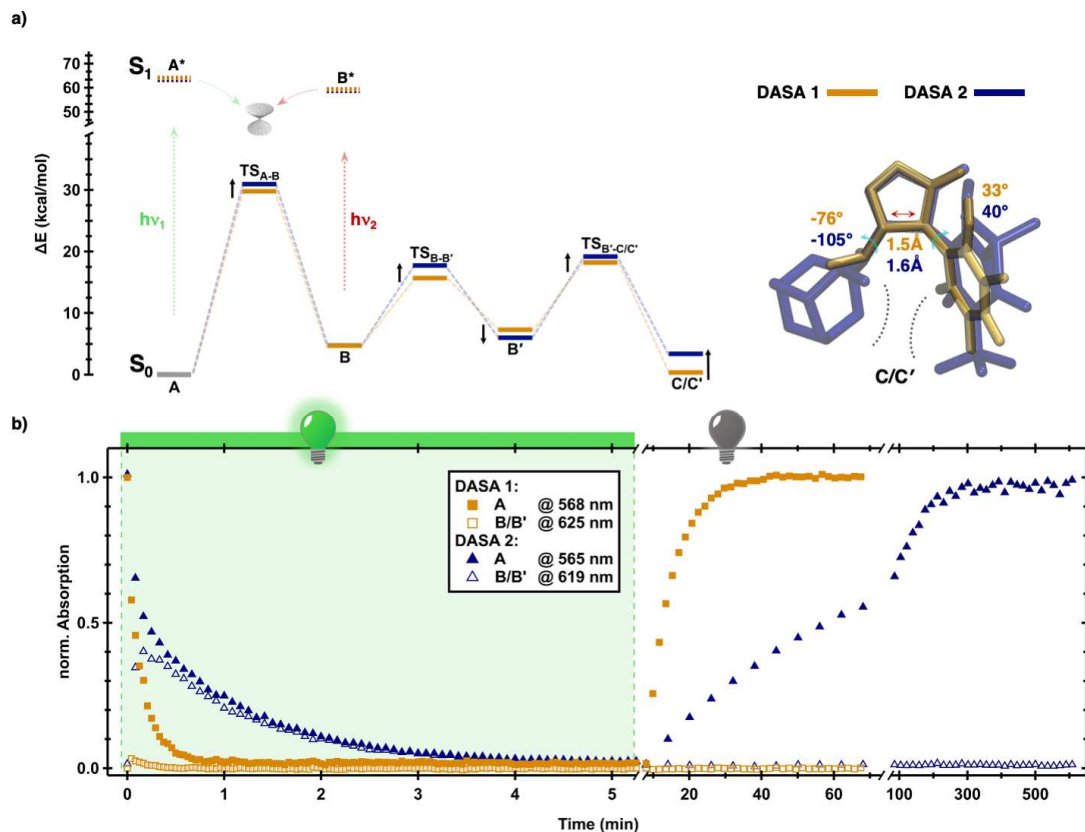


Figure 5.3. a) Potential energy surfaces of DASA 1 and 2 for the intermediates up to C' including the relevant changes leading to a stabilization of C computed at the ω B97xD3/def2-TZVP(-f) level of theory in COSMO ($\epsilon = 2.38$). DASA 2 does not access C but directly isomerizes to C' due to the planarization of the nitrogen inside the ring system. The potential energy surface for the full photoswitching mechanism is shown in **Figures 5.11-14**. The C/ C' structures are shown with dihedral angles ($^\circ$) and C-C bond distances (\AA) for DASA 1 (yellow) and 2 (blue). b) Time-dependent UV-Vis spectroscopy of DASA 1 and 2 at 10 μM in Toluene. The population of A and B/B' is observed by following their respective λ_{max} during irradiation with a 530 nm LED for 8 minutes and subsequent recovery in the dark. The results show differences under irradiation and in the thermal recovery in the dark for the two DASAs and the increase in the stability of B/B' for DASA 2. Originally published in *Nature Chemistry*.¹ Reprinted with permission from Springer Nature.

Driven by the design principles suggested from the computed potential energy surfaces, we experimentally analyzed the stability of Stage II (**B/B'**) in **DASA 2** using **DASA 1** as a control (**Figure 5.3b**). In agreement with previous studies, **DASA 1** exhibits a high thermodynamic equilibrium (88 % open in the dark) and a low solvatochromic shift of -44 nm, suggesting a charge-separated ground state in **A** (**Figure 5.19**, Table 5.6). The absorbance of **DASA 1** in Stage I (**A**, **Figure 5.3b**) disappears fully upon irradiation showing the formation of Stage III (**C**-isomers, **Figure 5.3b**). During irradiation, formation of a shoulder representing the **B/B'** intermediates of Stage II is only transiently observed quickly funneling to **C** (Stage III, **Figure 5.3b**).^{25,36}

Similar to **DASA 1**, **DASA 2** exhibits a high thermodynamic equilibrium of >95 % open form in the dark while the solvatochromic shift of -17 nm is similar to **DASA S3** (2-methylindoline donor with *N,N'*-dimethylbarbituric acid acceptor; -5 nm⁴¹, Supplementary Figure 14), suggesting an increased hybrid ground state structure.⁴¹ As a consequence, conjugation along the triene is weakened in **DASA 2** compared to **DASA 1**.⁴¹ Upon irradiation, **DASA 2** emulates **1** transforming from Stage I (**A**, **Figure 5.3b**) fully to Stage III (**C**-isomers, Figure 3b) and subsequently a full recovery to Stage I in the absence of light irradiation, albeit on an extended timescale (8 min vs 1 min from Stage I to III; 700 min vs. 60 min for reversal). The extended timescale of the forward reaction can be explained by the high population of Stage II (**B/B'**, Figure 3b) while the recovery is slower due to the stabilization of **C'''** and **C''''** (**Figures 6.5.8–9**) compared to **DASA 1**. The absorbance of the second Stage II isomers **B/B'** at 619 nm reaches 40 % of the initial absorbance of **A** before slowly converting into **C** isomers. (Figure 3b). Furthermore, the life-time of Stage II is extended in comparison to **DASA S1** with a half-life of 8 s (**Figure 6.5.21**).

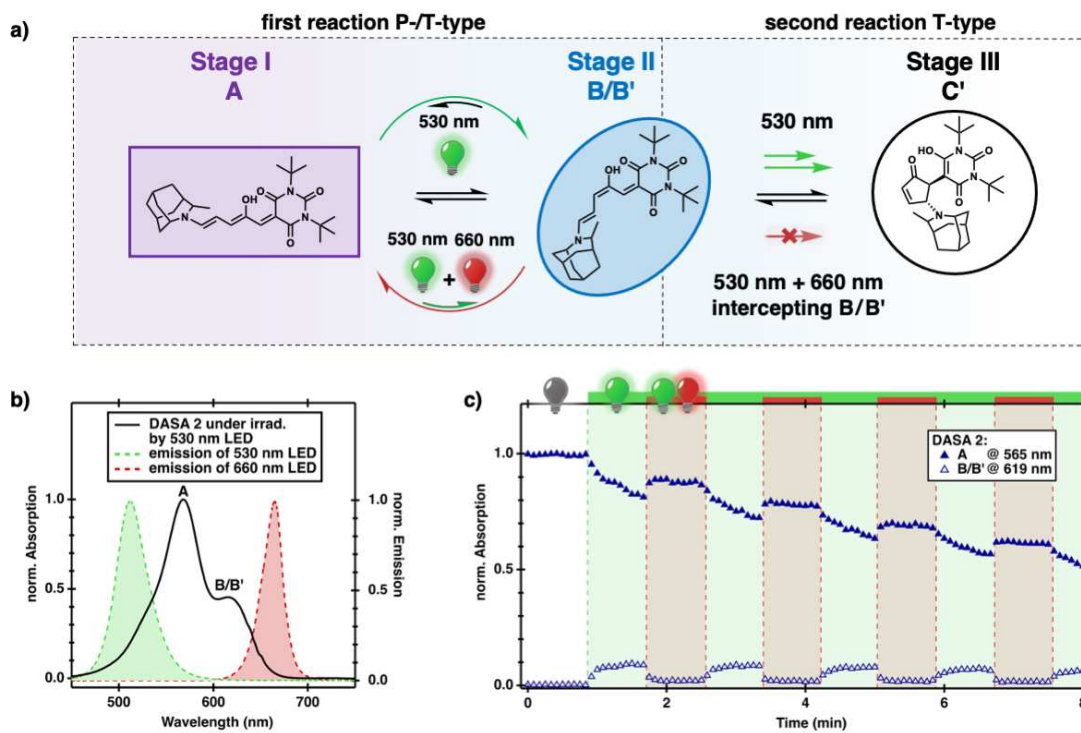


Figure 5.4. a) Schematic representation of A as Stage I, B/B' as Stage II and C' (and subsequent C-isomers) as Stage III. A secondary wavelength can be used intercept the switching mechanism at Stage II as observed in c). b) Absorption profile of DASA 2 under irradiation showing both molecules in Stage I (A) and II (B/B') and the emission profiles of the 530 nm and 660 nm LED used. c) Time-dependent pump-probe UV-Vis spectroscopy at 10 μM in Toluene of 2 showing both A and the B/B' intermediates. Transformation of A to C through irradiation with a 530 nm LED (1.2 mW/cm^2) can be interrupted by irradiation with a 660 nm LED (128.0 mW/cm^2) which promotes conversion of B/B' to A. Originally published in *Nature Chemistry*.¹ Reprinted with permission from Springer Nature.

Previously, this intermediate has only been observed transiently or at low-temperature ($< -40\text{ }^\circ\text{C}$).²⁷ Consistent with our calculations in **Figure 5.3a**, incorporating the large adamantyl group destabilizes the first isomer in Stage III (C', **Figure 5.2**) while stabilizing B', favoring (kinetically) the thermal recovery to Stage II. Upon extended irradiation the system can drain

toward the thermodynamically more stable Stage III isomers **C'''** and **C''''** resulting in an overall slower recovery. Furthermore, the *N,N'*-(*t*-butyl)barbituric acid acceptor group stabilizes Stage II (**B/B'**, **Figure 5.2**) by increasing the energy barrier of the reverse reaction from **B** to **A**, decreasing the forward and reverse rates of the photoswitching process (**Figures 5.3a-b**). See 6.5.12 for an extended discussion and systematic study on the role sterics play on the overall photoswitching pathway.

5.3 Multi-stage photoswitching through a stable **B/B'** population.

Increasing the stability of **B/B'** while retaining good reversible photoswitching opens up exciting new opportunities for DASA based photoswitches (**Figure 5.4a**). The Stage II population shows P-/T-type recovery to Stage I (**A**, **Figures 5.2, 5.4a**) and, for the first time, can be controlled through a secondary wavelength (here 660 nm, **Figures 5.4a-b**). This drives the Stage II back to Stage I instead of draining to Stage III. By enabling dual-wavelength control of DASA photoswitches the intermediate (Stage II) can be addressed through a wavelength which does not interact with either Stage I or III (**Figure 5.4b**). To illustrate this novelty, we first investigated the ability to impart dual-wavelength control by selectively irradiating and suppressing Stage II (**B/B'**, **Figure 5.4a**) with a 660 nm LED resulting in the reformation of Stage I out of Stage II (**A**, **Figure 5.4a**), effectively halting access to the closed isomer through a second wavelength of light (**Figure 5.4c, 30**). Molecules already in Stage III (**C**-isomers, **Figure 5.4a**), as expected from lack of absorbance in the visible region, seem not to be affected (**Figure 5.4c**). Furthermore, by controlling the ratio of intensities of the 530 and 660 nm light, we can either slow (e.g. a reduction of the PTSS – i.e. the equilibrium of the light driven forward reaction and the thermal driven back reaction⁴³ – from 93% to 56%, **Figure 5.31**) or effectively halt the forward reaction kinetics directly (**Figure 5.4c**). Interestingly, previously reported molecules, such as DASA **1**, show a notably reduced response to a secondary wavelength due to the lower population in Stage II (**Figure 5.33**).

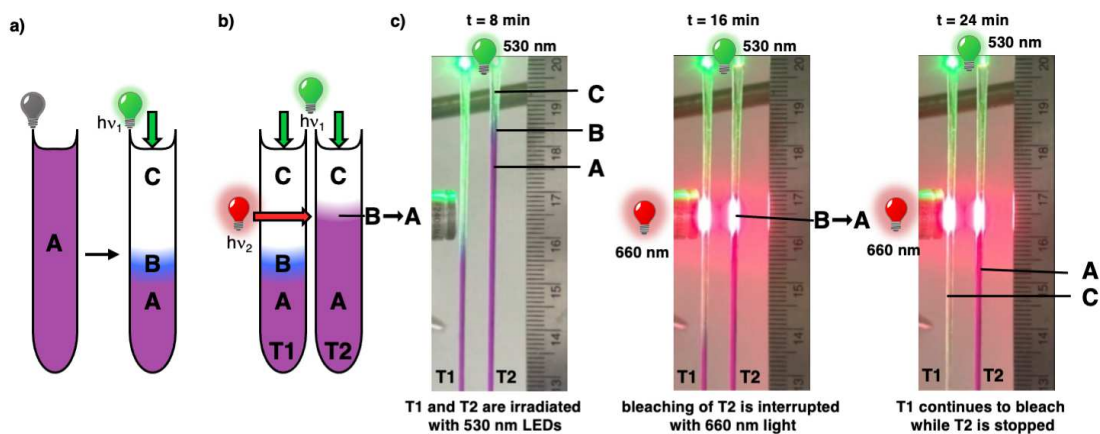


Figure 5.5. a) Irradiation of a negative three-stage photoswitch leads to a thin layer of the transient intermediate **B**. b) In a negative three-stage photoswitch perpendicular irradiation can be used to selectively stop the transformation from **A** to **C** through a volume filled with either **A** or **C** as seen in c while in a typical two-stage P-type photoswitch the $h\nu_2$ interacts with **B** and will get absorbed if passing through a volume filled with bleached sample. c) Photographic stills showing how 660 nm (73 mW) light can be used to stop the transformation from **A** to **C** in a secondary glass tube (T2) under constant irradiation with 530 nm (1 mW) through a glass tube (T1) containing already converted DASA 2 in isomer **C**. Originally published in *Nature Chemistry*.¹ Reprinted with permission from Springer Nature.

The unique ability to set the forward kinetics of DASA where the second wavelength of light preferentially interacts with an intermediate along the photoswitching pathway rather than the product enables new multi-stage photoswitching phenomena (**Figure 5.5**). In non-stirred media irradiation of negative photoswitches results in a bleaching front at which the photoswitch is transformed from absorbing to non-absorbing moving through the bulk sample at a fixed rate (**Figure 5.34**).^{44,45} The sample passed by the front is fully transformed to the metastable isomer (**B** for a two-stage photoswitch, **C** isomers for DASA) and the untouched

sample remains fully in **A**. The illustrations shown in **Figure 5.5a-b, 34** depict the benefit of controlling negative photochromic (irradiation leads to loss of absorbance at the excitation wavelength) multi-stage photoswitches in such an environment. DASA critically showcases negative photochromic properties both in Stage I (**A**) as well as Stage II (**B-isomers**). This moves beyond what is currently possible with state-of-the-art two-stage photoswitch platforms. The negative photochromic three-stage photoswitch results in a spatially controlled transient population of the photoproduct **B** (**Figure 5.5a**) addressable through a second wavelength of light; while the bleaching front interface the first wavelength of light interacts with Stage I, the colored absorbing species **A**, while the colorless non-absorbing product of the photoreaction, Stage III (**C**), does not interact with either the first or secondary wavelength allowing for an interaction with Stage II (**B**) through volumes of Stage I and III (**Figure 5.5b**). In traditional dual-wavelength controlled photoswitches, such as diarylethene or azobenzene, the second wavelength of light interacts with the product from the photoisomerization process driving the reaction back to the original state (i.e., on/off control of the two-stage photoisomerization reaction) (**Figure 5.34**).

To highlight the more complex photoswitching phenomena enabled by negative photochromic three-stage switching pathways, we first demonstrated that the transient population of the photoproduct **B/B'** in Stage II can be seen with the naked eye upon irradiation with 530 nm (**Figure 5.5a**). Using a fiber optic splitter that allows 530 and 660 nm light to be delivered from the top of the sample in parallel or individually enables control of the switching front depth (**Figure 5.34**). Continued irradiation with 530 nm or white light drives the reaction to Stage III in the regions not exposed to 660 nm light (Supplementary Figure 31). By setting the 660 nm LED perpendicular to the bleaching front, we can arrest the reaction at a set distance by interrupting Stage II. While fundamentally controlling a photostationary state and a bleaching front with a second wavelength of light could be achieved with a two-stage P-type photoswitch, it would be extremely challenging and require judicious choice of a negative

photoswitch coupled with a precise understanding of the photoswitching kinetics. Finally, to demonstrate true novelty, we set-up two glass tubes with **DASA 2** in toluene and a 530 nm LED on the top and a perpendicular 660 nm LED. Unique to this negative photochromic three-stage photoswitch is the fact that the secondary wavelength (660 nm) does not interact with the photoproduct in Stage III which is transparent. This enables light to pass freely through the closed isomers **C** through **C''''** in Stage III in the first tube and selectively stop the bleaching front in the neighboring glass tube **T2** (**Figure 5.5a-b**). While simultaneously controlling the bleaching front in tube **T2**, the photochromic switching process in tube **T1** is uninterrupted, enabling a continuous bleaching of **DASA 2**. This represents a photonic three-stage logic gate where the secondary wavelength solely negates the input of the primary wavelength. A similar experiment with a two-stage P-type photoswitch such as DAE or azobenzenes would lead to a reversion of the photoproduct upon irradiation with the second wavelength of light in the tube **T1**, thereby blocking light penetration and preventing control of the photoswitching process. We believe the selective interaction with the metastable intermediate **B/B'** in Stage II without interfering with the photoproducts **C** through **C''''** in Stage III will enable a number of exciting new applications where more complex switching phenomena are desired such as logic gates and additive manufacturing.⁴⁵ Isolating isomers along the reaction pathway of other multi-step photoswitches such as spiropyran or increasing the number of separate stages in multi-stage photoswitches will further enrich the toolbox for light responsive smart materials.

5.4 Conclusion

Using the powerful insight from both computation and synthesis we developed **DASA**-based photochromic compounds with steric demand on the both the donor and acceptor group that enable the first controlled three-stage single photochrome photoswitching system. Computed reaction pathways and pump probe UV-Vis spectroscopy together with NMR

spectroscopy serve to explain the influence each modification has on the light responsive behavior mainly focusing on the key intermediates **B/B'** and **C/C'**. This work showcases the relationship between sterics and photoswitching properties and the potential to move beyond simple two-stage photoswitches. Through the design insights from these studies, we demonstrate a dual wavelength responsive DASA for the first time by selectively intercepting the metastable intermediate **B/B'** and reverting it to **A**. This introduces a P-/T-type step which is directly followed by a thermal step enabling a negative photochromic three-stage photoswitch where the intermediate in Stage II, not the photoproduct in Stage III, is selectively addressed with a second wavelength of light. Indeed, the extent of this effect depends on the population of intermediates in Stage II and the ratio of intensities between the primary and secondary light source. This allows for spatial control of the transformation through samples containing either the stable isomer **A** or the metastable closed form in Stage III which is not possible with previously reported two-stage photoswitches. By coupling synthesis and computation, a detailed understanding of the energy landscape and lifetimes of key intermediates, leads to the design of a novel switching mechanism and associated photochromic properties for DASA derivatives. Significantly, these advances and principles are not restricted to a narrow sub-set of materials and support the development of new multi-stage photoswitches.

5.5 Additional Information

5.5.1 Experimental details

Materials: All commercially obtained reagents were bought from Sigma Aldrich, TCI Europe or Fisher Scientific and were used without purification, unless noted. Furfural was distilled before use and stored at -18 °C. Analytical thin-layer chromatography (TLC) was carried out with Merck silica gel 60 F254 glass plates and visualized using combination of UV and potassium permanganate staining or p-anisaldehyde. Flash column chromatography

was performed with Merck silica gel 60 (70-230 mesh). All chromatographic solvents were of ACS grade and used without further purification.

5.5.2 Characterization methods

ATR FT-IR: Attenuated total reflection Fourier-transform infrared (ATR FT-IR) spectra were recorded on a Varian 640-IR FT-IR spectrometer equipped with an ATR (attenuated total reflection) accessory or a Thermo Nicolet iS10 FTIR Spectrometer with a Smart Diamond ATR; applied as neat samples and absorbance bands reported as $1/\lambda$ in cm^{-1} .

Mass spectrometry: A Waters GCT Premier high-resolution Time-of-flight mass spectrometer is used. The instrument is equipped with electron ionization (EI), chemical ionization (CI), and field ionization/field desorption (FI/FD) ion sources. This instrument has a mass range up to m/z 800 in EI, CI, and FI modes and up to m/z 4000 in FD mode. Accurate mass measurement (<3 mDa) for elemental composition confirmation is available in EI, CI, and FI modes.

5.5.2.1 NMR-Spectroscopy:

^1H NMR spectra were recorded on Varian spectrometers (Agilent Technologies 400 MHz, 400-MR DD2 Spectrometer, Bruker Avance NEO 500 MHz, Varian Unity Inova 500 MHz, or a Varian Unity Inova AS600 600 MHz spectrometer) and are reported relative to the residual proteo-signal in deuterated solvents. Data for ^1H NMR spectra are reported as follows: chemical shift (δ ppm), multiplicity, coupling constant (Hz) and integration. ^{13}C NMR spectra were recorded on Varian Spectrometers (100, 125, or 150 MHz). Data for ^{13}C NMR spectra are reported in terms of chemical shift (δ ppm).

5.5.2.2 UV–Vis spectroscopy:

UV–Vis absorption spectra were recorded on Agilent 8453 UV–Vis spectrometer from 200 to 1200 nm wavelengths.

5.5.2.3 UV–Vis kinetic measurements:

The photoinduced optical absorption kinetics were measured on a pump-probe setup. The pump beam was generated by a light emitting diode (LED) source (Thorlabs) coupled into a multimode optical fiber terminated with an output collimator. The LED intensity was controlled through a digital-to-analog converter (National Instruments USB-6009) using LabVIEW. The probe beam was produced by High Power MINI Deuterium Tungsten Halogen Source w/shutter 200-2000 nm (Ocean Optics DH-MINI) coupled into a multimode fiber with an output collimator for the light delivery. The probe light was modulated by a shutter (Uniblitz CS25) which could be controlled manually or through a digital output port (National Instruments USB-6009) using LabVIEW. Pump and probe beams were overlapped using steering and focusing optics at a 90° angle inside a sample holder, which allowed for a 10x10 mm rectangular spectrophotometer cells that was connected to a circulating bath for temperature control. Additionally, the solutions were stirred during the measurements by a miniature stirring plate inserted into the sample holder (Starna Cells SCS 1.11). Both pump and probe beams were nearly collimated inside the cell with a diameter of about 2 mm. The pump beam was blocked after passing through the sample and the probe beam was directed by a system of lenses into the detector (Ocean Optics Flame-S1-XR spectrometer), which acquired spectra of the probe light. The detector was connected to a PC via USB port. The experiment was controlled by a National Instrument LabVIEW program which collected the probe light spectra, determined sample optical absorption spectra, controlled pump and probe light sources, and stored the data on the computer S3 hard drive according to the experimental

protocol. Experiments were performed at 10 μM concentration unless otherwise stated.

Samples were left to equilibrate overnight prior to measurements unless otherwise stated.

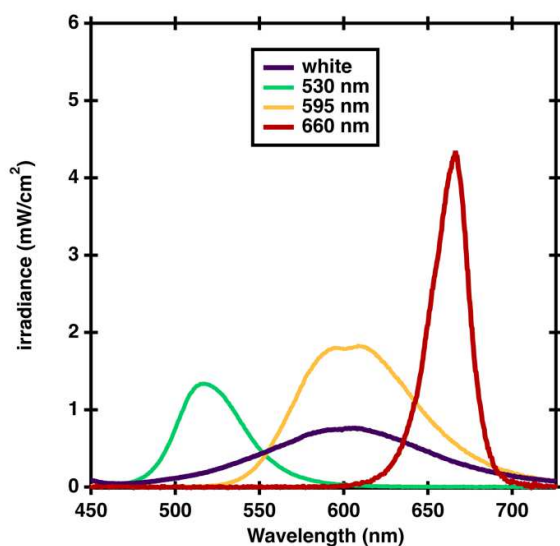


Figure 5.6. Irradiance of Thorlabs 530 nm, 595 nm and 617 nm LED used in

experiments. Total irradiance for white LED: 105 mW/cm²; 530 nm: 70 mW/cm²; 595 nm: 168 mW/cm²; 660 nm: 128 mW/cm² (unless otherwise specified). Measured using an Ocean Optics hand-held spectrometer with cosine corrector and radiometric calibration (model USB 4000). Values reported in mW are measured capturing the whole light output with a Newport Optical Power/Energy Meter (Model 842-PE) equipped with a 818-UV/DB Low-Power UV Photodetector and a 884-UVR attenuator.

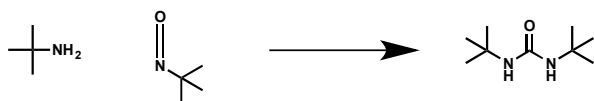
5.5.2.4 Video Capture and Processing:

Videos were taken with an iPhone 7 and processing was done using iMovie version 10.2.3. Singular frames were taken by exporting frames via iMovie. For photochemical transformations in the glass tubes spectrometer the LED was coupled into a multimode optical fiber terminated with a flat cleave and the intensity and ‘on’/‘off’ cycles were controlled with a T-cube LED driver (LEDD1B) from Thorlabs. To measure the power density of emission coming out of the fiber tip a Newport Optical Power/Energy Meter (Model 842-PE), equipped

with a 818-UV/DB Low-Power UV Photodetector and a 884-UVR attenuator, was used. To irradiate coaxially with two different LEDs a Wideband Multimode Circulator (WMC3L1S) from Thorlabs was used. The perpendicular LED was coupled into a multimode optical fiber terminated with an output collimator.

5.5.3 Synthesis Procedure:

Compound S1

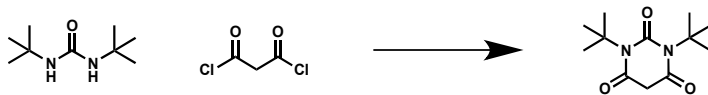


t-butylisocyanate (2.0 g, 0.02 mol, 1.0 eq., 2.3 ml) was added to THF (20 ml). *t*-butylamine (1.5 g, 0.02 mol, 1.0 eq., 2.1 ml) was added dropwise to the vigorously stirring solution. After continuous stirring for 30 min pentane (10 ml) was added, the solution was filtered and the solid dried under reduced pressure. The product was obtained as a colorless solid (2.9 g, 0.17 mol, 85 %).

¹H NMR (500 Mhz, Chloroform-*d*) δ/ppm: 1.31 (s, 18 H).

Characterization matches previously reported literature values.

Compound S2

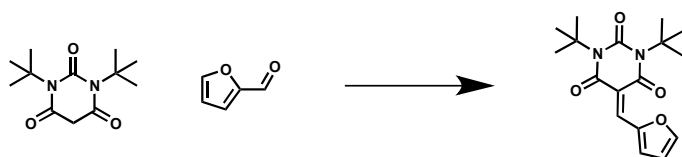


Malonyldichloride (0.73 g, 5.2 mmol, 1.1 eq) was added to a mixture of Compound **S1** (0.80 g, 4.7 mmol, 1.0 eq) in Chloroform (18 ml). The solution was refluxed at 70 °C for 4 h. After letting the solution cool 3 M HCl (18 ml) was added. After collecting the organic phase, the aqueous phase was washed with DCM (2x 20 ml). The organic phases were combined, dried over MgSO₄, filtered and then concentrated under reduced pressure. The remaining liquid was then subjected to a silica plug (SiO₂; Hexanes:EtOAc 4:1) to yield the product as a colorless solid (918 mg, 3.8 mmol, 81 %).

¹H NMR (500 Mhz, Chloroform-*d*) δ/ppm: 3.46 (s, 2H), 1.59 (s, 18H).

Characterization matches previously reported literature values.¹

Compound S3



Compound **S2** (1.2 g, 5 mmol, 1.0 eq.) was mixed with Furfural (3.4 g, 35 mmol, 7.0 eq.) and proline (120 mg, 10 w% regarding the carbon acid) and stirred at room temperature for 1 h. DCM (10 ml) and H₂O (100 ml) were added to the solution and the DCM was removed under reduced pressure. The resulting solid was filtered and purified by a silica plug (SiO₂; Hexanes:EtOAc 9:1). The product was isolated as a lead-tin-yellow colored solid (1.0 g, 3.1 mmol, 63 %).

^1H NMR (500 Mhz, Chloroform-*d*) δ /ppm: 8.34 (d, $J = 3.7$ Hz, 1H), 8.16 (s, 1H), 7.74 – 7.73 (m, 1H), 6.66 – 6.64 (m, 1H), 1.65 (s, 9H), 1.64 (s, 9H).

^{13}C -NMR (125 MHz, Chloroform-*d*) δ /ppm: 162.3, 161.6, 153.2, 151.1, 148.7, 137.7, 125.5, 116.5, 114.5, 61.8, 61.6, 29.6, 29.5.

HR-MS (ESI+) m/z 341.1480, calc. 341.1477 for $[\text{M} + \text{Na}]^+$.

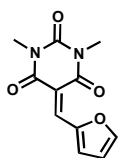
IR (ATR, cm^{-1}): 3030, 2980, 2930, 1741, 1664, 1578, 1554, 1481, 1466, 1396, 1343, 1303, 1229, 1178, 1153, 1108, 1087, 1020, 967, 950, 931, 897, 882, 856, 815, 795, 773, 741, 692, 674, 646, 605, 592, 527.

Compound S4



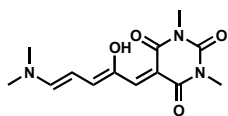
was synthesized in a multiple step synthesis according to literature. Characterization matches previously reported literature values.⁵⁶

Compound S5



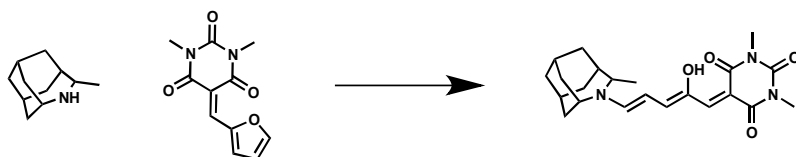
was synthesized after a literature procedure. Characterization matches previously reported literature values.⁴

DASA 1



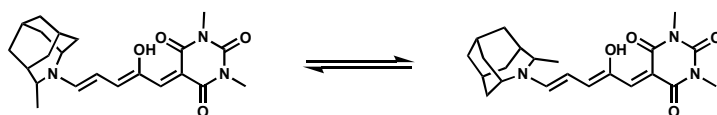
was synthesized after a literature procedure. Characterization matches previously reported literature values.⁵

DASA S1



Compound **S4** (200 mg, 1.21 mmol, 1.2 eq.) was dissolved in DCM (0.2 ml) with Compound **S5** (231 mg, 0.99 mmol, 1.0 eq.) and stirred for 2 h. After removing the solvent under reduced pressure, the remaining solid was subjected to column chromatography (SiO₂; Hexanes:EtOAc 2:1). After evaporating the solvent, the product was obtained as dark purple solid (70 mg, 0.18 mmol, 22 %).

¹H- and ¹³C-NMR show a 2:1 mixture between the following conformers:



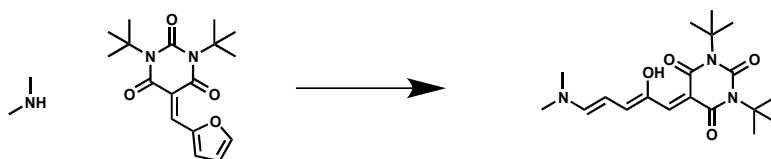
¹H NMR (500 Mhz, Chloroform-*d*) δ /ppm: 12.62 – 12.50 (m, 1H), 7.39 – 7.29 (m, 0.7H), 7.12 (s, 1H), 6.85 – 6.70 (m, 1H), 6.15 – 6.07 (m, 1H), 4.49 – 4.34 (m, 0.25H), 4.18 – 4.06 (m, 0.75H), 3.97 – 3.91 (m, 0.75H), 3.89 – 3.85 (m, 0.25H), 3.39 – 3.33 (m, 6H), 2.20 – 1.68 (m, 14H), 1.46 (d, *J* = 7.1 Hz, 1H), 1.42 (d, *J* = 6.9 Hz, 2H).

^{13}C -NMR (125 MHz, Chloroform-*d*) δ /ppm: 165.0, 163.5, 158.3, 158.2, 152.2, 152.1, 152.0, 146.5, 137.7, 137.4, 104.7, 103.8, 97.7, 68.0, 65.3, 60.7, 54.2, 40.6, 37.5, 35.7, 35.4, 35.3, 35.2, 35.1, 33.1, 32.7, 31.2, 30.9, 28.5, 28.3, 26.5, 26.3, 26.1, 25.8, 22.5, 18.8.

HR-MS (ESI+) m/z 422.2054, calc. 422.2056 for $[\text{M} + \text{Na}]^+$.

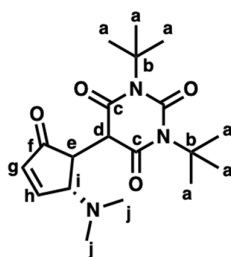
IR (ATR, cm^{-1}): 2907, 1690, 1587, 1545, 1467, 1406, 1358, 1322, 1277, 1238, 1196, 1112, 1060, 966, 949, 935, 902, 772, 721, 658, 635, 588, 546.

DASA S2



To Compound **S3** (250 mg, 0.78 mmol, 1.0 eq.) was mixed with Dimethylamine (2 M in THF, 0.4 ml, 0.78 mmol, 1.0 eq) and stirred for 2 h und exclusion from light. The dark purple mixture then was added to Hexanes (10 ml) at $-78\text{ }^{\circ}\text{C}$. The solution was quickly filtered and the solid dried under reduced pressure to yield the product as dark purple solid (145 mg, 0.40 mmol, 51 %).

Characterization of the closed isomer:



^1H NMR (500 MHz, Chloroform-*d*) δ /ppm: 7.79 – 7.62 (m, 1H, H_h), 6.38 – 6.28 (m, 1H, H_g), 4.28 – 4.19 (m, 1H, H_i), 3.78 – 3.73 (m, 1H, H_d), 3.43 – 3.37 (m, 1H, H_e), 2.38 (s, 6H, H_j), 1.66 – 1.60 (m, 9H, H_a), 1.59 – 1.54 (m, 9H, H_a).

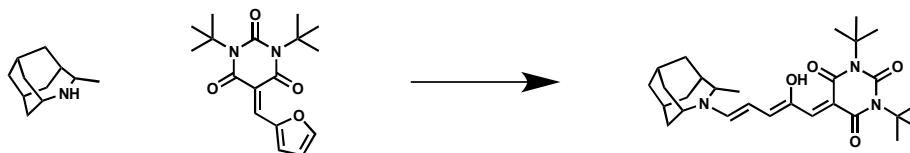
^{13}C -NMR (150 MHz, Chloroform-*d*) δ /ppm: 204.9 (C_f), 167.4 (C_c), 166.4 (C_c), 162.7 (C_h), 134.3 (C_g), 69.5 (C_i), 62.2 (C_b), 51.3 (C_d), 46.5 (C_e), 41.3 (C_j), 29.2 (C_a), 29.1 (C_a).

Assignment through HMBC and HSQC NMR see section 1.19.

HR-MS (ESI+) m/z 386.2059, calc. 386.2056 for $[\text{M} + \text{Na}]^+$.

IR (ATR, cm^{-1}): 2974, 2933, 1687, 1630, 1604, 1556, 1481, 1413, 1396, 1339, 1305, 1253, 1170, 1098, 1024, 979, 909, 850, 783, 731, 642.

DASA 2



Compound **S4** (200 mg, 1.21 mmol, 1.0 eq.) was dissolved in THF (0.2 ml) with Compound **S3** (385 mg, 1.21 mmol, 1.0 eq.) and stirred for 2 h. After removing the solvent under reduced pressure, the remaining solid was subjected to column chromatography (SiO_2 ; Hexanes:EtOAc 4:1). After evaporating the solvent, the product was obtained as dark purple solid (136 mg, 0.28 mmol, 23 %).

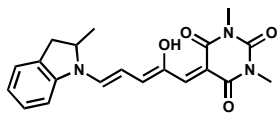
^1H NMR (400 MHz, Chloroform-*d*) δ /ppm: 12.52 – 12.40 (m, 1H), 7.20 – 7.16 (m, 1H), 7.12 – 6.99 (m, 1H), 6.59 – 6.46 (m, 1H), 5.95 – 5.85 (m, 1H), 4.31 – 4.25 (m, 0.3 H), 4.00 – 3.94 (m, 0.7H), 3.88 – 3.80 (m, 0.7H) 3.79 – 3.70 (m, 0.3H), 2.15 – 1.65 (m, 14H), 1.63 (s, 18H), 1.42 – 1.31 (m, 3H).

^{13}C -NMR (125 MHz, Chloroform-*d*) δ /ppm 166.0, 163.7, 154.6, 154.5, 146.8, 145.62, 141.5, 101.8, 100.8, 64.1, 61.3, 60.9, 59.8, 40.0, 35.9, 35.6, 35.5, 33.6, 31.3, 29.8, 29.8, 26.5, 26.0, 18.5.

HR-MS (ESI+) m/z 506.2992, calc. 506.2989 for $[\text{M} + \text{Na}]^+$.

IR (ATR, cm^{-1}): 2971, 2911, 1713, 1643, 1595, 1544, 1479, 1406, 1338, 1320, 1277, 1215, 1162, 1102, 1066, 1021, 977, 949, 935, 904, 805, 776, 720, 659, 616, 583, 545.

DASA S3



was synthesized after a literature procedure.⁶ Characterization matches previously reported literature values.

5.5.4 Computational details

We employ GPU-accelerated complete active space self-consistent field theory (SA-CASSCF)^{47–49} and Density Functional Theory (DFT) to study the complete photoswitching pathway for a series of first generation sterically hindered DASAs (**Figure 5.7**). **DASA 1** consists of a dimethyl amine donor and *N,N'*-dimethylbarbituric acid acceptor (**Figure 5.7**). **DASA 2** was constructed by switching the *N,N'*-dimethylbarbituric acid acceptor to the more sterically bulky *N,N'*-(*t*-butyl)barbituric acid (**Figure 5.7**). We introduced sterics to the donor side via an adamantyl derived amine. Lastly, we created DASA derivatives by substituting either the donor (**DASA S1**) or acceptor groups (**DASA S2**). All electronic structure calculations (i.e. energies, gradients, and nonadiabatic coupling vectors (NACV)) are performed with the TeraChem^{50–52} electronic structure package.

Electronic Structure Benchmarking: The computed energies for the ground-state minima were benchmarked using a series of hybrid and long-range-corrected exchange-correlation functionals with the Grimme's D3 dispersion model (i.e. PBE0-D3, B3LYP-D3, Becke half and half, ω PBEh, cam-B3LYP, and ω B97x-D3) including coupled-cluster singles, doubles, and perturbative triples (CCSD(T)) (**Figure 5.8**). The structures for each minimum were optimized at the ω B97x-D3/def2-TZVP(-f) level of theory using the COSMO solvation model.^{53,54} Single-point energies were computed using the labeled electronic structure method in COSMO ($\epsilon = 2.38$) and corresponding basis-set in **Figure 5.8**. The CCSD(T)⁵³ energies were computed in the gas phase due to computational cost for a system of this size. Basis-set size was explored using the def2-TZVP(-f) and def2-QZVP(-f) basis sets, which had little impact on the computed energies (**Figure 5.8**). Energies computed for the open-form DASAs (**A-B'**) were not sensitive to the selected method, with all DFT methods in relatively good quantitative agreement with CCSD(T). In contrast, the computed energies for the closed-form (**C''''**) depends heavily on the selected method, with considerable overestimations for both PBE0-D3 and B3LYP-D3 hybrid exchange-correlation functionals. Additionally, the

range-corrected exchange-correlation functionals ω PBEh and cam-B3LYP overestimate the relative energies of the closed-ring **C** intermediates. The ω B97x-D3 exchange-correlation functional improves the description of the short- and long-range interactions when compared to the other functionals and reproduces the qualitative trend between ground state intermediates shown in CCSD(T). For this reason, the ω B97x-D3 exchange-correlational functional with the def2-TZVP(-f) basis-set was used for all DFT calculations for the four studied sterically hindered DASA derivatives.

Actinic Step: To characterize the actinic step of these novel DASA derivatives, critical points (e.g. Frank-Condon point (FC), S_1 minimum, and S_1/S_0 minimum energy conical intersections (MECI) for α and β along the isomerization pathways) were computed using the DL-FIND¹⁵ optimization package (**Figure 5.9**). Cartesian coordinates, energies, CI vectors, and CASSCF natural orbitals are included in section **1.9**. We use an active space consisting of two electrons in two orbitals determined to minimize the average energy of the lowest three singlet states, in conjunction with the 6-31G** basis set, i.e. SA3-CAS(2,2)SCF/6-31G**. These critical points found to agree well with our previous *ab initio* nonadiabatic quantum molecular dynamics study of first-generation Meldrum's acid DASA.³⁵ Common features pertaining to the α and β nonradiative relaxation pathways, S_1 minima, and twisted S_1 minimum near the α MECI were found for all DASAs included in this study. The computed potential energy surfaces of DASAs **1**, **2**, **S1**, and **S2** show little change upon the introduction of steric demand into the donor and/or acceptor groups (**Figure 5.9**). For this reason, steric effects in the actinic step are likely to be minimal and we focus on the thermal steps in this study.

Thermal Step: To characterize the thermal step, geometries were optimized on the ground electronic state at the ω B97x-D3/def2-TZVP(-f) level of theory using the equilibrium Conductor-Like Screening Model (COSMO) to incorporate the polarization of the toluene

environment ($\epsilon = 2.38$). Minima were computed using a convergence criterion of root mean square of the nuclear gradient $\leq 10^{-5}$ a.u. and the maximum nuclear gradient component $\leq 10^{-5}$ a.u. The Hessian was determined to be positive definite at the observed minimum (i.e. all frequencies were positive). Transition states were computed using the following protocol: 1) Initial reaction pathways were determined from a geodesic interpolated⁶⁰ path between two minima along the photoswitching pathway of each sterically hindered DASA (**1**, **2**, **S1**, and **S2**). 2) These pathways were used to initiate minimum energy reaction pathway (MEP) searches using the climbing-image Nudged Elastic-Band (CI-NEB)⁵⁴ method with 21 images. 3) The transition state was computed by converging the climbing image from the MEP pathways (step 2) using the Dimer method⁵⁴ in ChemShell.⁵⁵ At the transition states, the Hessian possessed one negative eigenvalue (i.e. a single imaginary frequency) along the direction connecting the two initial minima (i.e., reactant and product). Geometries and energies for minima and transition states are included in the supplementary files. Additionally, movies constructed from the minima and transition states for all four DASAs are included in the supplementary files.

The influence of sterics on the specific donor-acceptor group are further examined in **Figures 5.7-8** for DASAs **1**, **2**, **S1**, and **S2**. **Figure 5.7** shows the relative electronic energies of the stage I (**A**) to stage II (**B**) transformation isolated to acceptor or donor substitutions. Changes in the acceptor and donor groups lead to collectively raising or lowering the energy barriers between intermediates, respectively. The subsequent thermal reaction potential energy surfaces in stage III (**C-C''''**) are shown in **Figures 5.8** and **5.9** for the four DASA derivatives.

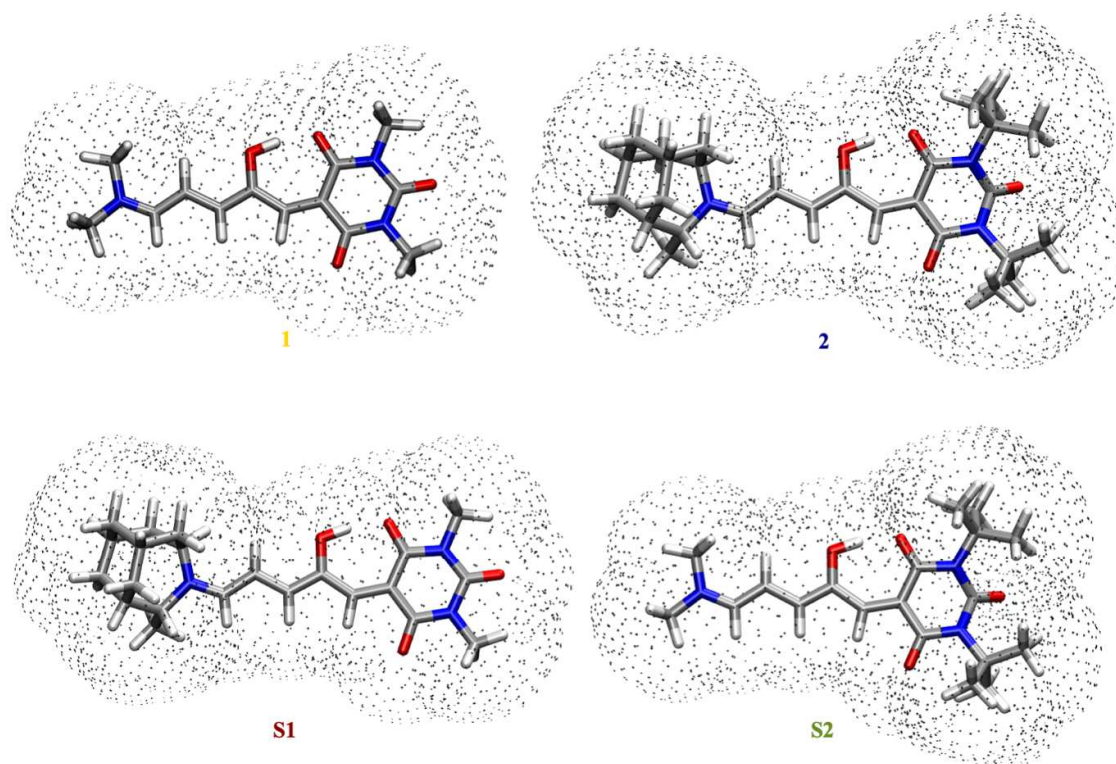
UV-Vis Electronic Absorption Spectrum: The UV-Vis electronic absorption spectra were generated from 250 geometries sampled according to a harmonic wigner distribution corresponding to the ω B97x-D3/def2-TZVP(-f) in COSMO ground-state optimized structure. Single-point energy calculations were performed at the same level of theory and their $S_0 \rightarrow S_n$

excitation energies (where $n = 1, 2, 3, 4, 5$) were homogeneously broadened using Gaussian functions, g , with a full-width half-maximum $\delta(\dots)$ of 0.1 eV according to:

$$\sigma(E) = \frac{\pi e^2}{2mc\epsilon_0} \sum_{J \neq I}^{N_{ex}} \left[\frac{1}{N_s^J} \sum_k^{N_s^J} f_{IJ}(\mathbf{R}_k) g(E - \Delta E_{IJ}(\mathbf{R}_k), \delta) \right]$$

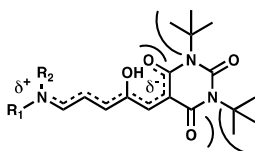
where N_{ex} is the number of excited electronic states, N_s^J is the total number of sampled points, and $\Delta E_{IJ}(\mathbf{R}_k)$ and $f_{IJ}(\mathbf{R}_k)$ are the excitation energy and oscillator strength for each point \mathbf{R}_k from the ground-state I to excited state J , respectively (**Figure 5.7**). After a 0.55 eV shift toward experiment, the computed and measured spectra agree well, with DASAs **1** and **2** being relatively close in energy (< 10 nm) with DASAs **S1** and **S2** red- and blue-shifted, respectively. This was compared to CASSCF which showed a similar trend in absorption maxima between the four DASA derivatives (S_0 minimum in **Figure 5.9**).

5.5.5 Size comparison of the four DASA compounds



DASA	# of Atoms	# of Surface Segments	Surface Area (Å ²)	Volume (Å ³)
1	37	1985	324.38	193.46
2	76	3740	522.45	296.96
S1	58	2903	428.22	248.08
S2	55	2850	419.75	243.53

Figure 5.7. The solvent accessible surface (SAS) for the open form (A) of DASAs **1**, **2**, **S1**, and **S2**. The SAS (grey) is constructed from apparent surface charge (ASC) segments with an effective radius of 1.2 times the radius of each atom. The table shows the number of atoms, total number of cavity segments, surface area of the cavity, and the cavity volume.



Scheme 5.1: Proposed interaction of the *t*-butyl sidechain leading to a destabilization of the partial double bond in the acceptor ring system resulting in a decreased conjugation along the triene for **DASA 2** and **S2**.

5.5.6 UV-Vis Spectroscopy: Theory & Experiment

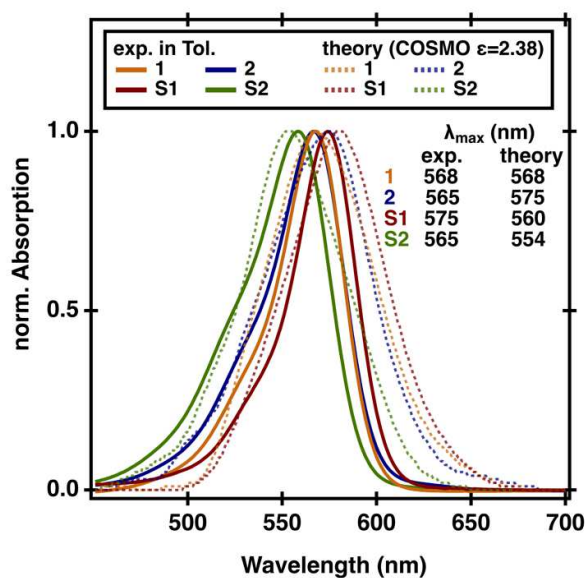
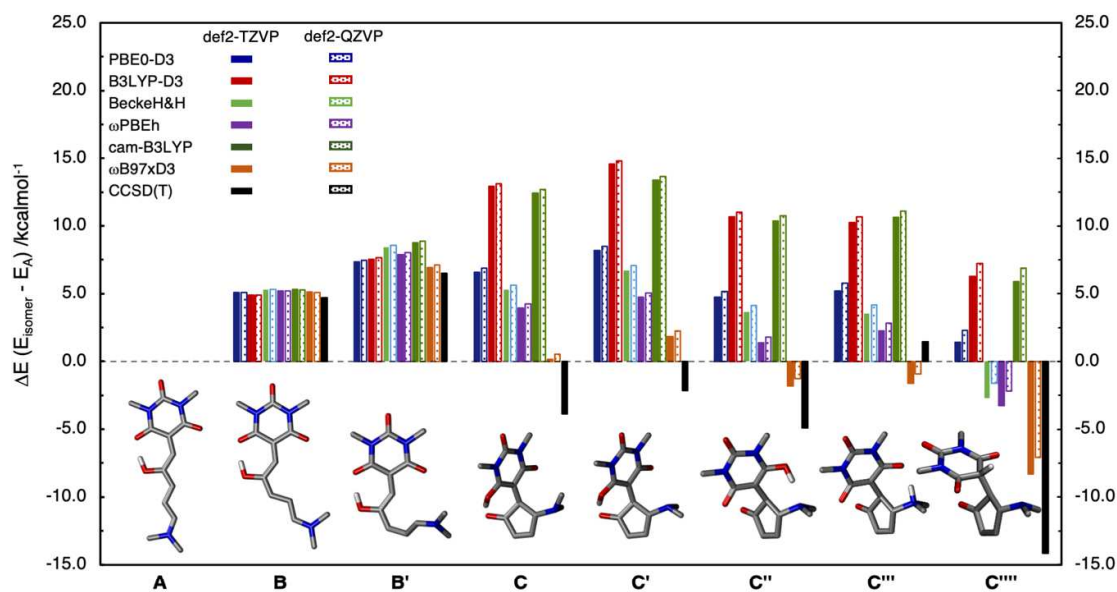


Figure 5.8. The measured (solid) and computed (dashed) UV-Vis electronic absorption spectra of DASA **1** (yellow) **2** (blue) **S1** (red) and **S2** (green) in toluene. Each normalized computed spectrum consisted of 250 structures sampled to a harmonic Wigner distribution and the lowest five singlet excitations (S_0 - S_n , $n = 1, 2, 3, 4, 5$) were homogeneously broadened using a Gaussian function with a FWHM = 0.1 eV and shifted to experiment by 0.55 eV using the (COSMO ($\epsilon = 2.38$)- ω B97x-D3/def2-TZVP(-f) level of theory. The corresponding spectrum maxima are shown in the inset.

5.5.7 Benchmarking Electronic Structure Methods on S₀ Minima



Method	$\Delta E (E_{\text{isomer}} - E_A) / \text{kcalmol}^{-1}$								
	A	B	B'	C	C'	C''	C'''	C''''	
PBE0-D3	0.00	5.09	7.33	6.58	8.19	4.73	5.19	1.41	
	0.00	5.08	7.46	6.88	8.51	5.16	5.76	2.28	
B3LYP-D3	0.00	4.90	7.52	12.92	14.57	10.67	10.26	6.29	
	0.00	4.88	7.64	13.14	14.82	11.00	10.69	7.22	
Becke H&H	0.00	5.31	8.44	5.28	6.71	3.66	3.53	-2.70	
	0.00	5.30	8.57	5.61	7.09	4.13	4.17	-1.60	
ω PBEh	0.00	5.21	7.90	3.94	4.73	1.36	2.26	-3.24	
	0.00	5.19	8.03	4.23	5.04	1.78	2.82	-2.18	
camB3LYP	0.00	5.32	8.75	12.44	13.39	10.36	10.64	5.87	
	0.00	5.30	8.88	12.69	13.68	10.74	11.10	6.87	
ω B97xD3	0.00	5.11	6.94	0.15	1.82	-1.80	-1.61	-8.31	
	0.00	5.10	7.11	0.55	2.25	-1.25	-0.90	-7.08	
CCSD(T)	0.00	4.71	6.52	-3.87	-2.13	-4.89	1.45	-14.14	

Figure 5.9. Ground-State Minima Benchmarking. The computed energies of the ground-state minima along the 4 π -electrocyclization in DASA 1 relative to the open-form A. Geometries were optimized at the COSMO ($\epsilon=2.38$) ω B97xD3/def2-TZVP(-f) level of theory and single-point energies were computed using the labeled methods. All single point energies were computed using the COSMO solvation model except for CCSD(T). The geometries of each intermediate are shown in the bottom of the plot.

5.5.8 Critical Points Along Isomerization Pathways in the Actinic Step

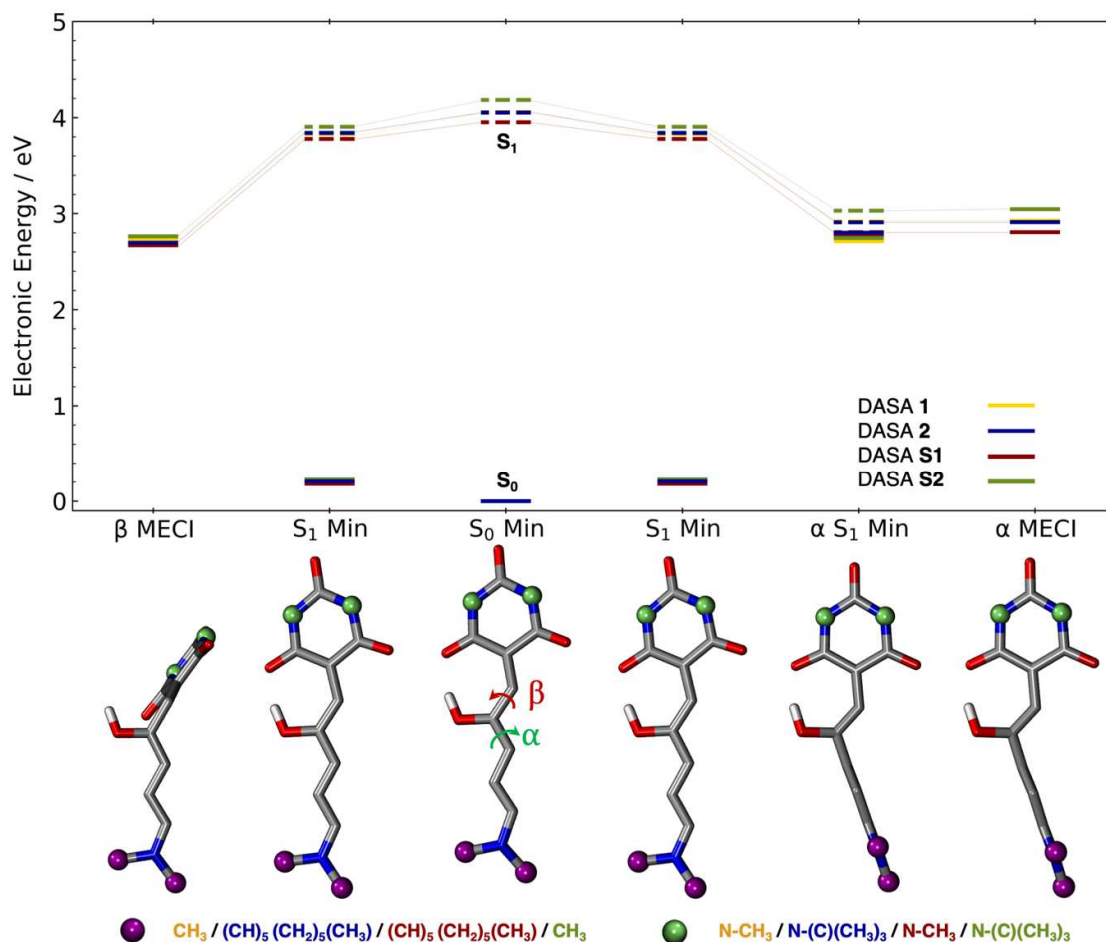


Figure 5.10. The Actinic Step for Sterically Hindered DASAs. Critical points along the different Z/E photoisomerization coordinates for the two lowest energy singlet states computed at the SA3-CAS(2,2)-SCF/6-31G** level of theory with reference to the ground-state energy of the S_0 minimum. Structures for each critical point along with the α (green) and β (red) torsion angles are shown in the bottom. The purple and green markers represent the locations of the substitution pertaining to each DASA derivative.

5.5.9 Critical Points Along the 4π electrocyclization in the Thermal Step

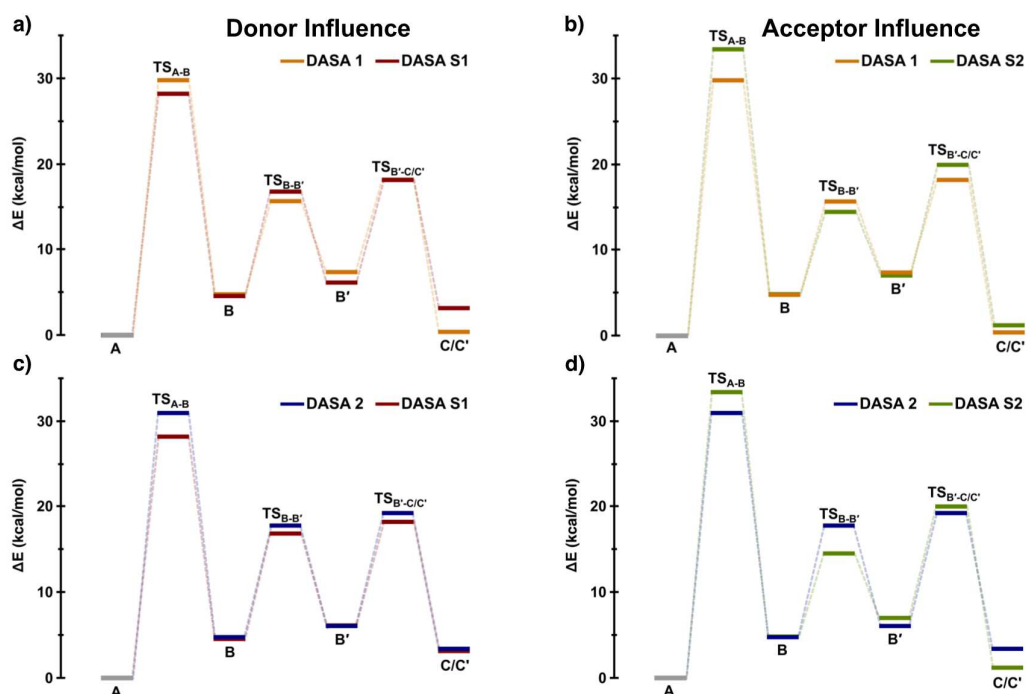


Figure 5.11. Computed 1D-potential energy surfaces of key intermediates in Stages I and II along the 4π -electrocyclization reaction coordinate for a) DASA **1** and DASA **S1**. b) DASA **1** and DASA **S2**. c) DASA **2** and DASA **S1**. d) DASA **2** and DASA **S2**. **a/c** and **b/d** highlight the influence of sterics isolated to donor or acceptor substitution, respectively. Energies are relative to the open-form intermediate, **A**. For adamantyl amine derived donors **C** is not accessed through the mechanism and instead **C'** is used as the first closed isomer.

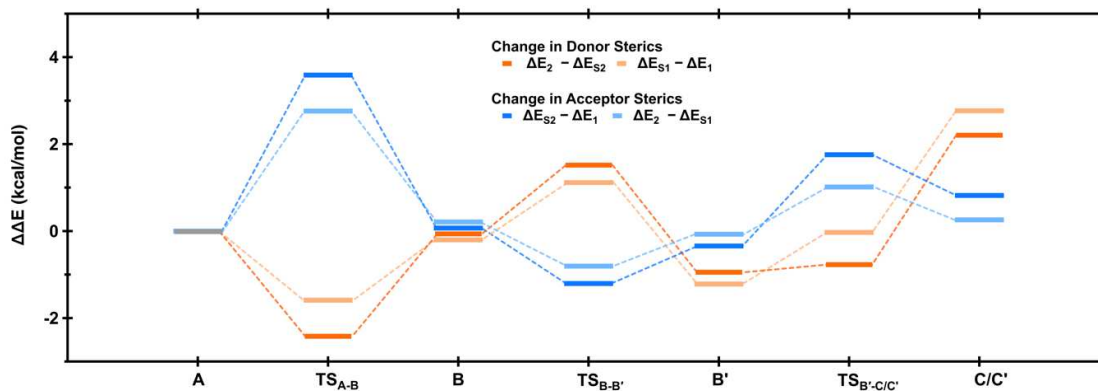


Figure 5.12. Influence of steric demand in the acceptor and donor moieties on the potential energy surface for stages I, II, and III, respectively. Unlike **Figure 5.10**, which shows the relative energies of each intermediate to **A**, here we show the relative change in the energy difference upon substitution in the acceptor and donor groups. For example, the **TS_{A-B}** energy barrier increases by approximately 3.5 – 4.0 kcal/mol when introducing steric demand into the donor group of DASAs **1** and **S2**. In contrast, steric demand introduced into the acceptor group leads to an overall decrease in the **TS_{A-B}** by approximately 2-2.5 kcal/mol shown in DASAs **S1** and **1**. For adamantyl amine derived donors **C** is not accessed through the mechanism and instead **C'** is used as the first closed isomer due to the pyramidalization of the nitrogen in the ring system.

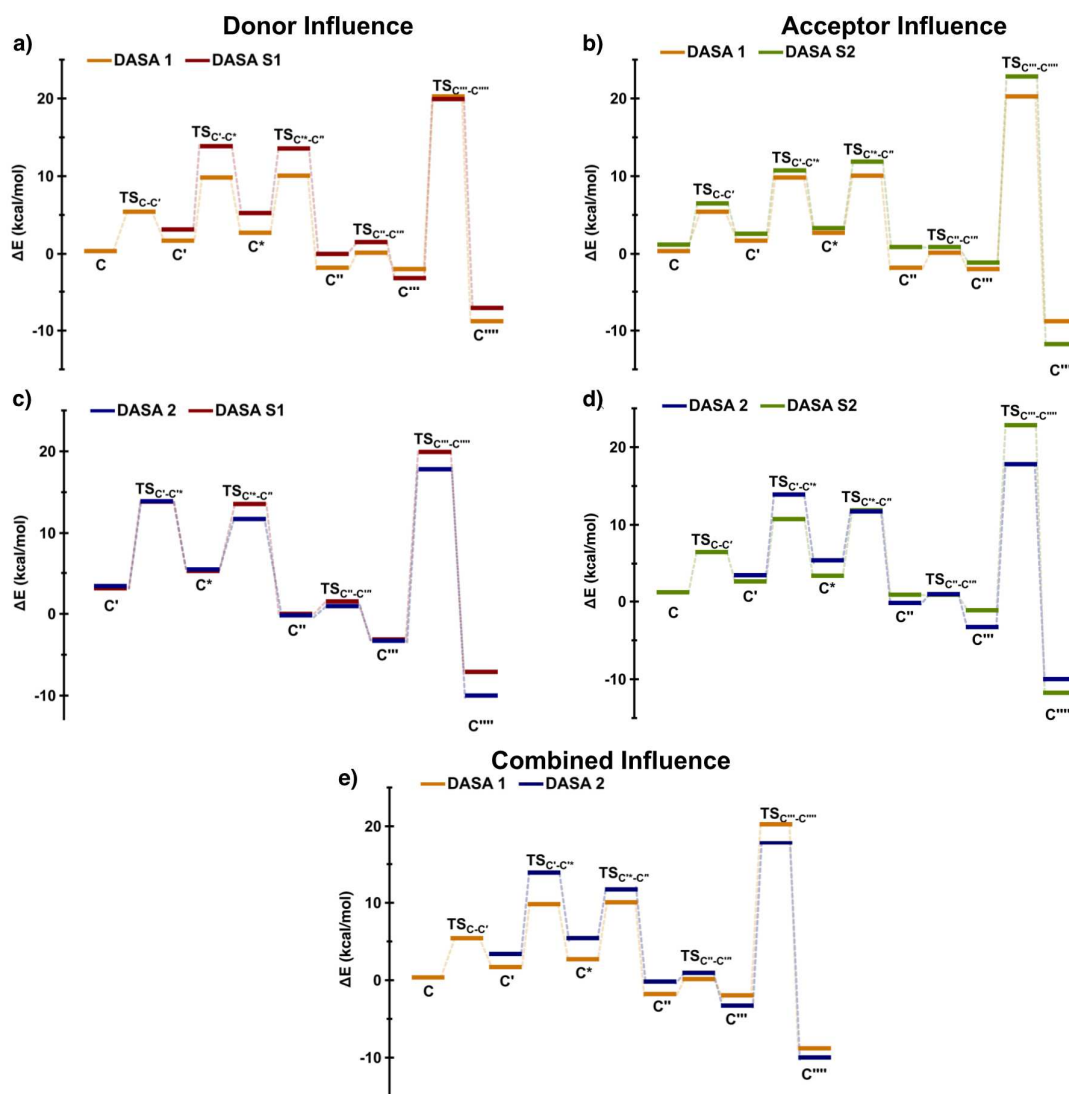


Figure 5.13. Computed 1D-potential energy surfaces of intermediates in Stages II and III after the 4π -electrocyclization reaction coordinate for a) DASA 1 and DASA S1 b) DASA 1 and DASA S2 c) DASA and DASA S1 d) DASA 2 and DASA S2. e) DASA 1 and DASA 2. Energies are relative to the open-form intermediate, **A**. Note: **C** is not accessed for adamantyl amine derived donors due to the pyramidalization of the nitrogen. **C*** is an intermediate corresponding to twisting of the acceptor group which was also computed for previous static potential energy surface calculations.²¹

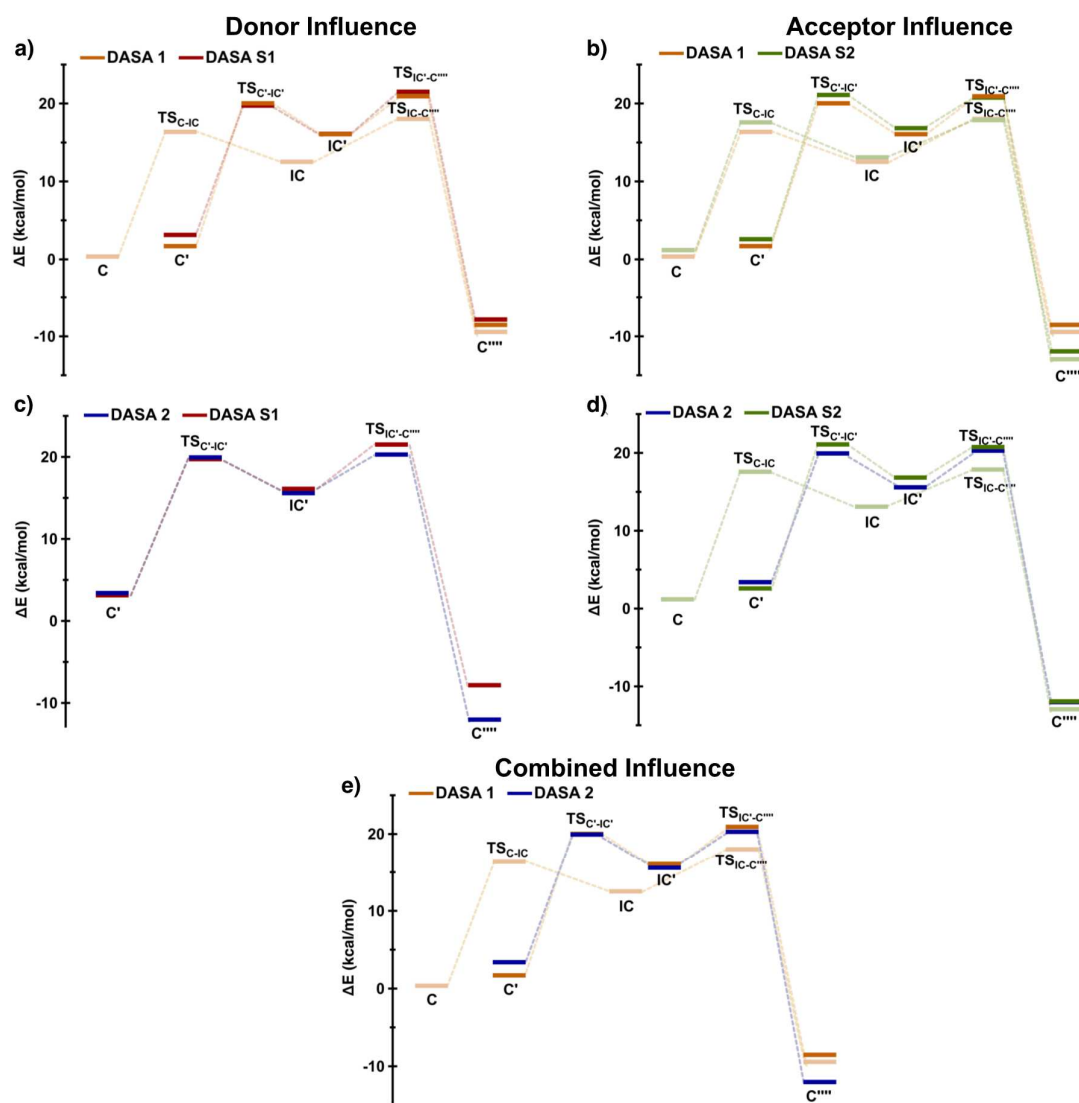


Figure 5.14. Computed 1D-potential alternative pathways along the energy surfaces of intermediates in Stages II and III after the 4π -electrocyclization reaction coordinate for a) DASA 1 and DASA S1 b) DASA 1 and DASA S2 c) DASA and DASA S1 d) DASA 2 and DASA S2. Energies are relative to the open-form intermediate, A. Note: C is not accessed for adamantyl amine derived donors due to the pyramidalization of the nitrogen.²² The keto

forming pathways involve proton transfer between the hydroxy and acceptor groups is shown but are considered minor channels due to their relatively high reaction barrier of ~18-20kcal/mol for all DASA derivatives. See supplemental files for trajectory of both pathways shown.

H	-2.3661820507	3.8199404773	-0.7297321007
H	-0.9923122208	3.3496236894	0.2578013569
C	-5.7593591886	-6.3179678481	-0.4439749443
H	-4.9208329317	-5.8052762294	-0.8930131857
H	-5.8454537538	-7.3031078524	-0.8730971983
C	-8.0290667736	-6.2879696854	-1.4889640211
H	-8.3200815323	-7.1843977566	-0.9588027337
H	-7.6271446993	-6.5561171590	-2.4564242820
H	-8.8919323182	-5.6534870068	-1.6219244847
H	-5.6099320213	-6.4055348275	0.6225194264

Energies & CI Eigenvectors:

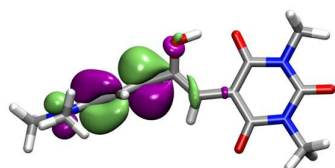
S₀ Energy (H): -964.91877632
 CI eigenvector: -0.60768684827168 A74 B75
 -0.60768684827168 B74 A75
 0.51127374685176 X74

S₁ Energy (H): -964.91877611
 CI eigenvector: 0.85934549776781 X74
 0.36154763785365 A74 B75
 0.36154763785365 B74 A75

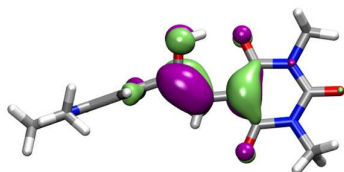
S₂ Energy (H): -964.68907435
 CI eigenvector: 0.99993776243999 X75

CI eigenvectors: *XYX* indicates that the *YY*th molecular orbital is doubly occupied, and *AYY/BYY* indicate that the *YY*th molecular orbital is singly occupied with alpha or beta spin, respectively.

Natural Orbitals:



Orbital 74



Orbital 75

*Purple and green correspond to isovalues +/- 0.05 e⁻/Å³, respectively.

β MECI

Coordinates (Å):

N	-9.1011360140	2.4893752267	3.2570886373
C	-9.6608350257	1.6596586279	4.1986913511
N	-9.1705059232	0.3752862660	4.2638564713
O	-10.5311881676	2.0430979755	4.9349119728
C	-9.6991305754	-0.5285039694	5.2795869472
C	-8.1870596268	-0.1304748748	3.4199750762
C	-7.6928945023	0.7320767628	2.3970468514
C	-8.1499910121	2.0950118871	2.3115749255
O	-7.7665411456	2.8912730166	1.4874064987
O	-7.8031536556	-1.2762570048	3.5811026317
C	-6.7295506192	0.2889699911	1.4785122048
C	-6.2919640741	-1.1040796251	1.3781289146

C	-6.8959572610	-2.0327280872	0.5321507638
C	-6.5061520727	-3.3683559327	0.4278630895
C	-7.1950540711	-4.2204631299	-0.4045462608
O	-5.2267209325	-1.5076889695	2.0326010978
N	-6.9545049976	-5.5088282649	-0.6013678819
H	-6.3279223670	0.9723294523	0.7552189140
H	-7.7290679818	-1.6674238060	-0.0383866808
H	-5.6888567882	-3.7184582720	1.0258316146
H	-8.0226437291	-3.8232545106	-0.9656917867
H	-4.9856449474	-0.8508178991	2.6700736636
H	-8.8974126215	-0.8711127584	5.9189238746
H	-10.4347571731	0.0029395796	5.8559723986
H	-10.1484991298	-1.3918918700	4.8077535821
C	-9.6068959842	3.8568481699	3.1783834062
H	-8.8059991557	4.4973592290	2.8500788404
H	-10.4230131802	3.9254220940	2.4680349946
H	-9.9600007780	4.1534277245	4.1509152782
C	-5.8782958028	-6.1832691773	0.1047884054
H	-4.9352216143	-5.6788199967	-0.0681408449
H	-5.7978503275	-7.1953316881	-0.2638880428
C	-7.8229391499	-6.3194104114	-1.4362237105
H	-8.3655562141	-7.0440738042	-0.8376055149
H	-7.2392880409	-6.8491345286	-2.1801499651
H	-8.5373979126	-5.6888799724	-1.9458593887
H	-6.0708919154	-6.2144909702	1.1721648113

Energies & CI Eigenvectors:

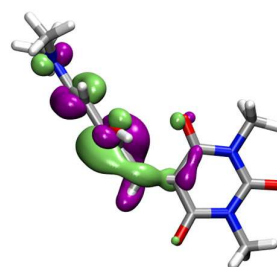
S₀ Energy (H): -964.92615734
 CI eigenvector: -0.70347941645262 A74 B75
 -0.70347941645262 B74 A75
 0.10115748614929 X74

S₁ Energy (H): -964.92615763
 CI eigenvector: 0.99484174726795 X74
 0.07153118639770 A74 B75
 0.07153118639770 B74 A75

S₂ Energy (H): -964.71109013
 CI eigenvector: 0.99997146914857 X75

CI eigenvectors: *XYX* indicates that the *YY*th molecular orbital is doubly occupied, and *AYY/BYY* indicate that the *YY*th molecular orbital is singly occupied with alpha or beta spin, respectively.

Natural Orbitals:



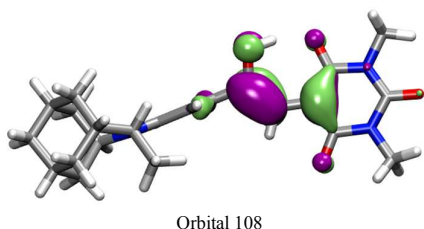
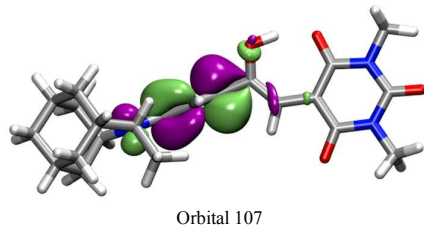
Orbital 74

CI eigenvector: -0.99908302207229 X107
-0.02932275443872 A107 B108
-0.02932275443872 B107 A108

S₂ Energy (H): -1312.53574670
CI eigenvector: 0.99994316712095 X108

CI eigenvectors: XYY indicates that the YYth molecular orbital is doubly occupied, and AYY/BYY indicate that the YYth molecular orbital is singly occupied with alpha or beta spin, respectively.

Natural Orbitals:



*Purple and green correspond to isovalues +/- 0.05 e-/Å³, respectively.

β MECI

Coordinates (Å):
N -9.1259974700 2.2702502265 3.4940144023
C -9.4522947146 1.4134398123 4.5178694794
N -8.8441059908 0.1790720777 4.5115096284
O -10.2251940462 1.7338971907 5.3817458570
C -9.1220143430 -0.7468650363 5.6042581223
C -7.9636499496 -0.2570188345 3.5260097030
C -7.7139693919 0.6276101247 2.4317544355
C -8.3039956637 1.9433805912 2.4128288431
O -8.1284143203 2.7543705355 1.5348502914
O -7.4536347044 -1.3569890099 3.6373548370
C -6.8737569084 0.2602760607 1.3742850292
C -6.3047702120 -1.0775345354 1.2108689445
C -6.9202681116 -2.0762893349 0.4667213302
C -6.4083721687 -3.3659221517 0.3020534155
C -7.1280104768 -4.2908757176 -0.4232720118
O -5.1138051086 -1.3512589454 1.7072740651
C -6.8939929867 -8.6943987691 -1.8673320872
C -7.3869495929 -7.3425089357 -2.4066292901
C -7.9021032905 -6.3579754578 -1.3429218106
C -5.6798384608 -7.6793346938 0.1342243025
C -5.5715048399 -8.5762558175 -1.1088094518
C -8.8046362804 -7.0540612656 -0.3140452842
C -6.8787195319 -8.1052277110 1.0090178691
C -7.9456052333 -9.3033505049 -0.9325669857
C -8.1889097881 -8.3425502885 0.2375250534
C -5.6170649122 -6.1587821895 -0.1205193389
N -6.8484058671 -5.5650146007 -0.6775663780
C -4.3972316859 -5.7422467775 -0.9509849718
H -6.6444642799 0.9794252563 0.6108541309
H -7.8625180111 -1.8108229702 0.0249129872
H -5.4763868661 -3.6095581638 0.7679234023

H -8.0562116444 -3.9482286197 -0.8457999698
H -4.8664364593 -0.6714745397 2.3168833661
H -6.7426882009 -9.3521933787 -2.7193954518
H -6.6234823595 -6.8621822235 -3.0110274816
H -8.2267139643 -7.5337187559 -3.0702938921
H -8.5001879403 -5.6266093195 -1.8709242000
H -4.7854506126 -7.8562299622 0.7262513900
H -4.7820792568 -8.2318697363 -1.7673237108
H -5.2753763228 -9.5696209136 -0.7797516784
H -9.0386044345 -6.3585580628 0.4867300078
H -9.7451319248 -7.3004532124 -0.8022757673
H -7.0377452467 -7.3769638378 1.8009074611
H -6.6111755447 -9.0371186067 1.5011431348
H -8.8759928303 -9.4828318952 -1.4666825347
H -7.6007957285 -10.2679552325 -0.5686745332
H -8.9029902030 -8.7852163863 0.9268671026
H -5.5070710705 -5.7249235083 0.8667849894
H -4.2862805837 -4.6656104435 -0.9606323269
H -3.4927463149 -6.1666642942 -0.5271050515
H -4.4779937821 -6.0705435741 -1.9791126219
H -8.2037265767 -0.9927722125 6.1193868813
H -9.8136132796 -0.2760107144 6.2793497568
H -9.5463300904 -1.6612743595 5.2125617706
C -9.7534561987 3.5888768822 3.4905502209
H -9.0652095959 4.2927460773 3.0539138480
H -10.6636882546 3.5802073800 2.9018421235
H -9.9905174918 3.8628418856 4.5039004580

Energies & CI Eigenvectors:

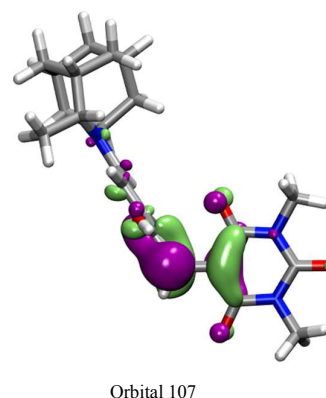
S₀ Energy (H): -1312.77090252
CI eigenvector: -0.68392382297953 A107 B108
-0.68392382297953 B107 A108
0.25395419692642 X10

S₁ Energy (H): -1312.7709023
CI eigenvector: 0.96718680227203 X107
0.17957785041872 A107 B108
0.17957785041872 B107 A108

S₂ Energy (H): -1312.55674836
CI eigenvector: 0.99997152190731 X108

CI eigenvectors: XYY indicates that the YYth molecular orbital is doubly occupied, and AYY/BYY indicate that the YYth molecular orbital is singly occupied with alpha or beta spin, respectively.

Natural Orbitals:



Energies & CI Eigenvectors:

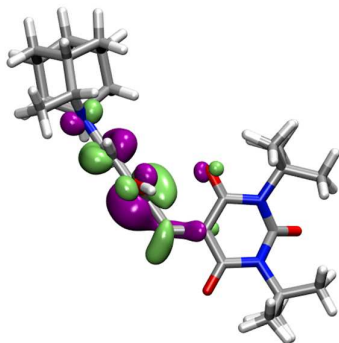
S₀ Energy (H): -1546.96052799
CI eigenvector: -0.99438276012071 X131
 -0.07464790040596 A131 B132
 -0.07464790040596 B131 A132

S₁ Energy (H): -1546.96052772
CI eigenvector: -0.70315552402365 A131 B132
 -0.70315552402365 B131 A132
 0.10556495958433 X131

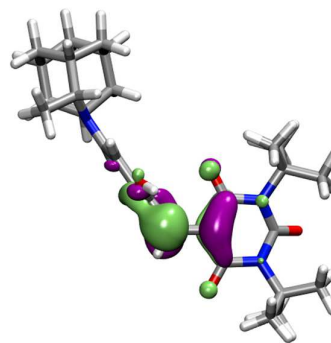
S₂ Energy (H): -1546.74571808
CI eigenvector: 0.99997051672402 X132

CI eigenvectors: XYY indicates that the YYth molecular orbital is doubly occupied, and AYY/BYY indicate that the YYth molecular orbital is singly occupied with alpha or beta spin, respectively.

Natural Orbitals:



Orbital 131



Orbital 132

*Purple and green correspond to isovalues +/- 0.05 e-/Å³, respectively.

5.5.11 Solvatochromic shift analysis

Table 5.1: The ten solvents and corresponding E_T^N solvent polarity value using the Dimroth—Reichardt E_T solvent polarity scale. The E_T^N scale is based on the electronic transitions of a polarity probe dye in a range of solvents which is normalized to nonpolar tetramethylsilane (TMS) ($E_T^N = 0$) and polar water ($E_T^N = 1.0$).²²

Solvent	Tol	Et ₂ O	THF	EtOAc	CHCl ₃	CH ₂ Cl ₂
E_T^N	0.099	0.117	0.207	0.228	0.259	0.309
Solvent	Acetone	DMSO	ACN	MeOH		
E_T^N	0.355	0.444	0.460	0.762		

By plotting the λ_{\max} vs E_T^N gives information about the ground state charge separation of DASA molecules.²³ A negative slope shows that the molecule is zwitterionic in nature. A neutral slope shows that the molecule is hybrid in nature.

Table 5.2: λ_{\max} (nm) values of DASA 1 in a range of solvents.

Solvent	Tol	Et ₂ O	THF	EtOAc	CHCl ₃
λ_{\max} (nm)	568	560	560	557	565
Solvent	CH ₂ Cl ₂	Acetone	DMSO	ACN	MeOH
λ_{\max} (nm)	562	551	547	546	537

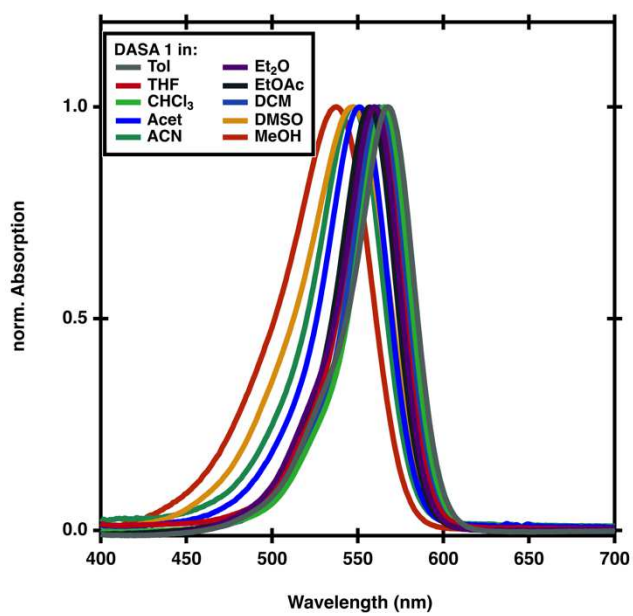


Figure 5.15. UV-Vis measurements showing the solvatochromic shift of DASA 1.

Table 5.3: λ_{max} (nm) values of DASA S1 in a range of solvents.

Solvent	Tol	Et ₂ O	THF	EtOAc	CHCl ₃
λ_{max} (nm)	575	567	567	563	567
Solvent	CH ₂ Cl ₂	Acetone	DMSO	ACN	MeOH
λ_{max} (nm)	567	558	547	555	546

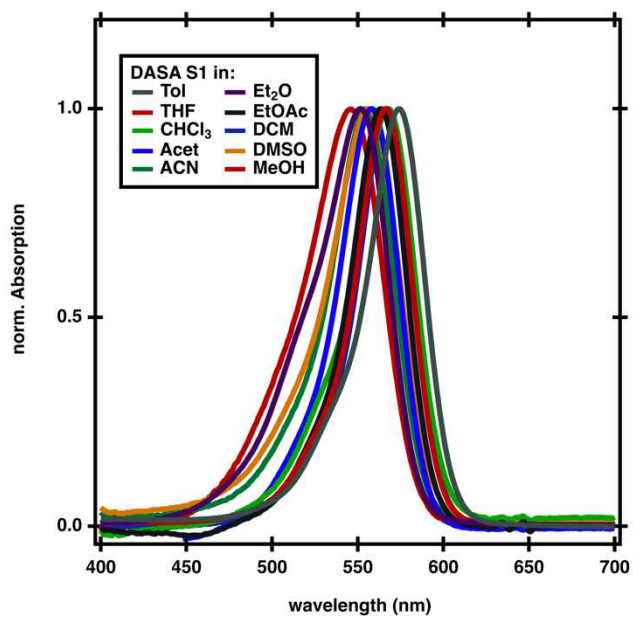


Figure 5.16. UV-Vis measurements showing the solvatochromic shift of DASA S1.

Table 5.4: λ_{max} (nm) values of DASA S2 in a range of solvents.

Solvent	Tol	Et ₂ O	THF	EtOAc	CHCl ₃
λ_{max} (nm)	556	552	558	554	559
Solvent	CH ₂ Cl ₂	Acetone	DMSO	ACN	MeOH
λ_{max} (nm)	558	553	554	550	546

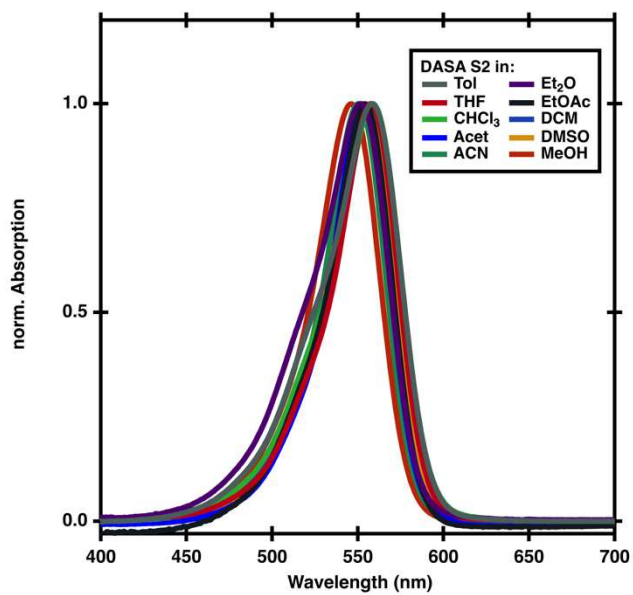


Figure 5.17. UV-Vis measurements showing the solvatochromic shift of DASA S2.

Table 5.5: λ_{\max} (nm) values of DASA 2 in a range of solvents.

Solvent	Tol	Et ₂ O	THF	EtOAc	CHCl ₃
λ_{\max} (nm)	565	560	565	561	568
Solvent	CH ₂ Cl ₂	Acetone	DMSO	ACN	MeOH
λ_{\max} (nm)	566	560	561	557	553

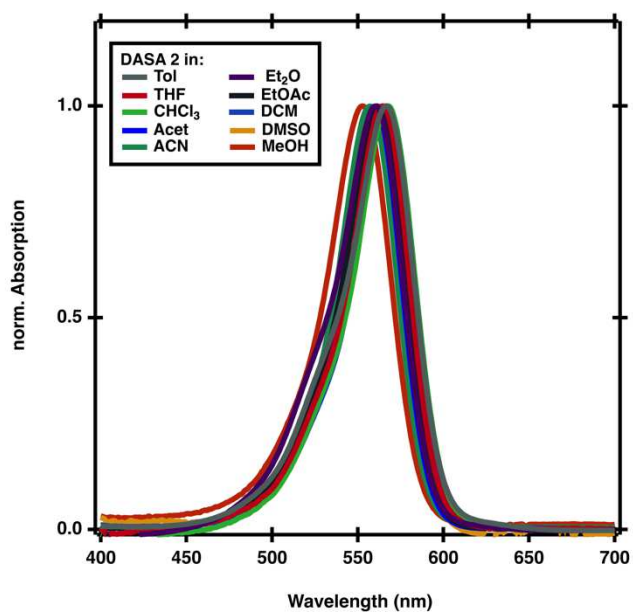


Figure 5.18. UV-Vis measurements showing the solvatochromic shift of DASA 2.

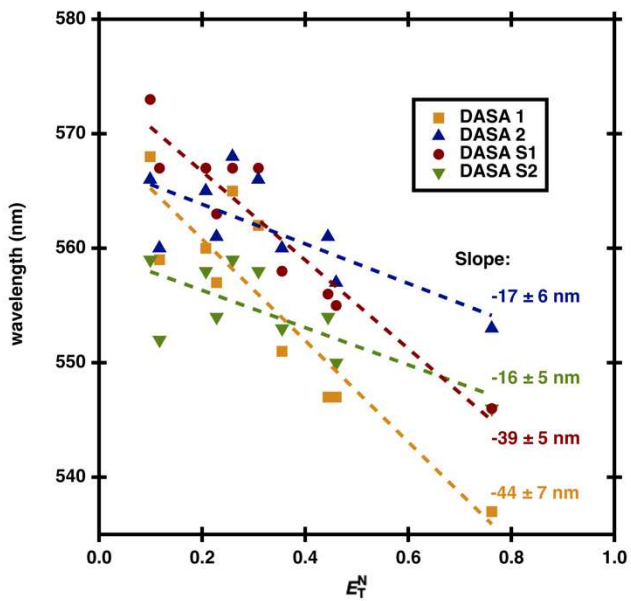


Figure 5.19. Solvatochromic slopes of DASA 1, 2, S1 and S2 with error.

5.5.12 Discussion on influence of donor and acceptor on photoswitching properties

Photoswitching Properties of DASA with Increased Sterics at the Donor Position.

In Figure **5.3a** and **Figures 5.11-14**, we show that the 4π -electrocyclization reaction coordinate can be dramatically influenced by modifying the sterics of the donor and/or the acceptor groups. The introduction of the bulky adamantyl donor group lowers the barrier from **B** to **A** when comparing DASA derivatives **1** vs. **S1** and **S2** vs. **2**. Furthermore the compound does not seem to go through the first closed isomer **C** but forms directly the second isomer **C'** due to the conformation of the nitrogen in the ring system. Additionally, our calculations indicate that the bulky donor group destabilizes the second closed isomer **C'** while stabilizing **B'**. The steric interactions of the adamantyl donor group in the 4,5-disubstituted cyclopentenone rotates the donor group of DASAs **S1** and **2** by 20.5° relative to DASA **1**, raising the energy of the closed isomer **C'**. This, together with the stabilization of **B'** and the **B** to **A** transition state (TS), suggests that the donor group favors the open-form at equilibrium in the dark, promoting the thermal back reaction when the irradiation is turned off. This is corroborated experimentally using ^1H NMR spectroscopy, where the thermodynamic equilibrium as a function of sterics on the donor group is measured the percent of the DASA in the open- vs. closed-form in the dark using ^1H NMR spectroscopy. DASAs **1**, **S1**, and **2** were dissolved in toluene- d_8 in an NMR tube and allowed to equilibrate overnight in the dark. In agreement with the computed potential energy surfaces, all three derivatives showed a high thermodynamic equilibrium (88% for DASA **1**, >95% for DASA **2** and **S1**) in the open form (Table 5.6). In contrast, only 9% of DASA **S2** is measured in the open-form at thermodynamic equilibrium. It is noteworthy that due to the light sensitivity and slow equilibration of DASA **S2**, light irradiation was used to switch the DASA adduct to the closed form and then the recovery to the thermodynamic equilibrium was monitored by ^1H NMR spectroscopy.

The role of the large donor group in destabilizing C' is further highlighted with DASAs **1** and **S1** in our measured UV-Vis spectra **Figure 5.25**). Irradiation of DASA **S1** with 530 nm light results in a 20% loss of absorbance at the λ_{max} (575 nm) compared to ~100% loss of absorbance for DASA **1** (**Figure 5.25**). For this reason, one could postulate that the adamantyl donor group lowers the PTSS from ~100% to 17% (i.e., conversion from the colored open-form **A** to the colorless closed form **C' → C''''**). However, the UV-Vis spectra shows that the loss in absorbance of DASA **2** does not correspond to the formation of the colorless closed-form isomer **C** as seen in DASA **1**, but rather the appearance of the red shifted shoulder at 630 nm corresponding to the open isomers **B/B'** of DASA **2** (**Figures 5.27-28**). Therefore, due to the inability of DASA **S1** to form **C'**, we can directly measure the kinetics of the thermal back reaction from **B/B'** to **A**. After irradiation is stopped, the **B/B'** population quickly reverts back to **A** with a k_{-1} of 4.008 min⁻¹ (**Figures 5.25-26** and Table 5.6). Here, the DASA **S1** is behaving analogous to a classic single-step *E-Z* isomerization based P/T-type photoswitch. Overall, these results are in agreement with previous reports by Beves and coworkers,⁴ thereby supporting the generality of these phenomena and the ability to use sterics of the donor as a design principle to tune the photoswitching properties of DASAs.

Effects of Sterics on Acceptor Groups on Photoswitching Properties.

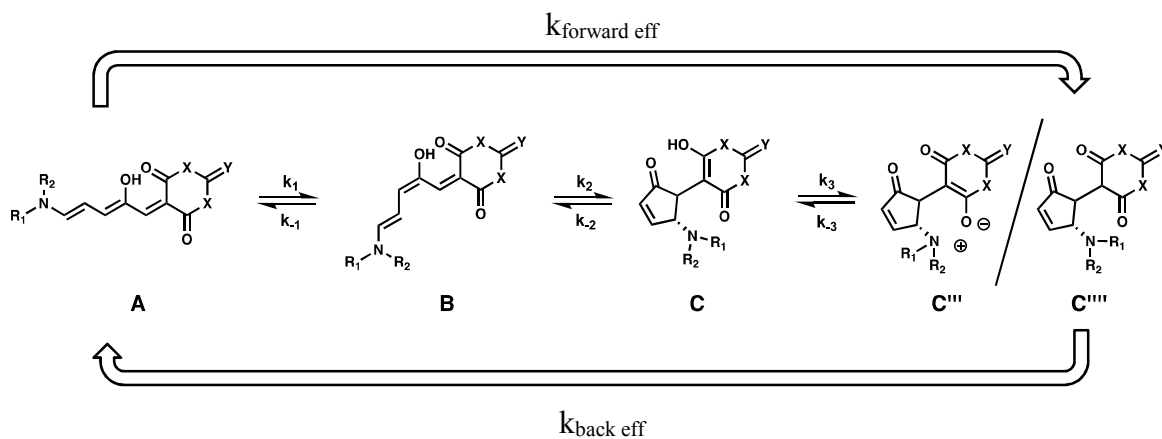
In contrast to the donor side, we show that by introducing sterics into the acceptor side the equilibrium ratio is inverted, favoring the closed-ring forms **C → C''''**. The relative energy differences computed in **Figure 5.3a** and **Figure 5.11** show that the reverse reaction barrier from **B** to **A** increases substantially when introducing sterics into the acceptor group for DASAs **S2** and **2**. Additionally, the TS between **B** to **B'** and the rate-determining step, **B'** to

C/C' are shifted towards the formation of C/C'. Lastly, we observe a significant stabilization of the computed closed metastable isomers, specifically isomer C'''' (Table 5.6). Collectively, this suggests that the equilibrium will shift towards the closed-ring isomers and favor a long thermal half-life. Notably, this is consistent with our experimental observations. For example, replacing the smaller *N,N'*-(dimethyl)barbituric acid acceptor in DASA 1 with the sterically larger *N,N'*-(*t*-butyl)barbituric acid in DASA S2 decreases the thermodynamic equilibrium from 88% to 9%, respectively (Table 5.6). Comparing the $k_{\text{back,eff}}$ enables us to experimentally probe the role the acceptor plays on modulating the transition state barrier from C/C' to B'. Here, we observe the $k_{\text{back,eff}}$ of DASA 1 ($k_{\text{back,eff}} = 0.13 \text{ min}^{-1}$) is faster than DASA S2 ($k_{\text{back,eff}} = 0.02 \text{ min}^{-1}$, it has to be noted that the recovery of DASA S2 was measured by ^1H NMR at 30 °C due to no observable recovery in UV-Vis due to the probe light.) (Table 5.6, **Figures 5.20-23**). This is significant because it demonstrates for the first time the dramatic impact sterics on the acceptor group plays in the photoswitching of DASAs. The impact of this structural modification is highlighted by the difference in photoswitching behavior of DASAs 2 vs. S1. As noted previously, irradiation of DASA S1 results in a single-step *Z* to *E* photoisomerization of A to B/B', but the formation of the closed isomer is not observed experimentally (i.e., we observe a PTSS of 0%). However, by simply modifying the sterics of the acceptor group, for example DASA 2, we can regain the full photoswitching properties of DASA and obtain a PTSS of ~100% upon irradiation with a $k_{\text{back,eff}}$ recovery rate of 0.013 min^{-1} (**Figure 6.8b**, Table 5.6). Therefore, this suggests that the state/stability of the metastable closed isomer, as well as the life-time of the B/B' intermediate, are governed by the sterics of the acceptor group. It is known that closed isomer C can rapidly convert to more stable closed isomers C', C'', C''' and C''''', with C'''' being the most stable.^{4,21,24} To support this

hypothesis, we used 2D-NMR spectroscopy in toluene and chloroform to determine the state of the closed-form of DASA **S2**. Interestingly, we only observed the keto metastable product **C''''** in toluene or chloroform (**Figures 5.39-43**), which is in contrast to previous studies by Beves and coworkers which have shown DASA **1** favors isomer **C'''** over **C''''** in chloroform.⁴ Presumably, the build-up of A_{1,2}-strain that would result from the formation of the enol- or enolate-bond within the barbituric acid ring (i.e., isomers **C** to **C'''**) results in the favored formation of **C''''**. This is supported by our calculations showing a stabilization of **C''''** upon introduction of the *N,N'*-(*t*-butyl)barbituric acid acceptor (**Figures 5.12-14**). In addition, the increase in barrier height of the TS between **B** to **A** and **B'** to **C** results in an overall stabilization of **B/B'**, which can be observed in the long-lived UV-Vis trace of **B/B'** under irradiation for both DASAs **2** (**Figure 5.28**) and **S2** (**Figure 5.29**). Taken together, these results reveal that the acceptor system provides a tunable lever to influence the transition states from **B** to **A** as well as **B'** to **C** and is key in influencing which closed-form isomer is ultimately formed. In summary, steric modification to the acceptor group provides a new and important design principle for DASA based photoswitches.

5.5.13 Photoswitching kinetics

Due to limitation in the observation of the intermediates only an effective rate constant from the overall forward and back reaction in the dark can be determined. **Scheme 5.2** shows the nomenclature used:



Scheme 5.2: Showing the rate constants determined by time dependent UV-Vis spectroscopy and by ^1H NMR in a simplified mechanism. For the full mechanism see **Figure 5.7a**.

Table 5.6: Photophysical properties of DASA 1, 2, S1, S2.

DASA ^[a]	λ_{max}	therm. equi.	$k_{\text{back eff}}$ (min^{-1})	$k_{\text{forward eff}}$ (min^{-1})	$k_{\text{forward eff}}/k_{\text{back eff}}$ ^[c]	PTSS (closed under irradi.)	Molar extinction coefficient
1	568	88 %	0.128	0.017	0.133	100 %	141 000
S1	575	>95%	4.008 ^[a]	0.027 ^[a]	0.007	17 % ^[b]	98 000
S2	556	9 %	0.022 ^[c]	0.237 ^[c]	10.772	100 %	115 000
2	565	>95%	0.013	0.001	0.077	100 %	82 000

All values in Toluene [a] k_{-1} not $k_{\text{back eff}}$ [b] PSS instead of PTSS. this refers to % A vs B/ B' [c] measured by NMR instead of UV-VIS spectroscopy @ 30 °C

5.5.14 Kinetic modelling of time dependent UV-Vis spectroscopy

The recovery data obtained from time-dependent UV-Vis spectroscopy was fit to an isomer equilibrium model assuming first order rates of opening and closing. The model used was of the form:

$$\frac{d[\text{Open}]}{dt} = -k_F[\text{Open}]_t + k_B([\text{Open}]_0 - [\text{Open}]_t)$$

For recovery:

$$[\text{Open}]_t = 1 - \frac{k_F + k_B e^{-(k_B+k_F)t}}{k_B + k_F} [\text{Open}]_0$$

where k_F , k_B , and $[\text{Open}]_0$ represent the rate of closing in the dark, the rate of opening in the dark, and the initial concentration. Samples were left to equilibrate overnight before irradiation, and thermodynamic equilibrium was used for initial concentration in UV-Vis experiments.

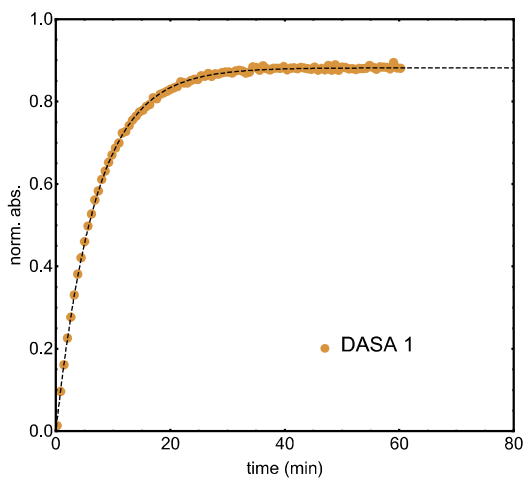


Figure 5.20. Time dependent UV–Vis spectroscopy of DASA 1 in Toluene followed at λ_{\max} 568 nm in the dark after irradiation including the fit used to determine equilibration rates. For rates see Table 5.6.

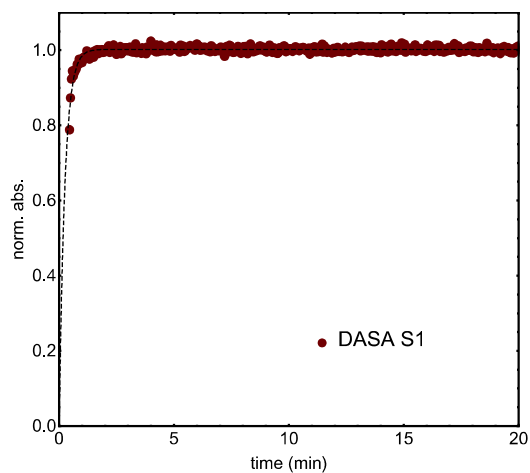


Figure 5.21. Time dependent UV–Vis spectroscopy of DASA S1 in Toluene followed at λ_{\max} 575 nm in the dark after irradiation including the fit used to determine equilibration rates. For rates see Table 5.6.

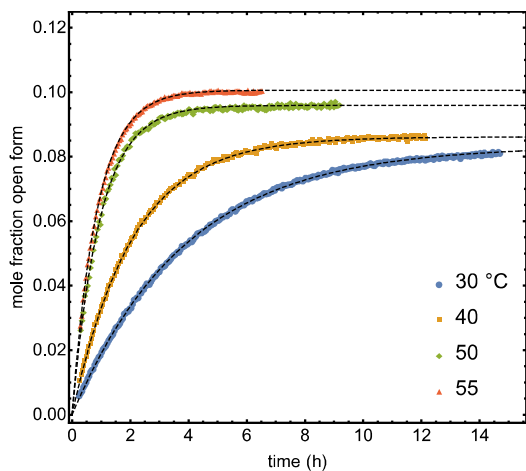


Figure 5.22. mole fraction of open form obtained by ^1H NMR spectroscopy of DASA S2 in Tol- d_8 in the dark after irradiation including the fit used to determine equilibration rates. For rates see Table 5.6 and 7.

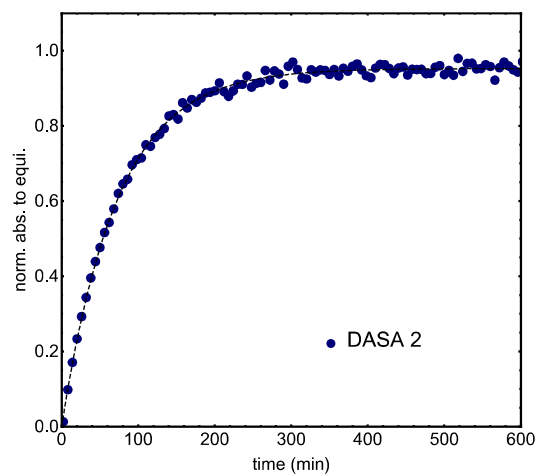


Figure 5.23. Time dependent UV–Vis spectroscopy of DASA 2 in Toluene followed at λ_{max} 565 nm in the dark after irradiation including the fit used to determine equilibration rates. For rates see Table 5.6.

5.5.15 Arrhenius Kinetics

Arrhenius kinetics could only be determined for DASA **S2** since DASA **1, 2** and **S1**'s rate equations could not be determined by NMR and therefore could not be measured at different temperatures.

Table 5.7: DASA S2

Temperature (°C)	$k_{\text{forward, eff}}(\text{s}^{-1})$	$k_{\text{back, eff}}(\text{s}^{-1})$	1/T (1/K)
30	0.00394953	0.00035833	0.00330
40	0.00739813	0.00069667	0.00320
50	0.01574685	0.00167	0.00310
55	0.01735433	0.00193333	0.00305
	$E_{\text{forward,eff}}$	$E_{\text{back,eff}}$	
	-12.30	-13.97	in kcal/mol

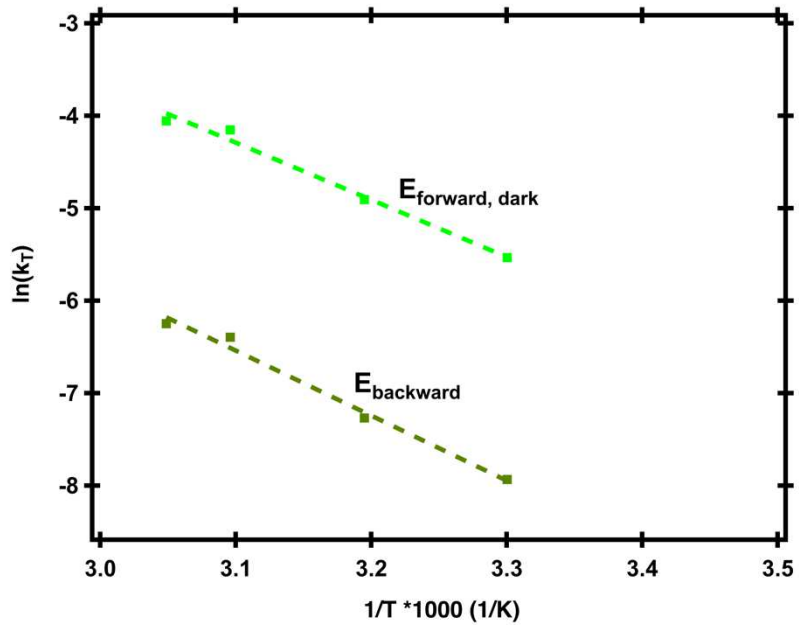


Figure 5.24. Arrhenius Plot for DASA S2.

5.5.16 Time dependent UV-Vis spectroscopy

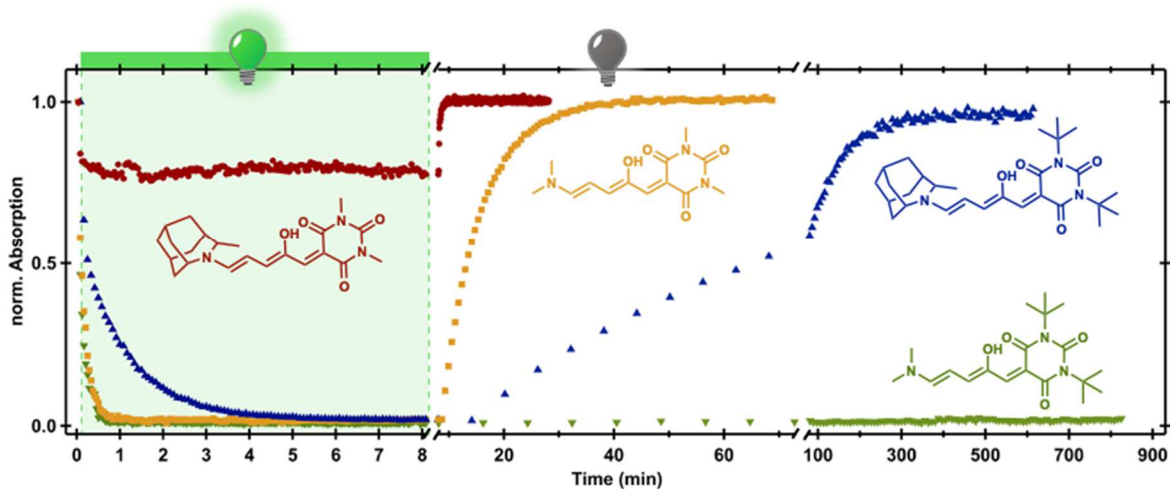


Figure 5.25. Time-dependent UV-Vis spectroscopy of DASA 1, 2, S1 and S2 at 10 μM in Toluene. Irradiation with a 530 nm LED for 8 minutes and subsequent recovery in the dark is observed by following their respective λ_{max} . The results show differences under irradiation and in the thermal recovery in the dark for the four DASAs.

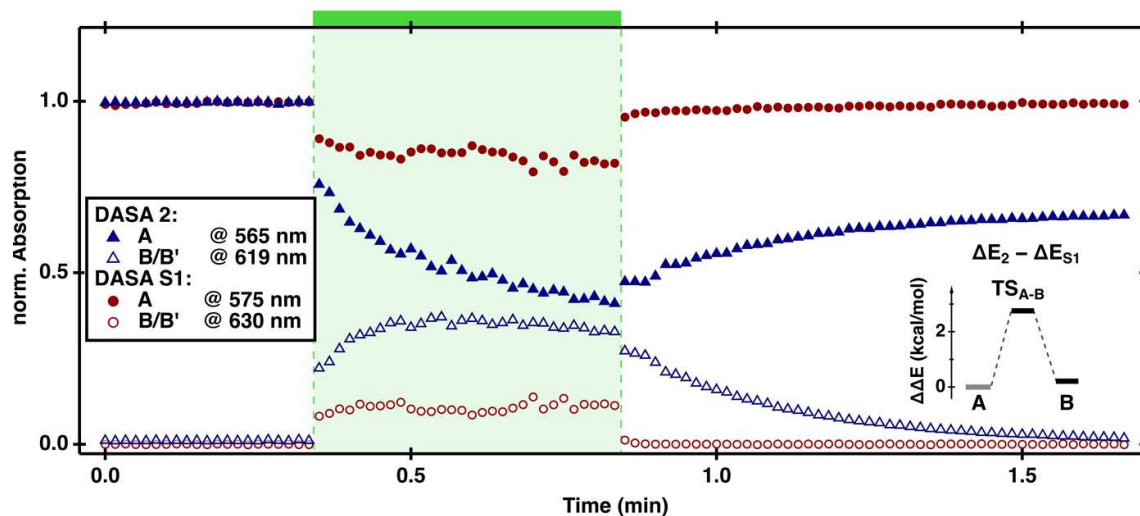


Figure 5.26. Time-dependent pump probe UV-Vis spectroscopy at 10 μ M in Toluene highlighting (irradiated with a 530 nm LED – 65 mW/cm²) the **B/B'** intermediates for **S1** and **2** highlighting the long half-life of **B/B'** in **2**. Inset: difference of the *N,N'*-(*t*-butyl)barbituric acid to *N,N'*-dimethylbarbituric acid carbon acid on the thermal barrier between **B** and **A** from **S1** to **2**.

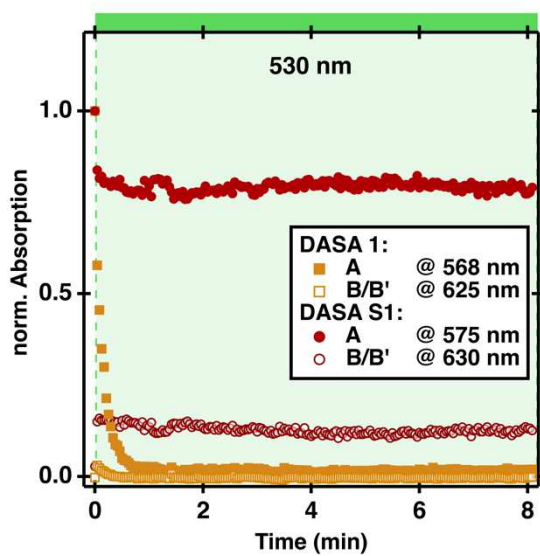


Figure 5.27. Time-dependent pump-probe UV-Vis spectrum at 10 μM in toluene under irradiation with a 530 nm LED ($65 \text{ mW}/\text{cm}^2$) and followed by the respective λ_{max} and maximum of the **B/B'** shoulder highlighting the **B/B'** intermediates for DASAs **1** and **S1**.

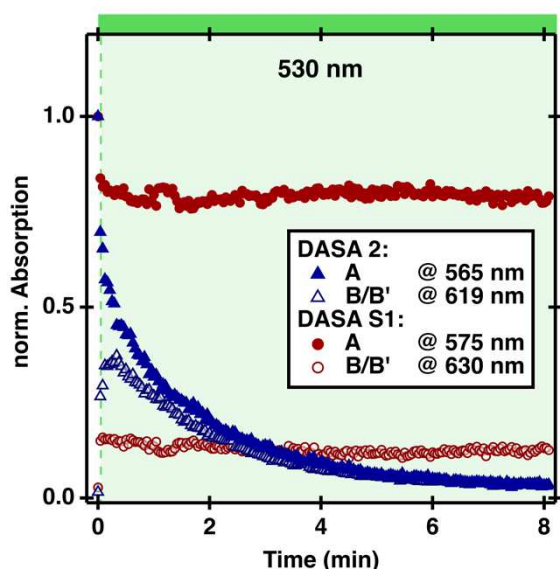


Figure 5.28. Time dependent UV-Vis spectroscopy of 10 μM DASA **S1** and **2** under irradiation with a 530 nm LED for 8 minutes followed at λ_{max} for **A** and at maximum of the shoulder for **B/B'**.

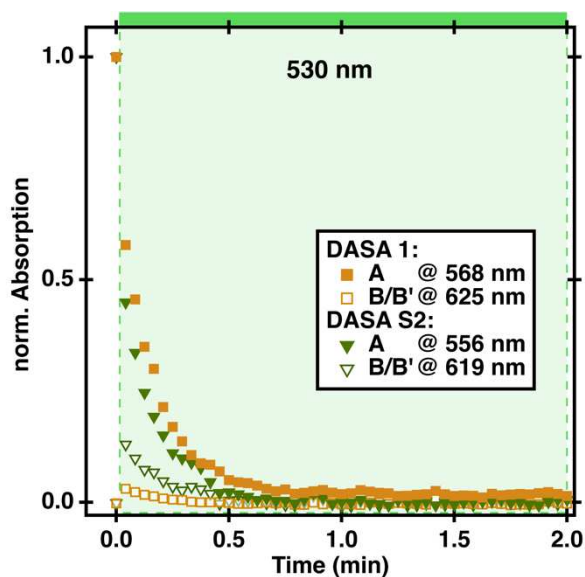


Figure 5.29. Time dependent UV-Vis spectroscopy of 10 μM DASA **1** and **S2** under irradiation with a 530 nm LED for 2 minutes followed at λ_{max} for **A** and at maximum of the shoulder for **B/B'**. This shows a smaller population of **B/B'** for **1** than for **S2** as expected by our theoretical predictions.

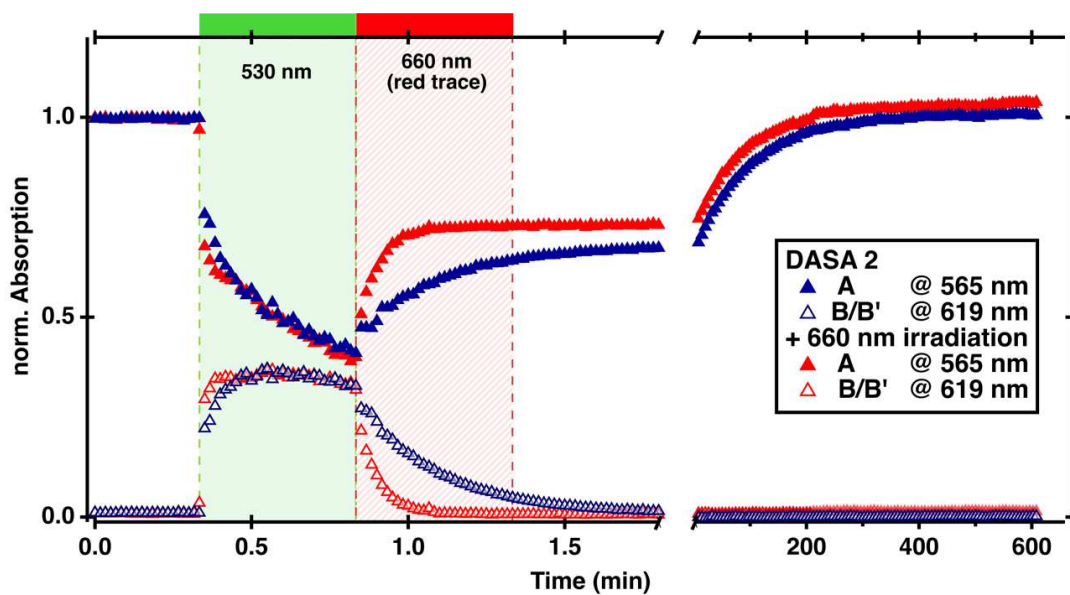


Figure 5.30. Time dependent UV-Vis spectroscopy of 10 μM DASA 2 in Toluene under irradiation with a 530 nm LED for 0.5 minutes followed at λ_{max} for **A** and at maximum of the shoulder for **B/B'**. The red trace is then irradiated with 660 nm LED ($128 \text{ mW}/\text{cm}^2$) showing the recovery of **A** upon irradiation of **B/B'**.

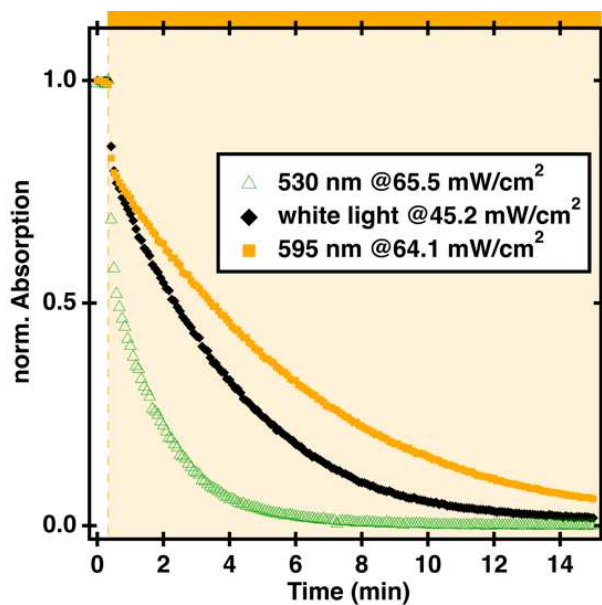


Figure 5.31. Time dependent UV-Vis spectroscopy of 10 μM DASA **2** in Toluene under irradiation with different light sources followed at λ_{max} for **A** (565 nm). This shows resistance to switching upon irradiation with a light source red shifted to the λ_{max} . Intensity is calculated for overlap of emission with UV-Vis spectrum of **2** as **A**.

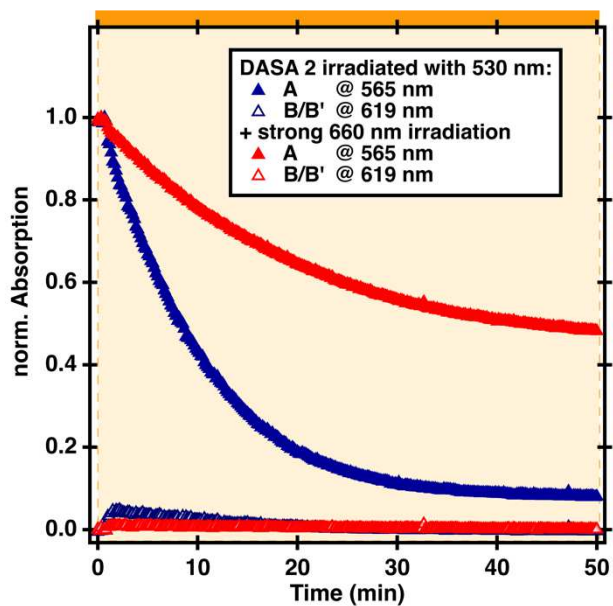


Figure 5.32. Time dependent UV-Vis spectroscopy of 10 μM DASA 2 in Toluene under irradiation with a 530 nm LED ($1.2 \text{ mW}/\text{cm}^2$) for 0.5 minutes followed at λ_{max} for **A** and at maximum of the shoulder for **B/B'**. The red trace is also irradiated with 660 nm LED ($128 \text{ mW}/\text{cm}^2$) increasing the PTSS from 93 % closed form under irradiation with 530 nm LED to 56 % closed under irradiation with both light sources.

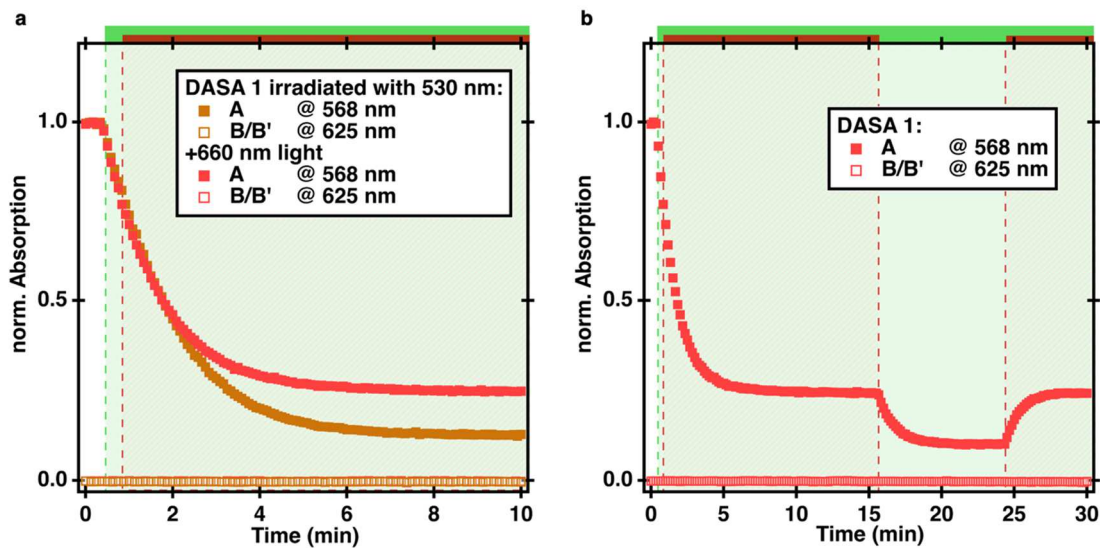


Figure 5.33. Time-dependent UV-Vis spectroscopy of DASA 1 at 10 μM in Toluene. a) DASA 1 is irradiated with 530 nm light (1.2 mW/cm^2 , dark orange trace) or both 530 nm light (1.2 mW/cm^2) and 660 nm (128.0 mW/cm^2) light (red trace). Even though Stage II (B/B') is not observable in DASA 1 irradiation with a secondary wavelength leads to a change in PTSS from 88 to 75 % in Stage III (C-isomers) under irradiation by influencing the forward reaction kinetics. b) When irradiation with the 660 nm light is stopped the PTSS moves from 75% to 88 % and upon subsequent restart of 660 nm light irradiation thermal recovery from Stage III to Stage I can be observed.

5.5.17 Comparison between two-stage and negative photochromic three-stage photoswitches

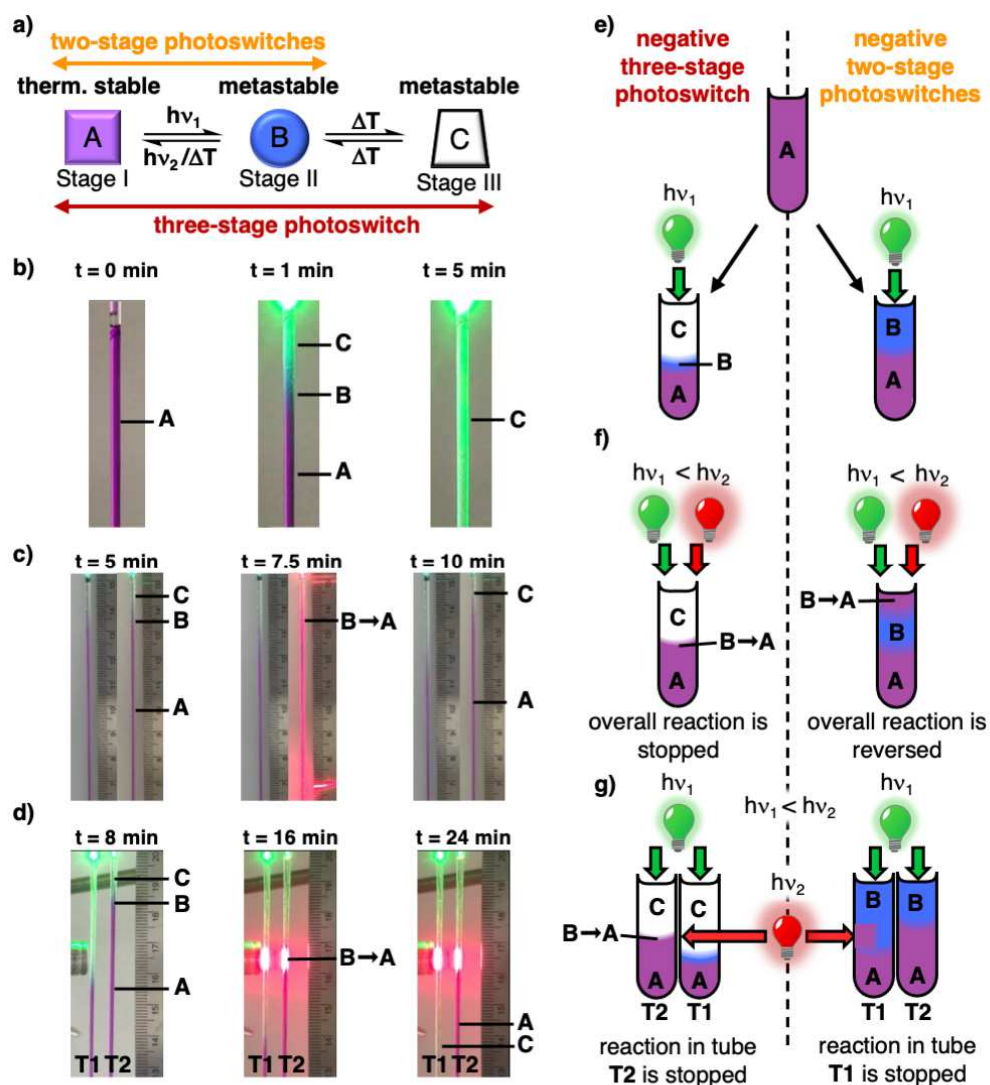


Figure 5.34. a) Schematic representation of a negative photochromic three-stage photoswitch presented in this work. b) Photographic stills showing A, the localization of B under irradiation with 530 nm (1 mW) and C under extended irradiation. c) Photographic stills showing how 660 nm (30 mW) light can be used to stop the transformation from A to C under constant irradiation with 530 nm (1 mW) light, locking in a bleaching front. d) Photographic stills showing how 660 nm (73 mW) light can be used to stop the transformation from A to C in a secondary glass tube (T2) under constant irradiation with 530 nm (1 mW) through a

glass tube (T1) containing already converted DASA 2 in isomer **C**. e) Irradiation of a negative photochromic three-stage photoswitch leads to a thin layer of the transient intermediate **B** as seen in a. f) Irradiation with two wavelengths can be used to stop the transformation from **A** to **C** as shown in c while a typical P-type photoswitch reverses the reaction to **A**. g) In a negative photochromic three-stage photoswitch perpendicular irradiation can be used to selectively stop the transformation from **A** to **C** through a volume filled with either **A** or **C** as shown in d while in a typical two-stage P-type photoswitch the $h\nu_2$ interacts with **B** and will get absorbed if it passes through a volume filled with sample.

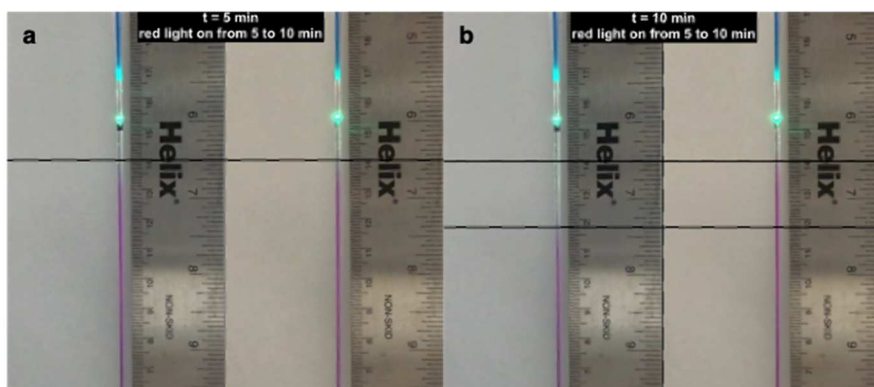


Figure 5.35. Photographic still 125 μM of DASA **2** in Toluene in a glass tube. Samples are continuously irradiated with 530 nm (1 mW). Right samples are irradiated with 660 nm (30 mW) light for 5 minutes in between screenshots. a) picture still at 5 min just before 660 nm LED is turned on for the right sample. b) picture still at 10 min just after 660 nm LED is turned off for the right sample. The left sample is continuously bleached while the photoswitching process in the right sample is interrupted through 660 nm LED.

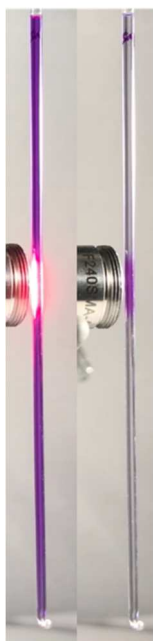


Figure 5.36. Photographic still of 250 μM of DASA **2** in Toluene in a glass tube. Samples are continuously irradiated with strong white light. 660 nm (73 mW) light is used to protect an area from bleaching. The left picture shows the sample prior to bleaching. The

right shows after the sample has bleach and the 660 nm is turned off. The area which was irradiated with 660 nm shows DASA 2 in the open form **A**.

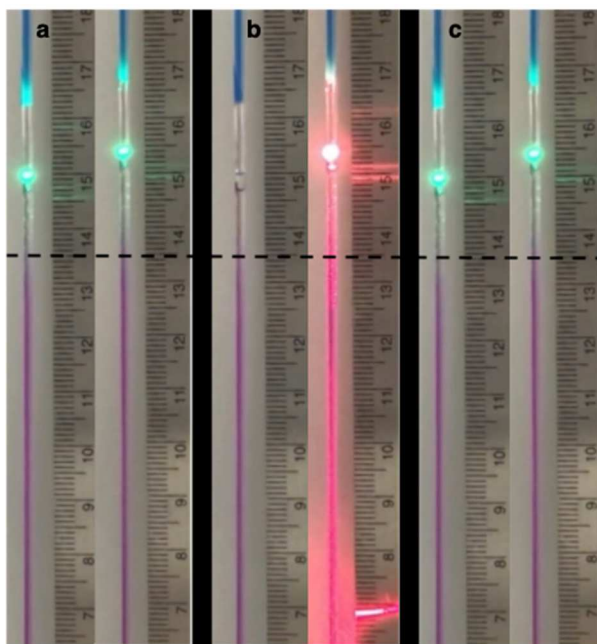


Figure 5.37. Photographic still of 125 μM of DASA 2 in Toluene in a glass tube.

Samples are irradiated with 530 nm LED (1 mW, a) and after 5 min the light is left: turned off; right: left on and a 660 nm (30 mW, coaxial) is turned on. After additional 5 minutes the 530 LED is turned back on for the sample on the left while in the right samples the 660 nm is turned off. This shows turning off the 530 nm light or irradiating with a 660 nm while irradiating the 530 nm light has similar effects.

5.5.18 Molar absorptivity

To measure the molar absorptivity for each DASA 3 different samples were prepared each diluted three times resulting in nine samples for each DASA. All samples were left to equilibrate overnight before measurement.

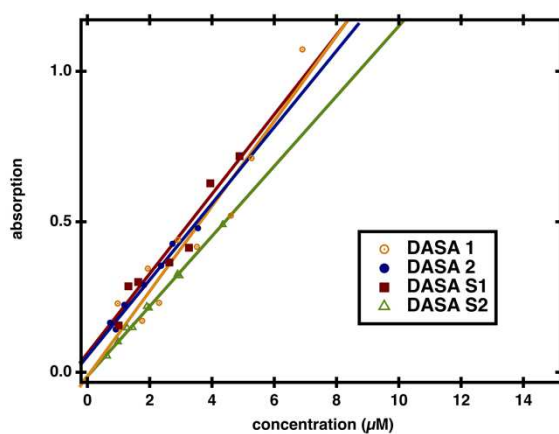


Figure 5.38. Molar absorptivity measurements for DASA 1, 2, S1 and S2. Results in Table 5.6.

5.5.19 2D NMR Spectroscopy

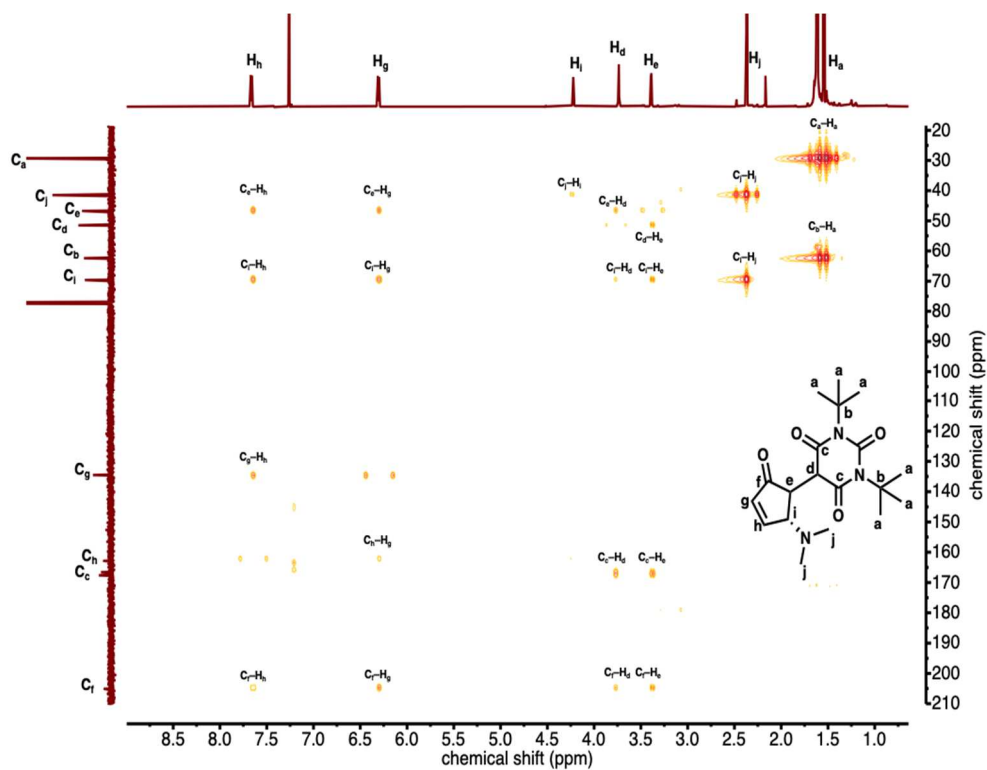


Figure 5.39. HMBC NMR (600 MHz, CDCl_3) spectra of DASA S2. Only the keto form can be observed.

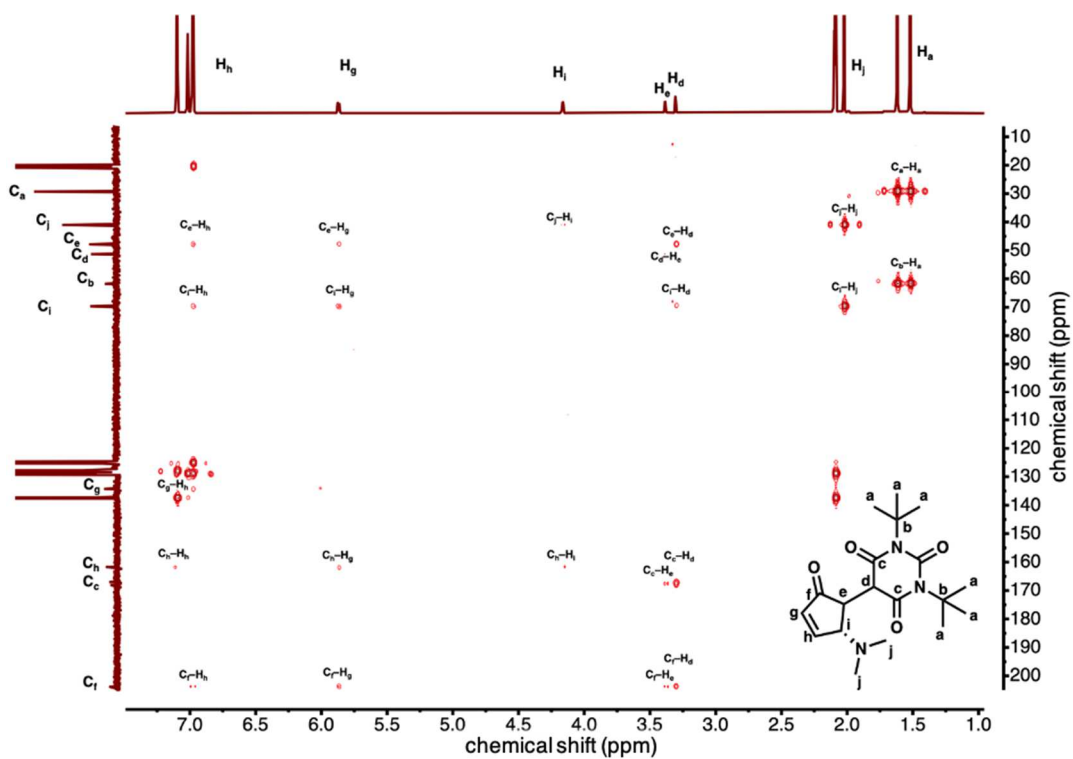


Figure 5.40. HMBC NMR (600 MHz, $\text{Tol-}d_8$) spectra of DASA S2. Only the keto form can be observed.

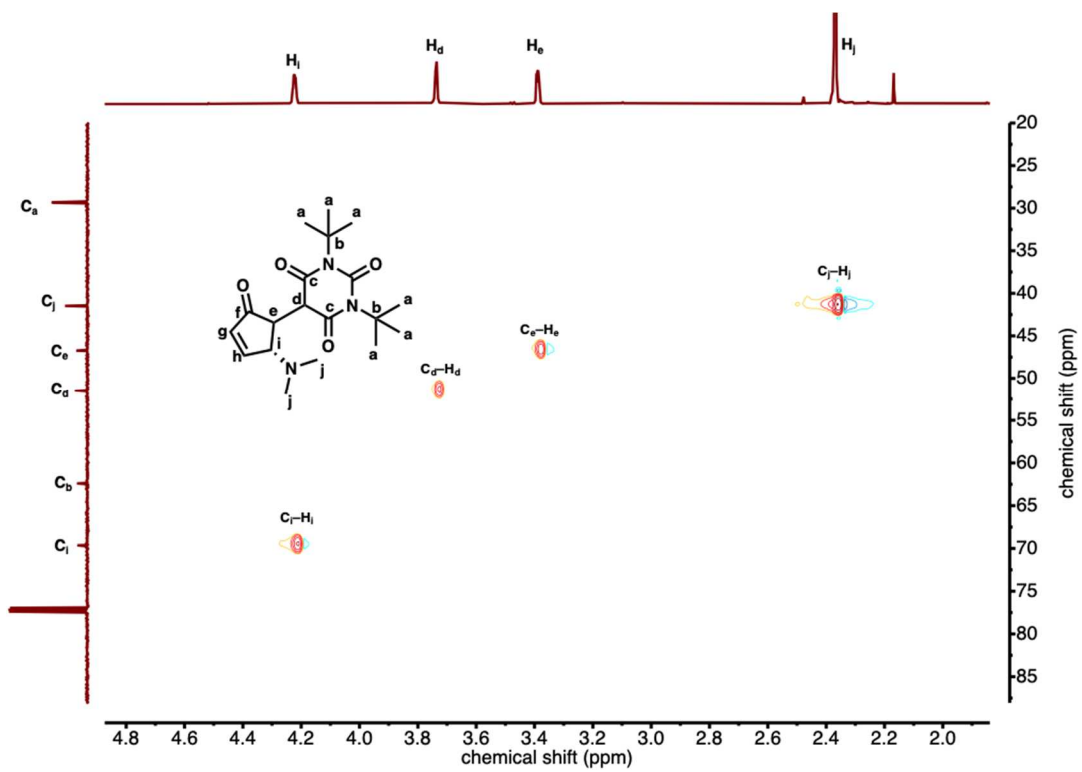


Figure 5.41. HSQC NMR (600 MHz, CHCl_3) spectra of DASA S2. Only the keto form can be observed.

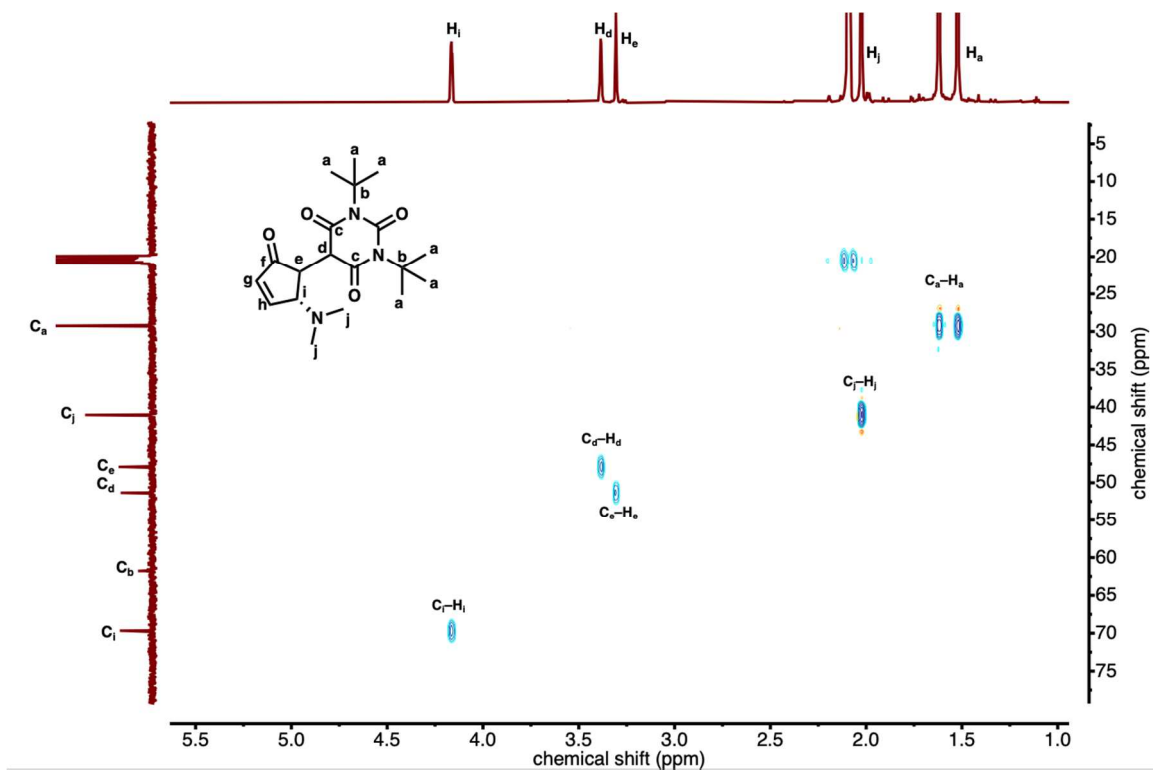


Figure 5.42. HSQC NMR (600 MHz, Tol- d_8) spectra of DASA S2. Only the keto form can be observed.

5.5.20 ^1H NMR Spectroscopy of minor isomers

The minor isomer *EZZ* is present at room temperature in CDCl_3 in **DASA 1**, **S1** and **2** at 5%, 4% and 2% respectively. While the increase in the steric demand on the donor side seems to have little to no effect on the population of the isomer, the introduction of the *t*-butyl sidechains on the acceptor seems to decrease and broaden the signals belonging to *EZZ*. This is in line with previous literature reports showing that decrease in the **DASA** conjugation decreases the population of this isomer.²¹

Minor isomers are assigned analogous to literature.²¹

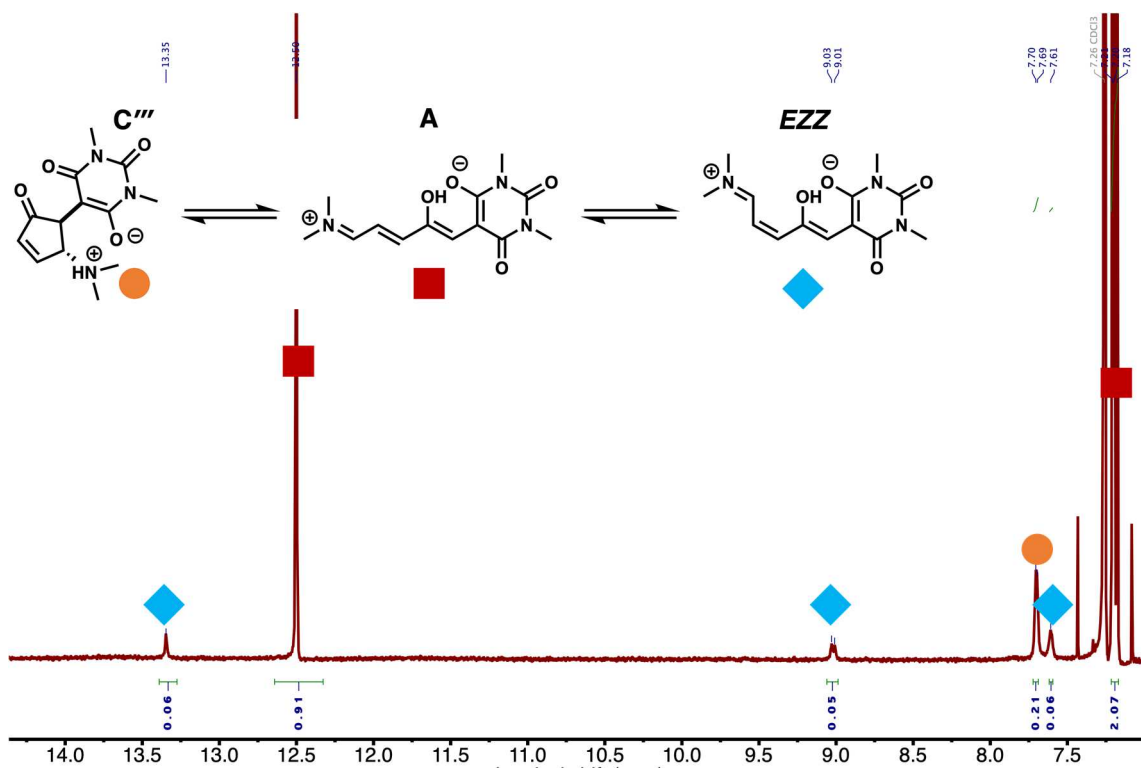


Figure 5.43. ^1H NMR (600 MHz, CDCl_3) at room temperature of **DASA 1**. The open isomer *EZZ* makes up $\sim 5\%$ of the open isomers.

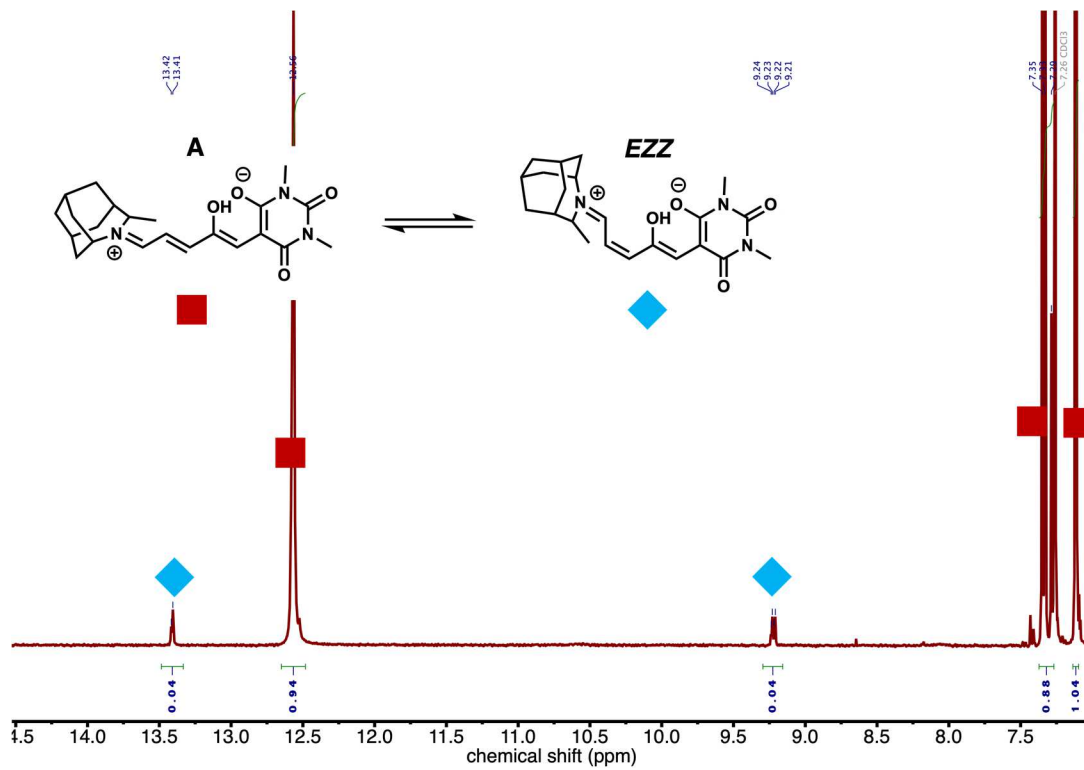


Figure 5.44. ^1H NMR (600 MHz, CDCl_3) at room temperature of DASA S1. The open isomer *EZZ* makes up $\sim 4\%$ of the open isomers.

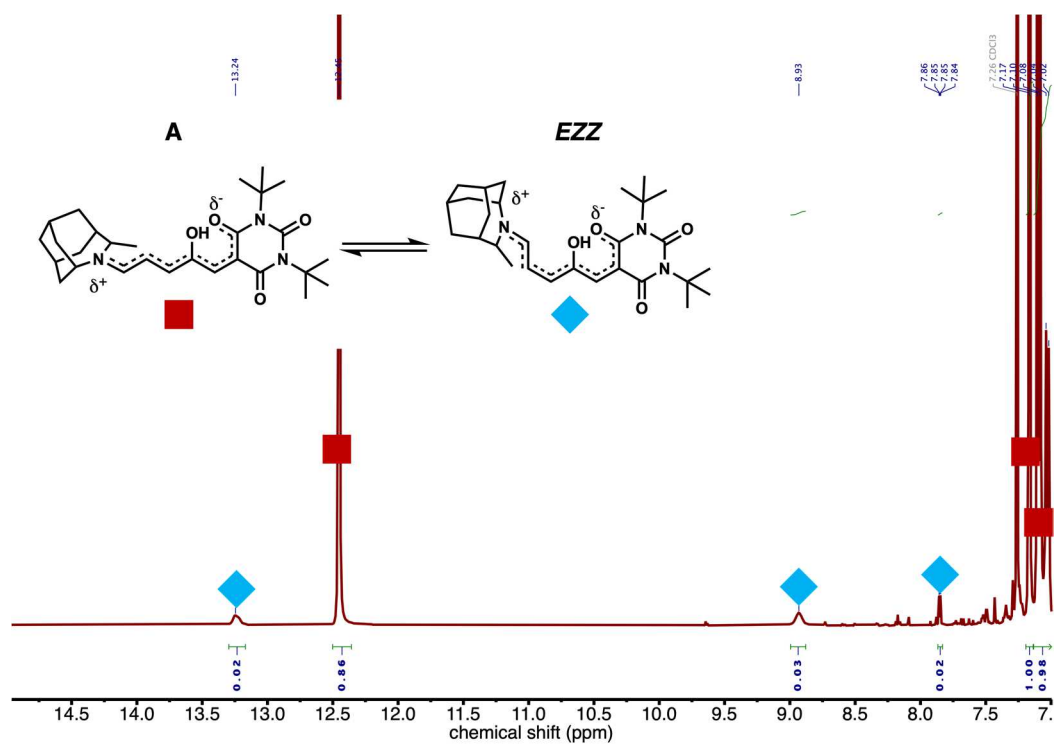


Figure 5.45. ^1H NMR (600 MHz, CDCl_3) at room temperature of DASA 2. The open isomer *EZZ* makes up $\sim 2\%$ of the open isomers.

5.5.21 NMR Spectroscopy

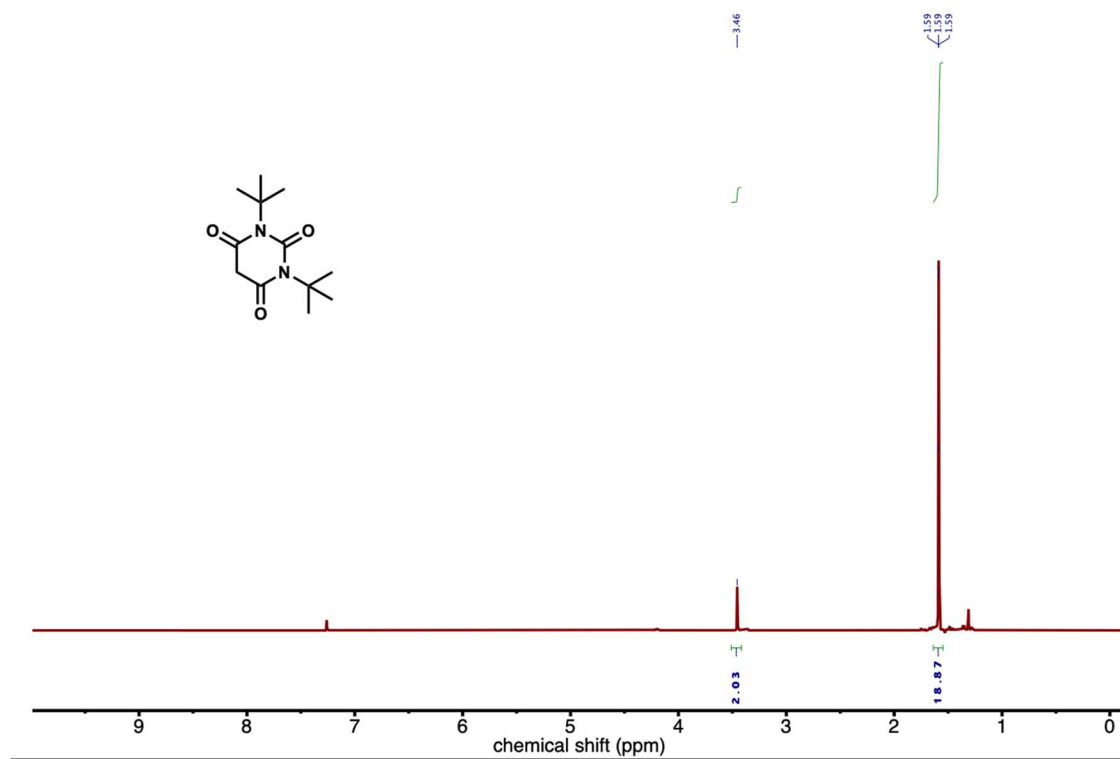


Figure 5.46. ¹H NMR (500 MHz, CDCl₃) spectra of Compound S2.

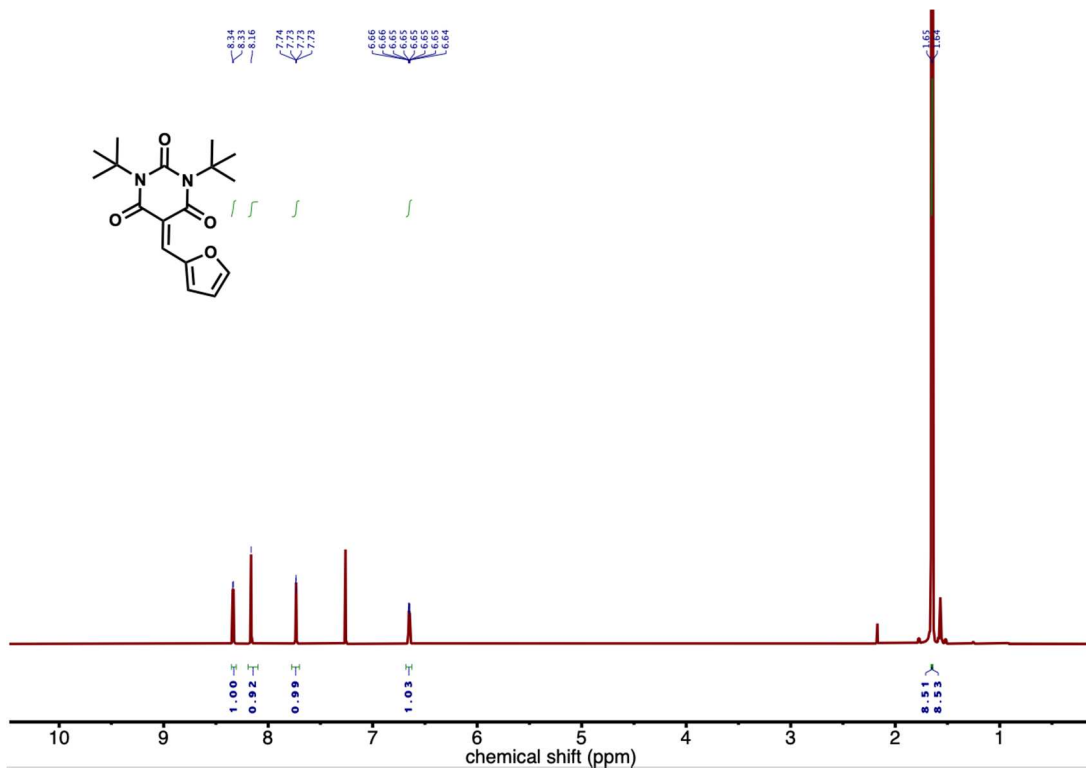


Figure 5.47. ¹H NMR (500 MHz, CDCl₃) spectra of Compound S3.

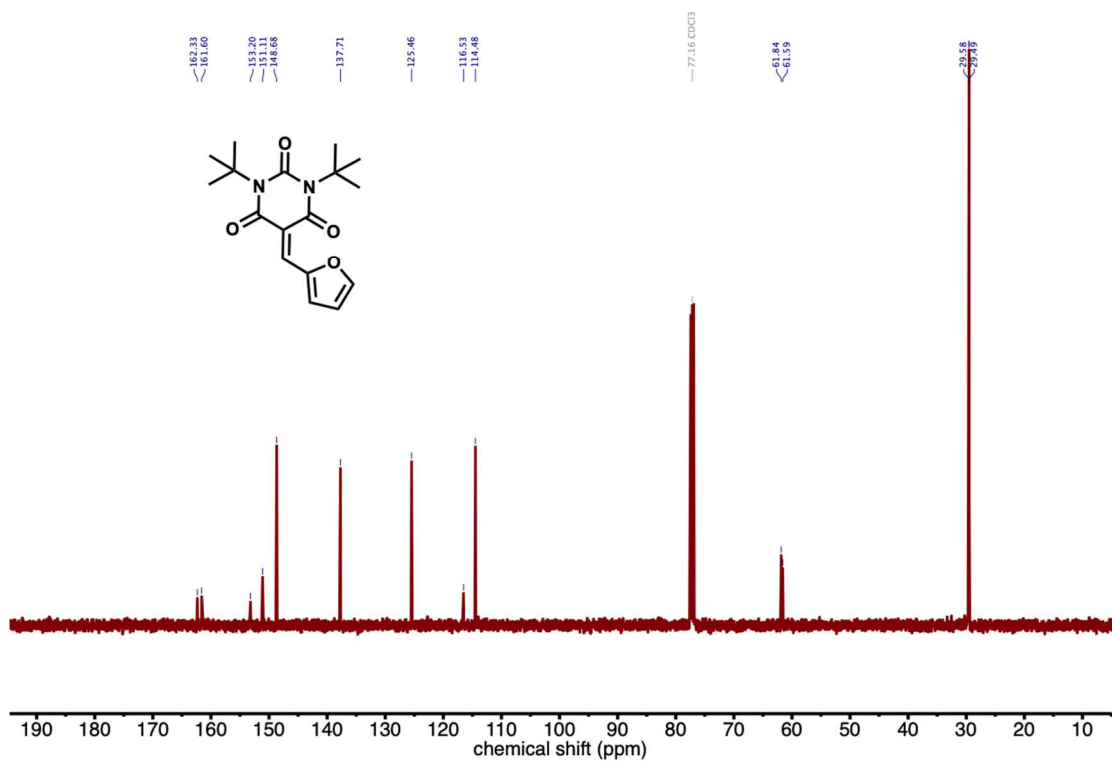


Figure 5.48. ¹³C NMR (125 MHz, CDCl₃) spectra of Compound S3.

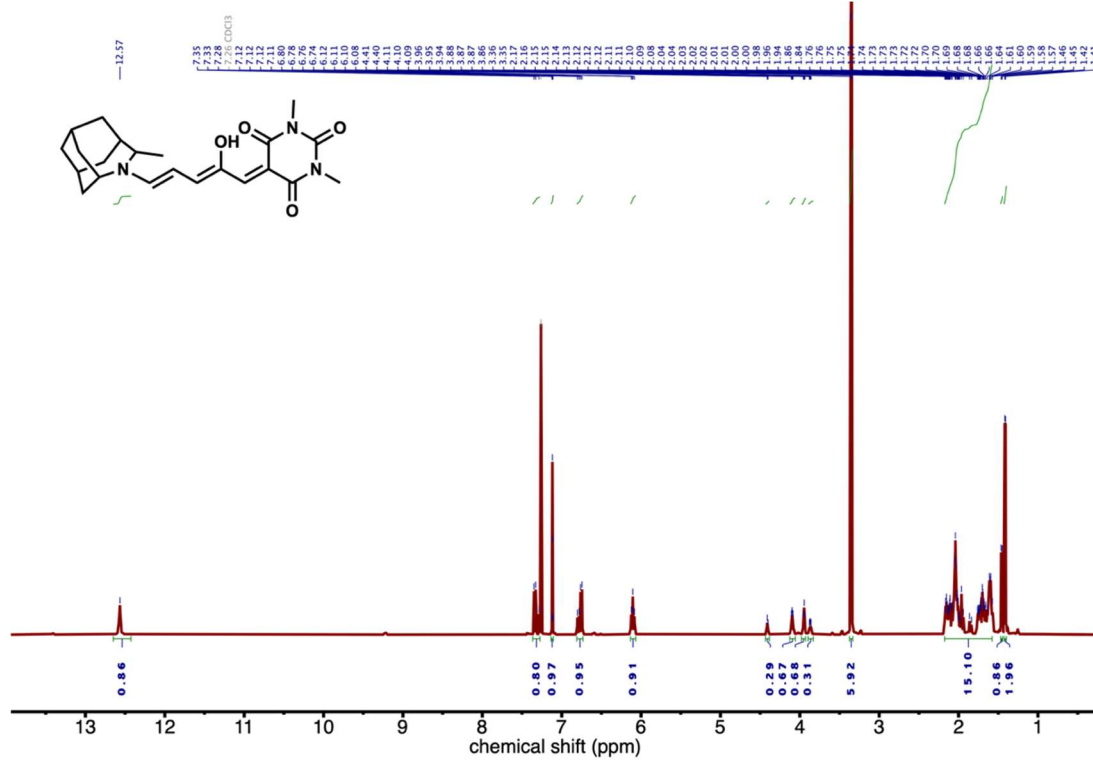


Figure 5.49. ¹H NMR (600 MHz, CDCl₃) spectra of DASA S1.

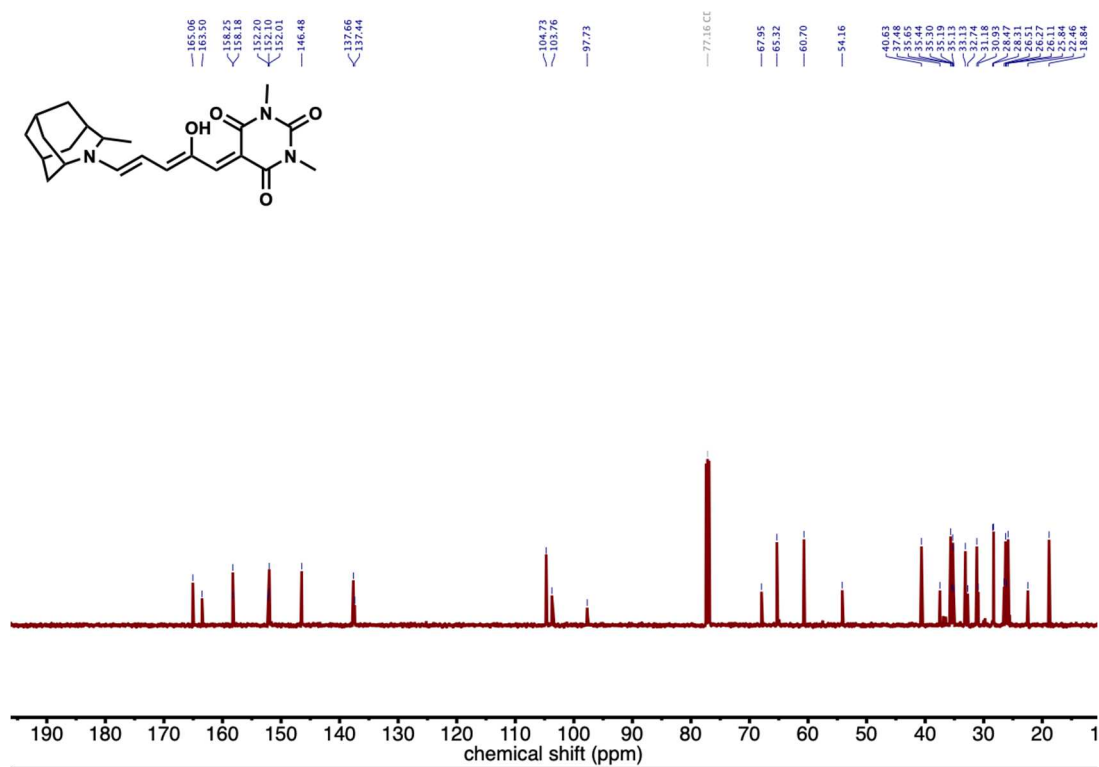


Figure 5.50. ¹³C NMR (125 MHz, CDCl₃) spectra of DASA S1.

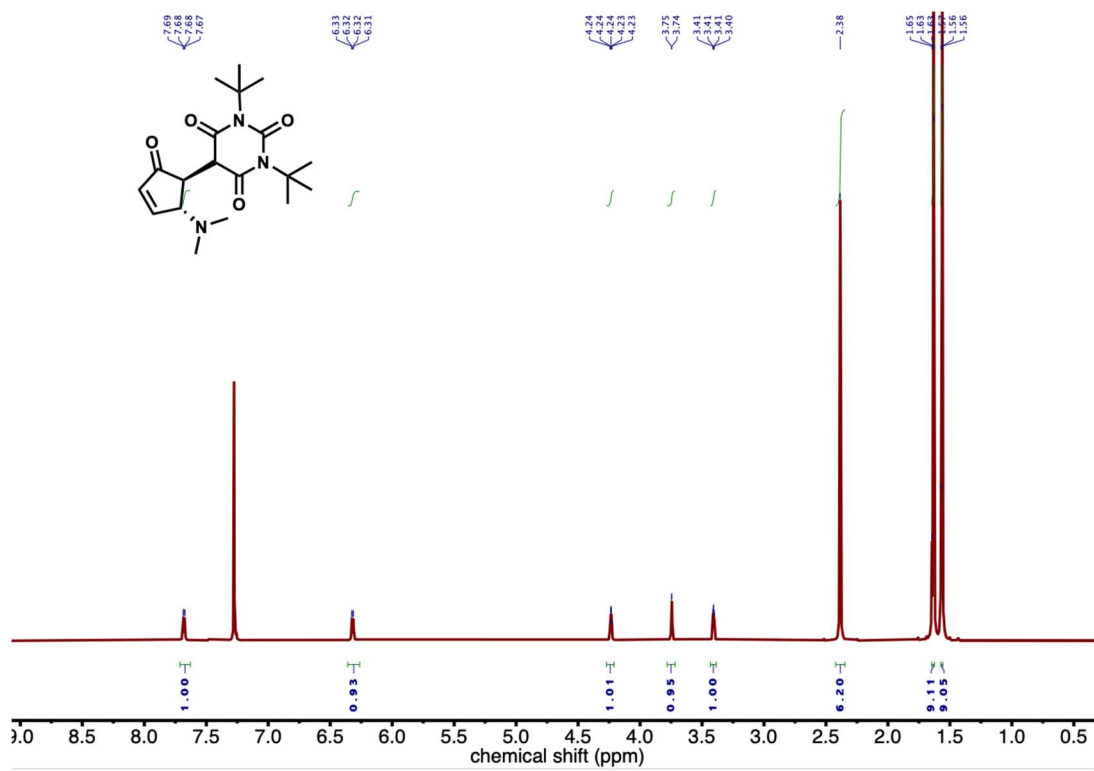


Figure 5.51. ¹H NMR (500 MHz, CDCl₃) spectra of DASA S2.

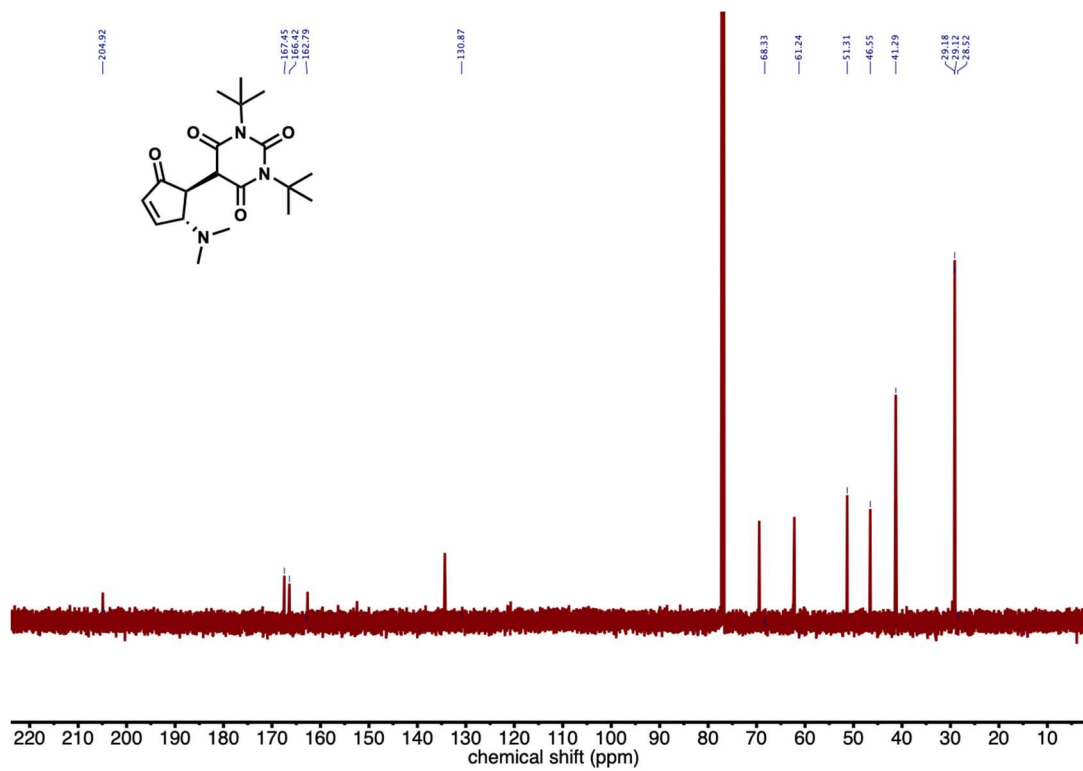


Figure 5.52. ^{13}C NMR (150 MHz, CDCl_3) spectra of DASA S2.

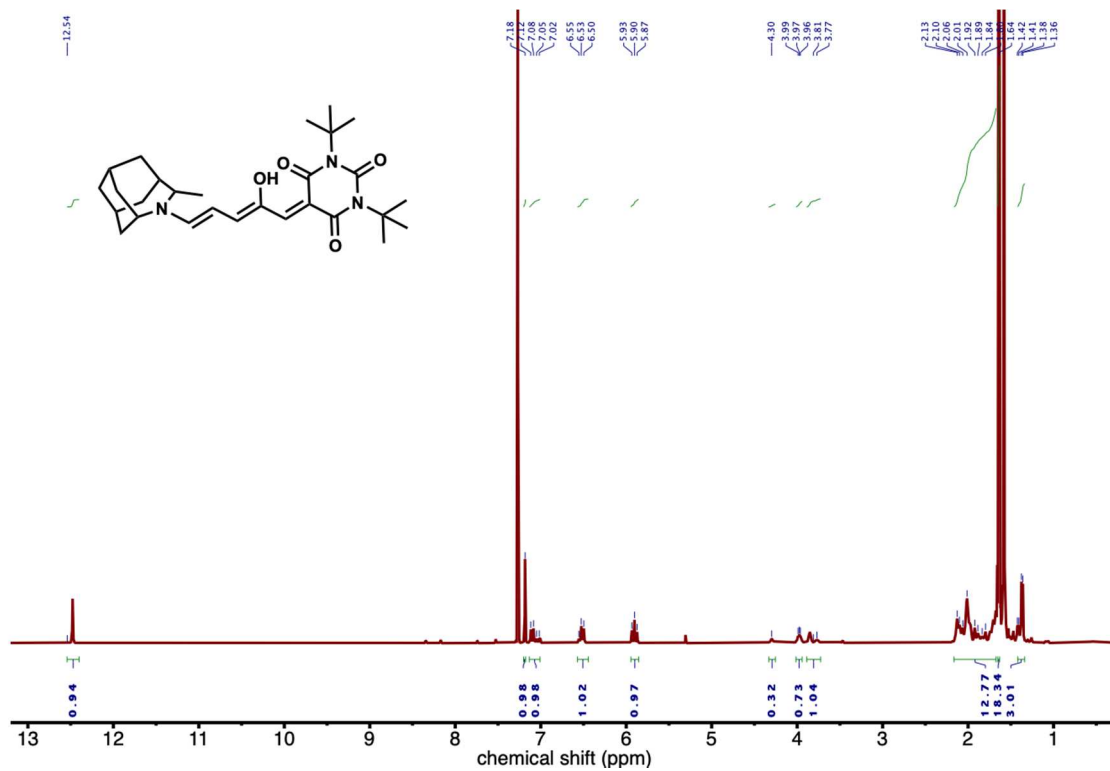


Figure 5.53. ¹H NMR (500 MHz, CDCl₃) spectra of DASA 2.

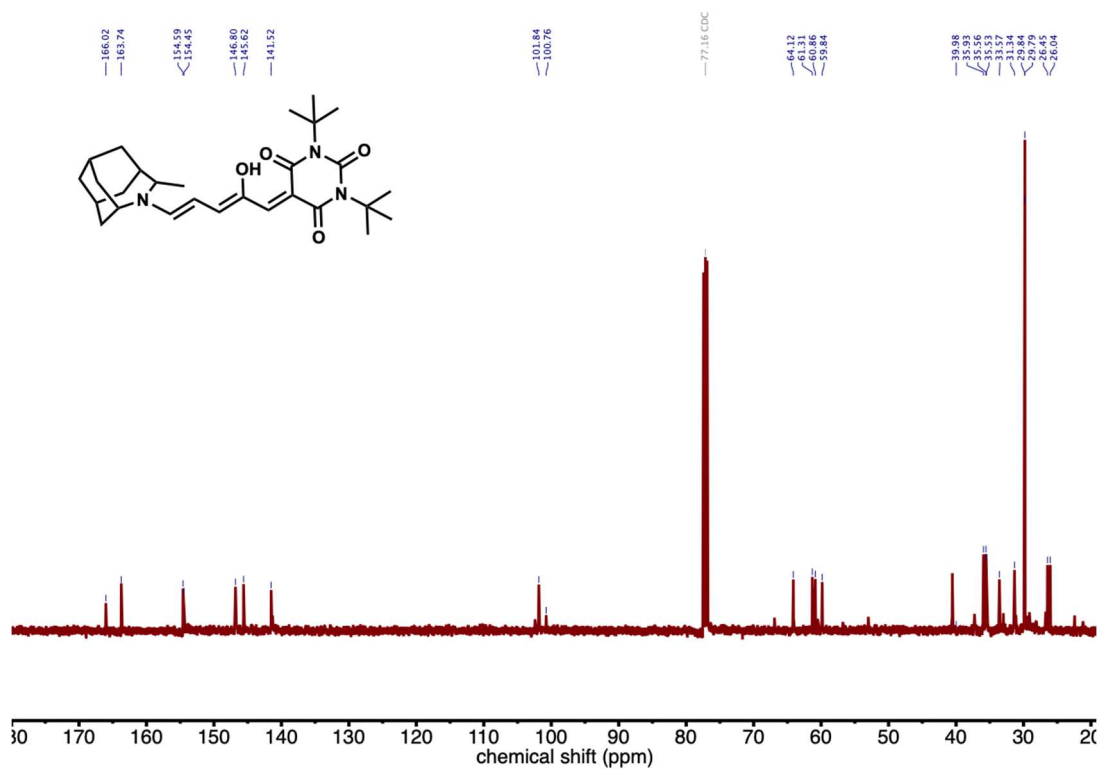


Figure 5.54. ¹³C NMR (125 MHz, CDCl₃) spectra of DASA 2.

5.5.22 Thermodynamic equilibrium

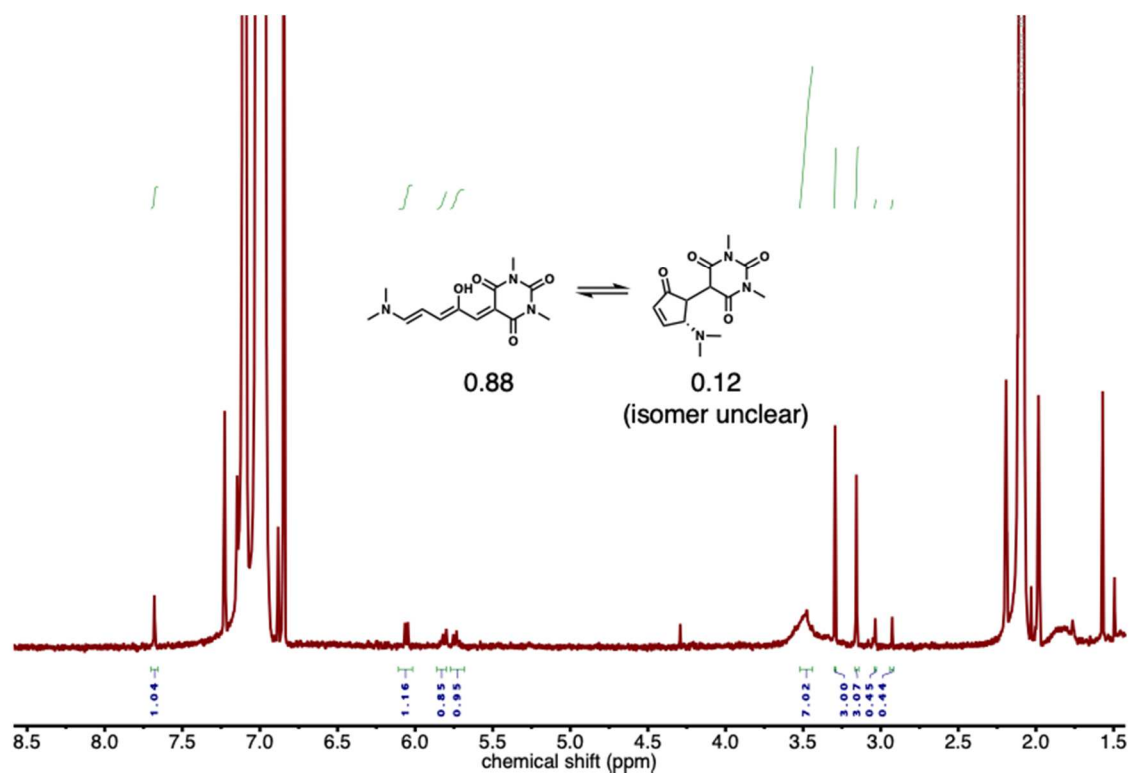


Figure 5.55. ¹H NMR (600 MHz, Tol-*d*₈) spectra of DASA 1 after 24h equilibration.

Solubility is limited in Toluene and the closed form isomer cannot be clearly identified.

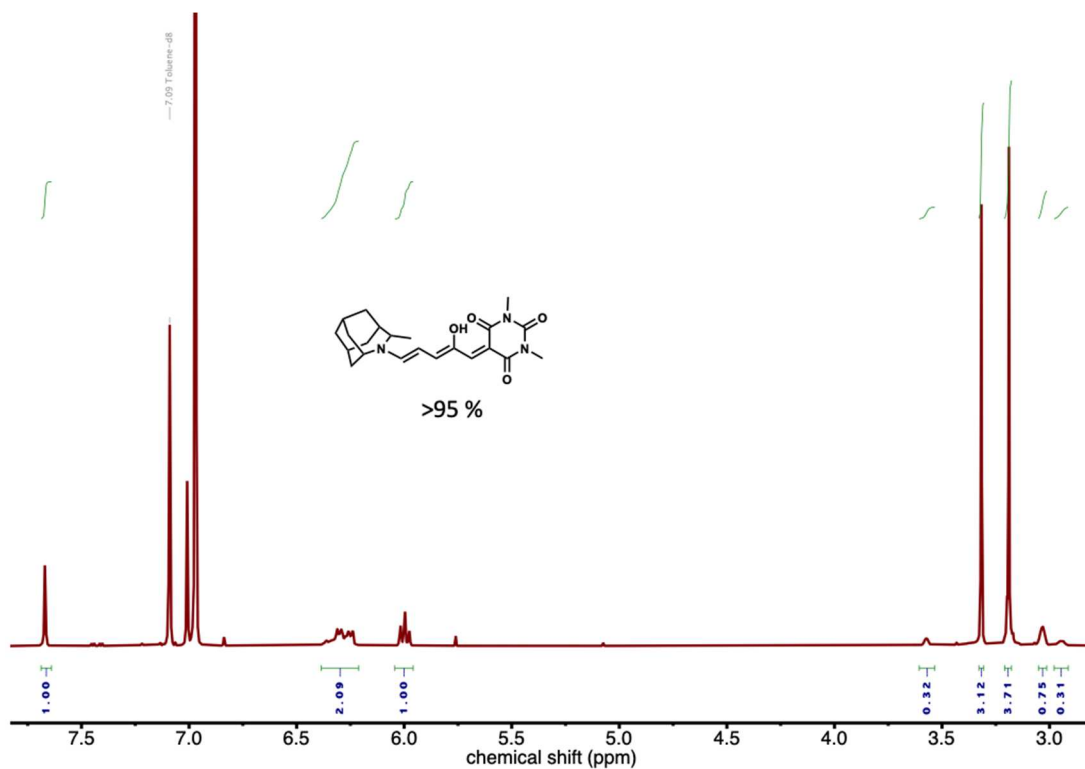


Figure 5.56. ^1H NMR (600 MHz, $\text{Tol}-d_8$) spectra of DASA S1 after 24h equilibration.

Only open form can be observed.

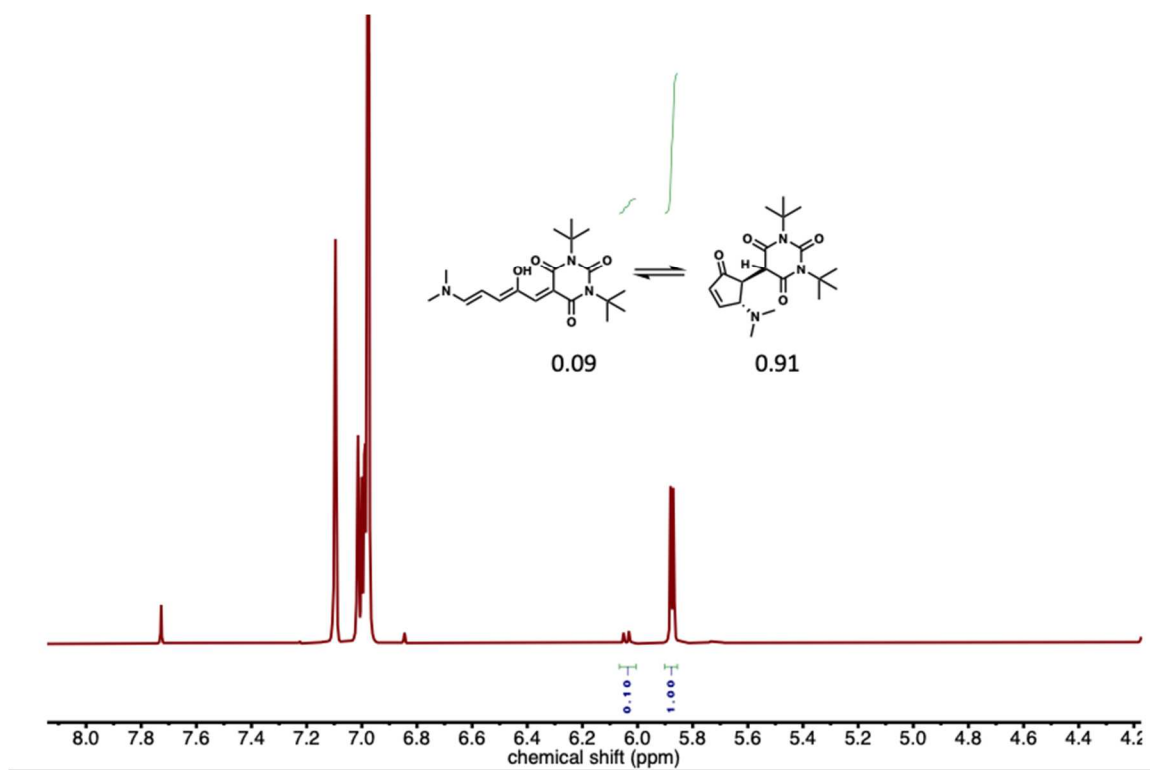


Figure 5.57. ^1H NMR (600 MHz, $\text{Tol-}d_8$) spectra of DASA S2 after 24h equilibration.

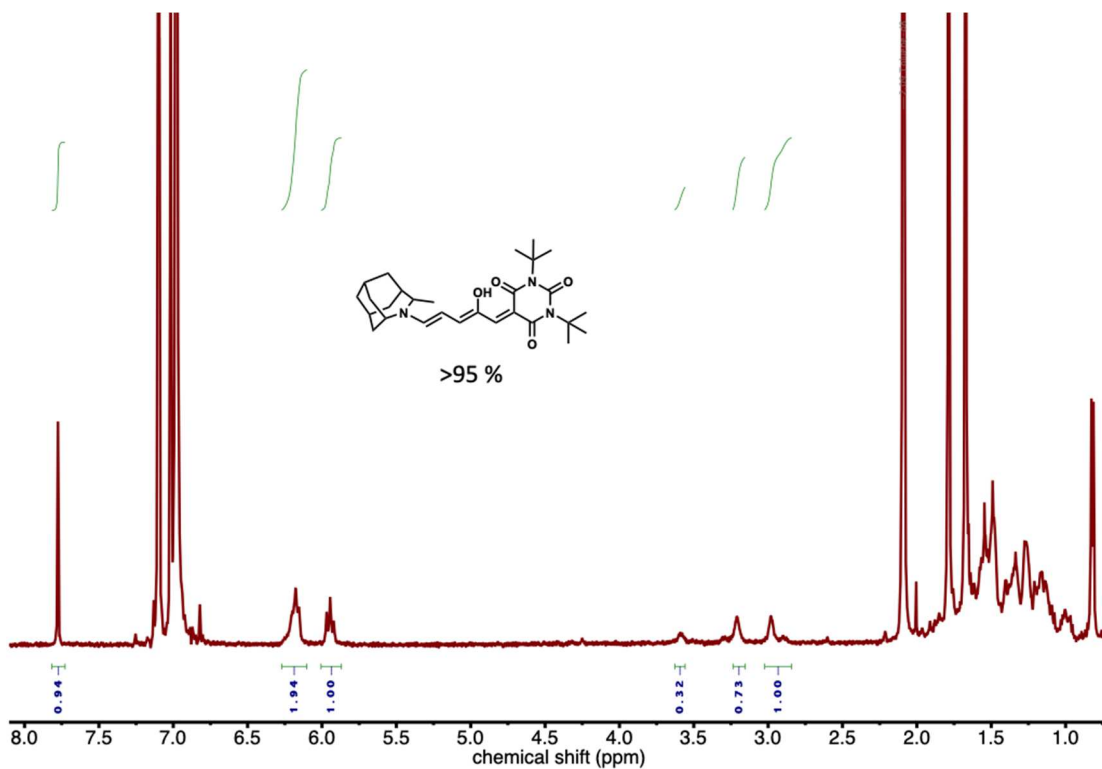


Figure 5.58. ^1H NMR (600 MHz, CDCl_3) spectra of DASA 2 after 24h equilibration.

Only open form can be observed.

5.6 References

- (1) Stricker, F., Sanchez, D. M., Raucci, U., Dolinski, N. D., Zayas, M. S., Meisner, J., Hawker, C. J., Martinez, T. J., Read de Alaniz, J., *Nature Chemistry*, **2022**, <https://doi.org/10.1038/s41557-022-00947-8>.
- (2) Feringa, B. L., Browne, W. R. *Molecular Switches*, Feringa, B. L., Browne, W. R., Eds., Wiley-VCH Verlag GmbH & Co. KGaA: Weinheim, Germany, 2011, Vol. 1. <https://doi.org/10.1002/9783527634408>.
- (3) Iamsaard, S., Aßhoff, S. J., Matt, B., Kudernac, T., Cornelissen, J. J. L. M., Fletcher, S. P., Katsonis, N. Conversion of Light into Macroscopic Helical Motion. *Nat. Chem.* **2014**, *6* (3), 229–235. <https://doi.org/10.1038/nchem.1859>.
- (4) Li, J., Zhou, X., Liu, Z. Recent Advances in Photoactuators and Their Applications in Intelligent Bionic Movements. *Adv. Opt. Mater.* **2020**, *8*, 2000886. <https://doi.org/10.1002/adom.202000886>.
- (5) Soberats, B., Uchida, E., Yoshio, M., Kagimoto, J., Ohno, H., Kato, T. Macroscopic Photocontrol of Ion-Transporting Pathways of a Nanostructured Imidazolium-Based Photoresponsive Liquid Crystal. *J. Am. Chem. Soc.* **2014**, *136* (27), 9552–9555. <https://doi.org/10.1021/ja5041573>.
- (6) Nie, H., Schausser, N. S., Dolinski, N. D., Hu, J., Hawker, C. J., Segalman, R. A., Read de Alaniz, J. Light-Controllable Ionic Conductivity in a Polymeric Ionic Liquid. *Angew. Chemie - Int. Ed.* **2020**, *59* (13), 5123–5128. <https://doi.org/10.1002/anie.201912921>.
- (7) Qiu, Q., Shi, Y., Han, G. G. D. Solar Energy Conversion and Storage by Photoswitchable Organic Materials in Solution, Liquid, Solid, and Changing Phases. *J. Mater. Chem. C* **2021**, *9* (35), 11444–11463. <https://doi.org/10.1039/D1TC01472B>.
- (8) Goulet-Hanssens, A., Eisenreich, F., Hecht, S. Enlightening Materials with Photoswitches. *Adv. Mater.* **2020**, *32*, 1905966. <https://doi.org/10.1002/adma.201905966>.
- (9) Browne, W. R., Feringa, B. L. Making Molecular Machines Work. *Nat. Nanotechnol.* **2006**, *1*, 25–35. https://doi.org/10.1142/9789814287005_0009.
- (10) Bandara, H. M. D., Burdette, S. C. Photoisomerization in Different Classes of Azobenzene. *Chem. Soc. Rev.* **2012**, *41* (5), 1809–1825.

- <https://doi.org/10.1039/c1cs15179g>.
- (11) Su, X., Aprahamian, I. Hydrazone-Based Switches, Metallo-Assemblies and Sensors. *Chem. Soc. Rev.* **2014**, *43* (6), 1963–1981. <https://doi.org/10.1039/c3cs60385g>.
- (12) Irie, M. Diarylethenes for Memories and Switches. *Chem. Rev.* **2000**, *100* (5), 1685–1716. <https://doi.org/10.1021/cr980069d>.
- (13) Irie, M., Fukaminato, T., Matsuda, K., Kobatake, S. Photochromism of Diarylethene Molecules and Crystals: Memories, Switches, and Actuators. *Chem. Rev.* **2014**, *114* (24), 12174–12277. <https://doi.org/10.1021/cr500249p>.
- (14) Minkin, V. I. Photo-, Thermo-, Solvato-, and Electrochromic Spiroheterocyclic Compounds. *Chem. Rev.* **2004**, *104* (5), 2751–2776. <https://doi.org/10.1021/cr020088u>.
- (15) Daub, J., Knöchel, T., Mannschreck, A. Photosensitive Dihydroazulenes with Chromogenic Properties. *Angew. Chemie Int. Ed. English* **1984**, *23* (12), 960–961. <https://doi.org/10.1002/anie.198409601>.
- (16) Bouas-Laurent, H., Dürr, H. Organic Photochromism. *Pure Appl. Chem.* **2001**, *73* (4), 639–665. <https://doi.org/10.1351/pac200173040639>.
- (17) Mrozek, T., Görner, H., Daub, J. Towards Multifold Cycloswitching of Biphotochromes: Investigation on a Bond-Fused Dihydroazulene/Vinylheptafulvene and Dithienylethene/Dihydrothienobenzothiophene. *Chem. Commun.* **1999**, 1487–1488.
- (18) Fihey, A., Perrier, A., Browne, W. R., Jacquemin, D. Multiphotochromic Molecular Systems. *Chem. Soc. Rev.* **2015**, *44* (11), 3719–3759. <https://doi.org/10.1039/c5cs00137d>.
- (19) Nie, H., Self, J. L., Kuenstler, A. S., Hayward, R. C., Read de Alaniz, J. Multiaddressable Photochromic Architectures: From Molecules to Materials. *Adv. Opt. Mater.* **2019**, *7*, 1900224. <https://doi.org/10.1002/adom.201900224>.
- (20) Perrier, A., Maurel, F., Jacquemin, D. Single Molecule Multiphotochromism with Diarylethenes. *Acc. Chem. Res.* **2012**, *45* (8), 1173–1182. <https://doi.org/10.1021/ar200214k>.
- (21) Andréasson, J., Pischel, U. Light-Stimulated Molecular and Supramolecular Systems for Information Processing and Beyond. *Coord. Chem. Rev.* **2021**, *429*, 213695.

- <https://doi.org/10.1016/j.ccr.2020.213695>.
- (22) Zulfikri, H., Koenis, M. A. J., Lerch, M. M., Di Donato, M., Szymański, W., Filippi, C., Feringa, B. L., Buma, W. J., Taming the Complexity of Donor–Acceptor Stenhouse Adducts: Infrared Motion Pictures of the Complete Switching Pathway. *J. Am. Chem. Soc.* **2019**, *141* (18), 7376–7384. <https://doi.org/10.1021/jacs.9b00341>.
- (23) Mallo, N., Tron, A., Andréasson, J., Harper, J. B., Jacob, L. S. D., McClenaghan, N. D., Jonusauskas, G., Beves, J. E. Hydrogen-Bonding Donor-Acceptor Stenhouse Adducts. *ChemPhotoChem* **2020**, *4* (6), 407–412. <https://doi.org/10.1002/cptc.201900295>.
- (24) Lerch, M. M., Szymański, W., Feringa, B. L. The (Photo)Chemistry of Stenhouse Photoswitches: Guiding Principles and System Design. *Chem. Soc. Rev.* **2018**, *47* (6), 1910–1937. <https://doi.org/10.1039/c7cs00772h>.
- (25) Helmy, S., Leibfarth, F. A., Oh, S., Poelma, J. E., Hawker, C. J., Read de Alaniz, J. Photoswitching Using Visible Light: A New Class of Organic Photochromic Molecules. *J. Am. Chem. Soc.* **2014**, *136* (23), 8169–8172. <https://doi.org/10.1021/ja503016b>.
- (26) Mallo, N., Brown, P. T., Iranmanesh, H., MacDonald, T. S. C., Teusner, M. J., Harper, J. B., Ball, G. E., Beves, J. E. Photochromic Switching Behaviour of Donor-Acceptor Stenhouse Adducts in Organic Solvents. *Chem. Commun.* **2016**, *52* (93), 13576–13579. <https://doi.org/10.1039/C6CC08079K>.
- (27) Lerch, M. M., Wezenberg, S. J., Szymanski, W., Feringa, B. L. Unraveling the Photoswitching Mechanism in Donor–Acceptor Stenhouse Adducts. *J. Am. Chem. Soc.* **2016**, *138* (20), 6344–6347. <https://doi.org/10.1021/jacs.6b01722>.
- (28) Lerch, M. M., Medved, M., Lapini, A., Laurent, A. D., Iagatti, A., Bussotti, L., Szymański, W., Buma, W. J., Foggi, P., Di Donato, M., Feringa, B. L., Tailoring Photoisomerization Pathways in Donor–Acceptor Stenhouse Adducts: The Role of the Hydroxy Group. *J. Phys. Chem. A* **2018**, *122* (4), 955–964. <https://doi.org/10.1021/acs.jpca.7b10255>.
- (29) Hemmer, J. R., Page, Z. A., Clark, K. D., Stricker, F., Dolinski, N. D., Hawker, C. J., Read de Alaniz, J. Controlling Dark Equilibria and Enhancing Donor-Acceptor Stenhouse Adduct Photoswitching Properties through Carbon Acid Design. *J. Am.*

- Chem. Soc.* **2018**, *140* (33), 10425–10429. <https://doi.org/10.1021/jacs.8b06067>.
- (30) Hemmer, J. R., Poelma, S. O., Treat, N., Page, Z. A., Dolinski, N. D., Diaz, Y. J., Tomlinson, W., Clark, K. D., Hooper, J. P., Hawker, C., Read de Alaniz, J., Tunable Visible and Near Infrared Photoswitches. *J. Am. Chem. Soc.* **2016**, *138* (42), 13960–13966. <https://doi.org/10.1021/jacs.6b07434>.
- (31) Lerch, M. M., Hansen, M. J., Velema, W. A., Szymanski, W., Feringa, B. L. Orthogonal Photoswitching in a Multifunctional Molecular System. *Nat. Commun.* **2016**, *7*, 12054. <https://doi.org/10.1038/ncomms12054>.
- (32) Di Donato, M., Lerch, M. M., Lapini, A., Laurent, A. D., Iagatti, A., Bussotti, L., Ihrig, S. P., Medved, M., Jacquemin, D., Szymański, W., Feringa, B. L., Shedding Light on the Photoisomerization Pathway of Donor-Acceptor Stenhouse Adducts. *J. Am. Chem. Soc.* **2017**, *139* (44), 15596–15599. <https://doi.org/10.1021/jacs.7b09081>.
- (33) Lerch, M. M., Di Donato, M., Laurent, A. D., Medved, M., Iagatti, A., Bussotti, L., Lapini, A., Buma, W. J., Foggi, P., Szymański, W., Feringa, B. L., Solvent Effects on the Actinic Step of Donor–Acceptor Stenhouse Adduct Photoswitching. *Angew. Chemie Int. Ed.* **2018**, *57* (27), 8063–8068. <https://doi.org/10.1002/anie.201803058>.
- (34) Laurent, A. D., Medved, M., Jacquemin, D. Using Time-Dependent Density Functional Theory to Probe the Nature of Donor–Acceptor Stenhouse Adduct Photochromes. *ChemPhysChem* **2016**, *17*, 1846–1851. <https://doi.org/10.1002/cphc.201600041>.
- (35) Sanchez, D. M., Raucci, U., Ferreras, K. N., Martínez, T. J. Putting Photomechanical Switches to Work: An Ab Initio Multiple Spawning Study of Donor-Acceptor Stenhouse Adducts. *J. Phys. Chem. Lett.* **2020**, *11* (18), 7901–7907. <https://doi.org/10.1021/acs.jpcllett.0c02401>.
- (36) Mallo, N., Foley, E. D., Iranmanesh, H., Kennedy, A. D. W., Luis, E. T., Ho, J., Harper, J. B., Beves, J. E. Structure-Function Relationships of Donor-Acceptor Stenhouse Adduct Photochromic Switches. *Chem. Sci.* **2018**, *9* (43), 8242–8252. <https://doi.org/10.1039/c8sc03218a>.
- (37) Clerc, M., Stricker, F., Ulrich, S., Sroda, M., Bruns, N., Boesel, L. F., Read de Alaniz, J. Promoting the Furan Ring Opening Reaction to Access New Donor–Acceptor Stenhouse Adducts with Hexafluoroisopropanol. *Angew. Chemie Int. Ed.* **2021**, *60*

- (18), 10219–10227. <https://doi.org/10.1002/anie.202100115>.
- (38) García-Iriepa, C., Marazzi, M., Sampedro, D. From Light Absorption to Cyclization: Structure and Solvent Effects in Donor-Acceptor Stenhouse Adducts. *ChemPhotoChem* **2019**, *3* (9), 866–873. <https://doi.org/10.1002/cptc.201900102>.
- (39) García-Iriepa, C., Marazzi, M. Level of Theory and Solvent Effects on DASA Absorption Properties Prediction: Comparing TD-DFT, CASPT2 and NEVPT2. *Materials (Basel)*. **2017**, *10*, 1025. <https://doi.org/10.3390/ma10091025>.
- (40) Berraud-Pache, R., Santamaría-Aranda, E., de Souza, B., Bistoni, G., Neese, F., Sampedro, D., Izsák, R. Redesigning Donor-Acceptor Stenhouse Adduct Photoswitches through a Joint Experimental and Computational Study. *Chem. Sci.* **2021**, *12* (8), 2916–2924. <https://doi.org/10.1039/d0sc06575g>.
- (41) Sroda, M. M., Stricker, F., Peterson, J. A., Bernal, A., Read de Alaniz, J. Donor–Acceptor Stenhouse Adducts: Exploring the Effects of Ionic Character. *Chem. - A Eur. J.* **2020**, *27* (12), 4183–4190. <https://doi.org/10.1002/chem.202005110>.
- (42) Sanchez, D. M., Raucci, U., Martínez, T. J. In Silico Discovery of Multistep Chemistry Initiated by a Conical Intersection: The Challenging Case of Donor–Acceptor Stenhouse Adducts. *J. Am. Chem. Soc.* **2021**, *143* (48), 20015–20021. <https://doi.org/10.1021/jacs.1c06648>.
- (43) Stranius, K., Börjesson, K. Determining the Photoisomerization Quantum Yield of Photoswitchable Molecules in Solution and in the Solid State. *Sci. Rep.* **2017**, *7* (January), 41145. <https://doi.org/10.1038/srep41145>.
- (44) Terrones, G., Pearlstein, A. J. Effects of Optical Attenuation and Consumption of a Photobleaching Initiator on Local Initiation Rates in Photopolymerizations. *Macromolecules* **2001**, *34* (10), 3195–3204. <https://doi.org/10.1021/ma001235y>.
- (45) Dolinski, N. D., Page, Z. A., Eisenreich, F., Niu, J., Hecht, S., Read de Alaniz, J., Hawker, C. J. A Versatile Approach for In Situ Monitoring of Photoswitches and Photopolymerizations. *ChemPhotoChem* **2017**, *1* (4), 125–131. <https://doi.org/10.1002/cptc.201600045>.
- (46) Dolinski, N. D., Page, Z. A., Callaway, E. B., Eisenreich, F., Garcia, R. V., Chavez, R., Bothman, D. P., Hecht, S., Zok, F. W., Hawker, C. J. Solution Mask Liquid Lithography (SMaLL) for One-Step, Multimaterial 3D Printing. *Adv. Mater.* **2018**, *30*

- (31), 1800364. <https://doi.org/10.1002/adma.201800364>.
- (47) Hohenstein, E. G., Luehr, N., Ufimtsev, I. S., Martínez, T. J. An Atomic Orbital-Based Formulation of the Complete Active Space Self-Consistent Field Method on Graphical Processing Units. *J. Chem. Phys.* **2015**, *142*, 224103. <https://doi.org/10.1063/1.4921956>.
- (48) Snyder, J. W., Curchod, B. F. E., Martínez, T. J. GPU-Accelerated State-Averaged Complete Active Space Self-Consistent Field Interfaced with Ab Initio Multiple Spawning Unravels the Photodynamics of Provitamin D3. *J. Phys. Chem. Lett.* **2016**, *7* (13), 2444–2449. <https://doi.org/10.1021/acs.jpcclett.6b00970>.
- (49) Snyder, J. W., Fales, B. S., Hohenstein, E. G., Levine, B. G., Martínez, T. J. A Direct-Compatible Formulation of the Coupled Perturbed Complete Active Space Self-Consistent Field Equations on Graphical Processing Units. *J. Chem. Phys.* **2017**, *146*, 174113. <https://doi.org/10.1063/1.4979844>.
- (50) Ufimtsev, I. S., Martinez, T. J. Strategies for Two-Electron Integral Evaluation. *J. Chem. Theory Comput.* **2008**, *4*, 222–231.
- (51) Ufimtsev, I. S., Martinez, T. J. Quantum Chemistry on Graphical Processing Units. 2. Direct Self-Consistent-Field Implementation. *J. Chem. Theory Comput.* **2009**, *5* (4), 1004–1015. <https://doi.org/10.1021/ct800526s>.
- (52) Ufimtsev, I. S., Martinez, T. J. Quantum Chemistry on Graphical Processing Units. 3. Analytical Energy Gradients, Geometry Optimization, and First Principles Molecular Dynamics. *J. Chem. Theory Comput.* **2009**, *5* (10), 2619–2628. <https://doi.org/10.1021/ct9003004>.
- (53) Kästner, J., Carr, J. M., Keal, T. W., Thiel, W., Wander, A., Sherwood, P. DL-FIND: An Open-Source Geometry Optimizer for Atomistic Simulations. *J. Phys. Chem. A* **2009**, *113* (43), 11856–11865. <https://doi.org/10.1021/jp9028968>.
- (54) Henkelman, G., Jónsson, H. A Dimer Method for Finding Saddle Points on High Dimensional Potential Surfaces Using Only First Derivatives. *J. Chem. Phys.* **1999**, *111* (15), 7010–7022. <https://doi.org/10.1063/1.480097>.
- (55) ChemShell, a Computational Chemistry Shell, See [Www.Chemshell.Org](http://www.chemshell.org).
- (56) Patel, D. G., Paquette, M. M., Kopelman, R. A., Kaminsky, W., Ferguson, M. J., Frank, N. L., A solution- and solid-state investigation of Medium Effects on Charge

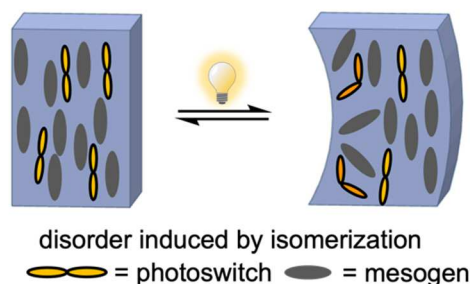
- Separation in Metastable Photomerocyanines, *J. Am. Chem. Soc.*, **2010**, *132*, 12568–12586. <https://doi.org/10.1021/ja100238h>
- (57) Werner, H. J., Knowles, P. J., Knizia, G., Manby, F. R., Schuetz, M., Celani, P., Gyoerffy, W., Kats, D., Korona, T., Lindh, R., Mitrushenkov, A., Rauhut, G., Shamasundar, K. R., Adler, T. B., Amos, R. D., Bennie, S. J., Bernhardsson, A., Berning, A., Cooper, D. K., Deegan, M. J. O., Dobbyn, A. J., Eckert, F., Goll, E., Hampel, C., Hesselmann, A., Hetzer, G., Hrenar, T., Jansen, G., Koepl, C., Lee, S. J. R., Liu, Y., Lloyd, A. W., Ma, Q., Mata, R. A., May, J., McNicholas, S. J., Meyer, W., Miller III, T. F., Mura, M. E., Nicklass, A., O'Neill, D. P., Palmieri, P., Peng, D., Petrenko, T., Pflueger, K., Pitzer, R., Reiher, M., Shiozaki, T., Stoll, H., Stone, A. J., Tarroni, R., Thorsteinsson, T., Wang, M., Welbron, M., MOLPRO version, a package of ab initio programs.
- (60) Zhu, X., Thompson, K. C., Martínez, T. J. Geodesic interpolation for reaction pathways. *J. Chem. Phys.* **2019**, *150*. <https://doi.org/10.1063/1.5090303>

6 DASA in Liquid Crystalline Materials.

6.1 Introduction

Liquid crystalline materials exhibit phase space with both liquid and crystalline properties. To do so they rely on mesogens, molecules which self-assemble into ordered, crystal-like structures while still being able to flow. These materials exhibit controllable anisotropy which results in interesting properties for applications in electronics,¹ optics, biological² and soft robotics.³ To control material properties mesogens can be incorporated into polymeric materials resulting in Liquid crystal polymers (LCPs). LCPs have been widely

a)



b)

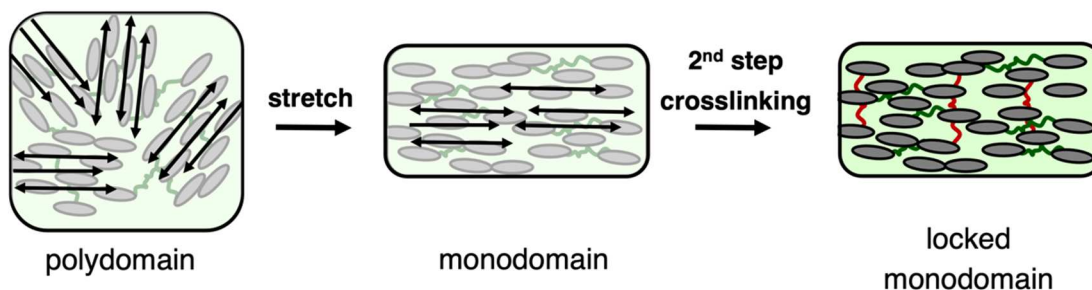


Figure 6.1. a) LC systems rely on mesogen to amplify external stimuli. Schematic of a photoresponsive LCP system amplifying the isomerization of a photoswitch into macroscopic deformation. b) Schematic representation of the mechanical alignment of Liquid Crystal Networks.

employed in stimuli responsive materials for mechano-,⁴ thermo-⁵, photo-responsive⁶ or a combination⁷ of these systems by using the LC induced order to amplify stimuli (**Figure 6.1a**).

To translate external stimuli into the most efficient macromolecular responses, liquid crystalline systems must be aligned into a singular domain.⁸ Alignment of Liquid Crystal Polymers (LCPs) into monodomain systems can be achieved by surface induction, rheological alignment, magnetic or electrical field and mechanical forces.⁹ Surface alignment is typically limited to thin film thicknesses, while rheological alignment requires judicious control of both material properties and polymerization during 3D printing. Magnetic field alignment tends to be restricted by the distance between the poles of the electromagnet¹⁰ while electric field alignment requires the introduction of polar functional groups like nitriles or halogens.⁹ Mechanical alignment is a simple and practical method to produce aligned LCPs samples by stretching the samples with a mechanical force after gelation occurs (for practical, handling purposes) and before full polymerization (**Figure 6.1b**). Subsequent polymerization then locks the strained state. To increase reproducibility, two separate stages of polymerization should be employed, for example, combining aza-Michael (Acrylate) step growth polymerization with a free radical photopolymerization.^{11,12} Such systems have been successfully employed in artificial muscles¹³ and color changing materials.⁴ However, the stimuli responsive nature of such materials has been limited by the harsh polymerization conditions including strong nucleophiles and radical chemistry (**Figure 6.2a**). To address this, several click chemistry systems have been introduced using aza-alkyne and furan-maleimide chemistry. However, these systems represent single step polymerizations and rely on their slow kinetics (up to days) to successfully strain the material after gelation but before full conversion.^{14,15}

A more selective and benign chemistry providing a two-step polymerization can reproducibly make LCPs and broaden the scope of responsive molecules which can be used to greatly improve the scope of easy-to-use responsive aligned LCPs. In this work, we aim to use the fast, metal free and quantitative reaction between a spiro cyclopentadiene (Cp) and maleimide (mal) to form the Diels–Alder (DA) adduct for a first step-growth polymerization^{16,17} and the thermally triggered retro Diels Alder (rDA) of a furan/maleimide (fu-mal) DA adduct to selectively produce more monomer upon heating (**Figure 6.2b**).¹⁸ This DA step-growth polymerization proves to be an efficient method for a two-step synthesis of Liquid Crystal Networks (LCNs).

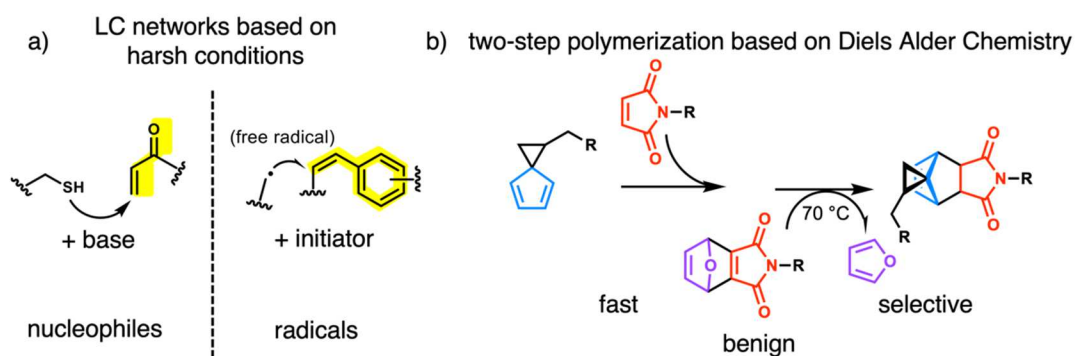


Figure 6.2. a) Previous chemistries used to fabricate mechanically aligned LC systems are based on harsh conditions. b) Schematic representation of new two-step DA-Click chemistry used to form Liquid Crystal Networks.

6.2 A Diels–Alder based liquid crystalline network.

We start the investigation of a new Diels–Alder platform for the introduction of sensitive molecules by design and synthesis of a mesogen, a chain extender and a thermally labile protected, mesogen. As shown in **Figure 6.3a**, the mesogen used is an analog of the commonly used in literature RM82 with maleimide instead of acrylate groups synthesized over 6 steps (**M1**). The strong electron withdrawing effect of the carbonyl groups in the maleimide makes

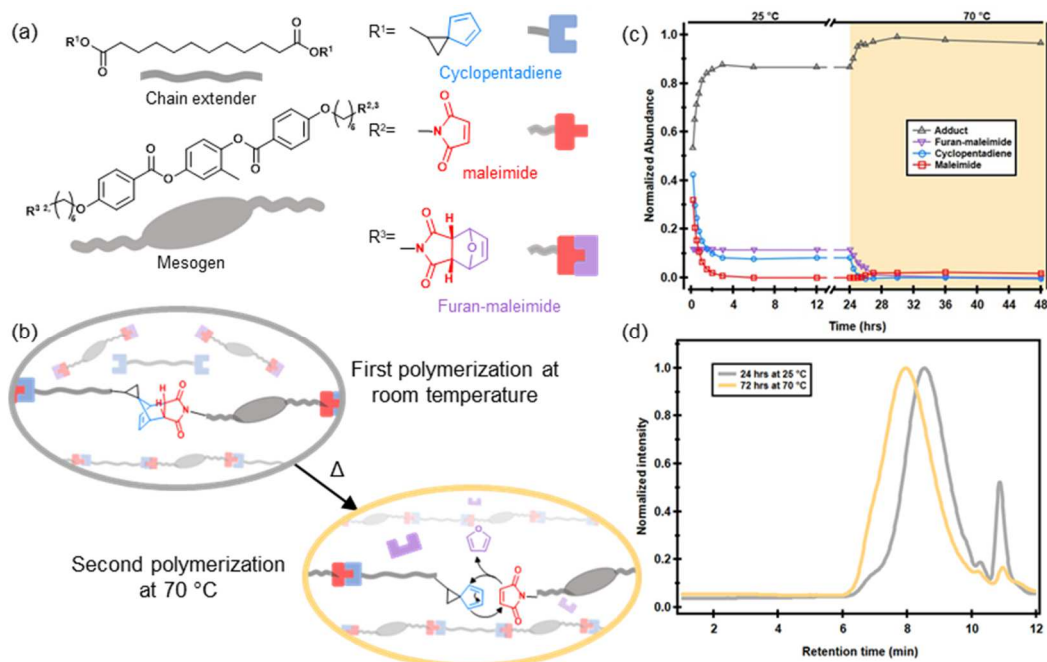


Figure 6.3. (a) Bifunctional monomers bearing maleimide and cyclopentadiene for step-growth DA polymerization. (b) Schematics of the temperature modulated polymerization (c) Kinetics of the linear polymerization followed by ^1H NMR. Consumption of maleimide (red), Cyclopentadiene (light blue), deprotection of the endo Furan-maleimide adduct (dark blue) and production of the Cp-mal DAA (gray) plotted as a function of time and temperature. (d) Gel Permeation Chromatography traces for the linear polymer after the first (gray) and second (yellow) polymerization.

the double bond of this moiety a very strong dienophile The chain extender is a bis-functional spiro cyclopentadiene with a 10-methylene alkyl chain via a two-step synthesis (**C1**). In this case, the spiro group enables stability to the cyclopentadiene preventing dimerization while retaining a strong diene character. It is the combined effect of a strong diene and strong dienophile that makes this reaction so selective yet quantitative., the endo-protected furan-maleimide DA adduct was synthesized over 5 steps (**M2**). Endo protection of maleimide with furan can be easily synthesized in gram scales and has shown to “hide” the reactivity of the dienophile which can be easily deprotected back to maleimide upon heating at 60°C.¹⁸ Detailed synthetic routes and characterization can be found in the Supporting Information, Section 2, synthesis.

To test Cp-mal step growth linear polymerization kinetics we followed a single pot reaction of **C1** (1.00 eq), **M1** (0.87 eq), and **M2** (0.13 eq) in 28 w% solution of toluene in ambient conditions by ^1H NMR, **Figure 6.7**. Chemical shifts followed, integrations and normalization can be found in **Table 6.1**. The normalized abundance of these functional groups was plotted as a function of time as shown in **Figure 6.3c**. After 4 hours at room temperature the first polymerization went to stoichiometric completion, i.e., total consumption of maleimide, 0.87 eq consumed of Cp and about 0.87 eq of the DA adduct produced while **M2** remained unreacted. After this time, the reaction was placed in a vacuum oven and the temperature was raised to 70 °C. At this temperature, quantitative deprotection of the **M2** was

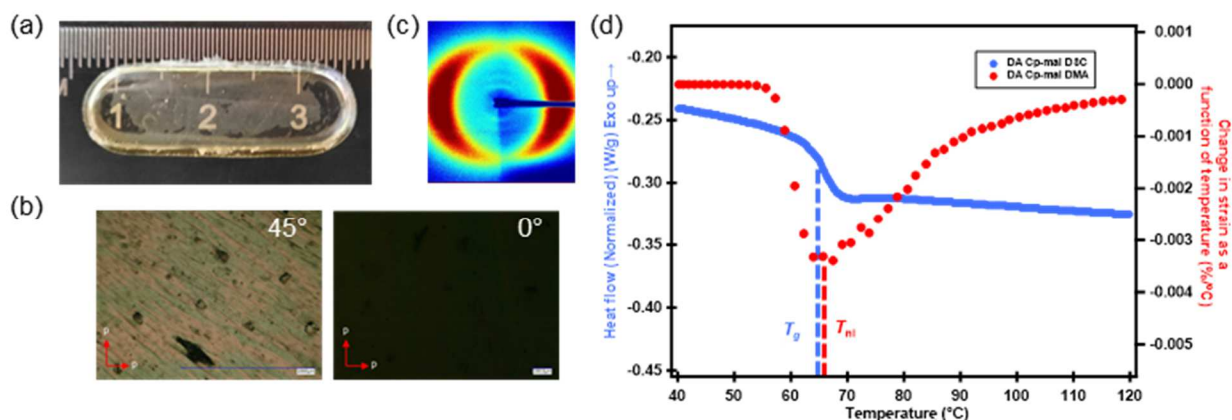


Figure 6.4. (a) Diels–Alder cyclopentadiene-maleimide Liquid Crystal Network. (b) Polarized Optical Microscopy of the DA Cp-mal LCN at 45° and 0° from the two light cross polarizers. (c) 2D-Wide Angle X-ray Diffraction of the DA Cp-mal LCN stretched at 400% its initial length. (d) Differential Scanning Calorimetry of the DA Cp-mal LCN where a glass transition temperature of 63 °C can be observed at a temperature ramp of 10 °C/min (left axis) and change in strain as a function of temperature measured by Dynamic Mechanical Analysis under a tensile constant force of 0.005N on a temperature ramp of 3 °C/minute (right axis). A nematic-to-isotropic temperature can be observed 67 °C.

observed after 4 hours while simultaneous consumption of **C1** and increase in adduct can be observed. This suggest that upon deprotection the newly produced maleimide reacts with cyclopentadiene to form more adduct. ¹H NMR kinetics indicates a fast, quantitative (0.99 eq of the DA Cp-mal adduct produced), stable, and controlled two-step polymerization of our monomers through temperature modulation.

To confirm that a two-step polymerization indeed takes place, we employed Gel Permeation Chromatography (GPC) **Figure 6.3d**. After 24 h at room temperature (gray trace) we observe two bands corresponding to 57.1 kg/mol and 1.1 kg/mol against a polystyrene standard in chloroform. Such peaks presumably correspond to the molecular weight distribution of the polymer and the unreacted **M2** respectively. Upon heating at 70 °C for 72 h we observe a shift of the major peak from 57.1 to 131.5 kg/mol while the signal at 1.1 kg/mol decreases considerably. This suggest that **M2** deprotected via rDA resulting in **M1** and further polymerization of oligomeric chains already formed increasing dramatically the molecular weight, thus confirming the thermally triggered two-step nature of our Diels–Alder based step growth polymerization. Full characterization of these polymers, M_n , M_w , PDI and T_g can be found in **Table 6.2** and **Figure 6.8**.

To form LCPs networks, a tetrafunctional-cyclopentadiene crosslinker (**C2**) was synthesized in three steps (see Scheme 6.2). To prepare a DA Cp-mal LCN 32.8 mg (0.87 eq, 0.075 mmol) of **C1**, 54.2 mg (0.87 eq, 0.075 mmol) of **M1**, 9.6 mg (0.13 eq, 0.011 mmol) of **M2** and 5.4 mg (0.013 eq, 0.00562 mmol) of **C2** were mixed in toluene and added to a 30 x 10 x 1 mm³ mold (see **Table 6.3**). The reaction was performed at room temperature, open to air, and without catalyst. The first polymerization produces a soft gel shown in **Figure 6.4a**. After 24 hours (time necessary to evaporate the toluene to produce a malleable gel) the film

is stretched 400% its initial size, aligning the mesogens (see **Figure 6.11**). After mechanical alignment, the second polymerization was triggered by an increase in temperature (70 °C under vacuum) that initiated the rDA reaction in the **M2** DA adduct. Through this simple preparation method, we are able to form aligned, controlled and reproducible two-step LCNs based on Diels–Alder Click chemistry.

6.3 Material Characterization

To characterize the alignment and crystalline packing in the fabricated LCN films, Polarized Optical Microscopy (POM), **Figure 6.4b**, and 2-Dimensional Wide Angle X-ray Diffraction (2D WAXS), **Figure 6.4c**, were performed. Through POM we observe interaction of the monodomain with polarized light if the films are set at 45 ° to the polarized optical filters while no interaction is observed at 90°. This is characteristic for a monodomain aligned film. Furthermore, 2D WAXS shows a ring of two symmetric regions of high intensity and a region of low intensity characteristic of a Liquid Single Crystal Polymer molecular packing, or, in other words, a monodomain. The order parameter S , determined as the half width of the intensity distribution of the Debye diffracted arc,¹⁹ was calculated to be 0.47. These results show that our two-step DA based LCN networks form well defined monodomain LCNs.

To characterize the thermo-mechanical properties of our LCN networks we performed Differential Scanning Calorimetry (DSC) and Dynamic Mechanical Analysis (DMA). DSC analysis show a T_g of 63 °C while no nematic-isotropic transition temperature (T_{ni}) is observable (**Figure 6.3e**). To determine T_{ni} we measured the strain as a function of temperature at low constant tensile force (0.005N) by DMA (**Figure 6.4f**).¹¹ We hypothesize

that the high T_g comes from bulkiness and stiffness of the Cp-mal DA adduct formed in the polymerization.

To confirm stability of our films at high temperature, Thermogravimetric Analysis (TGA) was done. TGA showed a decomposition temperature of about 400 °C (see **Table 6.6**). This result indicates high thermal stability which allows for thermal actuation up to a high

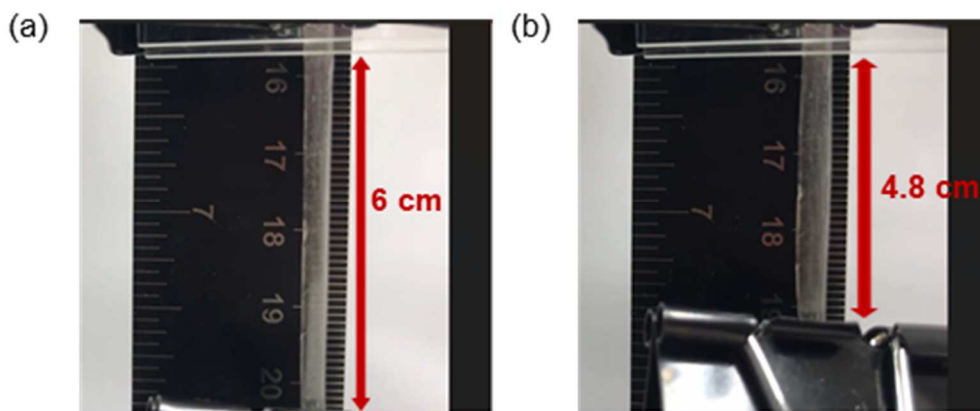


Figure 6.5. Images of the DA Cp-mal LCN before (a) and (b) after thermal actuation. A 6 cm, 12 mg film lifting 18.6 g, 1.4 cm when heated above the nematic-to-isotropic temperature.

value of temperature without the film showing any decomposition. To test the LC properties of our DA LCN networks we performed thermal actuation experiments (**Figure 6.5** and SXX). As seen in **Figure 6.5**, a thin film weighing 12 mg with 6 cm in length can lift 18.6 g a total distance of 1.4 cm After successfully performing work triggered by thermal energy with our LCN thin film, we characterized the strain and the normalized work by mass of our film seen in **Figure 6.28-29**. Interestingly, the maximum contraction (or negative strain) is about 25 % and slowly goes down upon increase of the lifting weight. In this plot we can also see a maximum weight lifted of 31.7 g. with a contraction of 10%. These results show that our system have a better contraction ratio than other high T_g LCNs,²⁰ (which have maximum strains

around 10%) as well as other LCEs which have contractions between 10 and 22%^{21–23} and better work output per mass than other Diels–Alder LCPs.¹⁵

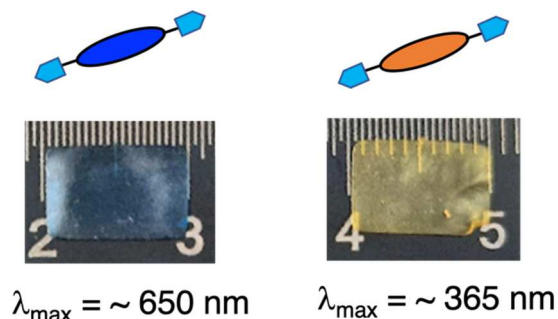


Figure 6.6. Images of the DA Cp-mal LCN with a DASA (**19**) and an azobenzene (**22**).

Furthermore, we can incorporate 2 mol% photoswitches (DASA or azobenzene) into our LCNs by copolymerizing with **19** and **22** respectively without any decomposition occurring. The mechanical properties of these materials match the pristine LCN (see section 6.5).

6.4 Conclusion

In conclusion, a thermally triggered two-step Diels Alder Liquid Crystal Network platform was synthesized using a fast and stable cyclopentadiene and a temperature-modulated concentration of maleimide through a step-growth polymerization. The polymerization was characterized by ¹H NMR and GPC proving to be efficient, fast, stable under ambient conditions and temperature controlled. To the best of our knowledge, this work represents the first one-pot two stage system controlled by a click chemistry for Liquid Crystalline materials. The Liquid Crystal Network resulting from this new chemistry was characterized by POM, 2D-WAXS, DSC and DMA. The system shows good thermomechanical with a glass transition temperature of 63 °C and performance similar or better to other LCNs and LCEs reported in the literature with a maximum contraction of 25%

and maximum weight lifted of 31.7 g by a 12 mg thin film. Furthermore, sensitive molecules like DASA can be incorporated without decomposition. This new chemistry implemented in Liquid Crystal Polymers opens an exciting opportunity for the introduction of nucleophile- or radical-sensitive molecules in the future. However, more work on the thermomechanical properties like T_g and T_{ni} needs to be done to optimize these parameters.

6.5 Additional information

6.5.1 General Experimental

6.5.1.1 Chemicals

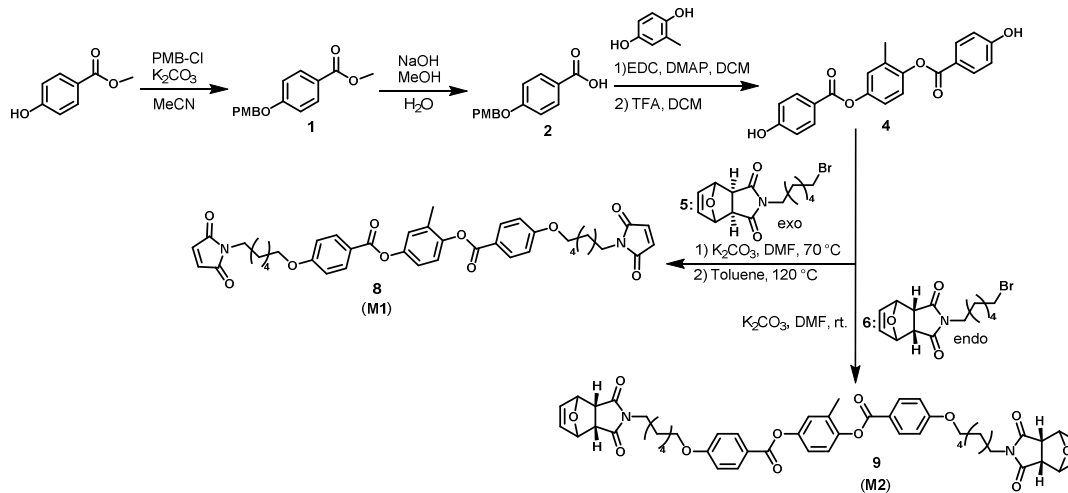
All commercially obtained reagents were bought from Sigma Aldrich, TCI Europe or Fisher Scientific and were used without purification. Anhydrous solvents were either obtained from Fischer Scientific or from a solvent purification system. Room temperature reactions were carried out between 22–25 °C. All reactions were performed under air conditions unless stated otherwise. Thin layer chromatography (TLC) was performed using Merck TLC plates (silica gel 60 F254 on aluminum) and visualized by UV light (254/ 366 nm) or staining with $\text{KMnO}_4/\text{NaOH}$. Silica gel chromatography was performed using silica gel from Sigma Aldrich (technical grade, 60 Å pore size, 40–63 μm particle size).

6.5.1.2 Instruments and Methods

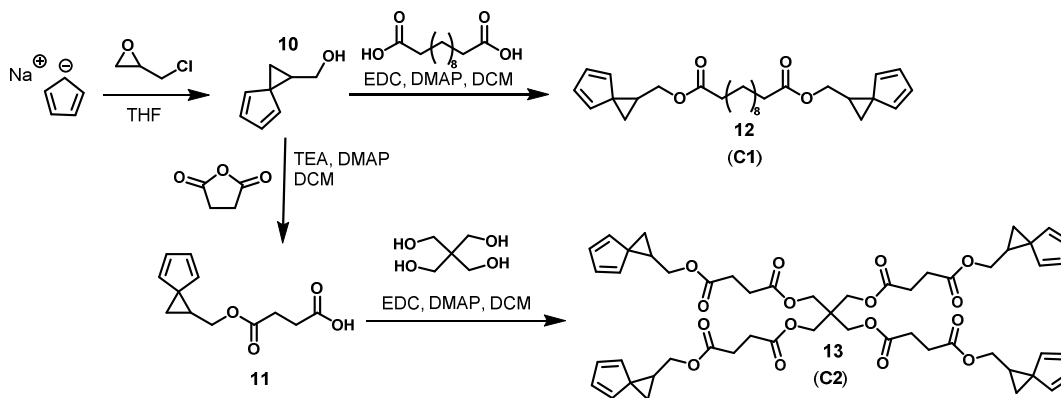
^1H NMR spectra was collected on a Bruker Avance NEO 500 MHz using CDCl_3 or $\text{DMSO-}d_6$ as a deuterated solvent. FTIR was measured with a Thermo Nicolet iS10 FTIR Spectrometer equipped with a Smart Diamond attenuated total reflectance (ATR) accessory. Differential Scanning Calorimetry was measured from -20 °C to 140 °C at a temperature ramp of 10 °C/min on a TA Instruments Q2000 DSC with 50 position autosampler. Sensitivity < 0.2 μW , and baseline drift < 10 μW . Gel permeation chromatography (GPC, Waters Alliance HPLC system) was measured using (PLgel, 5 μm MiniMIX-D, 250×4.6 mm columns with chloroform as the eluent. Dynamic Mechanical Analyzer was performed on a TA Instruments DMA 850. Thermogravimetric analysis was performed on a Discovery TGA Thermo-Gravimetric Analyzer with Mass Spectrometer Accessory.

6.5.2 Synthesis

6.5.2.1 Synthetic overviews



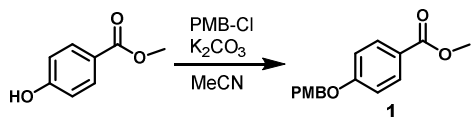
Scheme 6.1: Synthetic scheme of reactive **8** mesogen and **9** endo protected mesogen.



Scheme 6.2: Synthetic scheme of **12** Chain extender and **13** Crosslinker.

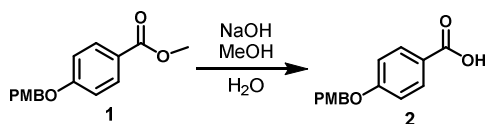
6.5.2.2 Synthetic procedures

Methyl 4-((4-methoxybenzyl)oxy)benzoate (1).



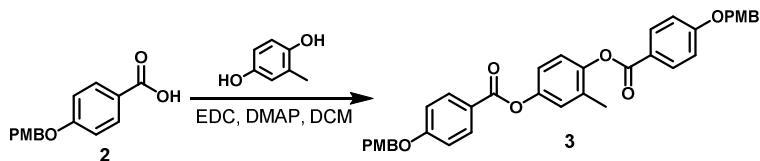
Compound **1** was prepared similarly to literature procedures and the spectral analysis matched literature data²⁴.

4-((4-methoxybenzyl)oxy)benzoic acid (2).



Compound **2** was prepared similarly to literature procedures and the spectral analysis matched literature data²⁴.

2-methyl-1,4-phenylene bis(4-((4-methoxybenzyl)oxy)benzoate) (3).

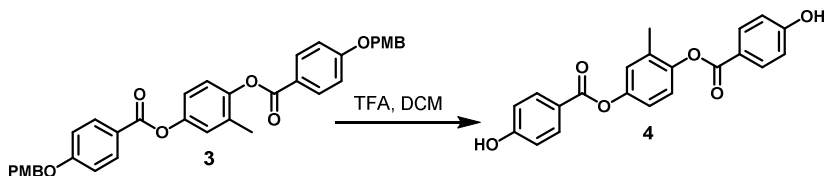


To a flame dried round bottom flask was added **2** (2.4 g, 9.3 mmol, 3.5 eq), methylhydroquinone (0.3 g, 2.7 mmol, 1.0 eq), N-(3-Dimethylaminopropyl)-N'-ethylcarbodiimide hydrochloride (EDC HCl salt, 2.1 g, 10.6 mmol, 4.0 eq) and 4-dimethylaminopyridine DMAP, (16 mg). The solids were dissolved in anhydrous dichloromethane and stirred at room temperature for 16 hours. Upon consumption of starting material by TLC, water and DCM were added to the solution. The organic phase was collected

and concentrated. Cold ethanol was added to the residue and the mixture filtered, washing again with cold ethanol. The filter cake was dried under high vacuum yielding the desired product **3** as a white powder which was used directly in the next reaction.

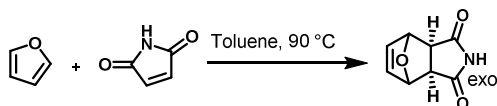
^1H NMR (500 MHz, CDCl_3) δ 8.22 – 8.13 (m, 4H), 7.41 – 7.36 (m, 4H), 7.21 – 7.08 (m, 3H), 7.08 – 7.04 (m, 4H), 6.97 – 6.92 (m, 4H), 5.09 (s, 4H), 3.83 (s, 6H), 2.25 (s, 3H). ^{13}C NMR (125 MHz, CDCl_3) δ 164.90, 164.51, 163.19, 163.15, 159.71, 148.43, 147.05, 132.34, 132.32, 131.80, 129.34, 129.33, 128.14, 124.14, 122.92, 121.92, 121.76, 120.06, 114.77, 114.72, 114.15, 70.05, 70.04, 55.35, 16.47.

2-methyl-1,4-phenylene bis(4-hydroxybenzoate) (4).



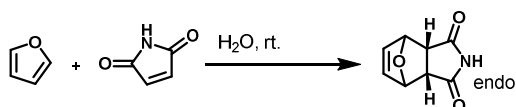
To a round bottom flask was added Compound **3** (~ 2.5 mmol). This was dissolved in DCM, then TFA (4 mL, excess) was added. The mixture was allowed to stir for 4 hours, turning a shade of purple in the process. Once starting material was consumed by TLC, the solution was concentrated under reduced pressure, filtered, and rinsed with cold DCM and cold water to yield the desired product (729 mg, 74% over two steps) as a white powder. Spectral data matches the one in literature.

(3aR,7aS)-3a,4,7,7a-tetrahydro-1H-4,7-epoxyisoindole-1,3(2H)-dione



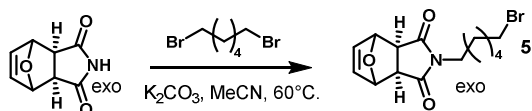
Exo-furan protected maleimide was prepared similarly to literature procedures and the spectral analysis matched literature data²⁵.

(3aR,7aS)-3a,4,7,7a-tetrahydro-1H-4,7-epoxyisoindole-1,3(2H)-dione



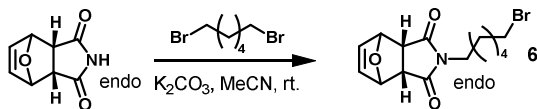
Endo-furan protected maleimide was prepared similarly to literature procedures and the spectral analysis matched literature data²⁶.

(3aR,7aS)-2-(6-bromohexyl)-3a,4,7,7a-tetrahydro-1H-4,7-epoxyisoindole-1,3(2H)-dione (5).



Compound **5** was prepared similarly to literature procedures and the spectral analysis matched literature data²⁷⁻²⁸.

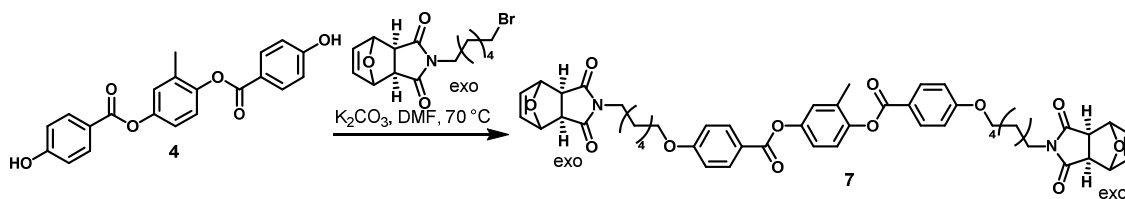
(3aR,7aS)-2-(6-bromohexyl)-3a,4,7,7a-tetrahydro-1H-4,7-epoxyisoindole-1,3(2H)-dione (6).



To a round bottom flask, endo maleimide (5.0 g, 30 mmol, 1.0 eq), 1,6-Dibromohexane (11.0 g, 45 mmol, 1.5 eq), Potassium carbonate (10.0 g, 72 mmol, 2.4 eq) and 50 mg of NaI were added. The mixture was dissolved in MeCN (300 mL) and stirred at 35 °C for 3 days. After dilution with water (200 mL), the mixture was extracted with ethyl acetate(3x 300 mL). The combined organic layer was dried over anhydrous Magnesium sulfate and evaporated under reduced pressure. The residue was purified by column chromatography in 70:30 hexanes:ethyl acetate to yield a colorless liquid (3.2 g, 9 mmol, 31%).

1H NMR (500 MHz, $CDCl_3$) δ 6.28 (d, $J = 1.2$ Hz, 2H), 5.25 – 5.13 (m, 2H), 3.39 (dd, $J = 3.7, 1.8$ Hz, 2H), 3.28 (t, $J = 6.8$ Hz, 2H), 3.18 (t, $J = 7.4$ Hz, 2H), 1.71 (dt, $J = 15.0, 6.7$ Hz, 2H), 1.36 – 1.28 (m, 4H), 1.19 – 1.11 (m, 2H). ^{13}C NMR (125 MHz, $CDCl_3$) δ 174.84, 134.37, 79.29, 77.51, 45.87, 38.26, 33.69, 32.45, 27.51, 27.25, 25.91. IR (ATR) 2936, 2859, 1768, 1690, 1397, 1343, 1282, 1142, 1019, 869, 730, 620 cm^{-1} .

2-methyl-1,4-phenylene bis(4-(((6-((3aR,7aS)-1,3-dioxo-1,3,3a,4,7,7a-hexahydro-2H-4,7-epoxyisoindol-2-yl)hexyl)oxy)benzoate) (7).



To a round bottom flask was added Compound **4** (0.6 g, 1.6 mmol, 1.0 eq), Compound **5** (2.0 g, 6.1 mmol, 4.0 eq) and anhydrous potassium carbonate (0.6 g, 4.6 mmol, 3.0 eq). Dimethylformamide was added as a solvent (15 mL) and the reaction was stirred for 16 hours at 55 °C. Upon consumption of starting material by TLC, the reaction was diluted with DCM and water. The organic phase was separated, concentrated, and washed with EtOH and diethyl ether, yielding Compound **6** (1.2 g, 91%) as an off-white solid.²⁷

¹H NMR (400 MHz, CDCl₃) δ 8.18 – 8.11 (m, 4H), 7.21 – 7.04 (m, 3H), 7.00 – 6.94 (m, 4H), 6.52 (s, 4H), 5.26 (s, 4H), 4.02 (t, 4H), 3.50 (t, *J* = 7.3 Hz, 4H), 2.83 (s, 4H), 2.24 (s, 3H), 1.86 – 1.76 (m, 4H), 1.65 – 1.58 (m, 4H), 1.53 – 1.45 (m, 4H), 1.41 – 1.32 (m, 4H). ¹³C NMR (125 MHz, CDCl₃) δ 176.33, 136.56, 132.30, 131.79, 124.13, 122.92, 120.05, 114.36, 114.31, 80.94, 68.07, 47.41, 38.85, 28.87, 27.47, 26.31, 25.51, 16.46. IR (ATR) 2940, 2860, 1690, 1600, 1510, 1400, 1250, 1160, 1070, 1010, 877, 764 cm⁻¹.

**2-methyl-1,4-phenylene
yl)hexyl)oxy)benzoate) (8).**

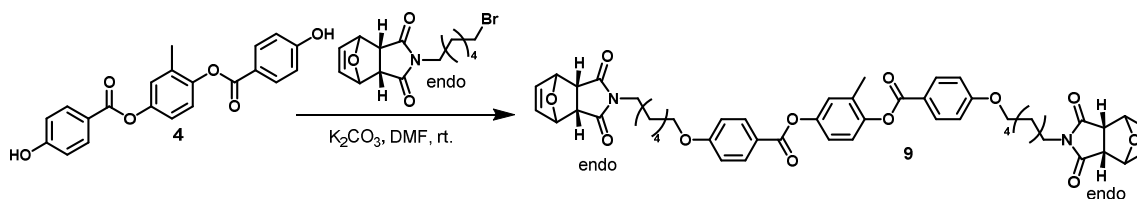
bis(4-((6-(2,5-dioxo-2,5-dihydro-1H-pyrrol-1-



To a round bottom flask was added **6** (0.2 g, 0.2 mmol, 1.0 eq). Toluene was added (20 mL) and the solution was heated to 120 °C for 16 hours. Upon completion by TLC, the solution was concentrated under reduced pressure to remove toluene, yielding the desired product as an off white powder. To ensure purity, this material was subjected to flash column chromatography (50:40:10 hexanes:ethyl acetate:DCM) giving the purified product **7** (0.1 g, 0.16 mmol 80%) as a bright white powder.²⁷

¹H NMR (500 MHz, CDCl₃) δ 8.20 – 8.10 (m, 4H), 7.20 – 7.05 (m, 3H), 6.99 – 6.94 (m, 4H), 6.68 (s, 4H), 4.08 – 4.00 (m, 4H), 3.54 (t, 4H), 2.24 (s, 3H), 1.85 – 1.78 (m, 4H), 1.67 – 1.60 (m, 4H), 1.55 – 1.47 (m, 4H), 1.41 – 1.33 (m, 4H).¹³C NMR (125 MHz, CDCl₃) δ 170.90, 164.96, 164.57, 163.49, 163.45, 148.42, 147.04, 134.08, 132.31, 132.30, 131.79, 124.13, 122.92, 121.58, 121.41, 120.06, 114.36, 114.30, 68.08, 68.06, 37.76, 28.94, 28.47, 26.47, 25.57, 16.46.; IR (ATR) 2940, 2860, 1700, 1600, 1510, 1410, 1250, 1160, 1060, 824, 730, 693 cm⁻¹; HRMS (ESI+) Exact mass calcd. for C₄₁H₄₂N₂O₁₀ [M+Na]⁺: 745.2737, found: 745.2745.

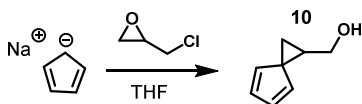
2-methyl-1,4-phenylene bis(4-(((6-((3aR,7aS)-1,3-dioxo-1,3,3a,4,7,7a-hexahydro-2H-4,7-epoxyisoindol-2-yl)hexyl)oxy)benzoate) (9).



To a round bottom flask, Compound **6** (2.2 g, 6.8 mmol, 2.5 eq), Compound **4** (1.0 g, 2.7 mmol, 1.0 eq), Potassium carbonate (0.7 g, 5.0 mmol, 1.9 eq) and 10 mg of NaI were added. The mixture was dissolved in 30 mL of DMF and stirred at 35°C for 3 days. After dilution with water (100 mL), the mixture was extracted with DCM (3x 100 mL). The combined organic layer was washed with water (2x 100 mL) and with brine (100 mL), dried over anhydrous Magnesium sulfate and evaporated under reduced pressure. The residue was purified by column chromatography in 65:35 ethyl acetate:hexanes to yield a white powder. (0.4 g, 0.5 mmol, 17%).

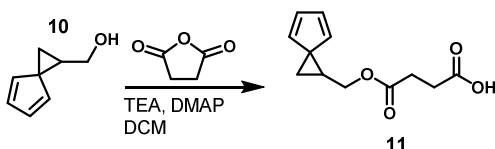
^1H NMR (500 MHz, CDCl_3) δ 8.21 – 8.06 (m, 4H), 7.22 – 7.03 (m, 3H), 6.96 (m, $J = 8.9$, 6.3 Hz, 4H), 6.39 (s, 4H), 5.32 (m, $J = 2.0$, 1.1 Hz, 4H), 4.08 – 4.00 (m, 4H), 3.51 (m, $J = 5.3$ Hz, 4H), 3.33 (t, $J = 7.5$ Hz, 4H), 2.24 (s, 3H), 1.80 (m, $J = 7.9$ Hz, 4H), 1.48 (m, $J = 8.4$ Hz, 9H), 1.41 – 1.25 (m, 5H). ^{13}C NMR (125 MHz, CDCl_3) δ 174.97, 164.93, 164.54, 163.45, 163.41, 148.42, 147.04, 134.43, 132.32, 132.31, 131.79, 124.13, 122.92, 121.63, 121.46, 120.06, 114.34, 114.28, 79.42, 68.03, 68.01, 45.96, 38.45, 28.94, 27.44, 26.57, 25.55, 16.46, 14.22. IR (ATR) 2973, 2858, 1725, 1691, 1602, 1511, 1250, 992, 896, 882, 872, 787, 629 cm^{-1} . HR-MS (ES+) $[\text{M}+\text{Na}]$ calc: 881.3262 m/z, found: 881.3286 m/z.

spiro[2.4]hepta-4,6-dien-1-ylmethanol (10)



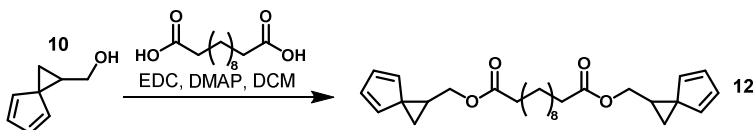
Compound **10** was prepared similarly to literature procedures and the spectral analysis matched literature data²⁸.

4-oxo-4-(spiro[2.4]hepta-4,6-dien-1-ylmethoxy)butanoic acid (11).



Compound **11** was prepared similarly to literature procedures and the spectral analysis matched literature data²⁸.

bis(spiro[2.4]hepta-4,6-dien-1-ylmethyl) dodecanedioate (12).

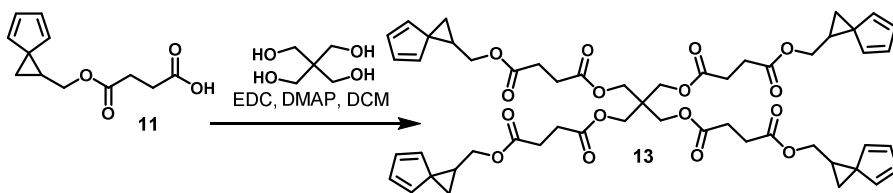


To a round bottom flask, 1,12-Dodecanedioic acid (0.4 g, 1.9 mmol, 1.0 eq), compound **10** (0.5 g, 4.1 mmol, 2.2 eq) and 80 mg of 4-dimethylaminopyridine (DMAP) were dissolved in DCM (10 mL). Then *N*-(3-Dimethylaminopropyl) -*N*'ethylcarbodiimide hydrochloride (EDC HCl salt, 1.1 g, 5.58 mmol, 3 eq) was added in portions over 1 minute. The reaction was stirred overnight, quenched with water (30 mL) and extracted with DCM (3x 30 mL). The organic layer was washed with brine (30 mL) and dried over anhydrous Magnesium sulfate. The

solution was concentrated under reduced pressure and purified via column chromatography 80:20 hexanes:ethyl acetate to yield a white powder (0.4 g, 0.9 mmol, 49%).

^1H NMR (500 MHz, CDCl_3) δ 6.56 (m, $J = 5.2, 1.8$ Hz, 1H), 6.50 – 6.45 (m, 1H), 6.22 (m, $J = 5.2, 1.8$ Hz, 1H), 6.06 (m, $J = 5.2, 1.9$ Hz, 1H), 4.35 – 4.27 (m, 1H), 4.16 (dd, $J = 11.7, 7.2$ Hz, 1H), 2.40 – 2.37 (m, 1H), 2.28 (t, $J = 7.5$ Hz, 2H), 1.83 (dd, $J = 8.7, 4.4$ Hz, 1H), 1.67 (dd, $J = 7.0, 4.4$ Hz, 1H), 1.59 (m, $J = 5.5$ Hz, 2H), 1.26 (d, $J = 5.5$ Hz, 6H). ^{13}C NMR (125 MHz, CDCl_3) δ 173.80, 138.95, 134.53, 131.13, 129.02, 65.77, 41.68, 34.27, 29.38, 29.24, 29.07, 25.49, 24.96, 17.32. IR (ATR) 2926, 2853, 1729, 1450, 1283, 1232, 1164, 1109, 981, 879, 795, 708, 674 cm^{-1} .

O,O'-(2,2-bis(((4-oxo-4-(spiro[2.4]hepta-4,6-dien-1-ylmethoxy)butanoyl)oxy)methyl)propane-1,3-diyl) bis(spiro[2.4]hepta-4,6-dien-1-ylmethyl) disuccinate (13).

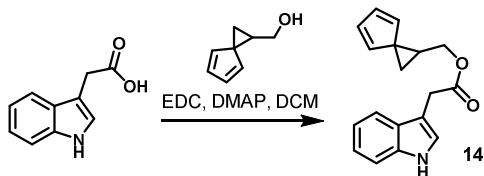


To a round bottom flask equipped with a stir bar was added Compound **11** (1.2 g, 5.62 mmol, 6.0 eq) pentaerythritol (0.1 g, 0.9 mmol, 1.0 eq), N-(3-Dimethylaminopropyl)-N'-ethylcarbodiimide hydrochloride (EDC HCl salt, 1.2 g, 6.5 mmol, 7.0 eq) and dimethylaminopyridine (DMAP, 10 mg). The reagents were dissolved/suspended in DCM (40 mL) and allowed to stir at room temperature for 15 h. The solvent was removed, and the residue was subjected to flash column chromatography with hexanes and ethyl acetate as

eluent (1:1, hexanes:ethyl acetate) to afford 0.8 g (0.8 mmol, 90%) of Compound **13** as a clear viscous oil.

^1H NMR (500 MHz, CDCl_3) δ 6.58 – 6.54 (m, 4H), 6.50 – 6.46 (m, 4H), 6.22 – 6.19 (m, 4H), 6.08 – 6.04 (m, 4H), 4.34 – 4.28 (m, 4H), 4.21 – 4.16 (m, 4H), 4.13 (s, 8H), 2.61 (s, 16H), 2.43 – 2.36 (m, 4H), 1.83 (dd, $J = 8.6, 4.5$ Hz, 4H), 1.67 (dd, $J = 7.1, 4.5$ Hz, 4H). ^{13}C NMR (125 MHz, CDCl_3) δ 172.02, 171.72, 138.95, 134.43, 131.24, 129.09, 66.41, 62.35, 42.09, 41.65, 28.90, 28.89, 25.30, 17.34. IR (ATR) 3050, 2960, 1730, 1360, 1260, 1150, 981, 795, 731 cm^{-1} ; MS (MALDI) Mass calcd. for $\text{C}_{53}\text{H}_{60}\text{O}_{16}$ $[\text{M}+\text{H}]^+$: 953.4, found: 953.7.

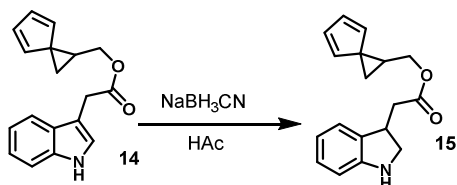
spiro[2.4]hepta-4,6-dien-1-ylmethyl 2-(1H-indol-3-yl)acetate (14).



To a round bottom flask, Compound **10** (1.0 g, 8.2 mmol, 1.0 eq), Indole-3-acetic acid (1.7 g, 9.7 mmol, 1.2 eq), 50 mg of 4-dimethylaminopyridine (DMAP) were dissolved in DCM (15 mL). Then *N*-(3-Dimethylaminopropyl)-*N*'ethylcarbodiimide hydrochloride (EDC HCl salt, 3.2 g, 16.3 mmol, 2.0 eq) is added. The reaction is for 2 hrs. quenched with water (50mL) and extracted with DCM (3x 30mL). The organic layer was washed with brine and dried over anhydrous Magnesium sulfate. The solution was concentrated under reduced pressure and purified via column chromatography 40:60 hexanes:ethyl acetate to yield a light red oil (1,3 g, 4.7 mmol, 56%).

¹H NMR (500 MHz, CDCl₃) δ 8.06 (s, 1H), 7.58 (d, *J* = 7.8 Hz, 1H), 7.35 (d, *J* = 7.9 Hz, 1H), 7.20 (t, *J* = 6.9 Hz, 1H), 7.16 – 7.10 (m, 2H), 6.60 – 6.54 (m, 1H), 6.52 – 6.47 (m, 1H), 6.23 – 6.19 (m, 1H), 6.09 – 6.05 (m, 1H), 4.43 – 4.34 (m, 1H), 4.25 – 4.18 (m, 1H), 3.77 (s, 2H), 2.47 – 2.38 (m, 1H), 1.85 – 1.80 (m, 1H), 1.70 – 1.64 (m, 1H). ¹³C NMR (126 MHz, CDCl₃) δ 171.97, 138.96, 136.10, 134.56, 131.18, 129.04, 127.23, 123.06, 122.23, 119.72, 118.95, 111.15, 108.42, 66.29, 41.74, 31.33, 25.47, 17.28. IR (ATR) 3403, 3058, 2980, 1721, 1240, 1154, 1044, 9799, 795, 739, cm⁻¹.

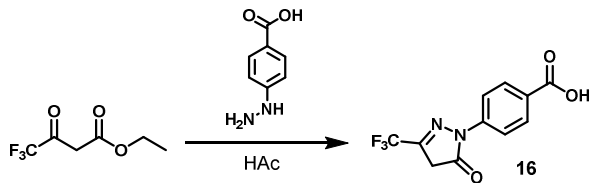
spiro[2.4]hepta-4,6-dien-1-ylmethyl 2-(indolin-3-yl)acetate (15).



To a round bottom flask, Compound **14** (0.8 g, 2.8 mmol, 1.0 eq) and Acetic acid (20 mL) was added, and the mixture was placed in an ice bath. To the solution, sodium cyanoborohydride (0.9 g, 13.8 mmol, 5.0 eq) was added in portions trying to not raise the temperature of the solution. and the reaction was stirred overnight at room temperature. The solution was basified with 4M NaOH to pH 10 and extracted with DCM (2x 20 mL). The organic layer was concentrated under reduced pressure and purified through a short silica plug in 1:1 hexanes:ethyl acetate to yield a colorless oil (0.5 g, 1.7 mmol, 63%).

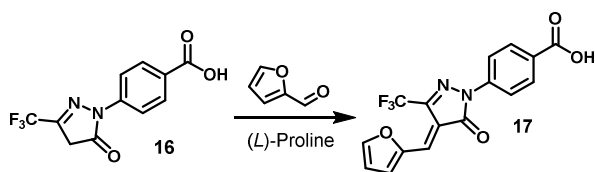
¹H NMR (500 MHz, CDCl₃) δ 7.11 – 7.02 (m, 2H), 6.77 – 6.69 (m, 1H), 6.68 – 6.62 (m, 1H), 6.62 – 6.55 (m, 1H), 6.53 – 6.48 (m, 1H), 6.28 – 6.21 (m, 1H), 6.13 – 6.05 (m, 1H), 4.46 – 4.36 (m, 1H), 4.26 – 4.17 (m, 1H), 3.79 – 3.65 (m, 2H), 3.56 (s, 1H), 3.32 – 3.18 (m, 1H), 2.82 – 2.72 (m, 1H), 2.62 – 2.50 (m, 1H), 2.50 – 2.39 (m, 1H), 1.89 – 1.82 (m, 1H), 1.74 – 1.66 (m, 1H). ¹³C NMR (125 MHz, CDCl₃) δ 172.26, 151.24, 151.22, 138.94, 134.51, 134.49, 131.30, 131.18, 129.14, 128.00, 123.94, 123.91, 118.78, 109.72, 66.17, 66.14, 53.26, 41.74, 38.92, 38.53, 38.51, 25.45, 25.43, 17.32, 17.30. IR (ATR) 3376, 3071, 2951, 2851, 1723, 1607, 1486, 1463, 1245, 1150, 976, 745 cm⁻¹.

4-(5-oxo-3-(trifluoromethyl)-4,5-dihydro-1H-pyrazol-1-yl)benzoic acid (16).



Compound **16** was prepared analogous to literature procedures and the spectral analysis matched literature data.²⁹

(E)-4-(4-(furan-2-ylmethylene)-5-oxo-3-(trifluoromethyl)-4,5-dihydro-1H-pyrazol-1-yl)benzoic acid (17).

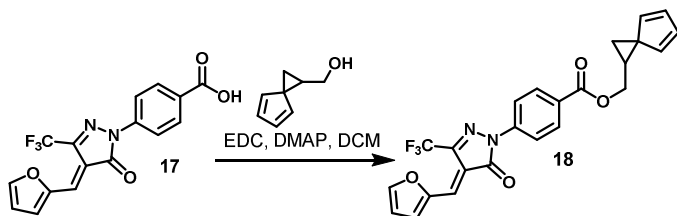


Compound **17** was prepared analogous to literature procedures and the spectral analysis matched literature data.²⁹

spiro[2.4]hepta-4,6-dien-1-ylmethyl

(E)-4-(4-(furan-2-ylmethylene)-5-oxo-3-

(trifluoromethyl)-4,5-dihydro-1H-pyrazol-1-yl)benzoate (18).

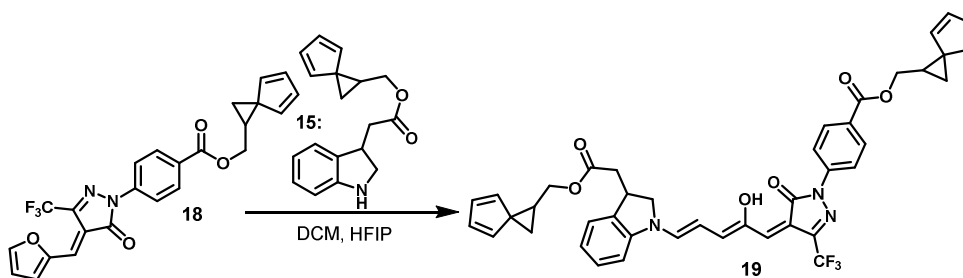


To a 20 mL scintillation vial, Compound **17** (0.5 g, 1.4 mmol, 1.0 eq), Compound **10** (0.2 g of 1.7 mmol, 1.2 eq), 20 mg of 4-dimethylaminopyridine (DMAP) and DCM (15 mL) were added. N-(3-Dimethylaminopropyl)-N'-ethylcarbodiimide hydrochloride (EDC HCl salt, 0.9 g of 4.3 mmol, 3.0 eq) was added and the reaction was stirred at room temperature overnight. The mixture was quenched with water (50 mL) and extracted with DCM (3x 50 mL). The organic layer was washed with brine (50 mL) and dried over anhydrous magnesium sulfate. The solution was concentrated under reduced pressure and purified via column chromatography 50:50 hexanes:ethyl acetate to yield a bright orange powder.(0.2 g, 0.4 mmol, 25%)

^1H NMR (500 MHz, CDCl_3) δ 8.91 (d, $J = 3.8$ Hz, 1H), 8.12 – 8.06 (m, 4H), 7.90 (d, $J = 1.7$ Hz, 1H), 7.70 (s, 1H), 6.82 (d, 1H), 6.61 – 6.57 (m, 1H), 6.52 – 6.48 (m, 1H), 6.32 – 6.28 (m, 1H), 6.13 – 6.07 (m, 1H), 4.59 (dd, $J = 11.7, 7.6$ Hz, 1H), 4.41 (dd, $J = 11.7, 7.1$ Hz, 1H), 2.60 – 2.51 (m, 1H), 1.94 – 1.88 (m, 1H), 1.82 – 1.76 (m, 1H). ^{13}C NMR (126 MHz, CDCl_3) δ 165.92, 161.50, 151.12, 150.74, 141.52, 140.98, 140.68, 138.98, 134.54, 131.97, 131.27, 130.75, 129.12, 128.48, 127.13, 120.86, 118.70, 118.47, 115.84, 115.32, 66.58, 41.71, 25.51,

17.59. IR (ATR) 3112, 1694, 1595, 1449, 1355, 1259, 1215, 1121, 1091, 1023, 973, 935, 781, 765 cm^{-1} .

spiro[2.4]hepta-4,6-dien-1-ylmethyl 4-((Z)-4-((2Z,4E)-2-hydroxy-5-(3-(2-oxo-2-(spiro[2.4]hepta-4,6-dien-1-ylmethoxy)ethyl)indolin-1-yl)penta-2,4-dien-1-ylidene)-5-oxo-3-(trifluoromethyl)-4,5-dihydro-1H-pyrazol-1-yl)benzoate (19).



Compound 18 (100 mg, 0.22 mmol, 1.0 eq) was dissolved in DCM (0.8 ml). Compound **15** (59 mg, 0.22 mmol, 1.0 eq.) and subsequent 1,1,1,3,3,3-hexafluoroisopropanol (HFIP, 0.2 ml) was added and the solution stirred for 4 h. The solvent was evaporated and the remaining solid was taken up in diethylether (1 ml) and triturated for 5 min. The solution was filtered and compound 19 (63 mg, 0.09 mmol, 41%) was obtained as a dark blue powder.

IR (ATR) 3068, 2951, 1730, 17707, 1601, 1499, 1463, 1366, 1152, 1111, 783, 719, 693 cm^{-1} .

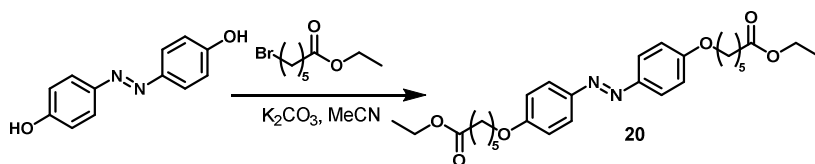
^1H NMR (600 MHz, CDCl_3) δ 8.16 – 7.99 (m, 4H), 7.73 – 7.65 (m, 1H), 7.35 – 7.29 (m, 1H), 7.26 – 7.21 (m, 1H), 7.18 – 7.11 (m, 1H), 7.10 – 7.06 (m, 1H), 6.77 – 6.71 (m, 1H), 6.66 – 6.56 (m, 2H), 6.55 – 6.48 (m, 2H), 6.36 – 6.28 (m, 2H), 6.24 – 6.21 (m, 1H), 6.15 – 6.08 (m, 2H), 4.64 – 4.44 (m, 2H), 4.45 – 4.38 (m, 2H), 4.35 – 4.26 (m, 1H), 4.24 – 4.11 (m,

1H), 4.03 – 3.75 (m, 2H), 3.03 – 2.80 (m, 1H), 2.70 – 2.55 (m, 2H), 2.50 – 2.38 (m, 1H), 1.96 – 1.84 (m, 2H), 1.83 – 1.78 (m, 1H), 1.76 – 1.62 (m, 1H).

¹³C NMR (125 MHz, CDCl₃) δ 139.4, 139.4, 138.6, 135.0, 134.9, 134.8, 131.7, 131.2, 131.0, 129.6, 129.5, 122.4, 119.6, 67.1, 66.8, 40.0, 37.6, 36.2, 36.1, 26.0, 25.9, 18.0.

HR-MS (ES⁺) [M+Na] calc: 758.2454 m/z, found: 758.2460 m/z.

diethyl 6,6'-((diazene-1,2-diylbis(4,1-phenylene))bis(oxy))(E)-dihexanoate (20).

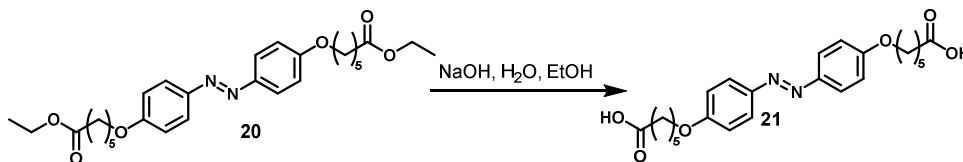


To a 500 mL round bottom flask, 4,4'-(diazene-1,2-diyl)diphenol (1.0 g 4.6 mmol, 1.0 eq), ethyl 6-bromohexanoate (2.5 g, 11.2 mmol, 2.4 eq) and potassium carbonate (2.6 g, 18.8 mmol, 4 eq) were added. The solids were dissolved in acetonitrile (200 mL) and the solution was refluxed overnight. The mixture was diluted with water (200 mL) and extracted with dichloromethane (3x 200 mL). The organic phase was combined, dried over anhydrous magnesium sulfate and the solvent was evaporated under reduced pressure. The crude product was purified by column chromatography 50:50 Hexanes:Ethyl acetate to yield the pure yellow solid. (1.6g, 3.2 mmol, 69%).

¹H NMR (500 MHz, CDCl₃) δ 7.85 (d, *J* = 9.0 Hz, 4H), 7.00 – 6.95 (m, 4H), 4.14 (q, *J* = 7.1 Hz, 4H), 4.04 (t, *J* = 6.4 Hz, 4H), 2.37 – 2.32 (m, 4H), 1.87 – 1.81 (m, 4H), 1.76 – 1.69 (m, 4H), 1.56 – 1.50 (m, 4H), 1.28 – 1.23 (m, 8H). ¹³C NMR (126 MHz, CDCl₃) δ 173.61, 161.06, 146.97 (d, *J* = 1.8 Hz), 124.32, 114.65, 67.95, 60.27, 34.24, 28.91, 25.64, 24.71, 14.26. IR

(ATR) 3067, 2938, 2871, 1734, 1599, 1579, 1474, 1314, 1304, 1231, 1160, 1147, 1100, 840,
552 cm^{-1} .

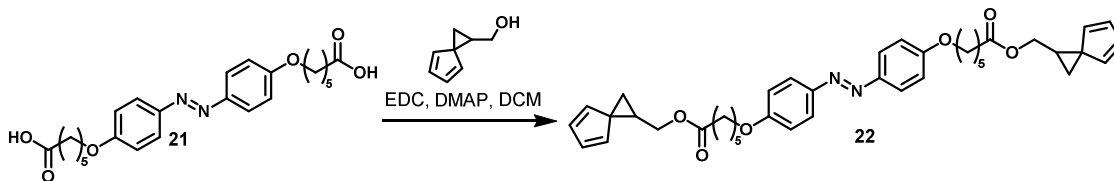
(E)-6,6'-((diazene-1,2-diylbis(4,1-phenylene))bis(oxy))dihexanoic acid (21).



To a round bottom flask, 2 g of Compound **20** (4 mmol) were added, dissolved in 100 mL of Ethanol and 50 mL of a 4M NaOH solution were added. The solution was refluxed at 90°C overnight. After cooling down to room temperature, the mixture was placed in an ice bath and acidified to pH 2 with concentrated HCl. The precipitate was filtered and rinsed with water and cold ethanol. The orange powder was dried under vacuum to yield the pure product (1.5 g, 3.4 mmol, 85%).

¹H NMR (500 MHz, DMSO) δ 12.00 (s, 2H), 7.86 – 7.79 (m, 4H), 7.13 – 7.06 (m, 4H), 4.06 (t, J = 6.5 Hz, 4H), 2.24 (t, J = 7.3 Hz, 4H), 1.80 – 1.69 (m, 4H), 1.61 – 1.53 (m, 4H), 1.48 – 1.37 (m, 4H). ¹³C NMR (125 MHz, DMSO-*d*₆) δ 174.89, 161.36, 146.55, 124.57, 115.42, 68.29, 34.08, 28.82, 25.58, 24.72. IR (ATR) 2944, 2870, 1697, 1600, 1580, 1255, 1243, 1148, 854, 842, 779, 731, 553 cm⁻¹.

bis(spiro[2.4]hepta-4,6-dien-1-ylmethyl) 6,6'-((diazene-1,2-diylbis(4,1-phenylene))bis(oxy))(E)-dihexanoate (22).



Compound **21** (1.0 g, 2.3 mmol, 1.0 eq) was crushed on a mortar to get a very fine powder. The powder was added to a round bottom flask along with Compound **10** (0.7 g, 5.6 mmol, 2.1 eq), 20 mg of 4-dimethylaminopyridine (DMAP) and dissolved in DCM (50 mL). N-(3-Dimethylaminopropyl)-N'-ethylcarbodiimide hydrochloride (EDC HCl salt, 10.0 g, 50 mmol, 22 eq) was added over the course of 2 hours and the reaction was stirred at room temperature overnight. The mixture was extracted with water, brine and dried over anhydrous Magnesium sulfate. The solution was concentrated under reduced pressure and purified via column chromatography 60:40 hexanes:ethyl acetate to yield a yellow powder (0.6 g, 0.9 mmol, 40%)

$^1\text{H NMR}$ (500 MHz, CDCl_3) δ 7.89 – 7.82 (m, 4H), 7.01 – 6.95 (m, 4H), 6.58 – 6.53 (m, 2H), 6.50 – 6.45 (m, 2H), 6.24 – 6.19 (m, 2H), 6.09 – 6.03 (m, 2H), 4.34 (dd, $J = 11.7, 7.3$ Hz, 2H), 4.17 (dd, $J = 11.7, 7.5$ Hz, 2H), 4.02 (t, $J = 6.4$ Hz, 4H), 2.45 – 2.38 (m, 2H), 2.34 (t, $J = 7.4$ Hz, 4H), 1.87 – 1.79 (m, 6H), 1.73 – 1.65 (m, 6H), 1.54 – 1.46 (m, 4H). $^{13}\text{C NMR}$ (125 MHz, CDCl_3) δ 173.53, 161.06, 146.99, 138.94, 134.52, 131.17, 129.05, 124.33, 114.65, 67.95, 65.90, 41.69, 34.15, 28.89, 25.57, 25.47, 24.82, 24.70, 17.31. IR (ATR) 2957, 1732, 1449, 1429, 1282, 1232, 943, 880, 706, 673, 653 cm^{-1} .

6.5.3 Linear Polymerization.

6.5.3.1 NMR Spectroscopy.

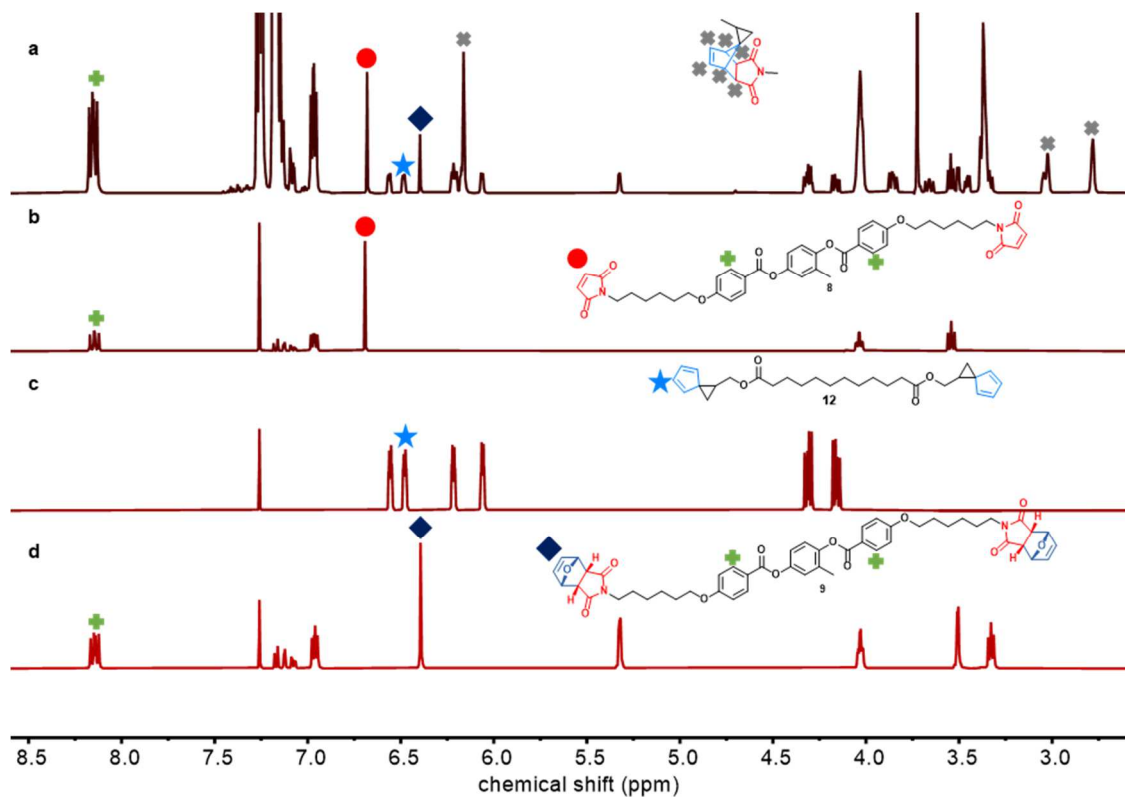


Figure 6.7 ^1H NMR (500 MHz, CDCl_3) spectra of **a**) linear step-growth polymerization of **8** Meso-mal, **12** CE-Cp and **9** Meso Fu-mal after 30 minutes at room temperature. **b**) **8** Meso-mal. **c**) **12** CE-Cp. **d**) **9** Meso Fu-mal.

Table 6.1. Kinetics of Linear polymerization of **8** Meso-mal, **12** CE-Cp and **9** Meso Fu-mal. Normalized abundance of the reactive functional groups and the Diels–Alder adduct product measured by ^1H NMR (500 MHz, CDCl_3) spectra as a function of time.

Time (h)	Adduct (2.85-2.79 ppm)		Fu-mal (6.41-6.37 ppm)		Cp (6.51-6.46 ppm)		Mal (6.70-6.67 ppm)	
	Integration	Normalized	Integration	Normalized	Integration	Normalized	Integration	Normalized
0.17	1.07	0.53	0.46	0.12	0.85	0.42	1.28	0.32
0.33	1.30	0.65	0.47	0.12	0.59	0.30	0.83	0.21
0.50	1.42	0.71	0.47	0.12	0.49	0.25	0.61	0.15
0.75	1.51	0.76	0.47	0.12	0.38	0.19	0.42	0.11
1.00	1.62	0.81	0.47	0.12	0.30	0.15	0.26	0.07
1.50	1.68	0.84	0.46	0.12	0.24	0.12	0.14	0.03
2.00	1.71	0.86	0.46	0.12	0.20	0.10	0.07	0.02
3.00	1.75	0.88	0.45	0.11	0.16	0.08	0.03	0.01
6.00	1.73	0.87	0.45	0.11	0.15	0.08	0.00	0.00
12.00	1.73	0.87	0.46	0.11	0.16	0.08	0.00	0.00
24.00	1.73	0.87	0.45	0.11	0.16	0.08	0.00	0.00
24.50	1.80	0.90	0.37	0.09	0.07	0.04	0.00	0.00
25.00	1.90	0.95	0.25	0.06	0.01	0.01	0.00	0.00
25.50	1.93	0.96	0.19	0.05	0.00	0.00	0.01	0.00
26.00	1.92	0.96	0.16	0.04	0.00	0.00	0.04	0.01
27.00	1.94	0.97	0.05	0.01	0.00	0.00	0.08	0.02
30.00	1.98	0.99	0.03	0.01	0.00	0.00	0.08	0.02
36.00	1.96	0.98	0.00	0.00	0.00	0.00	0.09	0.02
48.00	1.93	0.97	0.00	0.00	0.00	0.00	0.07	0.02
96.00	1.94	0.97	0.00	0.00	0.00	0.00	0.09	0.02

6.5.3.2 Gel Permeation Chromatography and Differential Scanning Calorimetry

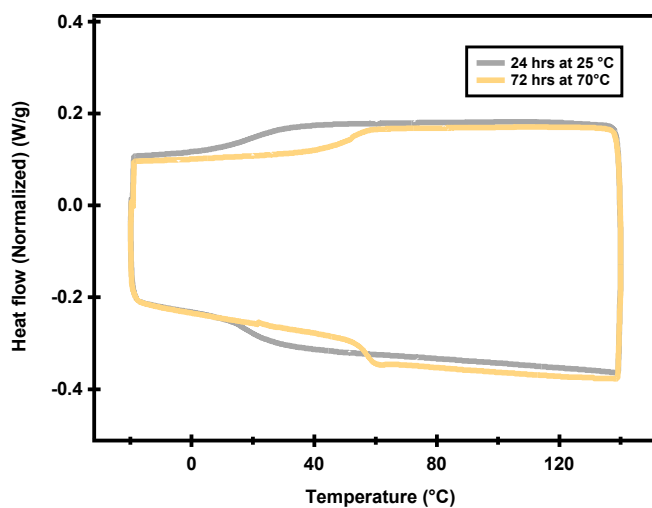


Figure 6.8 Differential Scanning Calorimetry of temperature controlled linear step-growth polymerization of **8** Meso-mal, **12** CE-Cp and **9** Meso Fu-mal. Traces at 24 hrs at room temperature and 72 hrs at 70 °C. Temperature ramp of 10 °C/min from -20 to 140 °C. Second cycle shown.

Table 6.2. Molecular weight, dispersity and glass transition temperature determined by Gel Permeation Chromatography and Differential Scanning Calorimetry to the linear polymerization of **8** Meso-mal, **12** CE-Cp and **9** Meso Fu-mal.

System	M_n	M_w	\mathcal{D}	T_g
	(g/mol)	(g/mol)		(°C)
Linear polymer	24 h at rt			
	20k	57k	2.8	23
	+72 h at 70 °C			
	34k	131k	3.9	56

6.5.4 Film fabrication.

6.5.4.1 Methodology

Stock solutions of monomers **9**, **12**, **13**, **19** and **22** were prepared by dissolving the pure compounds in dichloroethane (DCE). The concentration of the solutions was determined by evaporating 100 μL of the stock solution under reduced pressure and measuring the remaining mass. Stock solutions were stored at 0 $^{\circ}\text{C}$.

Aliquots of the stock solutions were added to a one dram vial (vial 1) and the solvent was evaporated under reduced pressure (quantities shown in **Table 6.1**). **8** (mesogen) was added to a one dram vial and 200 μL of toluene were added (vial 2). Vial 2 was heated in a water bath until complete dissolution of the mesogen. This solution was added to vial 1 containing **9** (endo-mesogen), **12** (chain extender), **13** (crosslinker) and (if applicable) **19** or **22** (the photoswitch). Vial 2 was then washed with a further 100 μL of toluene and added to vial 1. After mixing the combined monomers were quickly transferred into a Teflon mold and placed on a shaker for 24hrs. The resulting film was removed from the mold (**Figure 6.9**), and 1x0.5 cm samples were punched out (**Figure 6.10**). To form a monodomain the samples were stretched to 200% strain (**Figure 6.11**). The stretched or unstretched samples were then placed under reduced pressure at 70 $^{\circ}\text{C}$ for 3 days in a vacuum oven for the second step crosslinking.

Table 6.3. Composition of film synthesis.

Cmpds	MW (g/mol)	<i>f</i>	Film 1		Film 2		Film 3	
			mass (mg)	Eq.	mass (mg)	Eq.	mass (mg)	Eq
8 (Mesogen)	722.8	2	54.2	1.00	54.2	1.00	54.2	1
9 (Endo- mesogen)	875.9	2	9.6	0.15	9.6	0.150	9.6	0.150
12 (Chain extender)	438.5	2	32.8	1.00	32.2	0.980	32.2	0.980
13 (Crosslinker)	953.1	4	5.3	0.075	5.3	0.075	5.3	0.075
19 (DASA)	735.8	2	---	---	1.1	0.020	---	---
22 (Azobenzene)	650.8	2	---	---	---	---	1.0	0.020



Figure 6.9. Dimensions of films 1-3 on the polydomain after being taken out of the molds.

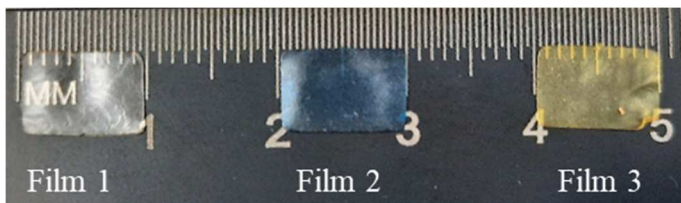


Figure 6.10. Dimensions of films 1-3 on the polydomain before stretching.

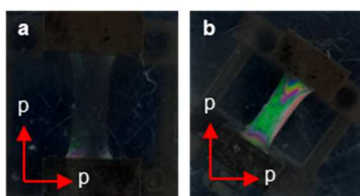


Figure 6.11. Film 1 (LCN) stretched 400% between two perpendicular light polarizers before the second polymerization **a**) at 0° and **b**) at 45°. Birefringence is observed.

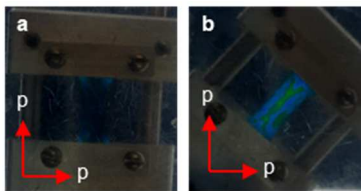


Figure 6.12. Film 2 (LCN+19 DASA) stretched 400% between two perpendicular light polarizers before the second polymerization **a)** at 0° and **b)** at 45° . Birefringence is observed.



Figure 6.13. Swelling of Films 1-3 in DCM. Gel fraction obtained after 24 hrs in DCM

6.5.5 Film characterization.

6.5.5.1 Thermogravimetric Analysis

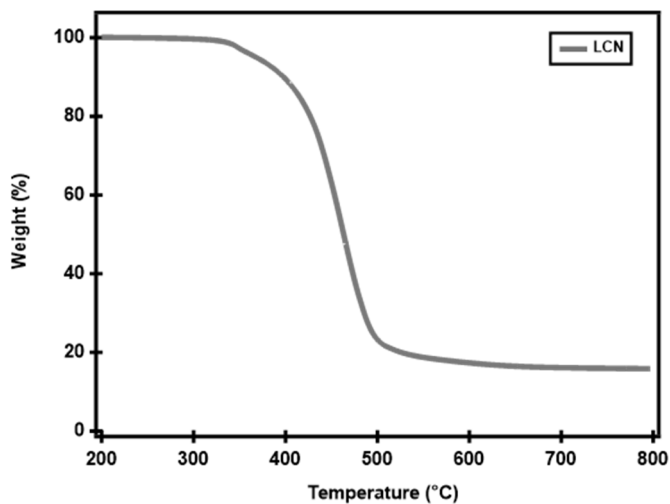


Figure 6.14. Thermogravimetric Analysis curve for **Film 1** (LCN) upon heating from 200 °C to 800 °C at a constant rate of 20 °C/min.

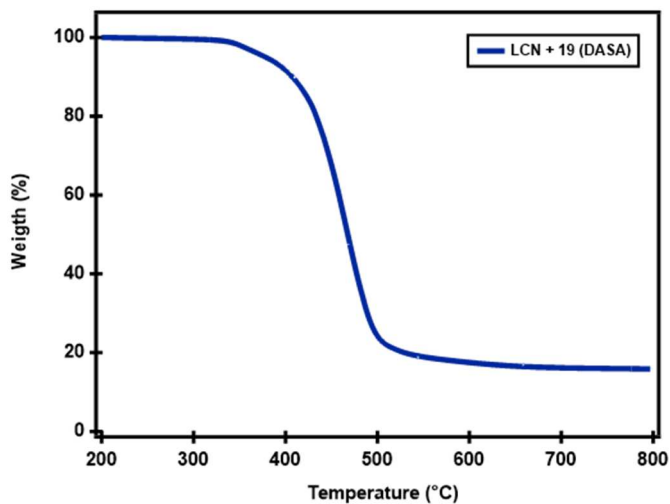


Figure 6.15. Thermogravimetric Analysis curve for **Film 2** (LCN+19 DASA) upon heating from 200 °C to 800 °C at a constant rate of 20 °C/min.

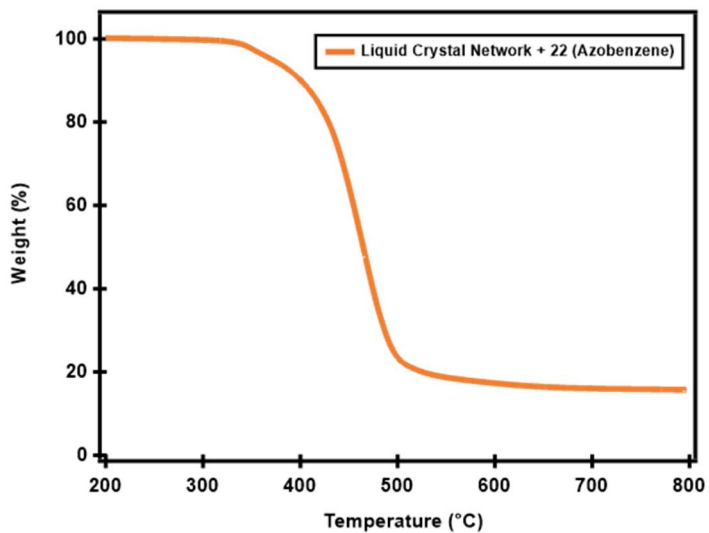


Figure 6.16. Thermogravimetric Analysis curve for **Film 3** (LCN+22 Azobenzene) upon heating from 200 °C to 800 °C at a constant rate of 20 °C/min

6.5.5.2 Differential Scanning Calorimetry

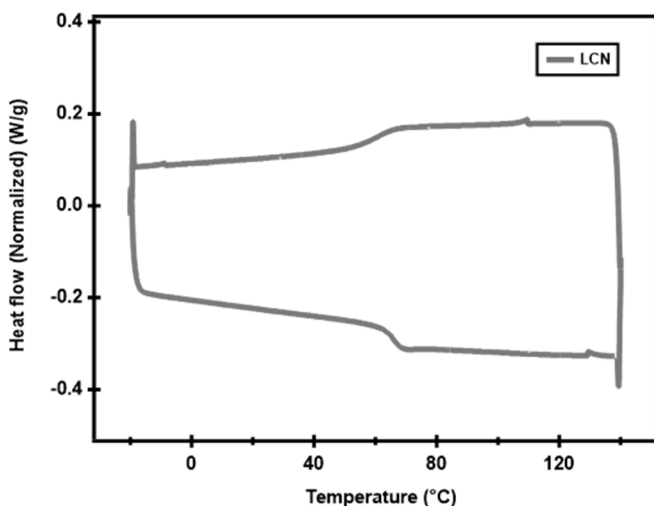


Figure 6.17. Differential Scanning Calorimetry of **Film 1** (LCN) from -20 °C to 140 °C at a temperature ramp of 10 °C/min. Third cycle shown. Glass transition temperature and nematic-isotropic temperature can be observed.

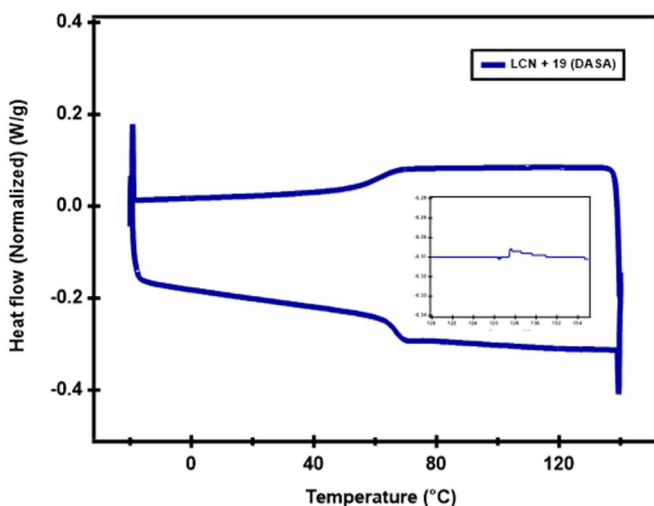


Figure 6.18. Differential Scanning Calorimetry of **Film 2** (LCN + 19 DASA) from -20 °C to 140 °C at a temperature ramp of 10 °C/min. Third cycle shown. Glass transition temperature can be observed. Nematic-isotropic temperature can be observed only on the first cycle.

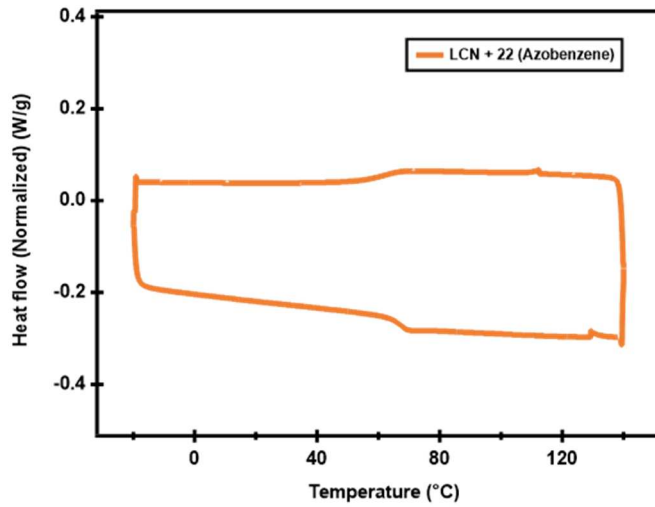


Figure 6.19. Differential Scanning Calorimetry of **Film 3** (LCN + **22** Azobenzene) from -20 °C to 140 °C at a temperature ramp of 10 °C/min. Third cycle shown. Glass transition temperature and nematic-isotropic temperature can be observed.

6.5.5.3 Dynamic Mechanical Analysis

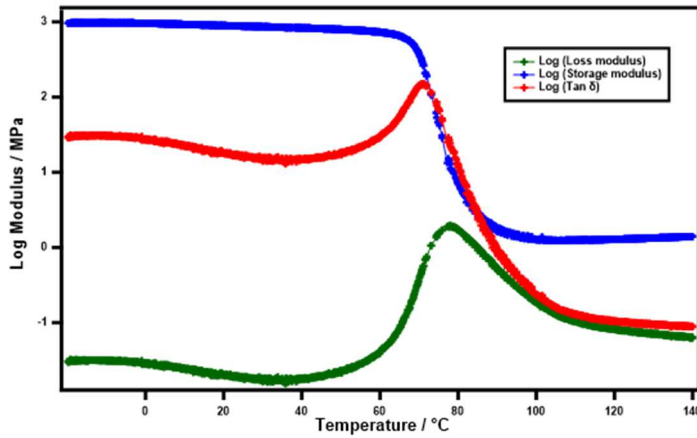


Figure 6.20. Dynamic Mechanical Analysis of **Film 1** (LCN) from -20 to 140 °C at 1 Hz on a temperature ramp of 5 °C / min. The logarithm of the storage modulus, loss modulus and the Tan δ as a function of the temperature.

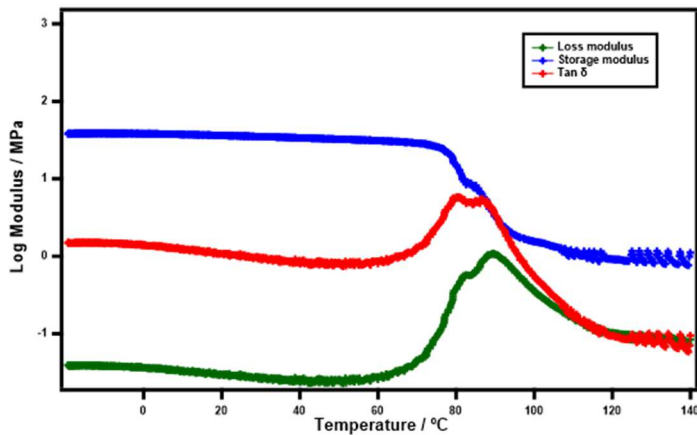


Figure 6.21. Dynamic Mechanical Analysis of **Film 2** (LCN + 19 DASA) from -20 to 140 °C at 1 Hz on a temperature ramp of 5 °C / min. The logarithm of the storage modulus, loss modulus and the Tan δ as a function of the temperature.

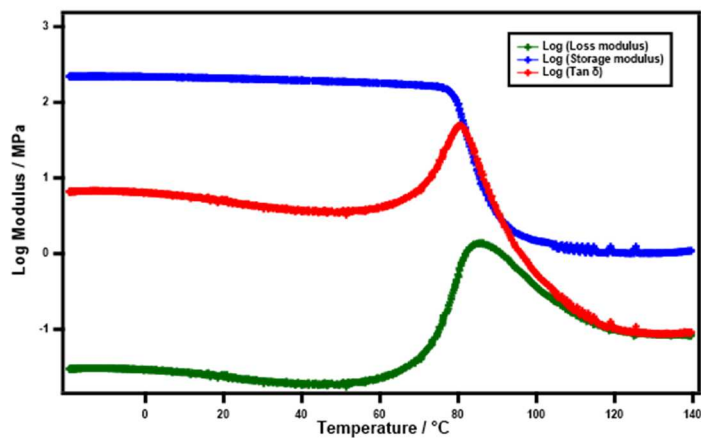


Figure 6.22. Dynamic Mechanical Analysis of **Film 3** (LCN + **22** Azobenzene) from -20 to 140 °C at 1 Hz on a temperature ramp of 5 °C / min. The logarithm of the storage modulus, loss modulus and the Tan δ as a function of the temperature.

6.5.5.4 Polarized Optical Microscopy.

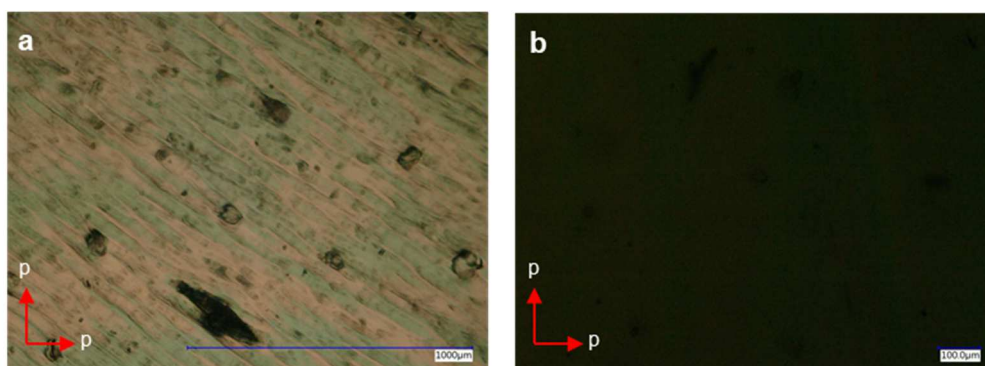


Figure 6.23. Polarized Optical Microscopy (POM) images of **Film 1** (LCN) after the second polymerization. **a)** 45° and **b)** 0°.

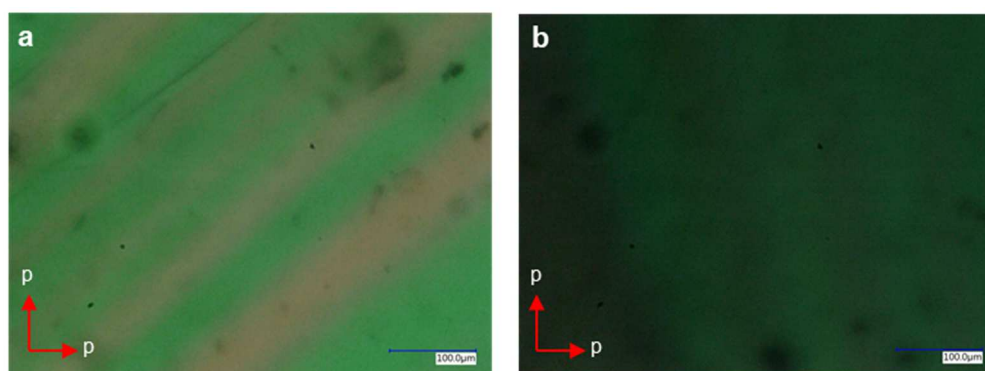


Figure 6.24. Polarized Optical Microscopy (POM) images of **Film 2** (LCN + 19 DASA) after the second polymerization. **a)** 45° and **b)** 0°.

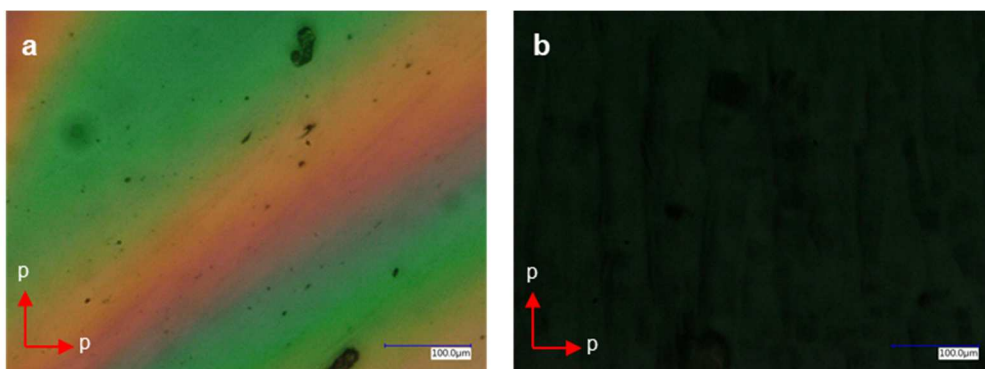


Figure 6.25. Polarized Optical Microscopy (POM) images of **Film 3** (LCN + **22** Azobenzene) after the second polymerization. **a)** 45° and **b)** 0°.

6.5.5.5 2D Wide Angle X-ray Scattering

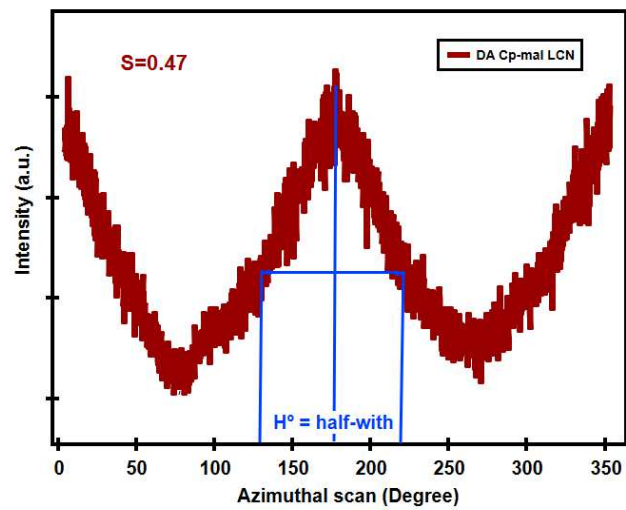


Figure 6.26. 2D Wide Angle X-ray Scattering of the DA Cp-mal LCN. The half-width of the distribution is shown. Order parameter determined to be $S = 0.47$.

6.5.6 Actuation

6.5.6.1 Thermal Actuation

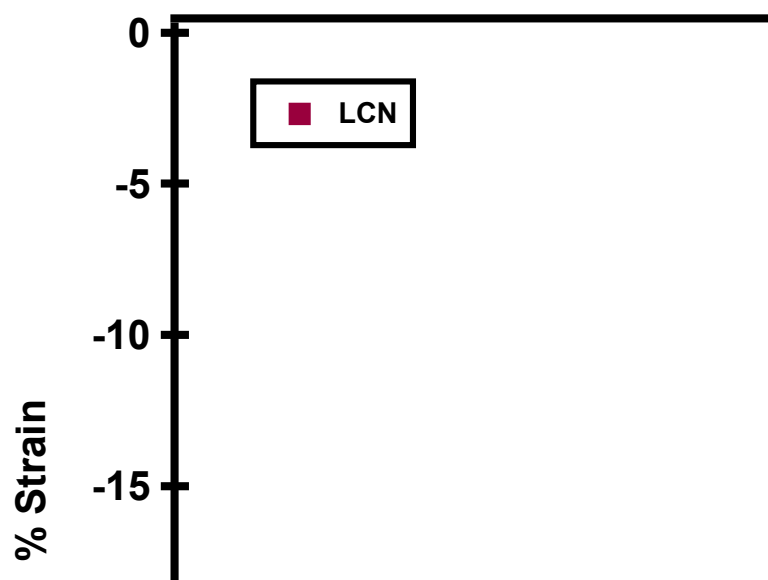


Figure 6.27. Percentage of strain by thermal actuation of a 12 mg DA Cp-mal DAA film, 6 cm in length, in function of the mass lifted.

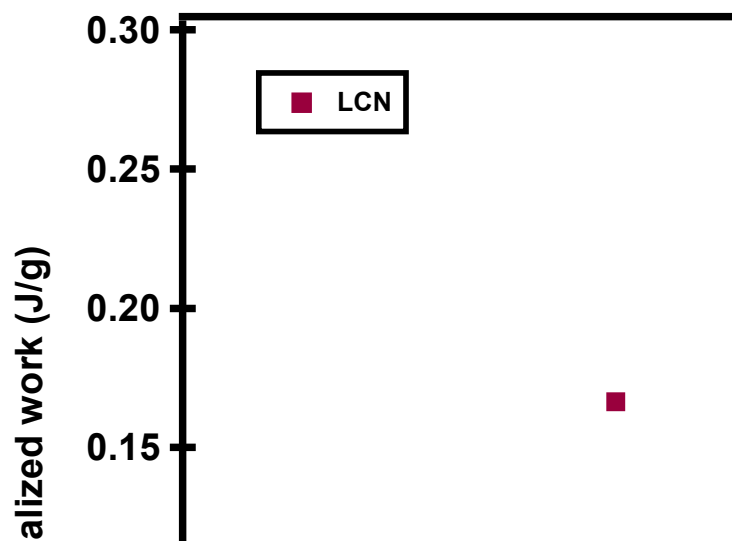


Figure 6.28. Normalized work output (by film mass) by thermal actuation of a 12 mg DA Cp-mal DAA film, 6 cm in length, in function of the mass lifted. Work output calculated as $[\text{mass lifted}] \times [\text{Gravitational constant}] \times [\text{distance of contraction}] / [\text{mass of the film}]$.

6.5.7 Spectra

6.5.7.1 NMR Spectra

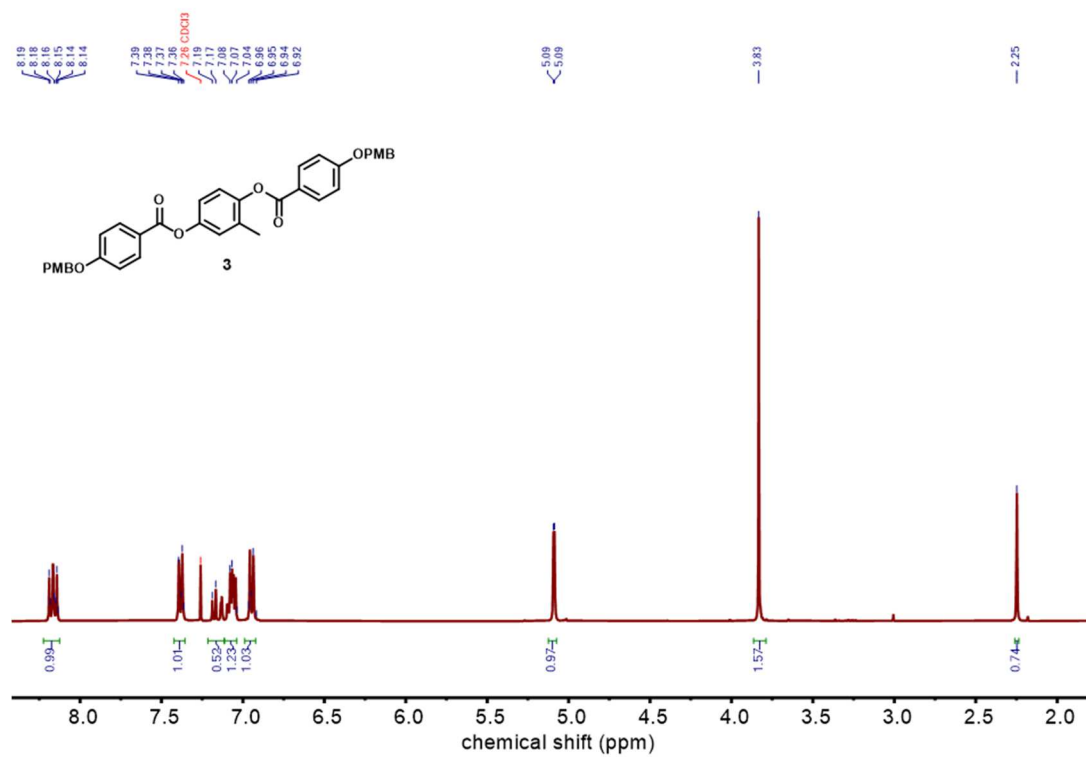


Figure 6.29. ¹H NMR (500 MHz, CDCl₃) spectra of **3**.

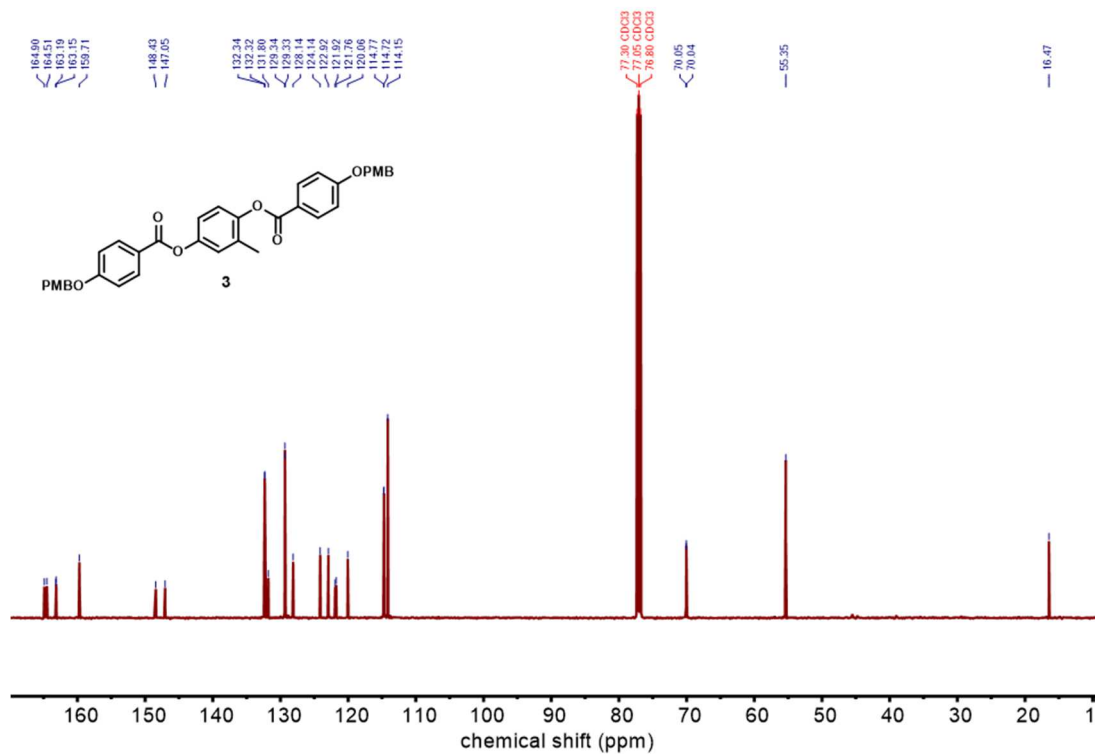


Figure 6.30. ^{13}C NMR (125 MHz, CDCl_3) spectra of **3**.

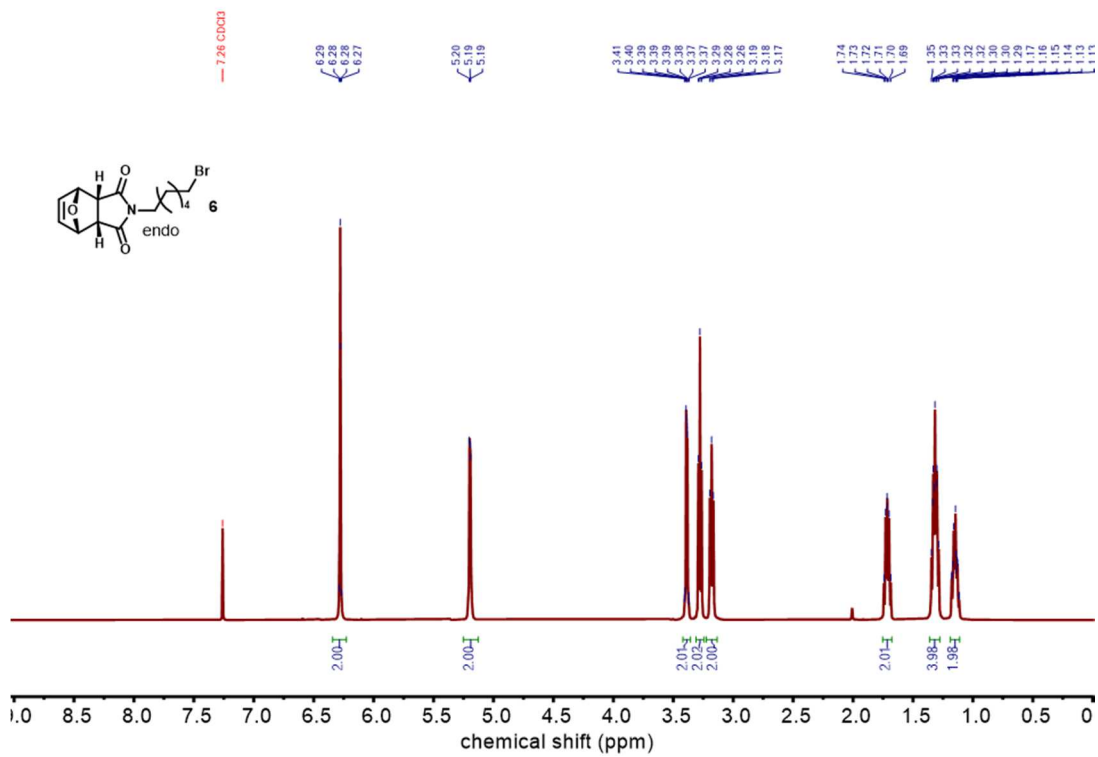


Figure 6.31. ^1H NMR (500 MHz, CDCl_3) spectra of **6**.

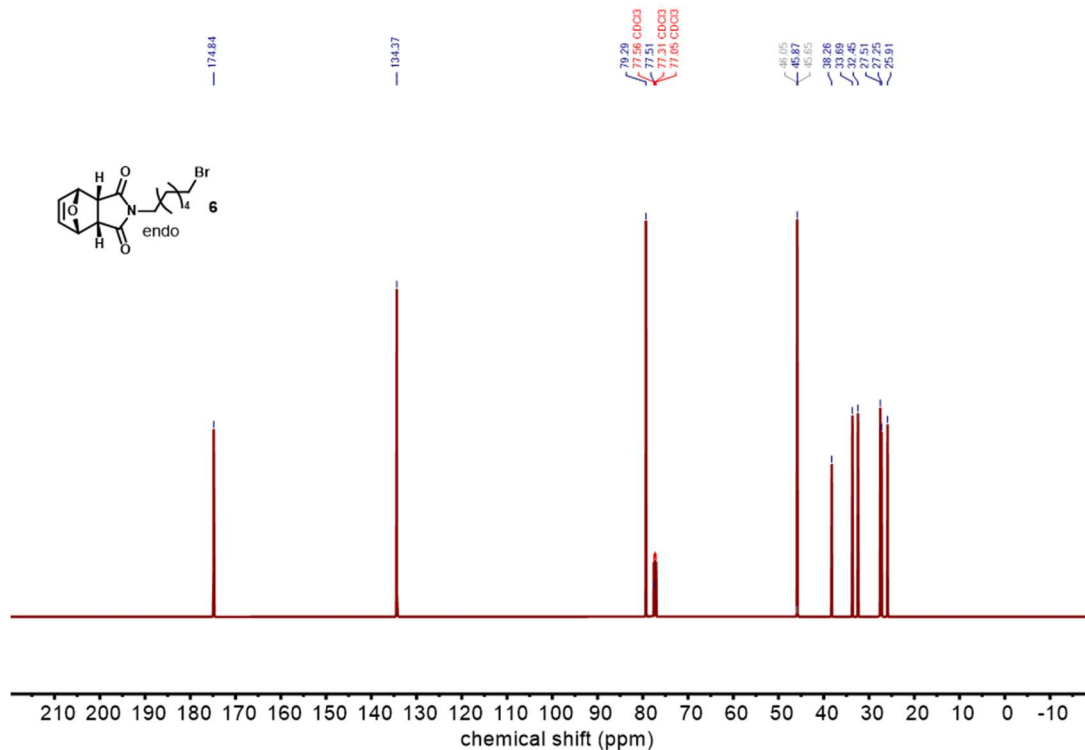


Figure 6.32. ^{13}C NMR (125 MHz, CDCl_3) spectra of **6**.

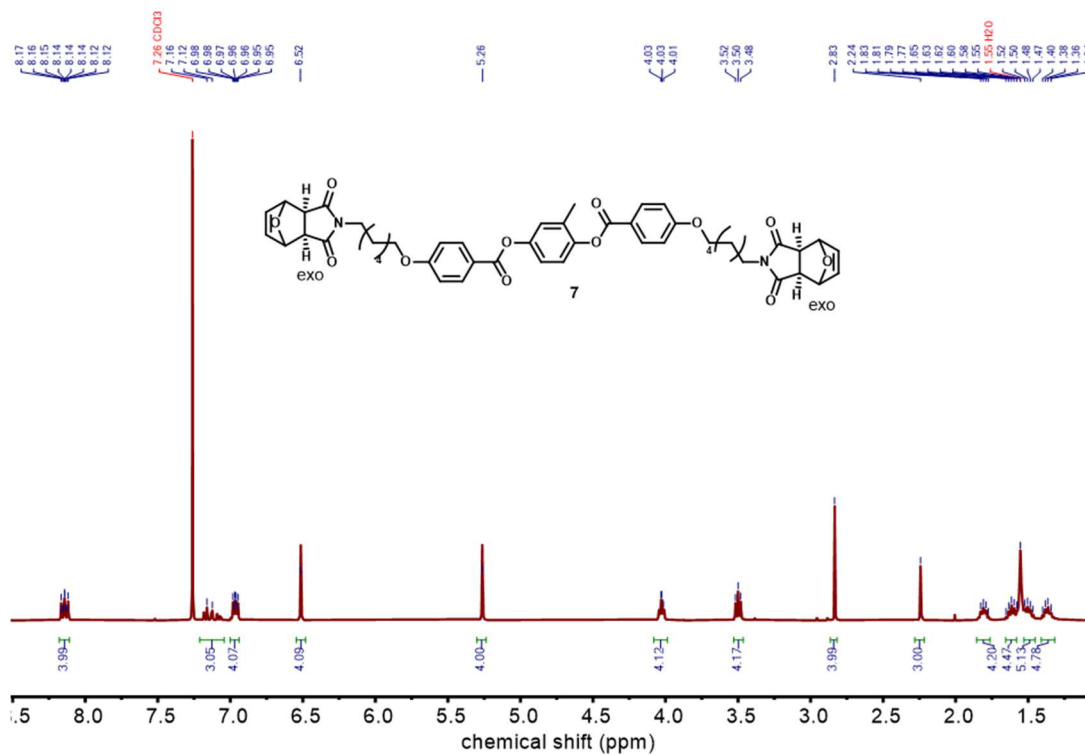


Figure 6.33. ^1H NMR (500 MHz, CDCl_3) spectra of **7**.

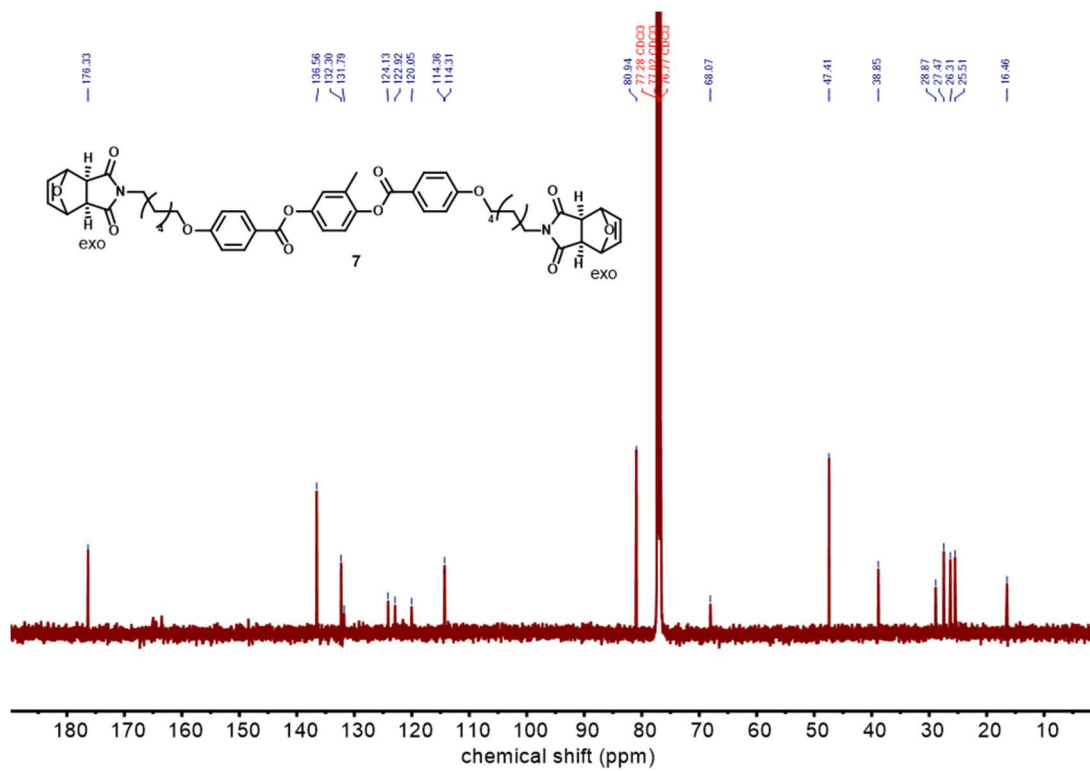


Figure 6.34. ¹³C NMR (125 MHz, CDCl₃) spectra of 7.

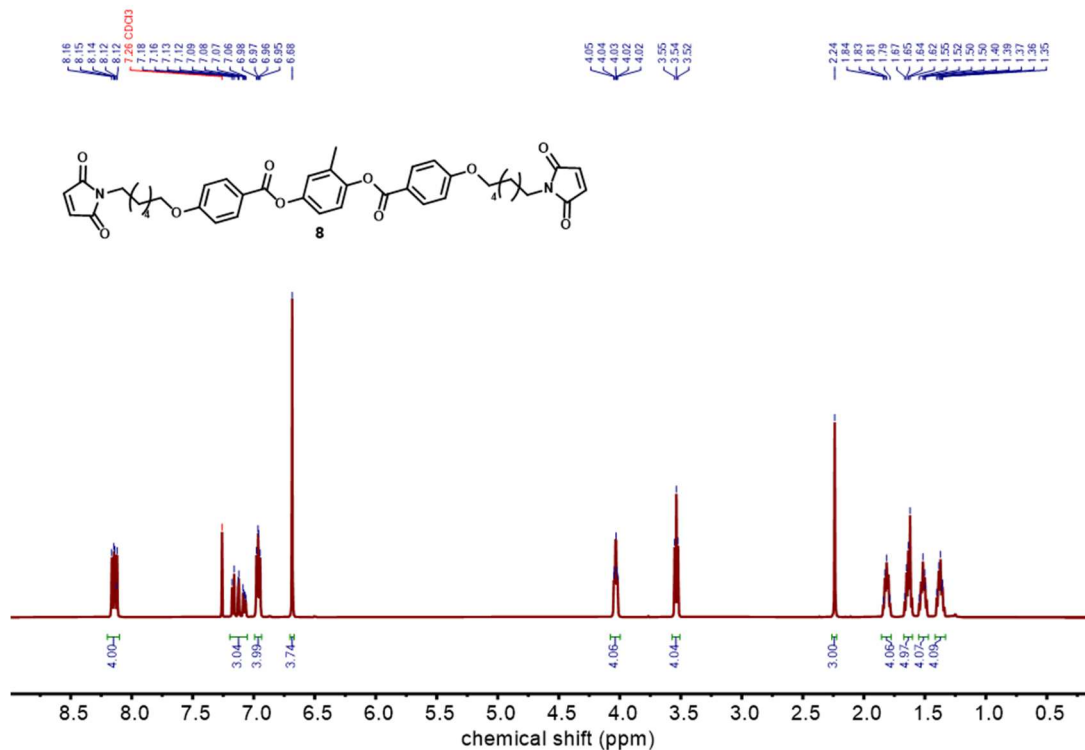


Figure 6.35. ^1H NMR (500 MHz, CDCl_3) spectra of **8**.

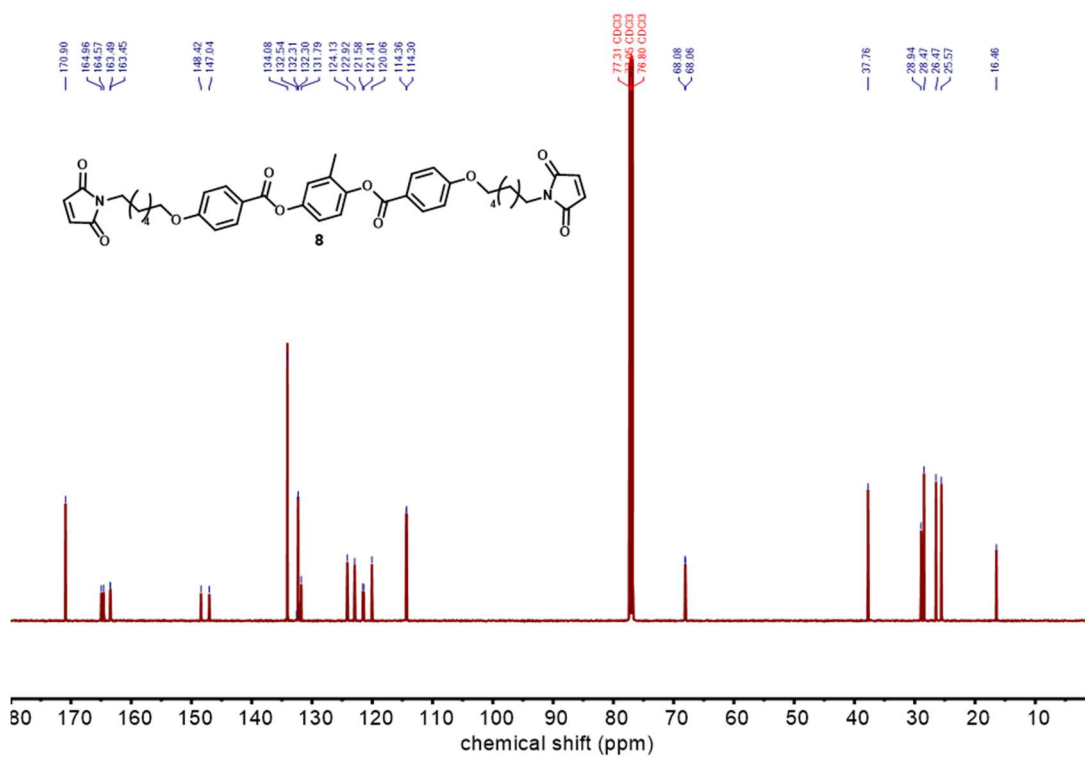


Figure 6.36. ^{13}C NMR (125 MHz, CDCl_3) spectra of **8**.

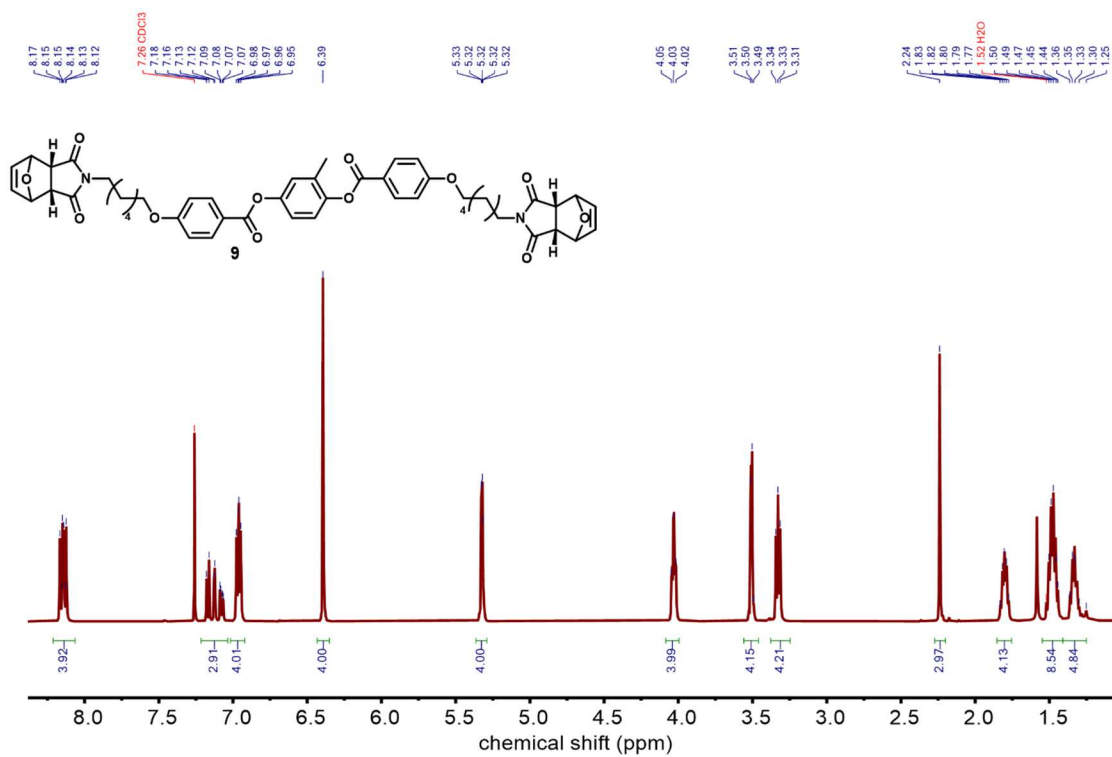


Figure 6.37. ^1H NMR (500 MHz, CDCl_3) spectra of **9**.

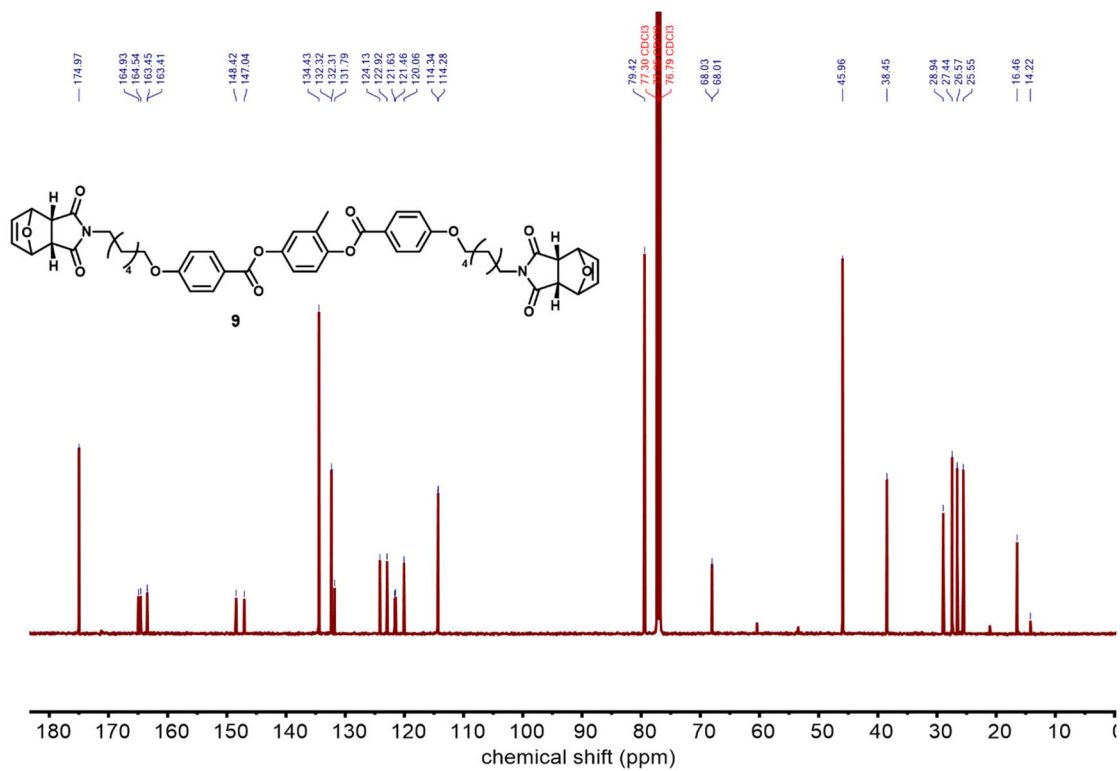


Figure 6.38. ^{13}C NMR (125 MHz, CDCl_3) spectra of **9**.

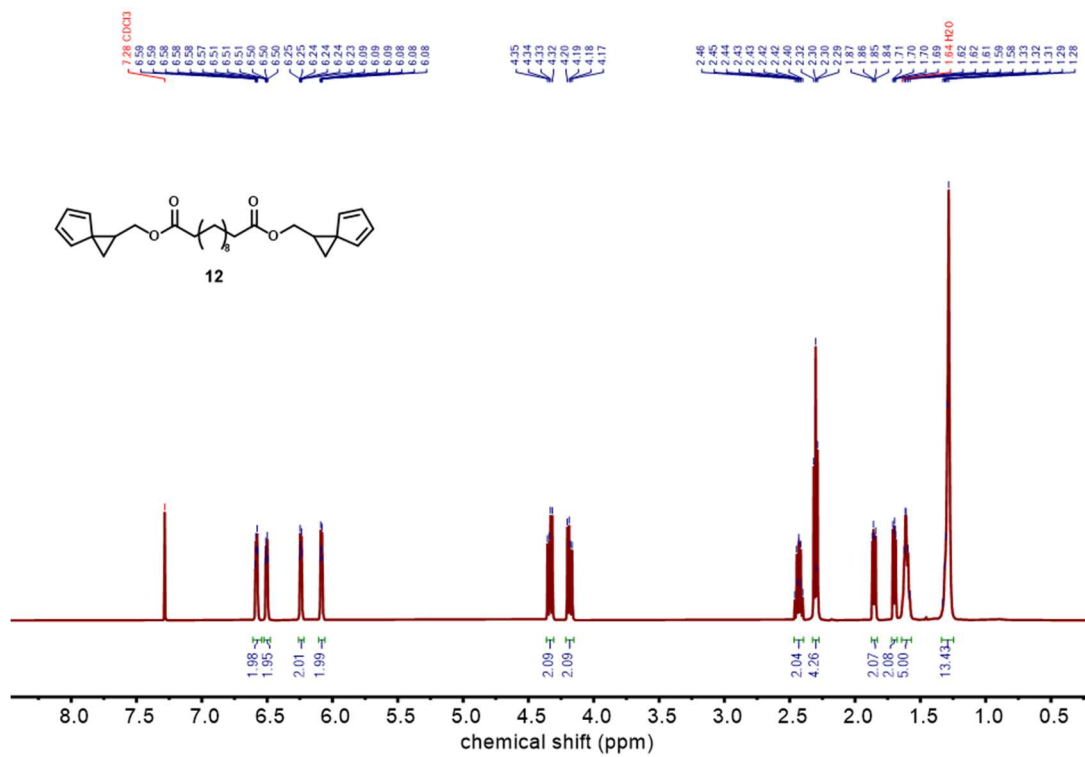


Figure 6.39. ¹H NMR (500 MHz, CDCl₃) spectra of **12**.

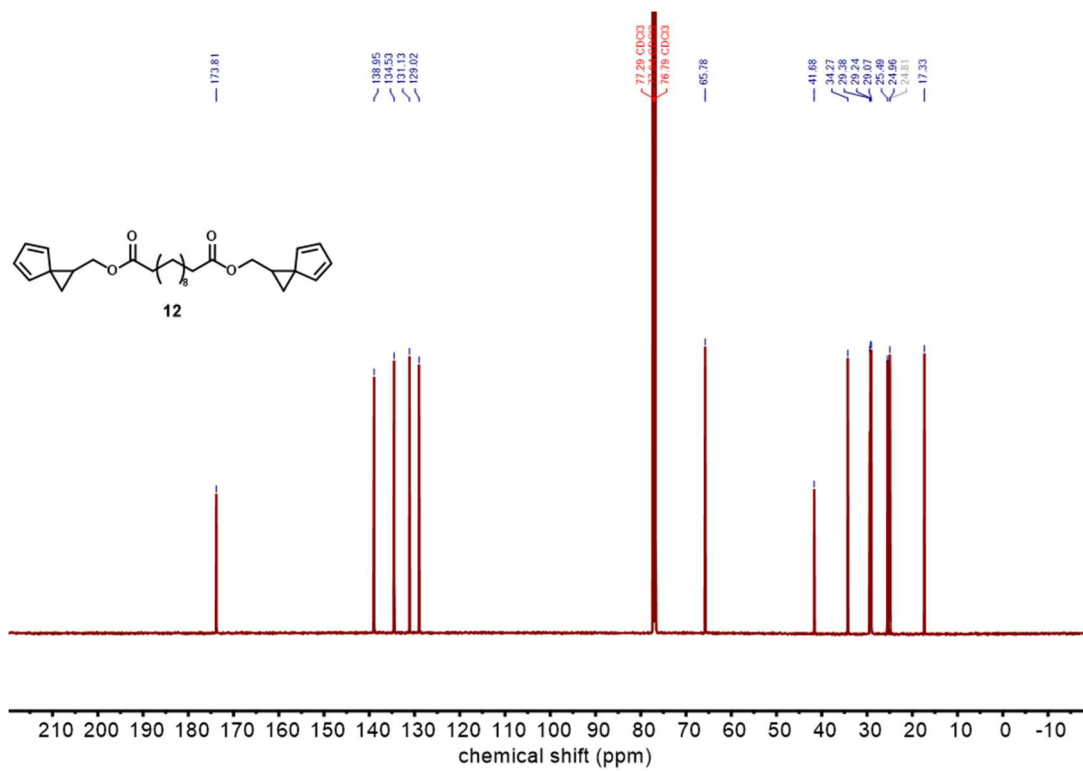


Figure 6.40. ¹³C NMR (125 MHz, CDCl₃) spectra of **12**.

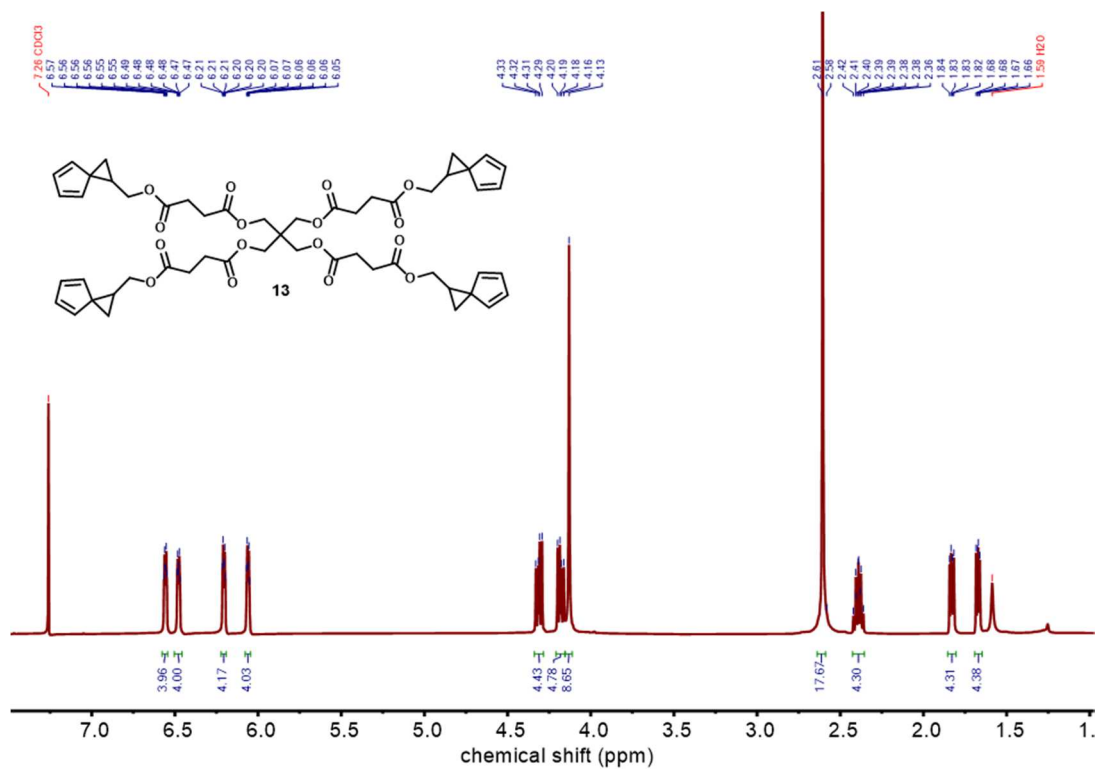


Figure 6.41. ^1H NMR (500 MHz, CDCl_3) spectra of **13**.

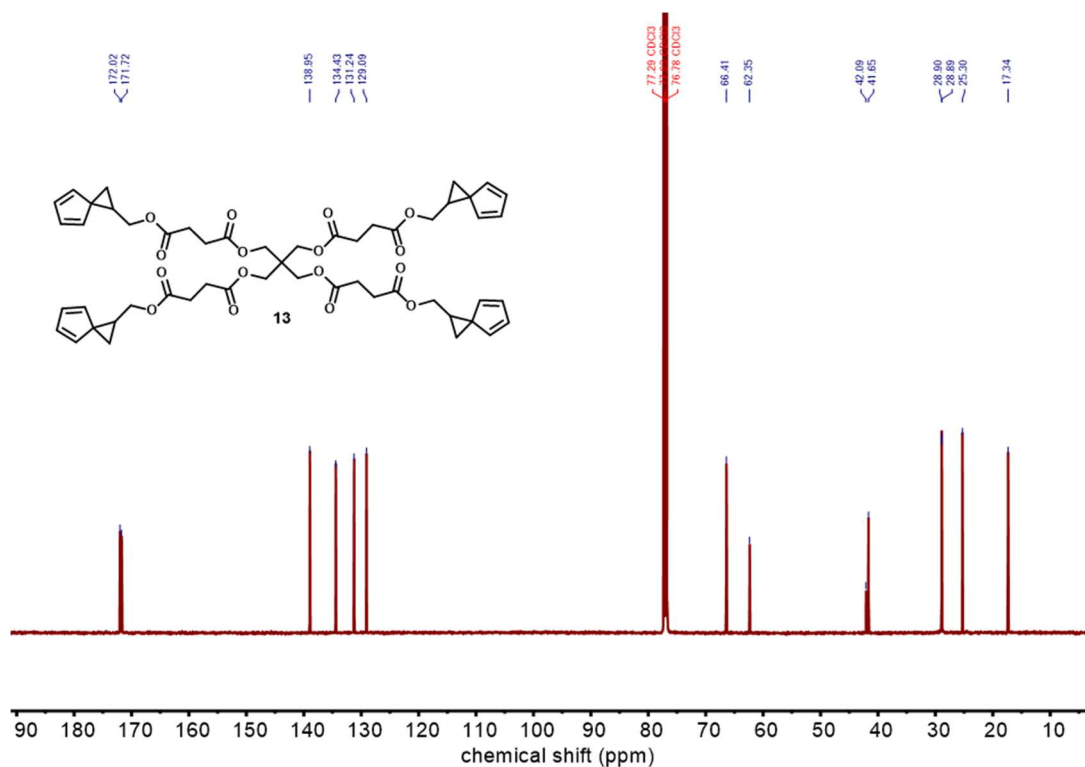


Figure 6.42. ¹³C NMR (125 MHz, CDCl₃) spectra of **13**.

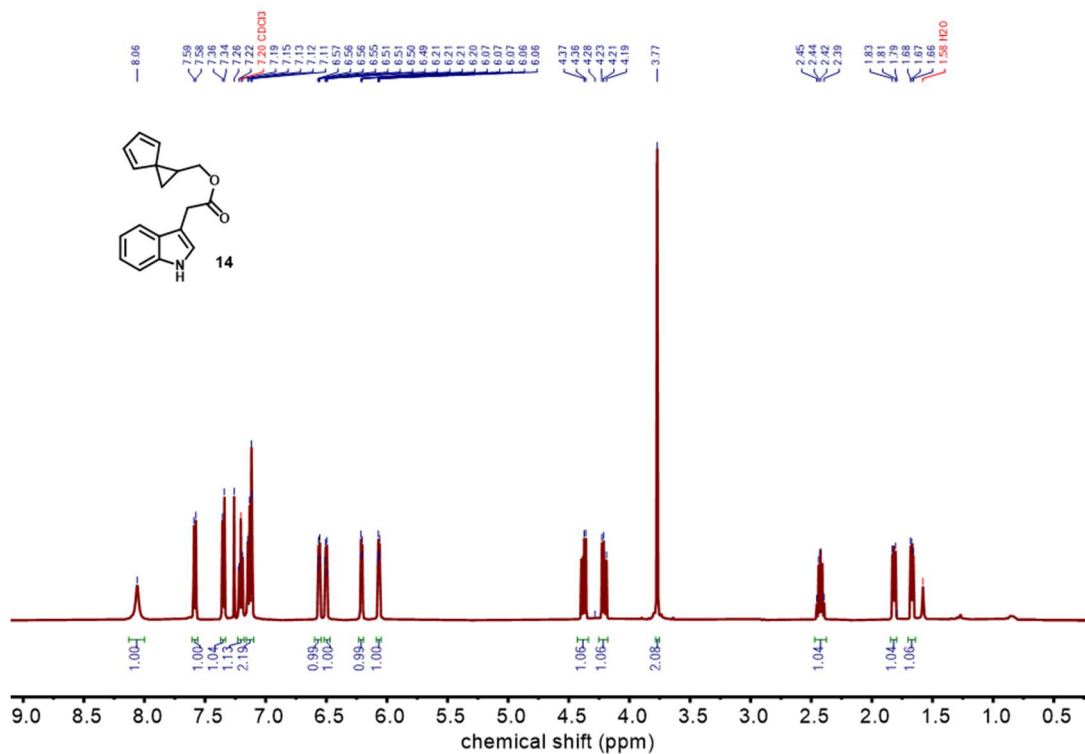


Figure 6.43. ¹H NMR (500 MHz, CDCl₃) spectra of **14**.

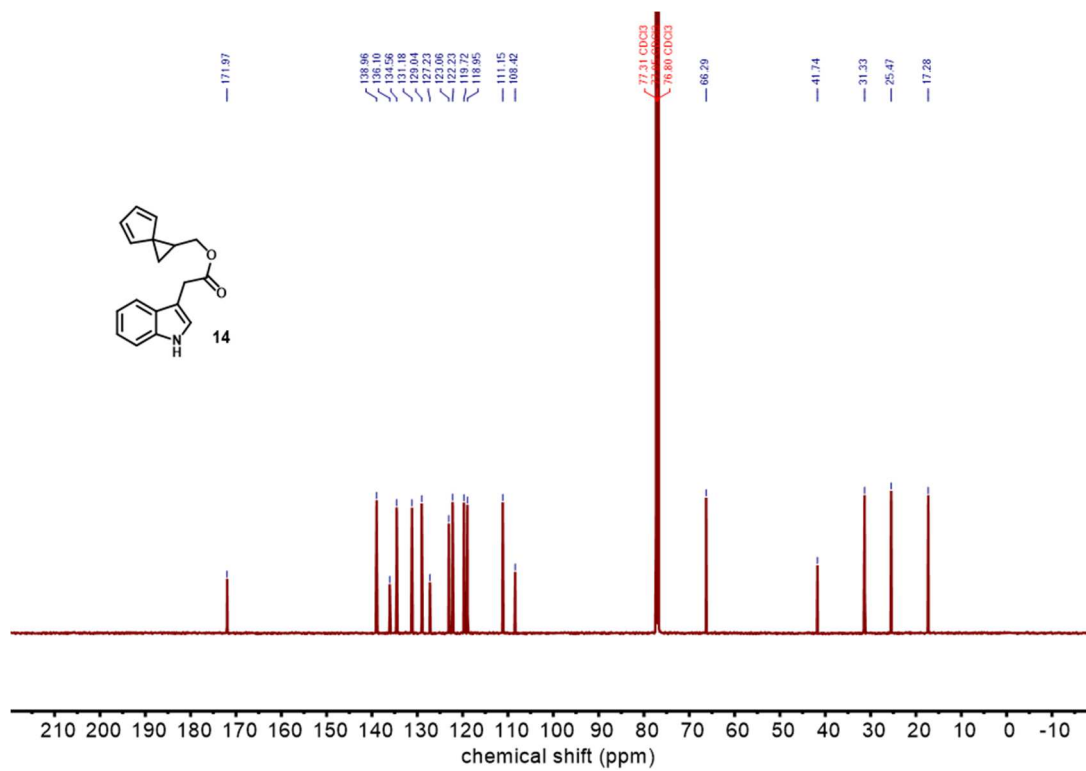


Figure 6.44. ^{13}C NMR (125 MHz, CDCl_3) spectra of **14**.

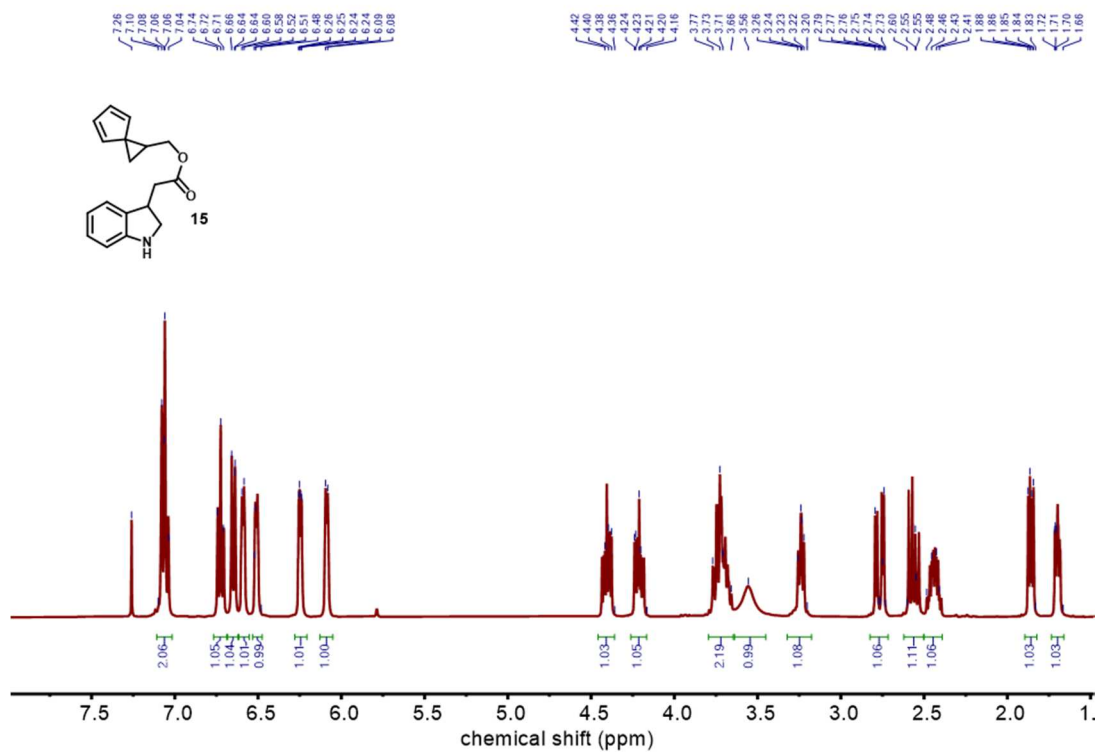


Figure 6.45. ^1H NMR (500 MHz, CDCl_3) spectra of **15**.

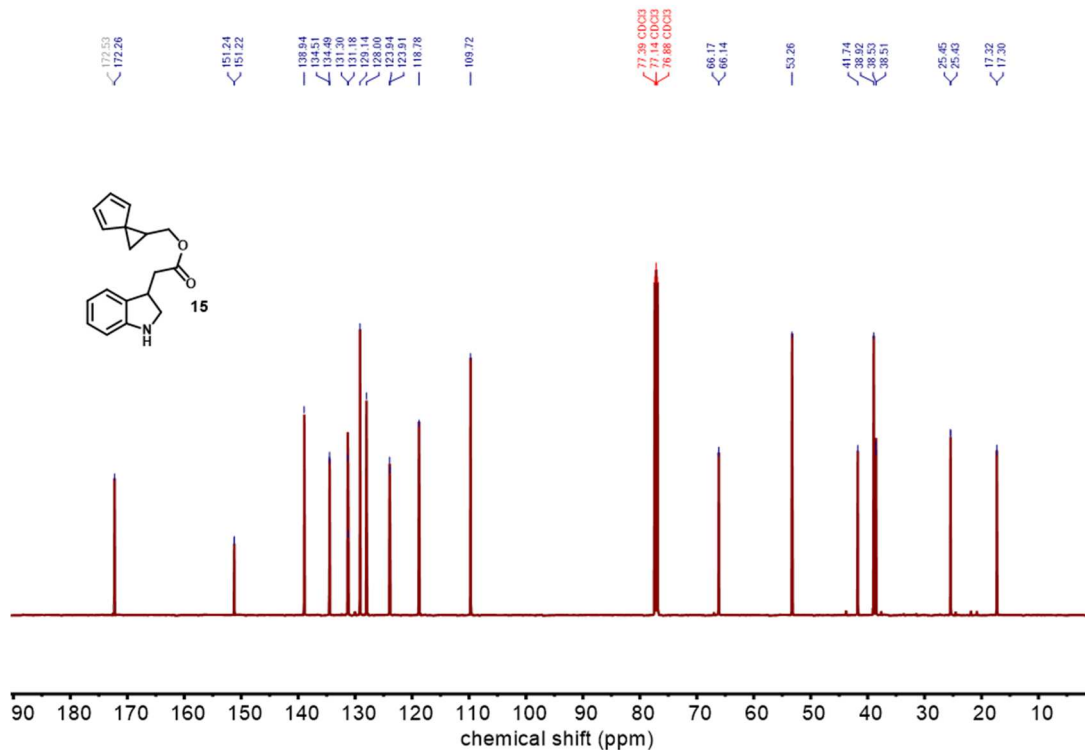


Figure 6.46. ¹³C NMR (125 MHz, CDCl₃) spectra of **15**.

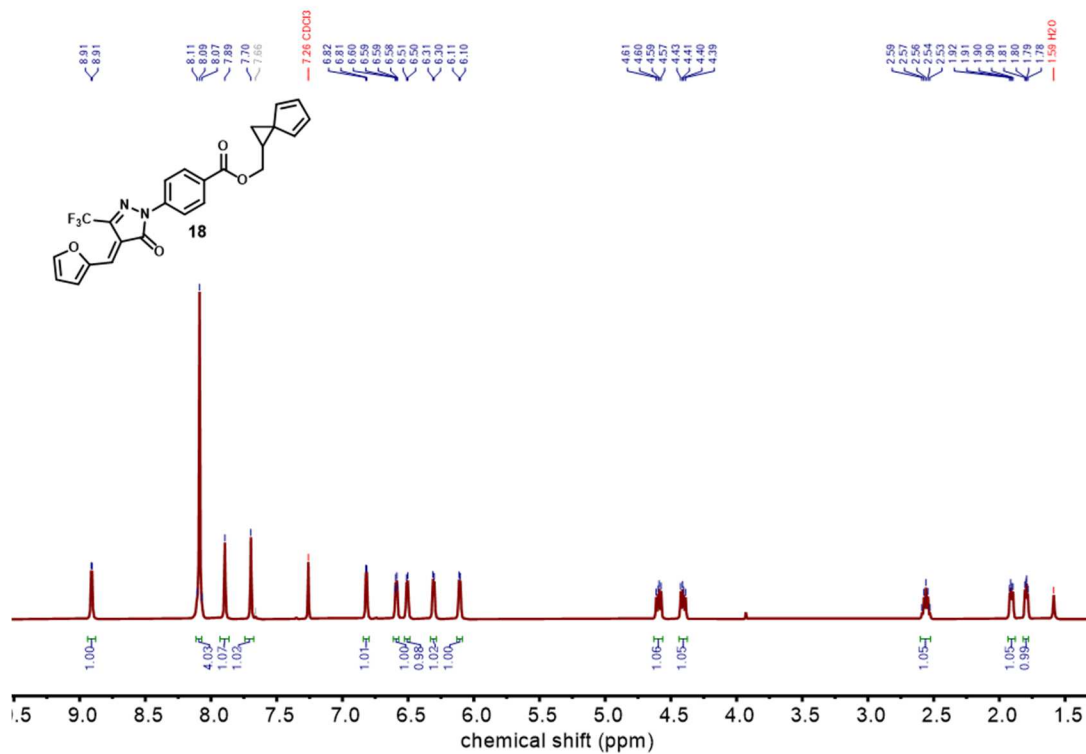


Figure 6.47. ¹H NMR (500 MHz, CDCl₃) spectra of **18**.

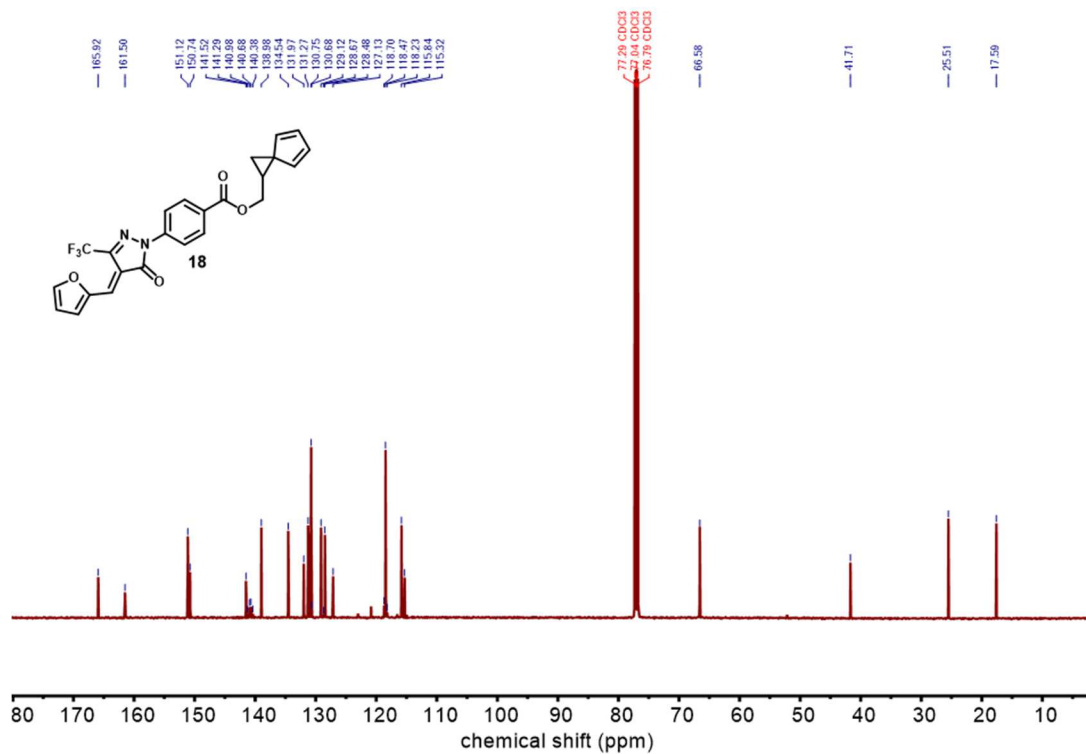


Figure 6.48. ¹³C NMR (125 MHz, CDCl₃) spectra of **18**.

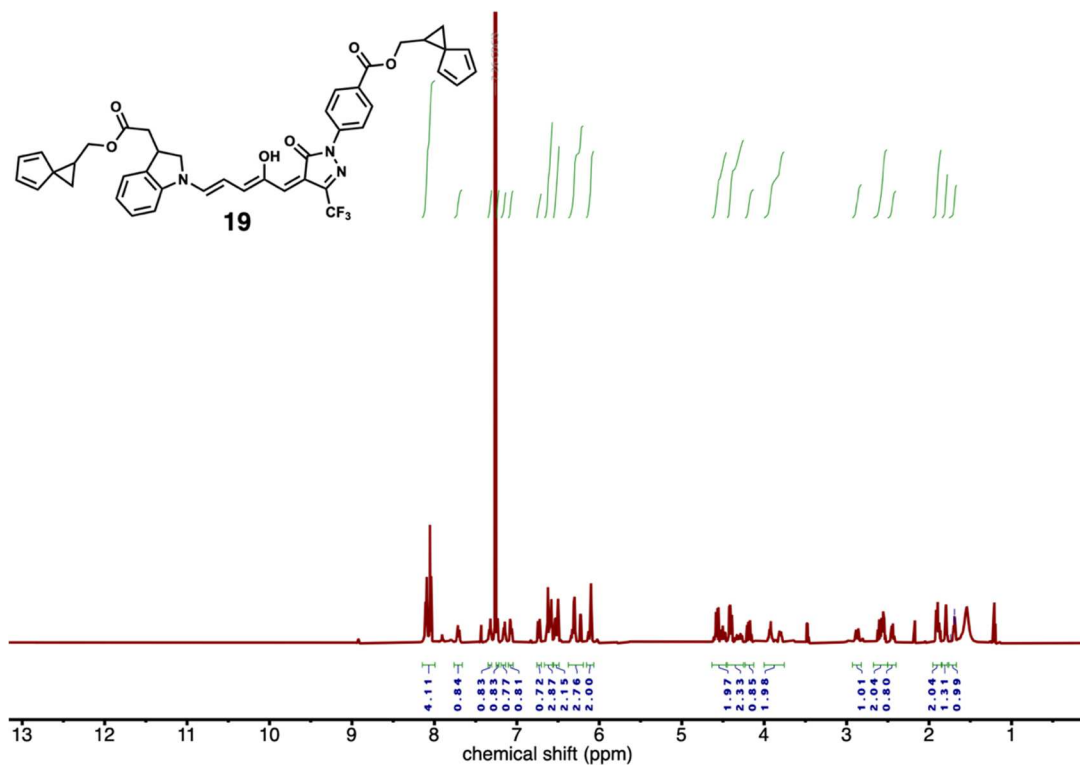


Figure 6.49. ¹H NMR (500 MHz, CDCl₃) spectra of **19**.

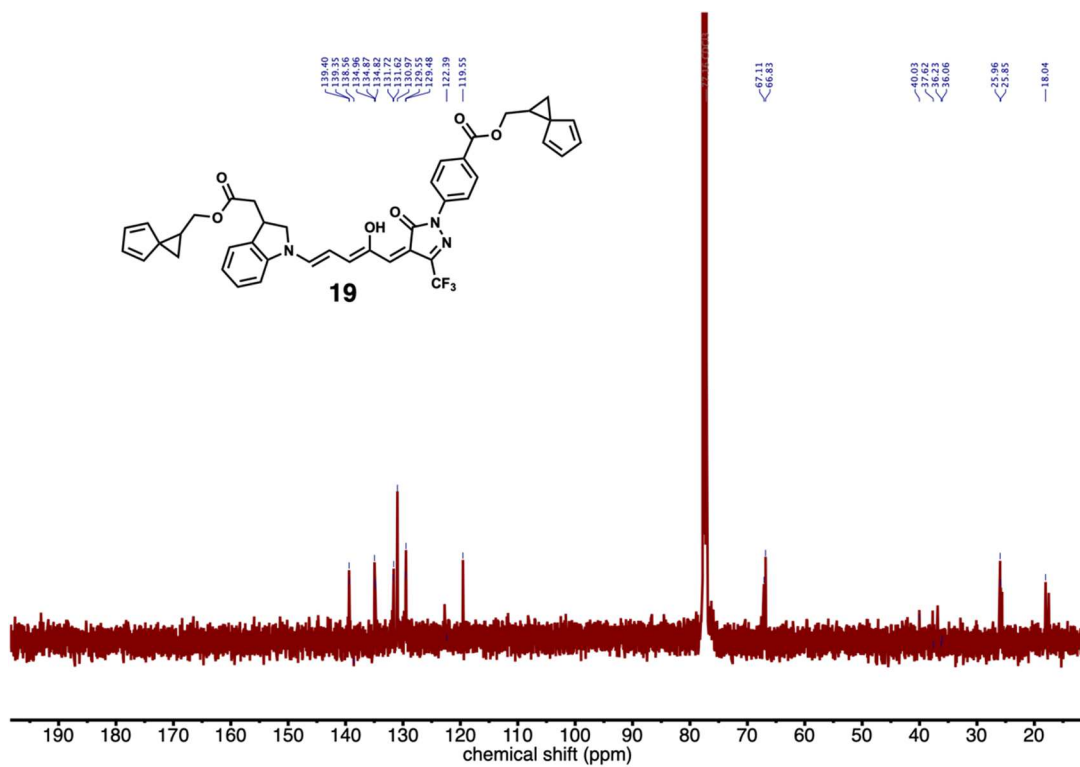


Figure 6.50. ¹³C NMR (125 MHz, CDCl₃) spectra of **19**.

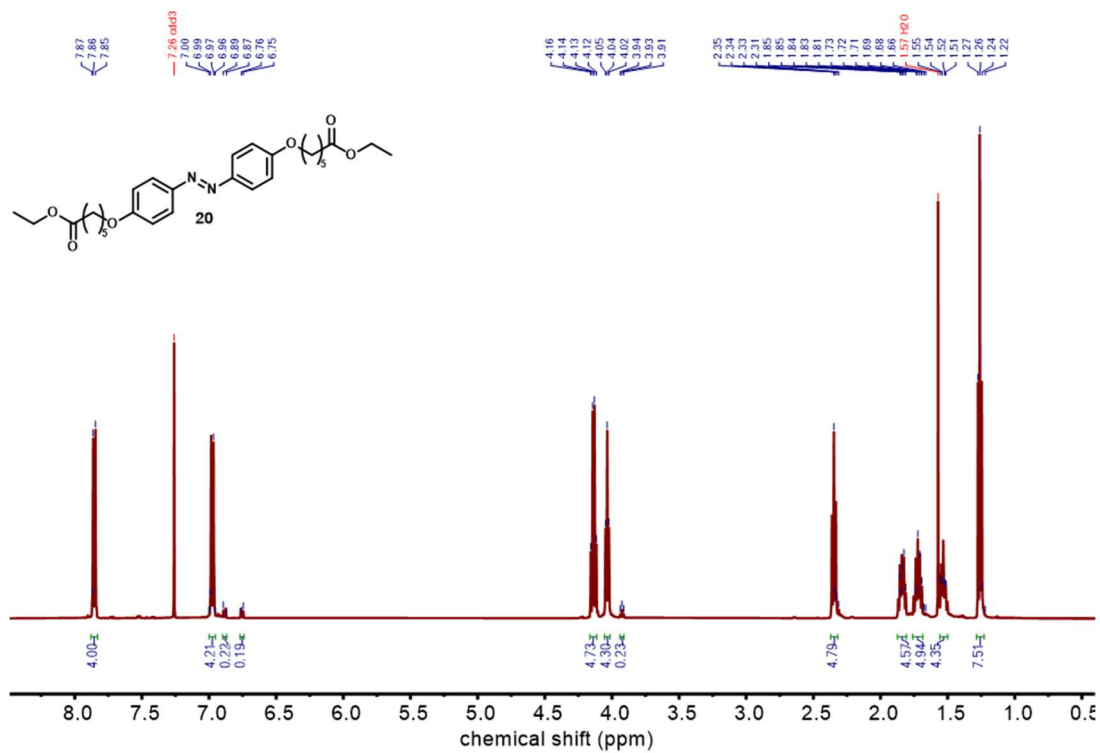


Figure 6.51. ¹H NMR (500 MHz, CDCl₃) spectra of **20**, traces of cis isomer can be observed.

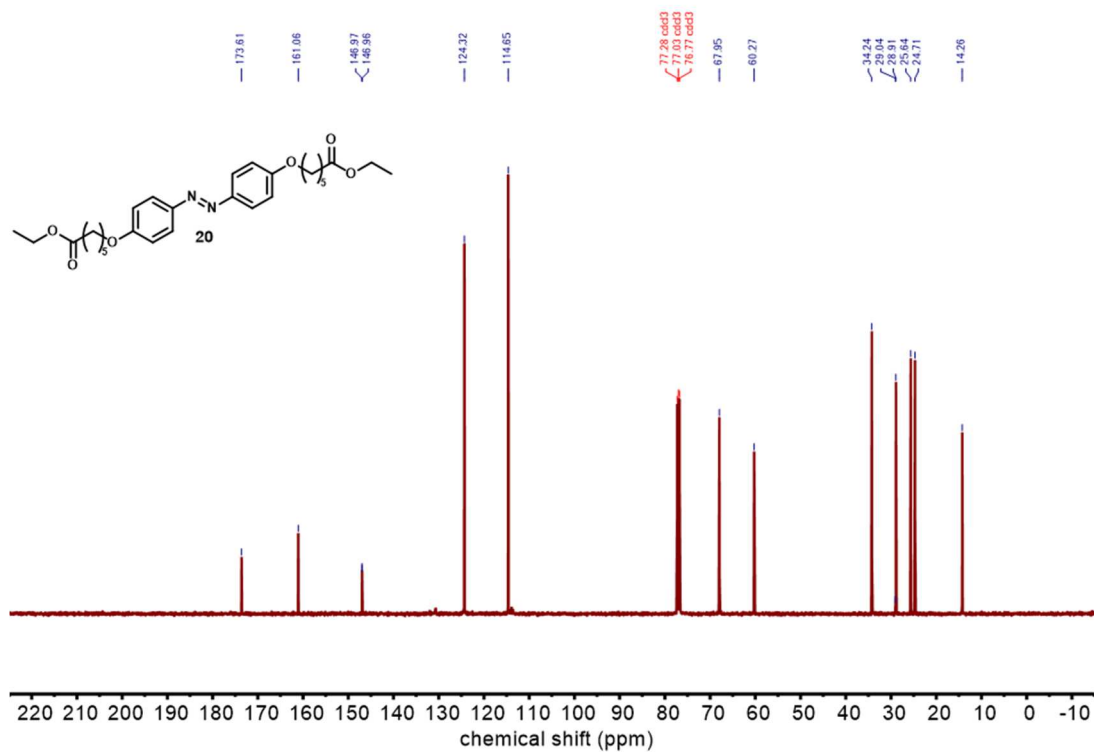


Figure 6.52. ^{13}C NMR (125 MHz, CDCl_3) spectra of **20**.

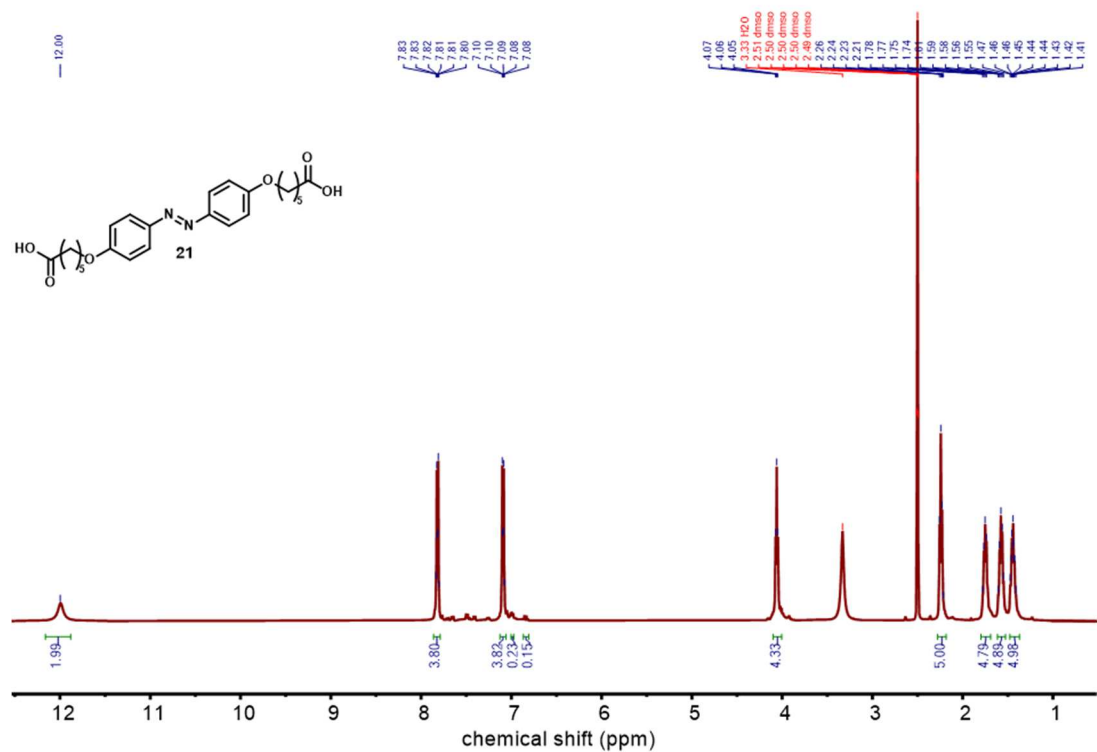


Figure 6.53. ^1H NMR (500 MHz, CDCl_3) spectra of **21**.

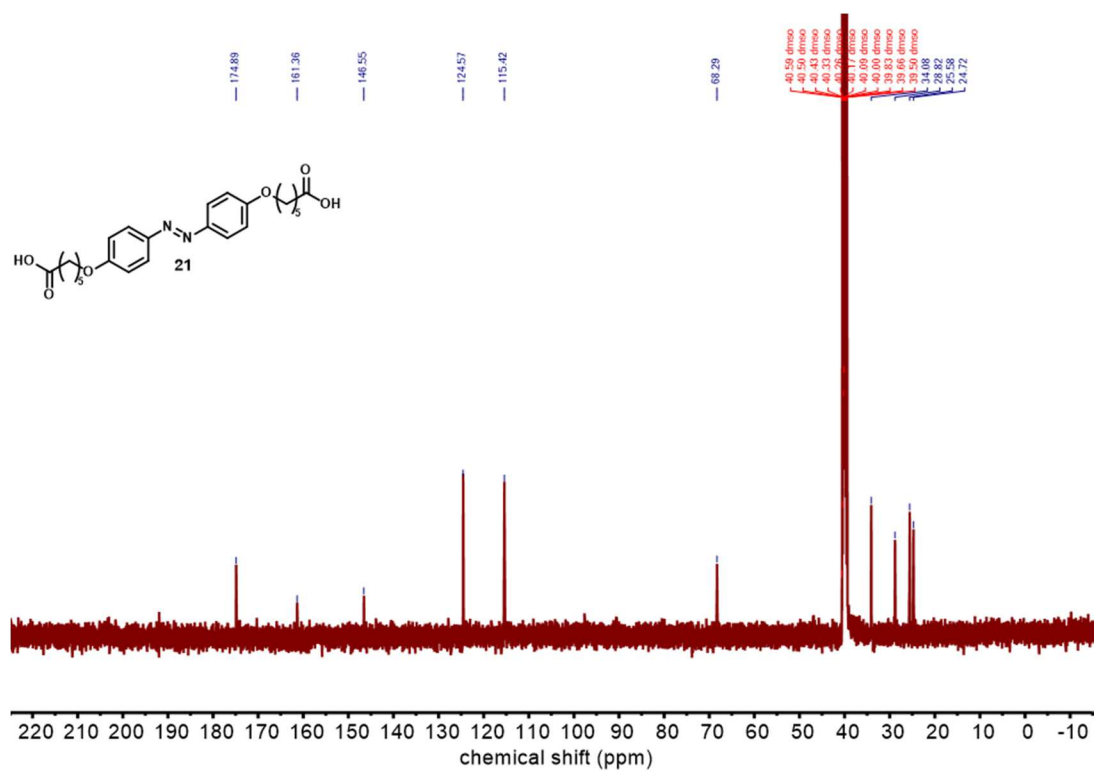


Figure 6.54. ^{13}C NMR (125 MHz, $\text{DMSO}-d_6$) spectra of **21**, cis isomer can be observed.

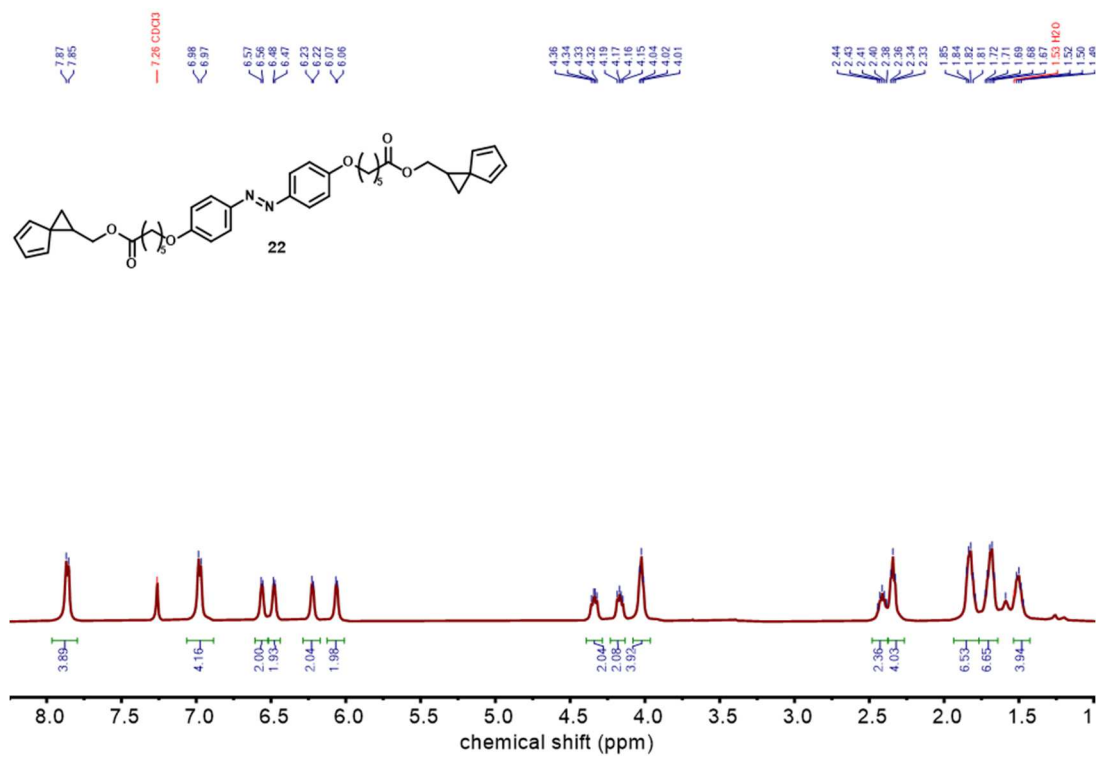


Figure 6.55. ¹H NMR (500 MHz, CDCl₃) spectra of **22** Azobenzene.

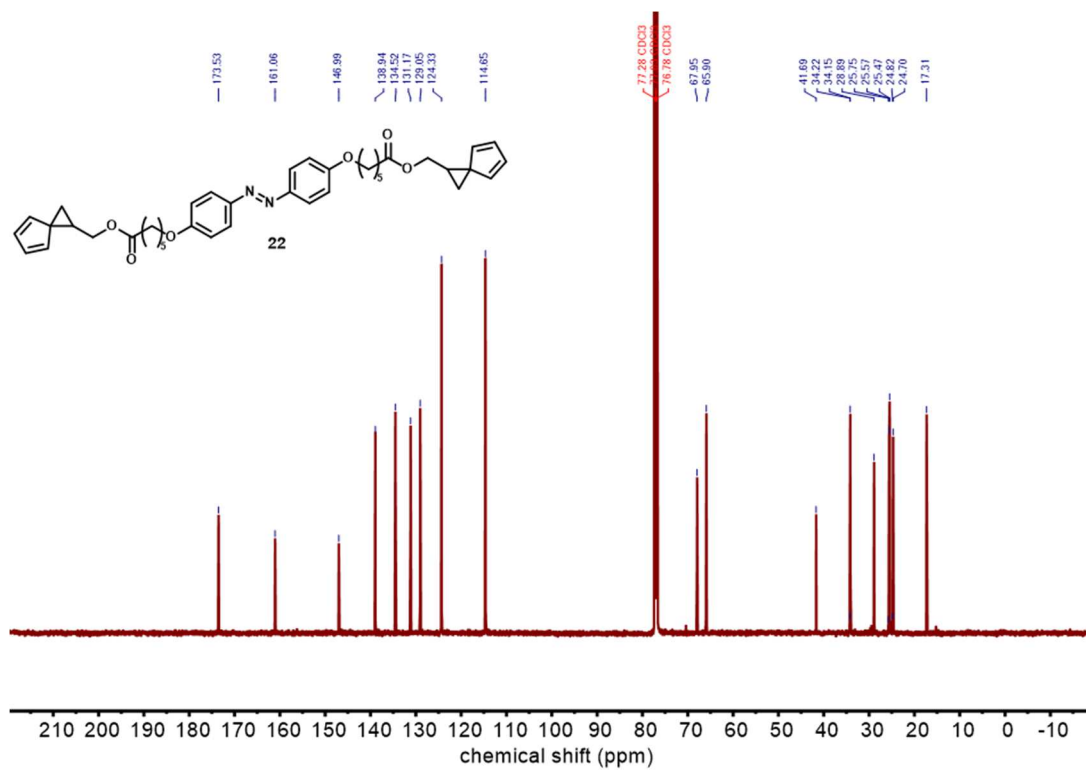


Figure 6.56. ^{13}C NMR (125 MHz, CDCl_3) spectra of **22** Azobenzene.

6.6 References

- (1) Chen, H. W., Lee, J. H., Lin, B. Y., Chen, S., Wu, S. T. Liquid Crystal Display and Organic Light-Emitting Diode Display: Present Status and Future Perspectives. *Light: Science and Applications*. Springer Nature March 1, **2018**, p 17168.
<https://doi.org/10.1038/lisa.2017.168>.
- (2) Lv, J. A., Liu, Y., Wei, J., Chen, E., Qin, L., Yu, Y. Photocontrol of Fluid Slugs in Liquid Crystal Polymer Microactuators. *Nature* **2016**, 537 (7619), 179–184.
<https://doi.org/10.1038/nature19344>.
- (3) Zhao, T., Fang, W., Fan, Y., Hu, Z., Wu, H., Feng, X. Q., Lv, J. an. Phototactic Miniature Soft Robots with Terrain Adaptability. *Advanced Materials Technologies* **2022**. <https://doi.org/10.1002/admt.202101660>.
- (4) Martinez, A. M., McBride, M. K., White, T. J., Bowman, C. N. Reconfigurable and Spatially Programmable Chameleon Skin-Like Material Utilizing Light Responsive Covalent Adaptable Cholesteric Liquid Crystal Elastomers. *Advanced Functional Materials* **2020**, 30 (35). <https://doi.org/10.1002/adfm.202003150>.
- (5) Kuepfer, J., Finkelmann, H. Nematic liquid single crystal elastomer. *Macromolecular Rapid Communications*. **1991**, 12, 717–726.
<https://doi.org/10.1002/marc.1991.030121211>
- (6) White, T. J. Light to Work Transduction and Shape Memory in Glassy, Photoresponsive Macromolecular Systems: Trends and Opportunities. *Journal of Polymer Science, Part B: Polymer Physics*. July 1, 2012, pp 877–880.
<https://doi.org/10.1002/polb.23079>.

- (7) Lahikainen, M., Zeng, H., Priimagi, A. Reconfigurable Photoactuator through Synergistic Use of Photochemical and Photothermal Effects. *Nature Communications* **2018**, *9*, 4148. <https://doi.org/10.1038/s41467-018-06647-7>.
- (8) Ge, F., Zhao, Y. Microstructured Actuation of Liquid Crystal Polymer Networks. *Advanced Functional Materials* **2020**, *30*, 1901890. <https://doi.org/10.1002/adfm.201901890>.
- (9) Herbert, K. M., Fowler, H. E., McCracken, J. M., Schlafmann, K. R., Koch, J. A., White, T. J. Synthesis and Alignment of Liquid Crystalline Elastomers. *Nature Reviews Materials*. Nature Research January 1, **2022**, 23–38. <https://doi.org/10.1038/s41578-021-00359-z>.
- (10) Li, M. H., Keller, P., Antonietti, M., Lacey, D., Meyer, R. B. Artificial Muscles Based on Liquid Crystal Elastomers. *Philosophical Transactions of the Royal Society A: Mathematical, Physical and Engineering Sciences* **2006**, *364* (1847), 2763–2777. <https://doi.org/10.1098/rsta.2006.1853>.
- (11) Hebner, T. S., Bowman, C. N., White, T. J. Influence of Orientational Genesis on the Actuation of Monodomain Liquid Crystalline Elastomers. *Macromolecules* **2021**, *54* (9), 4023–4029. <https://doi.org/10.1021/acs.macromol.1c00437>.
- (12) Yakacki, C. M., Saed, M., Nair, D. P., Gong, T., Reed, S. M., Bowman, C. N. Tailorable and Programmable Liquid-Crystalline Elastomers Using a Two-Stage Thiol-Acrylate Reaction. *RSC Advances* **2015**, *5* (25), 18997–19001. <https://doi.org/10.1039/c5ra01039j>.
- (13) Shahsavan, H., Aghakhani, A., Zeng, H., Guo, Y., Davidson, Z. S., Priimagi, A., Sitti, M. Bioinspired Underwater Locomotion of Light-Driven Liquid Crystal Gels. *Proc*

Natl Acad Sci U S A **2020**, *117* (10), 5125–5133.

<https://doi.org/10.1073/pnas.1917952117>.

- (14) Liu, Z. C., Zuo, B., Lu, H. F., Wang, M., Huang, S., Chen, X. M., Lin, B. P., Yang, H. A Copper(i)-Catalyzed Azide-Alkyne Click Chemistry Approach towards Multifunctional Two-Way Shape-Memory Actuators. *Polymer Chemistry* **2020**, *11* (22), 3747–3755. <https://doi.org/10.1039/d0py00217h>.
- (15) Jiang, Z. C., Xiao, Y. Y., Yin, L., Han, L., Zhao, Y. “Self-Lockable” Liquid Crystalline Diels–Alder Dynamic Network Actuators with Room Temperature Programmability and Solution Reprocessability. *Angewandte Chemie - International Edition* **2020**, *59* (12), 4925–4931. <https://doi.org/10.1002/anie.202000181>.
- (16) St Amant, A. H., Lemen, D., Florinas, S., Mao, S., Fazenbaker, C., Zhong, H., Wu, H., Gao, C., Christie, R. J., Read de Alaniz, J. Tuning the Diels–Alder Reaction for Bioconjugation to Maleimide Drug-Linkers. *Bioconjugate Chemistry*. **2018**, pp 2406–2414. <https://doi.org/10.1021/acs.bioconjchem.8b00320>.
- (17) St Amant, A. H., Huang, F., Lin, J., Lemen, D., Chakiath, C., Mao, S., Fazenbaker, C., Zhong, H., Harper, J., Xu, W., Patel, N., Adams, L., Vijayakrishnan, B., Howard, P. W., Marelli, M., Wu, H., Gao, C., Read de Alaniz, J., Christie, R. J. A Reactive Antibody Platform for One-Step Production of Antibody-Drug Conjugates through a Diels–Alder Reaction with Maleimide. *Bioconjugate Chemistry* **2019**, *30* (9), 2340–2348. <https://doi.org/10.1021/acs.bioconjchem.9b00436>.
- (18) Discekici, E. H., st. Amant, A. H., Nguyen, S. N., Lee, I. H., Hawker, C. J., Read de Alaniz, J. Endo and Exo Diels–Alder Adducts: Temperature-Tunable Building Blocks

- for Selective Chemical Functionalization. *J Am Chem Soc* **2018**, *140* (15), 5009–5013.
<https://doi.org/10.1021/jacs.8b01544>.
- (19) Yoon, H. H., Kim, D. Y., Jeong, K. U., Ahn, S. K. Surface Aligned Main-Chain Liquid Crystalline Elastomers: Tailored Properties by the Choice of Amine Chain Extenders. *Macromolecules* **2018**, *51* (3), 1141–1149.
<https://doi.org/10.1021/acs.macromol.7b02514>.
- (20) Lee, K. M., Bunning, T. J., White, T. J. Autonomous, Hands-Free Shape Memory in Glassy, Liquid Crystalline Polymer Networks. *Advanced Materials* **2012**, *24* (21), 2839–2843. <https://doi.org/10.1002/adma.201200374>.
- (21) Finkelmann, H., Nishikawa, E., Pereira, G. G., Warner, M. A New Opto-Mechanical Effect in Solids. *Physical Review Letters* **2001**, *87* (1), 015501/1-015501/4.
<https://doi.org/10.1103/physrevlett.87.015501>.
- (22) Li, M. H., Keller, P., Li, B., Wang, X., Brunet, M. Light-Driven Side-on Nematic Elastomer Actuators. *Advanced Materials* **2003**, *15* (7–8), 569–572.
<https://doi.org/10.1002/adma.200304552>.
- (23) Li, M. H., Keller, P., Yang, J., Albouy, P. A. An Artificial Muscle with Lamellar Structure Based on a Nematic Triblock Copolymer. *Advanced Materials* **2004**, *16* (21), 1922–1925. <https://doi.org/10.1002/adma.200400658>.
- (24) S. A. Swanger, K. M. Vance, T. M. Acker, S. S. Zimmerman, J. O. DiRaddo, S. J. Myers, C. Bundgaard, C. A. Mosley, S. L. Summer, D. S. Menaldino, H. S. Jensen, D. C. Liotta, S. F. Traynelis, *ACS Chem. Neurosci.* 2018, *9*, 306–319.
- (25) F. Han, Q. Shi, L. Zhang, B. Liu, Y. Zhang, Y. Gao, R. Jia, Z. Zhang, X. Zhu, *Polym. Chem.* 2020, *11*, 1614–1620.

- (26) W. H. Binder, C. Kluger, *Macromolecules* 2004, 37, 9321–9330.
- (27) Clark, K. D. (2020). *Micro to Macro: Translating the behavior of small molecules to functional materials through the use of external stimuli*. UC Santa Barbara. ProQuest ID: Clark_ucsb_0035D_14977. Merritt ID: ark:/13030/m5tx90xn. Retrieved from <https://escholarship.org/uc/item/1z92w9h5>
- (28) A. H. St Amant, D. Lemen, S. Florinas, S. Mao, C. Fazenbaker, H. Zhong, H. Wu, C. Gao, R. J. Christie, J. Read de Alaniz, *Bioconjug. Chem.* 2018, 29, 2406–2414.
- (29) J. Lee, M. M. Sroda, Y. Kwon, S. El-Arid, S. Seshadri, L. F. Gockowski, E. W. Hawkes, M. T. Valentine, J. Read de Alaniz, *ACS Appl. Mater. Interfaces* 2020, 12, 54075–54082.